Estimation of the Depth of Anaesthesia from Interacting Physiological Oscillators

THÈSE N^{O} 4197 (2008)

PRÉSENTÉE LE 10 OCTOBRE 2008

À LA FACULTE INFORMATIQUE ET COMMUNICATIONS

LABORATOIRE DE SYSTÈMES NON LINÉAIRES

PROGRAMME DOCTORAL EN INFORMATIQUE, COMMUNICATIONS ET INFORMATION

ÉCOLE POLYTECHNIQUE FÉDÉRALE DE LAUSANNE

POUR L'OBTENTION DU GRADE DE DOCTEUR ÈS SCIENCES

PAR

Kumiko OSHIMA

M.Sc. in electrical and electronic engineering, Sophia University, Tokyo, Japon
et de nationalité japonaise

acceptée sur proposition du jury:

Prof. M. A. Shokrollahi, président du jury
Prof. M. Hasler, directeur de thèse
Prof. A. Ijspeert, rapporteur
Prof. O. Sosnovtseva, rapporteur
Prof. M. Tanaka, rapporteur

ÉCOLE POLYTECHNIQUE
FÉDÉRALE DE LAUSANNE

Suisse
2008

Abstract

Nowadays, physiological monitoring is imperative for the safety of medical operations. However, systems which monitor the depth of anæsthesia are still far from reliable, such that still some patients may experience the trauma of remaining conscious under general anæsthesia during surgery.

The long term goal of our interdisciplinary project "BRACCIA" was to develop a device to measure the depth of anæsthesia. And, in view of this important goal, the main objective of research was to establish how the couplings between the cardiac, respiratory and cortical oscillations change in anæsthesia. Under the framework of this project, our objectives were: 1) The detection of the deep-light change of anæsthesia from experimental recordings on rats, and furthermore, the investigation of the interdependencies among three physiological activities, namely, the cardiac activity (H), respiration (R) and cortical activities (B) from experimental recordings of rats and humans, for each state of the depth of anæsthesia. 2) The modelling of the slow brain waves, and to consider the effect of anæsthesia on this realized model.

The analysis of the recordings were carried out with five methods. First method is the "S-estimator", which indirectly quantifies the amount of synchronization within a data set measuring the contraction of the embedding dimension of the state space. Second method is the "new S-estimator". In this new one, a linear transformation of the reconstructed state space trajectory orthonormalizes the state variables within each model such that global state space volume reduction becomes a measure of synchronization exclusively between the different models. Third method is the "embedding dimension analysis", which examines the time evolution of the embedding dimension obtained with false nearest neighbors method on each windowed time series. The last two methods consist in a more detailed analysis of the dependencies among three systems. Fourth method is the "coupling matrix". This calculates the coupling matrix, CM, which infers linear interactions between multivariate time series after constructing separately the self model of each signal from reconstructed states. The last method is the "nonparametric Granger causality". This method calculates the Granger causality, GC, which measures bivariate causal influence in frequency domain. Here, a nonparametric estimation approach was used to remove the difficulties such as uncertainty in model parameters. For this method, permutation tests are added to figure out the real causality.

From the obtained results, in most of the groups of experimental recordings, a change in the synchronization inside of the whole system between deep and light anæsthesia or between resting state and anæsthesia was found. For the results on Ketamine-Xylazine (KX) anæsthetized rats, a decrease of this synchronization was so clear that we succeeded

to detect the deep-light transition of the anæsthesia, and automatically in one group of the recordings. The changes in the synchronization exclusively between three sub-systems as measured with the "new S-estimator" was only found on the results on Pentobarbital anæsthetized rats. Interestingly, a change in the time evolution of the embedding dimension was found on B and H in most of the results of the recordings. Furthermore, some changes in the couplings were found according to the depth of anæsthesia. For KX anæsthetized rats and human, coupling direction change was also observed. The nonparametric GC agreed for some causality change obtained with coupling matrix, but still some disagreements remained.

From our literature study about the rhythmic activity of the brain, we deduce that it is generally accepted in the neuroscience community that the rhythms of the EEG are created by the interaction between the cortex and the thalamus. Consequently, we chose one of the Hodgkin-Huxley based model which considers the thalamocortical assemblies, the model of Bazhenov et al. This model includes four layers of neurons where two of them are for the thalamus (RE: thalamic reticular neuron, TC: thalamic relay neuron) and the other two are for the cortex (PY: pyramidal neuron, IN: interneuron). Not without having difficulties to set parameters and equations, we succeeded to reproduce this model and simulated it. Furthermore, we performed simulations on this model varying the parameter of maximal conductance of Ca^{2+} channels or the closing/opening rate of $GABA_A$ receptors from one simulation to another, and determined how the collective behavior of PY neurons, which should be interpreted as a field potential analogous to the EEG can be modified according to these parameter changes. Finally, to understand the model itself, some studies on the reproduced model were carried out.

As a results, from observing the collective spiking activity of the PY cells on the reproduced Bazhenov model, we confirmed the presence of slow oscillations, namely the δ-waves. The reaction of the model to changes of the parameters related to anesthetics showed that reinforcement of the inhibition that suppresses the spiking activities was effectively induced by all changes of the parameters, but the degree of this reaction was different in each case. From the studies of the size of the model, we found that the local synchrony and the mean field frequency is not influenced by the size of network, but the global synchrony is not preserved at larger sizes.

In conclusion, our data analysis studies showed a clear possibility for the detection of the depth of anæsthesia and a clear change in the interdependency changes depending on the anæsthesia. Moreover, our modelling study took an essential step for the investigation of the effect of anæsthesia on a brain model.

As future work, all the unsolved problems which appear in the analysis chapter of this thesis should be treated, but especially the embedding dimension analysis should be followed up in detail. For modelling, as we just made the first step, we should continue with the understanding of the model and the closing of the gap between the mathematical model and the reality.

Keywords

physiological oscillators, coupled oscillators, data analysis, anæsthesia, depth of anæsthesia, synchronization, interdependencies, brain modelling, thalamocortical assemblies, slow waves, effect of anæsthesia.

Version abrégée

Aujourd'hui, la surveillance physiologique est impérative pour la sécurité des opérations médicales. Cependant, les systèmes qui contrôlent la profondeur de l'anesthésie ne sont pas encore totalement sûrs, de telle sorte qu'encore quelques patients peuvent faire l'expérience traumatisante de rester conscient sous anesthésie générale pendant la chirurgie.

Le but à long terme de notre projet interdisciplinaire "BRACCIA" est le développement d'un appareil pour mesurer la profondeur de l'anesthésie. Et, en vue de cet important but, l'objectif principal de cette recherche est d'établir comment changent les couplages entre les oscillations cardiaques, respiratoires et corticales sous anesthésie. Dans le cadre de ce projet, nos objectifs sont: 1) La détection du changement d'anesthésie de profonde à légère, sur la base d'enregistrements expérimentaux sur les rats. Et l'examen des interdépendances parmi trois activités physiologiques qui sont l'activité cardiaque (H), la respiration (R) et les activités corticales (B), ceci depuis des enregistrements expérimentaux provenant de rats et d'humains pour chaque état de la profondeur d'anesthésie. 2) La modélisation des ondes lentes du cerveau, et la considération de l'influence de l'anesthésie sur le modèle réalisé.

Les enregistrements ont été analysés suivant cinq méthodes. La première est le "S-estimateur", qui définie indirectement la quantité de synchronisation dans un ensemble de données mesurant la contraction de la dimension intrinsèque de l'espace d'état. La seconde méthode est le "nouvel S-estimateur". Dans celle-ci, une transformation linéaire de la trajectoire reconstruite de l'espace d'état ortho-normalise les variables d'état pour chaque modèle. Ce qui implique que le volume réduit de l'espace d'état global devient donc une mesure de la synchronisation exclusivement entre les différents modèles. La troisième méthode est "l'analyse de la dimension intrinsèque", qui examine l'évolution dans le temps de la dimension intrinsèque obtenue avec la méthode des faux voisins les plus proches pour chaque fenêtre de série temporelle. Les deux dernières méthodes consistent en une analyse plus détaillée des dépendances parmi les trois systèmes. La quatrième nommée "matrice de couplage", après avoir construit séparément le modèle propre à chaque signal des états reconstruits, calcule la matrice de couplage (CM) qui déduit les interactions linéaires entre les séries temporelles multi variantes. La dernière méthode est la "causalité de Granger non paramétrique." Elle calcule la causalité de Granger (GC), qui mesure l'influence causale bivariante dans le domaine de la fréquence. Ici, une approche d'estimation non paramétrique a été utilisée pour retirer les difficultés telles l'incertitude en paramètres du modèle. Pour cette méthode, les tests de permutation sont ajoutés pour comprendre la causalité véritable.

Des résultats obtenus dans la plupart des groupes d'enregistrements , un changement a été trouvée dans la synchronisation à l'intérieur du système entier entre l'anesthésie profonde et légère, ou entre l'état de repos et sous anesthésie. Pour les résultats sur les rats anesthésiés par Ketamine-Xylazine (KX), une diminution de cette synchronisation est si

claire que nous avons réussi à détecter la transition de l'anesthésie légère à profonde même automatiquement en temps réel avec un léger retard. Par contre, la modification de la synchronisation exclusivement entre trois sous-systèmes, tel que mesurée avec le "nouvel S-estimateur", a seulement été trouvée sur les résultats des rats anesthésiés par Pentobarbital. De façon intéressante, une modification dans l'évolution temporelle de la dimension intrinsèque a été trouvée sur B et H dans la plupart des résultats des enregistrements. De plus, quelques modifications dans les couplages ont été trouvées selon la profondeur de l'anesthésie. Pour les rats anesthésiés par KX et les humains, un changement dans la direction de couplage a aussi été observé. Le GC non paramétrique a confirmé les changements de causalité obtenus avec la matrice de couplage, bien que quelques désaccords persistent.

De notre étude de la littérature ayant pour sujet l'activité rythmique du cerveau, nous déduisons qu'il est en général accepté dans la communauté de neuroscience que les rythmes de l'EEG sont créés par l'interaction entre le cortex et le thalamus. En conséquence, nous avons choisi un des modèles basés sur Hodgkin-Huxley qui considère l'ensembles thalamocorticaux: le modèle de Bazhenov et al. Ce modèle inclut quatre couches de neurones dont deux pour le thalamus (RE: neurone thalamique réticulaire, TC : neurone thalamique de relai), et deux autres pour le cortex (PY: neurone pyramidal, IN: inter neurone). Non sans difficultés pour définir les paramètres et les équations, nous avons réussi à reproduire ce modèle et à le simuler. De plus, nous avons exécuté des simulations sur ce modèle en variant le paramètre de la conductance maximum des canaux de Ca^{2+}, ou en variant le taux d'ouverture/fermeture des récepteurs $GABA_A$ d'une simulation à une autre. De cette manière nous avons déterminé comment le comportement collectif des neurones de PY peut être modifié par ces changements de paramètres. Ce comportement doit être interprété comme un champs moyen du potentiel analogue à l'EEG. Finalement, pour comprendre le modèle lui-même, quelques études sur le modèle reproduit ont été exécutées.

Depuis les observations de l'activité collective spontanée des cellules de PY sur le modèle reproduit de Bazhenov, nous avons confirmé la présence de δ-ondes. La réaction du modèle aux changements de paramètres indique, du point de vue anesthésique, l'élément suivant: le renforcement de l'inhibition qui empêche l'activité spontanée a effectivement été provoquée par tous les changements des paramètres, mais le degré de cette réaction est différent pour chaque cas. Depuis l'étude de la taille du modèle, nous avons déterminé que la synchronisation locale et la fréquence principale du champ ne sont pas influencées par la taille, mais que la synchronisation globale n'est pas préservée pour les grandes tailles.

En conclusion, nos analyses des données ont démontré une possibilité de déterminer la profondeur de l'anesthésie, et un changement clair des interdépendances selon l'anesthésie. En outre, notre étude de modélisation a franchi un pas essentiel dans l'examen de l'influence de l'anesthésie sur le modèle du cerveau.

En tant que futur travail, les problématiques non résolues dans cette thèse sont à traiter. Tout particulièrement un suivi plus approfondi de l'analyse de la dimension intrinsèque. En ce qui concerne la modélisation, nous devrions poursuivre la compréhension du modèle et atténuer l'écart entre le modèle mathématique et la réalité.

Mots-clés

oscillateurs physiologiques, oscillateurs couplés, analyse de données, anesthésie, profondeur d'anesthésie, synchronisation, interdépendances, modélisation du cerveau, ensembles thalamocorticaux, ondes lentes, effet d'anesthésie .

Acknowledgments

This doctoral dissertation was realized with many supports of my surroundings. Here, it is my great pleasure to thanks all of them.

First of all, I want to show my greatest and warmest thanks to Prof. Martin Hasler for giving me this opportunity to work with him here at EPFL in Switzerland. Thanks to him, I developed my capacities on how to initiate problems, how to assemble information, how to get organized, how to consider problems, how to tackle problems, how to interpret results... many many things! I'm sure these level up will be a big benchmark for my future career. Furthermore, I want to mention that I really appreciated to travel with him to conferences and project meetings. Every time, we had pleasant communication, nice meals and especially nice drinking time. For me, with a lot of respect, he was a great but friendly, charming and amiable professor. Again, thank you very much. It was a honor for me to work with you.

I want to thank Prof. Mamoru Tanaka, my previous supervisor in Sophia University in Tokyo. Thank you for giving me the chance to come here in Switzerland during my master study. Without this experience, never this thesis was initiated. Thank you also for keeping contact during my PhD thesis and settled a joint project with my laboratory, LANOS. Thank you also for accepting to come to my private thesis defense far from Japan. Thank you so much.

I want also to thank all my thesis committee for their hard work to read this voluminous thesis and their advices and comments at the private defense. Thanks to Prof. Shokrollahi for accepting to become the president of the committee. Thanks to Prof. Sosnovtseva for becoming one of my thesis committee, and also for giving me useful advises when visiting our lab for the first time. Thanks to Prof. Ijspeert also for becoming one of my thesis committee, and also for his kind attitude when I was searching for a PhD position at the very beginning of my doctoral school.

Next, I want to thank all my collaborators. Thanks to Cristian Carmeli for collaborating with me for the data analysis part. He was not only my collaborator but also my good friend. Thank you for a great memory that you gave to me. Thanks to Oscar De Feo for giving advices at any time. I also very much appreciate your goodwill to Japanese culture. Thanks to Borja Ibarz for collaborating with me for the brain modelling. Your funny character made me very happy. Thanks to Yuri Shiogai for collaborating with me at the very last moment on the data analysis. I was very happy to have Japanese colleague with me in LANOS. Thanks to all my partners in BRACCIA project for their useful comments.

I want to thank Bertrand Dutoit for his technical support. I'm very sorry to bother

you so many times. Every time, your smile made me so happy. Thank you also for your contribution for the enrollment to LANOS. I want to thank Erika Raetz, our secretary, for all her administrative help. I very much appreciated your smart and sharp arrangement. I want to thank Jugoslava Acimovic, my office mate. I was very happy to have a girl in my office and our discussion was very pleasant. I want to thank all my present colleagues, Mahdi Jalili, Alireza Khadivi, Marc Hafner, François Roy, Heinz Köppl, Ali Ajdari Rad, Leonidas Georgopoulos and Dongchuan Yu for warm environment. I want also to thank my past colleagues, Enno de Lange, Norman Urs Baier, Igor Belykh, Francesco Grilli and Svetlomir Stavrev. Special thanks to Slobodan Kozic and Thomas Schimming for their collaboration for my master thesis. Especially, thank you Thomas for all your advices from the beginning of my one year visit. I spent a great time with you and your wife, Changyan, not only during this year but also after my return to Switzerland.

I want to thank all my friends both in Japan and in Switzerland. I spent a great four years of my thesis thanks to all of them. Sorry for not to recite here all the names. But I want especially thank my best friends, Yukko and Mari in Japan. It was always a great pleasure to meet you when returning to my home town. Also to Zenichi. I really appreciated our coffee time organized from time to time. Thank you so much for your support. Furthermore, to Christiane, Anne, Paola and Gianluca.

Very special thanks to my future husband, Christophe Maillard for his presence during my hole period of my thesis. Without him, never I was managed to finish my thesis. I'm sorry for all the trouble that I made during this last six months. I'm so happy that we reached to our conclusion, our marriage, this year. I count on you also from now on! Additionally, I also want to thank your parents, Maguy and Paul-Henri for their warm support.

To end, I want to thank my parents in Japan for their strong support. Thank you for allowing me to come to Switzerland. I very much appreciated your financial, technical and mental backup. Thanks to both of you, I managed to reach this state. With all my heart, thank you.

ありがとう。 

Lausanne, October 10th, 2008
Kumiko Oshima

Table of contents

1 Introduction

1.1 Background

THE medical technology has been progressively advanced and provided revolutionary advancement in curing the sickness and the injury. Nevertheless, assuring 100% safety and success of surgery remains unsolved. One of these problems is the estimation of the depth of the anæsthesia under surgery. Millions of patients undergo surgery each year, but as shown in table 1.1, the incidence of awareness is nonzero. In other words, there are still a large number of patients who remain conscious during surgery due to lack of anæsthetic and who are unable to give any voluntary indication of waking up during surgery because of the muscle relaxant effect. This problem is particularly severe since, for clinical reasons, the anæsthesia should be kept as light as possible. Many monitors of the depth of anæsthesia

Author	Year	Sample	Awareness
Hutchinson	1960	656	1.2
Harris	1971	120	1.6
McKenna	1973	200	1.5
Wilson	1975	490	0.8
Liu et al	1990	1000	0.2
Sandin	1997-1998	11785	0.15
Myles	1993-2000	10811	0.11
Sebel	2001-2002	19575	0.13
Ekman et al	2003	7826	0.18
Lennmarken & Sandin	2004	1238	0.9
Rungreungvanick	2005	150000	0.07

Table 1.1 – *Incidence of awareness during surgery. [BRA, 2005][Bruhn et al., 2006]*

do exist. However as discussed in the next chapter, none of them are reliable to avoid these accidents, nightmares for the patients.

To tackle this problem, an interdisciplinary research project called "Brain, respiration and cardiac causalities in anæsthesia (BRACCIA)" where we participate has been set up. In this project, having input from anæsthetists (on human and on rats), dynamical systems theory, information theory, as well as control theory is applied in the biological sciences, treating the most complex mechanism ever to have existed - the heart, the lung and the brain. Our contributions to this project are: (1) the data analysis to detect the change point of deep-light anæsthesia from the recorded signals as well as to infer the interdependencies among recorded systems, and (2) the modelling of the slow brain waves considering the effect of the anæsthesia.

1.2 Objective and research plan

The aim of this thesis is to clarify further the mystery of the anæsthesia to help both patients and medical doctors (surgeons, anæsthetists, etc). Bearing in mind the big goal of our project "BRACCIA" which is to create a reliable monitor of the depth of anæsthesia, and our contributions to this project just mentioned before, the research plan is settled as follows:

1. Estimation of the effect of anæsthesia from recorded experimental data

- Detection of the deep-light transition of anæsthesia:
  Previously, from our project partners, Aneta Stefanovska and the others, the pertinence of using synchronization between cardio-respiratory activities for estimating the depth of ansthesia had been shown [Stefanovska et al., 2000]. Accordingly, taking brain activity into account and concentrating on the synchronization among these three physiological activities, we will try to detect the deep-light change of anæsthesia as precisely and quickly as possible.

- Understanding the mechanisms of the interaction with respect to the anæsthesia:
  Considering the three organisms, namely the heart, the lungs, and the brain as a coupled dynamical systems whose interactions depend on the depth of anæsthesia, the investigation on the coupling (the causality) and its direction will be carried out to see the interactions change between deep state and light state/awaken state.

2. Modelling of the slow brain waves

- Realization of the brain model:
  A lot of brain models do exist. So the first goal is to search for the mechanisms to realize the slow waves, especially the δ-waves. After that, the creation of the model with a large ensemble of locally and/or globally coupled identical and non-identical oscillators will be carried out. Here, each neuron is planned to be represented as one oscillator.

- Implementation of the effect of anæsthesia in the model:
  After establishing the model, first, the study on the physical effect of anæsthesia

will be carried out. After that, the investigation on the global behavior of the cortical neurons, such as the level of synchronization of the ensemble, changing various parameters which reflects the effect of anæsthesia, will be carried out.

1.3 Thesis structure

The topics treated in each chapter are the following.

- **Chapter 2:** Anæsthesia is first described in general to introduce readers to what this thesis stands on. More detailed explanation on the general anæsthesia, the depth of anæsthesia, as well as the anæsthetics used in this thesis are given afterwards. After that, a short introduction to dynamical systems is given.
- **Chapter 3:** The works of our partners are first shown in view of comparing their results with ours. After that, all the five analysis methods used in this work are described in detail. The obtained results are shown on each data set separately. At the end of both rats data and Human data analysis results, a summary of the obtained results is given.
- **Chapter 4:** We first begin with describing the basic knowledge acquired from literature studies. After that, we described the model of thalamocortical assemblies and show the obtained results. Then, the effect of anæsthesia on this model are implemented and tested. Finally, some analysis of the model itself is carried out.
- **Chapter 5:** The final conclusion is made and some future investigations are proposed.

Preacquaintance and state of the art

2

2.1 Anæsthesia

ANAESTHESIA is the process of blocking the perception of pain and other sensations. This allows patients to undergo surgery and other procedures without distress and pain they would otherwise experience.

The history of the anæsthesia begins in prehistory with the use of drug plants as opium, cannabis, etc. to the pain. After a long period of no progress, in 16th to 18th century, a lot of important discoveries for the anesthesiology had been made principally in Europe, and the basic use of the anesthetic to the surgery had set up in 19th century. The first general anæsthesia in the world was performed in 1804 by a Japanese surgeon Seishu Hanaoka on the operation of a breast cancer, by combining Chinese herbal medicine know-how and Western surgery techniques learned through "Rangaku", or "Dutch studies". The most reputable initialization of the general anæsthesia was demonstrated by a dentist, William Thomas Green Morton in 1846 who employed ether as an anæsthetic agent for the patient undergoing the surgical removal of a tumor (Fig. 2.1). The next year, in 1847, James Young Simpson found the use of chloroform for general anæsthesia and, in 1853, John Snow, who is the first anesthesiologist, gave this chloroform to Queen Victoria to perform painless delivery during the birth of Prince Leopold. Following these success of ether and chloroform to the general anæsthesia, rapid progress has been made and many improvements and developments of anesthetic techniques have been performed (Fig. 2.2).

From the end of the 19th century, to ensure the safety of the patients, monitoring the pulse rate, blood pressure, etc. during surgery has been pervaded, and the essential device, the monitor for the depth of anæsthesia has been developed. Recent well advertised monitor of the depth of anæsthesia is the bispectral index technique known as BIS[Scott and Kelly] which is widely employed in the hospitals all over the world. However the use of this approach is controversial because of its calculation procedure(Fig. 2.3). The BIS value is calculated according to the comparison with the previously collected database, and the

Figure 2.1 – *Contemporary re-enactment of Morton's October 16, 1846.*

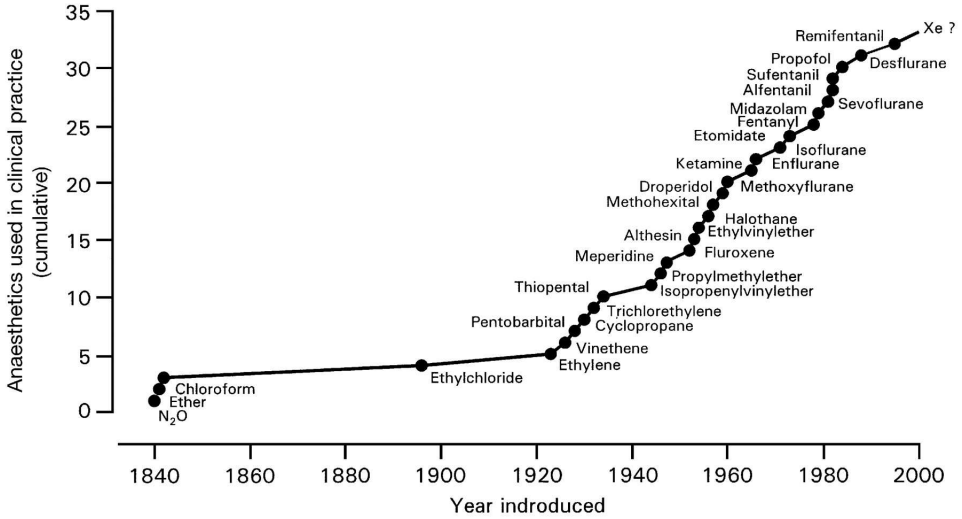

Figure 2.2 – *Dates of introduction of anaesthetic drugs.[Urban and Bleckwenn, 2002]*

mechanism behind is not published and kept as company secret. Consequently, the users can never be sure if the treated patients match the database criterion and can never be sure of the calculated BIS value. Other methods[Pomfrett, 2000][Bruhn et al., 2006] are also not 100% accurate, which lead to the results in table 1.1.

2.1.1 General anæsthesia

There are three types of the anæsthesia; regional, local and general one. In this thesis, we consider the general anæsthesia where the patients are deeply asleep (completely unconscious), don't have any sensation of pain and don't move.

From the clinical effect point of view, general anæsthesia consists of several components as shown in Fig. 2.4. The anæsthetist should balance these components regarding the demand of the patient who wants the amnesia and unconsciousness, the surgeon who wants an immobile patient, and the cardiologist who wants the patient's blood pressure and pulse

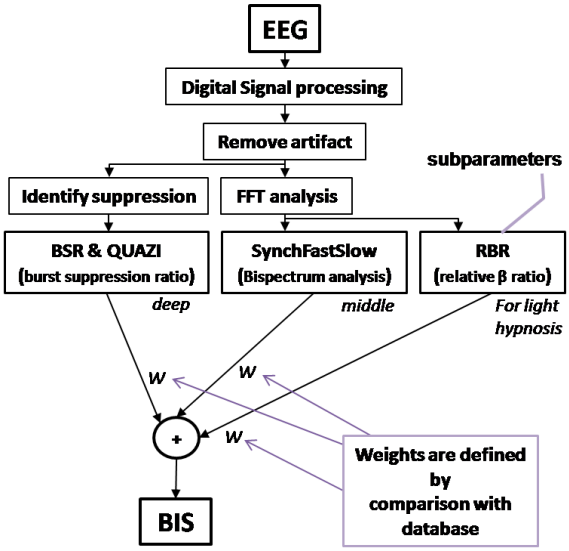

Figure 2.3 – *Schematic diagram of calculation paths to generate a BIS value.[BIS, 2005]*

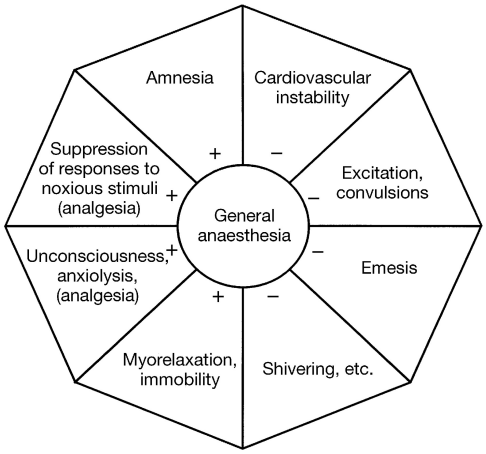

Figure 2.4 – *Components of general anæsthesia, those to be achieved and those to be avoided.[Urban and Bleckwenn, 2002]*

to remain within normal limits [Antognini and Carstens, 2002]. So, what are non-essential but desirable goals and what are the essential goals of general anæsthesia can depend on the demand of the concerned persons and the perspective of the anæsthetist. Consequently, it appears to exist no consensus defining general anæsthesia by its clinical effects [Urban and Bleckwenn, 2002].

In order to prevent the side effects that arise from high concentration, most anæsthetic procedures today involve the combination of different drugs, using anæsthetics in concentrations that are considerably smaller than those needed if one drug was to be used by itself. Modern general anæsthetic techniques typically involve the co-application of a hypnotic drug, an analgesic drug and a muscle relaxant. Many different combinations are possible, depending on which drugs are given together, on their relative concentrations with respect to each other, and on kinetics of their administration (bolus or continuously) [Urban et al.,

2006].

The general anæsthetics used for the experiments, whose recordings are treated in this thesis, are presented in next next subsection.

2.1.2 Depth of anæsthesia

The depth of anæsthesia was first mentioned by John Snow in 1847. He devided the effect of ether into five degrees, progressing from consciousness to deep coma, muscle flaccidity and respiratory paralysis. In 1937, Arthur Guedel described four stages of ether according to the eye signs, which is similar to those described by Snow (Fig. 2.5): In the first stage the patient was conscious but had analgesia. In the second stage (the delirium stage) the patient exhibited excessive motor activity, even to the point of violence. Eye movements were irregular and erratic, as was breathing. The third stage represented the surgical stage; four planes were originally described, with increasing anaesthetic depth as the patient progressed from the first to the last plane. Respiration became progressively weaker. In the fourth stage of anaesthesia, respiratory paralysis occurred. These classic signs have broad application, but it is clear that not all anaesthetics cause the same progression of clinical signs. Newer anaesthetics, in particular intravenous anaesthetics such as propofol, may not exhibit such signs. Many of the newer inhaled anaesthetics have low blood-gas solubilities and thus patients may pass from one stage to the next relatively quickly. Likewise, with intravenous anaesthetics patients are brought to deeper stages rapidly by bolus administration [Antognini and Carstens, 2002].

For only inhaled anæsthetic, another definition of the depth of anæsthesia can be obtained by minimum alveolar concentration (MAC) which shows the concentration of the vapour in the lungs that is needed to prevent movement in 50% of subjects in response to surgical stimulus (Fig. 2.6). The effective dose that results in 50% of patients hav-

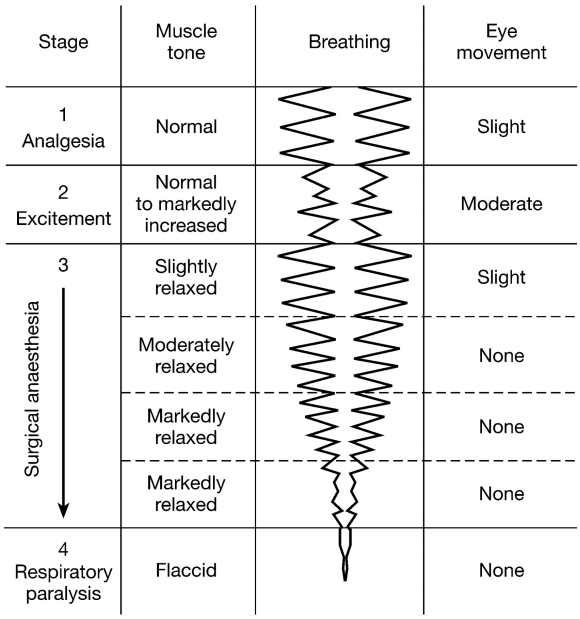

Figure 2.5 – *Guedel's stages and signs of anæsthesia.*

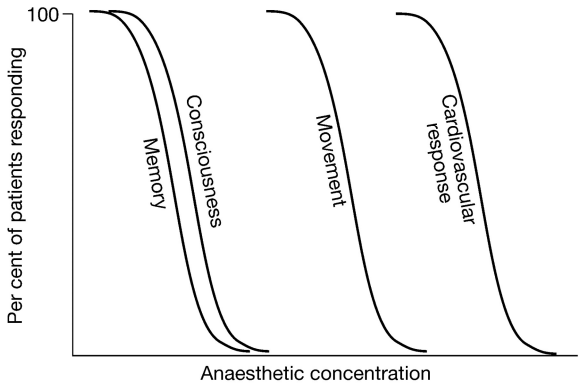

Figure 2.6 – *The dose-response curves for various end-points. [Antognini and Carstens, 2002]*

ing unconsciousness is called MAC-awake. This value is about 30-40% of MAC, although there are differences among anaesthetics. The anaesthetic concentration that blocks the cardiovascular response is called MAC-BAR. Today MAC serves as the standard of inhaled anesthetic potency. It allows quantitative comparisons of cardiorespiratory, neuromuscular, and central nervous system properties of inhaled anesthetics. It facilitates studies of the mechanisms by which inhaled anesthetics act. And clinicians use it to describe how deeply they anesthetize their patients and to appreciate the factors that influence anesthetic requirement (e.g., temperature) in a given patient [Eger, 2002].

In this thesis we will not use the depth of anæsthesia defined by Guedel (Snow), nor the MAC. What we are interested in, the most, is the moment when the anæsthetics begin to lose its effect and the patients state begin the transition toward the awaken state. Thereby, we will just take two levels of depth; deep and light, which are defined according to this moment of change. From this simple segmentation, we believe that we can develop the efficient monitoring method helping the anæsthetist to avoid incidents, the awareness of patients under surgery.

2.1.3 Anæsthetics used in this work

Ketamine

Ketamine* is commonly used in many laboratory species for anesthesia and chemical restraint. Ketamine is classified as a dissociative anesthetic, which means it produces dose-related unconsciousness and analgesia, but not classical anesthesia.

Its primary site of action in the central nervous system (CNS) appears to be the thalamoneocortical projection system. It selectively depresses neuronal function of the neocorticothalamic axis and the central nucleus of the thalamus while it stimulates parts of the limbic system, including the hippocampus.

Ketamine induces significant increase in cerebral blood flow, intracranial pressure, and cerebrospinal fluid pressure as a result of cerebral vasodilatation and elevated systemic blood pressure. In animals known to be epileptic, the administration of Ketamine has been

*This explanation is taken from a web site of Duke university and medical center. http://vetmed.duhs.duke.edu/guidelines_for_ketamine.htm

associated with the induction of seizures.

The cardiovascular effects of Ketamine are characterized by indirect cardiovascular stimulation. Various effects include sympathomimetic effects mediated within the CNS, inhibition of neuronal uptake of catecholamine by sympathetic nerve endings, direct vasodilatation of vascular smooth muscle, and an isotropic effect on the myocardium. Heart rate and arterial blood pressure increase as a result of direct stimulation of the CNS. Increased myocardial stimulation is associated with increased cardiac work and myocardial oxygen consumption.

The cardiovascular effect of Ketamine appears to depend on an intact and normally functioning CNS. Unlike most other anesthetics, Ketamine does not depress ventilatory responses to hypoxia. Skeletal muscle tone is maintained or even increased. Respiratory rate and minute volume may decrease initially after Ketamine administration, but return to baseline values within 15 minutes.

Ketamine may produce a transient apnea which appears to be dose dependent. Ketamine often causes increased salivation and respiratory secretions. Laryngeal and pharyngeal reflexes are usually well maintained during Ketamine anesthesia. In most species, Ketamine undergoes extensive hepatic metabolism. Rapid recovery following Ketamine administration is caused by rapid redistribution of Ketamine from the CNS to all body tissues (primarily body fat, lung, liver, and kidney).

Ketamine is rarely administered alone due to its poor muscle relaxation. Ketamine has been used in combination with various other anesthetic drugs, but it is most commonly combined with xylazine, acetylpromazine, or diazepam. These combined anæsthetics can be induced in the same time as Ketamine with one bolus injection.

Ketamine has a wide range of safety (i.e. wide dose range in most species). The duration of Ketamine anesthesia is very dose dependent and ranges from 15 minutes (dog), 20-45 minutes (cat) , 10-30 minutes (pig), and 10-20 minutes (rabbit).

Xylazine

Xylazine* hydrochloride (Rompun) is a medication commonly used in laboratory animal anesthesia. It is an alpha2-agonist with sedative and analgesic properties.

Specific actions are related to CNS depression mediated by stimulation of alpha2 receptors. Muscle relaxation is caused by inhibition of intra neural transmission within the CNS.

In several laboratory species (i.e. rodents, rabbits, ruminants, ferrets) xylazine has proven to be a safe anesthetic adjunct when coadministered with ketamine to induce short periods of surgical anesthesia. When combined with ketamine, muscle relaxation and visceral analgesia are improved, and emergence from anesthesia is smoother. Other anesthetic agents (i.e. butorphanol, guaifenesin, benzodiazepines) have also been combined with xylazine to obtain surgical anesthesia.

Major effects develop in approximately 10 to 15 minutes after intramuscular administration of xylazine and within 3 to 5 minutes following intravenous administration. When administered alone intravenously, xylazine induces bradycardia and a brief period of hyper-

*This explanation is also taken from a web site of Duke university and medical center. http://vetmed.duhs.duke.edu/guidelines_for_xylazine.htm

tension (5-10 minutes) followed by a longer period of decreased cardiac output and blood pressure.

The initial hypertension is caused by xylazines action at peripheral postsynaptic adrenergic receptors, which produces vascular smooth muscle contraction and vasoconstriction. Eventual reductions in blood pressure are due to decreased sympathetic tone resulting from xylazines activation of central and presynaptic sympathetic neuronal alpha2 adrenoceptors. Intramuscular administration of the drug does not produce this dramatic initial increase in blood pressure and vascular resistance.

The most commonly encountered arrhythmogenic effects of xylazine include sinoatrial block, atrioventricular block, bradycardia, first- and second-degree heart block, AV dissociation, and sinus arrhythmia. Respiratory rate decreases with the administration of xylazine.

Xylazine has a wide margin of safety. Increasing the dose does not in general increase the degree of sedation but rather the duration of effect.

Pentobarbital

Pentobarbital* is one of the most common injectable general anesthetic agents used in rodents. Pentobarbital is one of the drugs belonging to the class of anesthetics known as barbiturates. All barbiturates are derived from barbituric acid which, structurally, has had appropriate side-chain substitutions that result in central nervous system (CNS) depressant activity that varies in potency and duration with carbon chain length, branching, and saturation. The principal effect of a barbiturate is depression of the CNS by interference with passage of impulses to the cerebral cortex. Barbiturates act directly on CNS neurons in a manner similar to that of the inhibitory transmitter GABA. Barbiturate anesthesia is thought to be produced by the combined effect of enhanced inhibition and diminished excitation. The distinction between an anesthetic and an anticonvulsant barbiturate depends on the concentration at which amino acids modulation and GABA-mimicking activities occur.

The wide use of pentobarbital in rodents stems from its generalized availability, modest cost, widely available database for its use, rapid anesthetic onset, nonirritant nature, and ease of intraperitoneal injection to rodents of varying ages and body weights. Pentobarbital is a relatively poor analgesic. Higher doses are necessary to provide a surgical plane of anesthesia.

A mild excitement phase, during both anesthetic induction and recovery, is often observed with pentobarbital anesthesia. Pentobarbital causes respiratory depression which may result in hypercapnia with decreased tidal volume, minute volume, and respiratory rate. Reduced blood pressure, stroke volume, pulse pressure, and central venous pressure are common findings in pentobarbital-anesthetized animals. In prolonged anesthesia, the drug has also been shown to cause impaired myocardial contractility. Other reported effects include progressive decrease in core body temperature, decreased renal blood flow, reduced glomerular filtration rate, decreased intraocular pressure, and decreased urine output. Successful general anesthesia, using pentobarbital, is very dependent on good "support" (i.e.

*This explanation is also taken from a web site of Duke university and medical center. http://vetmed.duhs.duke.edu/guidelines_for_pentobarbital.htm

maintaining body temperature, maintaining hydration, etc.) during the anesthesia period. Environmental variables such as diet, environmental temperature, and type of bedding material the rodents are exposed to, can also affect the duration of pentobarbital-induced anesthesia. The effect of overdose of pentobarbital resembles the clinical signs produced by shock.

Sevoflurane

Sevoflurane* is a general inhalation anesthetic used for induction and maintenance of general anesthesia. It induces muscle relaxation and reduces pains sensitivity by altering tissue excitability. It does so by decreasing the extent of gap junction mediated cell-cell coupling and altering the activity of the channels that underlie the action potential. Used for induction and maintenance of general anesthesia in adult and pediatric patients for inpatient and outpatient surgery.

Although the mechanism of action has not been fully elucidated, sevoflurane may act by interfering with the release and re-uptake of neurotransmitters at post-synaptic terminals, and/or alter ionic conductance following receptor activation by a neurotransmitter. Sevoflurane may also interact directly with lipid matrix of neuronal membranes, thereby affecting gating properties of ion channels. In addition, this agent may activate gamma-aminobutyric acid (GABA) receptors hyperpolarizing cell membranes. This results in a general anesthetic effect, a decrease in myocardial contractility and mean arterial pressure as well as an increased respiratory rate†.

Sevoflurane is less irritating to the airway and therefore is useful to induce general anesthesia‡.

Propofol

The hypnotic agent propofol has pharmacokinetic characteristics that allow for rapid onset and offset of drug effect and fast elimination from the body. Elderly patients show a greater sensitivity to the hypnotic effect of propofol. The drug is extensively metabolized in the liver through the cytochrome P450 system and glucuronidation, with potential for drug interaction. Propofol does not cause significant inotropic depression at clinically relevant concentrations. But in vitro, propofol impairs isotonic relaxation of the heart and decreases free cytosolic Ca2+ concentrations in myocardial cells. In animal models, the cardioprotective effects of propofol derive in part from its antioxidant and free radical scavenging properties. Propofol decreases cerebral blood flow and cerebral metabolic rate dose-dependently. The neuroprotective effect of propofol in animal models is attributed to its antioxidant property, the potentiation of gamma-aminobutyric acid type A (GABAA)-mediated inhibition of synaptic transmission, and the inhibition of glutamate release. Subhypnotic doses of propofol induce sedative, amnestic, and anxiolytic effects in a dose-dependent fashion. Propofol impairs ventilation with a considerable effect on the control of ventilation and central chemoreceptor sensitivity. Propofol reduces the ventilatory response to hypercapnia and the ventilatory adaptation to hypoxia, even at subanesthetic doses. The drug

*Explanation taken from http://www.mongabay.com/health/medications/Sevoflurane.html
†http://www.cancer.gov/Templates/drugdictionary.aspx?CdrID=524061
‡http://health.kernan.org/altmed/drugs/sevoflurane-114365.htm

potentiates hypoxic pulmonary vasoconstriction, an effect caused by inhibition of K+ATP-mediated pulmonary vasodilatation. Most of the pharmacological actions of propofol result from interaction with the GABAA receptor or with calcium channels. Propofol prolongs inhibitory postsynaptic currents mediated by GABAA receptors, indicating that its effects are associated with enhanced inhibitory synaptic transmission, but propofol also influences presynaptic mechanisms of GABAergic transmission. Propofol modulates various aspects of the hosts inflammatory response. It decreases secretion of proinflammatory cytokines, alters the expression of nitric oxide, impairs monocyte and neutrophil functions, and has potent, dose-dependent radical scavenging activity similar to the endogenous antioxidant vitamin E [Schüttler and Schwilden, 2008].

Propofol does not have analgesic properties; pain should be treated with analgesic agents, propofol must be titrated separately from the analgesic agent*.

Cisatracurium (Curare)

Cisatracurium is used to adjunct to general anesthesia to facilitate endotracheal intubation and to relax skeletal muscles during surgery; to facilitate mechanical ventilation in ICU patients; does not relieve pain or produce sedation. It is classified as an intermediate-duration neuromuscular-blocking agent such that it blocks neural transmission at the myoneural junction by binding with cholinergic receptor sites. Maintenance of an adequate airway and respiratory support is critical†.

Remifentanil

Remifentanil is used as analgesic for use during the induction and maintenance of general anesthesia; for continued analgesia into the immediate postoperative period; analgesic component of monitored anesthesia. It binds with stereospecific mu-opioid receptors at many sites within the CNS, increases pain threshold, alters pain reception, inhibits ascending pain pathways. As it is an ultra short-acting medication, interruption of an infusion will result in offset of effects within 5-10 minutes‡.

2.2 Dynamical systems theory

A dynamical system is a system whose states are determined by the initial conditions and the temporal history of the inputs after the initialization. This dynamical system is usually described as:

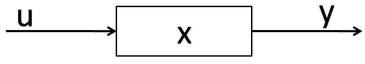

where u, x and y are respectively the input signal, the state and the output signal. These signals depend on the time $t \in T$ where T can be $\mathbb{R}$(continuous time systems) or $\mathbb{Z}$(discrete time systems). Very often, especially when we treat measurements, we limit our attention

*http://www.umm.edu/altmed/drugs/propofol-107675.htm
†http://www.taumed.com/content/adam/browse.jsp?pid=41&cid=029340
‡http://www.taumed.com/content/adam/browse.jsp?pid=41&cid=111575

to the signals from some initial time, typically t=0. In this case we would have $T = \mathbb{R}_+$ or $T = \mathbb{Z}_+$.

The temporal evolution of its states are mathematically formalized and written as differential/difference equations for continuous/discrete systems.

The differential calculus was introduced by two progenitors, Newton and Leibniz, who independently achieved the same outcome in the 15th century. At this epoch, of course, there was no possibilities to calculate on computers, and to solve a dynamical system required sophisticated mathematical techniques and only a small class of dynamical systems could handled. Recently, thanks to the development and calculation power of computers as well as new numerical methods, we manage to examine a wide range of complex dynamical systems.

The idea of dynamical systems theory is that the instantaneous configuration of a process is represented as a point, or "state", in a space of states, the "state space". The temporal evolution of the process can be represented as the motion of the state in the state space, called orbit or trajectory. The dimension of the state space is defined by the number of states which allows to specify uniquely the system's behaviow at each instant. If the dimension is low enough, we can visualize the trajectory [De Feo, 2001].

2.3 Influence of anaesthesia on the coupled oscillator model: state of the art

According to [Stefanovska and Bračič, 1999], the cardiovascular system can be considered as a noisy oscillatory dynamical system, and consequently can be macro-modelled as a collection of coupled oscillators plus noise. It has become clear that the oscillatory system - its amplitudes, frequencies, and especially its mutual couplings - can be used to characterize the state of the biological system.

In [Stefanovska et al., 2000], the use of mutual couplings of these oscillators has been implemented to characterize the state of the system during anæsthesia. This idea was tested on the physiological indicators (activity of heart(ECG) and respiration) of anæsthetized rats using synchronization indices and synchrograms. They claimed that this synchronization state could be used to characterize the depth of anæsthesia. More details are described in subsection 3.3.1. of this thesis. Using this method, it seems plausible that similar results may also be applied to humans, since, despite the cardiac and respiratory rhythms in rats being approximately four times faster than those in humans, the dynamics of these systems in rats and humans is very similar. However, applying this analysis to humans may not be reliable, because, in contrast to anaesthetized rats whose respiration does not need to be assisted, human respiration is often controlled by forced ventilation during surgery. Moreover, if the patients have some diseases in the heart or the lungs, the use of this method itself becomes suspicious. Therefore, a third system, the brain system, has been added for further studies.

Anæsthesia is a chemical pertubation of the organism which leads to a temporary loss of consciousness, but how this happens is still not very well understood. More over, despite highly intensive research on the brain, the mathematical models of the brain are far from the real one. Consequently to consider the effect of the anæsthesia on the brain waves is a very challenging problem, and should be a very important investigation.

Estimation of the depth of anaesthesia

3

- **Brief** - Five analyses of three recorded physiological signals, namely heart, respiration and brain signals, are carried out in order to detect the change from deep to light anæsthesia as well as to infer the interdependencies among these recorded systems under different depth of anæsthesia. First, the synchronization along the recordings is evaluated with a synchronization measure called "S estimator" to detect the change of subjects associated with the deep-light change of anæsthesia. A statistical assessment is afterward applied to the results of S estimator to detect precisely this deep-light change point of anæsthesia. Second, a new version of S estimator is applied to measure the synchronization exclusively between the different models created for each measured system. Third, an analysis on the embedding dimension of each recorded signal is performed to see the influence on the S estimator and to see the complexity change of the considered system under anæsthesia. Fourth, the coupling matrix between systems is assessed from reconstructed self models in order to see the interdependencies among these three organs under anæsthesia. Finally, the nonparametric Granger causality is calculated also to evaluate the interdependencies between these three systems and to be compared with the results of coupling matrix.

- **Contribution** - The S estimator, the new S estimator as well as the coupling matrix assessment used in this chapter were proposed by my colleagues in LANOS, Oscar De Feo and Cristian Carmeli. To see the time dependencies, I modified these methods adding the sliding window method. The application of these methods to the data of anæsthetised subjects and the analysis of the obtained results were my occupations. The method to estimate the embedding dimension is a very well known method, however to use this tool for the change of the complexity of the system was my idea. The Granger causality was proposed by Mukeshwar Dhamala from Georgia State University in US with whom we collaborate. The application of this method was carried out with my colleague of LANOS, Yuri Shiogai. The analysis of the results and the comparison with the coupling matrix were my occupations.

3.1 Motivation

THE development of the time series analysis techniques for the physiological signals is very important to create reliable medical monitors. During surgery, doctors rely not only on their five senses but also, mostly, on monitors to detect as quickly as possible the change of patients' condition. Accordingly, monitors must have real time data processing ability and clear display of the results. In the project BRACCIA, the big goal of the analysis is to construct a reliable monitor of the depth of anæsthesia which is able to show in real time the indication of the state of the anaesthesia measured from different physiological recordings and, moreover, inform anæsthetist when patients are moving toward the awaken state as clearly and quickly as possible*.

Many time series analysis methods have been established[Kantz and Schreiber, 2004]. However, to create or select one method which fits to our needs is a very difficult problem. Hence, extraction of the best analytical results seems to be a combination of different methods. As discussed in Chap.2, our project partners are confident that synchronization could be an indication of the depth of anæsthesia, and for this reason, they focused on the phase dynamics. Their methods based on these phase dynamics and their obtained results will be described more in detail in section 3.3. The way of their analysis seems to be very promising but still the definition of the phase, especially the phase of EEG signals, remains a big problem. Due to this problem, and also in order to avoid duplicating the work of our partners, and to combine afterward several methods to obtain a robust results, we took the entire dynamics and focussed on the correlation between the signals.

Previously, my colleagues of LANOS, Oscar De Feo and Cristian Carmeli, proposed two time series analysis tools based on this correlation between signals. One method is to measure the synchronization among multivariate time series[Carmeli et al., 2005][Carmeli, 2006]. More precisely, this method first reconstructs the state space from the observation signals. After that, it calculates the correlation matrix from the normalized reconstructed states. Finally, assuming that all the eigenvalues of this matrix are equal in a totally asynchronous case, and one eigenvalue is equal to one and the others are equal to zero in a synchronous case, the entropy of the distribution of the eigenvalues of the correlation matrix is calculated, and its complement is taken as the synchronization measure. More details will be discussed in section 3.4. The other method is to calculate the "coupling matrix" which infers the interaction among multivariate time series[De Feo and Carmeli, 2004][Carmeli et al., 2004][Carmeli, 2006]. More precisely, as the previous method, this method first reconstructs the state variables and creates a self model for each of the observations. After that, it calculates the linear interdependencies among the residual signals that can not be explained by its self models, and using an Euclidean norm, finally an estimate of the influence between systems, i.e. the coupling matrix is obtained. More details will be discussed in section 3.7. By C. Carmeli, these methods were tested with artificial toy models and their efficiency was proved. Also, the application of these methods to real data was performed, namely, to figure out the relationship between the visual stimuli and brain signals, the analysis of EEG data recorded on several electrodes applied to the scalp of subjects was carried out. The obtained results showed clear cooperativeness among certain EEG signals depending on the visual stimuli.

In this chapter, the root motivation was to apply these methods proposed by my col-

*At this moment, patients should be still under anæsthesia.

leagues to our data of anæsthetized subjects which contains three observation signals, namely electrocardiogram(ECG), chest band pressure for respiration and electroencephalogram(EEG), to test the use of these methods for the detection of the change of the depth of anæsthesia as well as the inference of the interdependencies among observed systems under different depth of anæsthesia, and then to improve these methods to consolidate the results.

Incidentally, at the end of my thesis, we began to collaborate with Mukeshwar Dhamala who is assistant professor in Georgia State University in Atlanta, US. He proposed us to use his method which calculates the Granger causality using a nonparametric approach[Dhamala et al., 2008] to our data. More precisely, this method estimates spectral density matrices by using direct Fourier transform of time series data, and then performing spectral density matrix factorization and Geweke's variance decomposition, it estimates the Granger causality. More details will be discussed in section 3.8. Accordingly, the comparison of this method with the coupling matrix described before was added to the motivation of this chapter to consolidate the analysis.

3.2 Data sets

3.2.1 First rats data

The experiments took place in the Institute of Pathophysiology in Ljubljana. These experiments were performed on two groups of adult, male Wistar rats weighing 250-300 g. Ten animals in the first group were anæsthetized with a single intraperitoneal injection of ketamine hydrochloride (KX, ketamine hydrocholride (45 mg/kg b.w.) and xylazine hydrochloride (7 mg/kg b.w.)). For convenience, let us call this group "Rats1". Ten animals in the second group were anæsthatised with a single intraperitoneal bolus of pentobarbital(PB, (60 mg/kg b.w.)). Let us call this group "Rats2". As soon as the rat could no longer hold its upright posture (10-15 minutes after administration of the drug), it was placed in a darkened Faraday cage where sensors were mounted and recording started immediately (See Fig. 3.1). In both groups, simultaneous recordings were made of: electrical

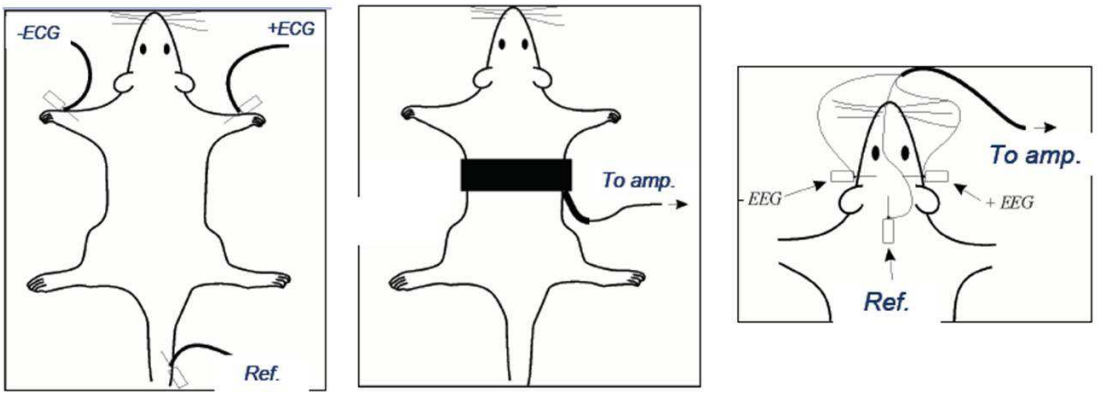

Figure 3.1 – *(Left) Electrode placement for the rat ECG. Two differential electrodes were attached to the animal's front legs. (Middle) Respiratory sensors: piezo probe on a belt was attached over the animal's chest. (Right) EEG sensors positioned over the left and right partial cortex*

activity of the heart (ECG); chest pressure for respiration; EEG over the left and right parietal cortex. The ECG was measured differentially ($V_{out} = A_d(V_+ - V_-), A_d = 20$) with three electrodes placed on the animal's tail and front paws. Respiration was monitored by recording chest wall movement using a piezoelectric probe attached over the animal's thorax. Three hypodermic needles, which served as EEG electrodes, were inserted under the animal's scalp. The EEG was differentially amplified ($V_{out} = A_d(V_+ - V_-), A_d = 10000$) and filtered (low-pass filter fc = 300 Hz). All three signals were then fed through a signal conditioning system (CardioSignals, developed by the Jožef Stefan Institute and the Faculty of Electrical Engineering, Ljubljana, Slovenia). They were each digitized at 1 kHz with 16-bit resolution (using a National Instruments multifunction I/O data acquisition board) and stored on the hard disk of a laptop computer. Depth of anæsthesia was assessed at 5 min intervals by a nociceptive stimulus, the skin pinch-test, applied to the sole of the animalfs front paw. The recording started with a negative test response, i.e. when the rat stopped responding with a reflex withdrawal of the limb. In the Rats1 group, monitoring was terminated on the reappearance of a positive pinch-test response, as the animal immediately started to move thereby terminating reliable data recording. The duration of recording varied from rat to rat and was on average 87 min. Monitoring of the Rats2 group continued for a limited period after the reappearance of a positive pinch-test, while the rat was still not fully awake. It was stopped 45-70 minutes after the reappearance of the positive pinch-test, thus allowing for recording during an interval of the waking state. Again, the duration of recording varied from rat to rat and was on average 92 min. All measurements were at constant room temperature (24±1°C). At the end of the recordings the animals were killed by administration of an overdose of the same anæsthetic. (Explanation taken from [Musizza et al., 2007].) Fig. 3.2 shows examples of 5 sec length of three recorded signals on one rat in each group.

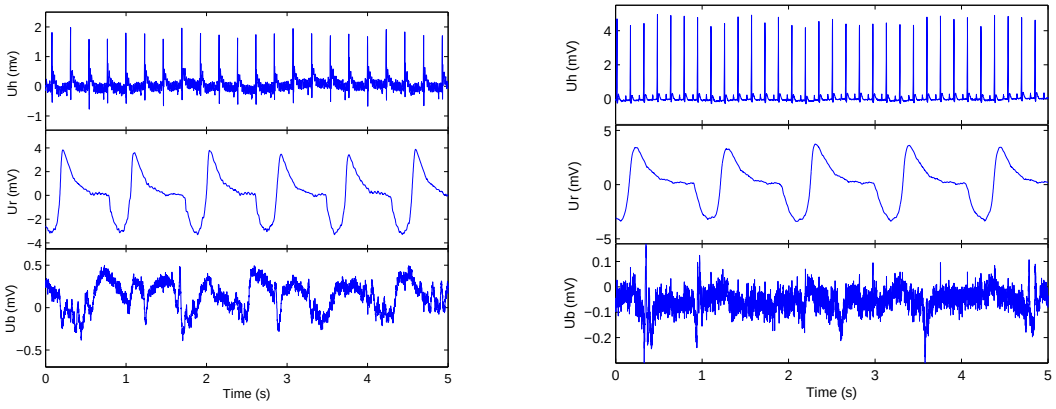

Figure 3.2 – *Example plots of three recorded time series of one rat in each group(left is KX and right is PB): ECG, U_h (top), respiratory signal, U_r (middle) and EEG, U_b (bottom)*

3.2.2 Second rats data

The experiments took place also in the Institute of Pathophysiology in Ljubljana with the same procedure mentioned in first data set except for the following: The EEG electrodes were implanted one to two weeks in advance. The reference electrode had a wire extension

and was placed between the rat's ears, while both signal electrodes were placed more to the front and on the top of the rat's head. Weight of rats were 250-350g. In the first group, sixteen rats were anæsthetized with re-injection of KX during recovery from anæsthesia with the same amount of anæsthetic as the first data sets, and eight of them were measured again after one week interval with single bolus injection of KX. Let us call the re-injection data set "Rats3" and the single injection "Rats5". The duration of recording also varied from rat to rat and was on average 159 min for Rats3 and 76 min for Rats5. In the second group, ten rats were anæsthetized with re-injection of PB during recovery from anæsthesia with the same amount of anæsthetic as the first data sets. Let us call this set "Rats4". Again, the duration of recording also varied from rat to rat and was on average 215 min. All signals were measured with a system developed by the Jožef Stefan Institute and the Faculty of Electrical Engineering, Ljubljana, Slovenia exclusively for the BRACCIA project and each digitized at 1.2kHz with 24-bit resolution.

3.2.3 Human data

The experiments took place in the Department of Anæsthesiology, Royal Lancaster Infirmary at the University Hospitals of Morecambe Bay NHS Trust, and in the Department of Anæsthesiology, Medical Faculty of Ullevael University Hospital at the University of Oslo. The measurements were performed while conscious and awaiting surgery (phase1), and then again, immediately after, being put under general anæsthetic (phase2). The measurement of phase1 started after all the measurement probes were set on the patient who is relaxing and lying on the operation table. He was asked not to move and not to sleep during measurement. When some events that might have disturbed the measurement happened, it was noted on a log file. The duration of measurement was around 25 min. Prior to the measurement of phase2, first, an intravenous line and anæsthesia monitoring equipment were established. In Lancaster, the measurement of phase2 started after the moment when the patient entered the steady state and the duration was around 25min in average. In Oslo, the first 5 subjects were measured in the same way as in Lancaster, but owing to the demand of our project leader, the other subjects measurements started before introduction of anæsthetic and ended at least 22 min after the moment when the patient entered the steady state. The duration of these measurements was around 35 min in average.

As induction of anæsthesia, there were two protocols. First one was with Sevoflurane: Anæsthesia was induced with Sevoflurane 8 % through inhalation (breathing the gas into the lungs) until endtidal concentration reached 5%. Spontaneous respiration was preferred but was assisted if necessary. The laryngeal mask (LMA) was inserted when the anæsthetist pronounced that the patient was deeply anæsthetized. After that, Sevoflurane was turned off until endtidal concentration decreased to 2%, and continued with Sevoflurane to maintain endtidal concentration at 2%. For half of the patients, Curare (0.15 mg/kg Cisatracurium, muscle relaxant) was injected into a vein after reaching "steady state", and forced ventilation was introduced because of the effect of Curare. Second one was with Propofol: Anæsthesia was induced with Propofol TCI=5 ng/ml by injecting into a vein. Spontaneous respiration was kept. The laryngeal mask (LMA) was inserted when the anæsthetist pronounced that patient was deeply anæsthetized. After that, Propofol was turned down to 3 ng/ml, and maintained. Again, for half of the patients, Curare (0.15mg/kg Cisatracurium, muscle relaxant) was injected in the same way as when Sevoflurane was used. These two protocols were determined randomly immediately prior to measurement.

The recordings were carried out with the same measuring system as second rats data set and sensors were attached as follows: For respiration, prior to all other sensors, a piezo probe on a belt was attached over the patient's chest and adjusted so that the signal occupied approximately a third of the sensor range. ECG electrodes were attached to the left shoulder, the right shoulder and the lowest rib on the left side of the body to obtain well defined ECG. For EEG, two BIS EEG electrodes were used crossing across the forehead in Lancaster. Lower electrode was connected on the right and higher one was connected on the left. Two channels were measured per electrode. In Oslo, only one BIS electrode was used on the left.

3.3 Analysis carried out by our project partners

In this section, I'll introduce two analyses carried out by our project partners. One is the study on synchronization states of the cardiorespiratory system which changes according to the effect of anæsthesia along the time. For this study, synchronization indices and synchrogram, calculated from the instantaneous phase, are used. The other one is the analysis on the interactions between cardiac, respiratory and EEG-δ oscillations using phase dynamics and mutual information. Later in this chapter, their results will be used to compare with our own results.

3.3.1 Previous studies on synchronization states of the cardiorespiratory system

This work had been carried out by Aneta Stefanovska and her collaborators[Stefanovska et al., 2000] before the beginning of the project "BRACCIA". The results of this study are very important since the general concept of BRACCIA is based on that. The data used in the development of this method were different from the data treated in this thesis*.

At the beginning, to see the change of state of both the cardiac and the respiratory system, their *instantaneous frequencies*, f_h and f_r, were calculated using the marker events method:

$$f(t) = \frac{1}{t_{k+1} - t_k}, \tag{3.1}$$

*Experiments were performed on adult male Wistar rats under general anesthesia with ketaminhydrochlorid 100 mg/kg b.w. and xylazinhydrochorid 20 mg/kg b.w., administered in a bolus, intraperitoneally. During the recording the animal was placed on a homeothermic operating table that enabled the body temperature to be kept constant at 37°C. The depth of anesthesia was assessed at 5 min intervals, starting from the moment at which the drugs were applied, by the animals response to touch and to painful stimulus with the skin pinch test. The plantar surface of the animals hind paws was stroked with the tip of a pair of tweezers (touch stimulus) or pinched (pain stimulus). The tests were considered positive if the animal responded by flexing its fingers or withdrawing its limb and were not perturbative to any of the quantities analyzed. The electric activity of the heart (ECG) and excursions of the thorax, which are proportional to respiratory activity, were noninvasively recorded while the breathing remained spontaneous and unassisted. Using a 16 bit A/D converter, each time series was digitized at a sampling rate of 2000 Hz and recorded over the entire duration of anesthesia (∼120 min). Recording started 5∼10 min after anesthetic drugs were injected and ended 5∼10 min after the first signs of recovered reflex responses, detected by a skin pinch test. Five rats were recorded in the same way. On each animal the recording was repeated after one week, using the same anesthetics and concentrations.(Explanation taken from [Stefanovska et al., 2000].)

where t_{k+1} and t_k are the time of two consecutive peaks[†]. The obtained results are shown in Fig. 3.3 a), b) and c).

Next, a *synchrogram* was drawn. Here, relying on the condition of (n,m)-phase synchronization, $\mid \varphi_{n,m} \mid = \mid n\phi_1 - m\phi_2 \mid < const$, we can understand the (n,m)-synchronization as the appearance of peaks in the distribution of the cyclic relative phase $\Psi_{n,m} = \varphi_{n,m} \mod 2\pi$ and interpret as the existence of a preferred stable value of phase difference between two oscillators. In such a case, the n:m phase locking manifests itself as a time variation of $\Psi_{n,m}$ around a horizontal plateau. When considering two interacting noisy oscillatory processes, n and m change in time. To analyse this kind of processes, we fix the value of m and observe changes of n in time. This analysis method is called a "synchrogram". The cardiorespiratory synchrogram was constructed by plotting the normalized relative phase of a heartbeat within m respiratory cycles and calculated as follows:

$$\Psi_m = \frac{1}{2\pi}(\phi_r(t_k) \mod 2\pi m), \tag{3.2}$$

where t_k is the time of kth heartbeat and ϕ_r is the instantaneous phase of respiration. From the fact that, in cardiorespiratory recordings, an integer value of the instantaneous frequency ratio was observed, m was fixed to $1(m = 1)$. The instantaneous phase was obtained as,

$$\phi(t) = 2\pi \frac{t - t_k}{t_{k+1} - t_k} + 2\pi, k, \qquad t_k \leq t < t_k + 1 \tag{3.3}$$

where t_k is the kth marker event. The obtained synchrogram with $m = 1$ is shown in Fig. 3.3 d).

Finally to characterize the strength of $n : m$ synchronization, they introduced a robust quantitative measure, the *synchronization index*, $\lambda_{n,m}$, based on conditional probability. Here, the idea is to use the distribution of the second oscillator's phase at fixed values of the phase of the first oscillator, θ, since in noisy systems, phase synchronization can be understood in a statistical sense as the existence of preferred values of generalized phase differences. The distribution of phases can be obtained as:

$$\eta = \phi_2 \mod 2\pi n \mid_{\phi_1 \mod 2\pi m = \theta} . \tag{3.4}$$

Concretely, the interval of each phase ϕ_1 and ϕ_2, respectively $[0, 2\pi m]$ and $[0, 2\pi n]$, is divided into N bins. The values of $\phi_1 \mod 2\pi m$ that belong to bin l are denoted as θ_l , while the number of points inside this bin is denoted as M_l. Using Eq. (3.3), the values of $\eta_{j,l} (j = 1, \ldots, M_l)$ are calculated. This $\eta_{j,l}$ shows an uniform distribution on the interval of $[0, 2\pi n]$ in asynchronous case, and shows an unimodal distribution concentrating around certain value in synchronous case. In order to rank the strength of the synchronization which evolves in time, they quantified this distribution using sliding window as:

$$r_l(t_k) = \frac{1}{M_l(t_k)} \sum_{i=1}^{M_l(t_k)} e^{i\phi_2(j)}, \tag{3.5}$$

for each j that $\phi_1(t_j)$ belongs to the lth bin and $t_k - t_p/2 \leq t_j \leq t_k + t_p/2$ (t_p is the window length fixed to 8 sec in their simulations). $M_l(t_k)$ is the number of points in this bin at the

[†]R peaks for EKG and maxima of inspiration for respiration signals

kth instant. As a result, $\mid r_l(t_k) \mid$ close to 0 indicates that there is no synchronization, and $\mid r_l(t_k) \mid = 1$ indicates complete synchrony. Finally, to improve reliability, the average over all bins was calculated to obtain the $n : m$ synchronization index,

$$\lambda_{n,m}(t_k) = \frac{1}{N} \sum_{l=1}^{N} \mid r_l(t_k) \mid . \tag{3.6}$$

The obtained synchronization indices are shown in Fig. 3.3 e) - h).

From Fig. 3.3 a) & b), dramatic changes of both instantaneous cardiac and respiratory frequencies during anæsthesia can be observed. During the first ∼25 min, f_h decreases from 4 to 3.2 Hz, then it increases and decreases again and, after ∼70 min, varies randomly between 3.5 and 4.5 Hz. The f_r slowly decreases from 2 to ∼0.8 Hz until at ∼40 min, then it begins to increases and returns again to its initial value of 2 Hz at ∼70 min, at which point it becomes highly variable, between 1 and 4 Hz. The ratio (f_h/f_r) shown in Fig. 3.3 c), first increases from 2 to 5, then decreases back to 2, and after ∼ 70 min, it becomes highly variable, spanning a wide amplitude range between 1 and 4. Observing these results, they found out that the effect of the anesthetic drugs seems to vanish at $\sim 70min$, and defined the period before this point "deep" anæsthesia and after this point "light" anæsthesia.

The synchrogram shown in Fig. 3.3 d) indicates immediately that several phase synchronization states occur with respect to the anæsthetic effects.

The time evolutions of the different synchronization indices, $\lambda_{1,n}$ shown in Fig. 3.3 e) - h) confirm what we observed in the synchrogram. During the first ∼40 min, all four states of synchronization, 1:2, 1:3, 1:4, 1:5, are clearly present and gradually switch one into the other (follow bold fleshes positions in time in Fig. 3.3). The next ∼40 to ∼70 min, the inverse evolution of phase synchronization is observed. And from ∼70 to until the end of recordings, no clear synchronization state can be seen.

To summarize, they showed that the cardiac and respiratory systems possesses dynamical properties and couplings that can synchronize their oscillations in a hierarchy of different phase-locked states. During the course of anæsthesia, the forward transition followed by the backward transition of the phase synchronization state are ascertained. Consequently, believing that these changes in phase synchronization state come from the nerve conductivity which decreases during the initial state of anæsthesia, and which causes changes in the overall nervous control of the cardiorespiratory system, they are persuaded that synchronization between the systems could be a useful measure of the depth of anæsthesia.

3.3.2 Interactions between cardiac, respiratory and EEG-δ oscillations

This work had been carried out with the first rats data set, in parallel with my thesis, by Bojan Musizza supervised by Aneta Stefanovska[Musizza et al., 2007] having in mind the studies described in the previous subsection. The principle method used in this work was proposed by Milan Paluš[Paluš et al., 2001][Paluš and Stefanovska, 2003] and Michael G. Rosenblum et al.[Rosenblum and Pikovsky, 2001][Rosenblum et al., 2002]. The results obtained in this work will be used to compare with my own results in the following sections.

To begin, the EEG power spectrum was divided into the conventionally-defined *frequency bands*: δ (0.5 - 3.5 Hz); θ (3.5 - 7.5 Hz); α (7.5 - 12.5 Hz); β (12.5 - 25 Hz); γ_1 (25 - 35 Hz); γ_2 (35 - 50 Hz); and γ_3 (50 - 100 Hz). The time evolution within each band was

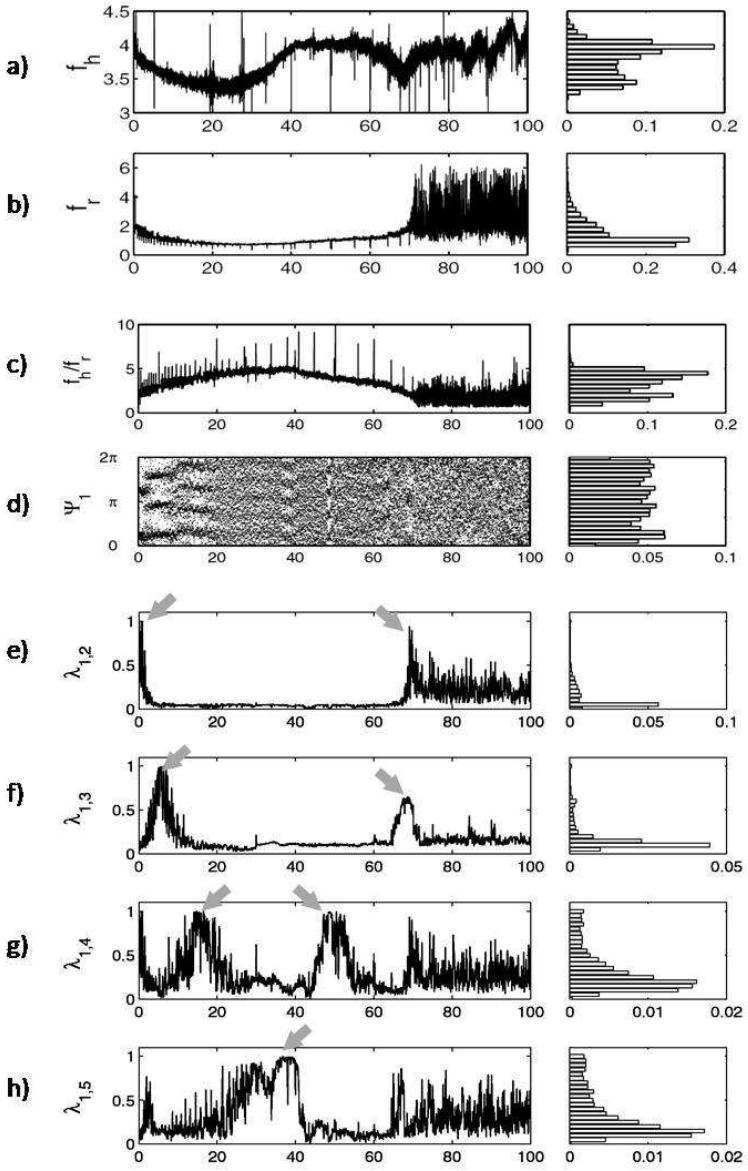

Figure 3.3 – *Evolution of phase synchronization measures during anæsthesia.[Stefanovska et al., 2000]: a)&b) the evolution of the instantaneous cardiac and respiratory frequencies. c) their ratio. d) cardiorespiratory synchrogram. e)-h) 1:2, 1:3, 1:4 and 1:5 synchronization indices, respectively. Bold fleshes indicate the pronounced phase-locked states. Occurrence of 1:n synchronization is demonstrated both in appearance of n plateaus in Ψ_1 and by $\lambda_{1,n}$ approaching unity. The right-hand column shows the corresponding distributions.*

separately calculated applying the continuous wavelet transform[Stefanovska and Bračič, 1999]. Fig. 3.4 shows typical time-frequency plots for the two groups. For the KX group, activity occurred mainly in the 0.5 - 3.5 Hz(δ range) and 3.5 - 7.5 Hz(θ range) bands. Note that, from the beginning, the δ-oscillations slightly increase in frequency and dramatically diminish in amplitude at ∼40 min, when the θ-oscillations begin to emerge. For the PB group, activity was only observed within 3.5 - 7.5 Hz (θ range) during the second part of the experiment. No δ-oscillations are observed. The sharp spectral peak near 1 Hz is

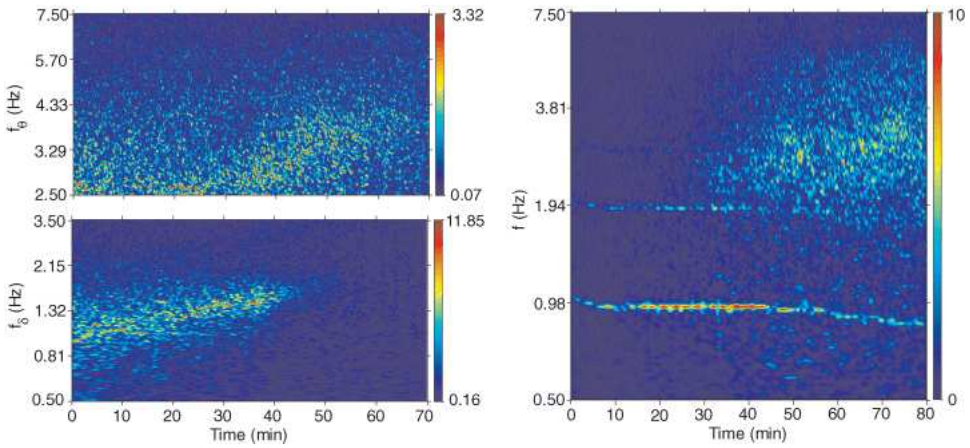

Figure 3.4 – *Evolution with time of the characteristic frequencies of EEG δ- and θ-oscillations during KX (left) and PB (right) anaesthesia. Data of rat No.9 for KX and No.8 for PB, respectively.*

spurious: it corresponds to the respiratory frequency and results from movement artifacts due to respiration. Its second harmonic can also be seen.

Next, as previous studies, in order to have an idea of the deep-light change point of anæsthesia, the *frequency analysis* was carried out. The cardiac and respiratory instantaneous phases were obtained using marker events as described in the previous subsection. The instantaneous phase of δ-oscillations in the EEG was obtained using Discrete Hilbert transform. Constructing a signal $\xi(t)$ defined as $\xi(t) = s(t)+is_H(t) = A(t)e^{i\phi(t)}$, where $A(t)$ is the amplitude and $\phi(t)$ is the phase of the signal $s(t)$, and $s_H(t)$ is its Hilbert transform, the instantaneous phase is given by $\phi(t) = \arctan \frac{s_H(t)}{s(t)}$.

Unfortunately, only the phases of the cardiac and respiratory oscillations could be determined reliably throughout the anaesthesia. The instantaneous phase of the δ-oscillations could be calculated only for the KX group, and only during the first section of the recording; in the second section, their amplitude became too small. The phase of δ-oscillations for the PB group was undetectable throughout. For both groups, the amplitude of θ-oscillations was significant only during the second part of the recordings. Under both anaesthetics, they spanned a large frequency interval (see Fig. 3.4) so that the notion of an instantaneous phase could not be defined unambiguously. Fig. 3.5 shows examples of cardiac, respiratory and δ instantaneous phases for one rat during KX (left) and PB (right) anaesthesia. For the result

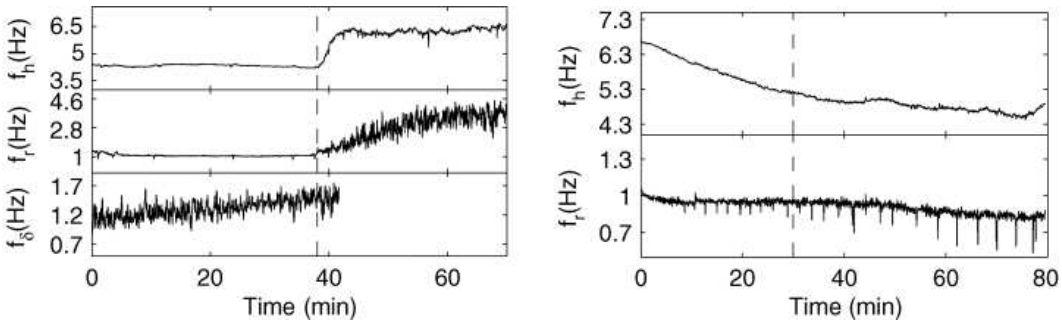

Figure 3.5 – *Evolution with time of the characteristic frequencies during KX (left) and PB (right) anaesthesia.Data of rat No.9 for KX and No.8 for PB, respectively.*

	Time of event for each rat (in min.)									
KX	1	2	3	4	5	6	7	8	9	10
Duration	62	57	168	72	73	73	100	71	71	122
f_r increase	18	36	59	52	43	43	47	33	38	73
f_δ diminish	17±4	36±5	60±2	52±4	46±2	43±3	45±3	34±5	38±5	76±4
PB	1	2	3	4	5	6	7	8	9	10
Duration	135	67	31	80	68	75	87	80	109	87
f_θ appear	60±3	16±4	2±1	20±3	14±5	30±5	27±5	28±4	30±4	35±3

Table 3.1 – *Times of characteristic events of 20 rats relative to the initiation of anæsthesia*

of KX anæsthetic, a remarkable change occurs ∼38 min in cardiac(f_h) and respiratory(f_r) frequencies. This point was defined as the change point of deep-light anæsthesia. In agreement with the previous study, the respiration frequency increased and became erratic at the transition, and the cardiac frequency increased. The frequency change point seen in the δ- and θ-oscillations (see Fig. 3.4) also coincide this transition point. For the result of PB anæsthetic, no particular changes in the instantaneous frequencies of cardiac and respiratory oscillations were observed during the whole recordings (see Fig.3.5). Therefore, using the similarity of θ-frequency behavior between KX and PB group, the deep-light change point of anæsthesia was defined by the appearance of θ-activity for the PB group. The observed event time for each rat used to define the transition point are given in Table 3.1. The increase in f_r was always clearly defined, but the decrease of δ-wave amplitude and the appearance of θ-wave amplitude was not possible to localized precisely such that intervals were specified.

Now, we come to the main point, the *detection of interactions* among these cardiac, respiratory and EEG-δ oscillators. First, I'll introduce the method which uses the phase dynamics introduced by Michael G. Rosenblum et al.[Rosenblum and Pikovsky, 2001][Rosenblum et al., 2002]. This technique was developed, assuming that the two observed signals represent weakly interacting oscillators, to reveal whether the interaction is bi- or unidirectional and quantify the degree of asymmetry in the coupling. They focused on the phase dynamics, since it is well-known that weak coupling first affects the phases of the oscillators, and not their amplitudes. The reduced phase dynamics of the concerned two observations can be represented as,

$$\dot{\phi}_{1,2} = \omega_{1,2} + \varepsilon_{1,2} f_{1,2}(\phi_{2,1}, \phi_{1,2}) + \xi_{1,2}(t). \tag{3.7}$$

where, $\omega_{1,2}$ are the natural frequencies, $f_{1,2}$ are 2π-periodic functions which consist of the phase dynamics of autonomous systems and the coupling between them, and $\xi_{1,2}$ describe noise. Small parameters $\varepsilon_{1,2} \ll \omega_{1,2}$ characterize the strength of coupling. Having the phase dynamics as Eq. (3.7), the directionality index was obtained in four steps.

First of all, the *increments of phases* during some fixed time interval τ were calculated as follows (see Fig. 3.6),

$$\Delta_{1,2}(t) = \phi_{1,2}(t+\tau) - \phi_{1,2}(t), \tag{3.8}$$

These increments can be considered as generated by some unknown two dimensional noisy map,

$$\Delta_{1,2}(t) = \omega_{1,2}\tau + \mathcal{F}_{1,2}(\phi_{2,1}(t), \phi_{1,2}(t)) + \eta_{1,2}(t). \tag{3.9}$$

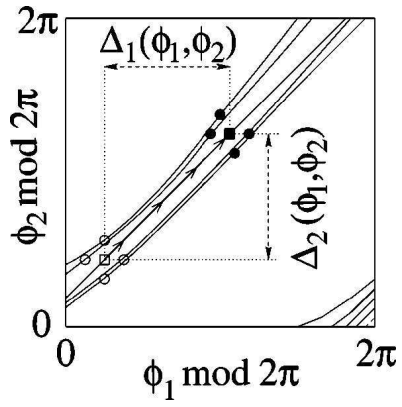

Figure 3.6 – *Evolution of neighboring trajectories on the torus (ϕ_1, ϕ_2) during the time interval τ. The points denoted by open symbols evolve with time to the positions shown by closed ones. The trajectory of one point (boxes) is shown by arrows. Here the increment of ϕ_1, $\Delta_1 = \phi_1(t+\tau) - \phi_1(t)$, depends on ϕ_2, hence, the phase of the first oscillator is influenced by the second one. On the contrary, the increment Δ_2 is constant, what indicates that there is no coupling in the direction from 1 to 2.*

The deterministic parts $\mathcal{F}_{1,2}$ of the map can be estimated from the time series $\Delta_{1,2}(t)$ and $\phi_{1,2}(t)$. For this purpose, secondly, the dependencies of Δ_1 and Δ_2 on ϕ_1 and ϕ_2 were fitted as a *probe function* using a finite Fourier series,

$$F_{1,2} = \sum_{m,l} A_{m,l} e^{im\phi_1 + il\phi_2}, \tag{3.10}$$

with $\mid l \mid \leq 3$ for $m = 0$, $\mid m \mid \leq 3$ for $l = 0$, and $\mid m \mid = \mid l \mid = 1$. Thirdly, the *cross dependencies* of phase dynamics of two systems were quantified using the results of fitting by means of the coefficients $c_{1,2}$ defined as,

$$c_{1,2}^2 = \int \int_0^{2\pi} \Big(\frac{\partial F_{1,2}}{\partial \phi_{1,2}} \Big)^2 d\phi_1 d\phi_2. \tag{3.11}$$

Finally, the *directionality index* was introduced as,

$$d_{(1,2)} = \frac{c_2 - c_1}{c_1 + c_2}. \tag{3.12}$$

Normalized in this way, the index varies from 1 in the case of unidirectional coupling $(1 \rightarrow 2)$ to -1 in the opposite case $(2 \rightarrow 1)$ with intermediate values $-1 < d_{(1,2)} < 1$ corresponding to bidirectional coupling. As a result, this index gives an integrated measure of how strong each system is driven and of how sensitive it is to the drive.

Let's introduce the second method which uses the mutual information introduced by Milan Paluš[Paluš et al., 2001][Paluš and Stefanovska, 2003]. This method considers two observation time series $x(t)$ and $y(t)$ as realization of two stationary ergodic stochastic processes $X(t)$ and $Y(t)$. Dependence structures between the two processes (time series) can be studied using the simple *mutual information*,

$$I(y; x_\tau) = H(y) + H(x_\tau) - H(y, x_\tau), \tag{3.13}$$

where, y represents $y(t)$ and x_τ stands for $x(t+\tau)$. The entropies $H(y)$,$H(x_\tau)$ and $H(y, x_\tau)$ are given in the usual Shannonian sense. This $I(y; x_\tau)$ measures the average amount of

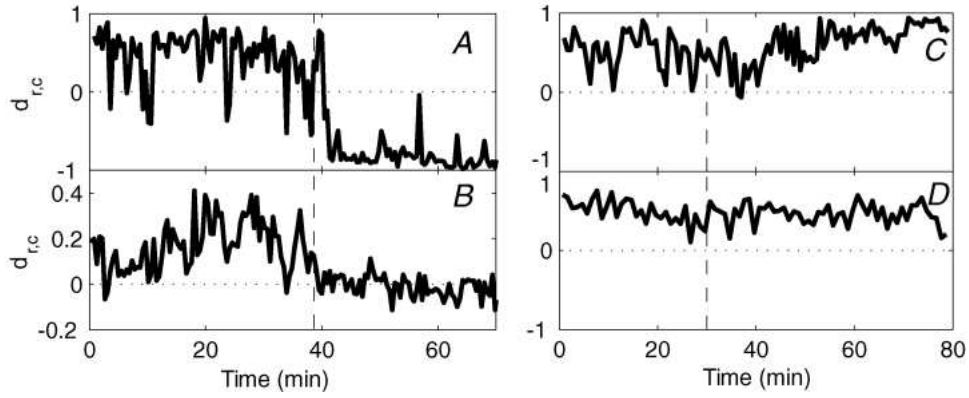

Figure 3.7 – *Direction of the cardio-respiratory interaction $d_{r,c}$ measured during KX (A and B) and PB (C and D) anæsthesia, obtained by phase dynamics based method (A and C) and mutual information based (B and D). Data of rat No.9 for KX and No.8 for PB, respectively.*

information contained in the process Y about the process X in τ-future(τ time units ahead). However, if processes X and Y are not independent, i.e. if $I(x;y) > 0$, this measure could also contain information about the τ-future of the process X contained in this process itself. Therefore, to estimate the 'net' information about the τ-future of the process X contained in the process Y, the *conditional mutual information*,

$$I(y; x_\tau \mid x) = H(y \mid x) + H(x_\tau \mid x) - H(y, x_\tau \mid x) \tag{3.14}$$

should be applied.

Reducing both systems into phase dynamics, the directionality of coupling between them was obtained as follows. As the method of Rosenblum et al., first, the phase increments $\Delta_{1,2}(t) = \phi_{1,2}(t+\tau) - \phi_{1,2}(t)$ were calculated. Next, how system 1 drives the other system 2, $i(1 \to 2)$ and vice versa, $i(2 \to 1)$ were calculated by the conditional mutual information using the obtained increments rather than simply substituting the series $x(t)$ and $y(t)$ by the phases $\phi_1(t)$ and $\phi_2(t)$,

$$i(1 \to 2) = I(\phi_1(t); \Delta_2(t) \mid \phi_2(t)), \tag{3.15}$$
$$i(2 \to 1) = I(\phi_2(t); \Delta_1(t) \mid \phi_1(t)). \tag{3.16}$$

Finally, in analogy with phase dynamics based method, the directionality index was obtained as,

$$d_{(1,2)} = \frac{i(1 \to 2) - i(2 \to 1)}{i(1 \to 2) + i(2 \to 1)}. \tag{3.17}$$

Cardio-respiratory directionality index, $d_{r,c}$ for both KX and PB anæsthetics were obtained by both phase dynamics based and mutual information based methods. The window-sliding method was applied to see the time evolution of the index. The obtained results are plotted in Fig. 3.7. In each case the interaction during KX (Fig. 3.7, left) is seen to undergo a marked and sudden change at the transition, at the same time as the onset of erratic respiration (Fig. 3.5, left) and the pronounced decrease in amplitude of the δ-oscillation (Fig. 3.4, left). Up to that point, the directionality index is positive, i.e. respiration drives cardiac activity as in the waking state. As the anæsthesia becomes shallow, however, this

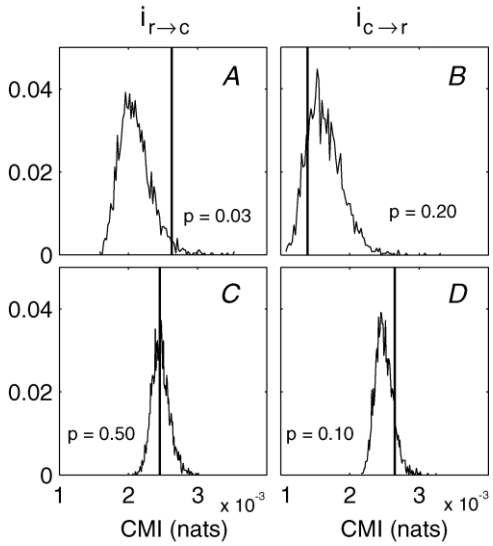

Figure 3.8 – *The histogram and the significance of the conditional mutual information (CMI) obtained using 2500 realizations of surrogate data created with KX anæsthetized rat(No,9). A and B refer to a period of deep anæsthesia, C and D refer to a period of light anæsthesia. The CMI characterizes the information flow (influence) from respiratory to cardiac activity $i_{r\to c}$ is shown on A and C, and in the opposite direction from cardiac to respiratory activity $i_{c\to r}$ is shown on B and D. The CMI for the original data is represented by the position of a vertical bar.*

is no longer true and, if anything, it is then the cardiac rhythm that drives respiration. On the contrary, no significant change in cardio-respiratory interactions can be observed during either phase of PB anaesthesia (Fig. 3.6, right). The results obtained from these two very different methods are clearly in good qualitative agreement.

Furthermore, the reliability of the measures was checked through the use of surrogate data*. Testing of significance was based on the CMI itself and not the directionality index (Eq. (3.17)) because of the reliability. For establishing the significance of the results, the absolute value of the CMI is irrelevant. Rather, it is its difference from the surrogate range that counts. The reason is that a particular data distribution and frequency content lead to a particular bias, and this bias is also preserved in the surrogate data. Consequently, only values that are significantly greater than those from the surrogate data can be taken as reliable evidence of interaction.

Fig. 3.8 shows the distribution of the obtained CMI values, calculated from 2500 realizations of surrogate data, in the form of a 100-bin histogram. If the value of CMI for the original data(presented as a vertical line) lies within this distribution, it is considered as statistical significance for accepting the null hypothesis, namely as no significant cou-

*These are artificially generated time series that preserve the statistical properties of the original data but are randomized such that any possible coupling is removed. They were constructed by random permutation of the RR intervals, and of the intervals between respiration and δ-wave maxima; and phases were computed using these randomized intervals as described above. This approach should have destroyed any dependence or causal relationship, if present in the original data, while preserving the basic statistical properties (i.e. distributions of cardiac, respiratory and δ-wave frequencies) of the original data which can be sources of bias and variance in estimation of the conditional mutual information (CMI).

	Significant level of the CMI for each rat										
KX(deep)	1	2	3	4	5	6	7	8	9	10	N
C→R	**0.03**	0.23	0.14	0.14	0.80	0.90	0.80	0.20	0.20	0.70	1
R→C	**0.00**	**0.00**	0.34	**0.02**	**0.00**	**0.00**	0.10	**0.00**	**0.03**	**0.00**	8
δ →R	0.50	0.25	0.33	0.70	0.08	0.40	0.05	0.50	0.07	0.22	0
R→ δ	0.30	**0.03**	0.70	0.26	**0.02**	0.07	**0.03**	0.18	0.16	0.05	3
δ →C	0.90	0.60	0.23	0.42	0.06	0.90	0.70	0.30	0.90	0.90	0
C→ δ	0.10	0.90	0.90	0.64	0.60	0.50	0.26	0.90	0.90	0.50	0
KX(light)	1	2	3	4	5	6	7	8	9	10	
C→R	0.45	**0.00**	0.90	0.60	0.90	**0.00**	**0.00**	0.90	0.10	0.90	3
R→C	0.70	0.90	0.70	0.60	**0.00**	0.07	0.40	0.70	0.50	0.50	1
PB(deep)	1	2	3	4	5	6	7	8	9	10	
C→R	**0.00**	0.10	-	0.79	-	**0.02**	0.90	0.72	0.41	**0.04**	3
R→C	**0.00**	**0.00**	-	**0.00**	-	**0.00**	**0.00**	**0.00**	**0.00**	**0.00**	8
PB(light)	1	2	3	4	5	6	7	8	9	10	
C→R	**0.04**	**0.00**	0.09	0.84	0.17	0.77	0.18	0.21	0.06	0.28	2
R→C	0.48	**0.00**	**0.00**	**0.00**	**0.00**	**0.00**	**0.00**	0.50	**0.00**	0.07	7

Table 3.2 – *Statistical tests of conditional mutual information(CMIS) for all 20 rats. Because of the problem defining the instantaneous phases, only the couplings that are possible to calculate are stated. The results are considered as significant for* $p < 0.05$ *and written in bold.* N *indicates the number of rats' data which shows significant influence.*

pling. According to the figure, only the case of CMI characterizes the information flow from respiratory to cardiac activity $i_{r\to c}$ during deep anæsthesia(shown on A) is statistically significant. From B and D, the $i_{c\to r}$ differs from deep period to light period, but it is still not significant. C is simply not significant. The summary of the statistical tests for all twenty rats are shown in Table. 3.2.

Fig. 3.9 summarizes schematically the main results of the study, based on all twenty rats analyzed. With KX anæsthetic, reversing the direction of coupling between cardiac activity and respiration between the periods of deep and light anæsthesia was admitted. With PB, solid influence from respiration to cardiac activity throughout the recording was consolidated, while the interaction $i_{c\to r}$ in the opposite direction became insignificant in the period of light anæshtesia. For the KX group, interactions with the EEG δ-oscillations in the deep phase of anaesthesia were also summarized. Statistically significant evidence for respiration driving the cortical δ-oscillations was established. No signature of cardiac-δ interactions was obtained for any of the rats so that there being no driving in either direction was presumed with a high probability.

To conclude, they found out that the effect on the cardiac activity, respiration and the brain waves caused by KX and PB anæsthetics differed a lot from one to the other. However, they succeeded to identify two distinct phases of anæsthesia for both KX and PB anæsthetics. With KX, the sudden change in the EEG-δ and -θ frequencies (f_{delta} and f_θ) and the directionality of cardio-respiratory interaction at the transition point of deep-light anæsthesia was admitted apart from the cardiac and respiratory frequency (f_h and f_r) changes reported in the previous study. Moreover, the evidence which shows the interactions between respiratory and EEG-δ oscillations, specifically, the former driving the latter, is very interesting. With PB, EEG-θ frequency change was consolidated at the

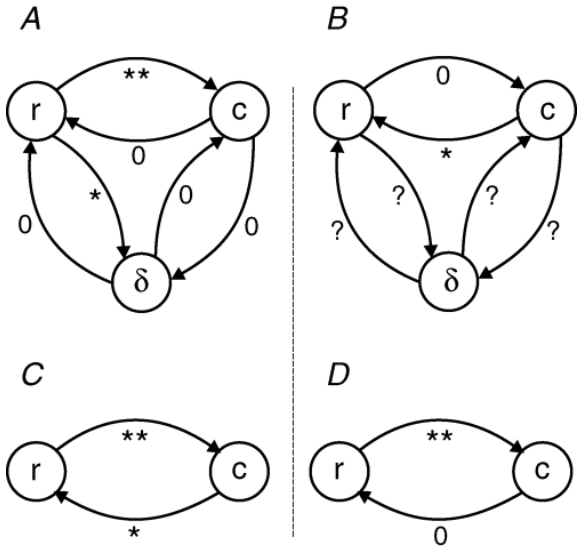

Figure 3.9 – *Schematic diagram illustrating the main results of the study in terms of the 3-oscillator model of respiratory (r), cardiac (c) and cortical (δ) mutual interactions (arrows). Inter-oscillator interactions during the period of deep anaesthesia (A and C) are compared with those during shallow anaesthesia (B and D) with KX (A and B) and PB (C and D), respectively. The significances of the calculated CMI are indicated by the numbers of stars (** for $N > 6$, * for $3 \leq N \leq 6$, and 0 for $N < 3$, where N is number of rats shown in Table. 3.2). A ? is used to indicate cases where an interaction could not be evaluated because of the definition of the instantaneous phases.*

transition, though the other frequencies do not change. The bidirectional interaction of cardio-respiratory systems during deep anæsthesia, and the driving of respiration of the cardiac oscillator in both phases of anæsthesia was demonstrated.

Such causal relationships during anæsthesia have not previously been reported. Further investigation to consolidate the method and implications of the method are highly expected.

3.4 The S estimator

As shown in the former section, the synchronization has a great potential for the detection of the change in anæsthesia. Consequently, placing the emphasis on the synchronization among the three recordings, i.e. ECG(heart activity), chest pressure(respiration) and EEG(brain waves), straightforwardly, a method which calculates a measure of synchronization called "S estimator" [Carmeli et al., 2005][Carmeli, 2006] is applied to the recordings of anæsthetized subjects. In this analysis, fast detection of the deep-light change of the depth of anæsthesia was expected for recordings of anæsthetized rats which were measured using single bolus injection of anæsthetic.

This S estimator was proposed by my colleagues of LANOS, Cristian Carmeli and Oscar De Feo. This is a linear approach to express the amount of cooperativeness within M interacting sub-systems, and it makes possible to examine directly the multivariate time series. It has a potential advantage of lower computational complexity and can be applied to a wide range of signals.

Though, there is no standard, unique and rigorous definition of the synchronization in the literature, here, it is defined as follows. The synchronization is defined as a process whereby two (or more) dynamical subsystems adjust some of their time-varying properties to a common behavior as a result of coupling or a common external force. More precisely, considering a large stationary, deterministic, finite dimensional time continuous dynamical system, which can be divided into $d^{(1)}$- and $d^{(2)}$- dimensional sub-systems, respectively

$$\begin{cases} \dot{\mathbf{x}}^{(1)}(t) = \mathbf{f}_1(\mathbf{x}^{(1)}(t), \mathbf{x}^{(2)}(t)), \\ \dot{\mathbf{x}}^{(2)}(t) = \mathbf{f}_2(\mathbf{x}^{(1)}(t), \mathbf{x}^{(2)}(t)). \end{cases} \tag{3.18}$$

We say that two sub-trajectories $\mathbf{x}^{(1)}(t) \in \mathbb{R}^{d^{(1)}}$ and $\mathbf{x}^{(2)}(t) \in \mathbb{R}^{d^{(2)}}$ of the whole system are synchronized with respect to the properties (time dependent measures) $\mathbf{g}^{(1)}$ and $\mathbf{g}^{(2)}$

$$\begin{cases} \mathbf{g}^{(1)} : \mathbb{R}^{d^{(1)}} \bigotimes \mathbb{R} \to \mathbb{R}^k \\ \mathbf{g}^{(2)} : \mathbb{R}^{d^{(2)}} \bigotimes \mathbb{R} \to \mathbb{R}^k \end{cases}, \qquad k \leq \min(m, n), \tag{3.19}$$

if there is a time-independent mapping $\mathbf{h} : \mathbb{R}^k \bigotimes \mathbb{R}^k \to \mathbb{R}^k$ such that

$$\mathbf{h}\big[\mathbf{g}^{(1)}(\mathbf{x}^{(1)}), \mathbf{g}^{(2)}(\mathbf{x}^{(2)})\big] = \mathbf{0} \tag{3.20}$$

This unifying definition covers most phenomena usually considered to be synchronization [Brown and Kocarev, 2000]. Condition Eq. (3.20) requires a property ($\mathbf{g}^{(1)}$) of the trajectory $\mathbf{x}^{(1)}(t)$ to be in a fixed relation ($\mathbf{h}$) with another property ($\mathbf{g}^{(2)}$) of the trajectory $\mathbf{x}^{(2)}(t)$, and it implies that synchronized sub-trajectories lie on an r-dimensional manifold, where r depends on $\mathbf{h}$ and is $1 \leq r \leq k$. Consequently, the dimensionality of synchronized dynamics ($d^{(1)} + d^{(2)} - r$) becomes smaller than that of generic asynchronous dynamics ($d^{(1)} + d^{(2)}$) in the whole system [Brown and Kocarev, 2000] [Boccaletti et al., 2002]. For instance, two identically synchronized two-dimensional periodic oscillators have dimension of the whole state space equals to four, but the embedding dimension of the synchronized dynamics equals only to two.

In the first subsection, the method is described in details. In the following subsection, a Wilcoxon rank sum test[Gibbons, 1985] is introduced in order to detect more precisely the time of change in state of the anæsthesia.

3.4.1 Detailed description of the method

By exploiting the above mentioned concepts of synchronization, the amount of synchronization within time series, which are multivariate, recorded from each system, is quantified by comparing the actual dimensionality of the set of samples of the trajectory with the expected full dimensionality of an asynchronous trajectory. This comparison can be performed by considering the Principal Component Analysis (PCA) technique. The PCA explains the variance-covariance structure of multivariate data through a few linear combinations of the original variables. A given multivariate time series with D components can be transformed into the population principal components by a linear transformation projecting the original time series into the eigenbase of the covariance matrix (correlation matrix, if the data have been de-trended to zero mean and normalized to unitary variance) of the time series itself [Joliffe, 2002]. In this coordinate system, the relative importance of each principal

component, in justifying the variance of the original time series, is given by the normalized eigenvalue associated with its corresponding eigenvector.

The S estimator is a measure of the amount of synchronization, S, using an information-theory-inspired measure defined as the complement of the entropy of the normalized eigenvalues of the corresponding correlation matrix. The more numerous the significant PCA components are (which means higher embedding dimension), the higher the entropy of the eigenspectrum is, and less synchronization is measured (Closer to the asynchronous case). On the contrary, the more concentrated the eigenspectrum, the fewer the significant PCA components are (which means a lower embedding dimension), the lower the entropy of the eigenspectrum, and higher synchronization measure is obtained (Closer to the complete synchronous case). Practically, the procedure to calculate the value S from the time series (observations) is as follows.

For sake of simplicity, first the method is explained without embedding. Very often, the time series that we should analyze can be formalized as a network model, given by the noise-driven system,

$$\dot{\mathbf{X}}(t) = \boldsymbol{\mathcal{F}}(\mathbf{X}(t)) + \boldsymbol{\eta}(t) \tag{3.21}$$

where the generic vector field $\boldsymbol{\mathcal{F}} : \mathbb{R}^D \to \mathbb{R}^D$ models the network dynamic law. The vector $\boldsymbol{\eta}(t) \in \mathbb{R}^D$, represents the modeling noise. $\mathbf{X}(t) \in \mathbb{R}^D$ is the state space vector of M dynamical sub-systems at time t, where

$$\mathbf{X}(t) = \begin{bmatrix} \mathbf{x}^{(1)}(t) \\ \vdots \\ \mathbf{x}^{(i)}(t) \\ \vdots \\ \mathbf{x}^{(M)}(t) \end{bmatrix}. \tag{3.22}$$

The components $\mathbf{x}^{(i)}(t) \in \mathbb{R}^{d^{(i)}}$ are the state variables of the generic $d^{(i)}$-dimensional sub-systems(i) at time t and $\sum_{i=1}^{M} d^{(i)} = D$. Taking into account that measurements are generally performed with a fixed uniform sampling interval Δt at times $t_0, t_0 + \Delta t, \ldots, t_0 + (L-1)\Delta t$, P observation signals* obtained from dynamical sub-systems are denoted as

$$\mathbf{O} = \begin{bmatrix} \mathbf{O}_0 \\ \mathbf{O}_1 \\ \vdots \\ \mathbf{O}_{L-1} \end{bmatrix} \tag{3.23}$$

where $\mathbf{O}_t \in \mathbb{R}^P$ is the t-th sample observation vector and L is the number of available samples. Without loss of generality, $\mathbf{O}$ can be de-trended to zero mean and normalized to unitary variance as $\tilde{\mathbf{O}}_t$, where, $\tilde{o}_t^{(i)} = (o_t^{(i)} - \bar{o}_t^{(i)})/\sigma_{o_t^{(i)}}$. The corresponding $P \times P$ correlation matrix is given by

$$C = \frac{1}{L} \sum_{t=0}^{L-1} \tilde{\mathbf{O}}_t^T \tilde{\mathbf{O}}_t. \tag{3.24}$$

*$P \leq D$ (number of observation signals $\leq$ number of states in the model)

Let $\lambda_1, \ldots, \lambda_P$ be the eigenvalues of C, and

$$\lambda_i' = \frac{\lambda_i}{\sum_{j=1}^{P} \lambda_j} = \frac{\lambda_i}{tr(C)} = \frac{\lambda_i}{P} \tag{3.25}$$

be the corresponding normalized eigenvalues. The entropy-like quantity

$$E = -\sum_{i=1}^{P} \lambda_i' \log(\lambda_i') \tag{3.26}$$

is a measure for the "dimension" of the observed dynamical phenomenon. Specifically, this E measures the diversity in the distribution of the normalized eigenvalues. In the case of P uncorrelated signals, $C = I$(Identity matrix), the normalized eigenvalues are all equal (uniform distribution), i.e. $\lambda_i' = \frac{1}{P}, \forall i$, and E equals to $\log(P)$. On the contrary, in the case of perfectly correlated identical signals, C has one unitary normalized eigenvalue and all the others zero (peaky distribution), i.e. $\lambda_1' = 1$ and $\lambda_i' = 0 (i \neq 1)$, and E equals to zero. To have a measure for the amount of synchronization, one can simply rearrange Eq. (3.26) and obtained the S value as

$$S^{(1,2,\ldots,P)} = 1 - \frac{E}{\log(P)}, \tag{3.27}$$

which gives zero for asynchronous signals, and gives one for complete synchronous ones.

Now let's move to the application of this method to the delay-embedded coordinates. The observation signals that were mentioned just before, usually are less numerous than all the D states of $\mathbf{X}(t)$ and the result of S estimator may not be adequate. Nevertheless, $\mathbf{O}_t$ is naturally considered to be related to $\mathbf{X}(t)$ with a measurement function $\mathcal{G} : \mathbb{R}^D \to \mathbb{R}^P$, which assumed to be a smooth function corrupted by some measurement noise $\boldsymbol{\nu}(t) \in \mathbb{R}^P$. Thus, the measurement equation of the network yielding a P-variate time series can be written as,

$$\mathbf{O}_t = \mathcal{G}(\mathbf{X}_t) + \boldsymbol{\nu}_t, \tag{3.28}$$

where subscripts indicate the discrete time values, with $t = 0, \ldots, L-1$, which leads to the reconstruction of state-space that is topological equivalent as the original one.

The state-space for each (i)-th sub-system is reconstructed using the delay embedding method which transforms a univariate time series $\{o_t^{(i)}\}$ into a multivariate one as

$$o_t^{(i)} \to \mathbf{Y}_t^{(i)} = [o_t^{(i)} \;\; o_{t+\tau^{(i)}}^{(i)} \;\; \cdots \;\; o_{t+(n^{(i)}-1)\tau^{(i)}}^{(i)}] \tag{3.29}$$

where the time delay $\tau^{(i)}$ and the embedding dimension $n^{(i)}$ can be obtained through the first minimum of the self-mutual information and the false nearest neighbors method, respectively [Kantz and Schreiber, 2004].

- Decision of τ with mutual information:
Mutual Information measures the general dependence of two variables, i.e. measures the information we already posses about the value of $s(t+\tau)$ if we know $s(t)$. The expression

we have to compute is based on Shannon's entropy. From the interval explored by the data, a histogram of resolution ϵ is created for the probability distribution of the data. Denote by p_i the probability that the signal assumes a value inside the i-th bin of the histogram, and let $p_{ij}(\tau)$ be the probability that $s(t)$ is in bin i and $s(t+\tau)$is in bin j. Then the mutual information for time delay τ reads

$$I_\epsilon(\tau) = \sum_{i,j} p_{ij}(\tau) \ln p_{ij}(\tau) - 2 \sum_i p_i \ln p_i. \tag{3.30}$$

For small τ, $I_\epsilon(\tau)$ will be large. It will then decrease more or less rapidly. In the limit of large τ, $s(t)$ and $s(t+\tau)$ have nothing to do with each other and p_{ij} thus factorizes to $p_i p_j$ and mutual information becomes 0. Consequently, the first minimum of $I_\epsilon(\tau)$ marks the time lag, where $s(t+\tau)$ adds maximal information to the knowledge we have from $s(t)$, in other words, the redundancy is least. See more details in [Kantz and Schreiber, 2004].

- Decision of n with false nearest neighbors:
The concept, called false nearest neighbors, was introduced by Kennel, Brown and Abarbanel[1992]. If we assume that the dynamics in phase space is represented by a smooth vector field, then neighboring states should be subject to almost the same time evolution. Hence, after a short time interval into the future, the two trajectories emerging from them should be still close neighbors, even if chaos can introduce an exponential divergence of the two. Owing to that, the basic idea of this false nearest neighbors is to search for points in the data set that are neighbors solely because of viewing the orbit (the attractor) in a too small embedding space. See example in Fig. 3.11.

The original procedure to choose the minimum embedding dimension is the following. If we are in n dimensions and we denote the r-th closest neighbor of $\mathbf{Y}_t$ by $\mathbf{Y}_{t,r}$, then from Eq. 3.29, the square of the Euclidian distance between the point $\mathbf{Y}_t$ and this neighbor is

$$R_n^2(t,r) = \sum_{k=0}^{n-1} [o_{t+k\tau} - o_{t+k\tau,r}]^2. \tag{3.31}$$

In going from dimension n to $n+1$ by delay embedding, the distance between $\mathbf{Y}_t$ and the same r-th nearest neighbor is

$$R_{n+1}^2(t,r) = R_n^2(t,r) + [o_{t+n\tau} - o_{t+n\tau,r}]^2. \tag{3.32}$$

A natural criterion for catching embedding errors is that the increase in distance between $\mathbf{Y}_t$ and $\mathbf{Y}_{t,r}$ is large when going from dimension n to dimension $n+1$. The increase in distance can be stated quite simply from Eqs. 3.31 and 3.32. Then, the criterion is defined by designating as a false neighbor any neighbor for which

$$\left(\frac{R_{n+1}^2(t,r) - R_n^2(t,r)}{R_n^2(t,r)} \right)^{1/2} = \frac{|o_{t+n\tau} - o_{t+n\tau,r}|}{R_n(t,r)} > R_{tol}, \tag{3.33}$$

where, R_{tol} is a threshold. The criterion that the embedding dimension is high enough is that the fraction of false neighbors is sufficiently small. See example in Fig. 3.10. See more details in [Kennel et al., 1992].

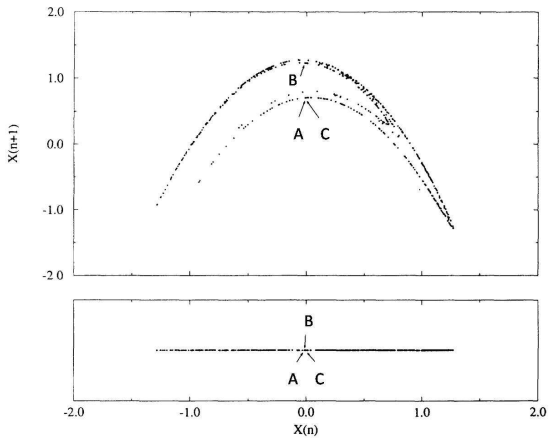

Figure 3.10 – *The R^1 and R^2 embeddings of the x coordinate of the Hénon map of the plane. It is known that for this map $d_E = 2$. A and B are false neighbors while the points A and C are true neighbors.[Kennel et al., 1992]*

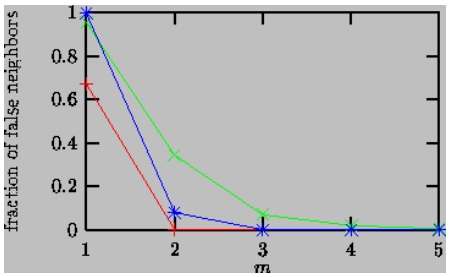

Figure 3.11 – *The fraction of false nearest neighbors as a function of the embedding dimension for noise free Lorenz (blue) and Hénon (red) time series, as well as a Hénon time series (green) corrupted by 10% of noise.[Rainer et al., 1999]*

In this study, we use a slightly modified method. The distance between neighbors is evaluated with a maximum norm instead of the Euclidean distance. Consequently, eq. (3.31) becomes,

$$R_n(t,r) = \max_{k<n} |o_{t+k\tau} - o_{t+k\tau,r}|, \tag{3.34}$$

and eq. (3.32) becomes,

$$R_{n+1}(t,r) = \max_{k<n+1} |o_{t+k\tau} - o_{t+k\tau,r}|, \tag{3.35}$$

then, the condition of false neighbors becomes,

$$\frac{R_{n+1}(t,r)}{R_n(t,r)} > R_{tol}. \tag{3.36}$$

Here R_{tol} is set to $R_{tol} = 15$. And the threshold of fraction of false neighbors is set to 0.05.

Suppose we have two observation signals ($P = 2$), with estimated delay times($\tau^{(1)}$ and $\tau^{(2)}$) and embedding dimensions ($n^{(1)}$ and $n^{(2)}$). Then, embedded multivariate trajectories are represented as $\mathbf{Y}_t = \{\mathbf{Y}_t^{(1)}, \mathbf{Y}_t^{(2)}\}_{t=0,\ldots,l}$ where $\mathbf{Y}_t \in \mathbb{R}^{(n^{(1)}+n^{(2)})}$, l is the minimum

number of samples available after the two reconstructions, and then, the S-estimator on the embedded time series is just calculated as a non-embedded $(n^{(1)} + n^{(2)})$-variate time series.

To complete the analysis on the synchronization, as we are interested in the time evolution of the S-estimator with respect to the depth of anæsthesia, the sliding window method is added to the whole analysis. This method works to separate the data for the analysis in several overlapping windows along the time scale (See Fig. 3.12).

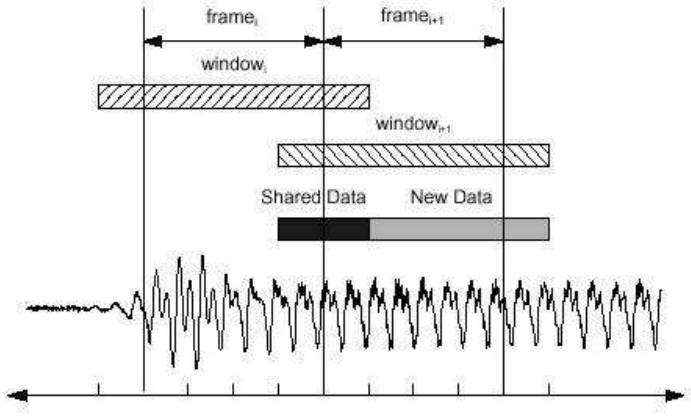

Figure 3.12 – *Graphical representation of the Sliding window method.*

First, for each window the embedding dimension and the delay are calculated. After that, to have unique embedding dimension and delay for comparison of value of S along the time, they are fixed taking the maximum value of the embedding dimension* and the mean value of the delay along the time. With these values, for each window the synchronization measure S is calculated and the time evolution $S(t)$ is obtained.

3.4.2 The statistical assessment

In order to detect statistically more precisely the state change point of anaesthesia, we calculated the statistical assessment value p using a Wilcoxon rank sum test. This test performs a two-sided rank sum test of the hypothesis that two independent samples come from distributions with equal medians, and yields the p-value from the test. p is the probability of observing the given result. In the extreme case, when the null hypothesis is true, i.e., the medians are equal, $p = 1$". Hence, the closer the p-value is to zero, the more confident we are in rejecting the null-hypothesis. The process of this assessment is to calculate this p on two sets of samples separated with a certain interval and move the selected two sets along the time axis. In this way, the trend analysis can be easily obtained, and later in subsec. 3.9.1, sudden decrease of Synchronization remarked in the results of single bolus injection of KX rats data can be detected numerically. For more details, please refer to the help of the MATLAB function "ranksum".

*For embedding dimension, the obtained results are checked manually, and comparing with the measurements, if the maximum value is due to some artifact, the lower value is taken as a unique embedding dimension.

3.5 The new S estimator

In the previous section, we performed the S estimator on reconstructed state space variables. Our concern in this studies is that we measured also the synchronization of the state variables within each considered model such that it may result in false conclusions concerning the interdependencies of the models. When Cristian Carmeli remarked this problem, he upgraded the S estimator to a new version [Carmeli et al., 2005][Carmeli, 2006]. In this new one, a linear transformation of the reconstructed state space trajectory orthonormalizes the state variables within each considered model such that global state space reduction becomes a measure of synchronization exclusively between the different models.

Apart from this new version, we can also calculate this exclusive inter-synchronization using the principal component analysis(PCA*) based embedding method [Joliffe, 2002][Kantz and Schreiber, 2004] instead of delay embedding method since this state-space reconstruction method creates the state-space already orthogonalized.

In the following subsection, the upgraded method and the PCA based embedding method are described in details.

3.5.1 Detailed description of the method

Consider again two observation signals ($P = 2$) mentioned in subsec. 3.4.1, with estimated embedding dimensions ($n^{(1)}$ and $n^{(2)}$). The corresponding estimated correlation matrix can be block partitioned to highlight the contribution of the two systems, i.e.

$$\mathcal{C} = \begin{bmatrix} \mathcal{C}^{(1,1)} & \mathcal{C}^{(1,2)} \\ {\mathcal{C}^{(1,2)}}^T & \mathcal{C}^{(2,2)} \end{bmatrix}, \tag{3.37}$$

where the $n^{(i)} \times n^{(i)}$ matrices $\mathcal{C}^{(i,i)}, i = 1, 2$, give the intra-sub-system correlation terms, namely the correlation between state variables of the same sub-system, while the $n^{(1)} \times n^{(2)}$ matrix $\mathcal{C}^{(1,2)}$ gives the inter-sub-system correlation terms. To correctly estimate the inter-dependence between the two delay embedded sub-systems, independently of the intra-dependencies, a suitable linear transformation of the reconstructed state space trajectory $\mathbf{Y}$ which reduces the $\mathcal{C}^{(i,i)}$ to identity matrices(I) is applied; precisely, we intra-orthogonalize the state variables of the two sub-systems. As a result of the transformation, the estimated correlation matrix for the transformed trajectory will have non-zero off-diagonal elements only within the inter-dependence block $\mathcal{C}^{(1,2)}$.

The transformation is given by

$$\mathbf{Z} = \begin{bmatrix} \mathbf{Z}^{(1)} & \mathbf{Z}^{(2)} \end{bmatrix} = \begin{bmatrix} \mathbf{Y}^{(1)} & \mathbf{Y}^{(2)} \end{bmatrix} \begin{bmatrix} \mathcal{T}^{(1)} & 0 \\ 0 & \mathcal{T}^{(2)} \end{bmatrix} = \mathbf{YT}, \tag{3.38}$$

with $\mathcal{T}^{(1)} = {\mathcal{C}^{(1,1)}}^{-\frac{1}{2}}$ and $\mathcal{T}^{(2)} = {\mathcal{C}^{(2,2)}}^{-\frac{1}{2}}$, i.e. the principal square root matrices of ${\mathcal{C}^{(1,1)}}^{-1}$ and ${\mathcal{C}^{(2,2)}}^{-1}$, respectively, where the inverses are guaranteed to exist if an appropriate

*The PCA is mathematically defined as an orthogonal linear transformation that transforms the data to a new coordinate system such that the greatest variance by any projection of the data comes to lie on the first coordinate (called the first principal component), the second greatest variance on the second coordinate, and so on. The low-order components often contain the "most important" aspects of the data and keeping only them, we can reduce the dimension of the system.

embedding is performed. Clearly, the estimated correlation matrix $\mathcal{R}$ for the $\mathbf{Z}$ trajectory turns out to be

$$\mathcal{R} = \begin{bmatrix} I & {\mathcal{T}^{(1)}}^T \mathcal{C}^{(1,2)} \mathcal{T}^{(2)} \\ {\mathcal{T}^{(2)}}^T {\mathcal{C}^{(1,2)}}^T \mathcal{T}^{(1)} & I \end{bmatrix} = \begin{bmatrix} I & \mathcal{R}^{(1,2)} \\ {\mathcal{R}^{(1,2)}}^T & I \end{bmatrix}, \tag{3.39}$$

which can then be used, through Eq. (3.26), to correctly quantify the interdependence between the two sub-systems. If the two sub-systems are uncorrelated, $\mathcal{R}^{(1,2)} = 0$, $\mathcal{R}$ will be diagonal, and $E = \log(n^{(1)} + n^{(2)})$, while if the two sub-systems are perfectly correlated, $\mathcal{R}^{(1,2)}$ will have ones on the main diagonal and zeros elsewhere. Under this "identical" case, the entropy of the normalized eigenvalues will depend on the embedding dimensions ($n^{(1)}$ and $n^{(2)}$). There is no closed formula to compute it, though it can be easily computed numerically and let us denote E_{min}. Knowing the extremes, we can finally rearrange Eq. (3.27) as

$$S^{(1,2)} = \frac{\log(n^{(1)} + n^{(2)}) - E}{\log(n^{(1)} + n^{(2)}) - E_{min}}, \tag{3.40}$$

getting a measure proportional to the amount of interdependencies and ranging from 0 to 1. Clearly, this procedure can be extended to estimate the whole cooperativeness within M interacting dynamical sub-systems.

- PCA based embedding method:
For each of the M observations $o^{(i)}$, first, a Toeplitz like matrix $TT^{(i)}$ is created from a de-trended to zero mean and normalized to unitary variance observation signal, $\tilde{o}_t^{(i)} = (o_t^{(i)} - \bar{o}_t^{(i)})/\sigma_{o_t^{(i)}}$,

$$TT^{(i)} = \begin{bmatrix} \tilde{o}_0^{(i)} & \tilde{o}_1^{(i)} & \tilde{o}_2^{(i)} & \cdots & \tilde{o}_{K-3}^{(i)} & \tilde{o}_{K-2}^{(i)} & \tilde{o}_{K-1}^{(i)} \\ \tilde{o}_1^{(i)} & \tilde{o}_2^{(i)} & \tilde{o}_3^{(i)} & \cdots & \tilde{o}_{K-2}^{(i)} & \tilde{o}_{K-1}^{(i)} & \tilde{o}_K^{(i)} \\ \tilde{o}_2^{(i)} & \tilde{o}_3^{(i)} & \tilde{o}_4^{(i)} & \cdots & \tilde{o}_{K-1}^{(i)} & \tilde{o}_K^{(i)} & \tilde{o}_{K+1}^{(i)} \\ \vdots & \vdots & \vdots & \ddots & \vdots & \vdots & \vdots \\ \tilde{o}_{L-(K+1)}^{(i)} & \tilde{o}_{L-K}^{(i)} & \tilde{o}_{L-(K-1)}^{(i)} & \cdots & \tilde{o}_{L-4}^{(i)} & \tilde{o}_{L-3}^{(i)} & \tilde{o}_{L-2}^{(i)} \\ \tilde{o}_{L-K}^{(i)} & \tilde{o}_{L-(K-1)}^{(i)} & \tilde{o}_{L-(K-2)}^{(i)} & \cdots & \tilde{o}_{L-3}^{(i)} & \tilde{o}_{L-2}^{(i)} & \tilde{o}_{L-1}^{(i)} \end{bmatrix}, \tag{3.41}$$

where, K is the row size of $TT^{(i)}$ and is decided as the first maximum of the self mutual information. Using $n^{(i)}$ eigenvectors $\mathbf{w}^{(i)}$, corresponding to the $n^{(i)}$ largest eigenvalues (Here the sum of these largest eigenvalues > 0.995, and the number of these eigenvalues = embedding dimension.) of the autocorrelation matrix of $TT^{(i)*}$, the sub-state-space $\mathbf{y}^{(i)}$ is obtained as,

$$\mathbf{y}^{(i)} = TT^{(i)} * \mathbf{w}^{(i)}. \tag{3.42}$$

This PCA based approach is suitable for its robustness to noise and for the orthogonality of the constructed state-space components. Here again, for window sliding, first the value of K and embedding dimension are calculated at each window, and after that, the unique values[†] are decided by taking their maximum along the time.

[*] Autocorrelation matrix $R_{ij} = C_{ij}/\sqrt{C_{ii}C_{jj}}$, where, C is the autocovariance matrix

[†] Again, for embedding dimension, the obtained results are checked manually, and comparing with the measurements, if the maximum value is due to some artifact, the lower value is taken as a unique embedding dimension.

3.6 The embedding dimension analysis

Comparing the results of the S-estimator and the new one , we remarked that the change of synchronization measure is mostly provoked by the synchronization within each model. Since this synchronization is measured by the contraction of the embedding dimension, it would be interesting to see the time evolution of the necessary embedding dimension, $ED(t)$, calculated on each window of recordings*. Conveniently, this analysis allows us to see also the complexity change of each system.

This $ED(t)$ obtained using false nearest neighbors method was already calculated during the analysis of sec. 3.4, and using eigenvalues of PCA based embedding method was calculated during the analysis of sec. 3.5. Consequently, we just need to plot these obtained $ED(t)$.

3.7 Coupling matix

To consider the structure of the interdependencies among a network of multivariate systems is an intriguing problem. Many investigations on the directional influence have been carried out in several applied sciences to understand the mechanisms of the network itself, to formalize the dynamical behavior, as well as to extract some change in features. Unfortunately, most of these methods assessing the strength and the direction of the coupling have been proposed for bivariate time series. The methods described in subsection 3.3.2 are also bivariate methods. If the two time series used in the analysis respond to a third system, some correlations can be exhibited without real causal connections and the obtained directional causalities may not indicate the real values.

Previously, my colleagues of LANOS, Oscar De Feo and Cristian Carmeli, proposed a method to estimate the strength and the direction of weak interdependencies among multivariate time series, assuming that such a network is composed of weakly coupled heterogeneous deterministic dynamical sub-systems[De Feo and Carmeli, 2004][Carmeli et al., 2004]. The approach of this method is very similar to the method proposed by Rosenblum et al. explained in subsection 3.3.2 [Rosenblum and Pikovsky, 2001][Rosenblum et al., 2002]. The only difference is that here it considers the whole dynamics instead of the reduced phase dynamics. In the thesis of Cristian Carmeli[Carmeli, 2006], the efficiency of the method was proven on artificial data, created by combining several dynamical oscillators as dynamical sub-systems of the network. It would be very interesting to apply this method to the data of anæsthetized subjects. It may confirm or disagree with the results presented in the subsec. 3.3.2, moreover it may find out new influences among systems.

In the following subsection, a detailed description of the method is given.

*This study was first initiated by Behnaz Bostanipour, supervised by myself, as a 3^{rd} year bachelor semester project. At the beginning of the project, she studied the use of the methods, namely the mutual information method for deciding the value of τ and the false nearest neighbors method deciding the value of ED, with an artificial toy model, i.e. the Lorentz system. After becoming familiar with the method, she applied it to our first anæsthetized rats data set. She did a great job, however because of the change in protocol, all the studies were redone by myself.

3.7.1 Detailed description of the method

Taking the model composed of Eqs. (3.21) and (3.22) in subsec. 3.4.1, and under the hypothesis of weak coupling, the equation governing the (i)-th dynamics can be written as,

$$\dot{\mathbf{x}}^{(i)}(t) = \boldsymbol{\mathcal{F}}_S^{(i)}(\mathbf{x}^{(i)}(t)) + \varepsilon \boldsymbol{\mathcal{F}}_C^{(i)}(\mathbf{X}(t)) + \boldsymbol{\eta}^{(i)}(t), \tag{3.43}$$

where, $\boldsymbol{\mathcal{F}}_S^{(i)} : \mathbb{R}^{d^{(i)}} \to \mathbb{R}^{d^{(i)}}$ describes the self dynamics of the sub-system (i) in the absence of interactions within the network, $\boldsymbol{\mathcal{F}}_C^{(i)} : \mathbb{R}^D \to \mathbb{R}^{d^{(i)}}$ describes the inter-sub-system interactions, the small constant ε indicates the weak couplings, and $\boldsymbol{\eta}^{(i)} \in \mathbb{R}^{d^{(i)}}$ is the (i)-th sub-vector of $\boldsymbol{\eta}$.

Under the assumption of Eq. (3.43), the average interdependencies along a given trajectory $\tilde{\mathbf{X}}(t)$ between the sub-system (i) and any other sub-system (j) can be naturally quantified as a matrix of dimension $d^{(i)} \times d^{(j)}$,

$$\mathcal{K}^{(i,j)} = \frac{1}{T} \int_0^T \varepsilon \frac{\partial \boldsymbol{\mathcal{F}}_C^{(i)}}{\partial \mathbf{x}^{(j)}} \bigg|_{\mathbf{X}=\tilde{\mathbf{X}}(\xi)} d\xi, \qquad \forall j \neq i, \quad i,j = 1,\ldots,M, \tag{3.44}$$

where T is the time horizon of the trajectory $\tilde{\mathbf{X}}(t)$. By means of a suitable arrangement of all the $\mathcal{K}^{(i,j)}$, the matrix $\mathcal{K}$ describing the connectivity within the network can be given as,

$$\mathcal{K} = \begin{bmatrix} \emptyset & \cdots & \mathcal{K}^{(1,i)} & \cdots & \mathcal{K}^{(1,j)} & \cdots & \mathcal{K}^{(1,M)} \\ \vdots & \ddots & \vdots & & \vdots & & \vdots \\ \mathcal{K}^{(i,1)} & \cdots & \emptyset & \cdots & \mathcal{K}^{(i,j)} & \cdots & \mathcal{K}^{(i,M)} \\ \vdots & & \vdots & \ddots & \vdots & & \vdots \\ \mathcal{K}^{(j,1)} & \cdots & \mathcal{K}^{(j,i)} & \cdots & \emptyset & \cdots & \mathcal{K}^{(j,M)} \\ \vdots & & \vdots & & \vdots & \ddots & \vdots \\ \mathcal{K}^{(M,1)} & \cdots & \mathcal{K}^{(M,i)} & \cdots & \mathcal{K}^{(M,j)} & \cdots & \emptyset \end{bmatrix}, \tag{3.45}$$

where the diagonal blocks represent the self-coupling, and by assumption set to zero and denoted by $\emptyset$.

In order to apply this method, we should have all the D states of $\mathbf{X}(t)$, however, as mentioned in subsec. 3.4.1, only some P observation signals $\mathbf{O}(t)$ are available for the analysis. Consequently, we need to reconstruct a state-space which is topologically equivalent to the original one.

Having $P = M$ observations available, the connectivity matrix $\mathcal{K}$ can be obtained in three steps.

1. **State-space reconstruction**
   The (i)-th observed time series denoted as $o_t^{(i)}, t = 0,\ldots,L-1$ is assumed to be only a function of $\mathbf{x}^{(i)}$, namely,
   $$o_t^{(i)} = \mathcal{G}^{(i)}(\mathbf{x}_t^{(i)}) + \boldsymbol{\nu}_t^{(i)}. \tag{3.46}$$
   Because of the weak interactions, by embedding the time series $o^{(i)}$, we can expect to obtain a state-space $\mathbf{y}^{(i)} \in \mathbb{R}^{n^{(i)}}$ that is equivalent to the original $\mathbf{x}^{(i)}$ and not the whole $\mathbf{X}$. This is done for all M measurements, getting the "mixed state-space", $\mathbf{Y} \in \mathbb{R}^N$ of the network, where $N = \sum_{i=1}^M n^{(i)}$.

The PCA based method* is applied to reconstruct the state-space since the orthogonality of the constructed state-space components is an advantage for the next two steps of identification.

2. **Self modelling**
Using this reconstructed sub-state-space $\mathbf{y}^{(i)}$ and moving to discrete time, Eq. (3.43) can be rewritten as,

$$\mathbf{y}_{t+1}^{(i)} = \boldsymbol{F}_S^{(i)}(\mathbf{y}_t^{(i)}) + \varepsilon \boldsymbol{F}_C^{(i)}(\mathbf{Y}_t) + \boldsymbol{\xi}_t^{(i)}, \tag{3.47}$$

where, again, $\boldsymbol{\mathcal{F}}_S^{(i)} : \mathbb{R}^{n^{(i)}} \to \mathbb{R}^{n^{(i)}}$ describes the self dynamics of the sub-system (i) in the absence of interactions within the network, $\boldsymbol{\mathcal{F}}_C^{(i)} : \mathbb{R}^N \to \mathbb{R}^{n^{(i)}}$ describes the inter-sub-system interactions, the small constant ε indicates the weak couplings, and $\boldsymbol{\xi}^{(i)} \in \mathbb{R}^{n^{(i)}}$ is the modelling noise.

Consider a generic reconstructed trajectory $\tilde{\mathbf{Y}}_t$ and assume that, without loss of generality, it has zero mean and $F_C^{(i)}(0) = 0$. Then, by Taylor expansion (up to the first order) about the average point of the trajectory (the origin) of the second term of Eq. (3.47), we get,

$$\mathbf{y}_{t+1}^{(i)} = \boldsymbol{F}_S^{(i)}(\mathbf{y}_t^{(i)}) + \sum_{j \neq i} \varepsilon \frac{\partial \boldsymbol{F}_C^{(i)}(\mathbf{Y})}{\partial \mathbf{y}^{(j)}} \Big|_{\mathbf{Y}=0} \mathbf{y}_t^{(j)} + \varepsilon \mathcal{O}(\|\mathbf{Y}_t\|^2) + \boldsymbol{\xi}_t^{(i)}, \tag{3.48}$$

where the $n^{(i)} \times n^{(j)}$ matrices $\varepsilon \frac{\partial \boldsymbol{F}_C^{(i)}}{\partial \mathbf{y}^{(j)}} \Big|_{\mathbf{Y}=0}$ describe the couplings directed from the $n^{(j)}$ state variables of sub-system (j) to the $n^{(i)}$ state variables of sub-system (i).

According to the hypothesis of weak interactions within the network, the second term on the right of Eq. (3.48), $\boldsymbol{\omega}_t^{(i)} = \sum_{j \neq i} \varepsilon \frac{\partial \boldsymbol{F}_C^{(i)}(\mathbf{Y})}{\partial \mathbf{y}^{(j)}} \Big|_{\mathbf{Y}=0} y_t^{(j)} + \varepsilon \mathcal{O}(\|\mathbf{Y}_t\|^2) + \boldsymbol{\xi}_t^{(i)}$ can be considered small with respect to the self-dynamics $\boldsymbol{F}_S^{(i)}(\mathbf{y}_t^{(i)})$. Therefore, given,

$$\mathbf{y}_{t+1}^{(i)} = \boldsymbol{F}_S^{(i)}(\mathbf{y}_t^{(i)}) + \boldsymbol{\omega}_t^{(i)}, \tag{3.49}$$

where $\boldsymbol{\omega}_t^{(i)}$ is considered as a small modelling noise, and neglecting its small dependence on $\boldsymbol{F}_S^{(i)}(\mathbf{y}_t^{(i)})$, the identification of $\boldsymbol{F}_S^{(i)}$ by using a least squares (in predictive sense) algorithm is carried out. Practically, for each sub-system (i), a model $\hat{\boldsymbol{F}}_S^{(i)}$ is estimated from data so as to minimize the total square prediction error, i.e.

$$\hat{\boldsymbol{F}}_S^{(i)} = \arg\min_{\boldsymbol{F}_S^{(i)}} \sum_{k=1}^{l^{(i)}-1} \left\| \mathbf{y}_k^{(i)} - \boldsymbol{F}_S^{(i)}(\mathbf{y}_{k-1}^{(i)}) \right\|^2, \tag{3.50}$$

where $\|\cdot\|$ stands for the 2-norm and $l^{(i)}$ is the number of samples available for sub-system (i) after the embedding.

For the identification of $\boldsymbol{F}_S^{(i)}$, first, a best linear estimation (in a least square sense) is obtained by Moore-Penrose inverse. This corresponds to have,

$$\boldsymbol{F}_S^{(i)}(\mathbf{y}_t^{(i)}) = A\mathbf{y}_t^{(i)} + \boldsymbol{\psi}, \tag{3.51}$$

*Described in subsection3.5.1.

where A represents the kernel of the image of $\mathbf{y}_{past}^{(i)}$ (the trajectory of the oscillator i up to time t), and $\boldsymbol{\psi}$ is the prediction error which lays in the linear null space of $\mathbf{y}_{past}^{(i)}$. If this $\boldsymbol{\psi}$ does not result to be a stationary gaussian process, it is modelled by Radial Basis Functions (RBF) as a second step. RBF provides a very flexible nonlinear model class and an efficient Matlab toolbox is available[Orr, 2001].

Finally, the identified self-model $\hat{\boldsymbol{F}}_S^{(i)}(\mathbf{y}_t^{(i)})$ is given by,

$$\hat{\boldsymbol{F}}_S^{(i)}(\mathbf{y}_t^{(i)}) = A\mathbf{y}_t^{(i)} + \hat{\boldsymbol{\psi}}(\mathbf{y}_t^{(i)}), \tag{3.52}$$

where, $\hat{\boldsymbol{\psi}}(\mathbf{y}_t^{(i)})$ is the estimated nonlinear part using RBF.

3. **Cross modelling**
Using the self-model $\hat{\boldsymbol{F}}_S^{(i)}$ estimated in the previous step, the modeling residuals $\mathbf{r}^{(i)}$ can be introduced as,

$$\mathbf{r}_t^{(i)} = \mathbf{y}_t^{(i)} - \hat{\mathbf{y}}_t^{(i)}, \tag{3.53}$$

where, $\hat{\mathbf{y}}_t^{(i)} = \hat{\boldsymbol{F}}_S^{(i)}(\mathbf{y}_{t-1}^{(i)})$ is the current state predicted on the basis of the only local past information $\mathbf{y}_{t-1}^{(i)}$. These residuals represent the dynamics unjustified by the estimated local self-models, and can be justified with the dynamical interactions within the network. According to Eq. (3.48), Eq. (3.53) can be rewritten as,

$$\mathbf{r}_{t+1}^{(i)} = \sum_{j \neq i} \varepsilon \frac{\partial \boldsymbol{F}_C^{(i)}(\mathbf{Y})}{\partial \mathbf{y}^{(j)}} \Bigg|_{\mathbf{Y}=0} \mathbf{y}_t^{(j)} + \boldsymbol{\epsilon}_t^{(i)}, \tag{3.54}$$

where, $\boldsymbol{\epsilon}_t^{(i)}$ accounts for the higher order terms of Eq. (3.48) and the modelling noise. This $\boldsymbol{\epsilon}_t^{(i)}$ is very small under the hypothesis of deterministic dynamics and weak interactions, and adding that the dependence to $\mathbf{Y}_t$ is also small, it is neglected from the consideration.

By means of a least squares linear regression (in predictive sense) over all the residual time samples, the $\hat{A}^{(i)}(n^{(i)} \times \sum_{j \neq i} n^{(j)})$ matrix is estimated as,

$$\hat{A}^{(i)} = \arg\min_{A^{(i)}} \sum_{k=1}^{min\{l^{(i)}\}-1} \left\| \mathbf{r}_k^{(i)} - A^{(i)} \mathbf{Y}_{k-1}^{(\neg i)} \right\|^2, \tag{3.55}$$

where, $\mathbf{Y}^{(\neg i)}$ is the state vector without the (i)-th sub-system components. Here a regularized ordinary least squares approach was used because of the high number of independent variables (i.e. state-space components) involved in this regression step.

As the estimated matrix $\hat{A}^{(i)} = [\hat{\mathcal{K}}^{(i,1)} \dots \hat{\mathcal{K}}^{(i,j \neq i)} \dots \hat{\mathcal{K}}^{(i,M)}]$ is the concentration of all the nonzero coupling matrices, finally, by a suitable rearrangement of the estimated

sub-blocks, the connectivity matrices $\hat{\mathcal{K}}^{(i,j)}(n^{(i)} \times n^{(j)})$ are obtained as

$$\mathcal{K} = \begin{bmatrix} \emptyset & \dots & \hat{\mathcal{K}}^{(1,i)} & \dots & \hat{\mathcal{K}}^{(1,j)} & \dots & \hat{\mathcal{K}}^{(1,M)} \\ \vdots & \ddots & \vdots & & \vdots & & \vdots \\ \hat{\mathcal{K}}^{(i,1)} & \dots & \emptyset & \dots & \hat{\mathcal{K}}^{(i,j)} & \dots & \hat{\mathcal{K}}^{(i,M)} \\ \vdots & & \vdots & \ddots & \vdots & & \vdots \\ \hat{\mathcal{K}}^{(j,1)} & \dots & \hat{\mathcal{K}}^{(j,i)} & \dots & \emptyset & \dots & \hat{\mathcal{K}}^{(j,M)} \\ \vdots & & \vdots & & \vdots & \ddots & \vdots \\ \hat{\mathcal{K}}^{(M,1)} & \dots & \hat{\mathcal{K}}^{(M,i)} & \dots & \hat{\mathcal{K}}^{(M,j)} & \dots & \emptyset \end{bmatrix}, \tag{3.56}$$

Normally, a single number $\mathcal{C}^{(i,j)}$ quantifying the influence from $o^{(j)}$ to $o^{i)}$ is more suitable than the estimated connectivity matrix $\hat{\mathcal{K}}^{(i,j)}$. For that reason, a norm of $\hat{\mathcal{K}}^{(i,j)}$ is proposed for that. Meanwhile, the elements of the connectivity matrices which may represent spurious dependencies should be set to zero. Hence a statistical procedure described below is added to the calculation of the norm.

To explain this statistical test, for the sake of simplicity, let us focus on a generic element of $\hat{\mathcal{K}}^{(i,j)}$, which, to simplify the notation, is denoted as $\hat{k}$. Thanks to the least squares procedure, the standard deviation of $\hat{k}$ can be easily obtained. Under the assumption that $\hat{k}$ is normally distributed, with mean μ and variance σ^2, the null hypothesis

$$H_0 : \mu = 0, \sigma = \hat{\sigma}$$

is tested against the alternative hypothesis

$$H_1 : \mu = \hat{k}, \sigma = \hat{\sigma}$$

From F-statistics*, the p-value is easily computed; namely, the probability of a *Type I error*, which is the probability that the null hypothesis, H_0 is wrongly rejected when it is true. Afterwards, the p-value can be used to compute the probability of a *Type II error*, i.e. the probability β that the hypothesis, H_1 is wrongly accepted when it is false. Usually, its complementary probability, $1 - \beta$, is called the "power" of the test of the hypothesis H_0 against the alternative hypothesis H_1. Under normal distribution hypothesis, the power is given by

$$1 - \beta = G\{\sqrt{L'}\hat{k}/\hat{\sigma} - z\}, \tag{3.57}$$

where, L' is the number of samples used to get the estimate $\hat{k}$, G is the standardized normal distribution function and z is such that $G(-z) = p$ holds. Fixing the threshold on the power of test of hypothesis to 0.95, that is 5% of *Type II error* is allowed, the value of $\hat{k}$ whose power computed in Eq. (3.57) exceeds this 0.95, i.e. $1 - \beta > 0.95$, is set to zero.

Finally, after repeating the same statistical procedure for all the elements of $\hat{\mathcal{K}}^{(i,j)}$, a 2-norm is applied to obtain an estimate of the influence of sub-system (j) on (i), the coupling

*For analyzing the quality of fits obtained with different parameter values, the variance of the fit (chi-square) is a very useful statistical quantity. The ratio of the chi-square of two fits is distributed like a Fisher (F) distribution. Therefore, this distribution can be used to judge if a given variance increase (e.g. after change of a parameter value) has a magnitude in a range that could occur just by statistical error in the data (assuming normally distributed noise), or if the variance increase is significant.

matrix $\mathcal{C}$.

$$\mathcal{C} = \begin{bmatrix} 0 & \dots & c^{(1,i)} & \dots & c^{(1,j)} & \dots & c^{(1,M)} \\ \vdots & \ddots & \vdots & & \vdots & & \vdots \\ c^{(i,1)} & \dots & 0 & \dots & c^{(i,j)} & \dots & c^{(i,M)} \\ \vdots & & \vdots & \ddots & \vdots & & \vdots \\ c^{(j,1)} & \dots & c^{(j,i)} & \dots & 0 & \dots & c^{(j,M)} \\ \vdots & & \vdots & & \vdots & \ddots & \vdots \\ c^{(M,1)} & \dots & c^{(M,i)} & \dots & c^{(M,j)} & \dots & 0 \end{bmatrix}, \tag{3.58}$$

At the end, as the previous "S estimator" method, the sliding window method is added to the whole analysis. As a results, for each window the coupling matrix $\mathcal{C}$ is calculated and the time evolution of this matrix $\mathcal{C}(t)$ is obtained.

3.8 Nonparametric Granger Causality

Close to the end of my thesis, we began to collaborate with Mukeshwar Dhamala, assistant professor of Georgia State University in United State. One of his interests is to identify the connectivity among physiological signals, especially brain signals, and he found our project on the interactions of brain and cardio-respiratory systems during anesthesia very interesting. He proposed us to look at the directed interactions among brain and cardio-respiratory systems using his recently developed nonparametric Granger causality method [Dhamala et al., 2008].

The Granger causality was proposed in 1969 [Granger, 1969] and recently has emerged as a leading statistical technique for extracting information flow in networks of coupled dynamical systems from the time series measurements of their activity. The definition of this Granger causality is based on the theory of linear prediction and its original estimation framework requires autoregressive (AR) modeling of time series data. Unfortunately, this parametric modeling methods often encounter difficulties such as uncertainty in model parameters and inability to fit data with complex spectral contents. To overcome this problem, our partner proposed a nonparametric approach to estimate the Granger causality from Fourier transforms of data, eliminating the need of explicit AR modeling. As the coupling matrix method proposed in the previous section is a parametric method, it will be interesting to compare results obtained by both methods.

In this section, first, the method is described in details including the parametric Granger causality. And then, for this method*, a permutation test that allows us to remove the false causality is described. The idea of this test is the same as the test of significance using surrogate data that is described in subsec. 3.3.2.

3.8.1 Detailed description of the method

First, for convenience, we start with the parametric approach.

*The coupling matrix method has very heavy computation such that permutation tests were impossible to realize.

- Granger causality with parametric estimation approach:
Consider two simultaneously recorded time series from two stationary stochastic processes ($\mathbf{X_1}$,$\mathbf{X_2}$).

$$\mathbf{X_1} = \begin{bmatrix} x_1(1) \\ x_1(2) \\ \vdots \\ x_1(t) \\ \vdots \end{bmatrix}; \mathbf{X_2} = \begin{bmatrix} x_2(1) \\ x_2(2) \\ \vdots \\ x_2(t) \\ \vdots \end{bmatrix}; \tag{3.59}$$

Using AR representations, we can construct bivariate linear prediction models for $x_1(t)$ and $x_2(t)$:

$$x_1(t) = \sum_{k=1}^{\infty} b_{11,k} x_1(t-k) + \sum_{k=1}^{\infty} b_{12,k} x_2(t-k) + \epsilon_{1|2}(t) \tag{3.60}$$

$$x_2(t) = \sum_{k=1}^{\infty} b_{21,k} x_1(t-k) + \sum_{k=1}^{\infty} b_{22,k} x_2(t-k) + \epsilon_{2|1}(t) \tag{3.61}$$

along with the univariate models:

$$x_1(t) = \sum_{k=1}^{\infty} \alpha_k x_1(t-k) + \epsilon_1(t) \tag{3.62}$$

$$x_2(t) = \sum_{k=1}^{\infty} \beta_k x_2(t-k) + \epsilon_2(t). \tag{3.63}$$

Here, ϵ are the prediction errors.

If $var(\epsilon_{1|2}(t)) < var(\epsilon_1)$ in some suitable statistical sense, then $\mathbf{X_2}$ is said to have a causal influence on $\mathbf{X_1}$. Similarly, if $var(\epsilon_{2|1}(t)) < var(\epsilon_2)$, then there is a causal influence from $\mathbf{X_1}$ to $\mathbf{X_2}$. These causal influences are quantified in time domain by

$$F_{j \to i} = \ln \frac{\mathrm{var}(\epsilon_i(t))}{\mathrm{var}(\epsilon_{i|j}(t))}, \tag{3.64}$$

where, $i = 1, 2$ and $j = 2, 1$.

As experimental processes are often rich in oscillatory content, it is natural to proceed to spectral analysis. The spectral decomposition of Granger's time domain causality was proposed by Geweke in 1982[Geweke, 1982].

To derive the frequency domain Granger causality, Eq. 3.62, 3.63 are rewritten in a matrix form with a lag operator $L : Lx(t) = x(t-1)$ as

$$\begin{pmatrix} b_{11}(L) & b_{12}(L) \\ b_{21}(L) & b_{22}(L) \end{pmatrix} \begin{pmatrix} x_1(t) \\ x_2(t) \end{pmatrix} = \begin{pmatrix} \epsilon_{1|2} \\ \epsilon_{2|1} \end{pmatrix}, \tag{3.65}$$

where,

$$b_{ij}(L) = \sum_{k=0}^{\infty} b_{ij,k} L^k \tag{3.66}$$

with $b_{ij,0} = \delta_{ij}$ (the Kronecker delta function). The covariance matrix of the noise term is

$$\mathbf{\Sigma} = \begin{pmatrix} \Sigma_{11} & \Sigma_{12} \\ \Sigma_{21} & \Sigma_{22} \end{pmatrix} \tag{3.67}$$

where, $\Sigma_{11} = \text{var}(\epsilon_{1|2})$, $\Sigma_{12} = \Sigma_{21} = \text{cov}(\epsilon_{1|2}, \epsilon_{2|1})$, and $\Sigma_{22} = \text{var}(\epsilon_{2|1})$. Fourier transforming Eq. 3.65 yields

$$\begin{pmatrix} B_{11}(f) & B_{12}(f) \\ B_{21}(f) & B_{22}(f) \end{pmatrix} \begin{pmatrix} X_1(f) \\ X_2(f) \end{pmatrix} = \begin{pmatrix} E_1(f) \\ E_2(f) \end{pmatrix}, \tag{3.68}$$

where the components of the coefficient matrix $[B_{ij}(f)]$ are

$$B_{lm}(f) = \delta_{lm} - \sum_{k=1}^{\infty} b_{lm,k} e^{-i2\pi fk}. \tag{3.69}$$

In terms of transfer function matrix ($\mathbf{H}(f) = [B_{ij}(f)]^{-1}$), Eq. 3.68 becomes

$$\begin{pmatrix} X_1(f) \\ X_2(f) \end{pmatrix} = \begin{pmatrix} H_{11}(f) & H_{12}(f) \\ H_{21}(f) & H_{22}(f) \end{pmatrix} \begin{pmatrix} E_1(f) \\ E_2(f) \end{pmatrix}. \tag{3.70}$$

Then, the spectral density matrix $\mathbf{S}(f)$ is given by

$$\mathbf{S}(f) = \mathbf{H}(f)\mathbf{\Sigma}\mathbf{H}^*(\mathbf{f}), \tag{3.71}$$

where, $*$ denotes matrix adjoint.

To examine the causal influence from X_2 to X_1, we need to look at the auto-spectrum of $x_1(t)$-series, which is

$$S_{11}(f) = H_{11}\Sigma_{11}H_{11}^* + 2\Sigma_{12}\text{Re}(H_{11}H12^*) + H_{12}\Sigma_{22}H_{12}^*. \tag{3.72}$$

Here, because of the cross-terms in this expression for S_{11}, the causal power contribution is not obvious. Therefore, Geweke [Geweke, 1982] introduced a transformation that eliminates the cross terms and makes an intrinsic power term and a causal power term identifiable. For X_1-process, this transformation is achieved by left-multiplying Eq. 3.68 on both sides with at the auto-spectrum of $x_1(t)$-series, which is

$$\begin{pmatrix} 1 & 0 \\ -\Sigma_{12}/\Sigma_{11} & 1 \end{pmatrix}, \tag{3.73}$$

which yields:

$$\begin{pmatrix} B_{11}(f) & B_{12}(f) \\ \tilde{B}_{21}(f) & \tilde{B}_{22}(f) \end{pmatrix} \begin{pmatrix} X_1(f) \\ X_2(f) \end{pmatrix} = \begin{pmatrix} E_1(f) \\ \tilde{E}_2(f) \end{pmatrix}, \tag{3.74}$$

where,

$$\tilde{B}_{21}(f) = B_{21}(f) - \frac{\Sigma_{12}}{\Sigma_{11}} B_{11}(f) \tag{3.75}$$

$$\tilde{B}_{22}(f) = B_{22}(f) - \frac{\Sigma_{12}}{\Sigma_{11}} B_{12}(f) \tag{3.76}$$

$$\tilde{E}_2(f) = E_2(f) - \frac{\Sigma_{12}}{\Sigma_{11}} E_1(f). \tag{3.77}$$

The elements of the new transfer function $\tilde{\mathbf{H}}(f)$ then become

$$\tilde{\mathbf{H}}(f) = \begin{pmatrix} \tilde{H}_{11}(f) & H_{12}(f) \\ \tilde{H}_{21}(f) & H_{22}(f) \end{pmatrix} = \begin{pmatrix} H_{11}(f) + \frac{\Sigma_{12}}{\Sigma_{11}} H_{12}(f) & H_{12}(f) \\ H_{21}(f) + \frac{\Sigma_{12}}{\Sigma_{11}} H_{22}(f) & H_{22}(f) \end{pmatrix}. \tag{3.78}$$

Here,

$$\tilde{\Sigma}_{12} = \tilde{\Sigma}_{21} = \mathrm{cov}(E_1, \tilde{E}_2) = 0 \tag{3.79}$$

and the new variance of $x_2(t)$ is

$$\tilde{\Sigma}_{22} = \Sigma_{22} - \frac{{\Sigma_{12}}^2}{\Sigma_{11}}. \tag{3.80}$$

Owing to this transformation, the auto-spectrum of $x_1(t)$ is now decomposed into two obvious parts:

$$S_{11}(f) = \tilde{H}_{11}\Sigma_{11}\tilde{H}_{11}^* + H_{12}\tilde{\Sigma}_{22}H_{12}^*, \tag{3.81}$$

where, the first term accounts for the intrinsic power of $x_1(t)$ and the second term for causal power due to the influence from X_2 to X_1. Since Granger causality is the natural logarithm of the ratio of total power to intrinsic power [Granger, 1969], causality from X_2 to X_1 is obtained as:

$$I_{2\to1}(f) = \ln \frac{S_{11}(f)}{S_{11}(f) - \tilde{\Sigma}_{22}|H_{12}(f)|^2}. \tag{3.82}$$

Similarly, the Granger causality $I_{1\to2}(f)$ from X_1 to X_2 is obtained by taking the transformation matrix as

$$\begin{pmatrix} 1 & -\Sigma_{12}/\Sigma_{22} \\ 0 & 1 \end{pmatrix}. \tag{3.83}$$

Furthermore, the time-domain Granger causality is obtained as

$$F_{2\to1} = \frac{1}{2\pi}\int_{-\pi}^{\pi} I_{2\to1}(f)df. \tag{3.84}$$

- Granger causality with nonparametric estimation approach:
Consider a bivariate process with time series $x_1(t)$ and $x_2(t)$. Let's denote $X_1(f)$ and $X_2(f)$ their Fourier transforms. Then, by using directly the Fourier transform of time series data, the spectral density matrix $\mathbf{S}(f)$ is obtained as

$$\mathbf{S}(f) = \begin{pmatrix} S_{11} & S_{12} \\ S_{21} & S_{22} \end{pmatrix}, \tag{3.85}$$

where, $S_{lm} = \langle X_l(f)X_m(f)^* \rangle$, and $\langle\cdot\rangle$ is the averaging over multiple realizations. This $\mathbf{S}(f)$ can be factored into a set of unique minimum-phase functions:

$$\mathbf{S} = \boldsymbol{\psi}\boldsymbol{\psi}^*, \tag{3.86}$$

where, * denotes matrix adjoint,

$$\boldsymbol{\psi}(e^{i\theta}) = \sum_{k=0}^{\infty} \mathbf{A}_k e^{ik\theta} \tag{3.87}$$

is defined on the unit circle $|z| < 1$, and

$$\mathbf{A}_k = (1/2\pi) \int_{-\pi}^{\pi} \boldsymbol{\psi}(e^{i\theta}) e^{-ik\theta} d\theta. \tag{3.88}$$

Moreover, $\boldsymbol{\psi}$ can be holomorphically extended to the inner disk $|z| < 1$ as

$$\boldsymbol{\psi}(z) = \sum_{k=0}^{\infty} \mathbf{A}_k z^k \tag{3.89}$$

where $\boldsymbol{\psi}(0) = \mathbf{A}_0$, a real, upper triangular matrix with positive diagonal elements. Similarly S and H can be defined as functions of z with $H(0) = I$. More precisely, comparing the right hand sides of Eq. 3.71 and Eq. 3.86 at $z = 0$, we get

$$\boldsymbol{\Sigma} = \mathbf{A}_0 \mathbf{A}_0^T. \tag{3.90}$$

Rewriting Eq. 3.86 as

$$\mathbf{S} = \boldsymbol{\psi} \mathbf{A}_0^{-1} \mathbf{A}_0 \mathbf{A}_0^T \mathbf{A}_0^{-T} \boldsymbol{\psi}^*, \tag{3.91}$$

and comparing with Eq. 3.71 and 3.86, we arrive at the expression for the transfer function:

$$\mathbf{H} = \boldsymbol{\psi} \mathbf{A}_0^{-1} \tag{3.92}$$

Now, by substituting the specific elements of the noise covariance and transfer function from Eq. 3.90 and 3.92 into Eq. 3.82, one can estimate pairwise Granger causality spectra. Here again, the sliding window method is employed to see the evaluation in time.

3.8.2 Permutation test

The purpose of this permutation test is to detect the level of background noise in order to select the significant Granger causality from the obtained results. The procedure of this test is the following: The first step is to pick 10-minute time series out of all the measurements. The second step is to create windows and segments out of the extracted a 10-minute time series with the same length used for the analysis of GC (mentioned as multiple realizations). Third, at each group of measurements, create a pool putting all the segments created in the step two. Then, the step four is to pick up randomly, from the pool created in step three, the segments that need to calculate GC for the decided window length and calculate the GC as one permutation test and retain its maximum value. This step four (randomization) is repeated 1000 times. The last step is to plot a histogram of the obtained 1000 maximum values and fit it with a gamma function, and then assign the value of GC which has the value of the fitted gamma function equals to 0.01 as the criteria of the analysis.

3.9 Results of our Analysis on Rats recordings

3.9.1 Rats1

Before all the analysis except nonparametric Granger causality, all the measurements were preprocessed, i.e. a 50Hz component was filtered out to remove the effect of the power supply of the measuring systems, and frequency components superior to 100Hz were filtered out since they were considered as measurement noise. For nonparametric GC, all the measurements were also preprocessed, but here, frequency components superior to 45Hz were filtered out. Moreover, the sampling frequency is down-sampled to 200Hz.

S-estimator

In order to decide the window length for the analysis, we began to analyze with the recordings of Rats1-9, that is specially reported in [Musizza et al., 2007].

From [Musizza et al., 2007], the slowest frequency of the ECG f_h is around 4Hz, and for the respiration f_r is around 1Hz. Moreover the range of the EEG that we are interested in is δ- and θ-waves, whose lower bound is 0.5Hz. Accordingly, the window length, l, for the sliding window method was first fixed to 2.5sec (2500 samples) in order to have at least one cycle of these signals, and after that we tried with longer windows, i.e. 5sec, 7.5sec, 10sec, 12.5sec and 15sec. Meanwhile, for the length of shifting, 0.5sec was chosen in order to be able to detect a sudden change in the value of $S(t)$.

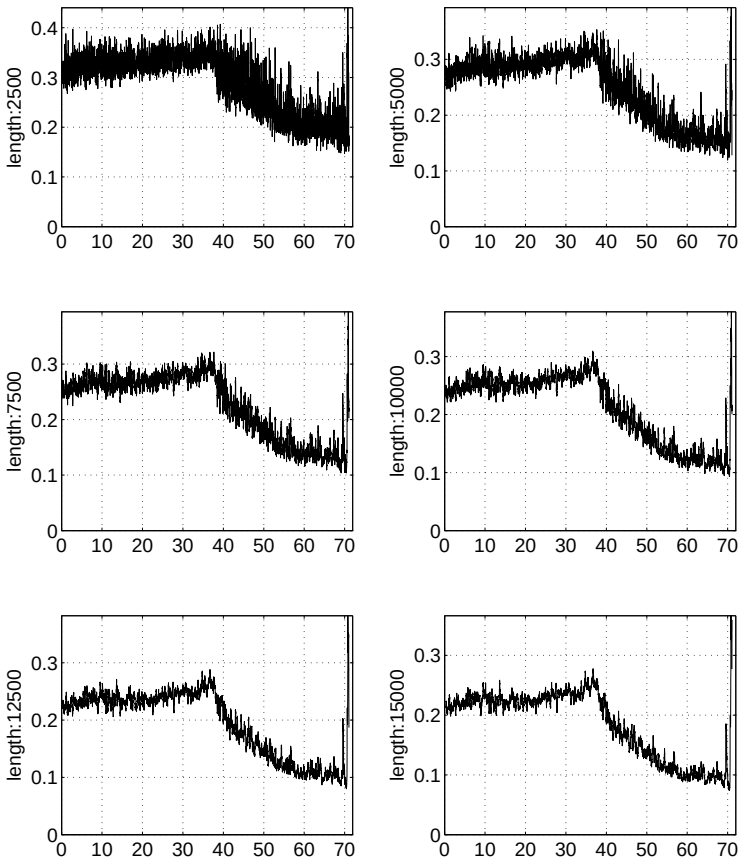

Figure 3.13 – *Synchronization measure $S(t)$ obtained by clustering three oscillators (ECG, Respiration and EEG) together on Rats1-9 using different window lengths. Horizontal axis is time (min).*

As we can see in Fig. 3.13, the longer the window length, the less effect of noise can be observed. However, longer window length results in heavy computation such that it does not fit to our purpose of real time detection. Thereby, in this work, 10sec of window length was chosen for the analysis.

Now, using the defined window length, we proceeded to the choice of the embedding dimension (ED) and time delay (τ). As mentioned in subsec. 3.4.1, we calculated these ED

and τ for all windows and took the maximum along the time for ED and took the mean for τ. However, if the maximum ED results from an artifact, smaller ED was manually chosen instead. Here is the table of the ED and τ used in this work.

Rats No: Rats1-		1	2	3	4	5	6	7	8	9	10
ED	ECG	8	10	8	7	6	8	10	8	8	8
	Resp	4	4	4	4	5	4	4	5	4	4
	EEG	7	7	7	7	7	7	7	7	7	7
τ	ECG	9	10	11	9	11	10	10	9	9	8
	Resp	33	28	24	24	30	29	25	31	25	41
	EEG	13	19	16	19	18	18	18	16	15	18

Table 3.3 – *Embedding dimension (ED) and time delay (τ(samples)) used in the studies.*

In Fig. 3.14, the synchronization measures obtained, for all the measurements in measurement group "Rats1", using the window length, shifted time, embedding dimension and time delay defined just before are shown. The values of $S(t)$ seems to increase slightly at the beginning for some rats, but suddenly begins to decrease for all rats. The beginning points of this decrease coincidence mostly with the results of [Musizza et al., 2007]. Consequently it seems appropriate to designate this point as the point of deep-light change of anæsthesia.

Here, we should remark that observing this real time plot of $S(t)$, we need at least more than 10 minutes to visually detect in real time the point of deep-light change in anæsthesia. So in order to detect numerically this point as precisely and quickly as possible, we add a statistical assessment which calculates a value p.

The statistical assessment:

Employing the obtained $S(t)$, we tested on two sets of samples/windows of 30 seconds length (60 samples) that were separated by 8 minutes (960 samples) of interval and moved them along the time axis. In this way, it is possible to detect the first pair where the second set statistically differs from the first set which is 8 min. in the past. In principle one could decide that a change has taken place as soon as a p-value below a certain threshold, typically, $p < 0.02$ has been detected. However, because of the effect of noise and small variabilities of the system, such p-values are encountered even before the change takes place. Therefore, we are obliged to look for a certain number of consecutive p-values below threshold. Practically, we traced the obtained p value along the time and checked the p-values smaller than 0.02. The point which we are interested in is the beginning of the longest sequence of p-values below threshold. This beginning point can be obtained precisely after the measurements (off-line) , and shown in fig. 3.15 with red markers. However our goal is to detect this point in real time. In this case we are obliged to have a delay in automatic detection. How long/How many p-values can be determined by examining the sequence of p-values of the time-series where we knows the point of change. The length/number must be longer/larger than the longest sequence of consecutive p-values below threshold before the change. For this data group "Rats1", the delay was 5.13 minutes and the obtained numerically detected point are also shown in fig. 3.15 with blue markers. Here below, the summary of the detection time is shown. From this table 3.4, we can remark that we succeeded to detect faster in time than our previous colleagues' work [Musizza et al., 2007] on 8/10 rats. Moreover, we succeeded to be much more precise on time and we think that

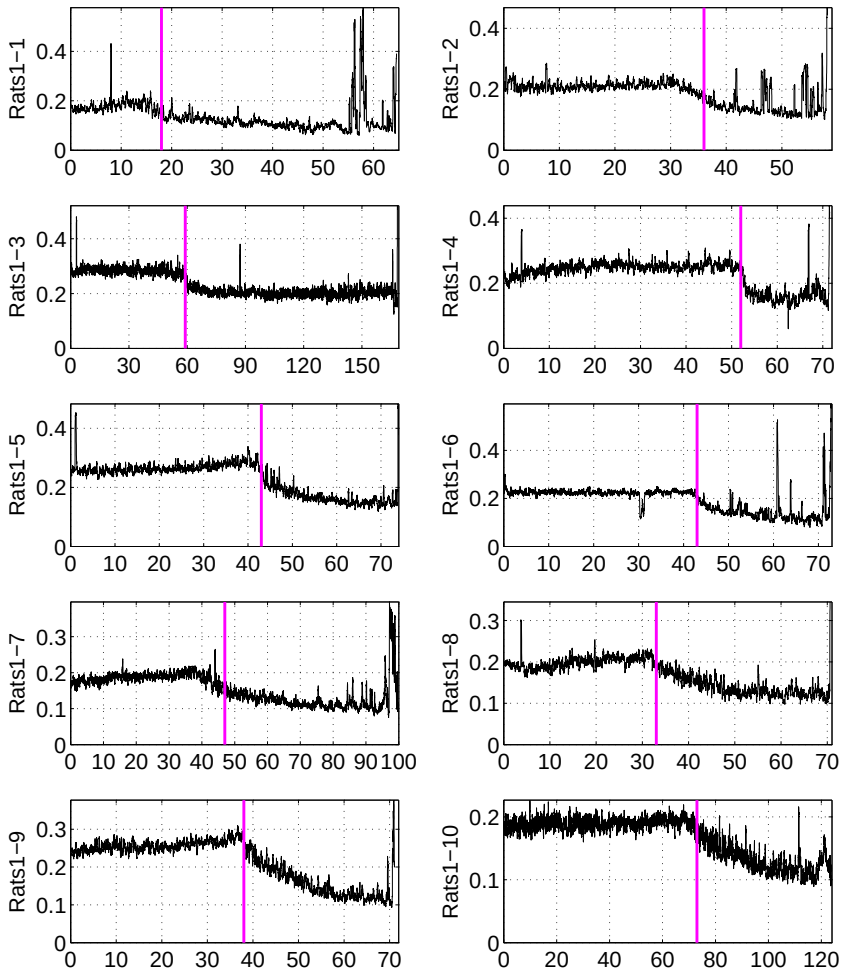

Figure 3.14 – *Synchronization measure $S(t)$ obtained by clustering three oscillators (ECG, Respiration and EEG) together on group "Rats1". Horizontal axis is time (min). The magenta lines indicate the deep-light change of anæsthesia detected in [Musizza et al., 2007]*

Rats No:	1	2	3	4	5	6	7	8	9	10
Musizza 2007	17±4	36±5	60±2	52±4	46±2	43±3	45±3	34±5	38±5	76±4
detected at	**16.3**	**32.6**	**57.6**	52.1	**42.7**	**42.1**	**44.4**	**32.5**	38.2	**72.0**
mini. delay	5.13	1.93	3.15	3.02	4.31	2.23	4.61	3.77	4.08	3.16

Table 3.4 – *Summary of the detected change (min) in anæsthesia and its corresponding minimum delay (min) for the subjects. The bold numbers indicates faster detection than in Musizza's work.*

we realized the automatic detection much faster than simple use of the S-estimator.

To evaluate the robustness of the statical detection, we changed the parameters, i.e., the window length, the interval length and the decision threshold, and calculated the p-value. To test the window length, the interval was fixed to 8 minutes and the decision threshold was fixed to 0.02.

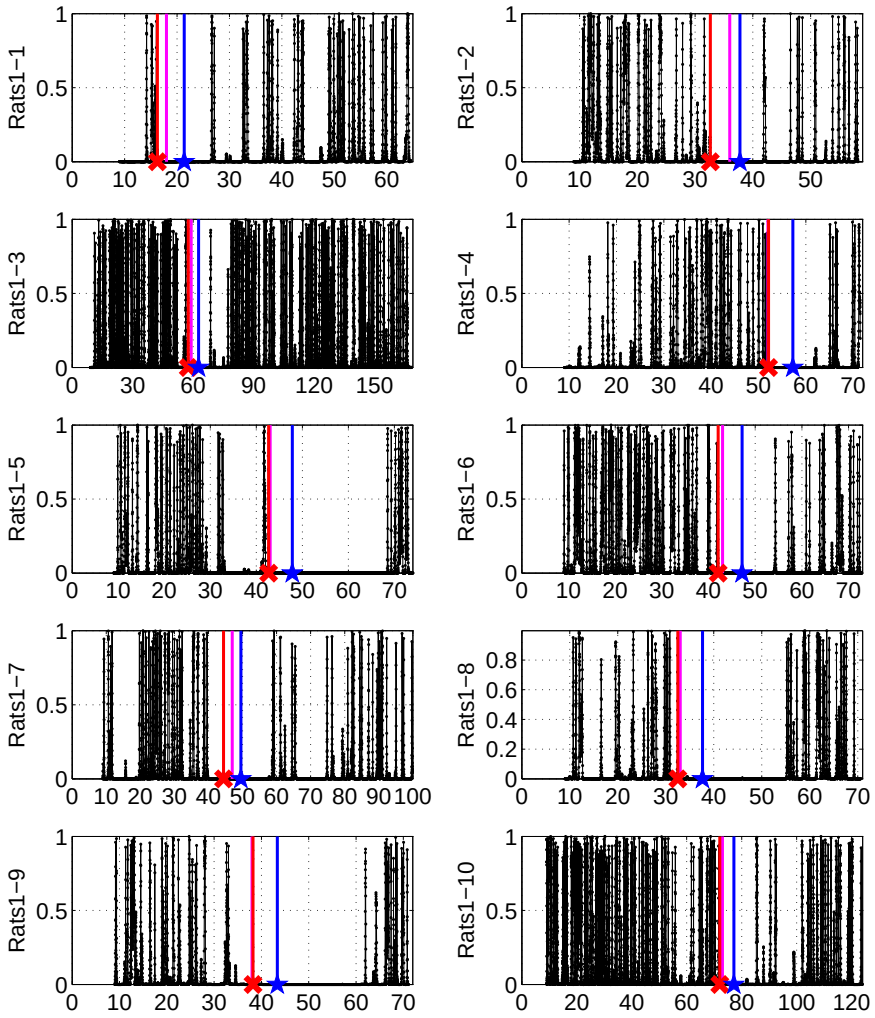

Figure 3.15 – *Statistical assessment value $p(t)$ of obtained S estimator on group "Rats1". Horizontal axis is time (min). The magenta lines indicate the deep-light change of anæsthesia detected in [Musizza et al., 2007]. The red lines with the crosses indicate the deep-light change detected by us (detected from the sequence of p-values below threshold). The blue lines with the stars indicate the auto-detected change point.*

Window length (sec)	5	15	20	30	60	120
detected at	40.55	39.55	39.6	**38.23**	38.54	39.02
mini. delay	2.14	3.28	3.28	**4.08**	7.2	15.18

Table 3.5 – *Summary of the detected change (min) in anæsthesia and its corresponding minimum delay (min) for Rats1-9 calculated using different window lengths. The bold numbers are chosen parameters results.*

From table. 3.5, we can remark that a good choice of the window length is necessary since the detected point can be changed more than 2 minutes. Moreover, we should not choose

a too large window length, otherwise the delay becomes too big. To test the interval, the window length was fixed to 30 seconds and the decision threshold was fixed to 0.02.

Interval (min)	4	6	8	10	12	14
detected at	38.41	38.45	**38.23**	38.35	39.95	38.51
mini. delay	3.37	3.12	**4.08**	8.91	5.57	6.09

Table 3.6 – *Summary of the detected change (min) in anæsthesia and its corresponding minimum delay (min) for Rats1-9 calculated using different intervals. The bold numbers are chosen parameters results.*

From table. 3.6, we can remark that the choice of the interval length is not so critical as the choice of the window length. But again, a too long interval results in a large delay. To test the interval, the window length was fixed to 30 seconds and the interval was fixed to 8 minutes.

Threshold	0.01	0.015	0.02	0.025	0.03	0.035	0.04	0.045	0.05
detected at	38.24	38.24	**38.23**	38.23	38.23	38.23	38.23	38.23	38.23
min. delay	4.05	4.06	**4.08**	4.08	4.08	4.09	4.10	4.10	4.11

Table 3.7 – *Summary of the detected change (min) in anæsthesia and its corresponding minimum delay (min) for Rats1-9 calculated using different decision threshold. The bold numbers are chosen parameters results.*

From table. 3.7, we can remark that the choice of this decision threshold is not critical at all and it has quite a wide range of choice.

Here again, The results of S-estimator with our detected points are shown in Fig. 3.16.

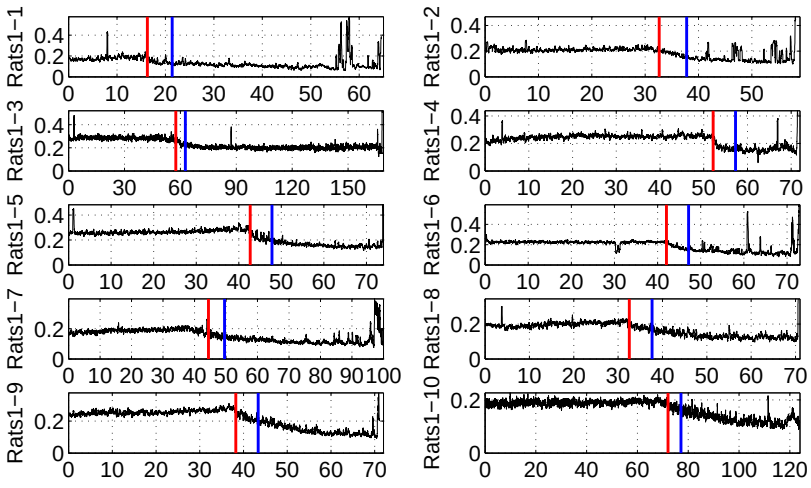

Figure 3.16 – *Synchronization measure $S(t)$ obtained by clustering three oscillators (ECG, Respiration and EEG) together on group "Rats1". Horizontal axis is time (min). The red lines indicate the deep-light change of anæsthesia detected by us. And the blue lines indicate the numerical auto-detected point.*

Also, we performed the S-estimator on sets of two sub-systems and the obtained results are shown in Fig. 3.17.

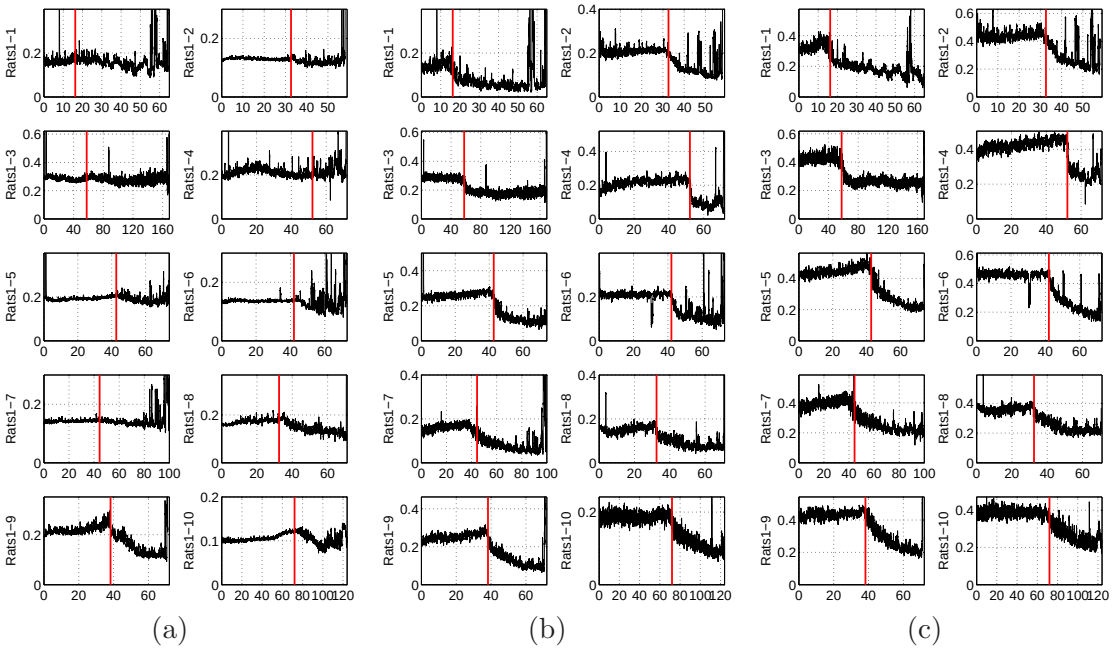

Figure 3.17 – *Synchronization measure $S(t)$ obtained by clustering two chosen oscillators together on group "Rats1". Horizontal axis is time (min). The red lines indicate the deep-light change of anæsthesia detected by us: (a) ECG and Respiration, (b) ECG and EEG, and (c) Respiration and EEG.*

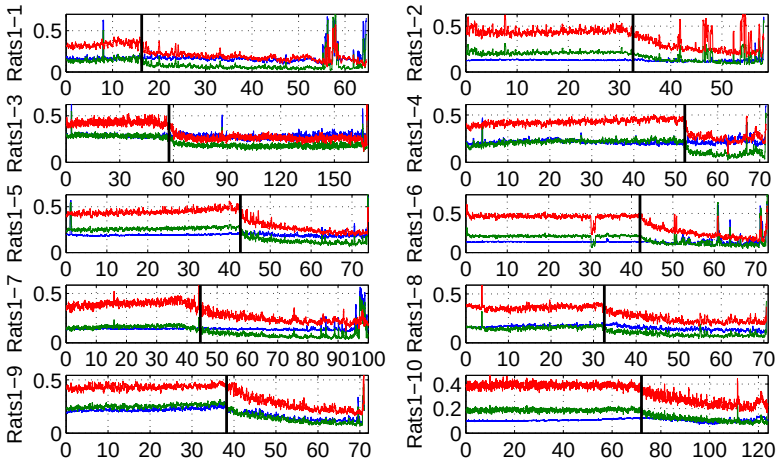

Figure 3.18 – *Comparison of the strength of $S(t)$ obtained by clustering two chosen oscillators together on group "Rats1". Horizontal axis is time (min). The black lines indicate the deep-light change of anæsthesia detected by us: (blue) ECG and Respiration, (green) ECG and EEG, and (red) Respiration and EEG.*

From Fig. 3.17, almost all $S(t)$ obtained with different clusters shows a sudden decrease at the detected change point of anæsthesia. However we can remark on the results obtained with the cluster of ECG and Respiration that the change at the point is not so remarkable in some rats. Furthermore, we observed that the synchronization between Respiration and EEG was the strongest (See Fig. 3.18).

new S-estimator

Now, let's move to the new S-estimator. As we mentioned in subsec. 3.5.1, the S-estimator includes the internal state synchronization such that the strength of the synchronization calculated previously (see Fig. 3.16 and 3.17) may not be correct when considering the synchronization exclusively between different systems.

In Fig. 3.19, we show the obtained results with the new S-estimator. From this Fig. 3.19, we can remark that there is no clear change in signal $S_{new}(t)$ at the change point in anæsthesia. Moreover the strength of the synchronization became about ten times smaller than the original S-estimator. Nevertheless, interestingly, we can remark a little higher synchronization at the moment close to the change point on 7/10 rats' results.

In Fig. 3.20, we plotted the results obtained with other clusters taking two sub-systems. From Fig. 3.20 (a), Rats1-1, Rats1-4 and Rats1-8 show high synchronization between ECG and Respiration, and moreover Rats1-8 shows clear change at the change point. However, looking generally at the results of (a), we cannot conclude anything. In (b), except Rats1-5 which shows clear change, it stays nearly constant at very low values. For (c), as we saw in Fig. 3.19, a little higher synchronization can be observed at the moment close to the

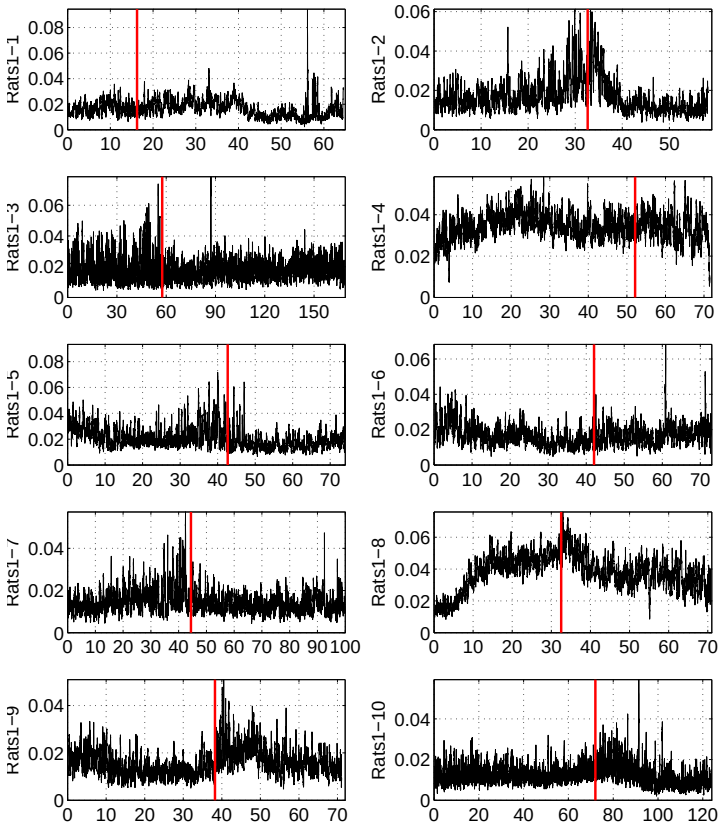

Figure 3.19 – *new Synchronization measure $S_{new}(t)$ obtained by clustering three oscillators (ECG, Respiration and EEG) together on group "Rats1". Horizontal axis is time (min). The red lines indicate the deep-light change of anæsthesia detected by us.*

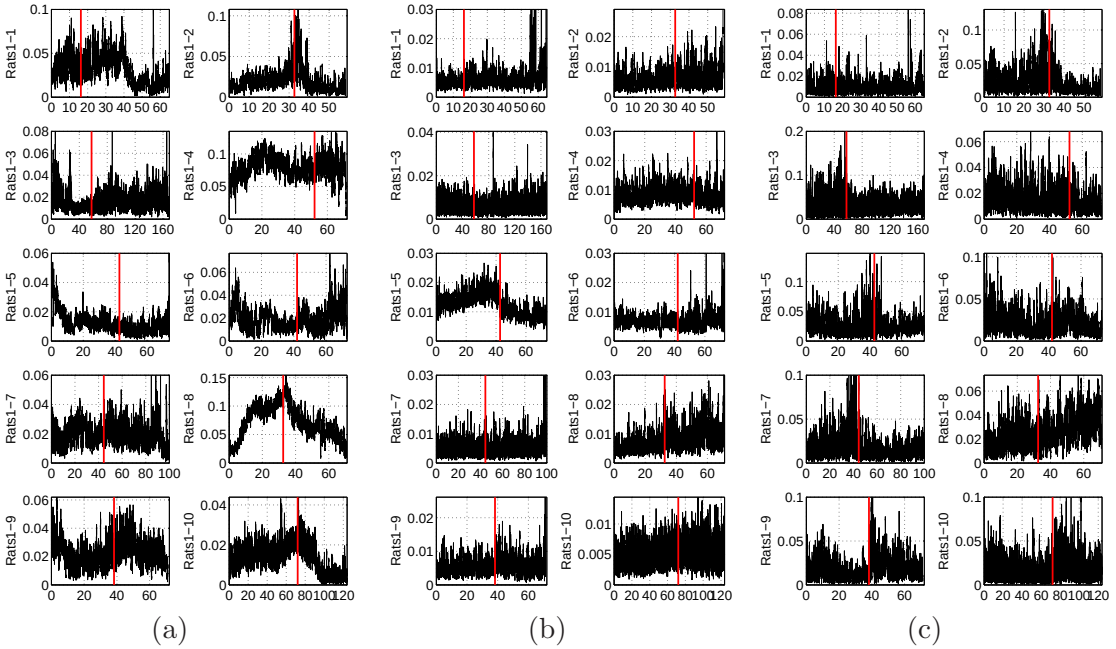

Figure 3.20 – *Synchronization measure $S_{new}(t)$ obtained by clustering two chosen oscillators together on group "Rats1". Horizontal axis is time (min). The red lines indicate the deep-light change of anæsthesia detected by us: (a) ECG and Respiration, (b) ECG and EEG, and (c) Respiration and EEG.*

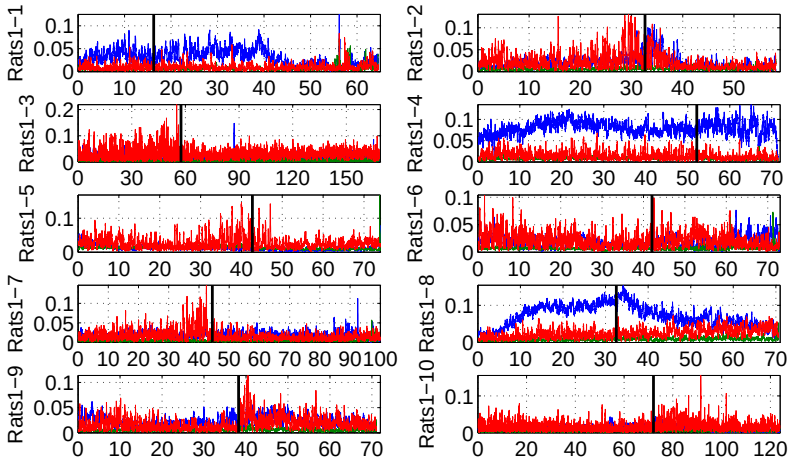

Figure 3.21 – *Comparison of the strength of $S_{new}(t)$ obtained by clustering two chosen oscillators together on group "Rats1". Horizontal axis is time (min). The black lines indicate the deep-light change of anæsthesia detected by us: (blue) ECG and Respiration, (green) ECG and EEG, and (red) Respiration and EEG.*

change point on some rats's result, but this variation is not enough for the detection of the change point. For the strength, little synchronization found on ECG-EEG cluster. For other two clusters, no big difference can be observed, except three rats's remarked in Fig. 3.20 (a) which indicate higher results for heart-respiration cluster (see Fig. 3.21).

Now, let's calculate the new S-estimator using the PCA based embedding method, which allows us to check the dependence on the embedding method. The embedding dimension

and the size of the Toeplitz like matrix used in this analysis are shown in table. 3.8.

Rats No: Rats1-		1	2	3	4	5	6	7	8	9	10
ED	ECG	7	7	10	7	8	7	7	7	7	7
	Resp	5	4	4	3	4	3	3	4	4	3
	EEG	9	10	10	10	11	12	9	10	9	10
K	ECG	20	22	33	21	22	22	22	21	21	22
	Resp	70	64	55	44	74	66	61	71	63	77
	EEG	31	40	38	39	44	40	37	38	35	40

Table 3.8 – *Embedding dimension (ED) and size of Toeplitz like matrix (K) used in the studies.*

Just to notice, this version of the new S-estimator went also through the linear transformation of the reconstructed states, since the length of the reconstructed states are unified to the length of one system which has minimum length (largest size of Toeplitz like matrix), such that the orthogonality of the states were lost. In Fig. 3.22 and 3.23, the obtained results are shown. From Fig. 3.22, apart from Rats1-3, Rats1-4, Rats1-5 and Rats1-6, the obtained results are not so far from the results of $S_{new}(t)$. This difference on four rats' results should be examined in the future. Nevertheless, from Fig. 3.23, we can see that this difference mostly comes from the synchronization between respiration and EEG. For the detection of the change point in anæsthesia, again as $S_{new}(t)$, this method cannot be used, since apart from Rats1-5, no clear variation at the change point is observed

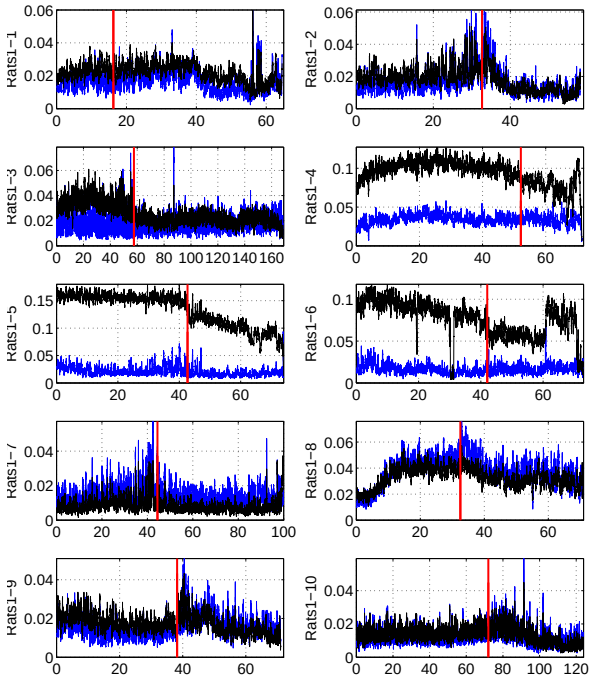

Figure 3.22 – *new Synchronization measure $S_{new,PCA}(t)$ obtained by clustering three oscillators (ECG, Respiration and EEG) together on group "Rats1". Horizontal axis is time (min). The red lines indicate the deep-light change of anæsthesia detected by us. The results of $S_{new}(t)$ is plotted in blue for reference.*

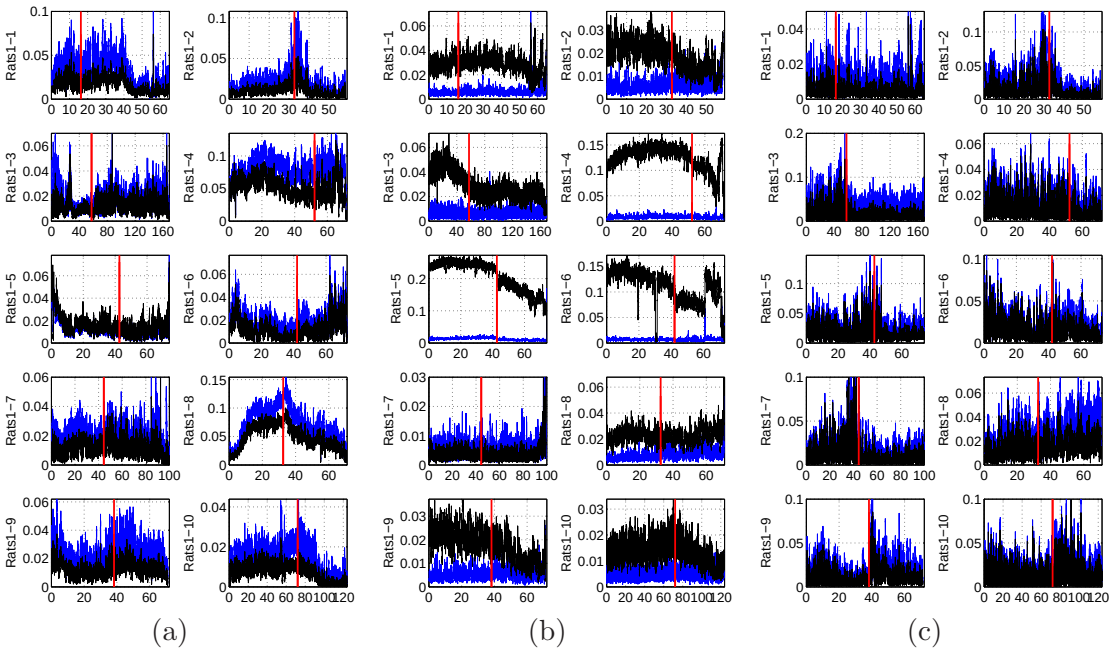

Figure 3.23 – *Synchronization measure $S_{new,PCA}(t)$ obtained by clustering two chosen oscillators together on group "Rats1". Horizontal axis is time (min). The red lines indicate the deep-light change of anæsthesia detected by us. The results of $S_{new}(t)$ is plotted in blue for reference: (a) ECG and Respiration, (b) ECG and EEG. and (c) Respiration and EEG.*

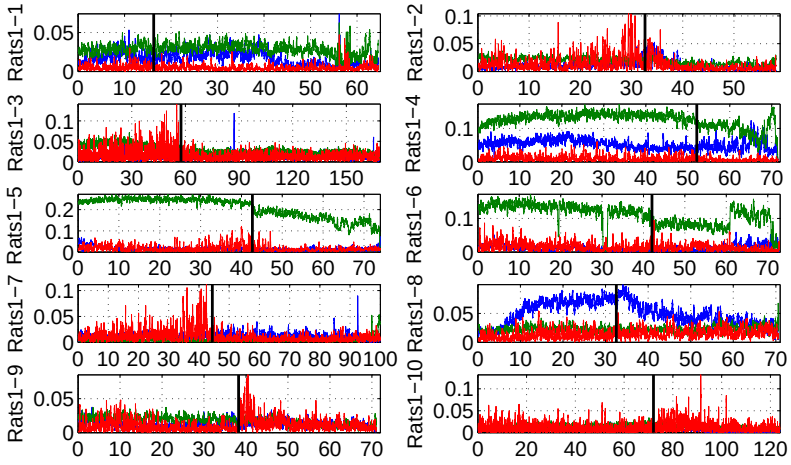

Figure 3.24 – *Comparison of the strength of $S_{new,PCA}(t)$ obtained by clustering two chosen oscillators together on group "Rats1". Horizontal axis is time (min). The black lines indicate the deep-light change of anæsthesia detected by us: (blue) ECG and Respiration, (green) ECG and EEG, and (red) Respiration and EEG.*

from the results. For the strength of the synchronization, there is no big difference among the clusters for Rats1-2, Rats1-7, Rats1-9 and Rats1-10. Besides, Rats1-1 and Rats1-3 to Rats1-6 has highest synchronization measure between ECG and EEG, and as reported in $S_{new}(t)$, Rats1-1, Rats1-4 and Rats1-8 has higher synchronization measure between ECG and respiration than between respiration and EEG(see Fig. 3.24).

Embedding dimension analysis

As mentioned in sec. 3.6, the embedding dimension and the time delay on each shifting window were calculated by the corresponding methods, i.e. false nearest neighbors, eigenvalues of correlation matrix and self mutual information, in the studies of the S-estimator and the new S-estimator. Accordingly, we just plotted the calculated values on figures.

In Fig. 3.25, we show the obtained results on embedding dimension (ED) for delay embedding. From this figure, we can remark that the ED calculated on the EEG windows, suddenly begins to increase at the change point in anæsthesia. Moreover, on 6/10, also the ED of the ECG windows increases around the change point. For respiration, no change can be remarked along the time. Owing to that, we understood that the complexity of the EEG and ECG signals change according to the effect of anæshtesia and it is lower in the deep state of anæshtesia. Comparing with Fig. 3.16, 3.17, 3.19, and 3.20 we remarked that the change of these ED are surely included in the results of $S(t)$ and we think that's why $S_{new}(t)$ has smaller value and has no clear variation at the change point. Adding to that, we remarked that the small increase around the change point seen in fig. 3.19 and 3.20 seems to correlate with the delay in the increase of ED to the change point.

In Fig. 3.26, we show the obtained results on time delay (τ) calculated as a first minima of the self mutual information. From the figure, we can remark a small decrease in the τ of EEG, and on the half of the τ of the respiration, the distribution of this τ suddenly increases, i.e. wider variation at the change point. In the analysis, the mean value was used as a unique parameter for τ, however this decision should be reconsidered in the future.

In Fig. 3.27, we show the obtained results on ED for PCA based embedding. From this figure, we can also remark a clear increase of ED of the EEG signals, however, the increase of ED of the ECG found with delay embedding is not present with this PCA based method. We tried to understand the difference between $S_{new}(t)$ and $S_{new,PCA}(t)$ (Fig. 3.19 and 3.22 or Fig. 3.20 and 3.23) but it seems that the difference is not coming from the ED but the reconstruction of the states itself.

In Fig. 3.28, we show the obtained results on the size of the Toeplitz like matrix (K) calculated as a first maxima of the self mutual information. As the method of this calculation is the same as the time delay, just the needed point is the maxima and not the minima, the structure of the plot is very similar to Fig. 3.26. As we took the maximum value along the time, we don't think that it makes problem to the analysis, but further investigation might be necessary.

From this analysis on the embedding dimension, we realized that the variation in the ED of the EEG signals can be also used to detect the change point in anæsthesia. Just, with the employed window length, the computation time is too long such that we should try with smaller window length and concretize the method. This is one of the future work.

Coupling matrix

In order to have more information about the influence between the observed systems, we proceeded to the analysis of the coupling matrix (CM). In this method, normally, the self model should be created considering the whole measurements, however because of the computation time, only the first 1 minute is considered for the creation of the self model. This decision was tested with a linear self model and verified at the results of the CM such

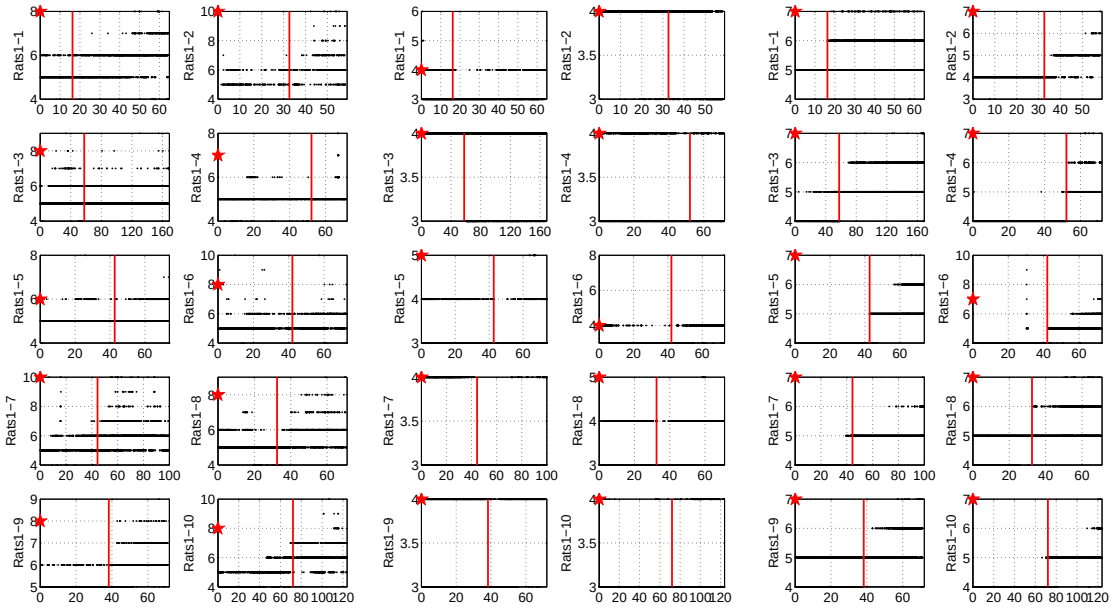

Figure 3.25 – *The study on the embedding dimension (ED) for delay embedding. Horizontal axis is time (min). The red lines indicate the deep-light change of anæsthesia detected by us. The red stars indicates the chosen parameters: (a) ECG, (b) Respiration and (c) EEG.*

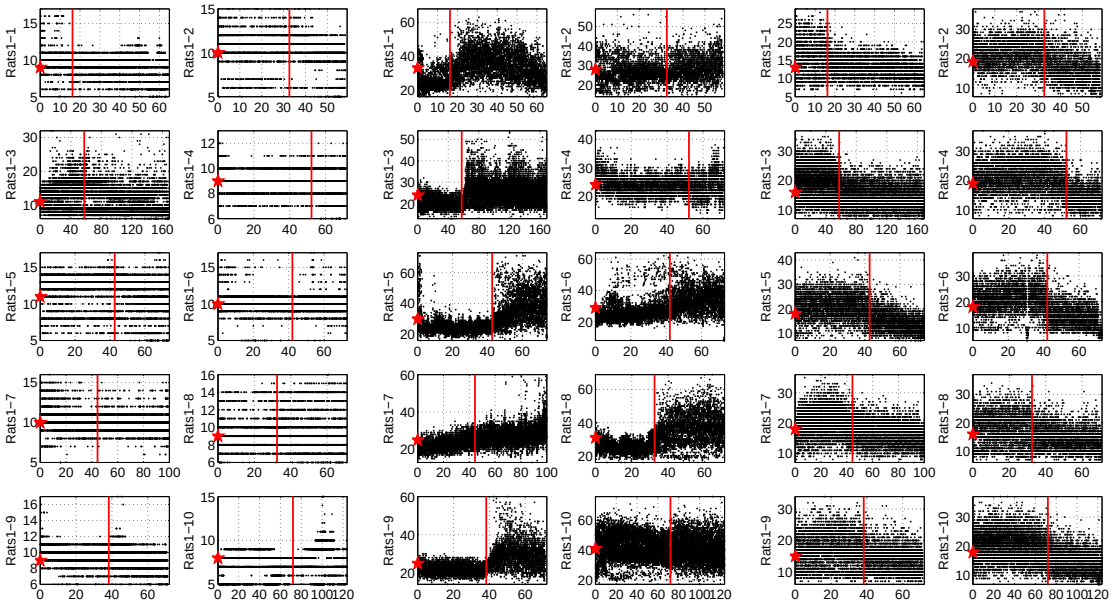

Figure 3.26 – *The study on the time delay (τ) (samples) for delay embedding. Horizontal axis is time (min). The red lines indicate the deep-light change of anæsthesia detected by us. The red stars indicates the chosen parameters: (a) ECG, (b) Respiration and (c) EEG.*

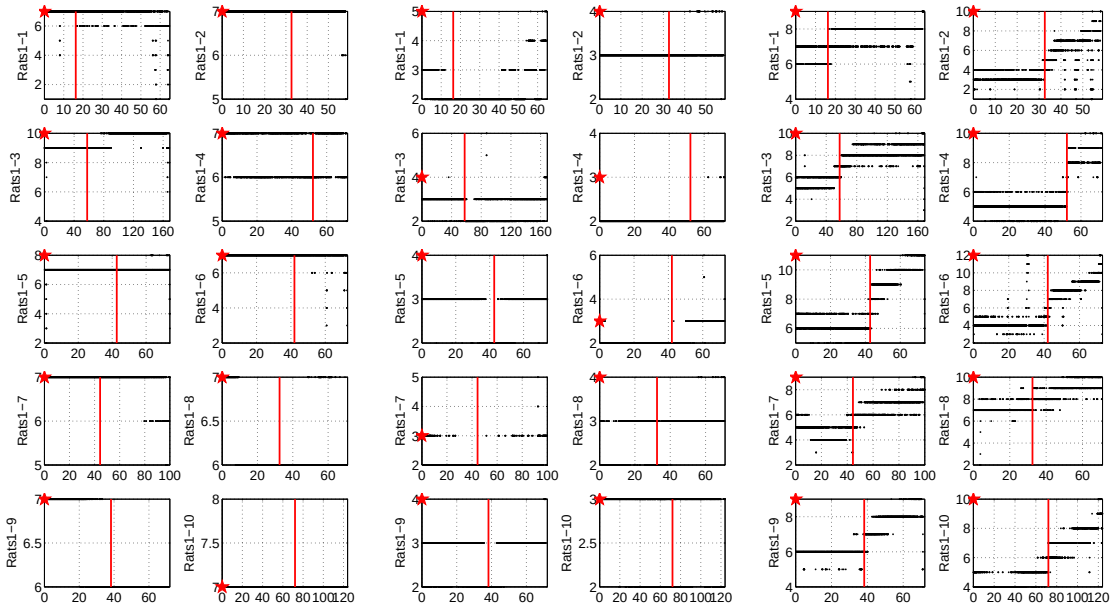

Figure 3.27 – *The study on the embedding dimension (ED) for PCA embedding. Horizontal axis is time (min). The red lines indicate the deep-light change of anæsthesia detected by us. The red stars indicates the chosen parameters: (a) ECG, (b) Respiration and (c) EEG.*

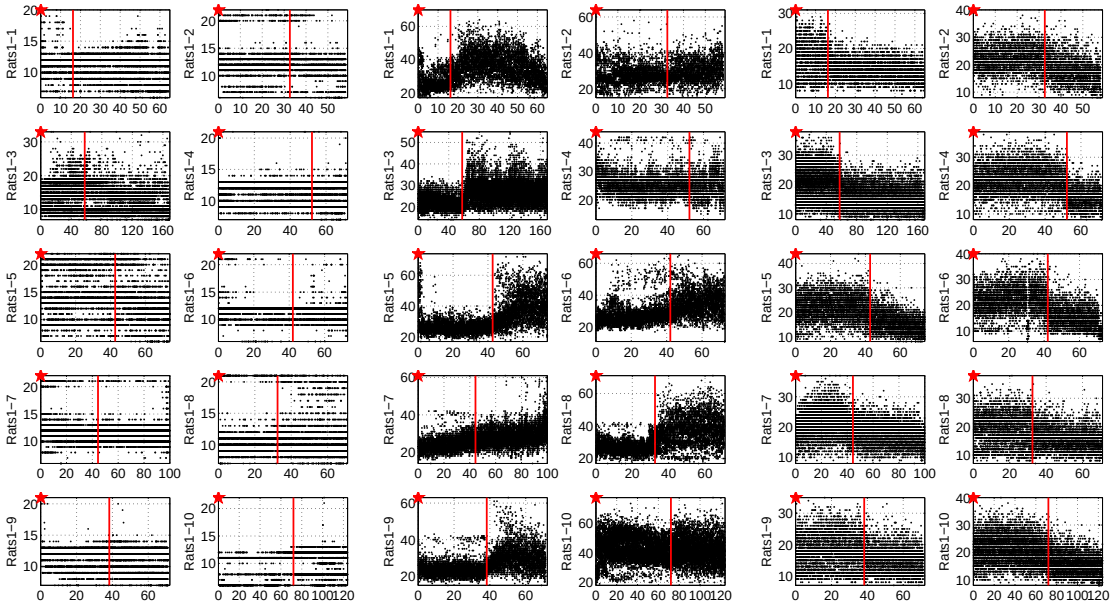

Figure 3.28 – *The study on the size of the Toeplitz like matrix (K) (samples) for PCA embedding. Horizontal axis is time (min). The red lines indicate the deep-light change of anæsthesia detected by us. The red stars indicates the chosen parameters: (a) ECG, (b) Respiration and (c) EEG.*

that no big difference was observed. Nevertheless, nonlinear system does not have the same property as the linear system that this decision should be tested on nonlinear system in the future. This analysis is very memory costing such that very long measurements cannot be analyzed. For this reason, Rats1-3 and Rats1-9 were removed from the analysis. In Fig. 3.29 , the obtained results are shown. From this figure set, comparing the two stage of anæsthesia, higher influence from EEG (B: Brain) to Respiration (R) and from ECG (H: Heart) to R can be remarked on all rats' results at the light state of anæsthesia. Moreover, a higher influence from R to B and from R to H are remarked on some rats at the deep state of anæsthesia. No clear variation can be found between B and H.

In order to check the directionality of the interactions, we calculated the directionality index in the same way as eq. 3.17 used in our collaborators study:

$$d_{(1,2)} = \frac{CM(1 \to 2) - CM(2 \to 1)}{CM(1 \to 2) + CM(2 \to 1)}. \tag{3.93}$$

The obtained results are shown in Fig. 3.30. From this figure, there is no unique relationship in all rats, though from main agreement, we can conclude that:
In deep anæsthesia:
Respiration drives both the brain activity and the heart activity.
In light anæsthesia:
Contrary to the deep state, the brain activity drives the respiration, and also the heart activity drives respiration.

This conclusion agrees with the study of our collaborators. Moreover, we succeeded to conclude the influence from brain to respiration under light anæsthesia that our collaborators did not manage to analyze.

Nonparametric Granger causality

In this study, the window length was set to 1 minute and shifted with 30 seconds. The segments inside of one window for multiple realizations were created with 4 seconds length with 2 seconds of overlap*. Here as we calculated the spectral density matrix, first, we plotted the power spectra and the coherence spectra† in Fig. 3.31 and 3.32. We can see that the plot of Rats1-9 in Fig. 3.31 is the same as the instantaneous frequency of our collaborator in Fig. 3.4 and 3.5 in subsec. 3.3.2, except the harmonics which are also present. In all rats' results, it agrees on the frequency of respiration which increases and becomes erratic, on the δ-oscillations which dramatically diminishes at the change point of anæsthesia, and on the θ-oscillations which begins to emerge at this change point. However, we remarked that the increase in heart frequency at the change point is just the case of Rats1-9. Fig. 3.32 gives, roughly, similar trend of relationship between systems as $S_{new}(t)$ in Fig. 3.20, nevertheless, concentrating in some frequencies, we can remark an increase between EEG and respiration and also between EEG and ECG in some rats. However, this change is not so obvious as the S-estimator, $S(t)$, moreover the changes are not unique in all rats, such that it is not possible to use for the detection of the depth of anæsthesia.

*We also analyzed with other window length and segment length, i.e. 30 seconds - 4 seconds and 2 minutes - 4 seconds, and 2 minutes - 12 seconds, and fined that there is no big difference in the obtained causality according to these parameters

†Coherence spectra is obtained as: $Re\frac{|S_{ij}|^2}{S_{ii}S_{jj}}$.

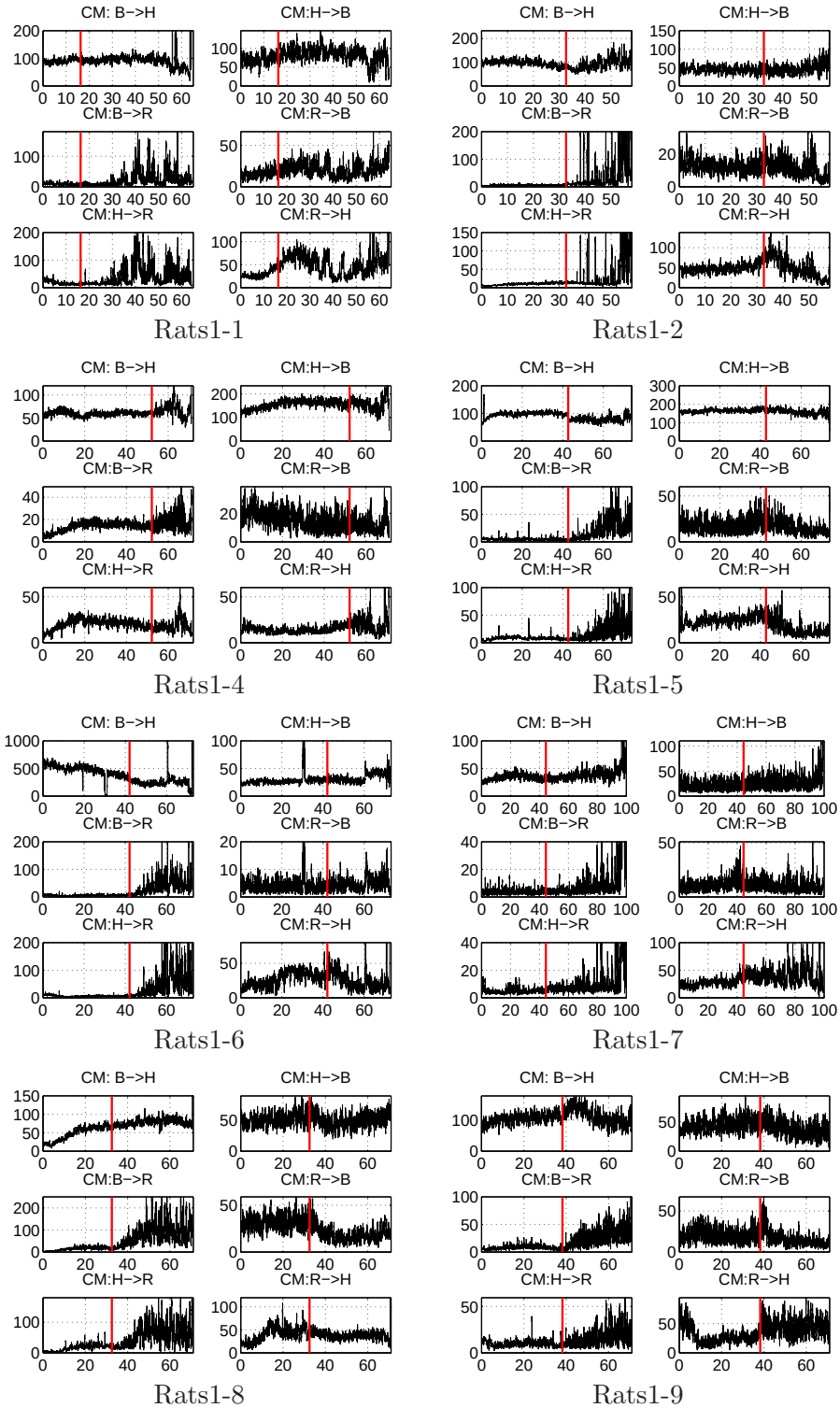

Figure 3.29 – *Coupling matrix $CM(t)$ obtained on "Rats1". Horizontal axis is time (min). The red lines indicate the deep-light change of anæsthesia detected by us. Rats1-3 and Rats1-10 were unable to analyze because of too long measurements: (B) EEG, (H) ECG, and (R) respiration.*

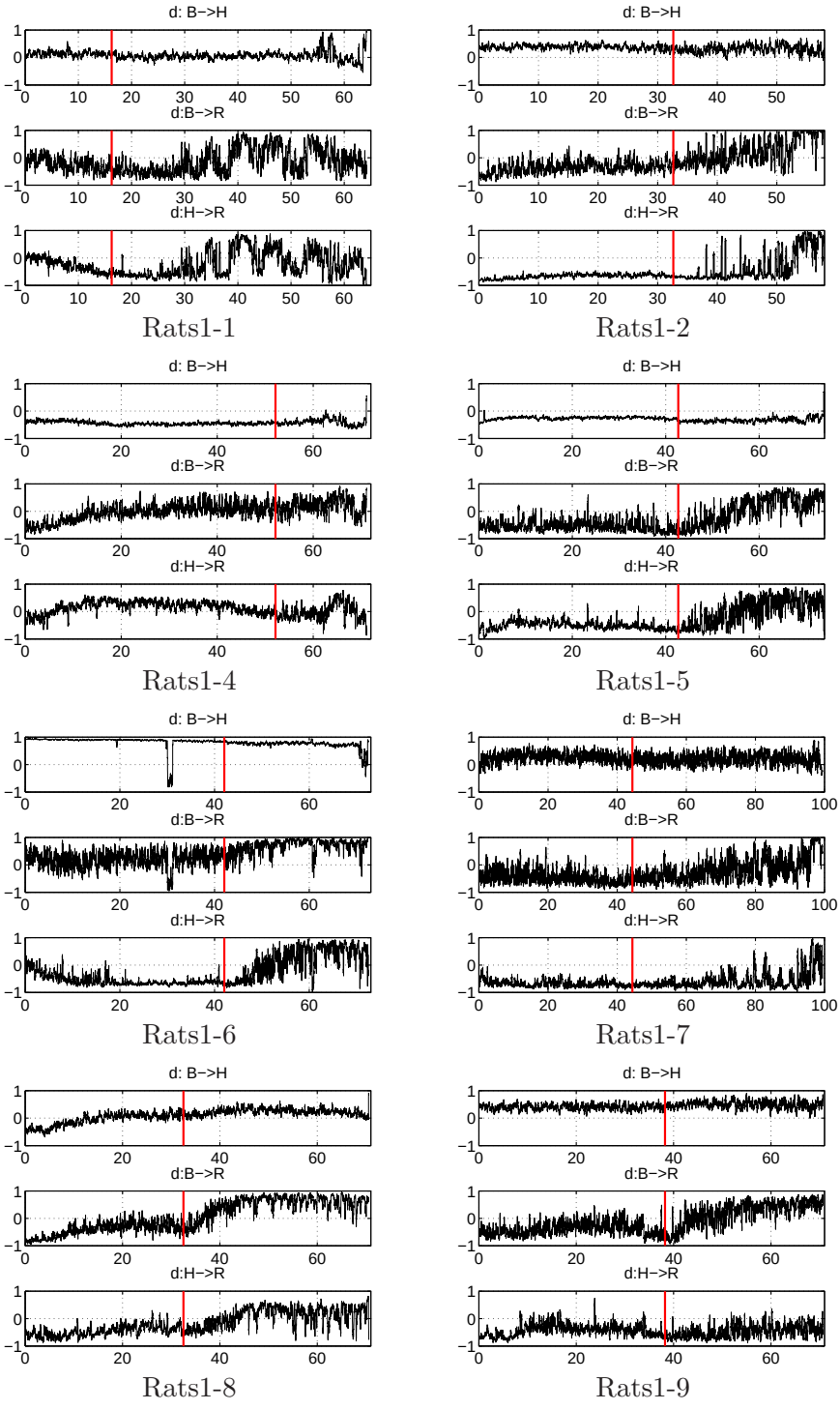

Figure 3.30 – *Direction of the interactions $d(t)$ obtained on "Rats1" using $CM(t)$. Horizontal axis is time (min). The red lines indicate the deep-light change of anæsthesia detected by us. Rats1-3 and Rats1-10 were unable to analyze because of too long measurements: (B) EEG, (H) ECG, and (R) respiration.*

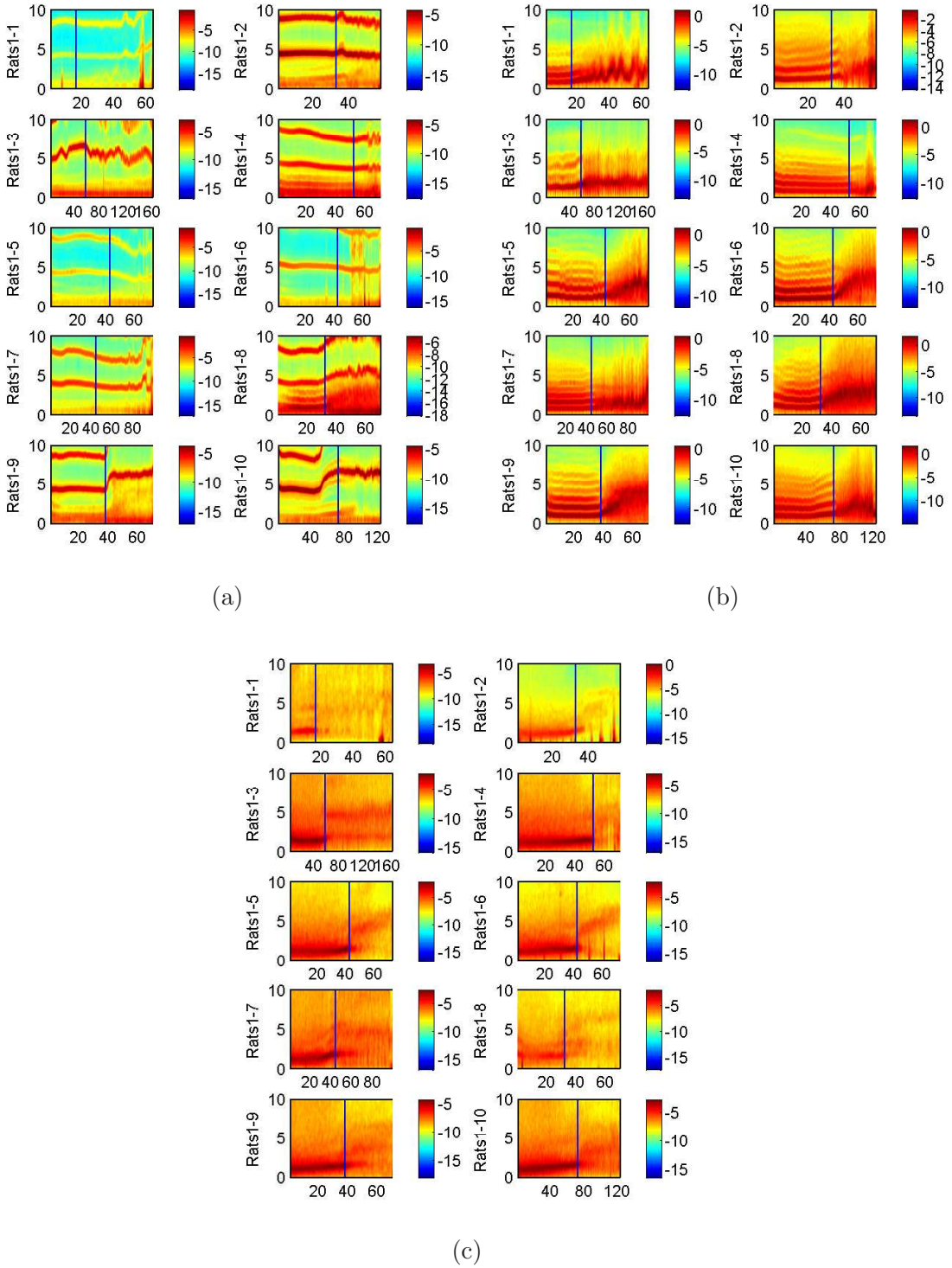

(a) (b)

(c)

Figure 3.31 – *Power spectra obtained on "Rats1". Horizontal axis is time (min). Vertical axis is frequency (Hz). The blue lines indicate the deep-light change of anæsthesia detected by us: (a) ECG, (b) Respiration, and (c) EEG.*

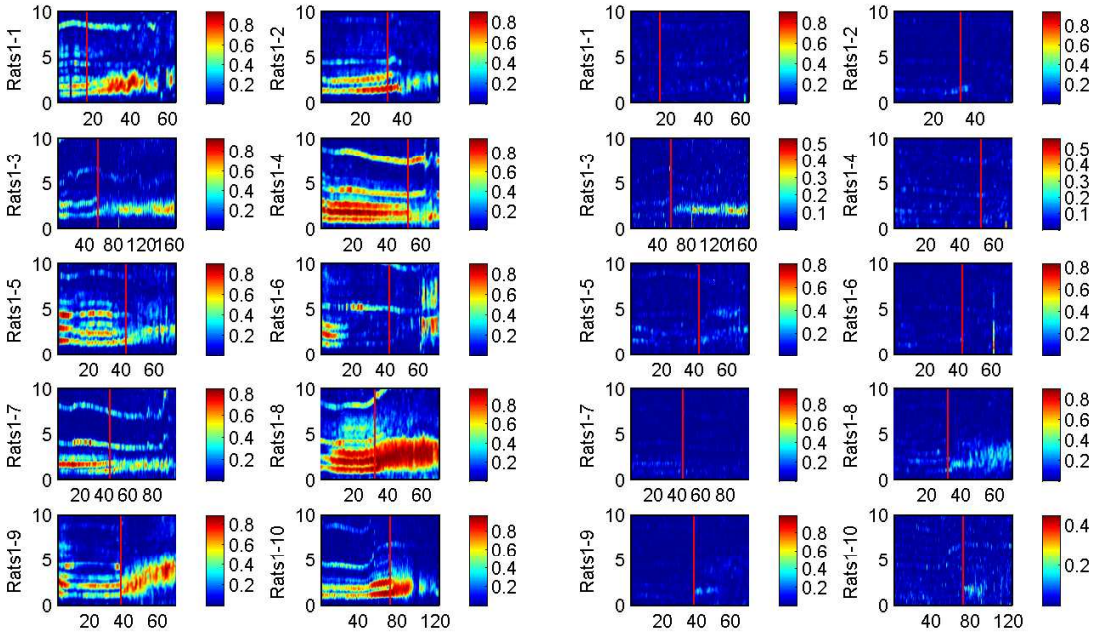

(a) (b)

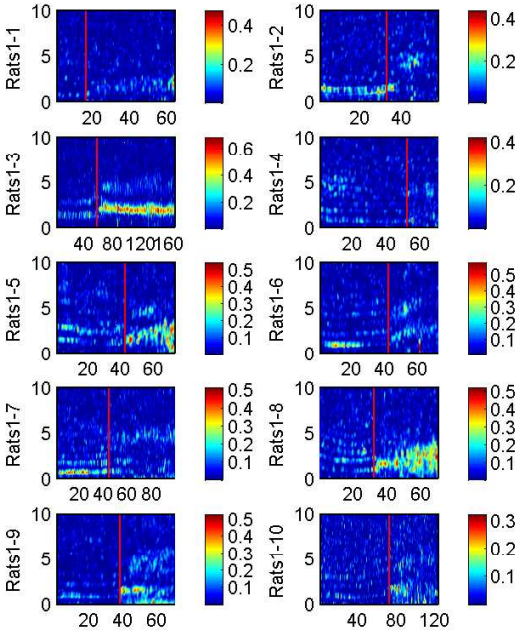

(c)

Figure 3.32 – *Coherence spectra obtained on "Rats1". Horizontal axis is time (min). Vertical axis is frequency (Hz). The red lines indicate the deep-light change of anæsthesia detected by us: (a) ECG and respiration, (b) EEG and ECG, and (c) EEG and respiration.*

In Fig. 3.33 and 3.34, we show the results of the nonparametric Granger causality $GC(t)$. In these figures, the $GC(t)$ smaller than threshold defined by the permutation test were set to zero. Here below, we show the thresholds obtained by the permutation test.

	GC:B→H	GC:H→B	GC:B→R	GC:R→B	GC:H→R	GC:R→H
threshold	0.09	0.1	0.1	0.09	0.1	0.1

Table 3.9 – *Threshold for nonparametric Granger causality $GC(t)$ defined by the permutation test for "Rats1": (B) EEG, (H) ECG, and (R) respiration.*

From fig. 3.33 and 3.34, we remarked the $GC(t) : B \rightarrow H$ increases around 2 Hz from the transition point of anæsthesia. Nothing can be remarked on $GC(t) : H \rightarrow B$, except Rats1-8 which indicates a clear increase from the change point. Half of the rats have the $GC(t) : B \rightarrow R$ which increase after the transition point in range of 0 to 5 Hz. Also, in half of the rats, the $GC(t) : R \rightarrow B$ show higher value around 2 Hz at the light state of anæsthesia. The $GC(t) : H \rightarrow R$ clearly shows high causality around 5 Hz at the deep stage. Finally, half of the rats have high $GC(t) : R \rightarrow H$ at the deep state, and in some rats at the light state, we can remark a frequency shift in the causality which relates to the frequency increase of ECG and respiration.

We also calculated the time domain Granger causality and its directionality, however, no change was observed at the transition point of the anæsthesia (See Appendix). Nevertheless, my colleague, Yuri Shiogai, analyzed the time-averaged Granger causality limiting her interest to certain frequencies which are major frequency of each system: around 1Hz for ECG, around 4Hz for respiration, δ-wave range and θ-wave range for EEG. So, in table. 3.10, H→ represents the causality from the heart around 4 Hz, R→ represents the causality

	Time average of the pairwise GC before and after transition										
Rats1(deep)	1	2	3	4	5	6	7	8	9	10	N
H→R	**0.19**	**0.31**	**0.14**	**0.48**	**0.47**	**0.47**	**0.55**	**0.38**	**0.35**	**0.30**	10
R→H	**0.24**	**1.10**	**0.46**	**0.59**	**0.53**	**0.28**	**0.30**	**0.66**	**0.41**	**1.71**	10
H→B	0.02	0.03	0.03	0.03	0.03	0.03	0.03	0.04	0.02	0.03	0
δ →H	0.03	0.06	0.03	0.01	0.03	0.04	0.05	0.03	0.02	0.02	0
R→B	0.05	0.04	0.04	0.03	0.06	0.07	0.09	0.06	0.04	0.03	0
δ →R	0.01	0.06	0.04	0.01	0.02	0.02	0.02	0.02	0.03	0.01	0
Rats1(light)	1	2	3	4	5	6	7	8	9	10	
H→R	0.08	0.08	**0.11**	**0.30**	**0.13**	**0.17**	**0.36**	**0.15**	0.10	0.07	6
R→H	**0.65**	**0.39**	**0.45**	**0.52**	**0.22**	**0.38**	**0.40**	**1.28**	**0.60**	**0.85**	10
H→B	0.03	0.03	0.03	0.03	0.03	0.03	0.03	0.03	0.02	0.03	0
δ →H	0.02	0.02	0.06	0.02	0.09	0.02	0.02	0.04	**0.13**	**0.12**	2
R→B	0.07	0.02	**0.32**	0.04	**0.18**	0.08	0.05	**0.22**	0.06	0.03	3
δ →R	0.01	0.03	0.10	0.02	**0.14**	0.04	0.03	0.03	**0.11**	0.06	2
θ →H	0.01	0.01	0.02	0.01	0.06	0.02	0.01	0.01	0.02	0.03	0
θ →R	0.02	0.06	0.04	0.03	0.04	0.05	0.05	0.03	0.04	0.02	0

Table 3.10 – *Table for time averaged GC before and after the transition time. If the causalities go beyond the thresholds calculated by a permutation test, they are significant and written in bold. N indicates the number of rat's data which shows significant influence: (H) ECG, (R) respiration, (B) EEG, (δ) δ-wave of EEG and (θ) θ-wave of EEG.*

from the respiration around 1 Hz, $\delta \rightarrow$ represents the causality from the δ wave of EEG and $\theta \rightarrow$ represents the causality from the θ wave of EEG. The averaging of the δ wave for the shallow stage were done only for 10 minutes. The θ-wave was not able to detect at the deep stage. From the obtained results on table 3.10, she conducted the Wilcoxon rank sum test between before and after transition point, and concluded that the influence from heart to respiration is weakened at the light stage of anaesthesia, and the coupling from δ wave to respiration is strengthened at the shallow stage of anaesthesia.

This conclusion agrees with coupling matrix analysis for the causality between brain and respiration. However the influence from heart to respiration is exactly the inverse. This disagreement should be followed-up in the future.

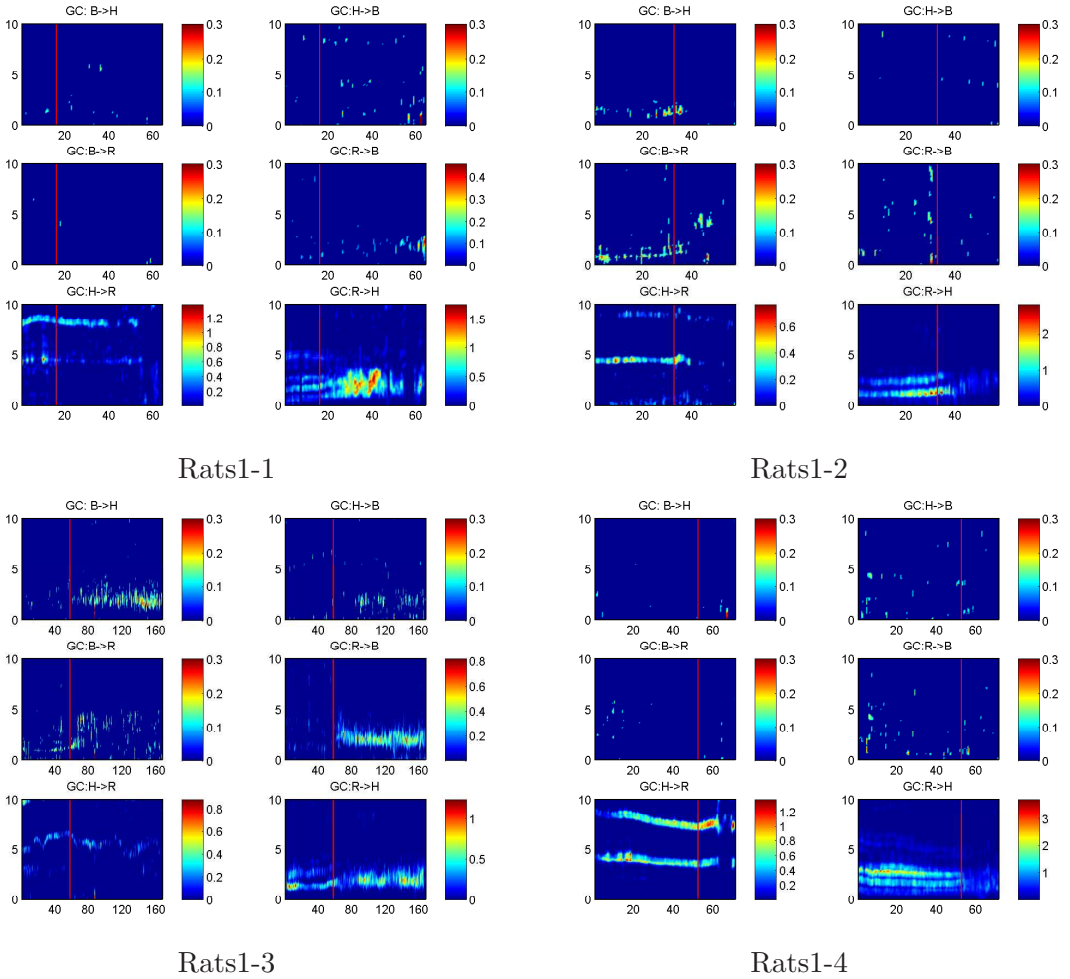

Figure 3.33 – *Nonparametric Granger causality $GC(t, f)$ obtained on "Rats1" PartI (Rats1-1 to Rats1-4). Horizontal axis is time (min). Vertical axis is frequency (Hz). The red lines indicate the deep-light change of anæsthesia detected by us: (B) EEG, (H) ECG, and (R) respiration.*

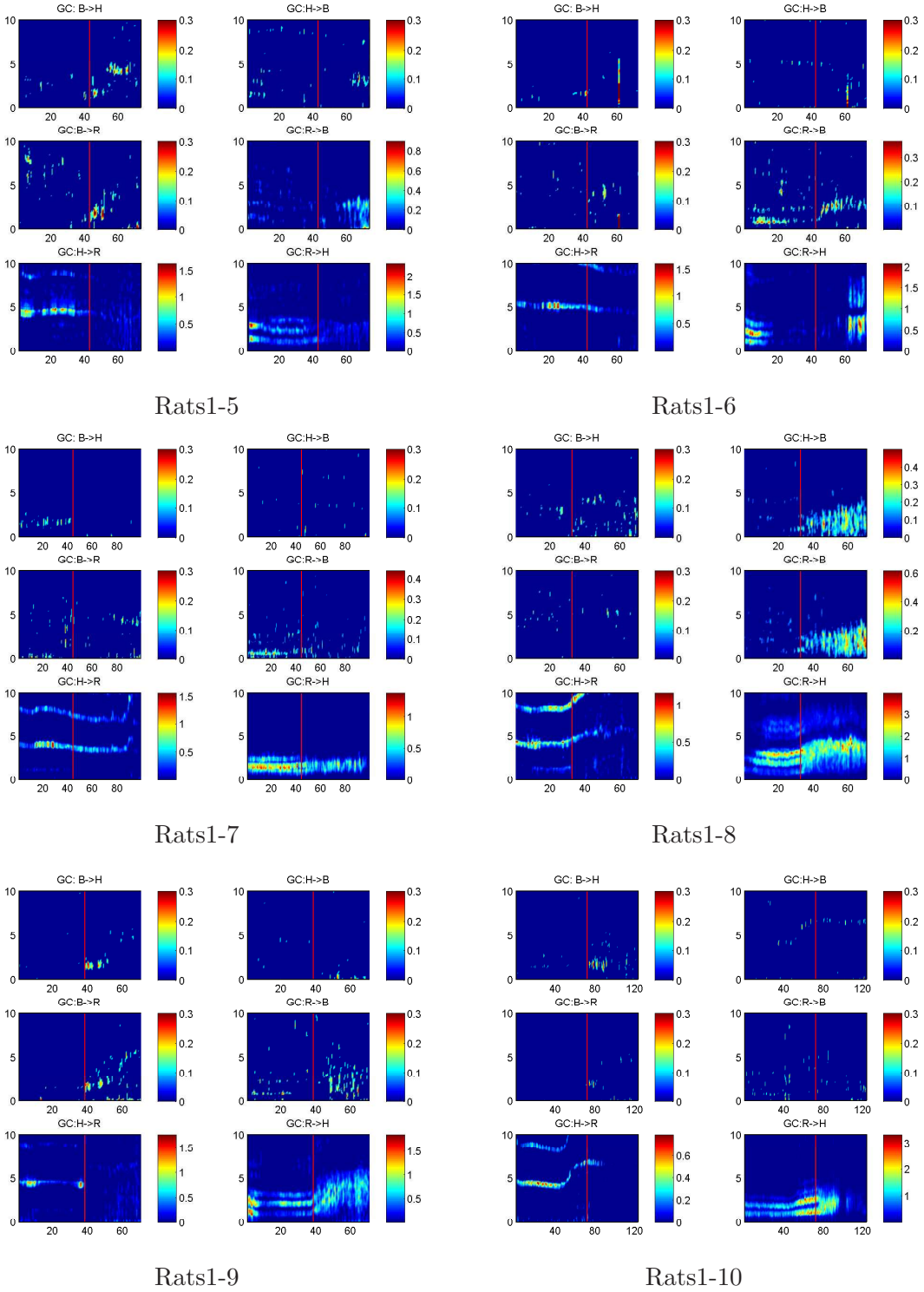

Figure 3.34 – *Nonparametric Granger causality $GC(t, f)$ obtained on "Rats1" PartII (Rats1-5 to Rats1-10). Horizontal axis is time (min). Vertical axis is frequency (Hz). The red lines indicate the deep-light change of anæsthesia detected by us: (B) EEG, (H) ECG, and (R) respiration.*

3.9.2 Rats2

The preprocessing was carried out in the same way as the group "Rats1".

S-estimator

The same length of sliding window (10 seconds) and the shifted time (0.5 second) as the group "Rats1" were used for the study. The embedding dimension (ED) and time delay (τ) used in this work are shown in the table below.

Rats No: Rats2-		1	2	3	4	5	6	7	8	9	10
ED	ECG	6	6	6	5	5	6	6	7	7	6
	Resp	4	4	4	4	4	4	4	4	4	4
	EEG	8	8	6	8	8	8	8	8	7	8
τ	ECG	7	9	6	8	6	9	8	9	9	7
	Resp	21	23	35	27	39	35	25	30	35	30
	EEG	16	9	20	15	14	14	13	14	13	11

Table 3.11 – *Embedding dimension (ED) and time delay (τ) used in the studies.*

In Fig. 3.35, the synchronization measures obtained for all the measurements are shown. The values of $S(t)$ seems to slowly increase along the time for some rats, but no clear

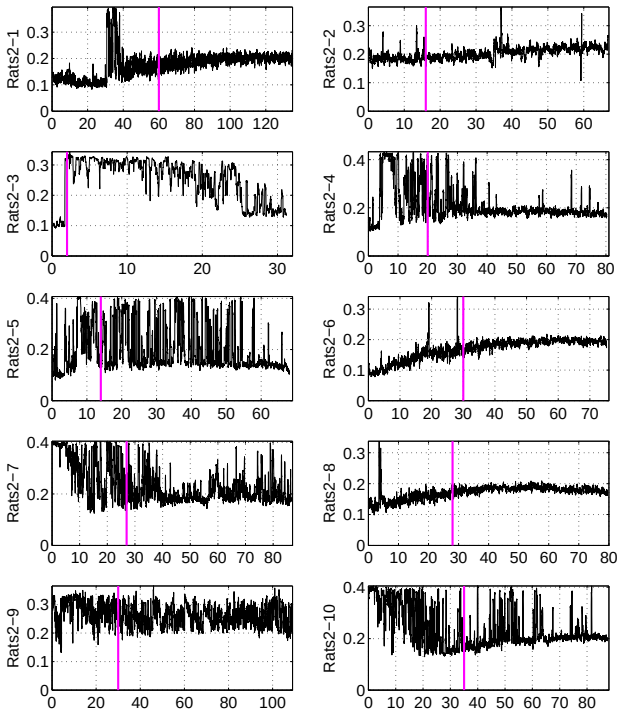

Figure 3.35 – *Synchronization measure $S(t)$ obtained by clustering three oscillators (ECG, Respiration and EEG) together on group "Rats2". Horizontal axis is time (min). The magenta lines indicate the deep-light change of anæsthesia detected in [Musizza et al., 2007]*

change can be observed at the transition point of the state of the anæsthesia. As a result, we realized that the detection of the depth of anæsthesia with the S-estimator depends on the kind of the anæsthetics and their effects. We presume that the difference among the results of "Rats2" comes from the difficulty of dose control of pentobarbital (PB) which mentioned in chap. 2. Moreover, as the reason of this failure of detection, the effect of PB and Ketamine (KX) on the respiratory-cardiovascular system which is known to be clearly different can be stated; PB decreases their function, whereas KX does not affect or even increase their function (See also chap. 2). As we didn't manage to define the transition point of anæsthesia by ourself, here after in the study of this group, the detection point of [Musizza et al., 2007] is used for reference change point.

In Fig. 3.36, the results of the S-estimator performed on sets of two sub-systems are shown. From these figures, we first remarked that the $S(t)$ obtained with the cluster of ECG and Respiration does not change at all during whole measurements. Then, we remarked that the results obtained by two other clusters are very similar. From these figures (Fig. 3.36(b) and (c)), we can conjecture that the EEG signal is the cause of the change since it is present in both analysis. However, this change may be result of the internal synchronization of the EEG reconstructed states. Consequently, we proceed to the new S-estimator. *

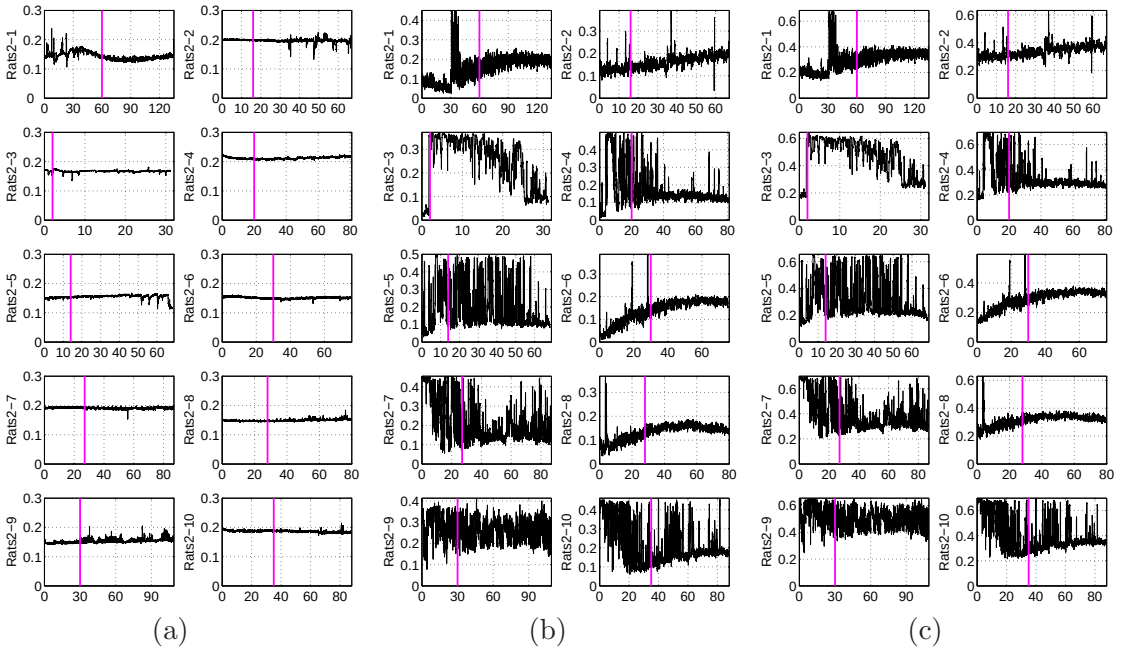

Figure 3.36 – *Synchronization measure $S(t)$ obtained by clustering two chosen oscillators together on group "Rats2". Horizontal axis is time (min). The magenta lines indicate the deep-light change of anæsthesia detected in [Musizza et al., 2007]: (a) ECG and Respiration, (b) ECG and EEG, and (c) Respiration and EEG.*

*Just for notice, the comparison of the strength of $S(t)$ seems to be unappropriate with $S(t)$ because of the internal state synchronization such that we just put the plot in appendix.

new S-estimator

In Fig. 3.37, we show the obtained results with the new S-estimator. From this figure, we can remark that, also as the case in "Rats1", the strength of the synchronization became about 5 to 10 times smaller than the original S-estimator. However, interestingly, we remarked that, contrary to "Rats1", there is a difference between deep and light stage of anæsthesia; the $S_{new}(t)$ is higher in the deep state of anæsthesia than shallow one. Unfortunately the decrease of $S_{new}(t)$ is not sharp at the transition point of the anæsthesia such that it can not be used for the detection of this point.

In Fig. 3.38, as we did in the original S-estimator, we plotted the results obtained with other clusters taking two sub systems. From these figures, we observed higher synchronization at the deep state of anæshtesia in most of rats in all clusters analysis. Especially Rats2-6 and Rats2-8 gives similar synchronization process such that we imagine that their dose control was a success. Focussing on this two rats, we can remark that the synchronization between ECG and respiration and between ECG and EEG decreases from the beginning, and they stabilize at the light state of anæsthesia. The synchronization between respiration and EEG increases at the beginning, then decreases, and then also stabilize at

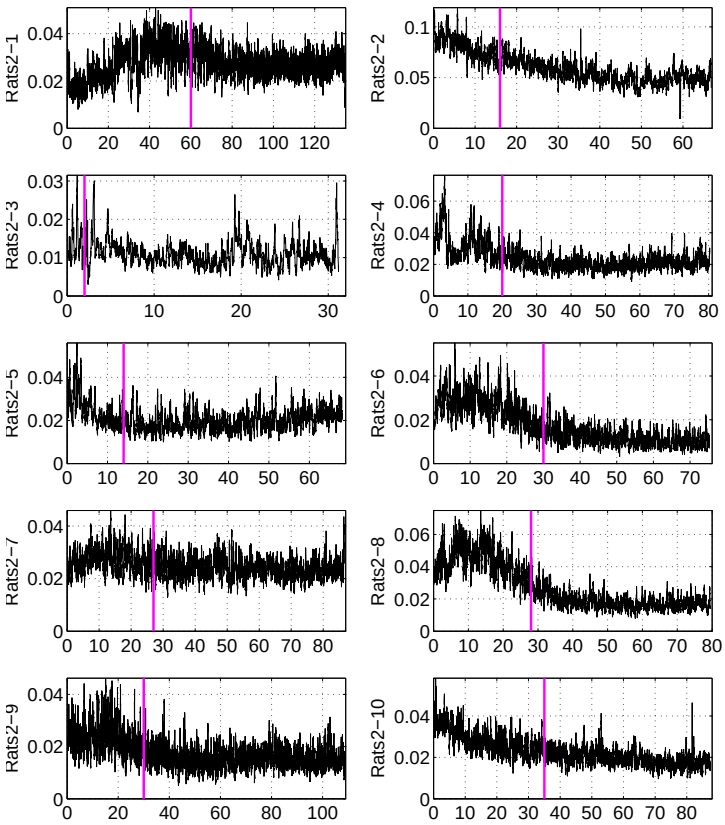

Figure 3.37 – *new Synchronization measure $S_{new}(t)$ obtained by clustering three oscillators (ECG, Respiration and EEG) together on group "Rats2". Horizontal axis is time (min). The magenta lines indicate the deep-light change of anæsthesia detected in [Musizza et al., 2007].*

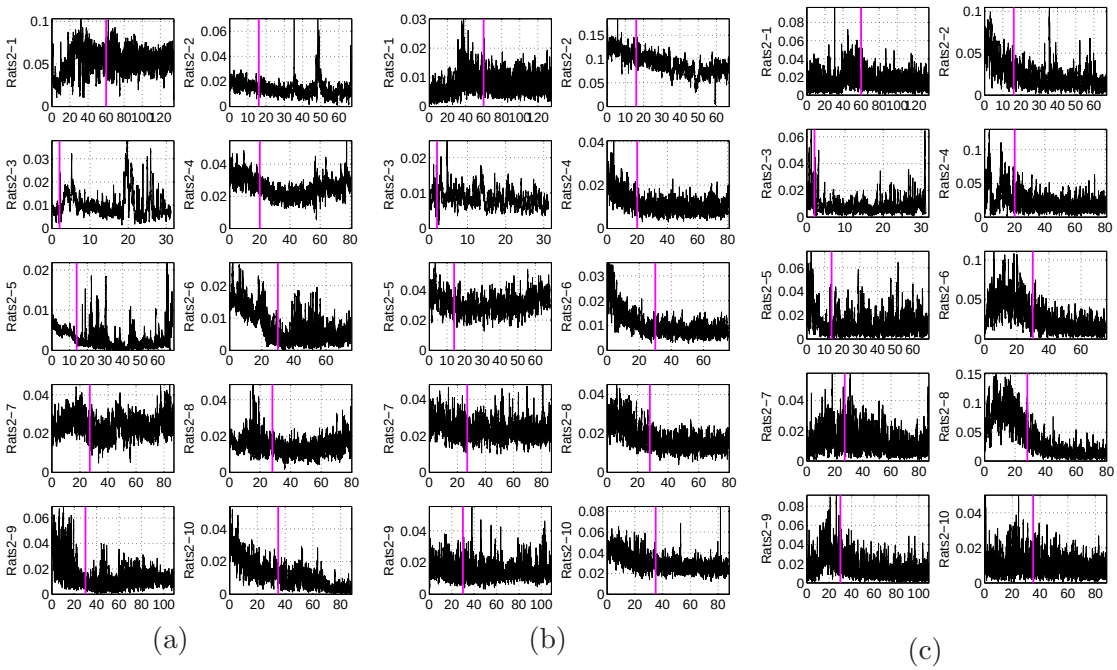

Figure 3.38 – *Synchronization measure $S_{new}(t)$ obtained by clustering two chosen oscillators together on group "Rats2". Horizontal axis is time (min). The red lines indicate the deep-light change of anæsthesia detected by us: (a) ECG and Respiration, (b) ECG and EEG, and (c) Respiration and EEG.*

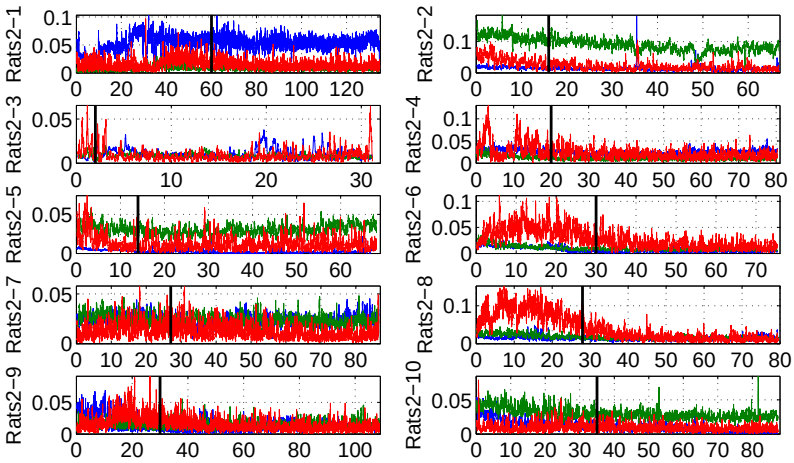

Figure 3.39 – *Comparison of the strength of $S_{new}(t)$ obtained by clustering two chosen oscillators together on group "Rats2". Horizontal axis is time (min). The black lines indicate the deep-light change of anæsthesia detected in [Musizza et al., 2007]: (blue) ECG and Respiration, (green) ECG and EEG, and (red) Respiration and EEG.*

the light stage. The variation change in this deep state might indicate the most strong effect of anæsthetic with the maximum value of $S_{new,EEG}(t)$. For the strength of the synchronization, there is no unique order of clusters can be defined. However, concentrating on the two rats mentioned before, the synchronization between respiration and EEG is the

strongest (see Fig. 3.39).

Now, let's calculate the new S-estimator using PCA based embedding method. The embedding dimension and the size of the Toeplitz like matrix used in this analysis are shown in table. 3.12.

Rats No: Rats2-		1	2	3	4	5	6	7	8	9	10
ED	ECG	7	7	5	4	5	5	5	7	7	5
	Resp	4	4	3	2	3	3	3	2	2	2
	EEG	11	9	10	11	10	10	9	10	12	10
K	ECG	21	21	12	12	12	12	12	21	21	12
	Resp	50	64	68	59	76	65	54	61	62	60
	EEG	40	28	41	41	37	33	35	36	42	36

Table 3.12 – *Embedding dimension (ED) and size of Toeplitz like matrix (K) used in the studies.*

In Fig. 3.40 and 3.41, the obtained results are shown. From Fig. 3.40, apart from Rats2-1 and Rats2-2, the obtained results does not have the same range in value as $S_{new}(t)$, but we can observe that the synchronization trend are very close. From Fig. 3.41(c), we remarked a good match between $S_{new}(t)$ and $S_{new,PCA}(t)$. Also in (a), we remarked that the difference between them is not so big. But in (b), the difference is big. This is exactly the same case as "Rats1"; the difference between $Snew(t)$ and $S_{new,PCA}(t)$ observed in fig. 3.40 mostly

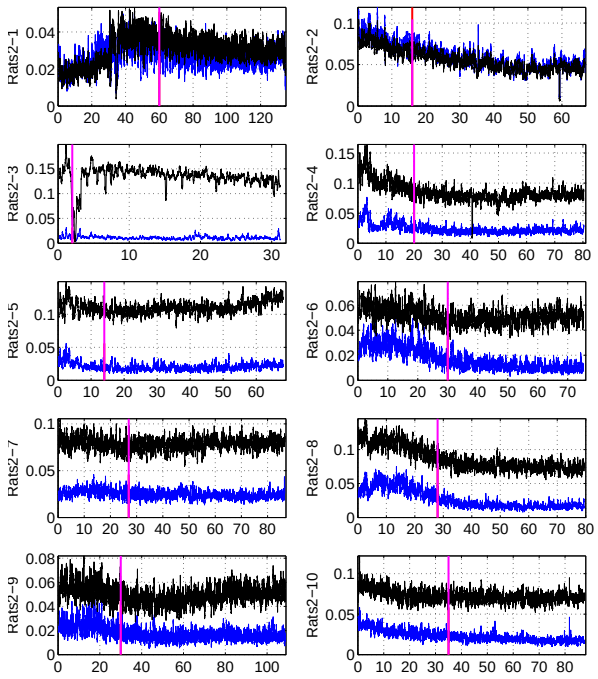

Figure 3.40 – *new Synchronization measure $S_{new,PCA}(t)$ obtained by clustering three oscillators (ECG, Respiration and EEG) together on group "Rats2". Horizontal axis is time (min). The magenta lines indicate the deep-light change of anæsthesia detected in [Musizza et al., 2007]. The results of $S_{new}(t)$ is plotted in blue for reference.*

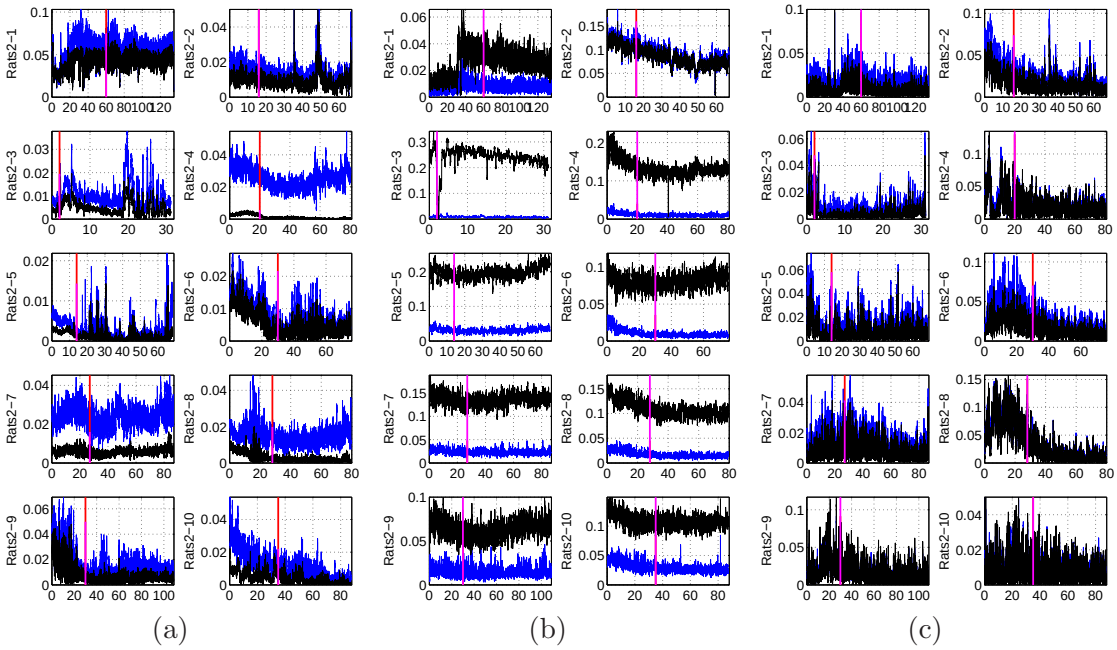

Figure 3.41 – *Synchronization measure $S_{new,PCA}(t)$ obtained by clustering two chosen oscillators together on group "Rats2". Horizontal axis is time (min). The magenta lines indicate the deep-light change of anæsthesia detected in [Musizza et al., 2007]. The results of $S_{new}(t)$ is plotted in blue for reference: (a) ECG and Respiration, (b) ECG and EEG, and (c) Respiration and EEG.*

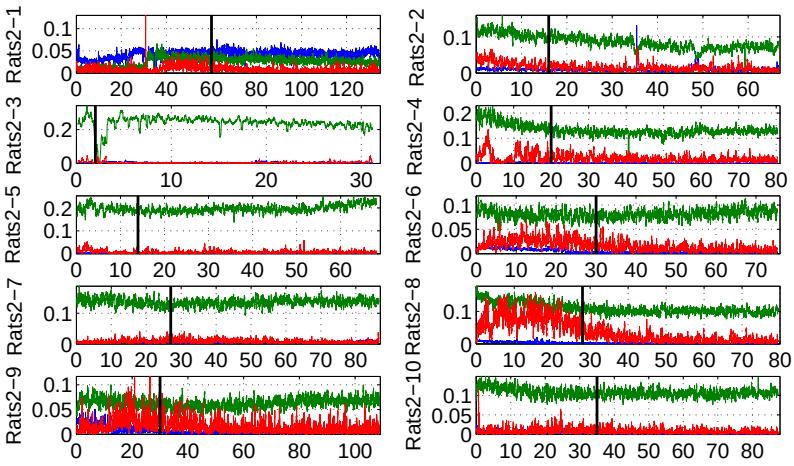

Figure 3.42 – *Comparison of the strength of $S_{new,PCA}(t)$ obtained by clustering two chosen oscillators together on group "Rats2". Horizontal axis is time (min). The black lines indicate the deep-light change of anæsthesia detected in [Musizza et al., 2007]: (blue) ECG and Respiration, (green) ECG and EEG, and (red) Respiration and EEG.*

comes from the synchronization between respiration and EEG. Again for the same reason as $S_{new}(t)$, this method cannot be used for the detection of the depth of anæsthesia. For the strength of the synchronization, the synchronization measure between respiration and EEG turns out to be the strongest(see Fig. 3.42).

Embedding dimension analysis

In Fig. 3.43, we show the obtained results on embedding dimension (ED) for delay embedding. From this figure, we remarked that the ED calculated on the EEG signals on half of the rats suddenly decrease around the transition point of the anæsthesia. But, on the ECG and respiration, we can not remark a change according to this transition point. Owing to that, we understood that the complexity of the EEG signals is higher in the deep state of anæsthesia. This is exactly the contrary as "Rats1". In "Rats1", we mentioned that one of the reason for the difference between $S(t)$ and $S_{new}(t)$ is the variation of the ED, but in this "Rats2", it seems not to be the case. Therefore, this reasoning that we stated in "Rats1" may not be true. In Fig. 3.44, we show the obtained results on time delay (τ) calculated as a first minima of the self mutual information. From the figure, we can remark an increase in the τ of EEG from around the transition point, and no change can be remarked for ECG and respiration. Again, in the analysis, the mean value was used as a unique parameter for τ, however this decision should be reconsidered in the future.

In Fig. 3.45, we show the obtained results on ED for PCA based embedding. From this figure, we can remark a clear decrease of ED of the EEG signals on Rats2-6 and Rats2-8. Apart from these two and Rats2-2, we remarked that the ED variate a lot compared to the ED calculated for delay embedding. We presume that this is because of the noise in the signals. This presumption can be confirmed comparing with the power spectrum plotted later on. Rats2-1 shows a clear decrease in the ED of the ECG, however this is only one case that nothing can be said globally. For respiration, nothing can be remarked. As mentioned in "Rats1,", the study on the size of the Toeplitz like matrix (K) is very similar to the

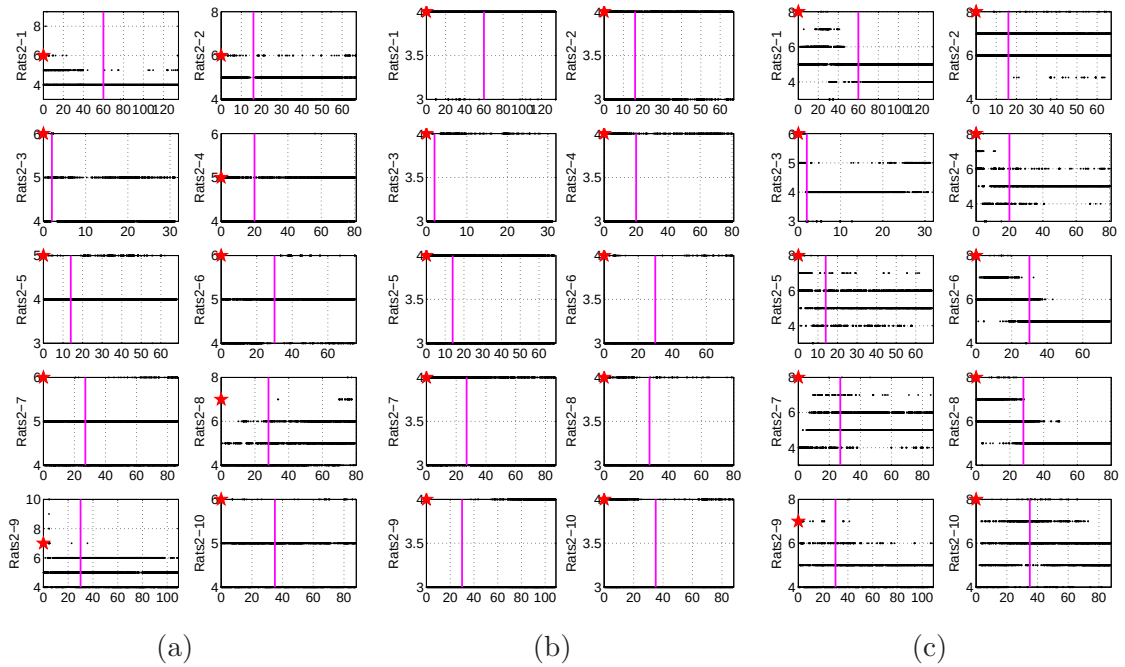

Figure 3.43 – *The study on the embedding dimension (ED) for delay embedding. Horizontal axis is time (min). The magenta lines indicate the deep-light change of anæsthesia detected in [Musizza et al., 2007]. The red stars indicates the chosen parameters: (a) ECG, (b) Respiration and (c) EEG.*

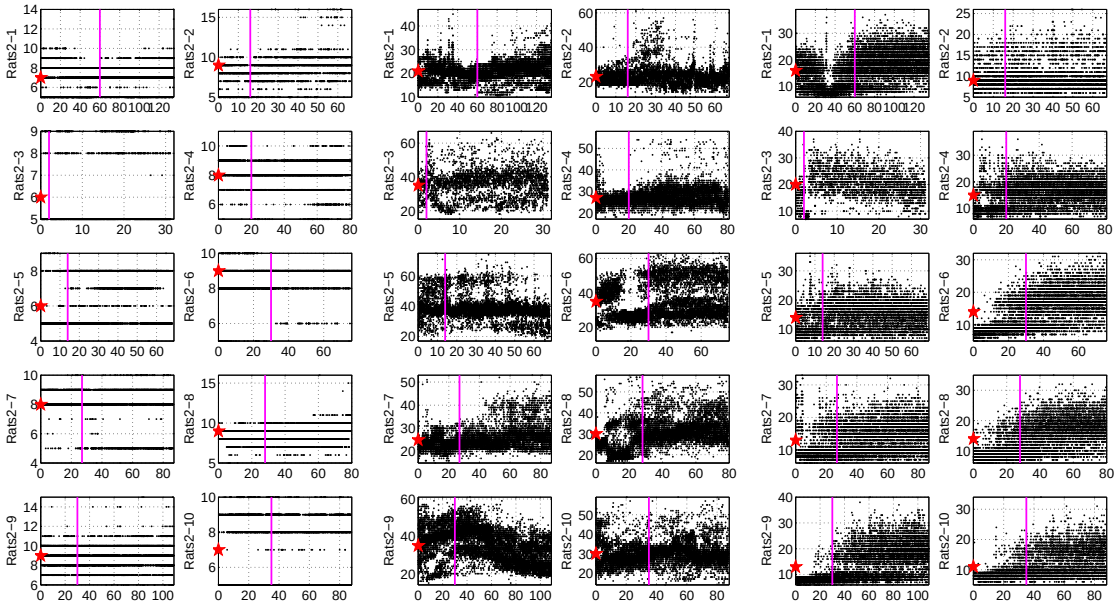

Figure 3.44 – *The study on the time delay (τ) (samples) for delay embedding. Horizontal axis is time (min). The magenta lines indicate the deep-light change of anæsthesia detected in [Musizza et al., 2007]. The red stars indicates the chosen parameters: (a) ECG, (b) Respiration and (c) EEG.*

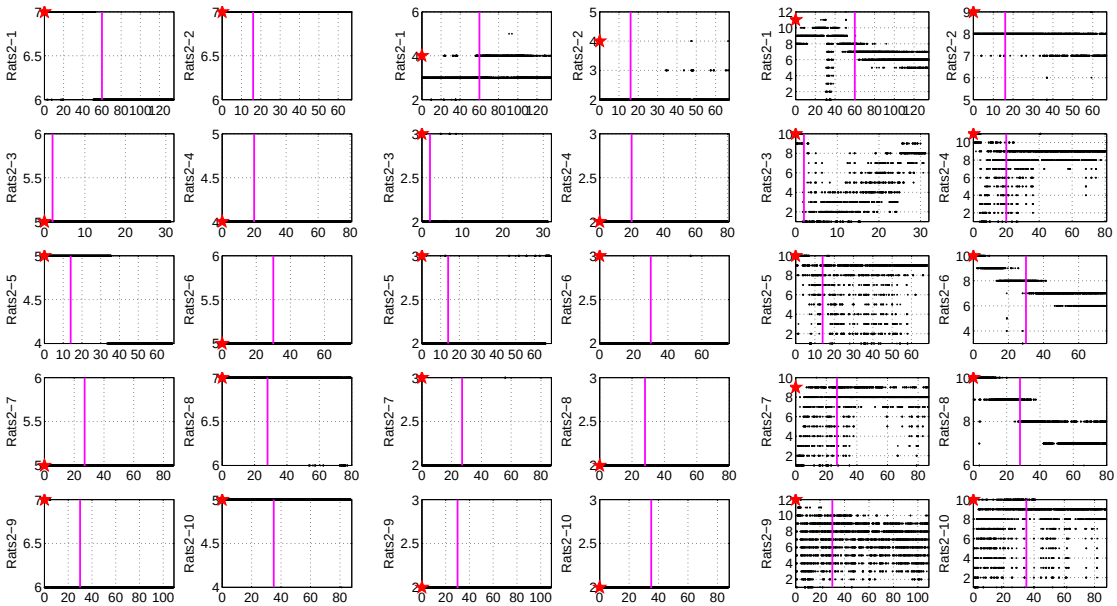

Figure 3.45 – *The study on the embedding dimension (ED) for PCA embedding. Horizontal axis is time (min). The magenta lines indicate the deep-light change of anæsthesia detected in [Musizza et al., 2007]. The red stars indicates the chosen parameters: (a) ECG, (b) Respiration and (c) EEG.*

study of the delay time τ such that the obtained plot is just shown in appendix.

Coupling matrix

Here again, in order to have more information about the influence between the observed systems, we proceeded to the analysis of the coupling matrix (CM). As "Rats1", the self model was created taking the first 1 minute time series of each signal. In Fig. 3.46 and 3.47, the observed results are shown. From these figures, compared to "Rats1", no common change of $CM(t)$ can be found in all causality between the two. Concentrating on some rats, a higher $CM(t) : B \rightarrow H$ and $CM(t) : R \rightarrow B$ can be remarked at the light stage of

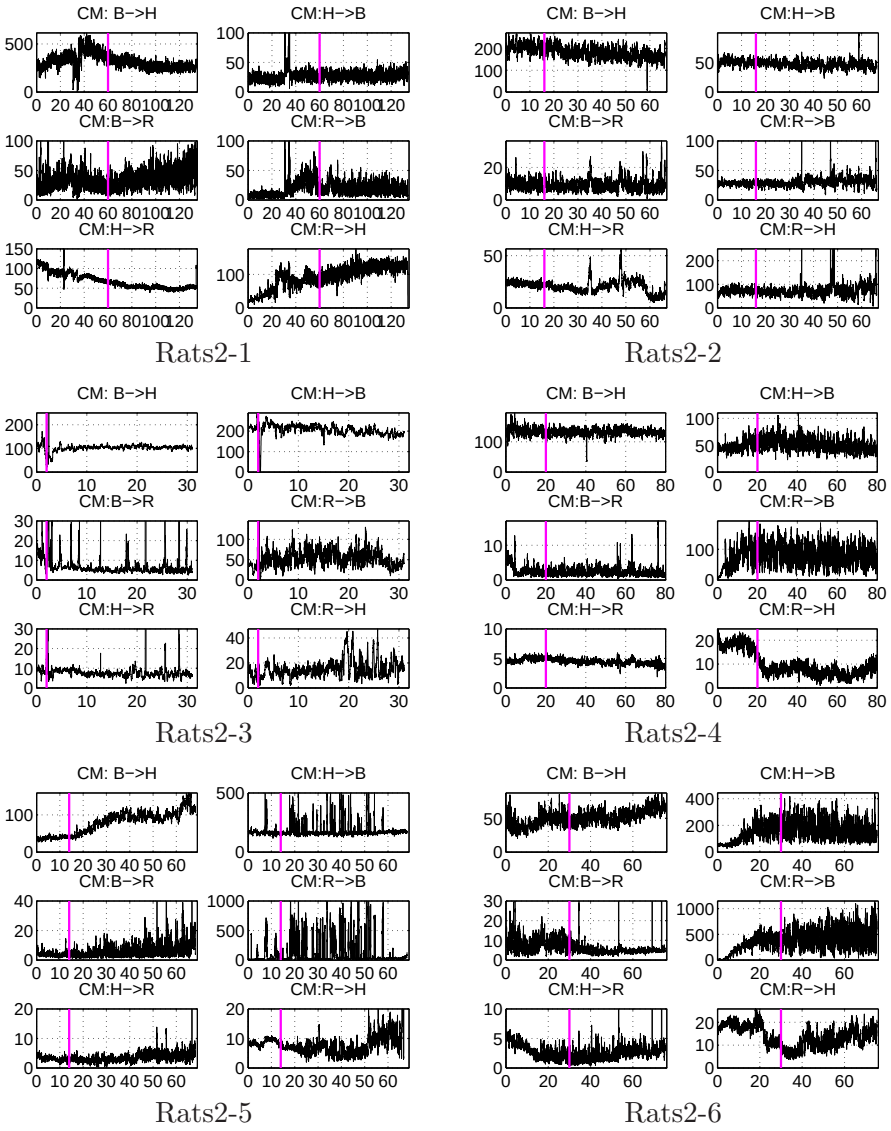

Figure 3.46 – *Coupling matrix $CM(t)$ obtained on "Rats2" PartI (Rats2-1 to Rats2-6). Horizontal axis is time (min). The magenta lines indicate the deep-light change of anæsthesia detected in [Musizza et al., 2007]: (B) EEG, (H) ECG, and (R) respiration.*

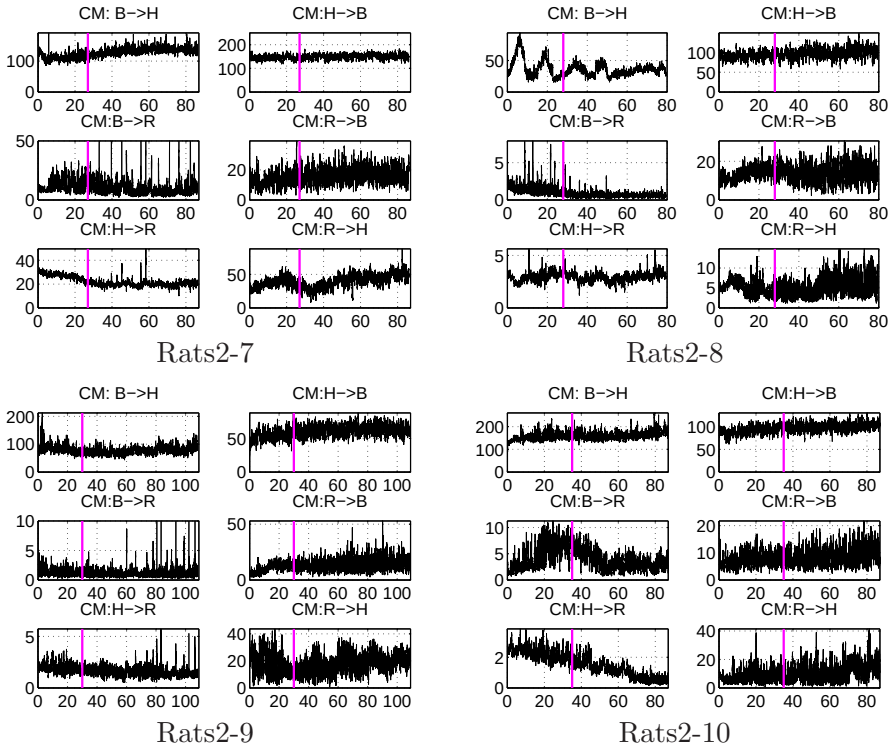

Figure 3.47 – *Coupling matrix $CM(t)$ obtained on "Rats2" PartII (Rats2-7 to Rats2-10). Horizontal axis is time (min). The magenta lines indicate the deep-light change of anæsthesia detected in [Musizza et al., 2007]: (B) EEG, (H) ECG, and (R) respiration.*

anæshtesia, and lower $CM(t) : H \rightarrow R$ and $CM(t) : R \rightarrow H$ can be remarked at the light stage of anæshtesia. Notice that, these remarks on the coupling matrix are different from what we observed on "Rats1".

In order to check the directionality of the interactions, we calculated the directionality index in the same way as "Rats1" and showed the obtained results in Fig. 3.48 and 3.49.

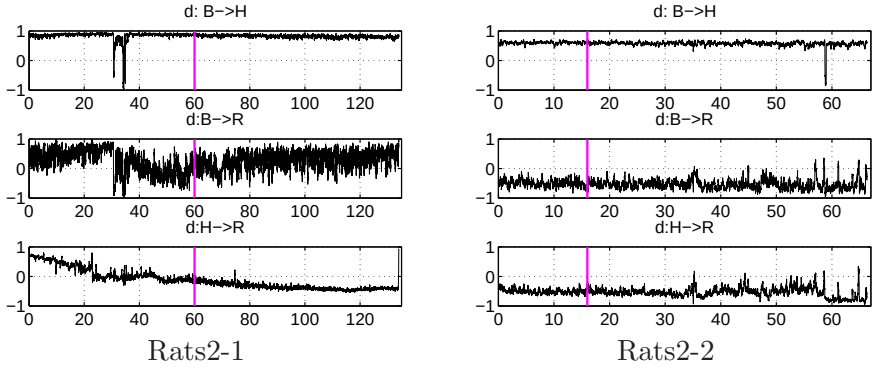

Figure 3.48 – *Direction of the interactions $d(t)$ obtained on "Rats2" using $CM(t)$ PartI (Rats2-1 to Rats2-2). Horizontal axis is time (min). The magenta lines indicate the deep-light change of anæsthesia detected in [Musizza et al., 2007]: (B) EEG, (H) ECG, and (R) respiration.*

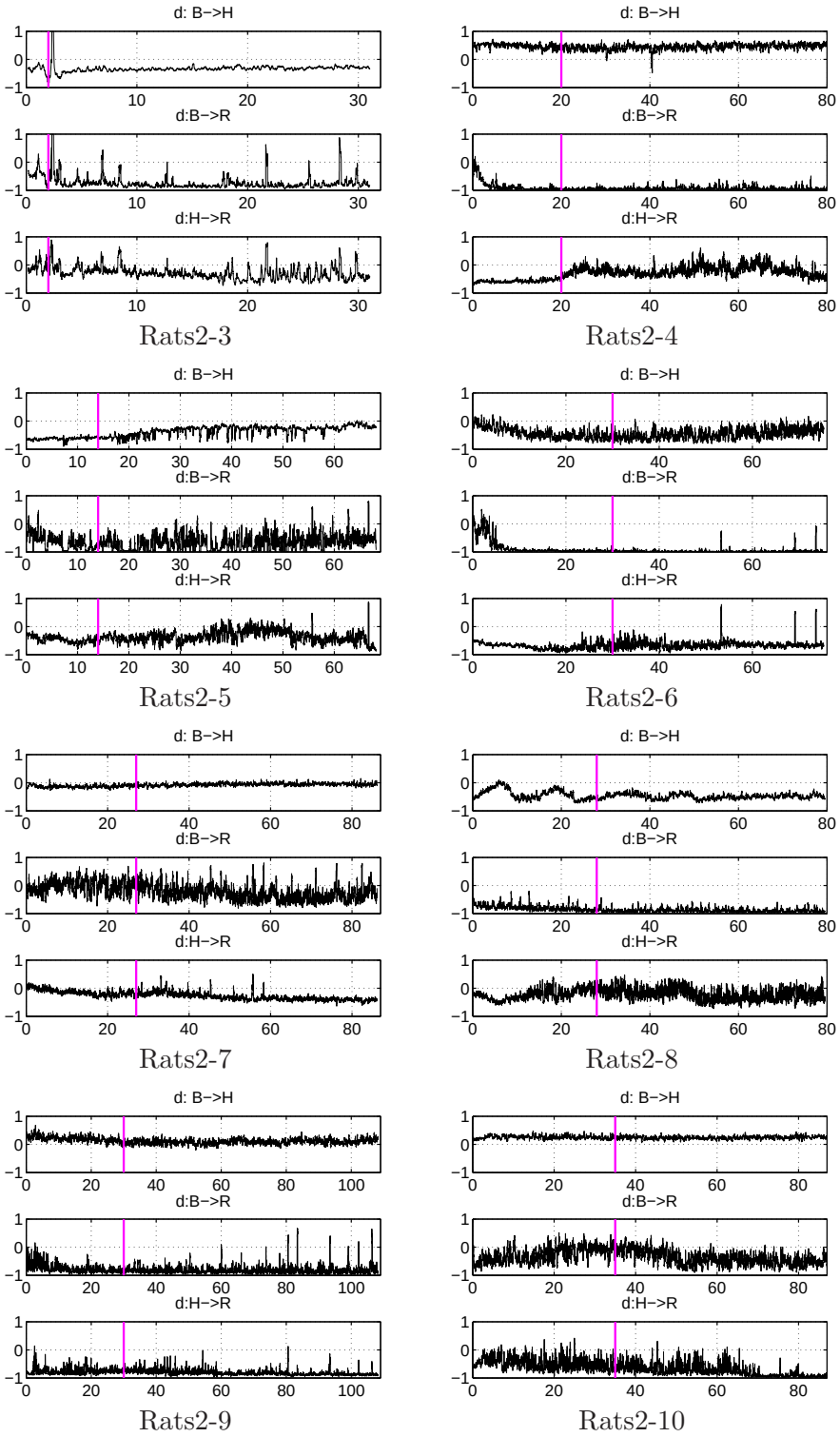

Figure 3.49 – *Direction of the interactions $d(t)$ obtained on "Rats2" using $CM(t)$ PartII (Rats2-3 to Rats2-10). Horizontal axis is time (min). The magenta lines indicate the deep-light change of anæsthesia detected in [Musizza et al., 2007]: (B) EEG, (H) ECG, and (R) respiration.*

From these figures, only $d(t) : H \rightarrow R$ shows clear change in direction at the transition point of anæsthesia. Therefore, no change in direction can be concluded for this group "Rats2",i.e. for PB anæsthetic. Nevertheless, there is major agreement on the directionality for whole measurements and we can conclude that:
In deep and light anæsthesia:
Respiration drives both the brain activity and the heart activity.

This conclusion for "Rats2" also agrees with the study of our collaborators. Moreover, we succeeded to conclude the influence from respiration to brain that our collaborators did not manage to analyze.

Nonparametric Granger causality

In this study, the length of window, shifted time, segments overlap time were set in the same way as "Rats1". First, the power spectra and the coherence spectra were plotted in fig. 3.50 and 3.51. We can see that the plot of Rats2-8 in Fig. 3.50 is the same as the instantaneous frequency of our collaborator in Fig. 3.4 and 3.5 in subsec. 3.3.2, except the harmonics which are also present. In all rats' results, it agrees on the frequency of respiration which does not change according to the change in anæsthesia and on the appearance of θ-oscillations at the transition point. However, we remarked that the decrease in heart frequency along the time is just the case of some rats. Fig. 3.51 gives similar trend between systems as the new S-estimator, $S_{new}(t)$ in Fig. 3.38, and as $S_{new}(t)$, we can remark a strong coherence at the deep stage of anæsthesia in some rats in all clusters. this decrease in coherence is obvious enough such that it may use for the detection of the depth of anæsthesia. However a numerical detection of this point will be difficult since this decrease is not unique for all rats.

In Fig. 3.52 and 3.53, we show the results of the nonparametric Granger causality. Again, the $GC(t)$ smaller than threshold, shown in the following table, defined by the permutation test were set to zero.

	GC:B→H	GC:H→B	GC:B→R	GC:R→B	GC:H→R	GC:R→H
threshold	0.11	0.11	0.11	0.12	0.11	0.12

Table 3.13 – *Threshold for nonparametric Granger causality $GC(t)$ defined by the permutation test for "Rats2": (B) EEG, (H) ECG, and (R) respiration.*

From figures 3.52 and 3.53, we remarked that most of the causality, no matter which two sub systems, show higher value in the deep stage of anæsthesia. Moreover, the frequency range of the remarkable causalities match the main frequencies of the influencing system.

As "Rats1", we also calculated the time domain Granger causality and its directionality, however, again, no change was observed at the transition point of the anæsthesia (See Appendix). Furthermore, my colleague, Yuri Shiogai, also analyzed this "Rats2" concentrating on the same main frequencies of the sub systems stated in "Rats1". The obtained results are shown in table. 3.14. Again, conducting the Wilcoxon rank sum test between the calculated time averaged values of before and after the transition point, she concluded that the coupling from respiration to heart is weakened at the light stage of anæsthesia. This conclusion agrees with the result of the coupling matrix. However, still other causalities are not statistically approved that we should also followed-up in the future.

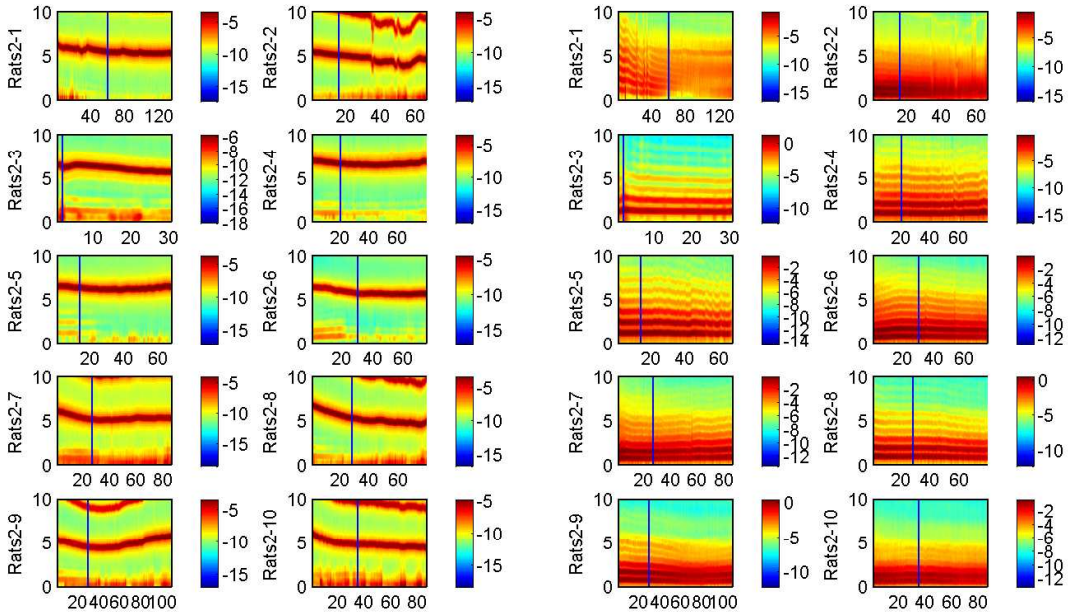

(a) (b)

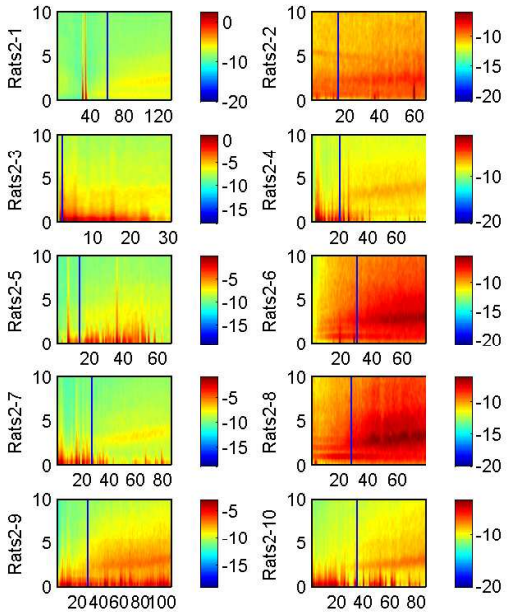

(c)

Figure 3.50 – *Power spectra obtained on "Rats2". Horizontal axis is time (min). Vertical axis is frequency (Hz). The blue lines indicate the deep-light change of anæsthesia detected in [Musizza et al., 2007]: (a) ECG, (b) Respiration, and (c) EEG.*

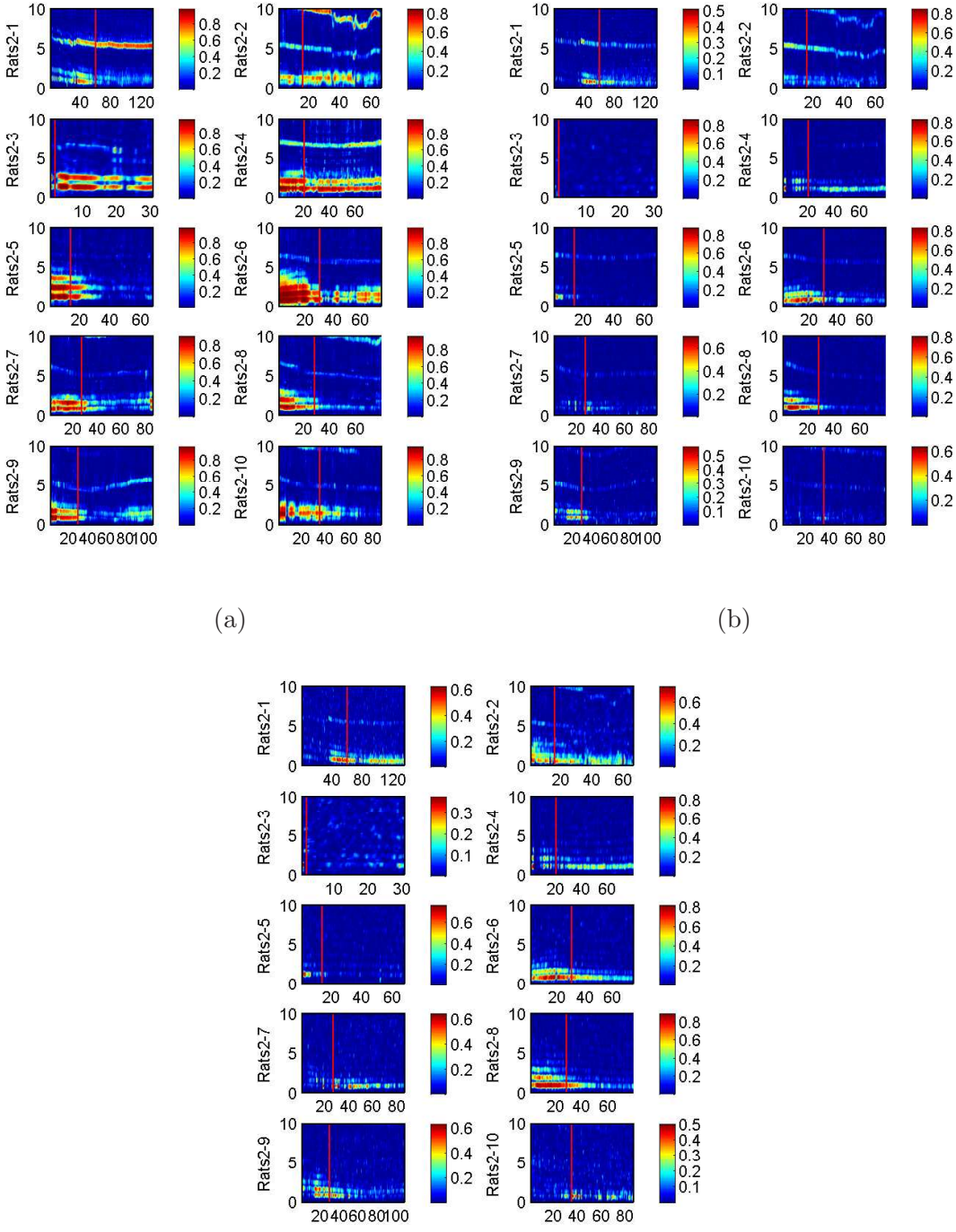

(a) (b)

(c)

Figure 3.51 – *Coherence spectra obtained on "Rats2". Horizontal axis is time (min). Vertical axis is frequency (Hz). The red lines indicate the deep-light change of anæsthesia detected in [Musizza et al., 2007]: (a) ECG and respiration, (b) EEG and ECG, and (c) EEG and respiration.*

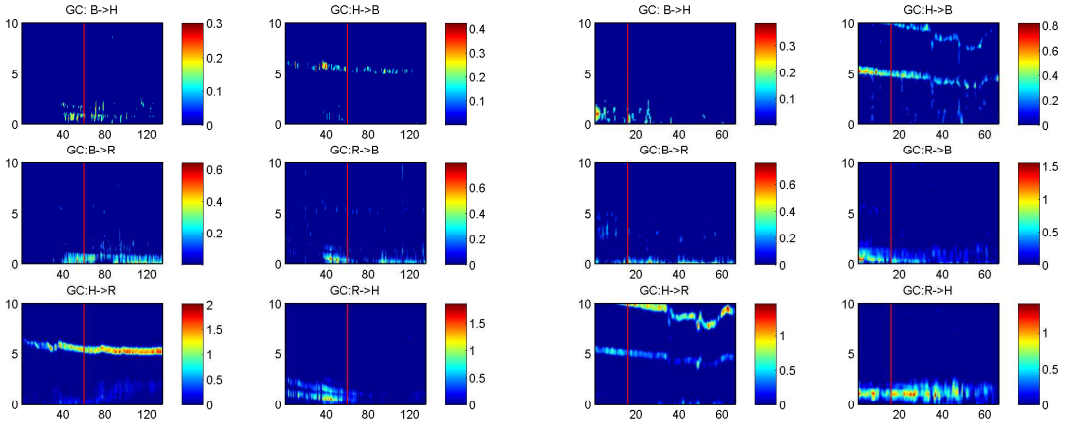

Rats2-1

Rats2-2

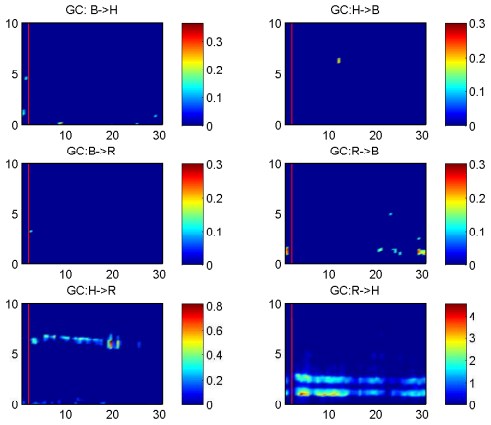

Rats2-3

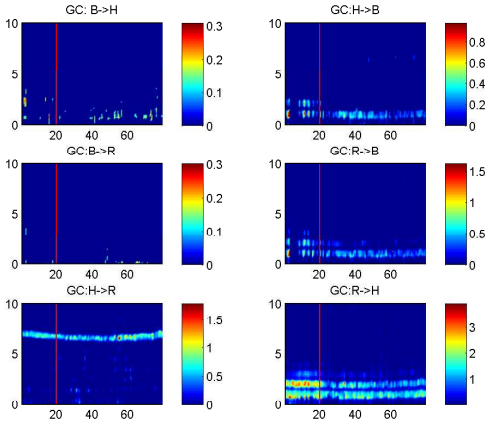

Rats2-4

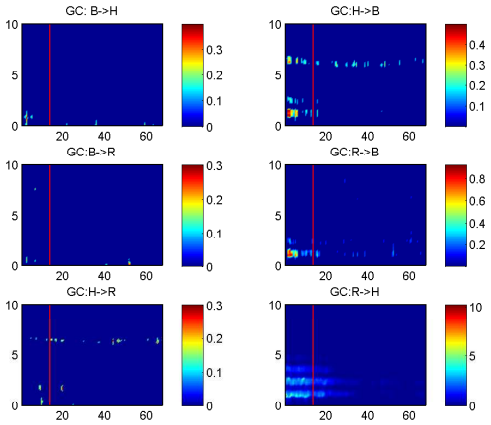

Rats2-5

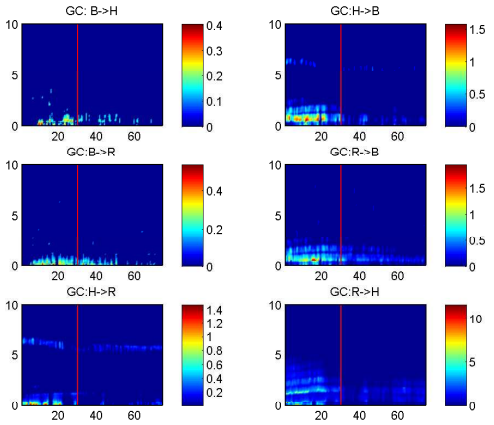

Rats2-6

Figure 3.52 – *Nonparametric Granger causality $GC(t, f)$ obtained on "Rats2" PartI (Rats2-1 to Rats2-6). Horizontal axis is time (min). Vertical axis is frequency (Hz). Red lines indicate the deep-light change of anæsthesia detected in [Musizza et al., 2007]: (B) EEG, (H) ECG, and (R) respiration.*

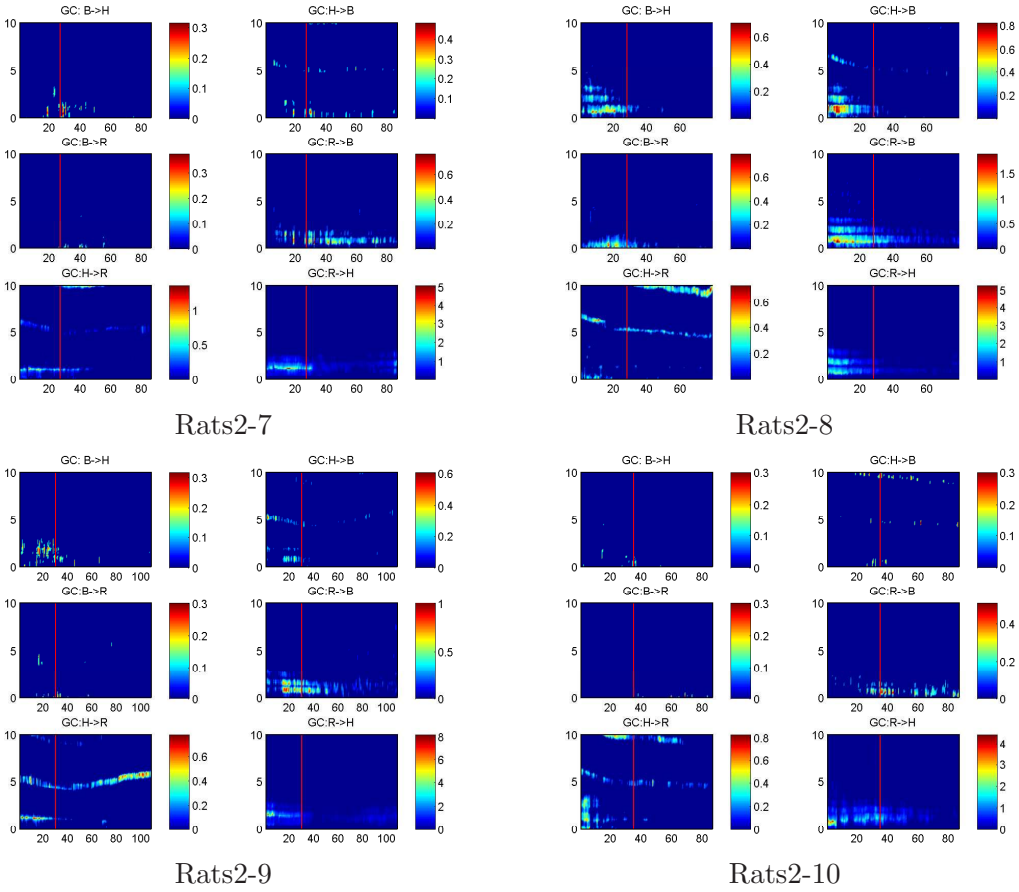

Figure 3.53 – *Nonparametric Granger causality $GC(t, f)$ obtained on "Rats2" PartII (Rats2-7 to Rats2-10). Horizontal axis is time (min). Vertical axis is frequency (Hz). Red lines indicate the deep-light change of anæsthesia detected in [Musizza et al., 2007]: (B) EEG, (H) ECG, and (R) respiration.*

	Time average of the pairwise GC before and after transition										
Rats2(deep)	1	2	3	4	5	6	7	8	9	10	N
H→R	**0.79**	**0.42**	0.08	**0.64**	0.05	**0.17**	**0.13**	**0.18**	**0.18**	0.11	7
R→H	**0.48**	**0.37**	**1.03**	**1.76**	**2.78**	**1.27**	**0.54**	**1.30**	**0.81**	**0.86**	10
H→ θ	0.10	**0.37**	0.02	0.03	**0.12**	0.11	0.06	**0.12**	**0.13**	0.04	4
R→B	0.09	**0.50**	0.10	**0.33**	**0.30**	**0.60**	0.09	**0.81**	**0.36**	0.07	6
Rats2(light)	1	2	3	4	5	6	7	8	9	10	
H→R	**1.35**	**0.24**	**0.12**	**0.64**	0.04	**0.12**	0.08	**0.13**	**0.26**	0.09	7
R→H	0.11	**0.42**	**1.40**	**1.41**	**0.48**	**0.70**	**0.22**	**0.23**	**0.19**	**0.16**	9
H→ θ	0.08	**0.18**	0.03	0.03	0.07	0.06	0.04	0.03	0.04	0.04	1
θ →H	0.05	0.02	0.02	0.01	0.01	0.01	0.01	0.01	0.01	0.01	0
R→B	0.05	**0.15**	0.05	**0.31**	0.06	**0.20**	**0.20**	**0.23**	**0.15**	0.11	6
θ →R	0.04	0.03	0.01	0.01	0.01	0.02	0.01	0.02	0.02	0.01	0

Table 3.14 – *Table for time averaged GC before and after the transition time. If the causalities go beyond the thresholds calculated by a permutation test, they are significant and written in bold. N indicates the number of rat's data which shows significant influence: (H) ECG, (R) respiration, (B) EEG and (θ) θ-wave of EEG.*

3.9.3 Rats3

In group "Rats1", we saw that the effect of Ketamine (KX) can be analyzed in different ways on three measured signals (EEG, ECG and respiration). As a result; we managed to detect the deep-light transition point of anæsthesia visually and numerically. And, we clarified that the interactions among these systems change according to the depth of anæsthesia. Here on group "Rats3", we will see if what we concluded in "Rats1" hold with reinduction of the anæsthetic (KX). Moreover, as we changed the measurement protocol for the EEG signals, we will proceed the analysis paying more attention to the change in the EEG related results.

All the measurements of this group were preprocessed in the same way as previous two groups. Now let us begin with the S-estimator.

S-estimator

The parameters, i.e. sliding window length and shifted time length were the same as "Rats1". However, the sampling frequency was 1200Hz and not 1000Hz such that there were more samples inside one window. The embedding dimension (ED) and time delay (τ) used in this work are shown in the following table.

Rats3-		1	2	3	4	5	6	7	8	9	10	11	12	13	14	15	16
ED	ECG	6	8	5	6	6	7	6	5	10	5	10	5	5	6	9	8
	Resp	4	4	4	4	4	4	4	4	4	4	4	4	4	4	4	4
	EEG	7	6	6	6	6	7	6	6	6	6	6	6	7	5	5	6
τ	ECG	11	10	9	11	12	11	11	12	11	9	9	9	9	13	11	11
	Resp	30	40	37	44	38	43	31	39	43	29	41	34	35	30	33	27
	EEG	15	18	17	16	16	14	18	14	16	15	15	14	14	20	18	14

Table 3.15 – *Embedding dimension (ED) and time delay (τ) used in the studies.*

In fig. 3.54, the obtained $S(t)$ for each rats are shown. In the figure, we remarked that, same as "Rats1", $S(t)$ increases when the anæsthetic begins to effect, and decreases when it looses the effect. However, as the increase rate of $S(t)$ is bigger than the case of "Rats1", the statistical assessment tool that we used in "Rats1" for numerical detection of the deep-light transition point of the anæsthesia did not work. We presume that this comes from the protocol change of the EEG signals. Consequently, the transition point was estimated comparing the result of the S-estimator and the power spectra that we obtained at the analysis of the nonparametric Granger causality, using the knowledge that we obtained from the study on "Rats1" and from the study of [Musizza et al., 2007]. More precisely, at first, we tried to detect this transition point looking at the variation change of the frequency of the EEG, i.e. diminishing δ-wave and appearing θ-wave, as well as the frequency of the respiration which slightly increased and became erratic on the plotted results of the power spectra (See fig. 3.61). After that, we checked if the detected change point coincide with the variation change point (increasing to decreasing) of the value of $S(t)$ which was the main result of the S-estimator on "Rats1", and adapted the timing of the transition point. The obtained transition time is shown in table. 3.16. Just to notice, these estimated transition timing are detected visually such that they may not precise. From fig. 3.54, we can remark

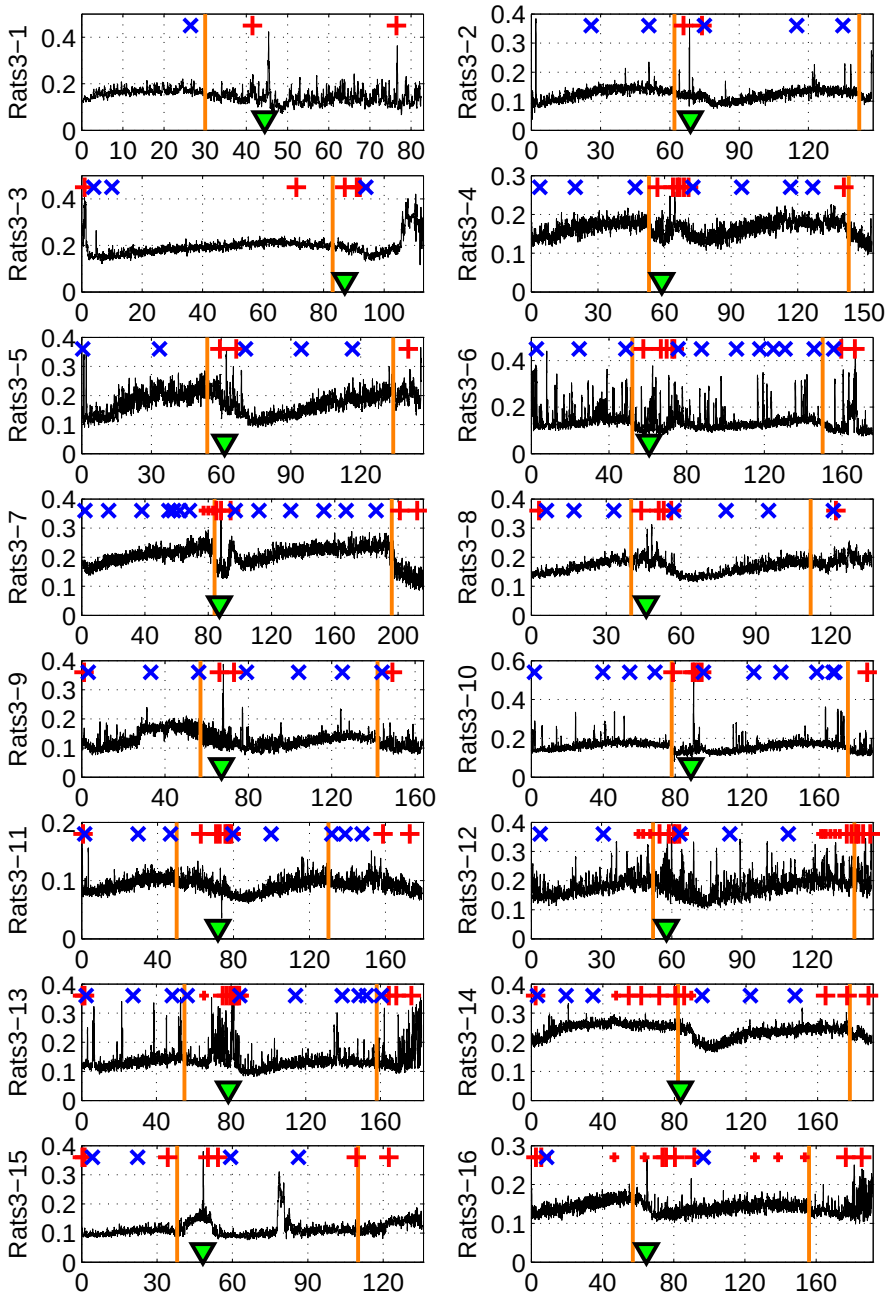

Figure 3.54 – *Synchronization measure $S(t)$ obtained by clustering three oscillators (ECG, Respiration and EEG) together on group "Rats3". Horizontal axis is time (min). The downward triangles show the reinduction timing. Blue 'x' means negative reaction, Red '+' means positive reaction, and smaller red '+' means weak positive reaction to the pinch test. Orange lines indicate the estimated deep-light change of anæsthesia.*

Rats3-	1	2	3	4	5	6	7	8	9	10	11	12	13	14	15	16
1st	30	62	83	53	54	52	84	40	57	78	50	52	55	82	38	57
2nd	-	142	-	143	134	150	196	112	142	176	130	138	158	178	110	156

Table 3.16 – *The estimated deep-light transition point of the anæsthesia (min). No 2nd transition was remarked for Rats3-1 and Rats3-3.*

that sometimes, the positive reaction to the pinch test precedes the estimated deep-light transition. We didn't see the experiments with our eyes such that we don't know if the rats were conscious or not when they had positive reaction. If they were also conscious, we should revise our detection methods.

Here below, we show the $S(t)$ obtained by clustering two sub-systems. From the figure, we remarked that the synchronization on ECG-Respiration cluster do not show a big change at the transition point, except on Rats3-5. As also in "Rats1", it was also difficult to remark the change at the transition of the anæshtesia on this cluster, we presume that the degree of the synchronization on ECG-Respiration system remains unchanged with the effect of KX even if there is a phase synchronization change reported in our collaborators studies. The other two clusters show similar plot as the cluster with all the three, and they also show a variation change at the transition point.

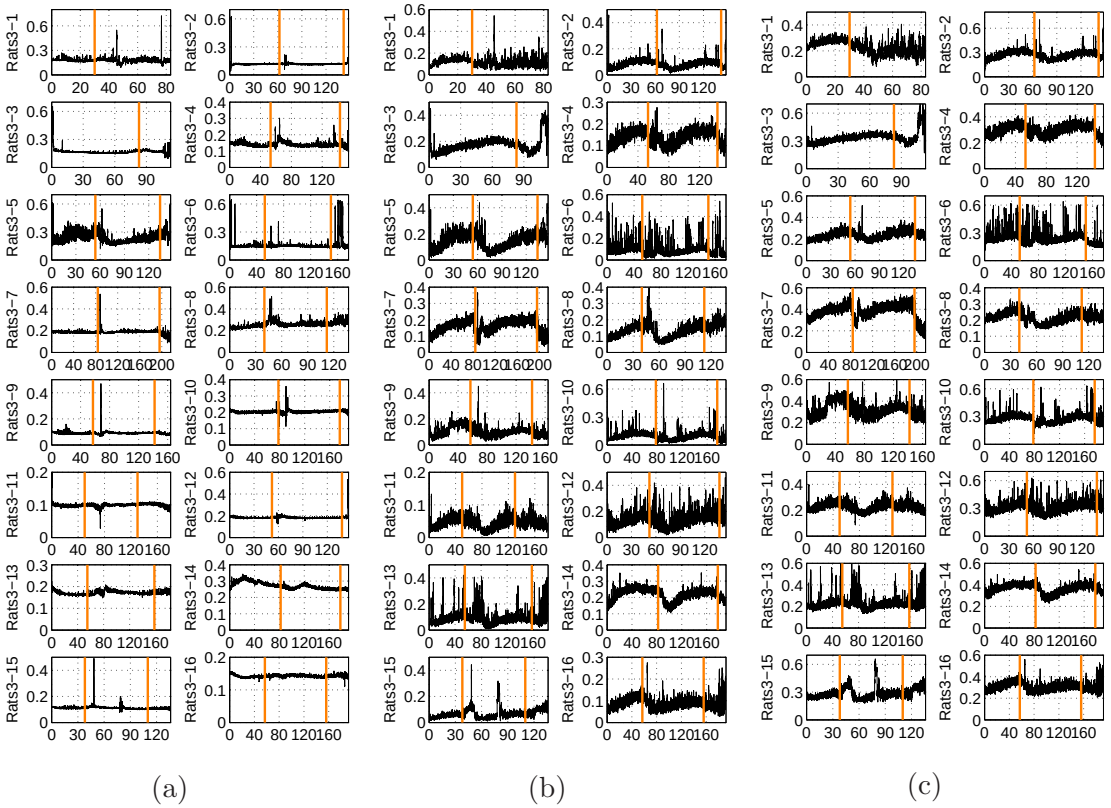

(a) (b) (c)

Figure 3.55 – *Synchronization measure $S(t)$ obtained by clustering two chosen oscillators together on group "Rats3". Horizontal axis is time (min). Orange lines indicate the estimated deep-light change of anæsthesia: (a) ECG and Respiration, (b) ECG and EEG, and (c) Respiration and EEG.*

new S-estimator

As the group before, we proceed to the new S-estimator to see the inter-synchronization without intra-synchronization. The obtained results are shown in fig. 3.56. From this figure, in the majority, we can confirm the result of "Rats1", i.e. there is no clear and unique variation change at the transition point except Rats3-5 and Rats3-7 which show a sudden decrease at this point. Again as previous two group of rats, the strength of the synchronization becomes 10 times smaller than $S(t)$. However, we cannot see a slight increase around the change point that we observed in "Rats1". But, we can see a spike of the $S_{new}(t)$ at the moment of the induction of anæsthetic which surely be a strong external stimuli.

In fig. 3.57, the results of $S_{new}(t)$ obtained with clusters of two systems are shown. From fig. 3.57(c), we remarked a very clear variation increase in $S_{new}(t)$ towards the transition points on Rats3-5, Rats3-6, Rats3-7, Rats3-12 and Rats3-13. This increase suddenly stop at the transition point and $S_{new}(t)$ suddenly decrease. Looking only this decrease, we can observe also on Rats3-1 and Rats3-16. This is very interesting, but as it is not the case for all rats, we can not conclude the relation between this phenomena and the effect of anæsthesia.

Fig. 3.58 is shown to compare the strength of synchronization among clusters of two systems. From the figure, we saw that there is little synchronization between ECG and EEG. For the other two, the order of the strength of synchronization is not unique such that nothing can be concluded.

We also calculated this new S-estimator with PCA based embedding method. The employed ED and K are shown in table below. 3.17.

Rats3-		1	2	3	4	5	6	7	8	9	10	11	12	13	14	15	16
ED	ECG	7	4	7	5	9	7	7	7	7	7	7	5	5	6	7	7
	Resp	5	4	6	3	4	3	6	3	3	4	3	4	4	4	4	3
	EEG	7	8	9	8	7	7	8	7	8	8	8	8	8	8	8	8
K	ECG	25	14	25	15	34	25	25	27	25	25	25	14	15	25	25	25
	Resp	66	89	78	85	82	89	72	82	88	79	87	78	76	78	76	71
	EEG	34	41	42	41	35	30	41	33	40	37	37	36	37	43	41	35

Table 3.17 – *Embedding dimension (ED) and size of Toeplitz like matrix (K) used in the studies.*

The obtained results gave us very similar results as the results with delay embedding method, such that we just putted the obtained results in appendix.

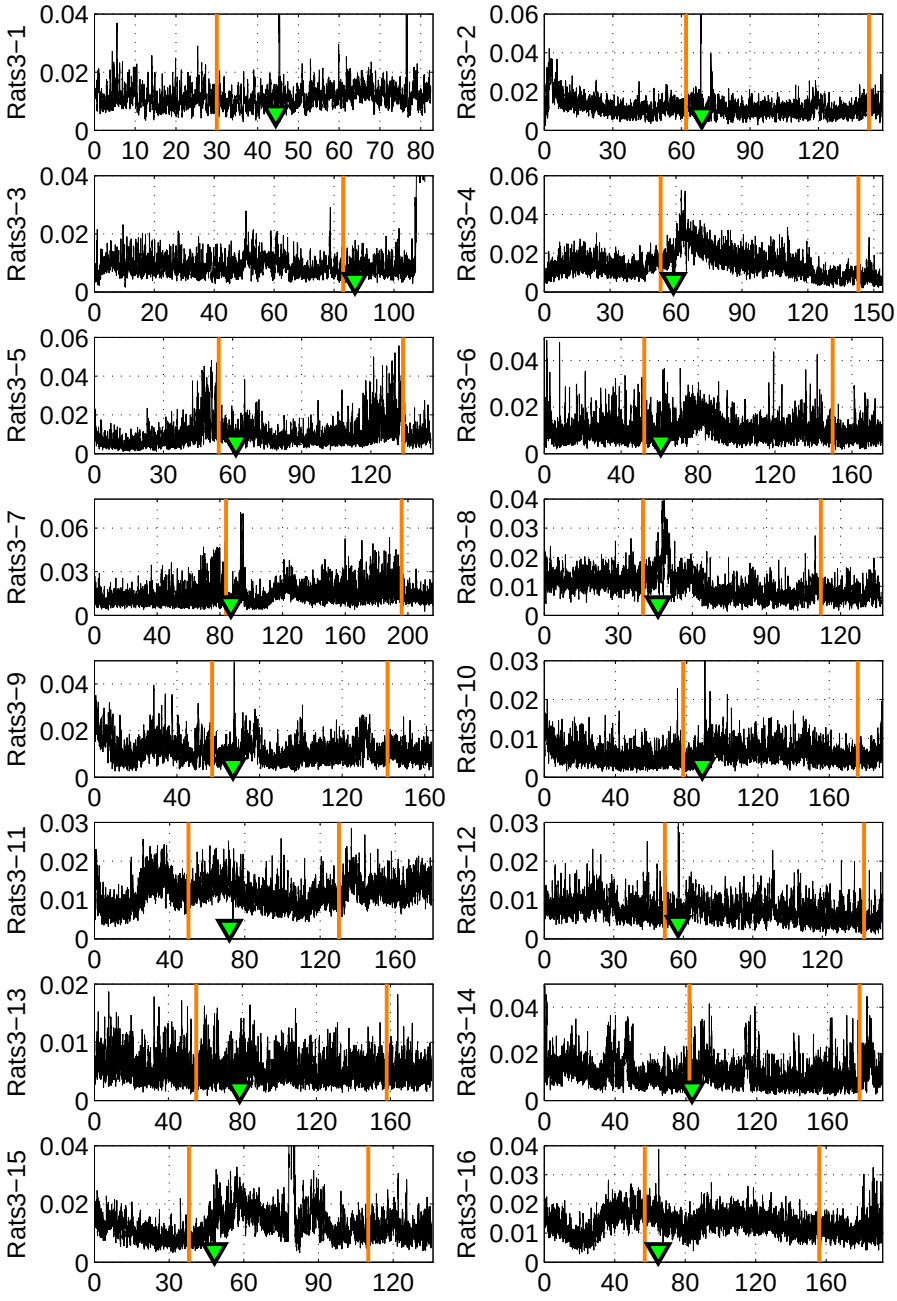

Figure 3.56 – *Synchronization measure $S_{new}(t)$ obtained by clustering three oscillators (ECG, Respiration and EEG) together on group "Rats3". Horizontal axis is time (min). Orange lines indicate the estimated deep-light change of anæsthesia. The downward triangles which indicate the reinduction timing are also shown as a reference of strong external stimulation. Sometimes, high value of $S_{new}(t)$ is not plotted since we zoomed in in order to see the variation around the transition point.*

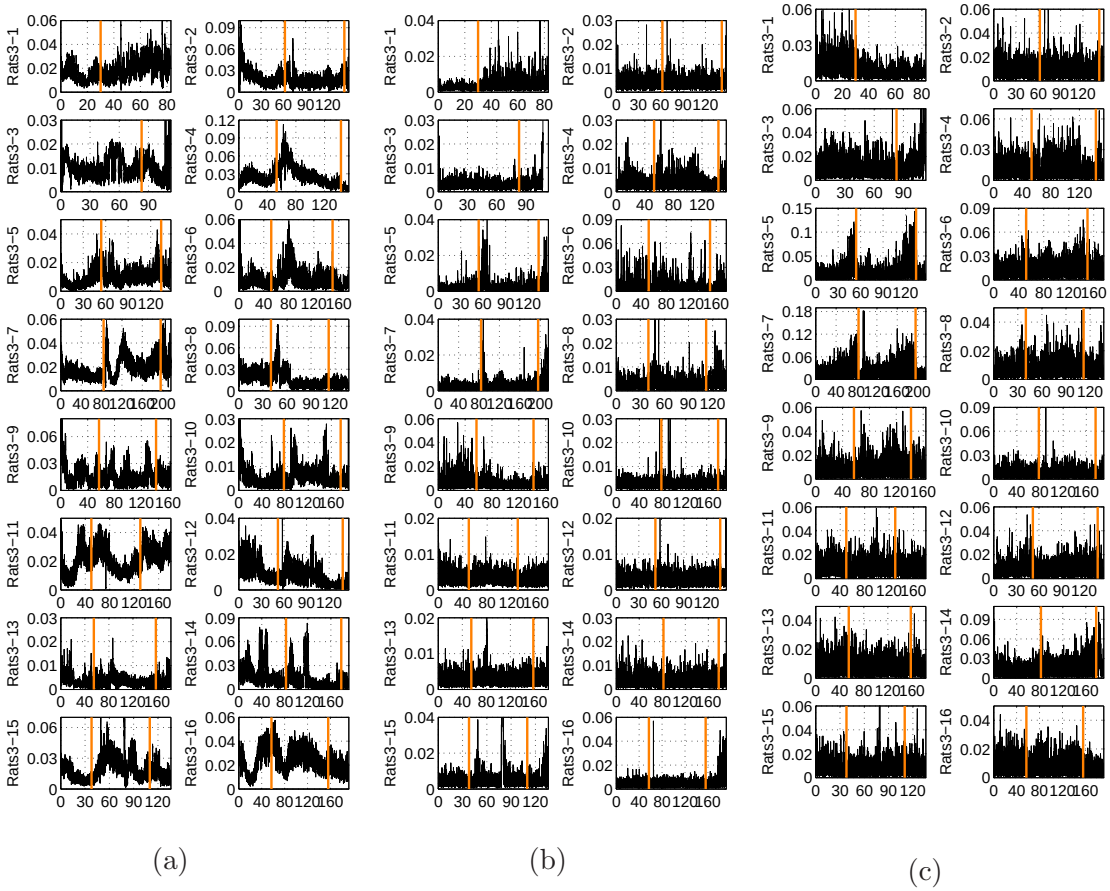

Figure 3.57 – *Synchronization measure $S_{new}(t)$ obtained by clustering two chosen oscillators together on group "Rats3". Horizontal axis is time (min). Orange lines indicate the estimated deep-light change of anæsthesia: (a) ECG and Respiration, (b) ECG and EEG, and (c) Respiration and EEG.*

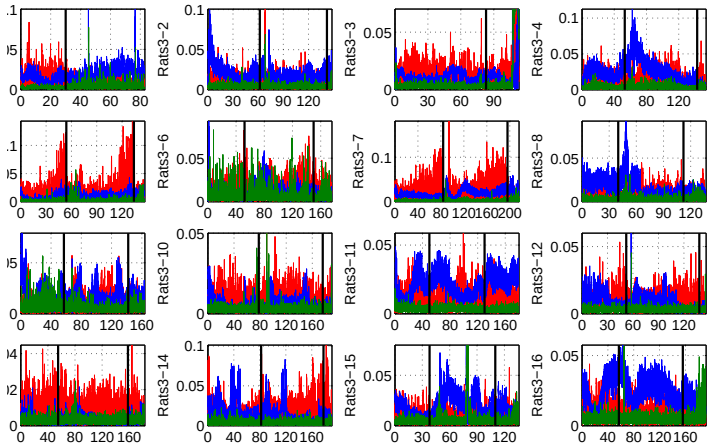

Figure 3.58 – *Comparison of the strength of $S_{new}(t)$ obtained by clustering two chosen oscillators together on Group "Rats3". Horizontal axis is time (min). The black lines indicate the estimated deep-light change of anæsthesia: (blue) ECG and Respiration, (green) ECG and EEG, and (red) Respiration and EEG.*

Embedding dimension analysis

In Fig. 3.59, we show the obtained results on embedding dimension (ED) for delay embedding*. On this figure, same as "Rats1", we remarked an increase in ED of EEG at the transition points on most of the rats, and also in ED of ECG around the transition points on more than half of the rats. No change was remarked for ED of respiration. Consequently, we can confirm the conclusion in "Rats1", i.e. the complexity of the EEG and ECG signals change according to the effect of anæshtesia and it is lower in the deep state of anæshtesia. Moreover, in this group, we have not only two times the transition from deep to light but also we have the transition from light to deep anæsthesia, such that we have more samples of ED change on the obtained figures, and we can give comment on this ED shift; right biased triangle structures of ED at the change point of anæsthesia appears on the results of ECG ED. From that, we presume that the effect of anæsthesia on heart activity slowly weakens along the time from the beginning of effective anæsthetic and rapidly strengthen with the reinduction of the anæsthetic. As a result, the ED of the ECG signals increases and decreases with respect to it. This presumption is very interesting, however, this is not

*the obtained results on the time delay are shown in appendix.

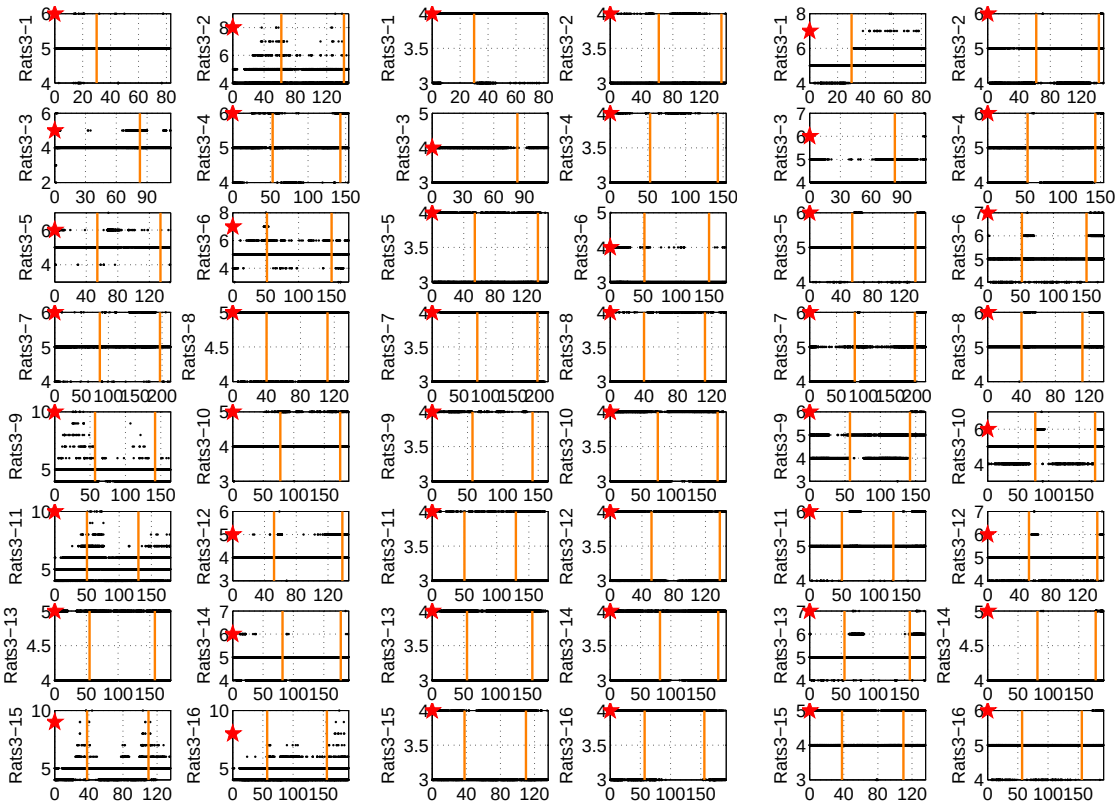

(a) (b) (c)

Figure 3.59 – *The study on the embedding dimension (ED) for delay embedding. Horizontal axis is time (min). Orange lines indicate the estimated deep-light change of anæsthesia. The red stars indicates the chosen parameters: (a) ECG, (b) Respiration and (c) EEG.*

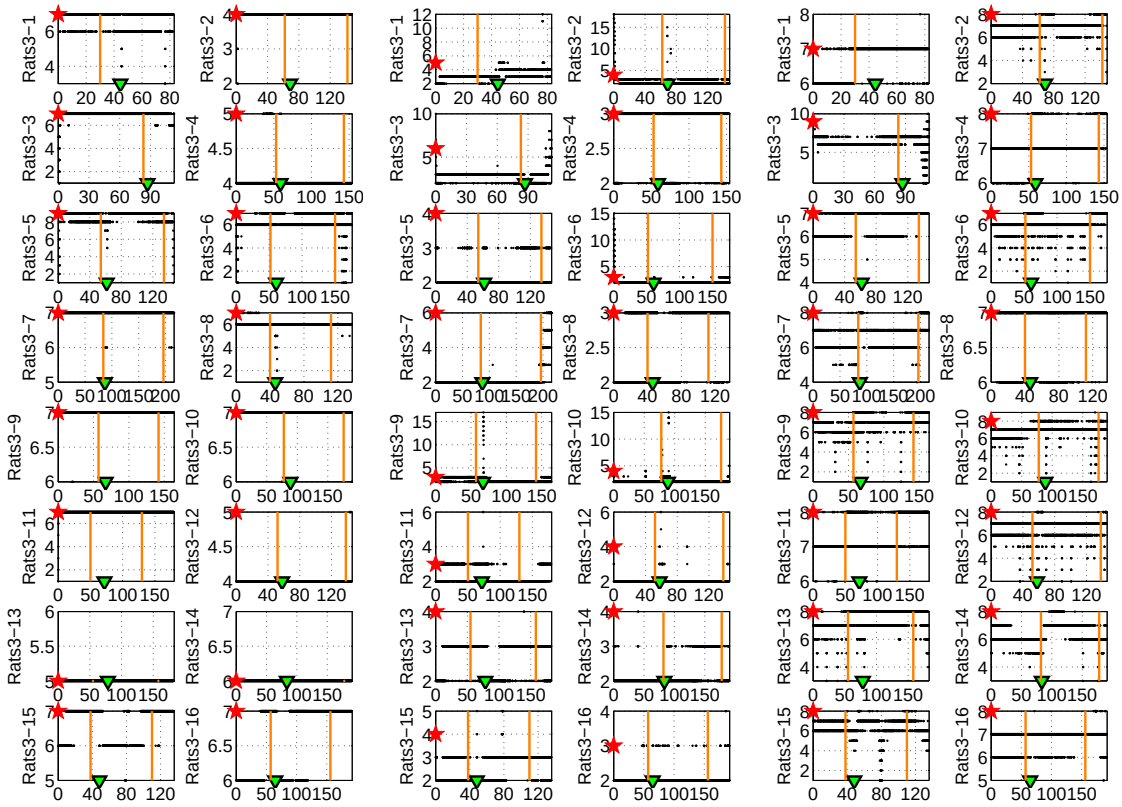

Figure 3.60 – *The study on the embedding dimension (ED) for PCA based embedding. Horizontal axis is time (min). Orange lines indicate the estimated deep-light change of anæsthesia. The downward triangles show the reinduction timing. The red stars indicates the chosen parameters: (a) ECG, (b) Respiration and (c) EEG.*

the case for all rats such that more detailed analysis is needed in the future. We cannot find this long time scale transition of ED with respect to the effect of anæsthesia on the result of the EEG signals, but we can remark the quick shift of the ED value at the change point of anæsthesia which is more straightforward than the group "Rats1". We presume that it is because of the protocol change of the EEG measurement and should be also taken care in the future.

In Fig. 3.60, we show the obtained results on embedding dimension (ED) for PCA based embedding method*. From these figures, at first, we remarked that the obtained results show a lot of spike-like short fluctuations. We can imagine that these are artifacts, since PCA based embedding is a linear method and can be easily affected from a sudden big influence on the signal. To verify, we plotted the reinduction timing on the obtained results, which represents the time index of the strong external stimuli, i.e. the cause of artifacts. Exactly, most of the reinduction timing match the spike of the value of ED. For the results of the ED of EEG signals, we also saw matches between spike-like fluctuation

*the obtained results on the size of the Toeplitz like matrix are shown in appendix.

and the pinch test*. Despite of these artifacts, the ED change of the EEG can be still seen with this PCA based method. But as the case of "Rats1", the change of ED of the ECG cannot be seen.

Nonparametric Granger causality

As mentioned in subsec. 3.2.2, the recordings on this group were very long, i.e. 159 min on average, such that it was impossible to analyze with the coupling matrix method because of the memory limitation on the computing servers†. Accordingly, this CM analysis for this group "Rats3" was omitted in this thesis.

Again, in this study, the length of window, shifted time, segments overlapped time were set with the same value as "Rats1". The power spectra and the coherence spectra were shown in fig. 3.61 and 3.62. In fig. 3.61, we can see that our estimated deep-light change

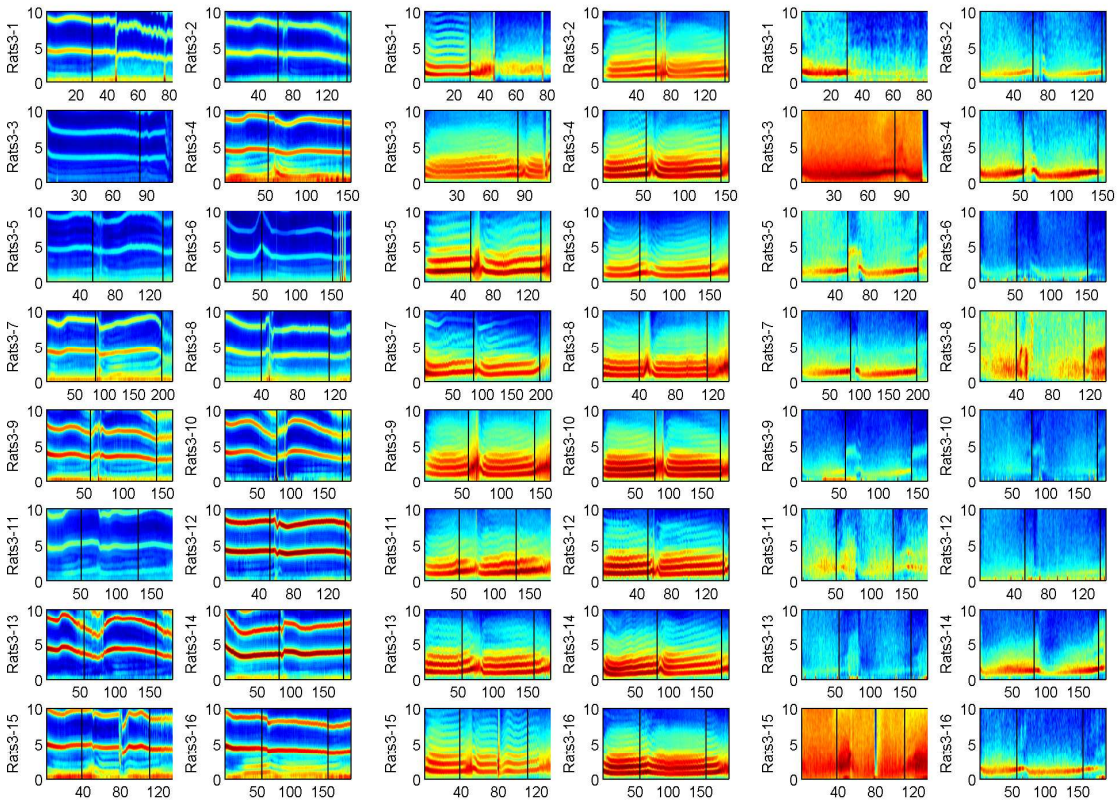

Figure 3.61 – *Power spectra obtained on "Rats3". Horizontal axis is time (min). Vertical axis is frequency (Hz). Color axis is omitted. Black lines indicate the estimated deep-light change of anæsthesia: (a) ECG, (b) Respiration, and (c) EEG.*

*The timing of the pinch test is not shown here since figures become messy.

†The maximum size of the memory was 16G

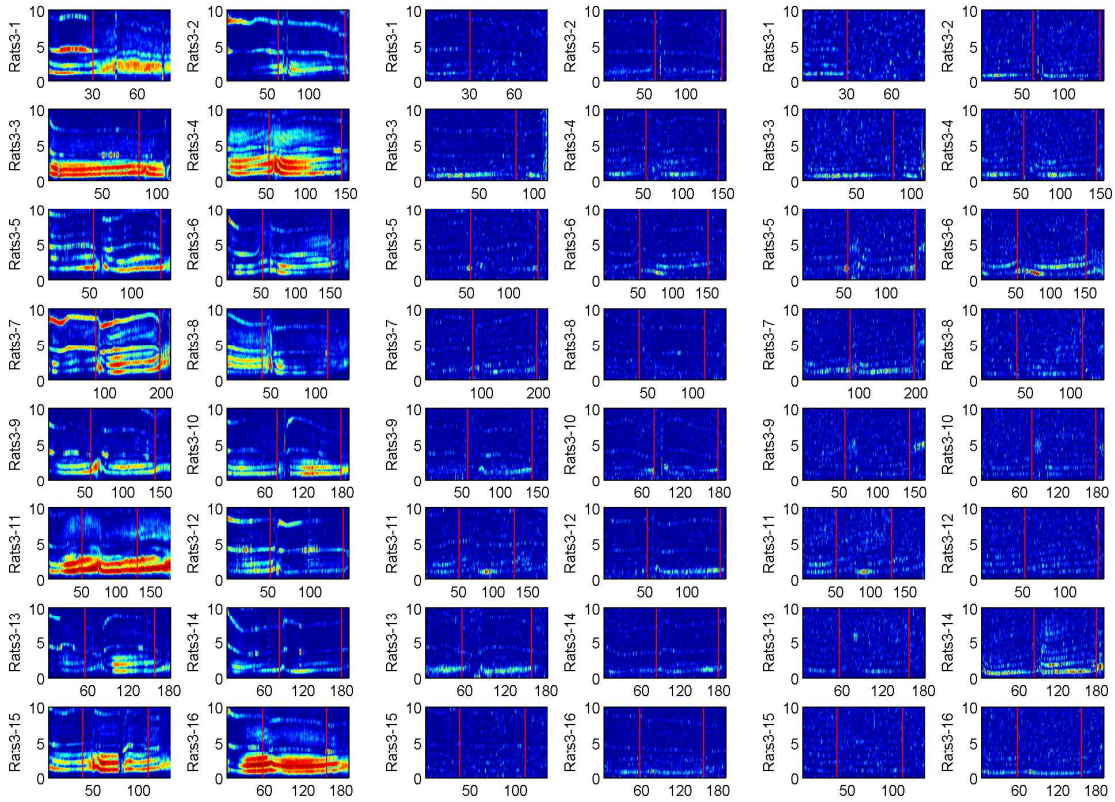

Figure 3.62 – *Coherence spectra obtained on "Rats3". Horizontal axis is time (min). Vertical axis is frequency (Hz). Orange lines indicate the estimated deep-light change of anæsthesia: (a) ECG and respiration; color axis [0 1], (b) EEG and ECG; color axis [0 0.4], and (c) EEG and respiration; color axis [0 0.4].*

points of anæsthesia were well defined to see the increase of the respiration frequency, diminishing δ-wave and appearance of θ-wave. No unique frequency change according to the anæsthesia can be observed for ECG. From fig. 3.62, as "Rats1", strong coherence can be observed between ECG and respiration. But in the contrary, the others show weak coherence. Nevertheless, it seems stronger in deep stage of anæsthesia at low frequency in both case. Looking carefully, again it gives similar trend as the new S-estimator.

In fig. 3.63, 3.64 and 3.65, we show the results of the nonparametric Granger causality. As previous two group, the $GC(t)$ smaller than threshold, shown in the following table 3.18, defined by the permutation test* were set to zero. From fig. 3.63, 3.64 and 3.65, few causality can be found between brain (B) and heart(H), and also between B and respiration (R). Consequently, we cannot remark an increase in the causality from B to R at the light stage of anæsthesia found in group "Rats1". This may result also because of the short recordings of the period of light stage of anæshtesia. The causality from H to R seems to

*For this permutation test on "Rats3", 10 min data around the first transition points are taken to the test.

	GC:B→H	GC:H→B	GC:B→R	GC:R→B	GC:H→R	GC:R→H
threshold	0.09	0.09	0.10	0.09	0.10	0.09

Table 3.18 – *Threshold for nonparametric Granger causality $GC(t)$ defined by the permutation test for "Rats3": (B) EEG, (H) ECG, and (R) respiration.*

decrease at the light stage of anæsthesia as we found in "Rats1". The causality from R to H can be found mostly on whole period of recordings, and some decrease can be remarked at the light stage of anæsthesia.

As the recorded data of this group "Rats3" were only available at the end of April 2008, i.e. only three months before my thesis submission, we didn't have much time to analyze. Owing to this, the time averaged GC analysis tracing specific frequency range was not reported on this thesis. As a result, we didn't manage to concretize any interdependencies between the brain, heart and respiration activities for this group.

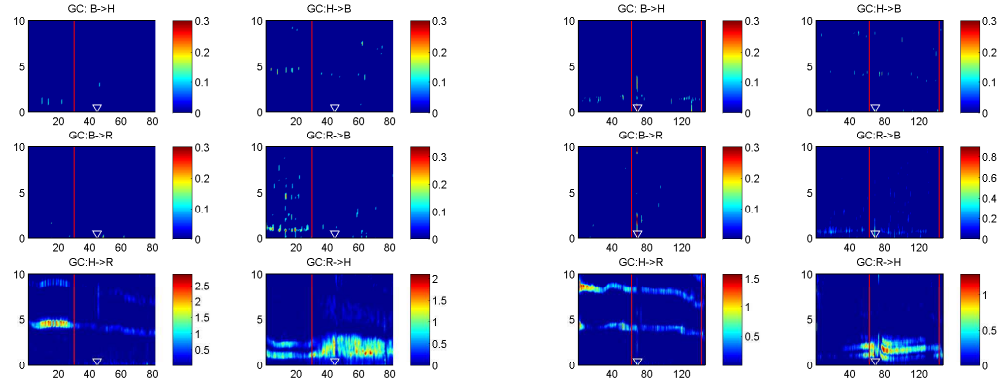

Rats3-1

Rats3-2

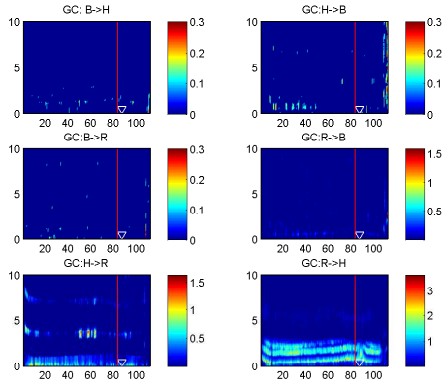

Rats3-3

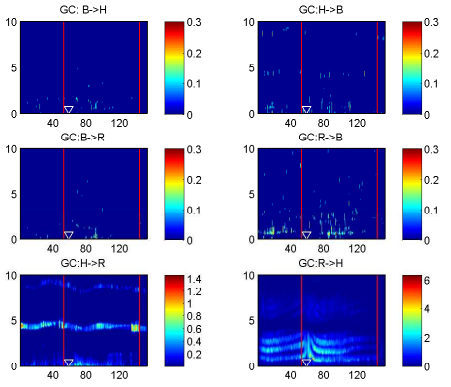

Rats3-4

Figure 3.63 – *Nonparametric Granger causality $GC(t, f)$ obtained on "Rats3" PartI (Rats3-1 to Rats3-4). Horizontal axis is time (min). Vertical axis is frequency (Hz). Red lines indicate the estimated deep-light change of anæsthesia. The downward triangles show the reinduction timing: (B) EEG, (H) ECG, and (R) respiration.*

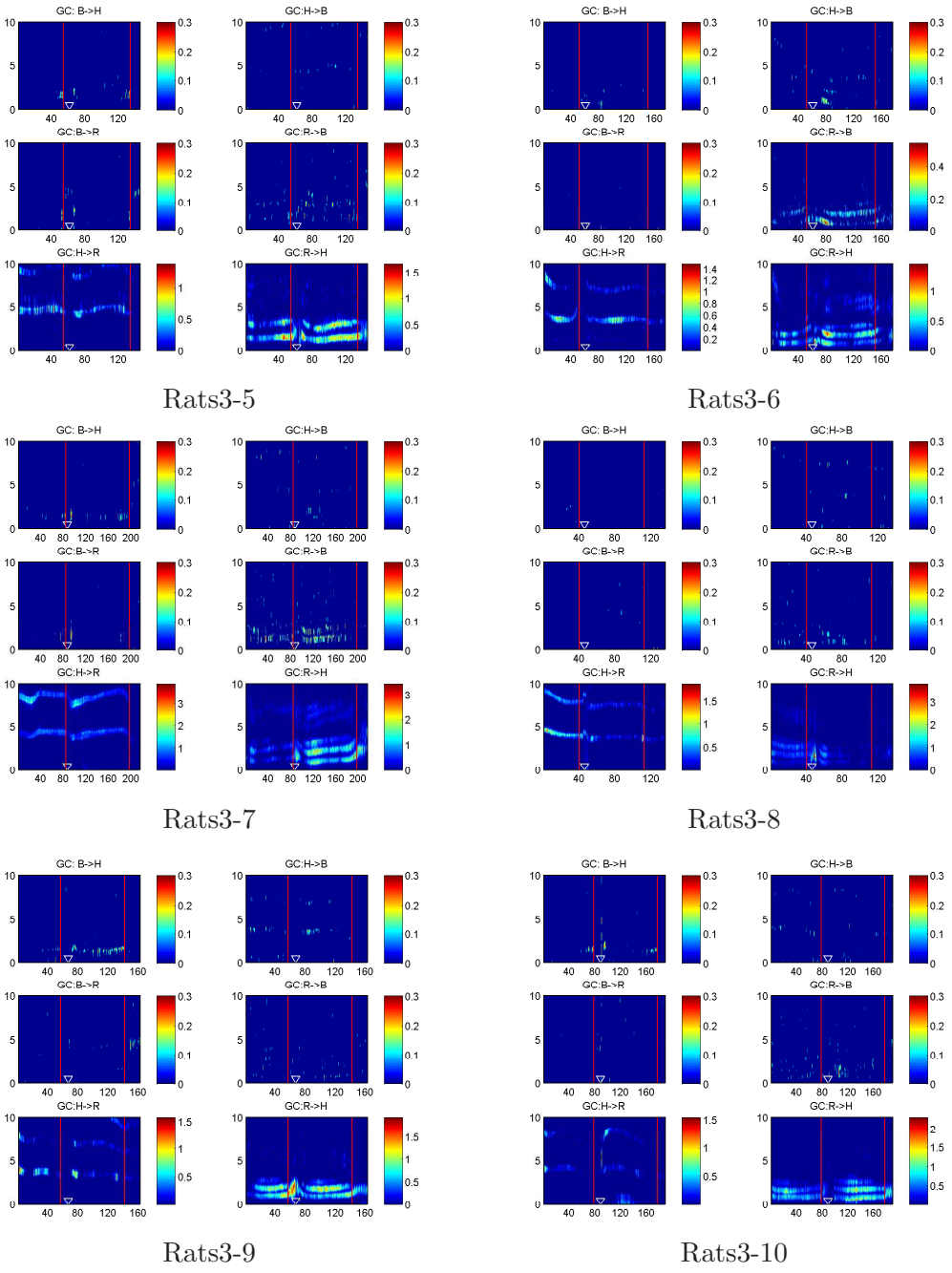

Figure 3.64 – *Nonparametric Granger causality $GC(t, f)$ obtained on "Rats3" PartII (Rats3-5 to Rats3-10). Horizontal axis is time (min). Vertical axis is frequency (Hz). Red lines indicate the estimated deep-light change of anæsthesia. The downward triangles show the reinduction timing: (B) EEG, (H) ECG, and (R) respiration.*

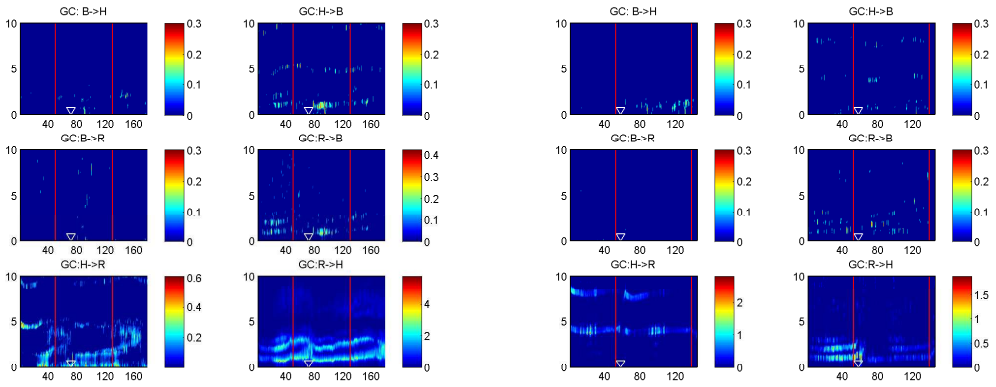

Rats3-11 Rats3-12

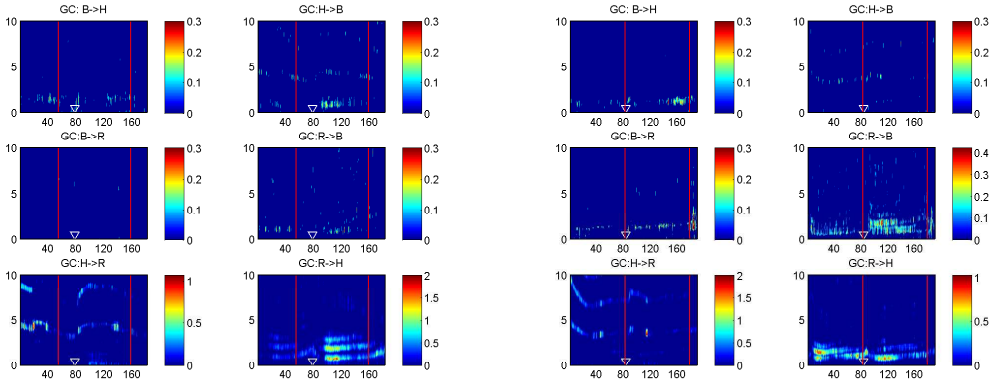

Rats3-13 Rats3-14

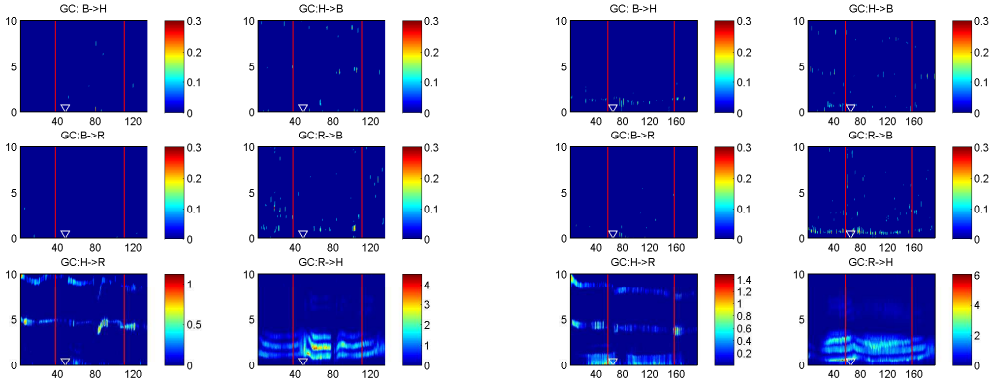

Rats3-15 Rats3-16

Figure 3.65 – *Nonparametric Granger causality $GC(t, f)$ obtained on "Rats3" PartII (Rats3-11 to Rats3-16). Horizontal axis is time (min). Vertical axis is frequency (Hz). Red lines indicate the estimated deep-light change of anæsthesia. The downward triangles show the reinduction timing: (B) EEG, (H) ECG, and (R) respiration.*

3.9.4 Rats4

As "Rats3", this group "Rats4" has reinduction of the anæsthetic and change of protocol for the EEG measurements. So the idea is to compare the results obtained here with the results of "Rats2" anæsthetized with the same anæsthetic, Pentobarbital (PB). In "Rats2", we encountered the difficulties to define the deep-light change of anæsthesia as well as the difficulties to differentiate the two stage of anæsthesia with our analysis method. Here we will see if this "Rats4" is the same case as "Rats2".

All the measurements of this group were preprocessed in the same way as previous groups. Now, let us begin with the S-estimator.

S-estimator

The length of sliding window and the length of time shift were set as previous groups. But again as "Rats3", the sampling frequency was 1200Hz, such that there were more samples in one window than "Rats2". The embedding dimension (ED) and the time delay (τ) used in this study are shown in the following table.

Rats No: Rats4-		1	2	3	4	5	6	7	8	9	10
ED	ECG	7	7	5	7	7	7	10	7	6	7
	Resp	4	4	4	4	4	4	4	4	4	4
	EEG	5	6	6	6	5	5	5	5	6	6
τ	ECG	10	10	10	10	9	9	10	9	8	10
	Resp	28	31	42	25	24	40	37	29	26	33
	EEG	19	17	16	18	18	19	19	19	15	17

Table 3.19 – *Embedding dimension (ED) and time delay (τ) used in the studies.*

In Fig. 3.66, the synchronization measures, $S(t)$ obtained for all the measurements are shown. From the figure, we immediately remark big fluctuation at the reinduction of anæsthesia on 8/10 rats. No slow increase found in "Rats2" can be observed. Furthermore, we remarked that the decision of the deep-light anæsthesia is impossible to make from these results. Consequently, this transition point of the anæsthesia was estimated by the appearance of the θ-wave in the power spectra obtained in the analysis of the Granger causality. As this appearance of the θ-wave is not clear in all rats, the points are visually and roughly decided, then adapted from the results of the S-estimator and the new S-estimator. The obtained transition time is shown in table below.

Rats4-	1	2	3	4	5	6	7	8	9	10
1st	60	49	36	30	25	43	16	10	-	42
2nd	111	141	149	168	146	150	173	130	192	139

Table 3.20 – *The estimated deep-light transition point of the anæsthesia (min). No 1st transition was remarked for Rats4-9.*

From fig. 3.66, the estimated deep-light transition seems to indicate the end of the fluctuation. This means that the synchronization is higher at the deep state of the anæsthesia. However, this change at the transition point was not found in "Rats2" such that we proceed

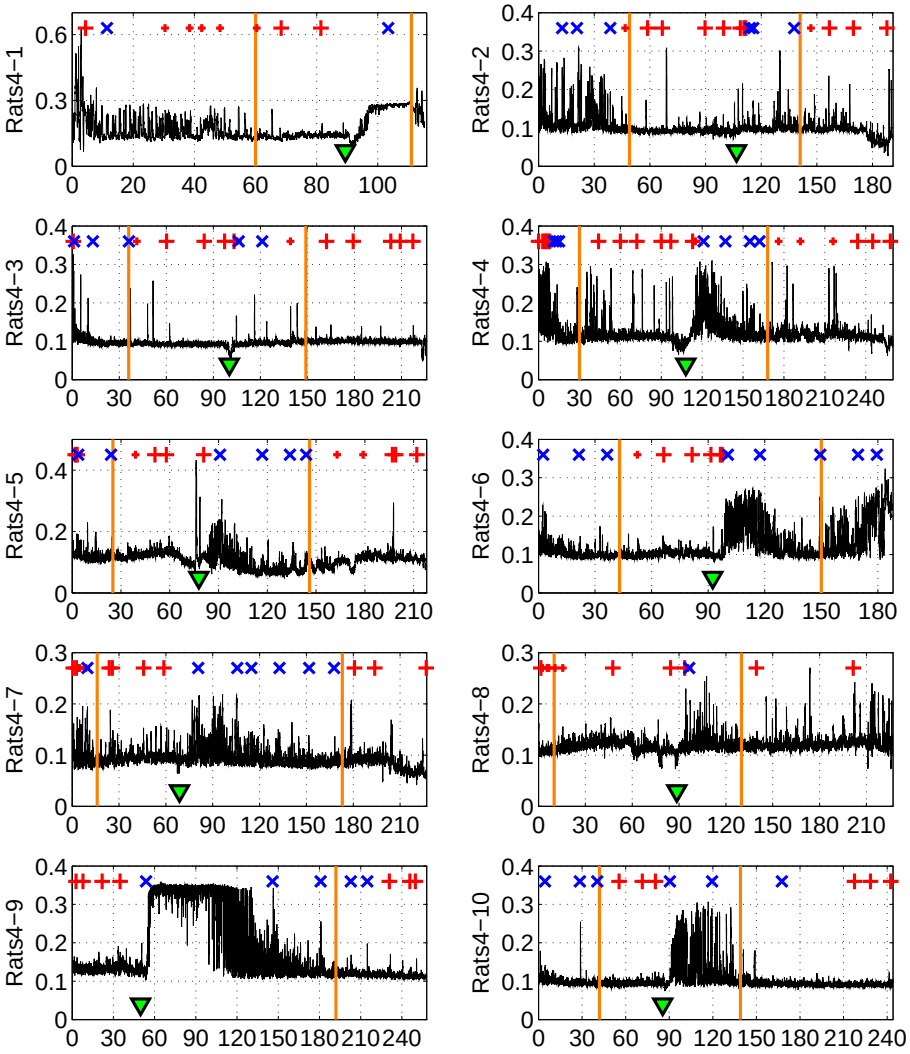

Figure 3.66 – *Synchronization measure $S(t)$ obtained by clustering three oscillators (ECG, Respiration and EEG) together on group "Rats4". Horizontal axis is time (min). The downward triangles show the reinduction timing. Blue 'x' means negative reaction, Red '+' means positive reaction, and smaller red '+' means weak positive reaction to the pinch test. Orange lines indicate the estimated deep-light change of anæsthesia.*

to the next analysis to comment on that. In fig. 3.67, we show the $S(t)$ obtained by clustering two sub-systems. From the figure, as "Rats2", we remarked that the $S(t)$ obtained with the cluster of ECG and Respiration does not change at all during whole measurements, and the results obtained by two other clusters are very similar to the results of $S(t)$ calculated on the cluster with all the three systems. Consequently, what we comment on the dominance of EEG change on the influence to the $S(t)$ can be confirmed. Let us go to the next analysis, the new S-estimator.

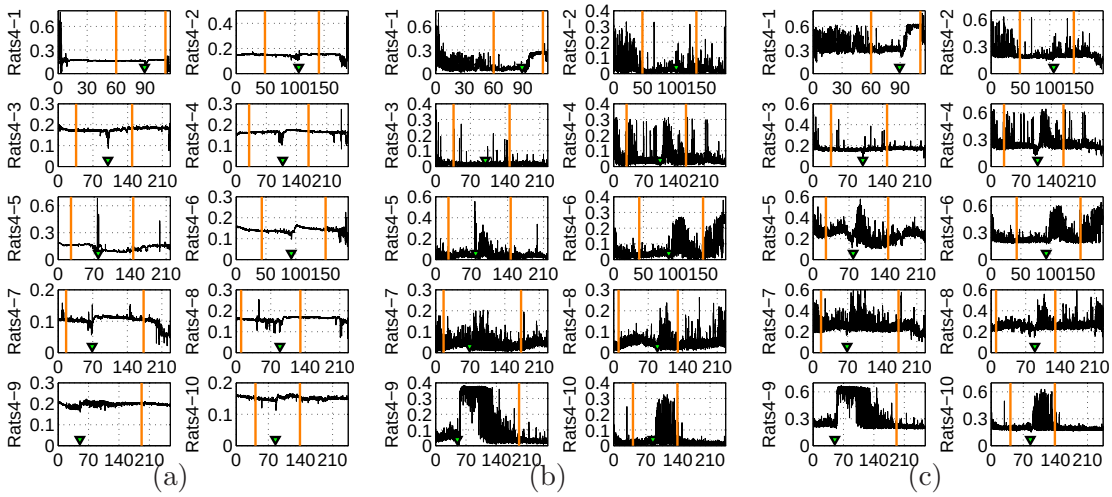

Figure 3.67 – *Synchronization measure $S(t)$ obtained by clustering two chosen oscillators together on group "Rats4". Horizontal axis is time (min). Orange lines indicate the estimated deep-light change of anæsthesia. The downward triangles show the reinduction timing: (a) ECG and Respiration, (b) ECG and EEG, and (c) Respiration and EEG.*

new S-estimator

In Fig. 3.68, we show the obtained results with the new S-estimator. From the figure, as in "Rats2", we remark that the strength of the synchronization became about 5 to 10 times

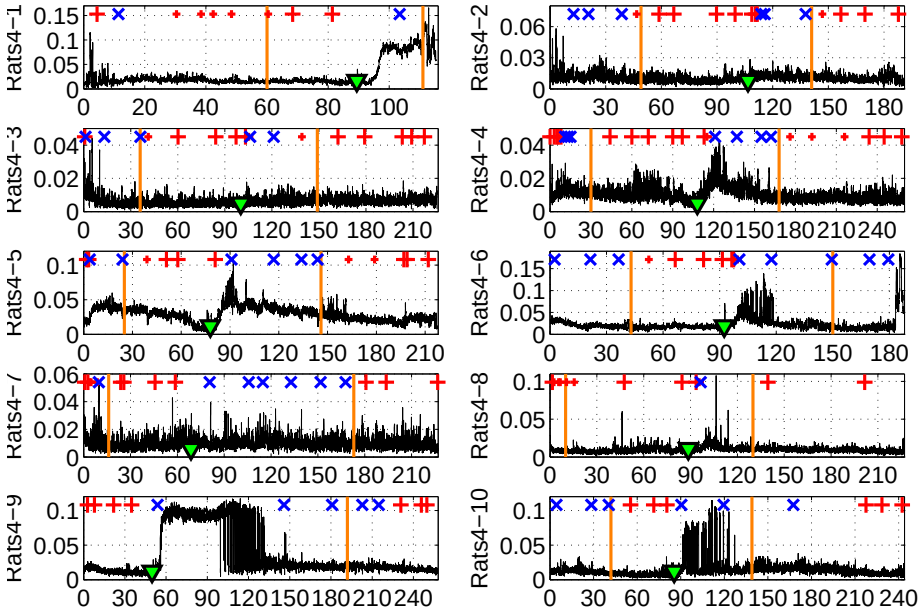

Figure 3.68 – *new Synchronization measure $S_{new}(t)$ obtained by clustering three oscillators (ECG, Respiration and EEG) together on group "Rats4". Horizontal axis is time (min). The downward triangles show the reinduction timing. Blue 'x' means negative reaction, Red '+' means positive reaction, and smaller red '+' means weak positive reaction to the pinch test. Orange lines indicate the estimated deep-light change of anæsthesia.*

smaller than the original S-estimator. However, it gives very similar structure of the plot as the $S(t)$ which differs from $S_{new}(t)$ of "Rats2" which was completely different from $S(t)$. In "Rats2", we managed to find that the $S_{new}(t)$ is higher at the deep stage of the anæsthesia, but here in "Rats4", we cannot see any change at this transition point.

In Fig. 3.69, as we did in the original S-estimator, we plotted the results obtained with other clusters taking two sub systems. From fig. 3.69(a), we can remark an increase of $S_{new}(t)$ on the clusters of ECG and respiration from the reinduction point, and after a while a decrease can be observed. But this change from increase to decrease do not coincidence

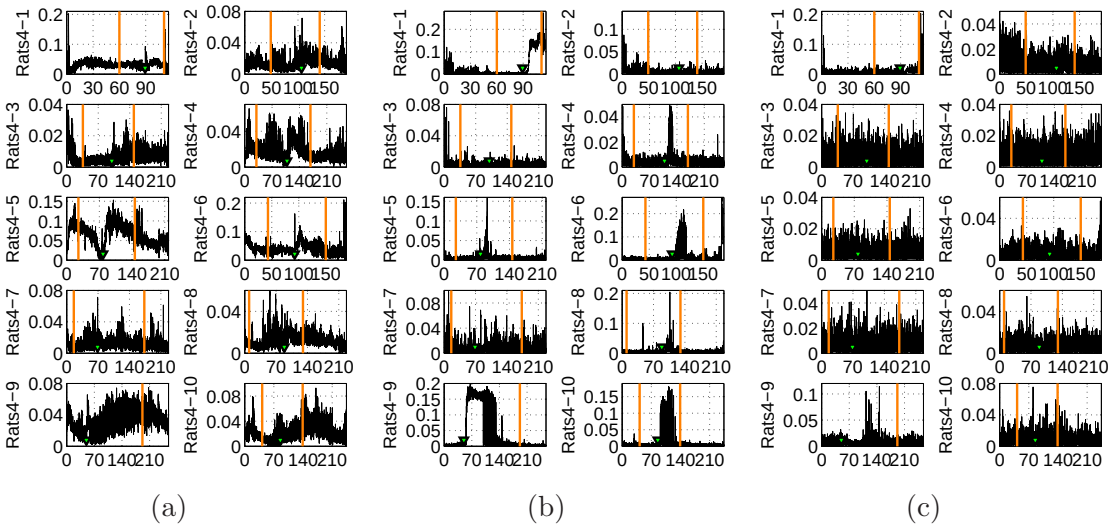

Figure 3.69 – *Synchronization measure $S_{new}(t)$ obtained by clustering two chosen oscillators together on group "Rats4". Horizontal axis is time (min). Orange lines indicate the estimated deep-light change of anæsthesia. The downward triangles show the reinduction timing: (a) ECG and Respiration, (b) ECG and EEG, and (c) Respiration and EEG.*

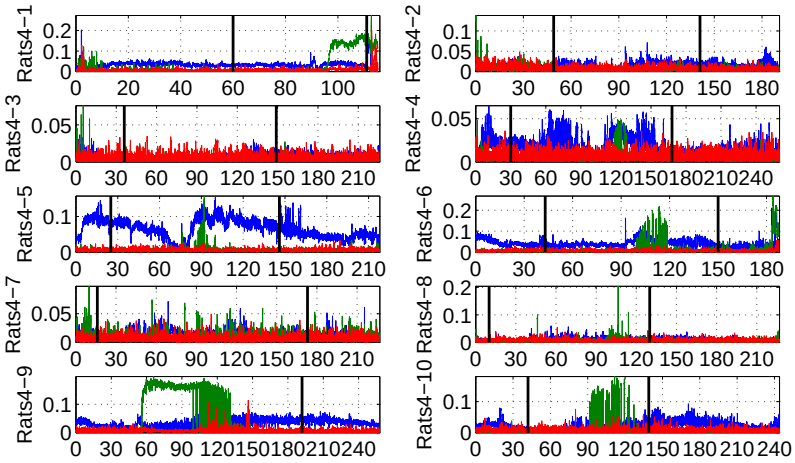

Figure 3.70 – *Comparison of the strength of $S_{new}(t)$ obtained by clustering two chosen oscillators together on group "Rats4". Horizontal axis is time (min). Black lines indicate the estimated deep-light change of anæsthesia: (blue) ECG and Respiration, (green) ECG and EEG, and (red) Respiration and EEG.*

with the transition point of the anæsthesia. From (c), we can remark that there is no change in $S_{new}(t)$ on the cluster of EEG-respiration along the time. From (b), we can understand that the fluctuation that we had on $S_{new}(t)$ on the clusters of all three systems came from the synchronization between ECG and EEG. From fig. 3.70, we can remark that mainly the ECG-respiration synchronization is the strongest, but the ECG-EEG synchronization is the strongest after a while induction of the anæsthetic.

We also calculated this new S-estimator with PCA based embedding method. The employed ED and K are shown in table below. 3.21.

Rats No: Rats4-		1	2	3	4	5	6	7	8	9	10
ED	ECG	7	7	7	7	7	6	7	4	5	7
	Resp	8	5	4	4	8	4	4	4	3	4
	EEG	9	8	8	9	8	9	9	9	8	8
K	ECG	25	25	25	25	25	25	24	14	14	25
	Resp	76	81	83	62	64	73	85	63	73	79
	EEG	42	38	36	40	39	44	45	39	35	36

Table 3.21 – *Embedding dimension (ED) and size of Toeplitz like matrix (K) used in the studies.*

The obtained results gave us similar results as the results with delay embedding method, such that again as "Rats3", we just putted the obtained results in appendix.

Embedding dimension analysis

In fig. 3.71 and 3.72, we show the obtained results on embedding dimension (ED) calculated for delay embedding* and PCA based embedding method†, respectively. On fig. 3.71(c), we first remark that we cannot see a decrease of ED as we found in "Rats2". This is probably because of the change in the EEG measurement protocol, since also in "Rats3", we saw less change in ED(t) calculated for delay embedding. From (a), we can see that the ED of ECG signals increase at the light stage of the anæsthesia, which was not observed in "Rats2". On (b), no change was observed for respiration. Consequently, Taking both "Rats2" and "Rats4" into consideration, we cannot conclude anything about the change of the embedding dimension.

In fig. 3.72, again we immediately remark many fluctuations. For ECG and respiration shown on (a) and (b), these fluctuations seems to mainly come from the external stimuli, i.e. reinduction of anæsthetic (PB) and pinch test. However, for EEG, some rule can be seen: After the reinduction of PB, the ED of EEG begins to vary from more and more low dimension to high dimension, and then decrease the variation and stay at high dimension. This change can be seen as a downward triangle structure on fig. 3.72(c). Our estimated transition point of anæsthesia mostly coincide with the end point of this downward triangle, such that our estimated point may be well defined. Nevertheless, much more investigation is necessary to really define this transition point.

*the obtained results on the time delay are shown in appendix.

†the obtained results on the size of the Toeplitz like matrix are also shown in appendix.

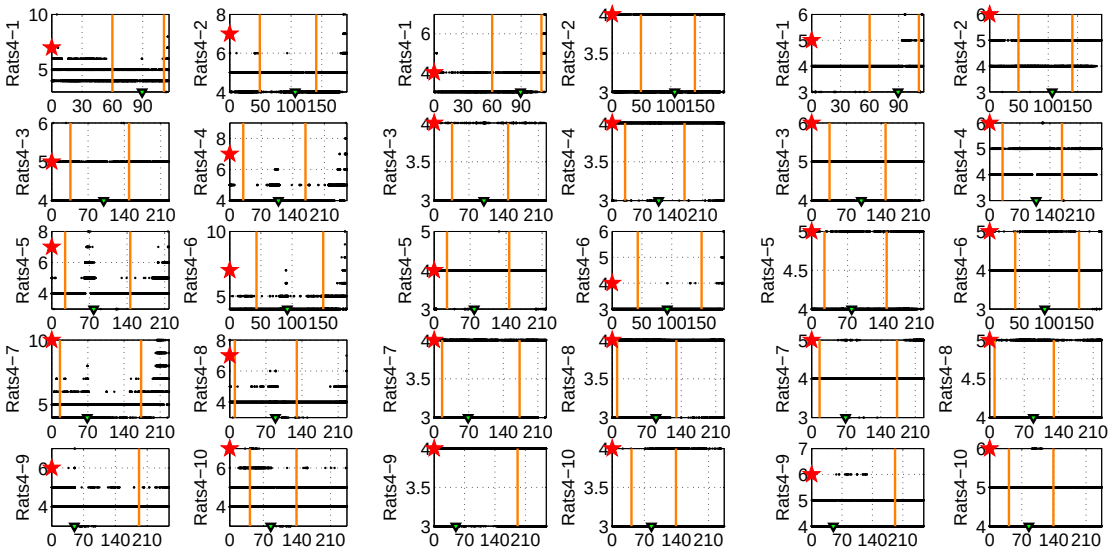

Figure 3.71 – *The study on the embedding dimension (ED) for delay embedding. Horizontal axis is time (min). Orange lines indicate the estimated deep-light change of anæsthesia. The downward triangles show the reinduction timing. The red stars indicates the chosen parameters: (a) ECG, (b) Respiration and (c) EEG.*

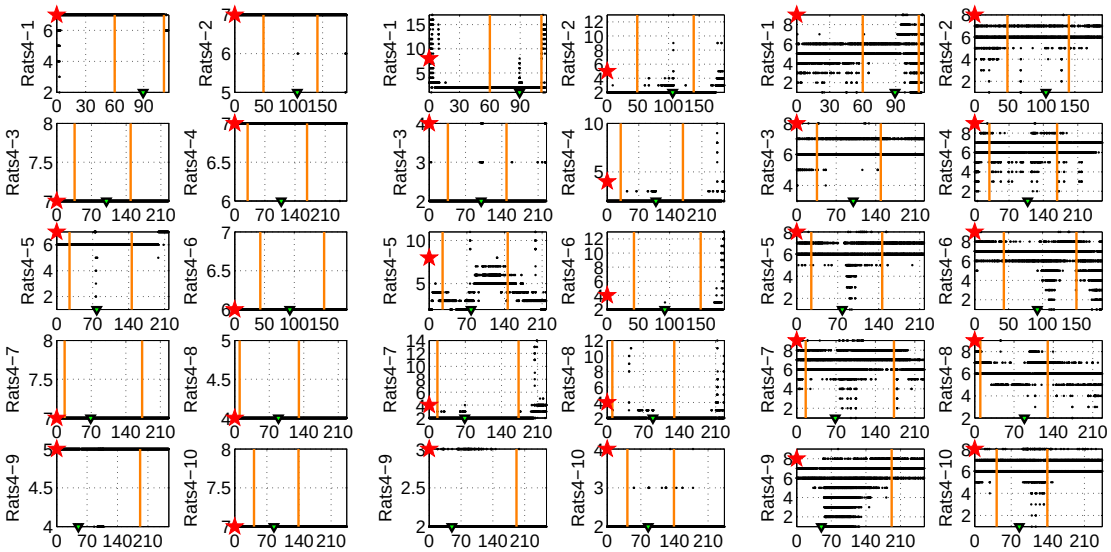

Figure 3.72 – *The study on the embedding dimension (ED) for PCA based embedding. Horizontal axis is time (min). Orange lines indicate the estimated deep-light change of anæsthesia. The downward triangles show the reinduction timing. The red stars indicates the chosen parameters: (a) ECG, (b) Respiration and (c) EEG.*

Nonparametric Granger causality

Again, this group "Rats4" has very long measurements data set such that the "Coupling matrix" analysis for this group was also omitted in this thesis study. Thereby, let us move to the nonparametric Granger causality analysis.

The same window length and the same shifted time length as previous groups were used. At first, we show the power spectra of the EEG signals in fig. 3.73, since this is the figure that allowed us to estimate the deep-light change of anæsthesia. From this figure, we can remark that it is very difficult to find where the θ-wave begins to appear. Consequently, the estimation of the deep-light transition of the anæsthesia was really a tough work*.

In fig. 3.74 and 3.75, we show the remaining power spectra (ECG and respiration) and the coherence spectra, respectively. From fig. 3.74, we can see on both ECG and respiration that frequencies are affected by the reinduction of the anæsthesia, but no clear change appears at the estimated deep-light change point of the anæsthesia. From fig. 3.75(a), we remarked a high coherence between heart and respiration activity, especially after the reinduction of the anæsthetic, i.e. at the deep state of the anæsthesia. However,

*Even been settled, we are still not sure of this definition. However, we had no way to improve it at this moment such that our analysis was based on that.

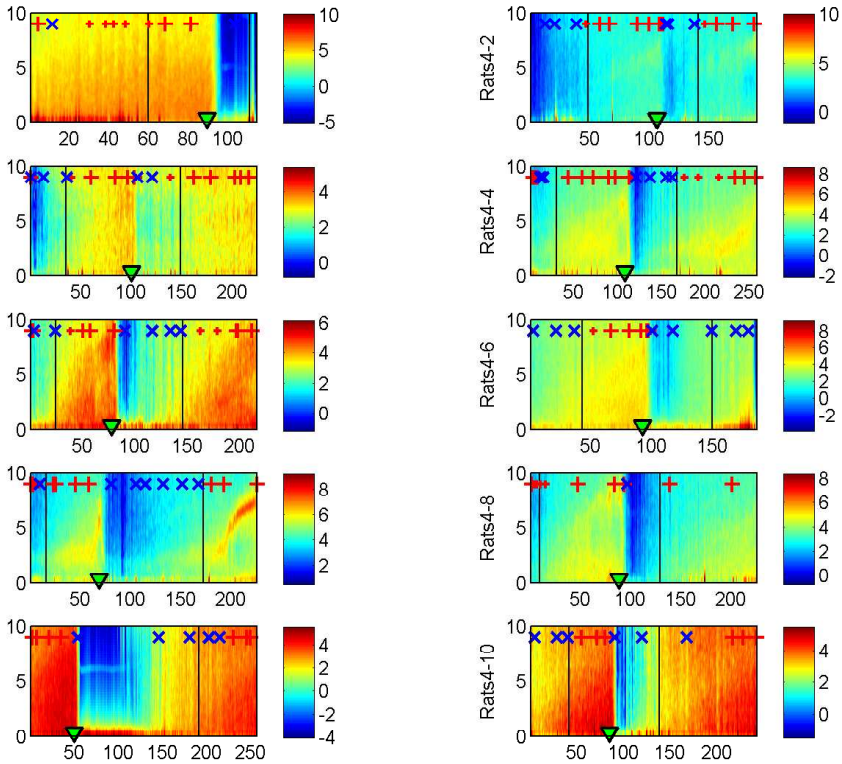

Figure 3.73 – *Power spectra obtained on "Rats4". Horizontal axis is time (min). Vertical axis is frequency (Hz). The downward triangles show the reinduction timing. Blue 'x' means negative reaction, Red '+' means positive reaction, and smaller red '+' means weak positive reaction to the pinch test. Orange lines indicate the estimated deep-light change of anæsthesia.*

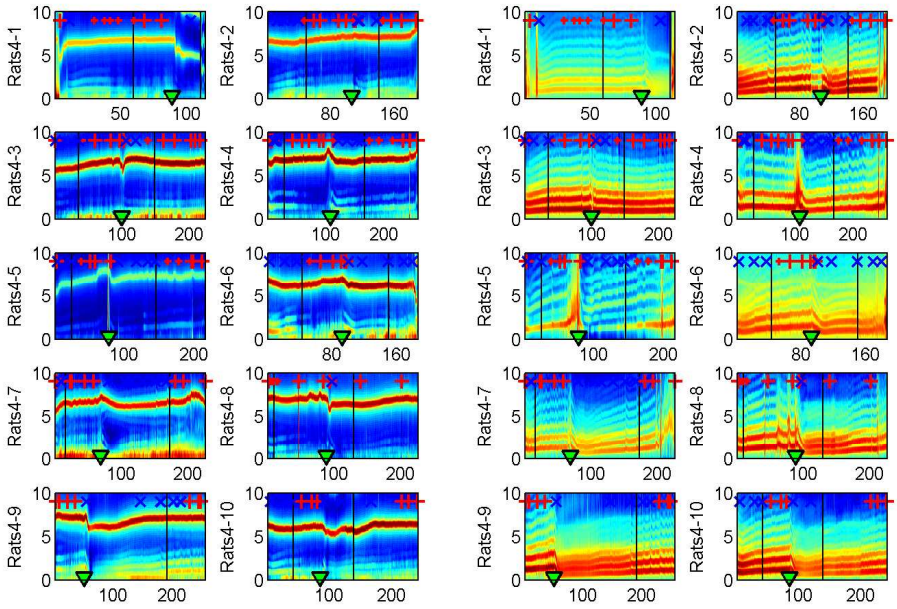

Figure 3.74 – *Power spectra obtained on "Rats4". Horizontal axis is time (min). Vertical axis is frequency (Hz). Color axis is omitted. Black lines indicate the estimated deep-light change of anæsthesia. The downward triangles show the reinduction timing: (a) ECG and (b) Respiration.*

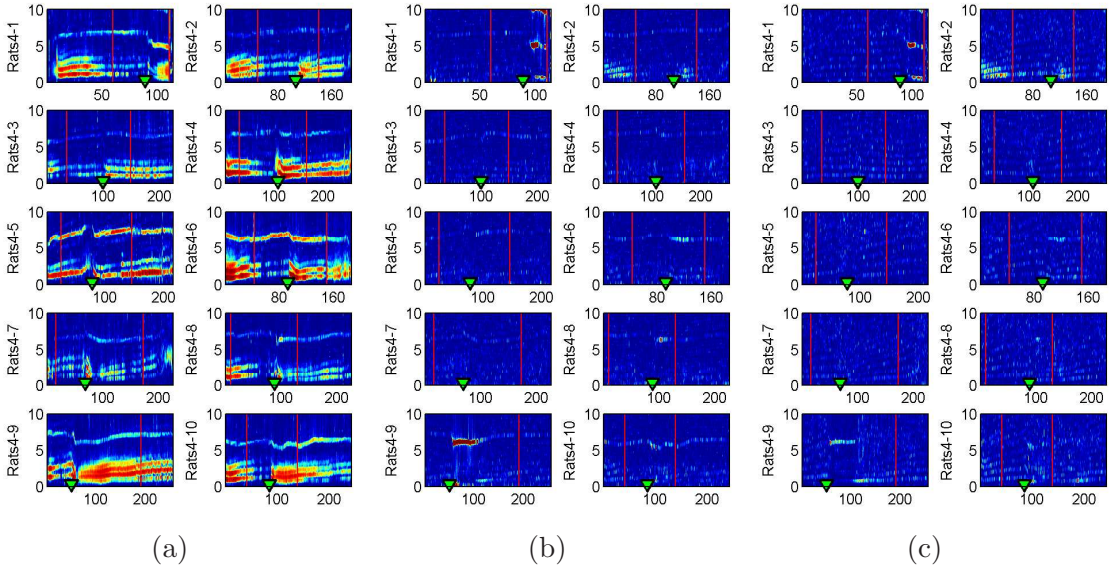

Figure 3.75 – *Coherence spectra obtained on "Rats4". Horizontal axis is time (min). Vertical axis is frequency (Hz). Orange lines indicate the estimated deep-light change of anæsthesia. The downward triangles show the reinduction timing: (a) ECG and respiration; color axis [0 1], (b) EEG and ECG; color axis [0 0.4], and (c) EEG and respiration; color axis [0 0.4].*

few coherence was found for the other results shown in (b) and (c). Nevertheless, it seems also stronger at the deep stage of the anæsthesia. Looking carefully, as previous groups, we

can remark a similar trend as the new S-estimator.

In Fig. 3.76 and 3.77, we show the results of the nonparametric Granger causality. Again, the $GC(t)$ smaller than threshold, shown in the following table, defined by the permutation test were set to zero.

	GC:B→H	GC:H→B	GC:B→R	GC:R→B	GC:H→R	GC:R→H
threshold	0.10	0.10	0.10	0.10	0.10	0.10

Table 3.22 – *Threshold for nonparametric Granger causality $GC(t)$ defined by the permutation test for "Rats4": (B) EEG, (H) ECG, and (R) respiration.*

From fig. 3.76 and 3.77, few causality can be found between brain (B) and heart(H), and also between B and respiration (R). In "Rats2", the causality between them was found at the deep stage of the anæsthesia. We presume that the cause of this difference comes from the change of the EEG measurement protocol but it should be verified in the future. Otherwise, we can remark the change in causality, $GC(t, f)$, at the transition point of the anæsthesia between R and H in both direction: They show higher $GC(t, f)$ at the deep

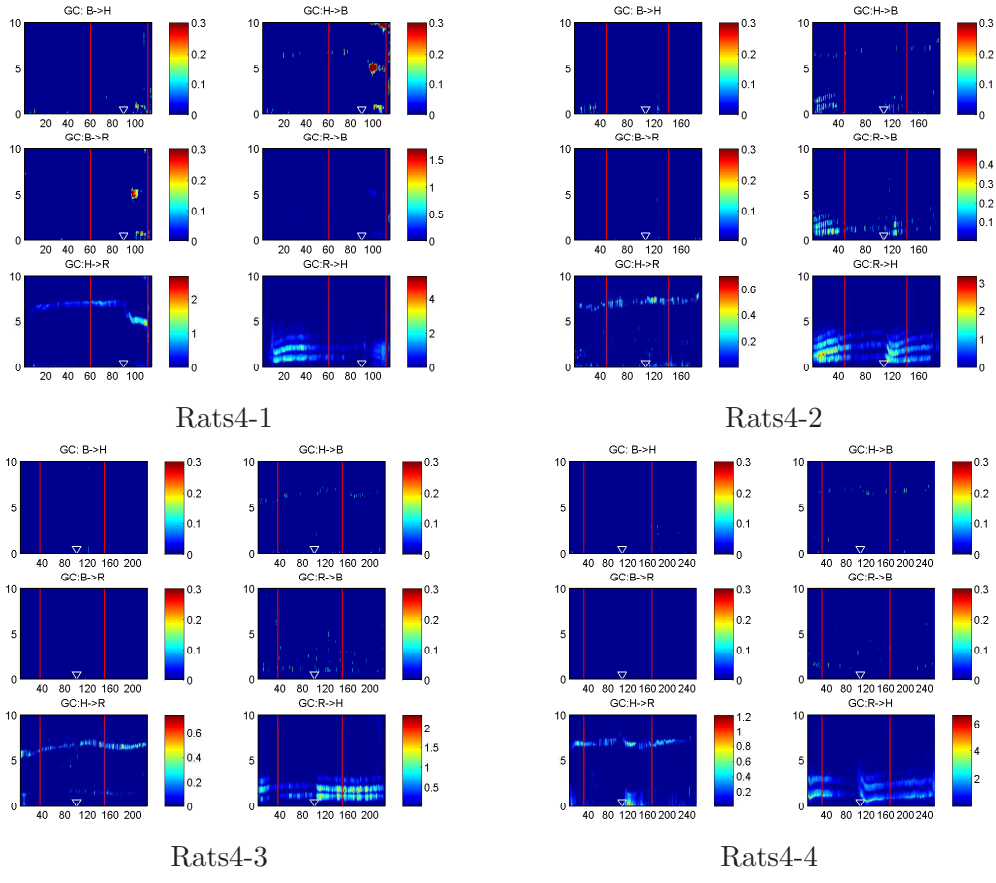

Figure 3.76 – *Nonparametric Granger causality $GC(t, f)$ obtained on "Rats4" PartI (Rats4-1 to Rats4-4). Horizontal axis is time (min). Vertical axis is frequency (Hz). Red lines indicate the estimated deep-light change of anæsthesia. The downward triangles show the reinduction timing: (B) EEG, (H) ECG, and (R) respiration.*

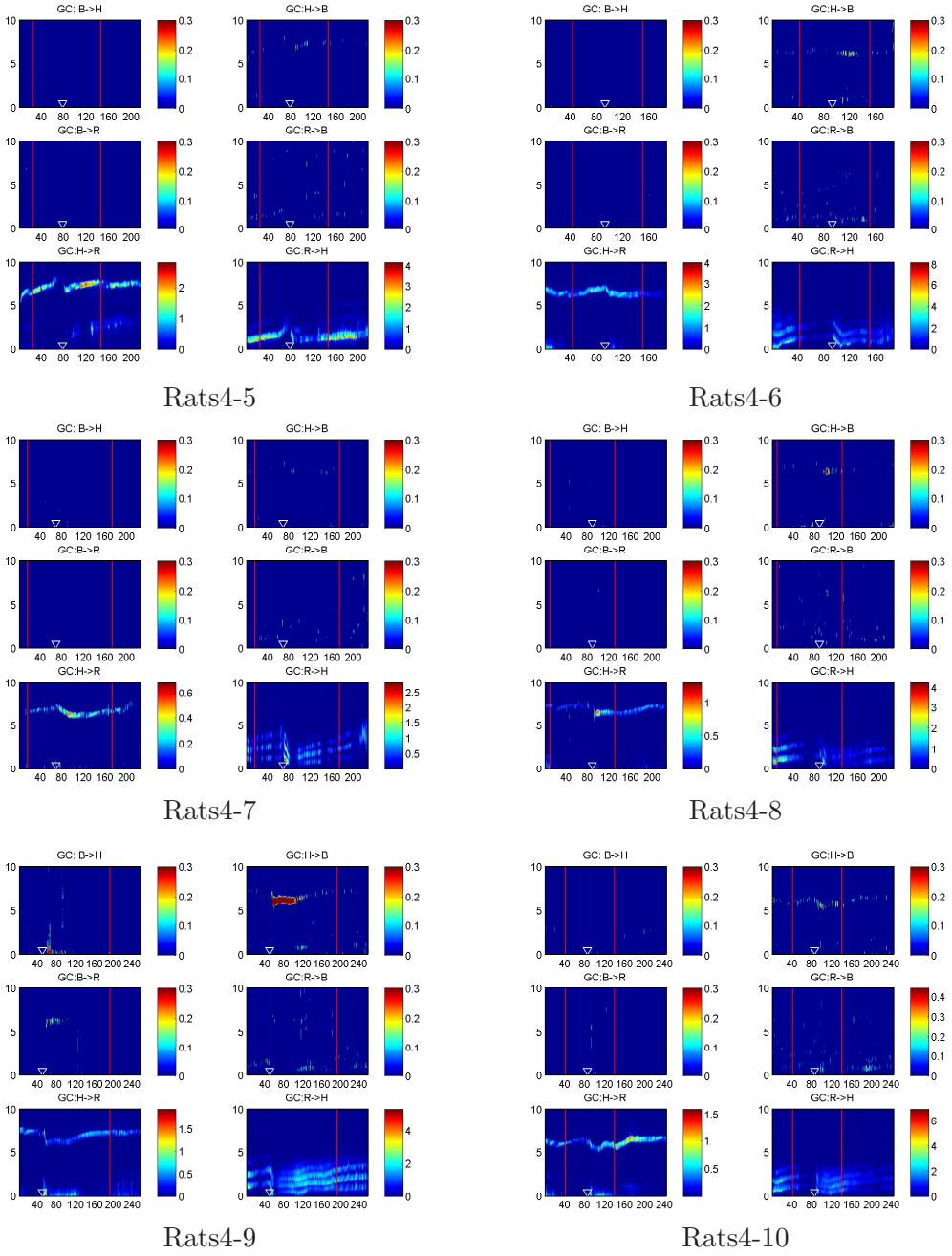

Figure 3.77 – *Nonparametric Granger causality $GC(t, f)$ obtained on "Rats4" PartII (Rats4-7 to Rats4-10). Horizontal axis is time (min). Vertical axis is frequency (Hz). Red lines indicate the estimated deep-light change of anæsthesia. The downward triangles show the reinduction timing: (B) EEG, (H) ECG, and (R) respiration.*

stage than light stage of anæsthesia.

The recorded data of this "Rats4" also arrived in the same time as "Rats4", such that we didn't have time to analyze the time averaged Granger causality tracing specific frequency range. As a result, the interdependencies found in this study should be concretized in the future.

3.9.5 Rats5

In this group "Rats5", the goal is to compare with "Rats3" to see if the anæsthesia repeated after one week changes the effectiveness of the anæsthetic, i.e. KX. As the measurements of "Rats5" were recorded on half of the rats in group "Rats3", here below we show the correspondence of the rat numbers.

Rats5-	1	2	3	4	5	6	7	8
Rats3-	4	5	6	9	11	14	15	16

Table 3.23 – *The correspondence of the rat number between "Rats3" and "Rats5".*

Furthermore, comparing with "Rats1", the influence on the analysis results by the change of the EEG measurement protocol will be investigated more closely. Here again, all the measurements of this group were preprocessed in the same way as previous groups.

S-estimator

As previous groups, the parameters, i.e. sliding window length and shifted time length were set to 10 seconds and 0.5 second, respectively. The number of samples inside of one window was the same as "Rats3". The embedding dimension (ED) and the time delay (τ) used in this study are shown in the following table.

Rats No: Rats5-		1	2	3	4	5	6	7	8
ED	ECG	7	5	6	8	6	6	5	5
	Resp	4	4	4	4	4	4	4	4
	EEG	6	6	6	6	6	5	5	6
τ	ECG	11	10	10	11	9	11	10	10
	Resp	34	48	38	38	42	38	43	38
	EEG	16	16	14	15	16	18	19	14

Table 3.24 – *Embedding dimension (ED) and time delay (τ) used in the studies.*

In fig. 3.78, the obtained $S(t)$ for each rats are shown. From the figure, we remarked that, except Rats5-3 and Rats5-4, there is no sudden decrease of the $S(t)$ such that we cannot estimate the deep-light change point of anæsthesia from these results. Consequently, as the case of "Rats3", we estimated this transition point by the frequency change of the EEG and respiration signals obtained in the figure of the power spectra (See fig. 3.88). For Rats5-1 to Rats5-4, there were clear change at these frequencies such that the estimation was a easy task. However, for Rats5-5 to Rats5-8, the decision was very difficult to make from the changes of the frequencies and the results of $S(t)$. Accordingly, it was approximately defined referring to all the other analysis results. The obtained transition time is shown in table. 3.25.

Rats5-	1	2	3	4	5	6	7	8
at	65	57	60	67	62	70	50	79

Table 3.25 – *The estimated deep-light transition point of the anæsthesia (min).*

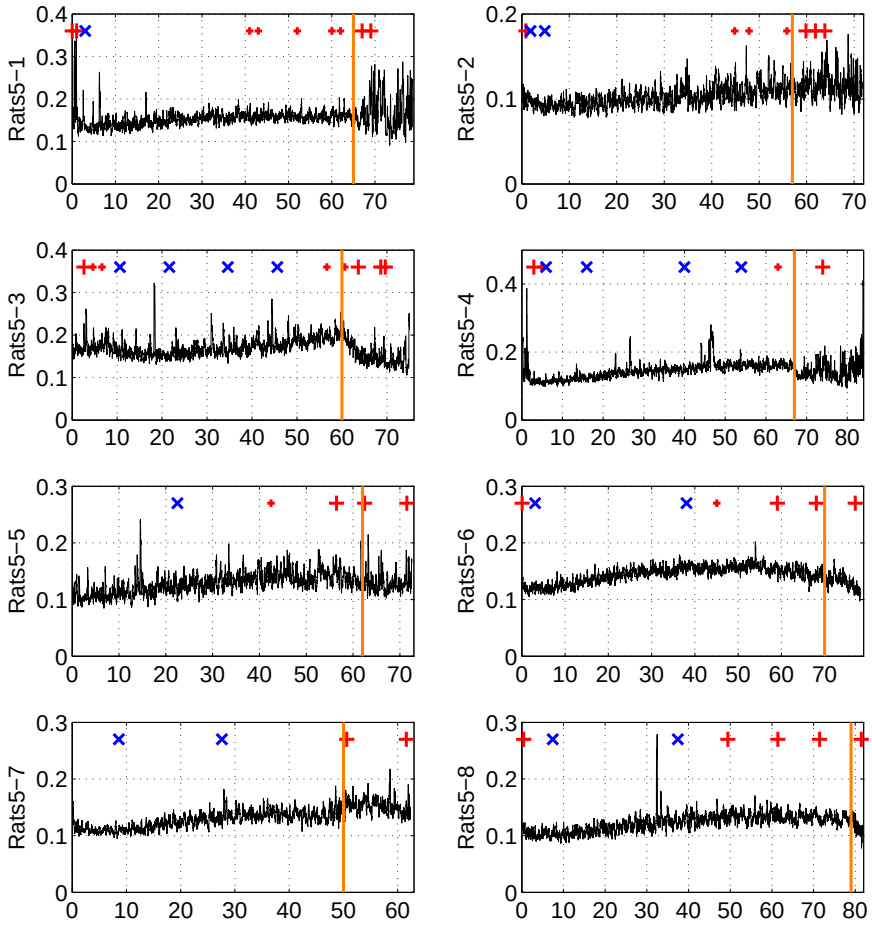

Figure 3.78 – *Synchronization measure $S(t)$ obtained by clustering three oscillators (ECG, Respiration and EEG) together on group "Rats3". Horizontal axis is time (min). Blue 'x' means negative reaction, Red '+' means positive reaction, and smaller red '+' means weak positive reaction to the pinch test. Orange lines indicate the estimated deep-light change of anæsthesia.*

Coming back to fig. 3.78, we can see that Rats5-3 and Rats5-4 have the coincidence between variation change of $S(t)$ and the transition point. However Rats5-5 and Rats5-6 have the change of $S(t)$ quicker than the estimated transition point. But as we remarked before, the change of $S(t)$ is not so clear that it is impossible to define the transition point according to $S(t)$ even if it seems better choice. As a result, on 7/8 rats, our estimated transition points indicate the time which we had already positive response of the pinch test. This should be discussed at the final meeting of our project held on September 2008. Furthermore, comparing with "Rats3", we remarked that the strength of the synchronization did not change, but the variance became smaller (significance level of 0.1049, tested with Wilcoxon rank sum test. See fig. 3.79). We suppose this might be the reason for the failure of the detection of the transition point with $S(t)$, but as the significance is not so low and the number of samples are only eight that we need to analyze more in the future.

In fig. 3.80, we show the $S(t)$ obtained by clustering two sub-systems. From the figure,

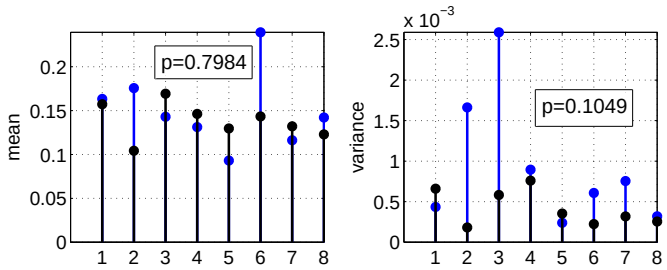

Figure 3.79 – *Mean and variance calculated on $S(t)$. x axis is the rat number of group "Rats5": (black) Rats5, (blue) corresponding "Rats3". p is the result of the Wilcoxon rank sum test.*

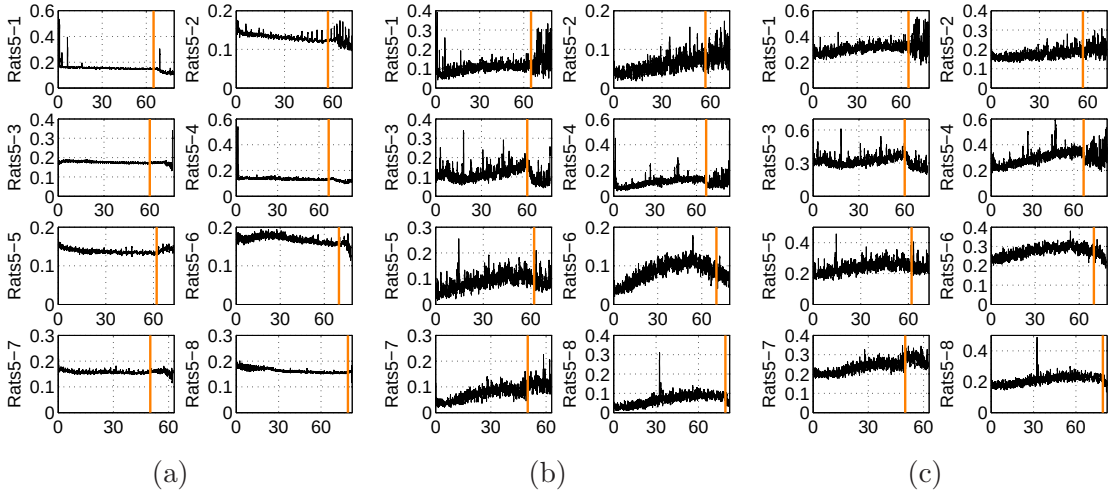

Figure 3.80 – *Synchronization measure $S(t)$ obtained by clustering two chosen oscillators together on group "Rats5". Horizontal axis is time (min). Orange lines indicate the estimated deep-light change of anæsthesia: (a) ECG and Respiration, (b) ECG and EEG, and (c) Respiration and EEG.*

we confirmed the results of other groups, i.e. the degree of the synchronization on ECG-Respiration system remains almost unchanged with the effect of KX. Also, we saw that the other two clusters show similar plot as the cluster with all the three such that we understood that the EEG signals make un important role in this analysis of $S(t)$.

new S-estimator

In fig. 3.81, the obtained results of $S_{new}(t)$ are shown. From this figure, we can confirm again the result of "Rats1" as "Rats3", i.e. there is no clear and unique variation change at the transition point, and the strength of the synchronization becomes 10 times smaller. Also, we cannot see a slight increase around the change point that we observed in "Rats1", such that we can conclude this increase as the artifact of the EEG measuring system. So, according to what we obtained as $S(t)$ and $S_{new}(t)$ in "Rats1", "Rats3" and "Rats5", we can say that the synchronization among all the state variables change according to the effect of KX, but if we concentrate on the synchronization exclusively between systems, there is no change of synchronization with respect to the effect of KX.

In fig. 3.82, the results of $S_{new}(t)$ obtained with clusters of two systems are shown. In (c) on Rats5-2 and Rats5-4, again as "Rats3", we can see an increase in $S_{new}(t)$ towards

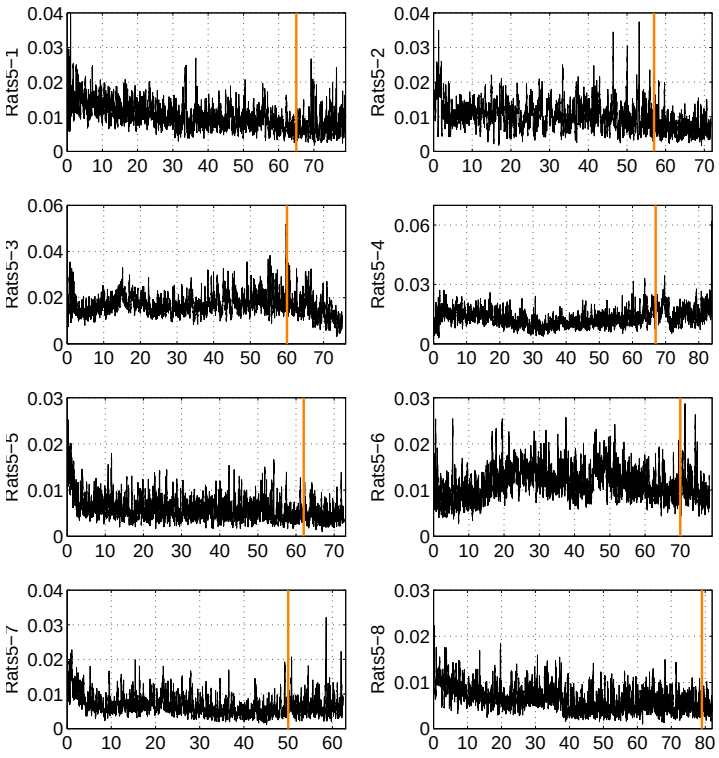

Figure 3.81 – *Synchronization measure $S_{new}(t)$ obtained by clustering three oscillators (ECG, Respiration and EEG) together on group "Rats5". Horizontal axis is time (min). Orange lines indicate the estimated deep-light change of anæsthesia.*

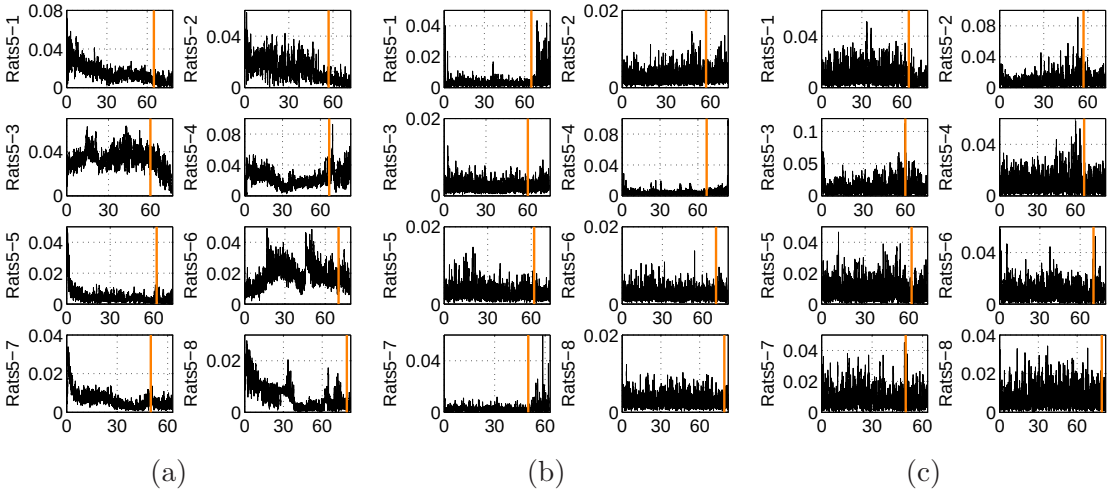

Figure 3.82 – *Synchronization measure $S_{new}(t)$ obtained by clustering two chosen oscillators together on group "Rats5". Horizontal axis is time (min). Orange lines indicate the estimated deep-light change of anæsthesia: (a) ECG and Respiration, (b) ECG and EEG, and (c) Respiration and EEG.*

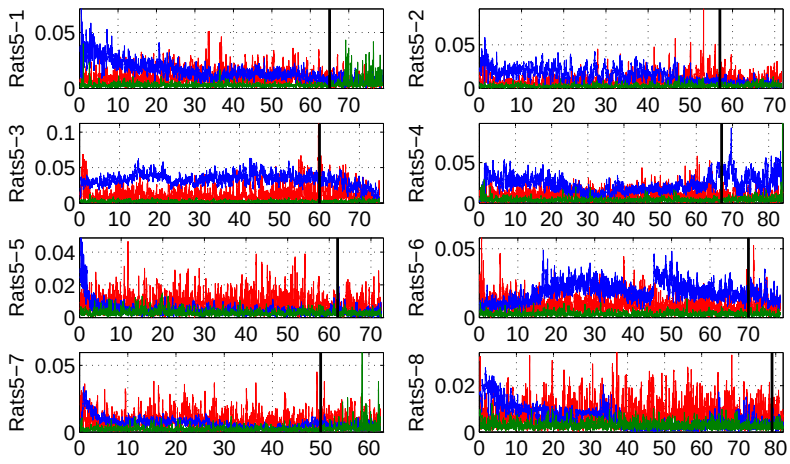

Figure 3.83 – *Comparison of the strength of $S_{new}(t)$ obtained by clustering two chosen oscillators together on Group "Rats5". Horizontal axis is time (min). The black lines indicate the estimated deep-light change of anæsthesia: (blue) ECG and Respiration, (green) ECG and EEG, and (red) Respiration and EEG.*

the transition point and sudden decrease at this transition point. On Rats5-1 and Rats5-5, only the decrease at the change point of anæsthesia is observed. But as we mentioned in "Rats3", this is not the case for all rats such that we cannot conclude the relation between this phenomena and the effect of anæsthesia.

Fig. 3.83 is shown to compare the strength of synchronization among clusters of two systems. From the figure, as "Rats3", we remark little synchronization between ECG and EEG. And also for the other two, the order of the strength of synchronization is not unique such that nothing can be concluded.

We also calculated this new S-estimator with PCA based embedding method. The employed ED and K are shown in table below. 3.26.

Rats No: Rats5-		1	2	3	4	5	6	7	8
ED	ECG	7	7	7	7	5	7	5	5
	Resp	4	3	3	4	3	4	3	3
	EEG	8	8	7	8	8	7	7	7
K	ECG	26	25	25	25	14	25	15	16
	Resp	78	90	68	76	86	87	81	74
	EEG	38	35	32	40	35	38	37	32

Table 3.26 – *Embedding dimension (ED) and size of Toeplitz like matrix (K) used in the studies.*

The obtained results gave us very similar results as the results with delay embedding method, such that we just putted the obtained results in appendix. To conclude for this new S-estimator, the choice of the embedding method seems not to make big difference for the results of the synchronization exclusively between the system.

Embedding dimension analysis

In Fig. 3.84, we show the obtained results on embedding dimension (ED) for delay embedding*. On this figure, again as "Rats1" and "Rats3", we can remark an increase in ED of EEG at the transition points on the results of all rats. So definitively, the ED of EEG increases according to the effect of KX, and it leads to the conclusion that the complexity of the EEG signals change according to the effect of KX, and which is low at the deep stage and high at the light stage, probably up to the awaken state. Furthermore, the ED of the ECG increases also at the transition point on half of the rats, which again confirm the results of "Rats1" and "Rats3". So, we presume that there is also a change of the complexity on ECG signals according to the effect of KX, but before to concretize, we should seek why half of the rats did not show the ED change at the transition point. For respiration, we can definitively conclude that there is no change in the complexity of the signal.

In Fig. 3.85, we show the obtained results on embedding dimension (ED) for PCA based embedding method†. From these figures, we can again remark some artifacts that we mentioned in "Rats3". Nevertheless, the ED change of the EEG can be still remarked in all rats and no change of the ED for the ECG and respiration can be confirmed.

From the studies of the embedding dimension carried out on all groups of rats, the analysis of ED calculated for delay embedding seems to give us more information about the complexity change. Moreover it seems to be more robust on the noise, and especially, it handles nonlinear systems. The use of this ED analysis for the complexity of the signals was unplanned at the beginning of my thesis since we didn't expect to have the complexity change like the results obtained here. Consequently, concentrating on the ED analysis using

*the obtained results on the time delay are shown in appendix.

†the obtained results on the size of the Toeplitz like matrix are shown in appendix.

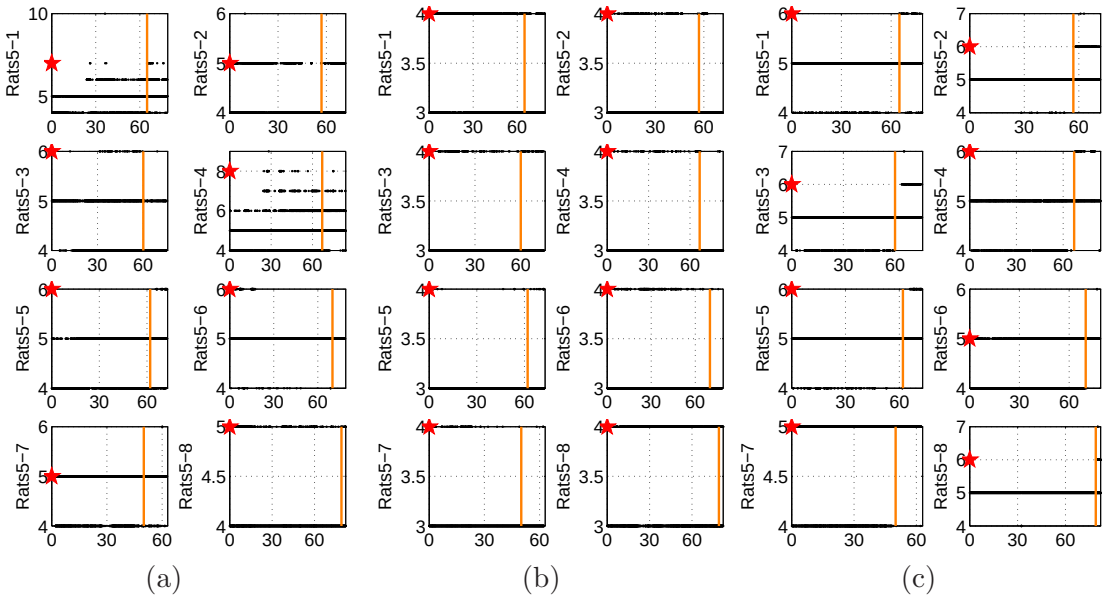

Figure 3.84 – *The study on the embedding dimension (ED) for delay embedding. Horizontal axis is time (min). Orange lines indicate the estimated deep-light change of anæsthesia. The red stars indicates the chosen parameters: (a) ECG, (b) Respiration and (c) EEG.*

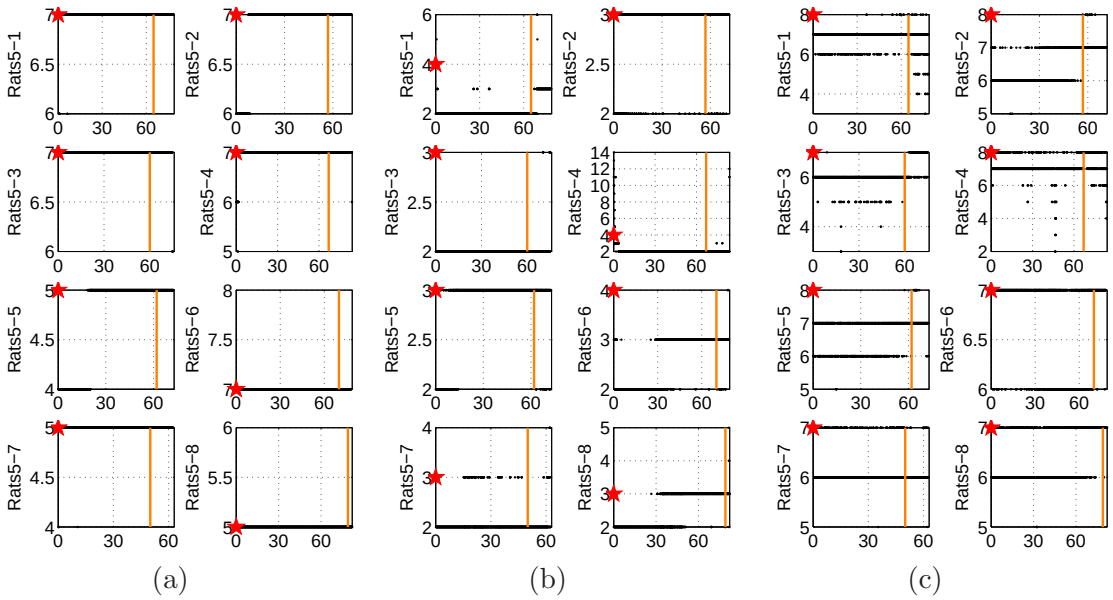

Figure 3.85 – *The study on the embedding dimension (ED) for PCA based embedding. Horizontal axis is time (min). Orange lines indicate the estimated deep-light change of anæsthesia. The red stars indicates the chosen parameters: (a) ECG, (b) Respiration and (c) EEG.*

false nearest neighbors for delay embedding, we should followed-up much more closely in the future.

Coupling matrix

We managed to analyze the "Coupling matrix" for this "Rats5". As "Rats1", the self model was created from the first 1 minute of the measurements. In Fig. 3.86 , the observed results are shown. From this figure, not on all rats's results but, we can see higher influence from EEG (B: Brain) to Respiration (R) and from ECG (H: Heart) to R at the light state of anæsthesia. Also, a higher influence from R to B and from R to H are remarked in some rats at the deep state of anæsthesia. No unique variation can be found between B and H. This results agree with the results in "Rats1". Now let's check the directionality.

In fig. 3.87, we show the calculated directionality index. From this figure, again as "Rats1", we cannot remark a unique causality in all rats. Moreover, the causalities that we conclude at "Rats1" can be observed less clearly than in "Rats1". We presume that this is because of the change in the EEG measurement protocol or the effect to be anæsthetized twice in a week interval (Need to be specified also in the future). Nevertheless, the trend of these indices are similar as "Rats1" that it seems appropriate to conclude the same interdependencies:
In deep anæsthesia:
Respiration drives both the brain activity and the heart activity.
In light anæsthesia:
Contrary to the deep state, the brain activity drives the respiration, and also the heart activity drives respiration.

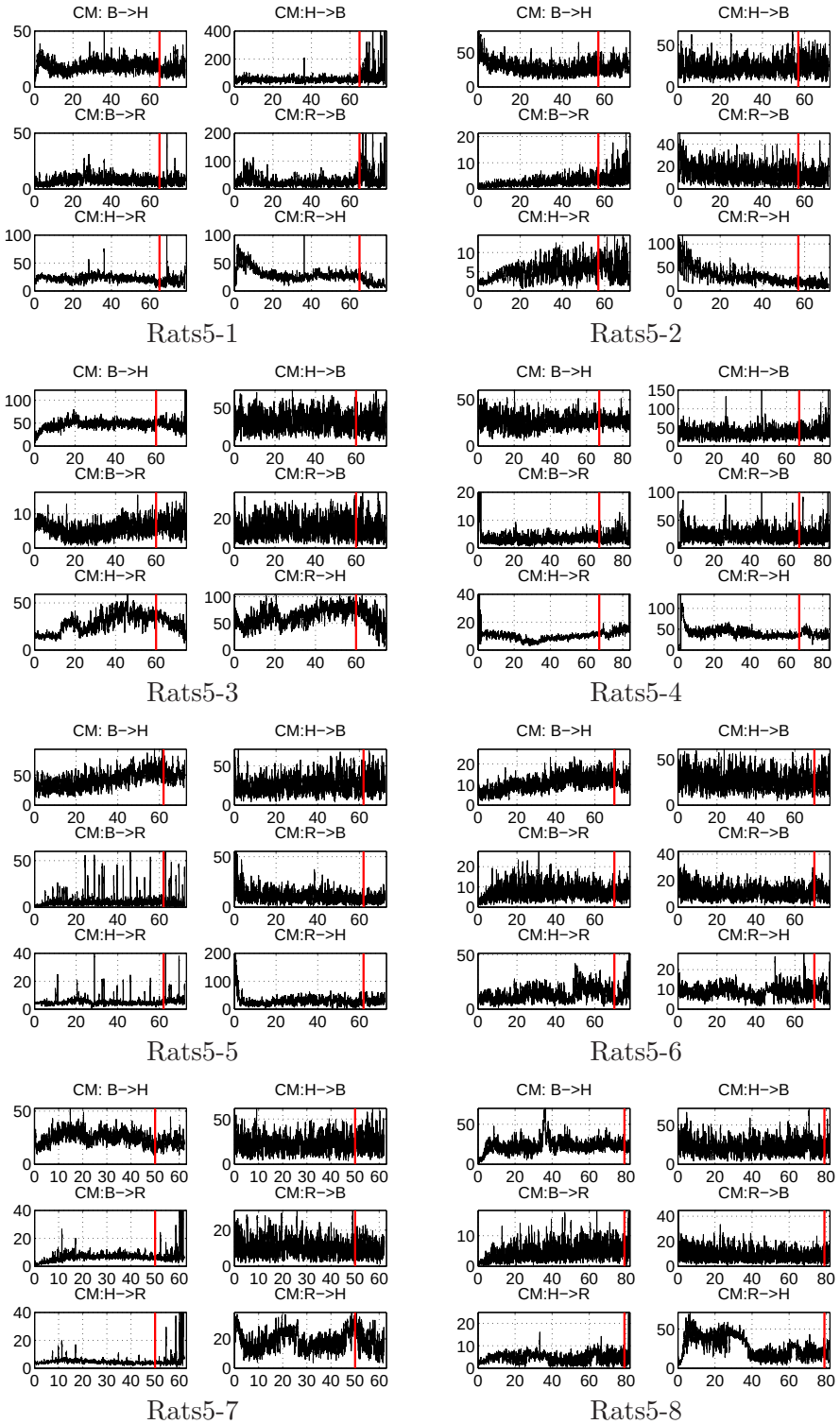

Figure 3.86 – *Coupling matrix $CM(t)$ obtained on "Rats5". Horizontal axis is time (min). Orange lines indicate the estimated deep-light change of anæsthesia: (B) EEG, (H) ECG, and (R) respiration.*

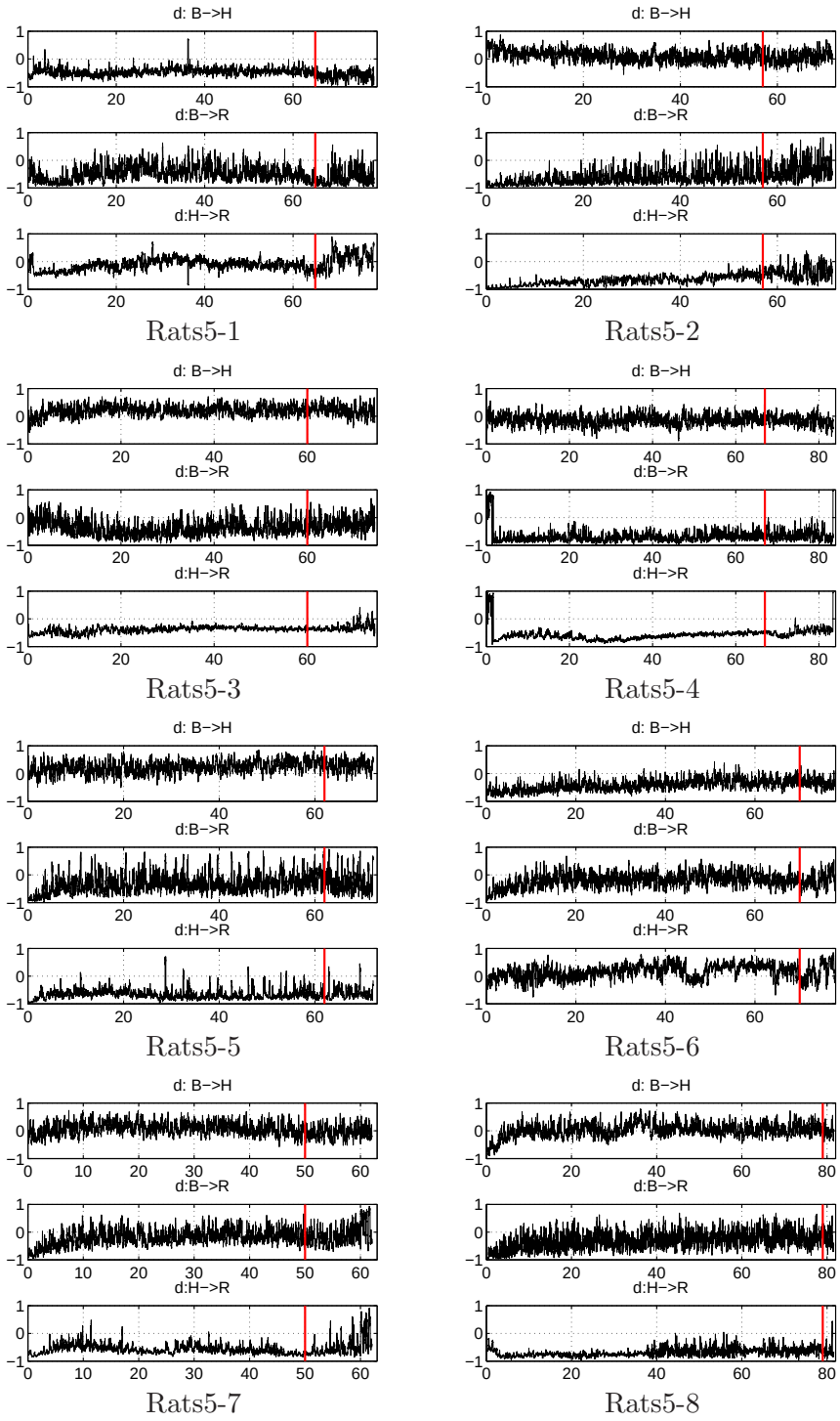

Figure 3.87 – *Direction of the interactions $d(t)$ obtained on "Rats5" using $CM(t)$. Horizontal axis is time (min). Orange lines indicate the estimated deep-light change of anæsthesia: (B) EEG, (H) ECG, and (R) respiration.*

Nonparametric Granger causality

Again, in this study, the length of window, shifted time, segments overlapped time were set with the same value as "Rats1" and "Rats3", i.e. 1min, 30sec, 4sec and 2sec, respectively. The power spectra and the coherence spectra were shown in fig. 3.88 and 3.89. In fig. 3.88,as mentioned at the S-estimator, on Rats5-1 to Rats5-4, we can see that our estimated deep-light change points of anæsthesia were well defined to see the increase of the respiration frequency, diminishing δ-wave and appearance of θ-wave. The other four rats, especially

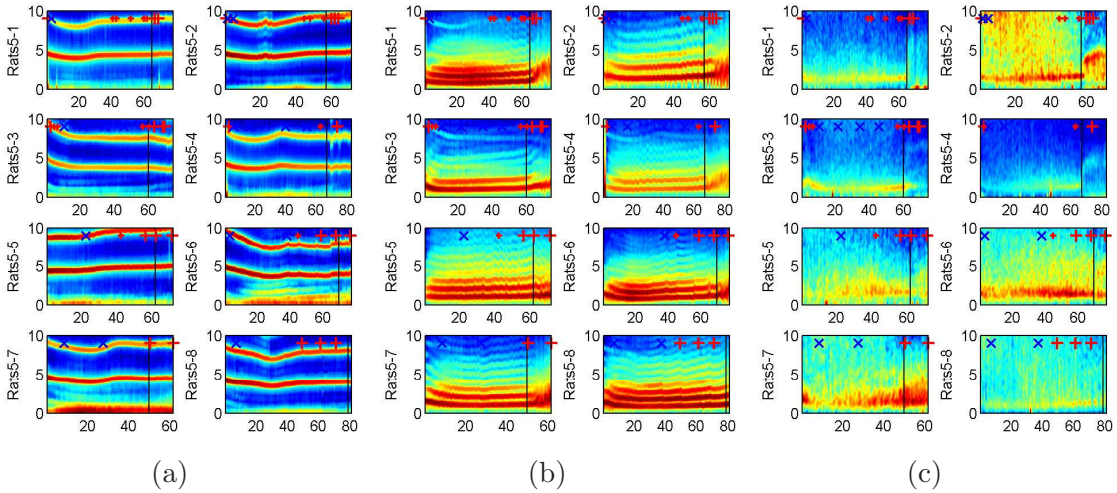

Figure 3.88 – *Power spectra obtained on "Rats5". Horizontal axis is time (min). Vertical axis is frequency (Hz). Color axis is omitted. Black lines indicate the estimated deep-light change of anæsthesia. The results of pinch test is added for reference ("+" positive, "x" negative): (a) ECG, (b) Respiration, and (c) EEG.*

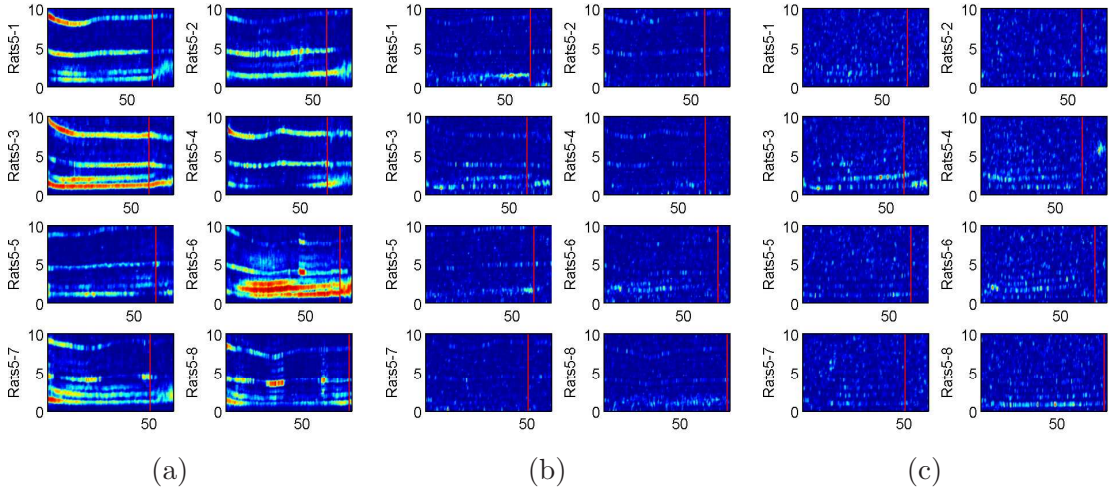

Figure 3.89 – *Coherence spectra obtained on "Rats5". Horizontal axis is time (min). Vertical axis is frequency (Hz). Orange lines indicate the estimated deep-light change of anæsthesia: (a) ECG and respiration; color axis [0 1], (b) EEG and ECG; color axis [0 0.4], and (c) EEG and respiration; color axis [0 0.4].*

Rats5-8, do not show clear change in frequency. No unique frequency change according to the anæsthesia can be observed for ECG. From fig. 3.89, as "Rats1" and "Rats3", strong coherence can be observed between ECG and respiration for all duration of the measurements. But in the contrary, the others show very weak coherence, even weaker than the case of "Rats3". Accordingly, nothing can be commented with respect to the transition point. We presume that this is because of the repeat of the experiments in one week interval. Again,looking carefully, some similar trend as the new S-estimator can be found.

In fig. 3.90 and 3.91, we show the results of the nonparametric Granger causality. As previous groups, the $GC(t)$ smaller than threshold, shown in the following table, defined by the permutation test were set to zero.

	GC:B→H	GC:H→B	GC:B→R	GC:R→B	GC:H→R	GC:R→H
threshold	0.09	0.09	0.09	0.09	0.09	0.09

Table 3.27 – *Threshold for nonparametric Granger causality $GC(t)$ defined by the permutation test for "Rats5": (B) EEG, (H) ECG, and (R) respiration.*

From fig. 3.63 and 3.64, few causality can be found between brain (B) and heart(H), and also between B and respiration (R), such that again we cannot remark an increase in the causality from B to R at the light stage of anæsthesia found in group "Rats1". The causality from H to R seems to decrease at the light stage of anæsthesia as we found in "Rats1" and "Rats3". The causality from R to H can be found mostly on whole period of recordings. Some decrease remarked at the light stage of anæsthesia in "Rats3" cannot be found in this group. We suppose this is also because of the remeasurements after one week.

This group also arrived very late such that the time averaged specified frequency analysis is not carried out yet. Consequently, nothing can be concretized for the interdependencies between the brain, heart and respiration activities also in this group.

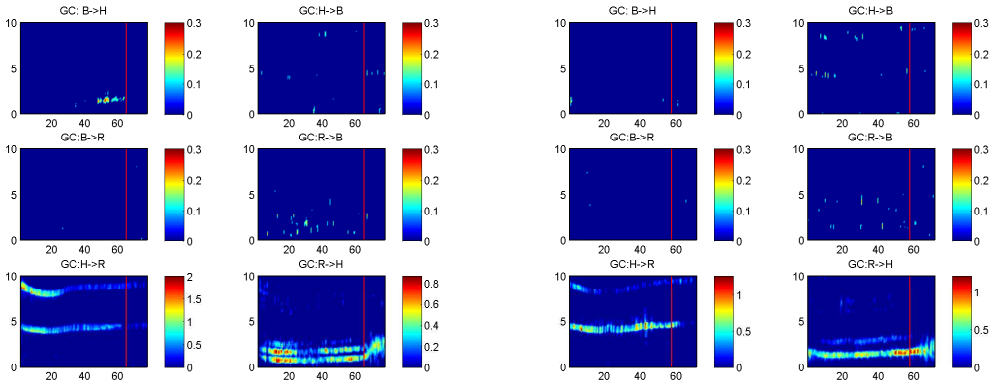

Rats5-1 Rats5-2

Figure 3.90 – *Nonparametric Granger causality $GC(t, f)$ obtained on "Rats5" PartI (Rats5-1 to Rats5-2). Horizontal axis is time (min). Vertical axis is frequency (Hz): (B) EEG, (H) ECG, and (R) respiration.*

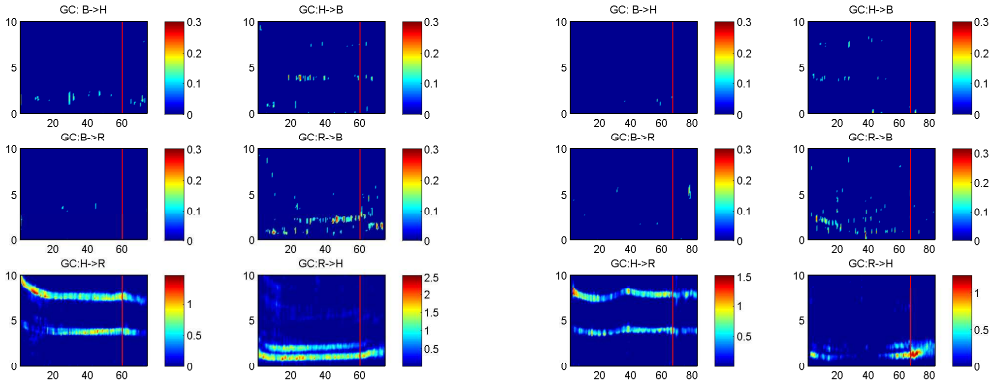

Rats5-3

Rats5-4

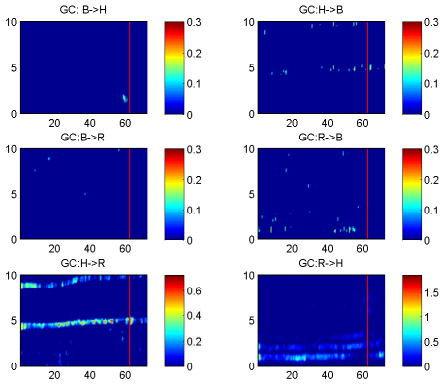

Rats5-5

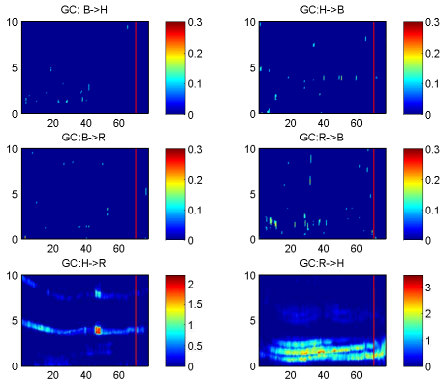

Rats5-6

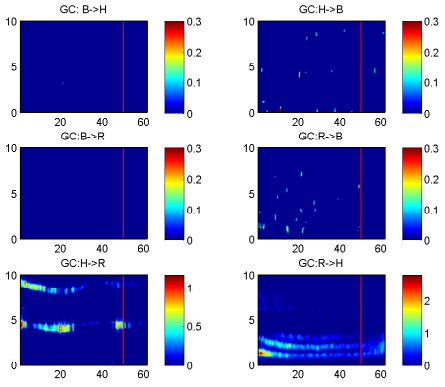

Rats5-7

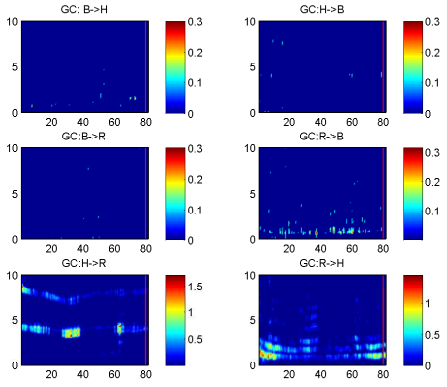

Rats5-8

Figure 3.91 – *Nonparametric Granger causality $GC(t, f)$ obtained on "Rats5" PartII (Rats5-3 to Rats5-8). Horizontal axis is time (min). Vertical axis is frequency (Hz): (B) EEG, (H) ECG, and (R) respiration.*

3.9.6 Summary of the interdependency for rats recordings

In this subsection, as the results of data analysis are shown on more than 70 pages, we summarized the results focussing on the interdependency according to the induced anæsthetics. The analysis results on the embedding dimension are also summarized since these are our brand-new findings. Here, the abbreviation B(brain) for EEG, H(heart) for ECG and R for respiration are used. The effect of the change in the measurement protocol of EEG and the effect of repeating measurement with one week interval are commented at the end of each anæsthetic.

Ketamine-Xylazine (KX)

The synchronization inside of whole system decreases at the light state of anæsthesia:

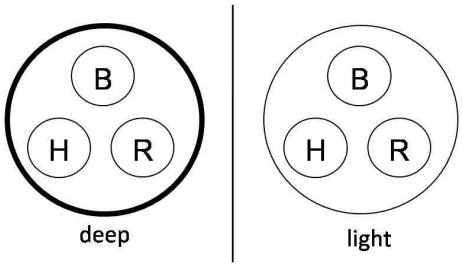

- Numerical detection was possible only for group "Rats1" with about 5min delay.
- When taking only two sub-systems into account, we can also see a decrease on B-H and B-R system, but no change can be remarked on H-R system*.

No change in the synchronization exclusively between sub-systems according to KX:

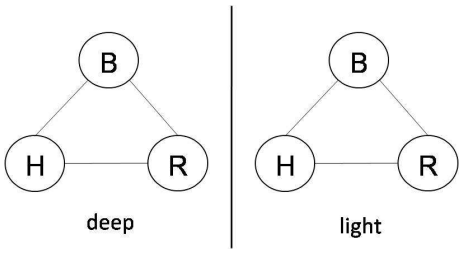

- The level of synchronization is about 10 times smaller than synchronization inside of whole system.
- When taking only two sub-systems into account, we remarked a decrease on B-R system on some rats. No change was observed on H-R system. Furthermore, little synchronization was found on B-H system. There is no unique order in the strength of synchronization on H-R and B-R system among the results.

*This leads to conclude that brain is the most influenced sub-system according to the effect of KX.

Embedding dimension increases at the light stage on B and H:

- The increase on ECG was not observed on all results.
- This implies that the complexity of the EEG and ECG increase at the light stage.
- We remark also that the variations of the calculated ED(t) of EEG and ECG are bigger at the light stage.

Coherence increases between B and R, and B and H at the light stage:

- High coherence was observed between H and R, but no change can be remarked at the change point of anæsthesia.
- The coherence between B and R is weak, but the coherence between B and H is even weaker.

The change in coupling strength found with "coupling matrix (CM)":

- The coupling from B to R and from H to R increase at light stage on all results.
- The coupling from R to B and from R to H decrease at light stage on some results.
- The directionality change in coupling happens like the figure below.

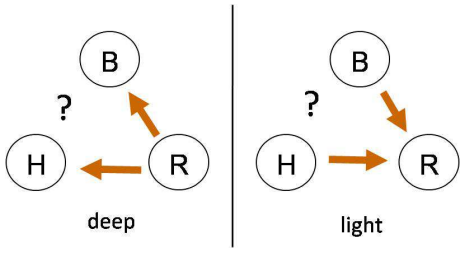

The change in causality strength found with "nonparametric Granger causality (GC)":

- The causality from H to R significantly decreases at light stage on all results. This disagrees with CM.
- The causality from B to R significantly increases at light stage on some results, and only on group "Rats1". This agrees with CM.
- The causality from R to H decreases at light stage on some results, but not on "Rats5".
- The causality from B to H and from R to B increase at light stage only on "Rats1".
- The causality between B and H, and B and R were not observed on group "Rats3" and "Rats5".

- The directionality of causality do not change according to KX and stays like the figure below.

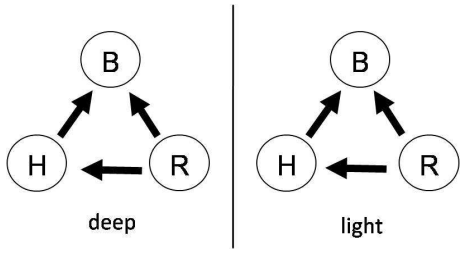

The effect of the change in the measurement protocol of EEG are:

- Numerical detection of the change of the depth of anæsthesia with $S(t)$ is not possible.
- Higher $S_{new}(t)$ around the change point is not observed, which make this unknown short increase an artifact.
- The shift of the ED of EEG at the transition point of anæsthesia is faster.
- The coherence between B and the other becomes smaller.
- The change of directionality of $CM(t)$ becomes less clear if this is not because of the repeating measurement after one week.
- The causality between B and the other almost disappears.

The effect of repeating measurement with one week interval:

- The sudden decrease of $S(t)$ cannot be seen except two rats.
- The coherence between B and the other becomes smaller.

Pentobarbital (PB)

The synchronization inside of whole system decreases at the light state of anæsthesia:

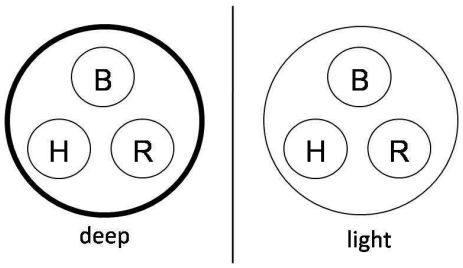

- This decrease at the transition point of anæsthesia cannot be seen on "Rats2".
- The reason why the obtained $S(t)$ differs from rats to rats should be the dose control problem.

- When taking only two sub-sytems into account, we can also see a decrease on B-H and B-R system, but no change can be remarked on H-R system*.

The synchronization exclusively between subsystems decreases at the light state of anæsthesia:

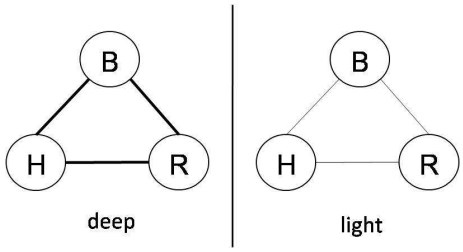

- The level of synchronization is about 5-15 times smaller than synchronization inside of whole system.
- The synchronization between B and R is the strongest.
- When taking only two sub-systems into account, we can also see a decrease on system with any two sub-systems, except B-R system in "Rats4".
- B-H system show sudden high synchronization at the moment of induction on "Rats4".

Nothing can be concluded on embedding dimension for PB:

- A decrease of EEG ED was remarked on half of rats in "Rats2", but no change was observed on EEG ED on "Rats4".
- No change was remarked on ECG ED on "Rats2", even if we observed an increase on "Rats4"

Coherence decreases between all two sub-systems at the light stage:

- High coherence was observed between H and R.
- The coherence between B and R and between B and H are weak.

The change in coupling strength found with "coupling matrix (CM)":

- There is no general agreement.
- Focussing on some rats, the coupling between H and R in both direction decrease at the light stage.
- The coupling from B to H and from R to B increase at the light stage.

*This leads to conclude that, as KX, brain is the most influenced sub-system according to the effect of PB.

- No change was remarked on the directionality of coupling.

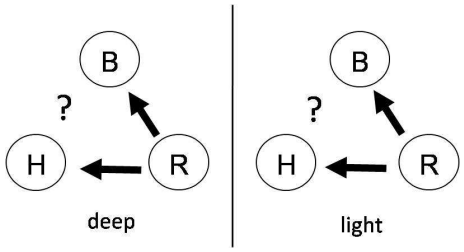

- This results on CM was analyzed only on 10 rats such that it may not correct.

The change in coupling strength found with "nonparametric Granger causality (GC)":

- All the causalities decrease at the light stage on "Rats2", but the causalities between B and the other cannot be observed on "Rats4".
- There is a significant decrease of causality from R to H on " Rats2". This agrees with CM.
- The directionality of causality do not change according to PB and stays like the figure below.

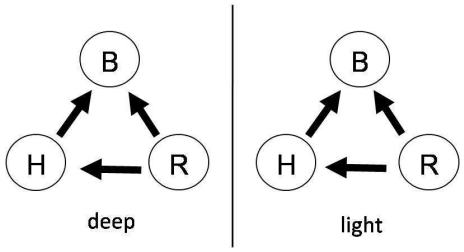

The effect of the change in the measurement protocol of EEG are:

- There is no decrease in EEG ED, and there is an increase in ECG ED.
- The coherence between B and the other becomes smaller.
- The causality between B and the other almost disappears.

3.10 Results of our Analysis on Human recordings

Now let us move to human data. As the physiological signals of rat are very similar as the signals of human, just they are four times faster, we can expect to detect the difference between deep and light anæsthesia on human recordings. Of course the anæsthetic differs with the drugs used for rats, such that we may have completely different results (as the results for KX and PB were different).

The human measurements are carried out on two separate phase*, i.e. resting state and anæsthetized state, such that the recordings do not contain the deep-light change point of anæsthesia. Moreover, we have multiple EEG recordings compared to rat data. Consequently, the objective of the analysis on human data are: See the difference in the level of synchronization and seek for the possibilities of the deep-light transition of anæsthesia. See the interdependencies among brain, heart and respiration activities. Seek the effective usage of the multiple EEG recordings.

Before all the analysis except nonparametric Granger causality, all the recordings were preprocessed, i.e. a 50Hz component was filtered out to remove the effect of the power supply of the measuring systems, and more than 100Hz components were filtered out since they were considered as measurement noise. After that, they are down-sampled to 300Hz. For nonparametric GC, all the recordings were also preprocessed, but here, more than 45Hz were filtered out. Furthermore, the sampling frequency is down-sampled to 200Hz.

3.10.1 Human in Lancaster

S-estimator

Taking account that the rhythms of human physiological systems are four times slower than rats, the window length was set to 40 seconds. As we down-sampled to 300Hz, the number of samples inside of one window is 12000 points, which is the same as "Rats3" to "Rats5". The shifted time length was set to 0.5 second as the case of rats, to assure the sudden change in the obtained results. To compare the resting state (from now on let us call "p1") and the anæsthetized state (from now on let us call "p2"), we calculated the $S(t)$ on each state. We show the used ED and τ in fig. 3.92. From this figure, we first remarked that, on more than half of the subject, the ED of EEG signals for "p2" are smaller than "p1". Also on some subject the ED of ECG signals for "p2" are smaller than "p1". This is exactly the same case as rats. For respiration, even if half of them were assisted, no difference was remarked. Furthermore, no difference was remarked according to the anæsthetics used in the studies. Let see more in details later at the embedding dimension analysis†. Just to add, we can remark higher τ for EEG signals for "p2", which should illustrates smaller EEG frequencies under anæsthesia.

As we didn't know how to manage with four EEG signals, we simply calculated four $S(t)$ taking ECG signal, respiration signal and each of the EEG signals independently. In fig. 3.93, the obtained $S(t)$ for each subjects on "p1" and "p2" are shown respectively. From these figures, we can remark that the level of the synchronization remains constant along

*See subsec. 3.2.3 for more details.

†The reason why the ED of ECG for subject no.8 was low is also described later at the embedding dimension analysis.

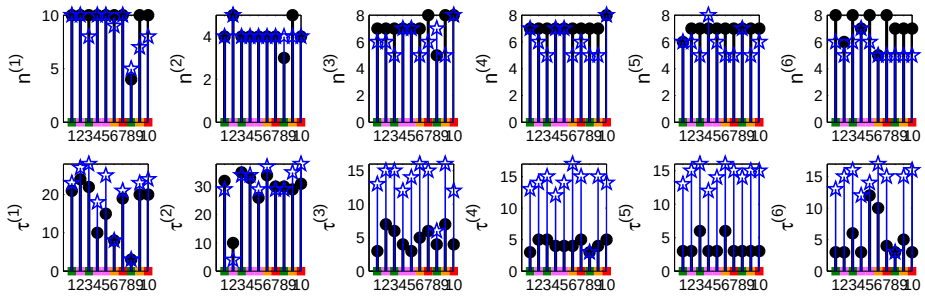

Figure 3.92 – *Embedding dimension (ED) and time delay (τ(samples)) used in the studies. Horizontal axis is the subjects number. Number in (.) means: (1) ECG (2) Respiration (3) EEG1 (4) EEG2 (5) EEG3 (6) EEG4. The black rounds are for "p1". The blue stars are for "p2". The colored squares above subject numbers are: (green) Propofol, (orange) Propofol+Curare, (red) Sevoflurane, and (pink) Sevoflurane+Curare.*

the time in both phase, and also we remarked that there is no big difference between the chosen EEG signals. It means that, we may use only one of these channels, and moreover, the position of the electrode does not matter. Furthermore, to compare the state "P1" and "P2", we calculated mean and variance of $S(t)$ for each subject at each state. From the obtained results shown in fig. 3.94, we observed that the synchronization under anæsthesia is smaller than the awaken state, and also we observed that the variance is bigger at the awaken state. However, these $S(t)$ on each state are calculated with different ED such that

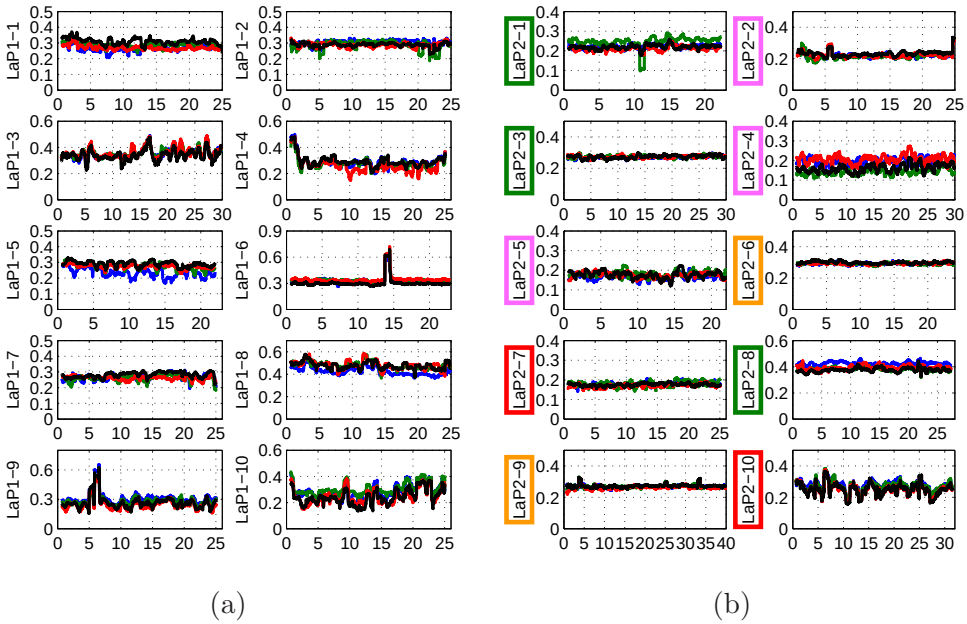

Figure 3.93 – *Synchronization measure $S(t)$ obtained by clustering three oscillators (ECG, Respiration and one of EEG1 to EEG4) together on group "Lancaster". Horizontal axis is time (min). Blue lines are with EEG1, green lines are with EEG2, red lines are with EEG3, and black lines are with EEG4: (a) resting (b) anæsthetized (Green boxes: Propofol, orange boxes: Propofol+Curare, red boxes: Sevoflurane, and pink boxes: Sevoflurane+Curare.)*

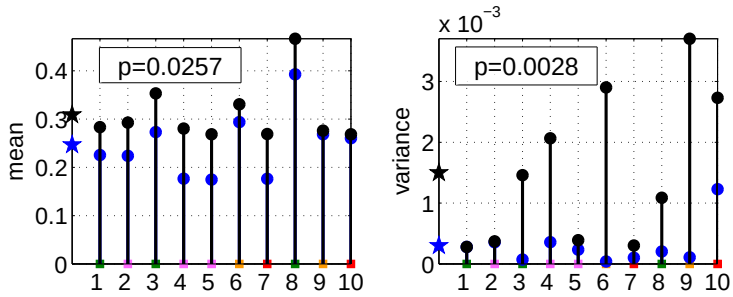

Figure 3.94 – *Mean and variance calculated on $S(t)$. x axis is the subject number of group "Lancaster". p is the result of the Wilcoxon rank sum test: (black round) "p1", (blue round) "p2", (black star) mean of "p1" (blue star) mean of "p2". The colored squares above subject numbers are: (green) Propofol, (orange) Propofol+Curare, (red) Sevoflurane, and (pink) Sevoflurane+Curare.*

we are not sure of the comparison. Consequently, we calculated the $S(t)$ at "p2" using the ED settled for "p1". From fig. 3.95, we can see that the $S(t)$ are slightly small when the ED for "p1" are used, i.e. ED are big. Again, using this $S(t)$, we compared the two state. From fig. 3.122, now we are confident to declare that the synchronization is lower under anæsthesia than the awaken state (significance level of 0.064), and the variance is also lower under anæsthesia (significance level of 0.0073). Interestingly, this low synchronization under anæsthesia is exactly the inverse case of rats which synchronization was higher under anæsthesia. As the $S(t)$ remains constant during each state and there is a difference between "p1" and "p2", there is a strong possibilities to use this $S(t)$ for the detection of the depth of anæsthesia, and moreover we may expect the numerical detection with our statistical assessment.

To finish with the S-estimator calculated on a cluster with three sub-systems, we tried

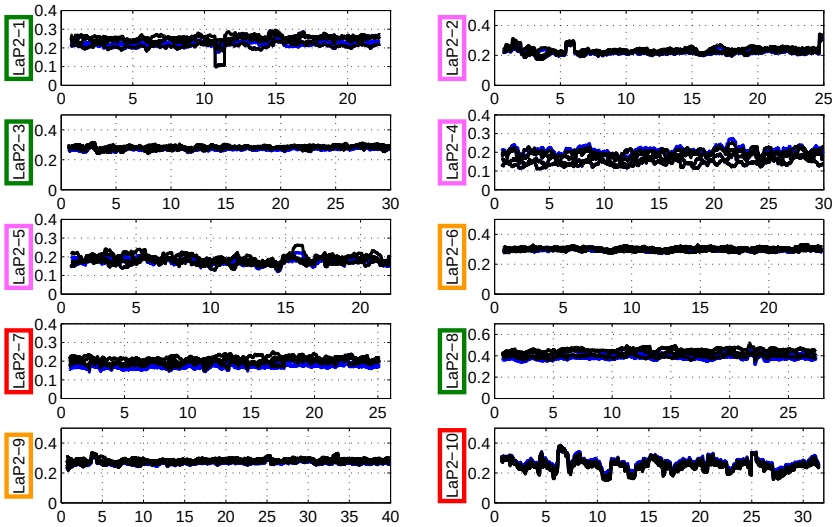

Figure 3.95 – *Comparison of $S(t)$ obtained on phase "p2" by clustering three oscillators (ECG, Respiration and one of EEG1 to EEG4) together on group "Lancaster" using the ED settled for "p1" and "p2": (black) ED of "p1" and (blue) ED of "p2". (green boxes: Propofol, orange boxes: Propofol+Curare, red boxes: Sevoflurane, and pink boxes: Sevoflurane+Curare.)*

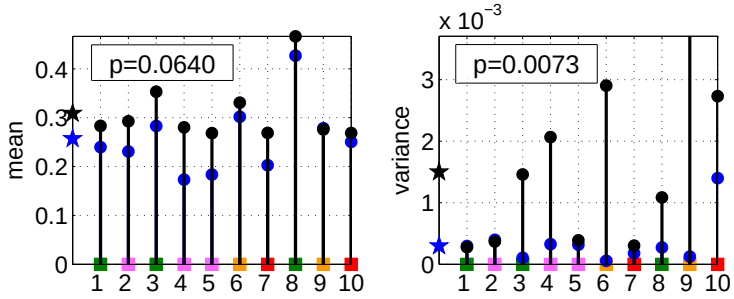

Figure 3.96 – *Mean and variance calculated on $S(t)$ obtained with the same ED for "p1" and "p2". x axis is the subject number of group "Lancaster". p is the result of the Wilcoxon rank sum test: (black round) "p1", (blue round) "p2", (black star) mean of "p1" (blue star) mean of "p2". The colored squares above subject numbers are: (green) Propofol, (orange) Propofol+Curare, (red) Sevoflurane, and (pink) Sevoflurane+Curare.)*

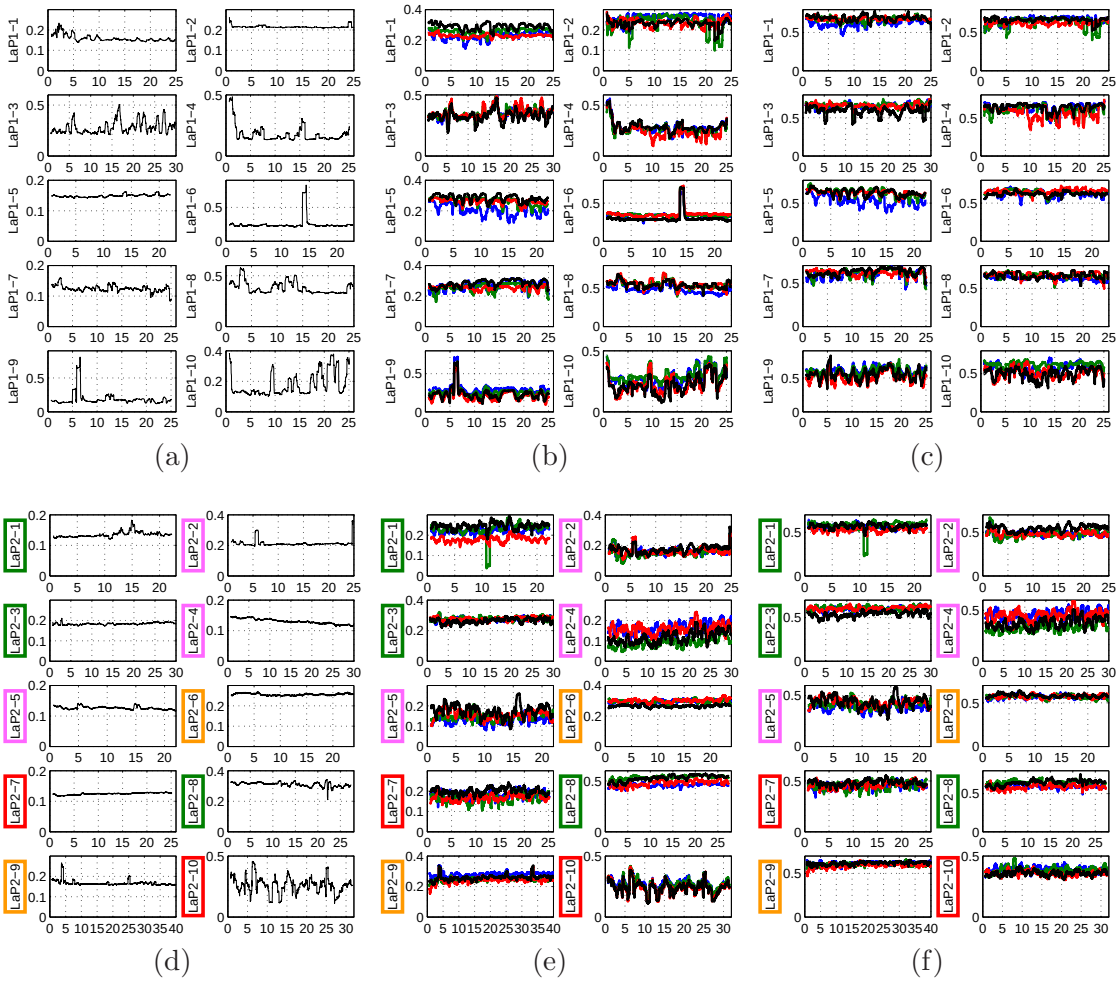

Figure 3.97 – *Synchronization measure $S(t)$ obtained by clustering two chosen oscillators together on group "Lancaster". Horizontal axis is time (min). The ED for "p1" was also used for "p2": (a,b,c) "p1" and (d e f) "p2" (green boxes: Propofol, orange boxes: Propofol+Curare, red boxes: Sevoflurane, and pink boxes: Sevoflurane+Curare.). (a,d) ECG and Respiration, (b,e) ECG and EEG, and (c,f) Respiration and EEG. For (b,c,e,f): (blue) EEG1, (green) EEG2, (red) EEG3, and (black) EEG4.*

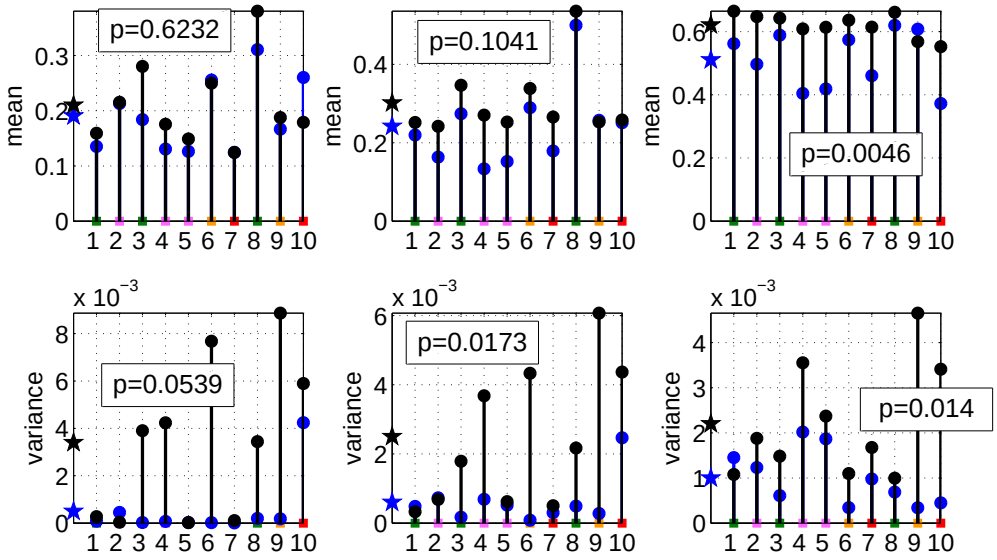

Figure 3.98 – *Mean and variance calculated on $S(t)$ with clusters of two sub-systems obtained with the same ED for "p1" and "p2". x axis is the subject number of group "Lancaster". p is the result of the Wilcoxon rank sum test:(left) ECG-Resp (middle) ECG-EEG (right) Resp-EEG. (black round) "p1", (blue round) "p2", (black star) mean of "p1" (blue star) mean of "p2". The colored squares above subject numbers are: (green) Propofol, (orange) Propofol+Curare, (red) Sevoflurane, and (pink) Sevoflurane+Curare.)*

to differentiate with respect to the anæsthetics. From fig. 3.122, Propofol with/without Curare seems to have higher $S(t)$ under anæsthesia more than Sevoflurane with/without Curare. However, since the subject number is only eight such that there is no certainty for this remark. From the other figures, no difference can be seen between the kind of anæsthetics used for the measurements.

In Fig. 3.97, the results of the S-estimator performed on sets of two sub-systems are shown. Here we directly plot the $S(t)$ at "p2" obtained with the same ED settled for "p1". From these figures, again we can remark that there is no huge difference among the results obtained with different EEG signals. We also compared mean and variance of the obtained results on each state, and show them on fig. 3.98. Paying attention on star markers, we remarked that the synchronization and its variance are lower under anæsthesia in all clusters. However, taking $p < 0.05$ as significance threshold, we can only conclude that $S(t)$ on EEG-Resp cluster decreases at "p2". Additionally, the variance of $S(t)$ on ECG-EEG and EEG-Resp clusters decreases at "p2".

new S-estimator

Now let us check the synchronization exclusively between sub-systems using the new S-estimator. In Fig. 3.99, we show the obtained results. From these figures, we remarked that the the strength of synchronization became about 10 times smaller than $S(t)$ as the case of rats. Again, no big difference can be observed among results obtained with different EEG signals usage. However we remarked that the level of synchronization variate along

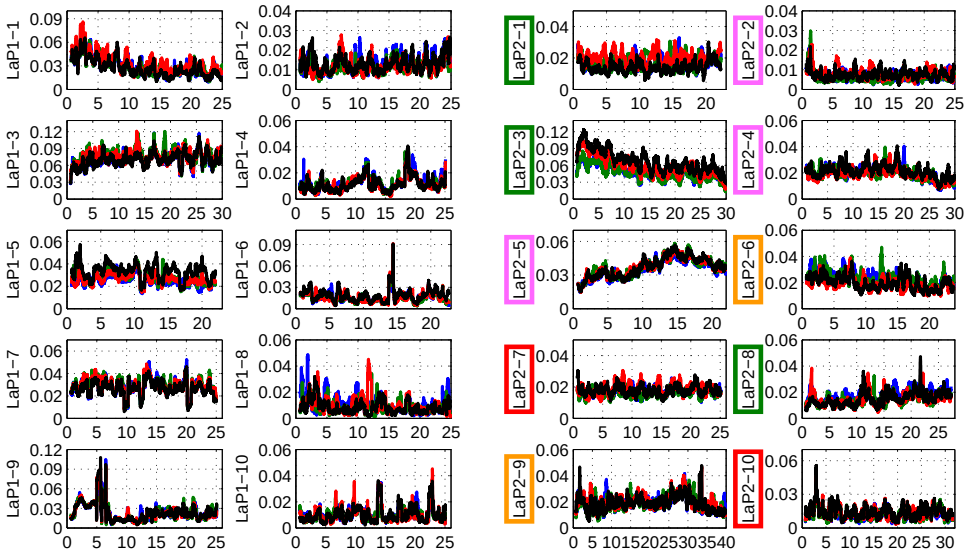

Figure 3.99 – *New synchronization measure $S_{new}(t)$ obtained by clustering three oscillators (ECG, Respiration and one of EEG1 to EEG4) together on group "Lancaster". Horizontal axis is time (min). Blue lines are with EEG1, green lines are with EEG2, red lines are with EEG3, and black lines are with EEG4: (a) resting (b) anæsthetized (Green boxes: Propofol, orange boxes: Propofol+Curare, red boxes: Sevoflurane, and pink boxes: Sevoflurane+Curare.)*

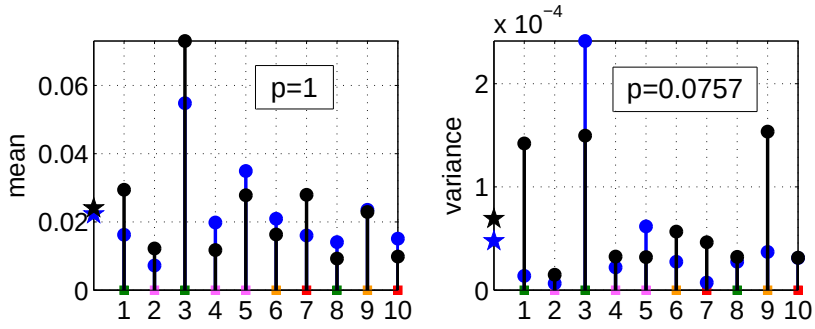

Figure 3.100 – *Mean and variance calculated on $S_{new}(t)$ obtained with the same ED for "p1" and "p2". x axis is the subject number of group "Lancaster". p is the result of the Wilcoxon rank sum test: (black round) "p1", (blue round) "p2", (black star) mean of "p1" (blue star) mean of "p2". The colored squares above subject numbers are: (green) Propofol, (orange) Propofol+Curare, (red) Sevoflurane, and (pink) Sevoflurane+Curare.)*

the time compare to the original $S(t)$. The comparison between state "p1" and "p2" was carried out using directly the $S_{new}(t)$ obtained with the same ED settled for "p1". From fig. 3.127, we observed that there is little difference between the "p1" and "p2 on the strength of the synchronization. This is also the same case as rats. Furthermore, also variance did not give significant difference.

In Fig. 3.101, as we did in the original S-estimator, we plotted the results obtained with other clusters taking two sub systems. From these figures, we remarked the results obtained with Propofol with/without Curare have more difference on the $S_{new}(t)$ obtained

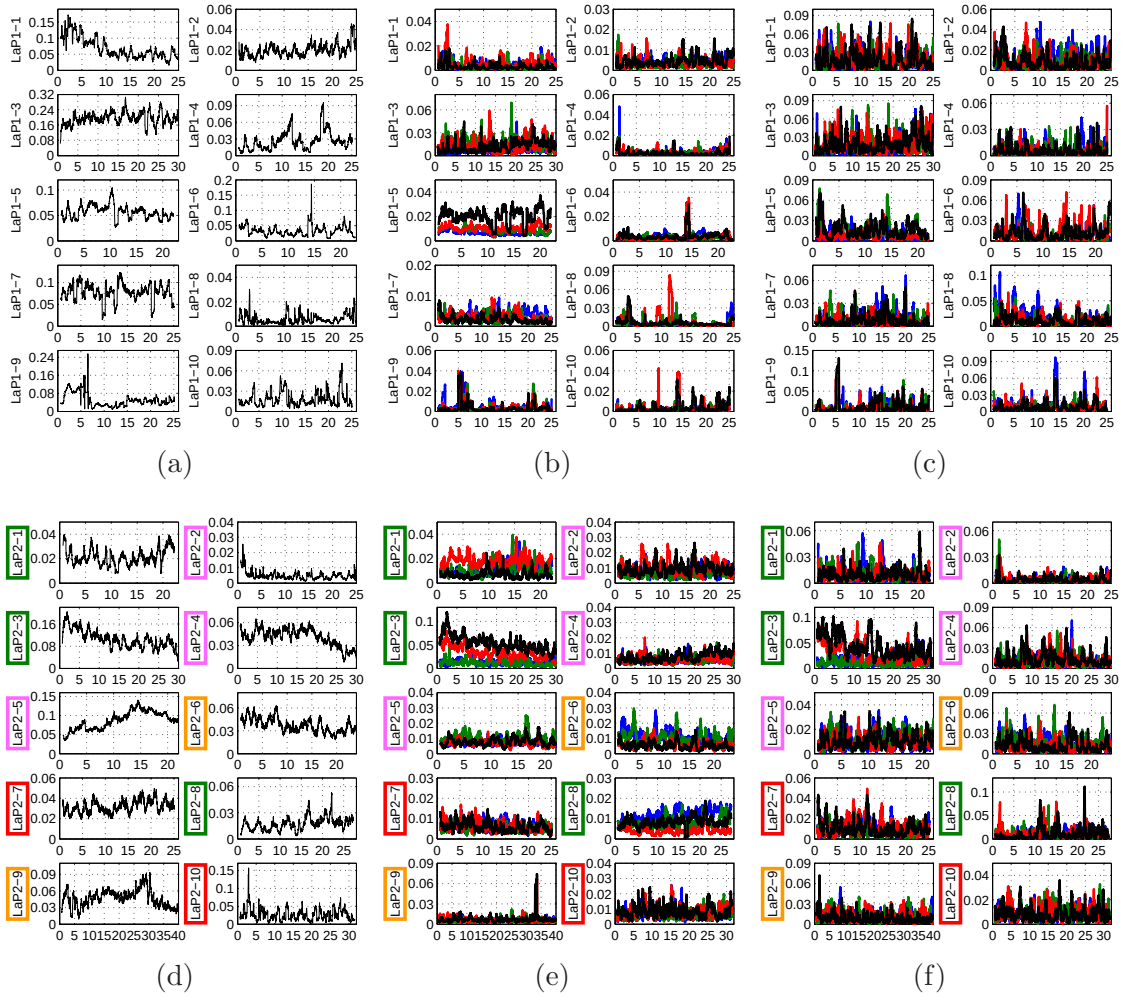

Figure 3.101 – *Synchronization measure $S_{new}(t)$ obtained by clustering two chosen oscillators together on group "Lancaster". Horizontal axis is time (min). The ED for "p1" was also used for "p2": (a,b,c) "p1" and (d e f) "p2". (a,d) ECG and Respiration, (b,e) ECG and EEG, and (c,f) Respiration and EEG. For (b,c,e,f): (blue) EEG1, (green) EEG2, (red) EEG3, and (black) EEG4. (green boxes) Propofol, (orange boxes) Propofol+Curare, (red boxes) Sevoflurane, and (pink boxes9 Sevoflurane+Curare.*

with different EEG signals than Sevoflurane with/without Curare. Furthermore, we found more fluctuation on $S_{new}(t)$ calculated on the ECG-Resp cluster. Here again, we compared "p1" and "p2" with mean and variance. The obtained results shown on fig. 3.102 shows significant difference at the level of synchronization on ECG-EEG cluster which increase under anæsthesia. Interestingly, this is exactly the inverse as the original S-estimator (See. fig 3.98). Consequently, we can imagine that the synchronization of the state variables inside of each subsystems decrease with the effect of anæsthetic, but the synchronization exclusively between ECG and EEG increases with the effect of anæsthetic.

As in the original S-estimator, we tried to differentiate the obtained results according to the kind of employed anæsthetics, and we found on fig. 3.98 that Sevoflurane with/without Curare seems to decrease more the value of $S(t)$ calculated on ECG-EEG and EEG-Resp clusters under anæsthesia. From that, we presume that Sevoflurane influences EEG signals

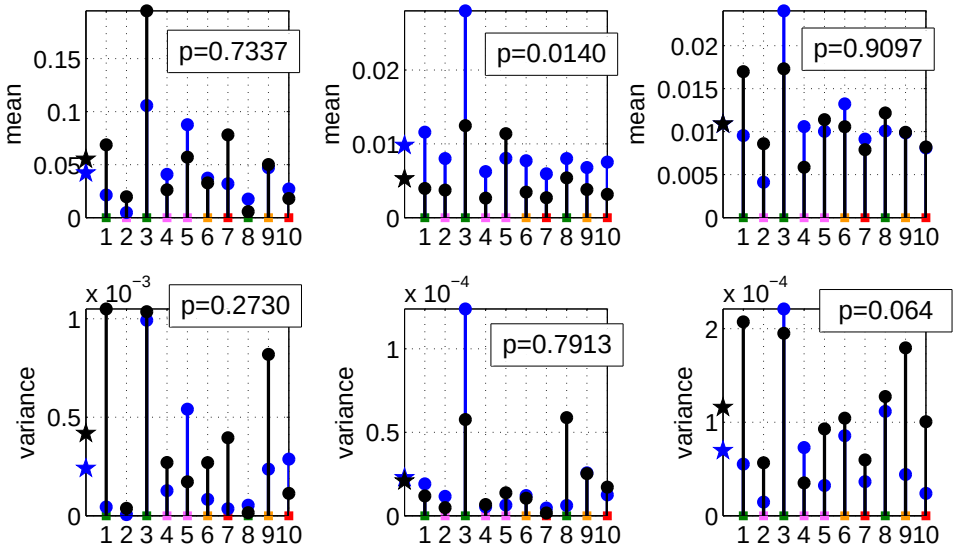

Figure 3.102 – *Mean and variance calculated on $S_{new}(t)$ with clusters of two sub-systems obtained with the same ED for "p1" and "p2". x axis is the subject number of group "Lancaster". p is the result of the Wilcoxon rank sum test:(left) ECG-Resp (middle) ECG-EEG (right) Resp-EEG. (black round) "p1", (blue round) "p2", (black star) mean of "p1" (blue star) mean of "p2". The colored squares above subject numbers are: (green) Propofol, (orange) Propofol+Curare, (red) Sevoflurane, and (pink) Sevoflurane+Curare.*

stronger than Propofol. No difference was observed on the other results.

In the studies of rats data, we carried out the analysis on the new S-estimator using PCA based embedding method. There, we saw that the embedding method does not matter the results of the new S-estimator. Consequently, in the studies on human data, this analysis with PCA based embedding method is omitted in this thesis*.

Embedding dimension analysis

In Fig. 3.103 and 3.104, we show the obtained results on embedding dimension (ED) for delay embedding. From these results, we remarked that there are much more fluctuation on the ED of ECG than the case of rats, except subject no.8. In fact, this subject was on a beta-blocker† for over 24hrs prior to the measurement. As this is a short acting drug and as this was dosed for anxiety and not for any heart disease, it was deemed suitable for inclusion into the trial. In our analysis of synchronization, we didn't see a grossly difference on this subject such that we cannot make judgement if it is worth pointing this out or not. For this reason, this case of beta blocker should be discussed with our collaborators, especially with our anæsthetists in the next final meeting of our project BRACCIA. Apart from this subject no.8, we remarked that most of the ED of ECG signals are equal to 10 at each measurement phase. In fact, in our decision of the ED using false nearest neighbors for the

*We verified outside of thesis that indeed the results of the new S-estimator with different embedding method gives approximately the same results.

†These drugs can be used as a heart medication.

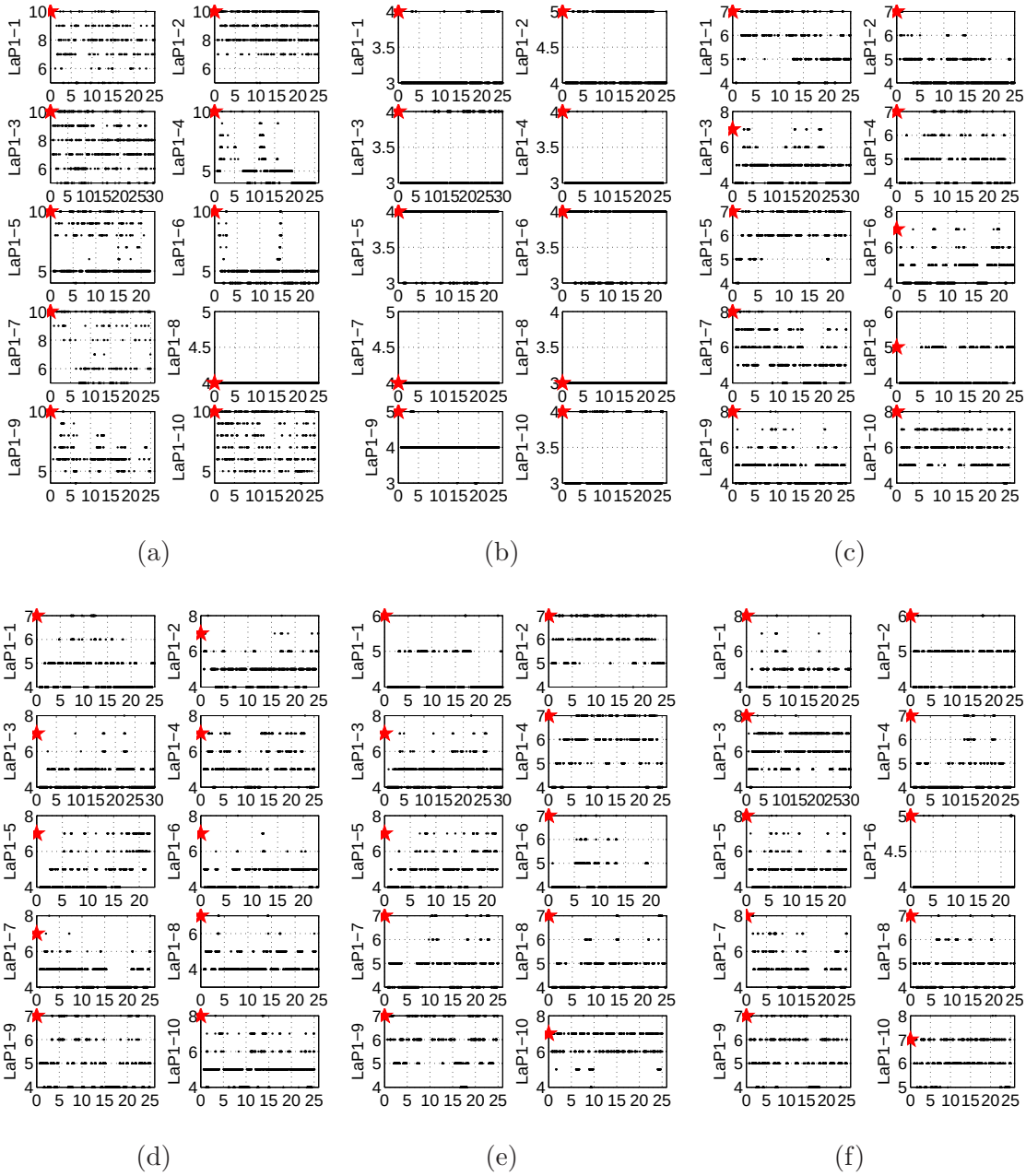

Figure 3.103 – *The study on the embedding dimension (ED) for delay embedding at the awaken(resting) state.Horizontal axis is time (min). The red stars indicates the chosen parameters: (a) ECG, (b) Respiration, (c) EEG1(d) EEG2, (e) EEG3 and (f) EEG4.*

delay embedding, we limited the maximum at 10*. This seems not to bother the analysis on rats, but, maybe, it will be worth to increase this limit for the analysis on human such that we may differentiate the two phase according to the effect of the anæsthesia. As we mentioned in the studies of rats, this is an interesting investigation for the future. The ED

*We limited to 10 since more we increase this limit more heavier the computation.

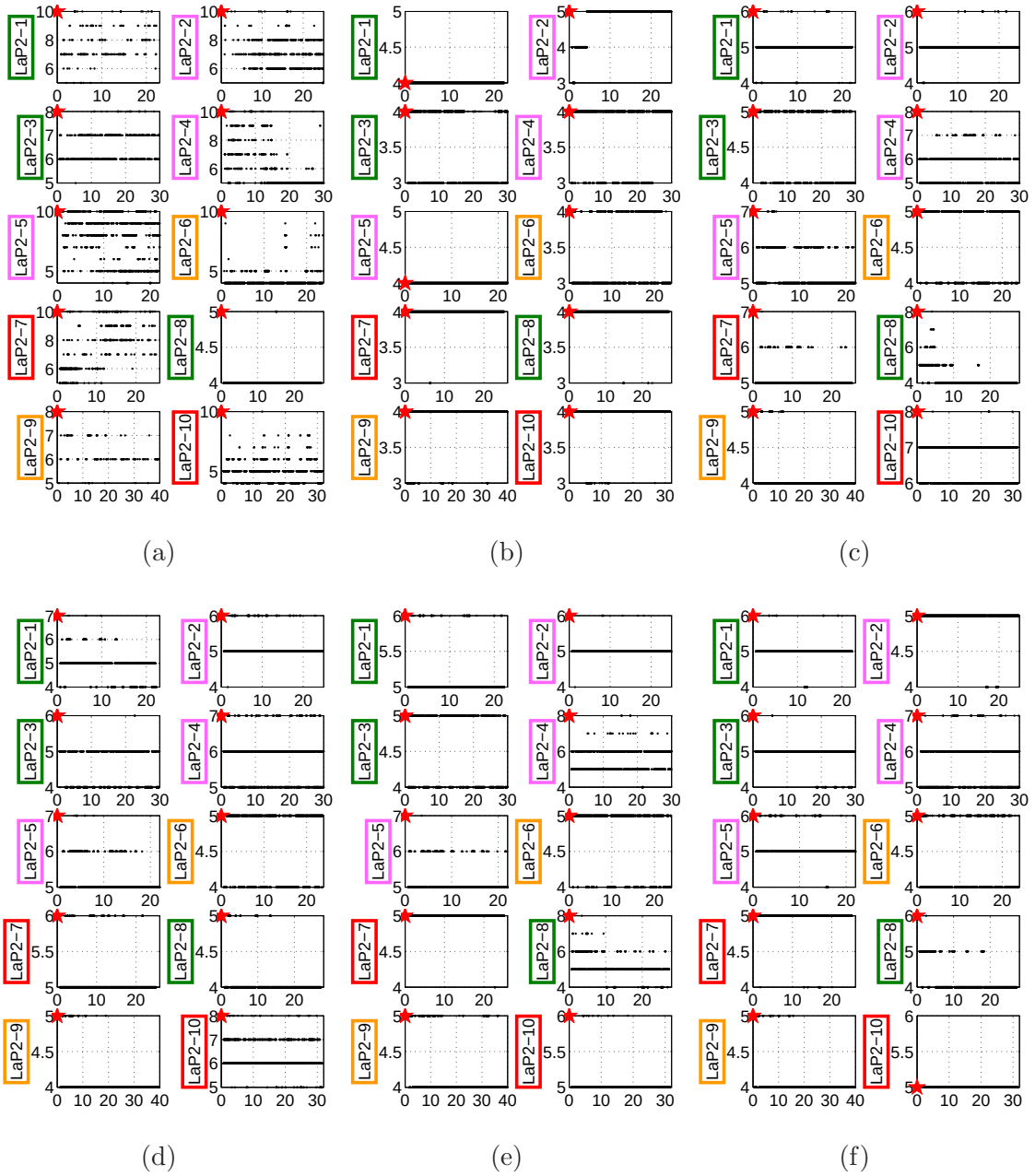

Figure 3.104 – *The study on the embedding dimension (ED) for delay embedding under anæsthesia. Horizontal axis is time (min). The red stars indicates the chosen parameters: (a) ECG, (b) Respiration , (c) EEG1 (d) EEG2, (e) EEG3 and (f) EEG4. (green) Propofol, (orange) Propofol+Curare, (red) Sevoflurane, and (pink) Sevoflurane+Curare.*

of respiration signal seems to be stable as we remarked in the studies of rats. The ED of EEG signals seem to have similar fluctuation degree as the studies of rats, but the $ED(t)$ obtained form each EEG signals are not exactly the same.

In fig. 3.105 , we compared the state "p1" and "p2" in the same way as the S-estimators. From the figures, we remarked that the mean values do not change according to the anæs-

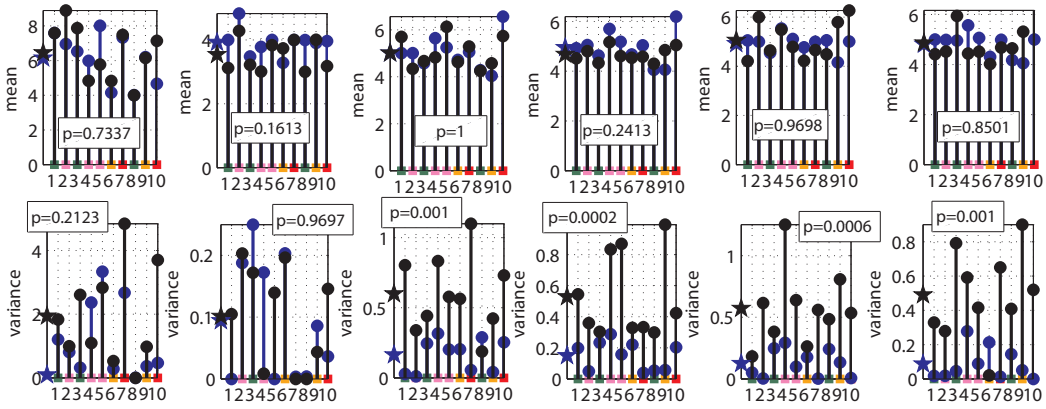

Figure 3.105 – *Mean and variance calculated on Embedding dimension (ED) at each state. Horizontal axis is the subjects number. From the left: ECG, Respiration, EEG1, EEG2, EEG3 and EEG4: (black round) "p1", (blue round) "p2", (black star) mean of "p1" (blue star) mean of "p2". The colored squares above subject numbers are: (green) Propofol, (orange) Propofol+Curare, (red) Sevoflurane, and (pink) Sevoflurane+Curare.*

thesia even if their maximum value decrease according to that (See fig. 3.92). However the variance of the embedding dimensions of the EEG signals definitively decrease under anæsthesia. As this was the same case as rats, as we mentioned before, the more detailed analysis will be very interesting as future work.

Just to remark, we didn't find any difference between the employed anæsthetics in this study of ED. The analysis with the PCA based embedding method was omitted from this human studies, since the obtained $ED(t)$ are very noisy such that the comparison between "p1" and "p2" seems meaningless.

Coupling matrix

Now let us proceed to coupling matrix to infer the interdependencies among sub-systems. Here, as the case of rats, not whole measurements were used to create the self model, but 4 minutes recordings were taken. Here below, we show the used ED and size of the Toeplitz like matrix K are shown in fig. 3.106. From this figure, we remarked again a decrease in the ED of EEG signals under anæsthesia as the case of delay embedding. Also, associated with the time delay τ, we remarked an increase in K of EEG signals under anæsthesia. However as we mentioned before, this calculation of the ED for PCA embedding is very noise sensitive such that the obtained values of ED are much bigger for EEG signals. Owing to this high ED, the analysis with coupling matrix had very heavy computation such that nearly one month was spent for the creation of the self model for the large ED. Some of them were still running at this moment*. Consequently, in fig.3.107 and 3.108, we show the obtained results on each state that we managed to finish. Apart from subject no.8, we remarked that the CM(t) obtained with different EEG signals gave us similar results. Subject no.10 under anæsthesia show huge CM(t): B→R and H→R. Checking the recordings of this subject, we

*We began the analysis on the human recordings this March 2008, such that we had only three month to analyze them. Furthermore, we had some unexpected trouble, like electricity cut, servers down for update,...etc., such that we didn't manage to finish before the submission of my thesis.

found very noisy ECG signals compared to the other subjects. Moreover, for resting state, no clear increase nor decrease was observed. But for under anæsthesia, an increasing trend can be seen in some results.

As the case of rats, we compared the two phase of measurements with mean and variance. We show the obtained results on fig. 3.109 and 3.110. To compare the strength of the coupling, the obtained mean value are summarized in the table below*.

	CM:B→H	CM:H→B	CM:B→R	CM:R→B	CM:H→R	CM:R→H
resting	8.48	18.11	7.43	9.95	13.16	6.42
anæsthesia	3.43	9.81	8.80	3.86	6.96	2.86

Table 3.28 – *Mean calculated on coupling matrix $CM(t)$.*

From this table, we remarked that the coupling from H to B is the strongest and the coupling from R to H is the smallest in both phase of measurements. From our knowledge, it seems to be more plausible the inverse case, since the heart and respiration is much closer than the brain and the heart. Consequently, deeper investigation in the future is an absolute requirement. We also remarked that all the mean values of CM except CM:B→R decrease under anæsthesia. Furthermore, from fig. 3.109, we observed significant decrease of the coupling on CM:B→H, CM:H→B, CM:R→B and CM:R→H under anæsthesia. And from fig. 3.110, we observed a significant decrease in the variance of CM(t) on CM:H→B and CM:R→B.

We checked also the directionality of these couplings, and show the obtained results on fig 3.111 and 3.112. From these figures, we remarked that H drives B in both phase, R drives B in resting state, B drives R under anæsthesia on some subjects. No remarkable coupling between H and R was observed. As the number of subjects is limited to ten, to conclude with this coupling will be done in the study on recordings of "Oslo".

To finish with this coupling matrix, we tried to distinguish the results according to the kind of anæsthetics, however, no big difference was observed in all results with coupling matrix.

*The mean values for B→R and H→R were recalculated without subject no.10.

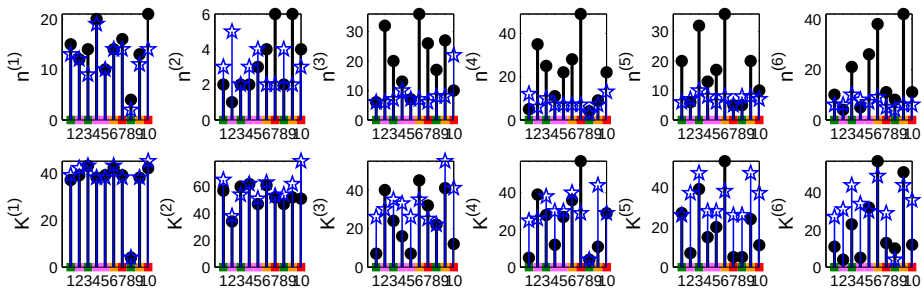

Figure 3.106 – *Embedding dimension (ED) and size of the Toeplitz like matrix (K(samples)) used in the studies. Horizontal axis is the subjects number. Number in (.) means: (1) ECG, (2) Respiration, (3) EEG1, (4) EEG2, (5) EEG3 and (6) EEG4. The black rounds are for "p1". The blue stars are for "p2".*

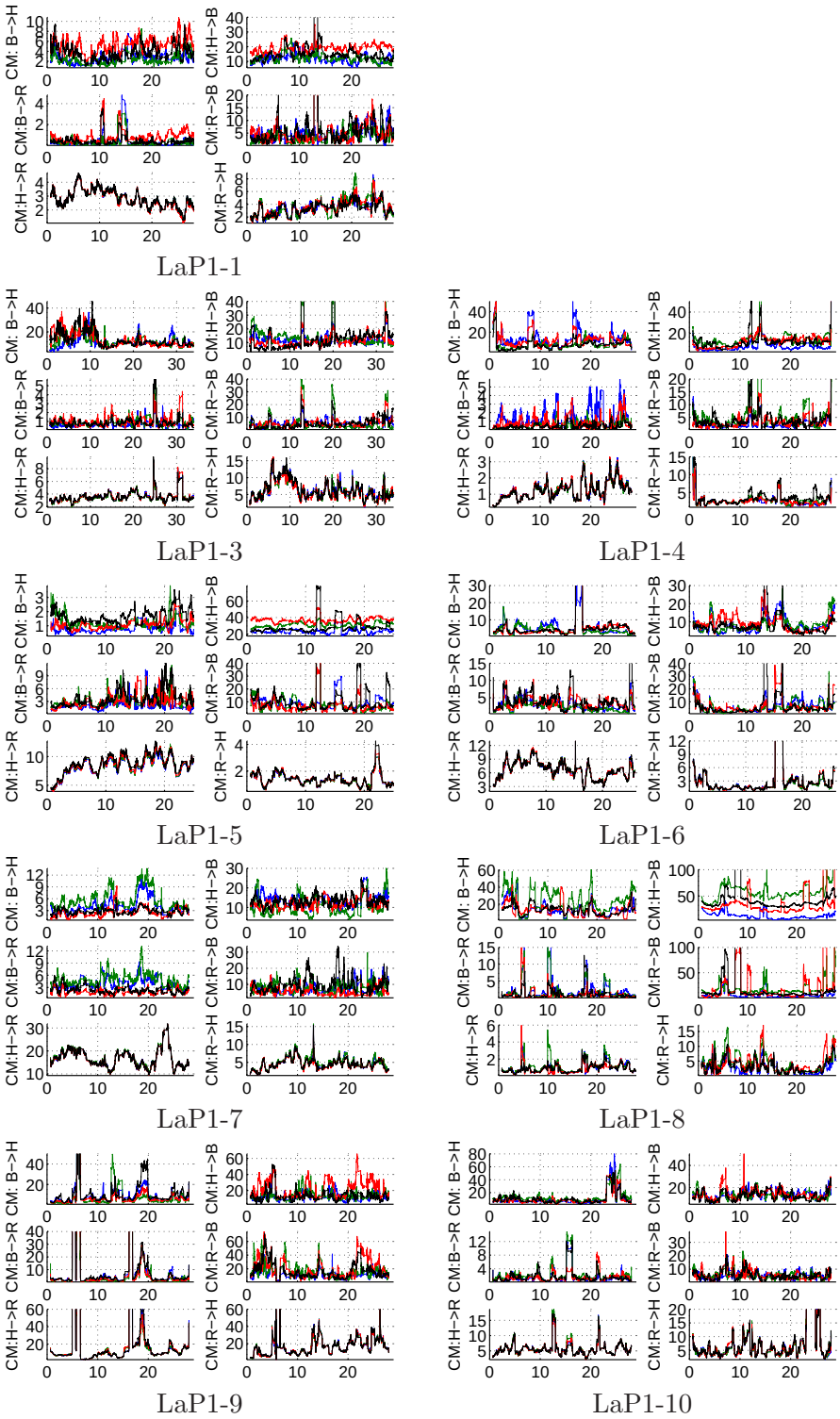

Figure 3.107 – *Coupling matrix $CM(t)$ obtained on "Lancaster" at resting (awaken) state. Horizontal axis is time (min). Subject no.2 is missing: (B) EEG, (H) ECG, and (R) respiration. Note that the results are zoomed to see the major part.*

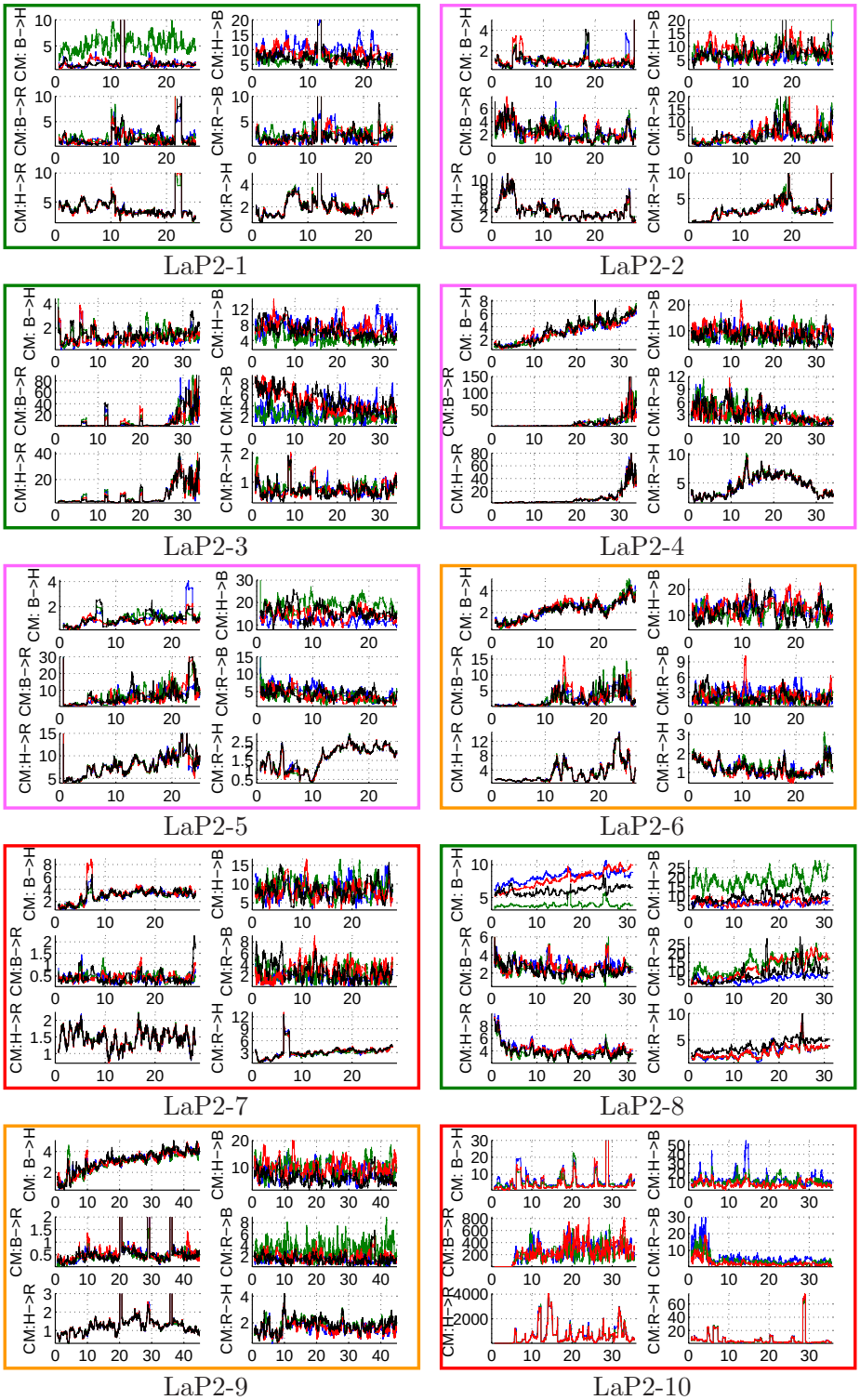

Figure 3.108 – *Coupling matrix $CM(t)$ obtained on "Lancaster" under anæsthesia. Horizontal axis is time (min). Subject no.10 miss the result with EEG4: (B) EEG, (H) ECG, and (R) respiration. Note that the results are zoomed to see the major part.*

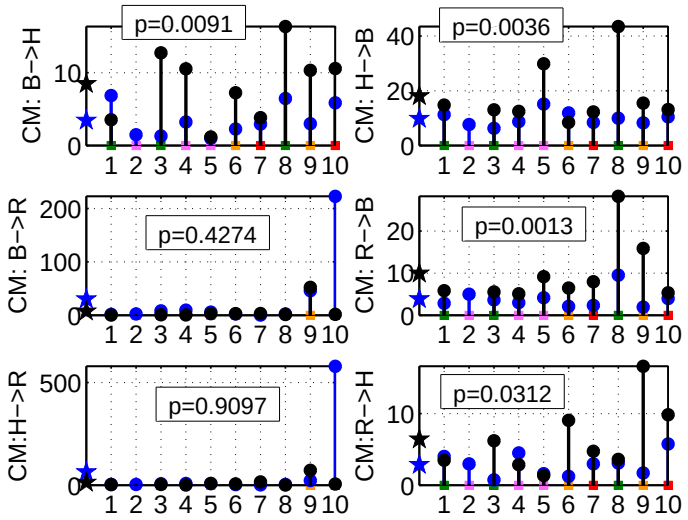

Figure 3.109 – *Mean calculated on CM(t) at each state. Horizontal axis is the subjects number. The black rounds are for "p1". The blue rounds are for "p2". The colored squares above subject numbers are: (green) Propofol, (orange) Propofol+Curare, (red) Sevoflurane, and (pink) Sevoflurane+Curare.*

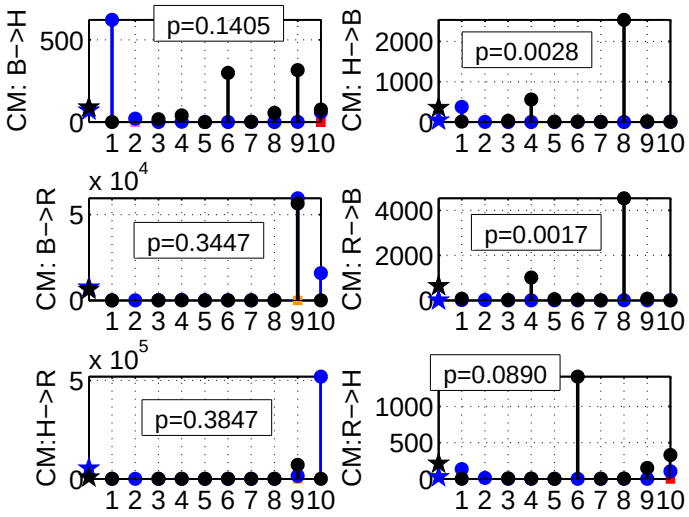

Figure 3.110 – *Variance calculated on CM(t) at each state. Horizontal axis is the subjects number. The black rounds are for "p1". The blue rounds are for "p2". The colored squares above subject numbers are: (green) Propofol, (orange) Propofol+Curare, (red) Sevoflurane, and (pink) Sevoflurane+Curare.*

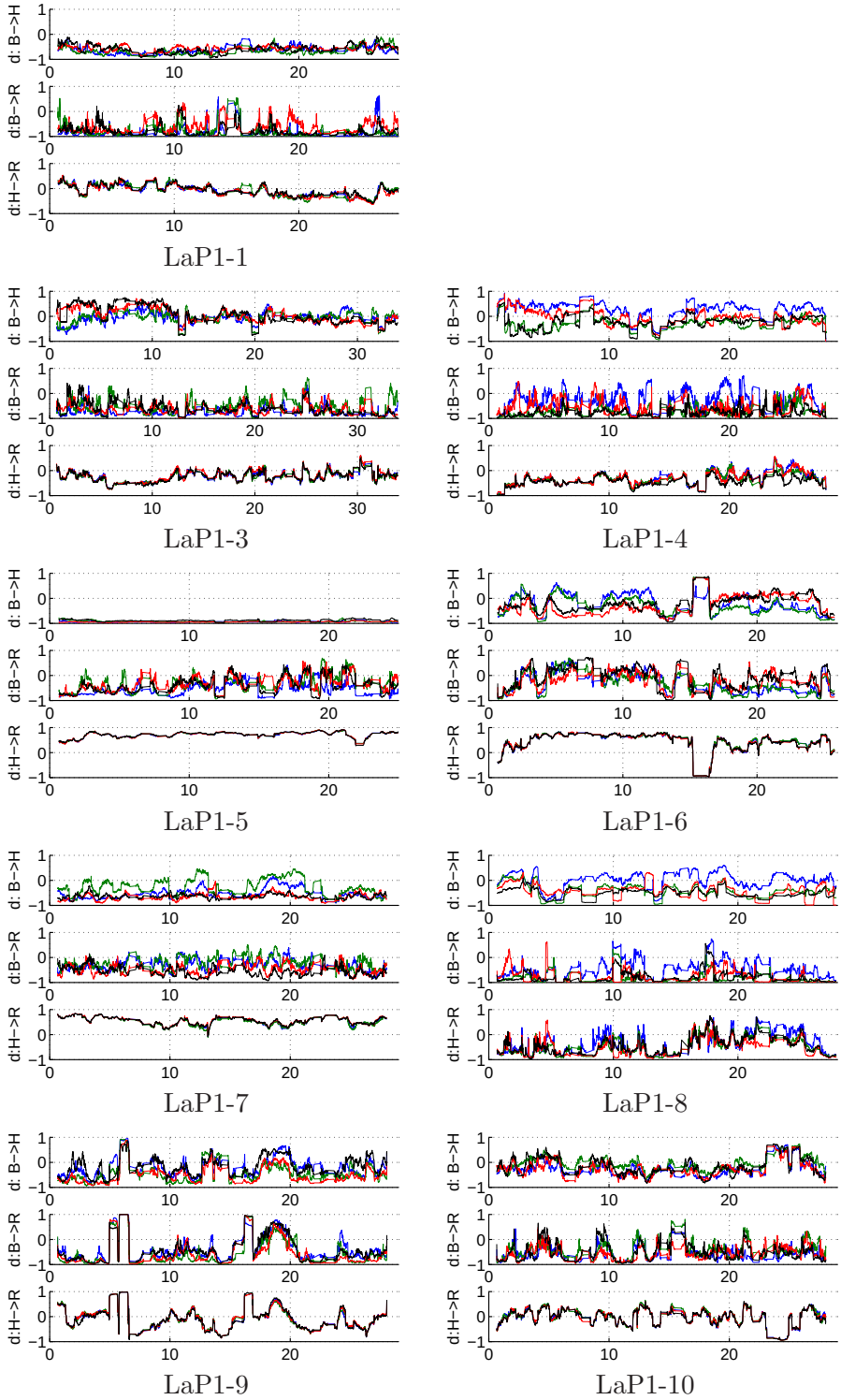

Figure 3.111 – *Direction of the interactions $d(t)$ obtained on "Lancaster" at resting (awaken) state. Horizontal axis is time (min). Subject no.2 is missing: (B) EEG, (H) ECG, and (R) respiration.*

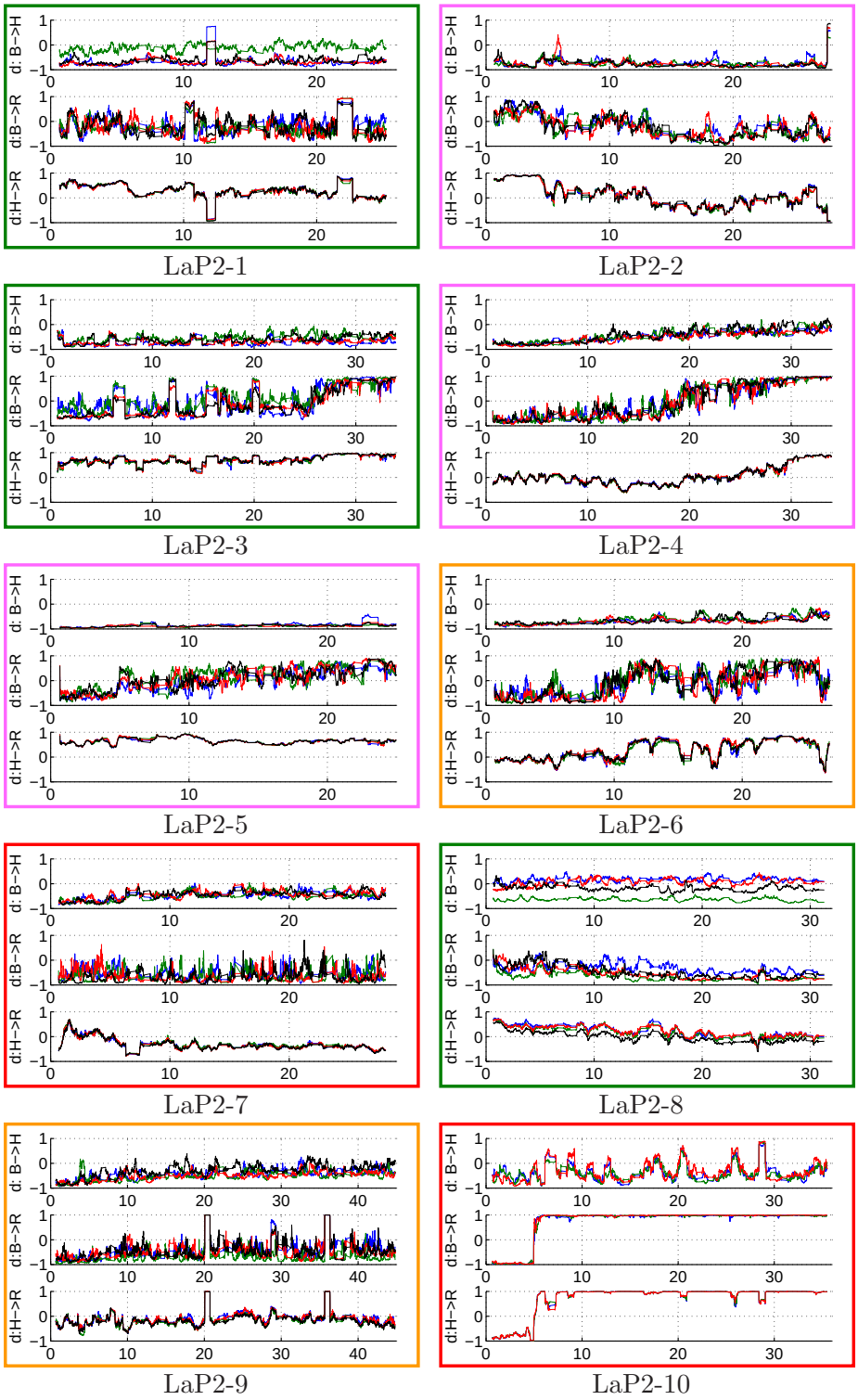

Figure 3.112 – *Direction of the interactions $d(t)$ obtained on "Lancaster" under anæsthesia. Horizontal axis is time (min). Subject no.10 miss the result with EEG4: (B) EEG, (H) ECG, and (R) respiration.*

Nonparametric Granger causality

In this study, the window length was set to 1 minute and shifted with 30 seconds as the case of rats studies, but the segments inside of one window for multiple realizations were created with 16 seconds length with 14 seconds of overlap. Here below, first, we show the obtained power spectra in fig. 3.113 and 3.114. From these figures, we remarked that the spectra of ECG signals show wavy form at the resting state and show straight lines under

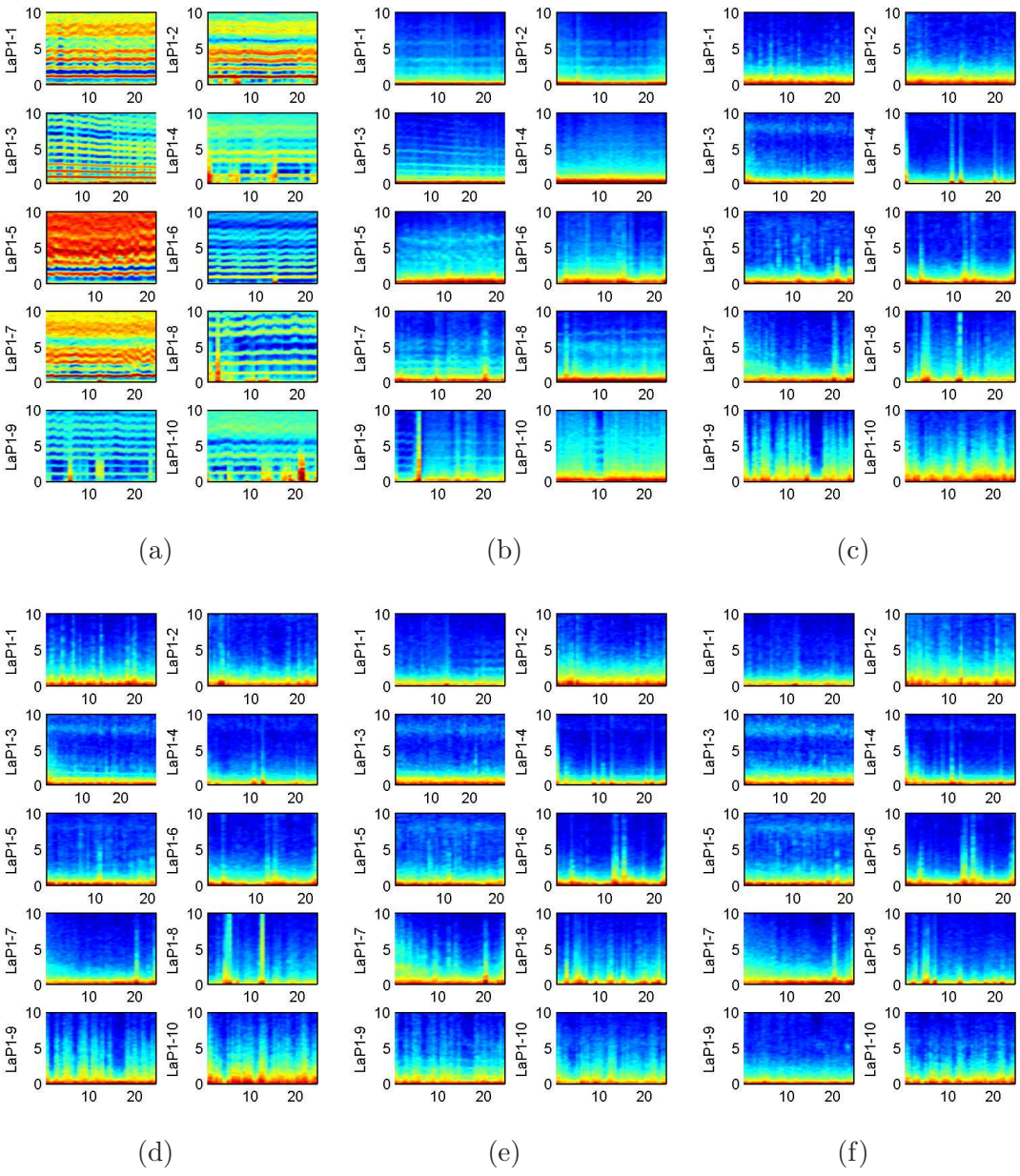

Figure 3.113 – *Power spectra obtained on "Lancaster" at resting (awaken) state. Horizontal axis is time (min). Vertical axis is frequency (Hz). Color axis is omitted: (a) ECG, (b) Respiration, (c) EEG1, (d) EEG2, (e) EEG3 and (f) EEG4.*

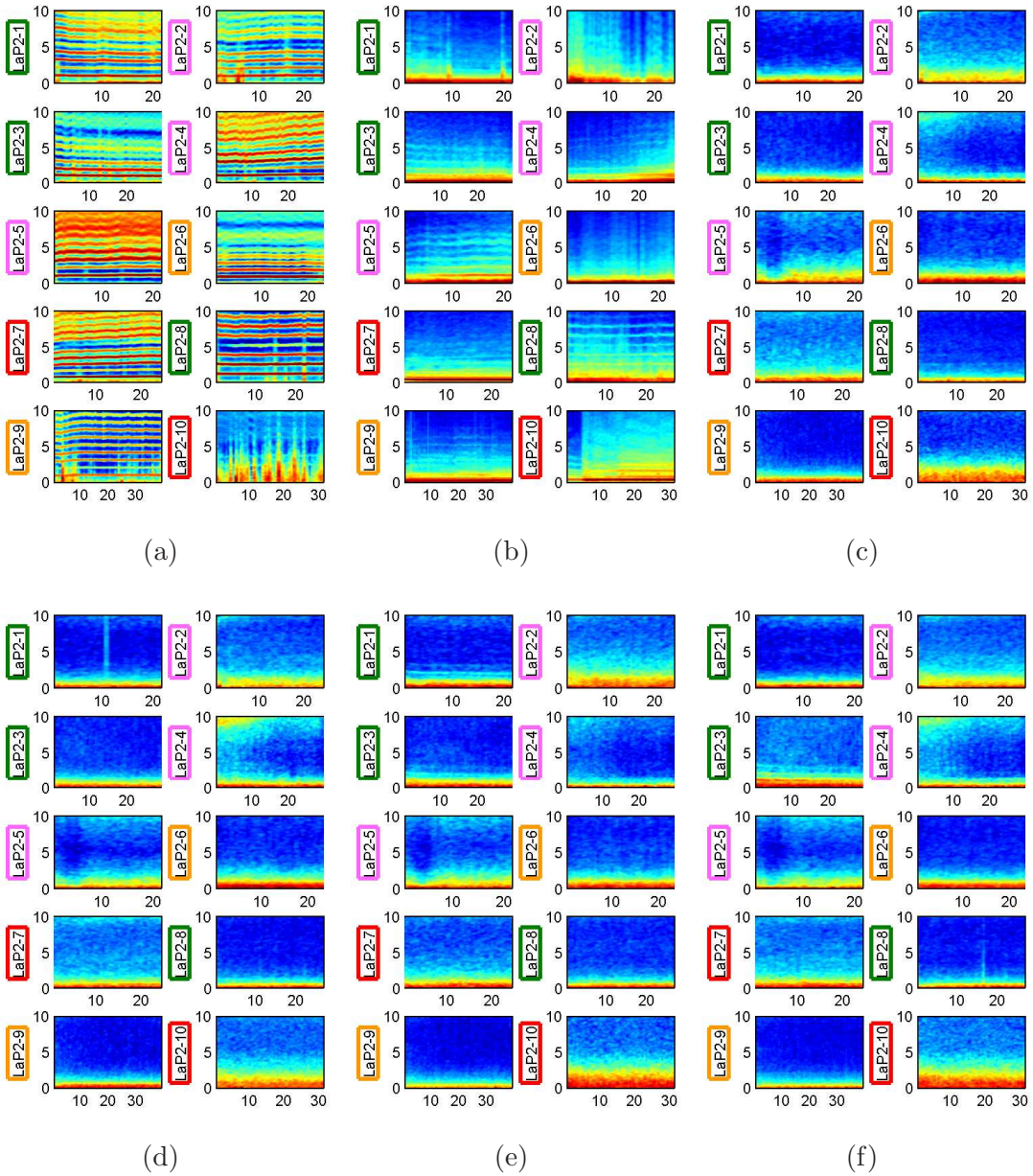

Figure 3.114 – *Power spectra obtained on "Lancaster" under anæsthesia. Horizontal axis is time (min). Vertical axis is frequency (Hz). Color axis is omitted: (a) ECG, (b) Respiration, (c) EEG1, (d) EEG2, (e) EEG3 and (f) EEG4. Boxes: (green) Propofol, (orange) Propofol+Curare, (red) Sevoflurane, and (pink) Sevoflurane+Curare.*

anæsthesia. As mentioned in coupling matrix analysis, the ECG recordings of subject no. 10 under anæsthesia was very noisy such that this spectra also shows high noise. The spectra of the respiration signals are concentrated at the very low frequency in both phase of measurements. To check the difference we zoomed in the figures at the low frequency (See in appendix), and we found that with Sevoflurane without Curare the frequency slightly increases under anæsthesia. No increase nor decrease of the frequency between two states

was observed for the other. Furthermore, we expected that the results with Curare shows clear straight lines since mechanical ventilation was used, but this was not the case. For the spectra of the EEG signals, again we remarked that they are concentrated at the very low frequency in both phase, and as ECG signals, we remarked straighter form under anæsthesia. Additionally, in the results with Sevoflurane with/without Curare, we can see the shadow around 10Hz. So, we zoomed out the figures (See appendix) and saw that α-waves(8-12Hz) appear on all the results under anæsthesia, and especially we saw greater amplitude with this Sevoflurane with/without Curare.

Now let us check the coherence spectra. Here in Human, we introduced also the permutation test. The used thresholds calculated with the test are shown in the table below.

		Coh:H-R	Coh:B-H	Coh:B-R
P1	EEG1	0.22	0.21	0.21
	EEG2	0.27	0.27	0.26
	EEG3	0.25	0.25	0.24
	EEG4	0.24	0.25	0.23
P2	EEG1	0.26	0.28	0.28
	EEG2	0.25	0.25	0.24
	EEG3	0.21	0.21	0.22
	EEG4	0.27	0.26	0.27

Table 3.29 – *Thresholds for coherence spectra defined by the permutation test for "Lancaster": (B) EEG, (H) ECG, and (R) respiration. Four cases in each phase are shown according to the chosen EEG signal: (P1) resting (P2) anæsthesia.*

In this table we remark that the defined thresholds are not close between the chosen EEG signals. This is because the chosen randomized segments used for the permutation test are different from one to the other. In fig. 3.115 and 3.116, we show the obtained coherence spectra. Just to notice, the results obtained with different EEG signals was very similar such that, for Coh:B-H and Coh:B-R, the mean result among this four cases is shown. From these figures, we remark a high coherence between heart (H) and respiration (R) in both phases. Here it is very difficult to comment which is stronger. The coherence between brain (B) and H is also present in both phase and it seems weaker under anæsthesia. Furthermore, apart form subject no. 3, nearly no coherence was found between B and R in both state.

Now let us proceed to the main analysis of this subsubsection, the nonparametric Granger causality. Here below we show the defined thresholds obtained with the permutation test.
In fig. 3.117 and 3.118, we show the obtained results. Here again, the results obtained with different EEG signals was very similar such that, the mean result among this four cases is shown in these figures. At first sight, we remark strong causality from heart (H) to respiration (R) at the resting state and slightly weaker under anæsthesia. The causality from R to H can be seen on some subjects at the very low frequency in both phase of measurements, and it looks higher under anæsthesia. Furthermore, borderline causality from H to brain (B) on some subjects can be observed in both state. No noticeable causality was found between B and R except subject no. 3. Let us again postpone the conclusion until the analysis on the recordings of "Oslo".

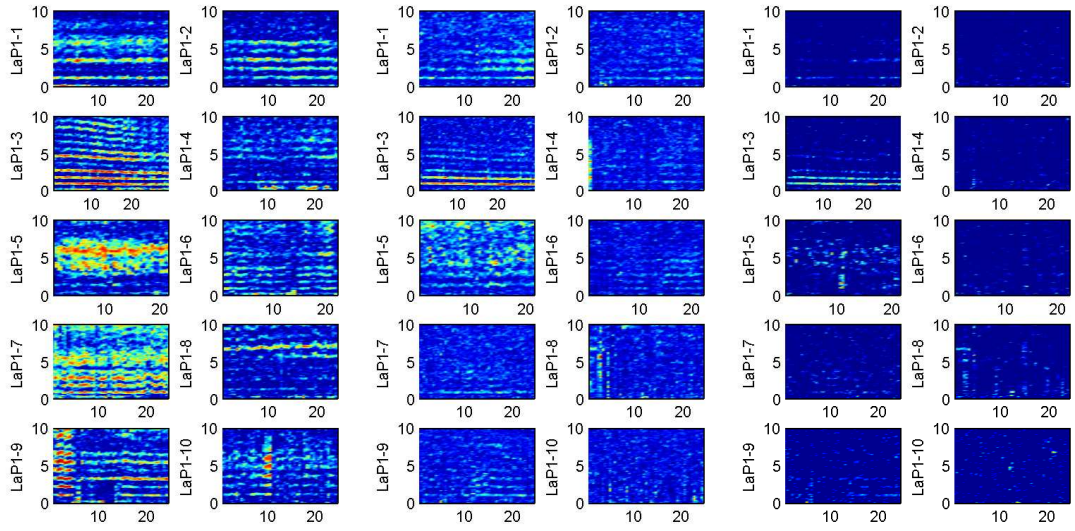

(a) (b) (c)

Figure 3.115 – *Coherence spectra obtained on "Lancaster". Horizontal axis is time (min). Vertical axis is frequency (Hz): (a) ECG and respiration; color axis [0 1], (b) EEG and ECG; color axis [0 0.6], and (c) EEG and respiration; color axis [0 0.6].*

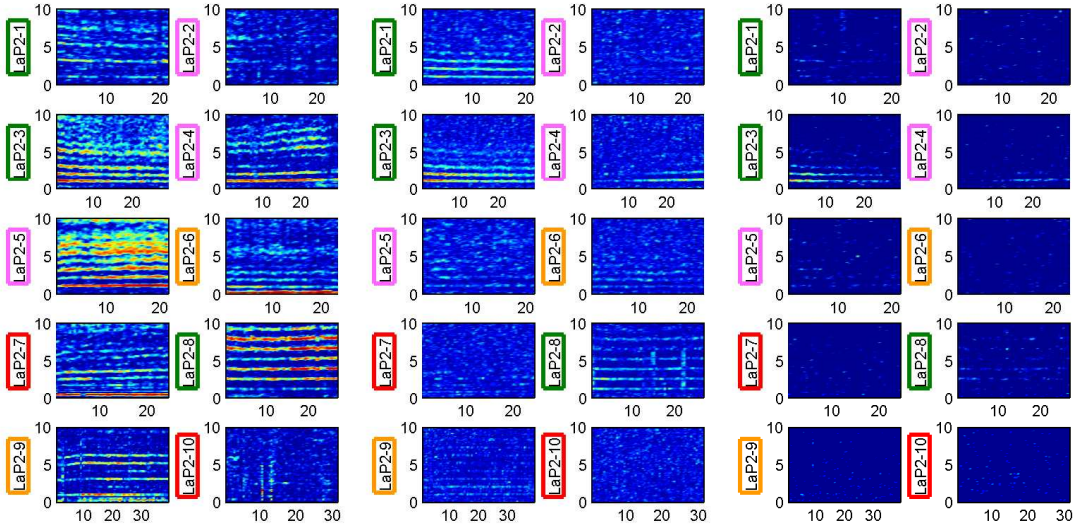

(a) (b) (c)

Figure 3.116 – *Coherence spectra obtained on "Lancaster". Horizontal axis is time (min). Vertical axis is frequency (Hz): (a) ECG and respiration; color axis [0 1], (b) EEG and ECG; color axis [0 0.6], and (c) EEG and respiration; color axis [0 0.6]. Boxes: (green) Propofol, (orange) Propofol+Curare, (red) Sevoflurane, and (pink) Sevoflurane+Curare.*

Here again, no difference was found between the results of different inducted anæsthetics.

		GC:B→H	GC:H→B	GC:B→R	GC:R→B	GC:H→R	GC:R→H
P1	EEG1	0.15	0.15	0.16	0.15	0.15	0.16
	EEG2	0.20	0.19	0.20	0.20	0.19	0.20
	EEG3	0.17	0.17	0.17	0.17	0.17	0.17
	EEG4	0.17	0.16	0.17	0.17	0.16	0.17
P2	EEG1	0.19	0.18	0.19	0.19	0.18	0.18
	EEG2	0.21	0.20	0.18	0.20	0.20	0.18
	EEG3	0.17	0.16	0.16	0.17	0.16	0.16
	EEG4	0.19	0.20	0.19	0.18	0.20	0.18

Table 3.30 – *Thresholds for nonparametric Granger causality $GC(t)$ defined by the permutation test for "Lancaster": (B) EEG, (H) ECG, and (R) respiration. Four cases in each phase are shown according to the chosen EEG signal: (P1) resting (P2) anæsthesia.*

3.10.2 Human in Oslo

S-estimator

In this study on the recordings from Oslo, same window length and same shift time length as Lancaster were used, i.e. 40sec and 0.5sec, respectively. In fig. 3.119, we show the ED and τ employed in this analysis. As we mentioned at subsec. 3.2.3, most of the recordings under anæsthesia had been recorded before steady state, so here, the ED under anæsthesia were chosen only taking the results after beginning of steady state into the consideration. From this fig. 3.119, as the case of Lancaster, we can again remark lower ED on the ECG and EEG signals, and larger τ on the EEG signals at state "p2". Moreover we remarked a high ED of respiration signal at resting state on subject no.11. Looking at the recordings, we observed that the respiration signal of this subject was much more noisy compared to the others. Also we found high τ of EEG signals on subject no. 9, but we didn't manage to know the reason just looking at the recordings.

The recordings of Oslo contains only two EEG signals. Consequently, the obtained two $S(t)$ calculated on a cluster of three sub-systems, where one took only EEG1 channel into the consideration and the other took only EEG2 channel into account, are shown in fig. 3.120 and 3.121. From fig. 3.120, we can remark fluctuations on some of the subject but generally it stays close to the same value along the time. Furthermore, some difference can be found between taken EEG signals, but this difference is not so large. On fig. 3.121, we first remark that the $S(t)$ obtained on subject no. 6 to 20 decrease from the beginning of the measurement toward the starting point of the steady state. After this point the $S(t)$ stay quasi-constant except subject no.1. Looking at the recordings, we found that all the recordings of this subject had disturbing signals after 7.7 minutes after the beginning of the recordings. Consequently, here after, only the results before 7.7 minutes obtained on this subject will be taken into account. Compared to the resting state, the difference between EEG signals became very small. Again as the same procedure as the case of Lancaster, we calculated mean and variance of $S(t)$ for each subject at each state (only steady state under anæsthesia), using directly the $S(t)$ on the state "p2" obtained with the same ED settled for "p1". The obtained results are shown in fig. 3.122. From this figure, we observed a significant (p=0.0179) decrease of synchronization under anæsthesia, and moreover, we found this change in the value of mean very close to the change of

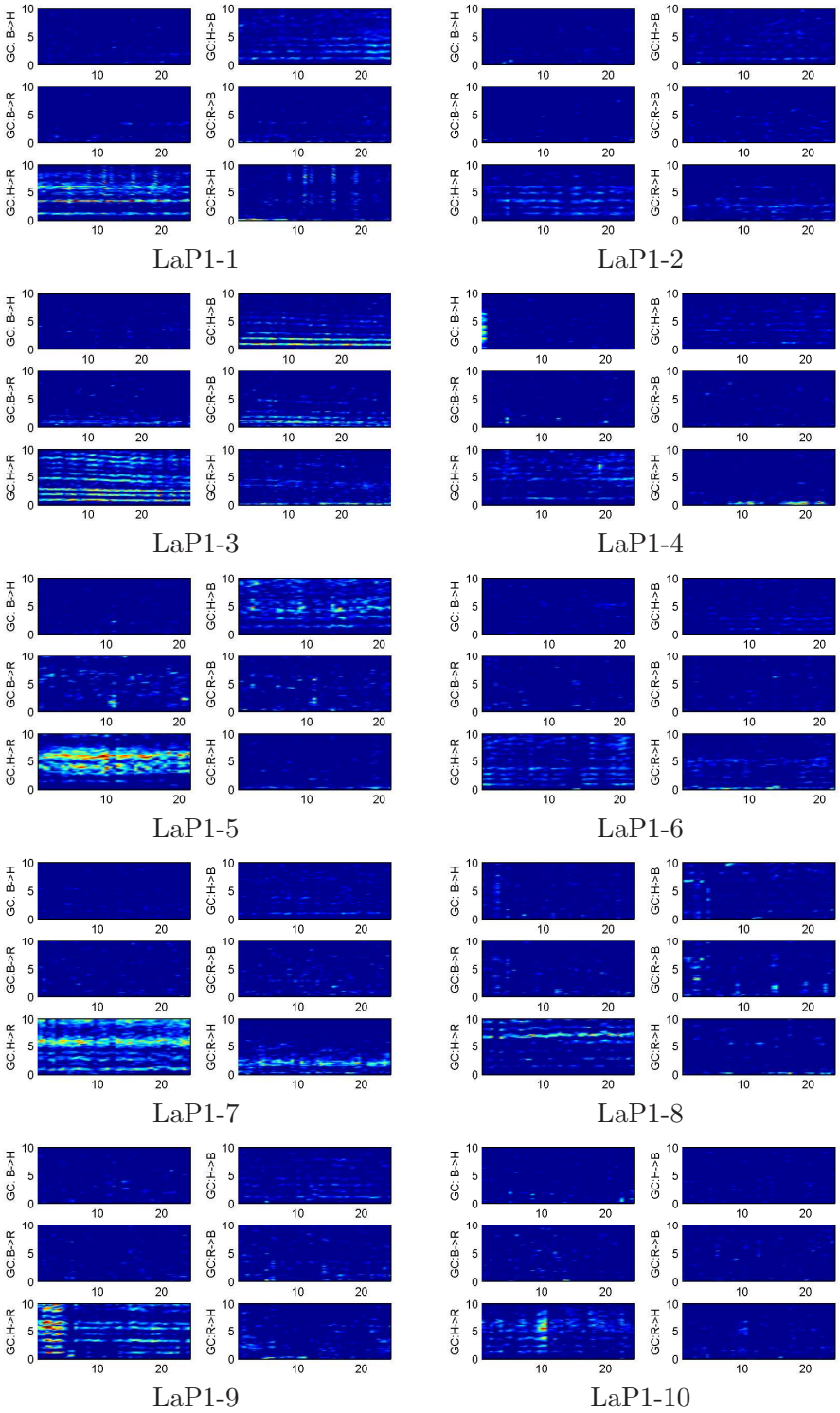

Figure 3.117 – *Nonparametric Granger causality $GC(t, f)$ obtained on "Lancaster" at resting (awaken) state. Horizontal axis is time (min): (B) EEG, (H) ECG, and (R) respiration. Color axis: B↔H [0 1], B↔R [0 0.5] and H↔R [0 2].*

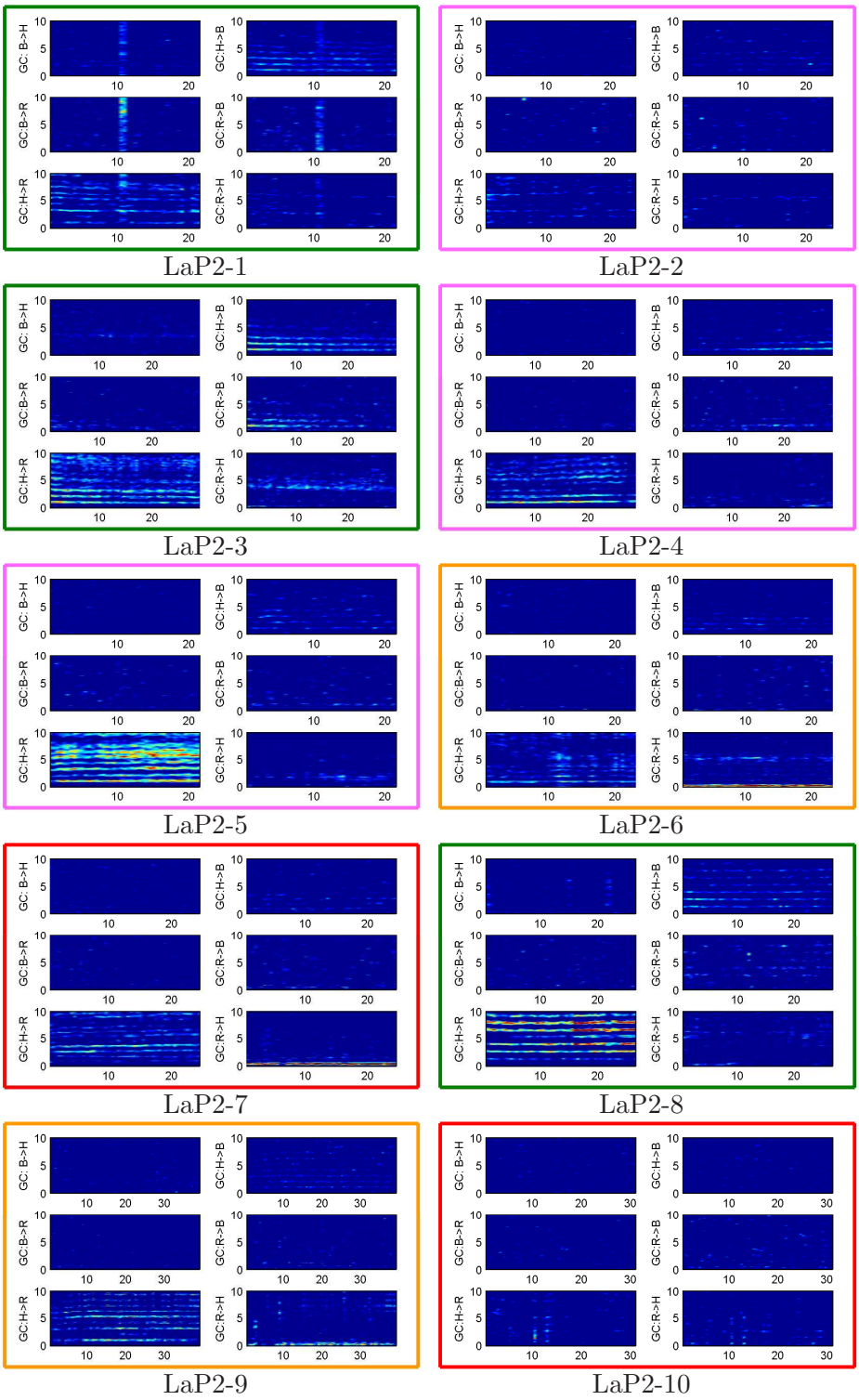

Figure 3.118 – *Nonparametric Granger causality $GC(t, f)$ obtained on "Lancaster" under anæsthesia. Horizontal axis is time (min): (B) EEG, (H) ECG, and (R) respiration. Color axis: B↔H [0 1], B↔R [0 0.5] and H↔R [0 2]. Boxes: (green) Propofol, (orange) Propofol+Curare, (red) Sevoflurane, and (pink) Sevoflurane+Curare.*

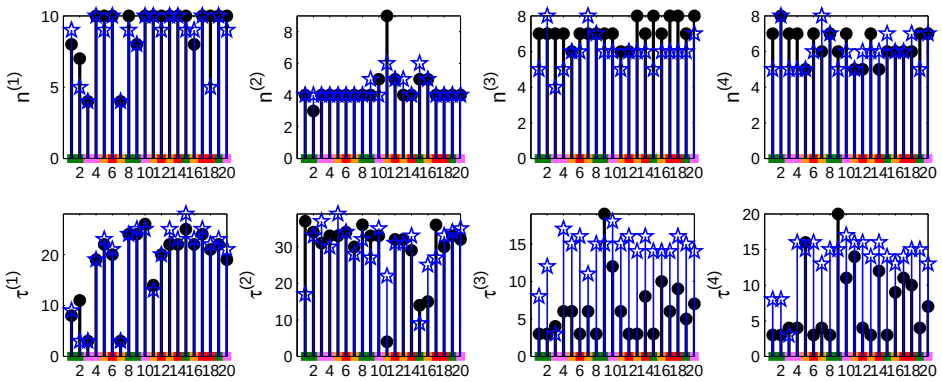

Figure 3.119 – *Embedding dimension (ED) and time delay (τ(samples)) used in the studies. Horizontal axis is the subjects number. Number in (.) means: (1) ECG (2) Respiration (3) EEG1 (4) EEG2. The black rounds are for "p1". The blue stars are for "p2".*

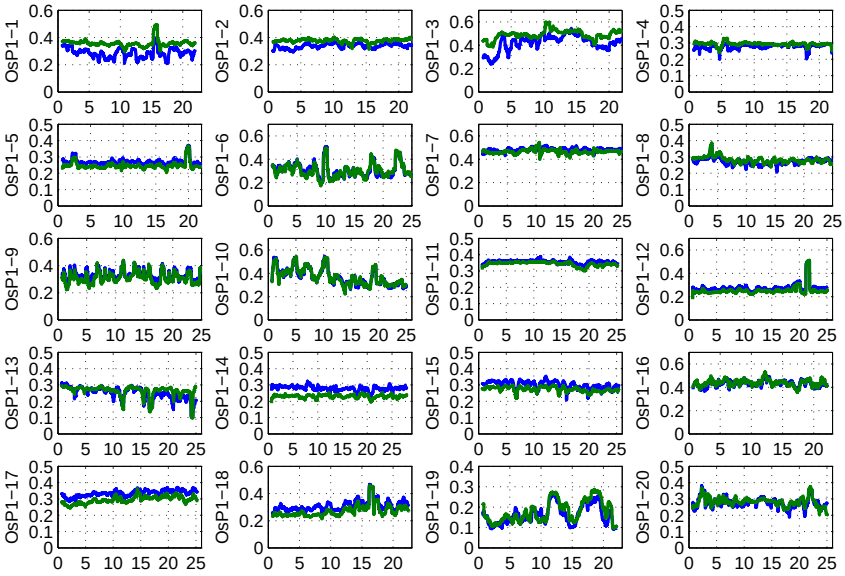

Figure 3.120 – *Synchronization measure $S(t)$ obtained at resting (awaken) state by clustering three oscillators (ECG, Respiration and one of EEG1 to EEG4) together on group "Oslo". Horizontal axis is time (min). Blue lines are with EEG1 and green lines are with EEG2.*

"Lancaster", i.e., $\sim$0.31$\rightarrow\sim$0.25 in both case. Additionally, we saw the variance is lower (significance level of 0.0223) under anæsthesia, except subject no. 2 and 8. We presume that this high variance on this two subjects results from the moving artifact noted in the log file. Consequently, these observation confirms what we concluded in the S-estimator study on the recordings of "Lancaster". Just to remark, the mentioned decrease of synchronization can be visually seen in fig. 3.121 before the starting point of the steady state. We expect to have an increase in the synchronization when the effect of anæsthesia diminishes such that the detection of the depth of anæsthesia with this S-estimator is highly expected.

In "Lancaster" we mentioned that Propofol seems to have higher S(t) under anæsthesia

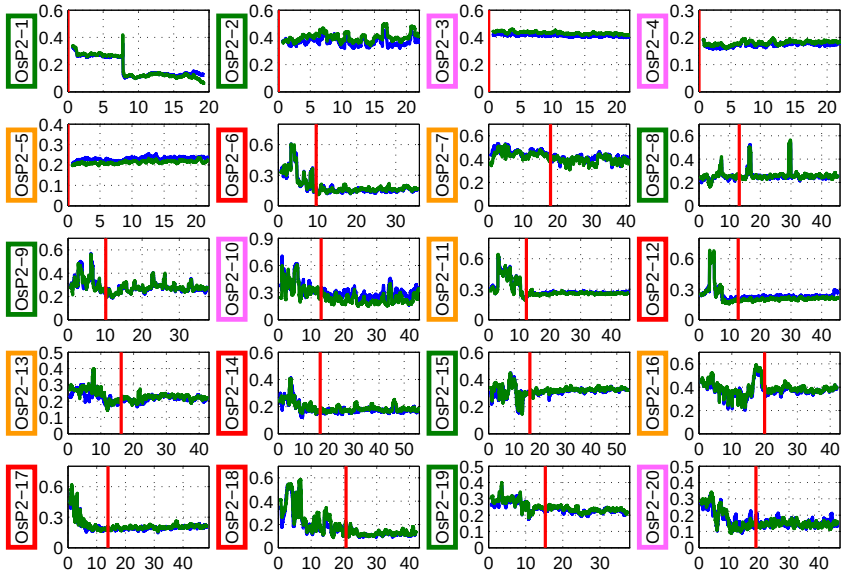

Figure 3.121 – *Synchronization measure $S(t)$ obtained under anæsthesia by clustering three oscillators (ECG, Respiration and one of EEG1 to EEG4) together on group "Oslo". Horizontal axis is time (min). Blue lines are with EEG1 and green lines are with EEG2. The red lines indicate the beginning of the steady state: The boxes around subject numbers are: (green) Propofol, (orange) Propofol+Curare, (red) Sevoflurane, and (pink) Sevoflurane+Curare.*

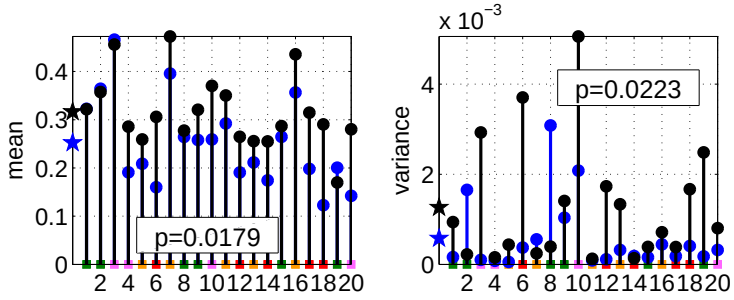

Figure 3.122 – *Mean and variance calculated on $S(t)$ obtained with the same ED for "p1" and "p2". x axis is the subject number of group "Oslo". p is the result of the Wilcoxon rank sum test: (black round) "p1", (blue round) "p2", (black star) mean of "p1" (blue star) mean of "p2". The colored squares above subject numbers are: (green) Propofol, (orange) Propofol+Curare, (red) Sevoflurane, and (pink) Sevoflurane+Curare.)*

than Sevoflurane. From fig. 3.122, we can roughly confirm on this differentiation in "Oslo". However not all the subjects agree with this difference in $S(t)$ such that we should continue analyzing more data.

In Fig. 3.123, the results of the S-estimator performed on sets of two sub-systems are shown. Here again, we directly plot the $S(t)$ at "p2" obtained with the same ED settled for "p1". From these figures, we remarked that there is more difference between the results obtained with different EEG signals at the resting state than under anæsthesia. However, as the S(t) obtained on a cluster of three sub-systems, we found this difference not so large. The comparison between "p1" and "p2" was again carried out using the mean and

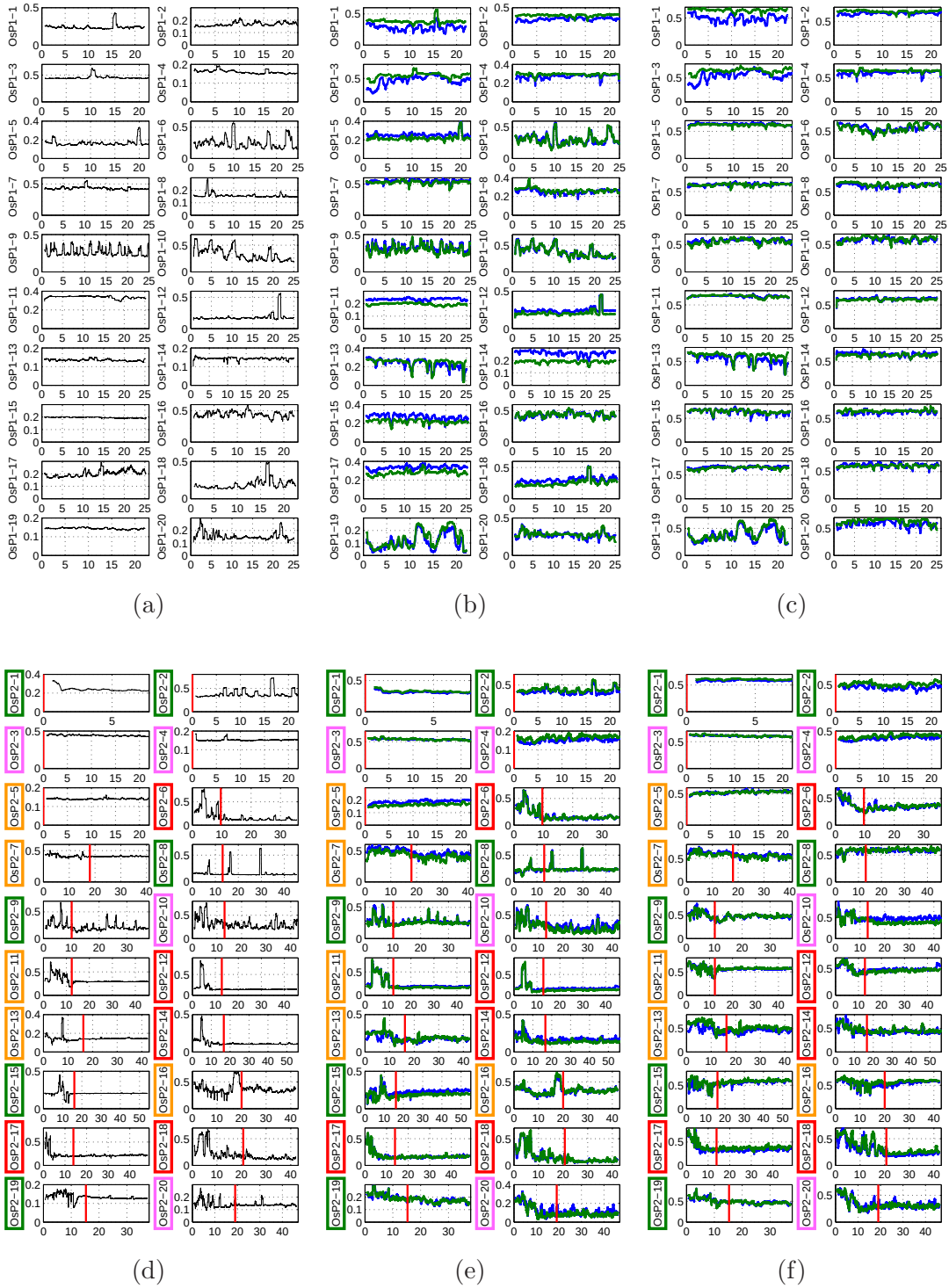

Figure 3.123 – *$S(t)$ obtained by clustering two chosen sub-systems on group "Oslo". Horizontal axis is time (min). The same ED was used: (a,b,c) "p1" and (d e f) "p2". (a,d) ECG and Respiration, (b,e) ECG and EEG, and (c,f) Respiration and EEG. For (b,c,e,f): (blue) EEG1 and (green) EEG2. Boxes:(green) Propofol, (orange) Propofol+Curare, (red) Sevoflurane, and (pink) Sevoflurane+Curare.*

variance. In fig. 3.124, we remark again low synchronization and low variances under

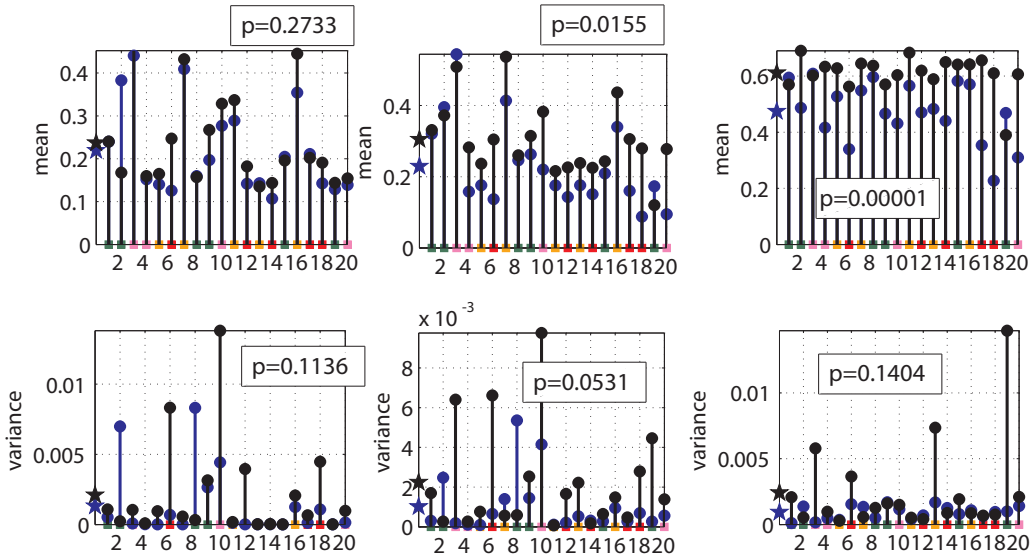

Figure 3.124 – *Mean and variance calculated on $S(t)$ with clusters of two sub-systems obtained with the same ED for "p1" and "p2". x axis is the subject number of group "Oslo". p is the result of the Wilcoxon rank sum test:(left) ECG-Resp (middle) ECG-EEG (right) Resp-EEG. (black round) "p1", (blue round) "p2", (black star) mean of "p1" (blue star) mean of "p2". The colored squares above subject numbers are: (green) Propofol, (orange) Propofol+Curare, (red) Sevoflurane, and (pink) Sevoflurane+Curare.)*

anæsthesia referring to star markers. When taking $p < 0.05$ as significance threshold, we can conclude that $S(t)$ on ECG-EEG and EEG-Resp clusters decrease at "p2". Here, we cannot confirm the significant decrease in the variance concluded at "Lancaster".

new S-estimator

Let proceed to the new S-estimator. The obtained results are shown in fig. 3.125 and 3.126. From these figures, we confirm again that the strength of the synchronization became more than 10 times smaller than $S(t)$. We confirm also that the proportional variation of $S_{new}(t)$ along the time became bigger. And, furthermore, no big difference found with respect to the chosen EEG signals. We compared the two state "p1" and "p2" calculating the mean and variance and show the obtained results on fig. 3.127. On the $S_{new}(t)$ obtained with the recordings of "Lancaster", we didn't find any significant difference, but here with the data of "Oslo", both mean and variance show significant decrease under anæsthesia. However looking carefully, there are two subjects on each results at resting state which have remarkably high value compared to the others. The significance p that we obtained might be because of them. To clarify, we need to analyze much more recordings.

Let check this $S_{new}(t)$ on clusters of two sub-systems. The obtained results are shown in fig. 3.128 and 3.129. From these figures, again the effect of Propofol with/without Curare seems to agree with the results of Lancaster having more difference on the $S_{new}(t)$ obtained with different EEG signals. To compare the state "p1" and "p2", the mean and variance were again calculated and the obtained results are shown in fig. 3.130. In the analysis of the

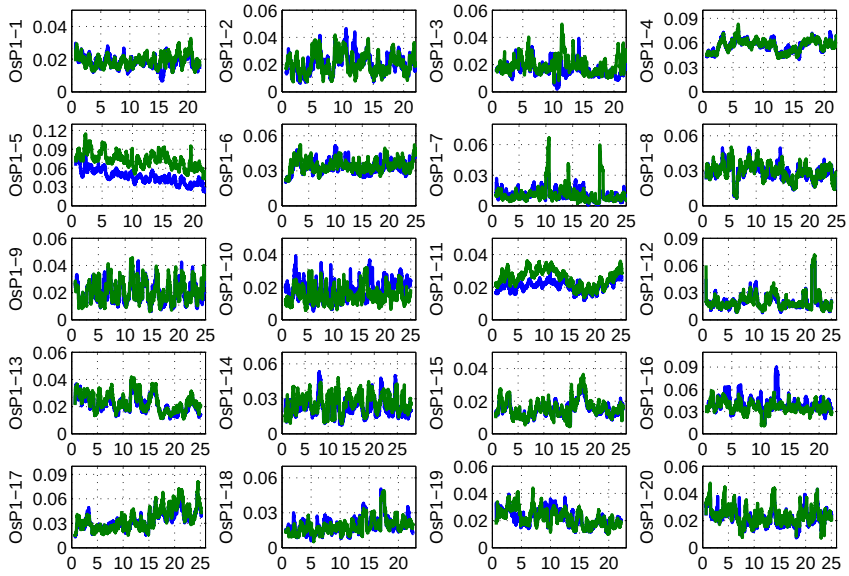

Figure 3.125 – *Synchronization measure $S_{new}(t)$ obtained at resting (awaken) state by clustering three oscillators (ECG, Respiration and one of EEG1 to EEG4) together on group "Oslo". Horizontal axis is time (min). Blue lines are with EEG1 and green lines are with EEG2.*

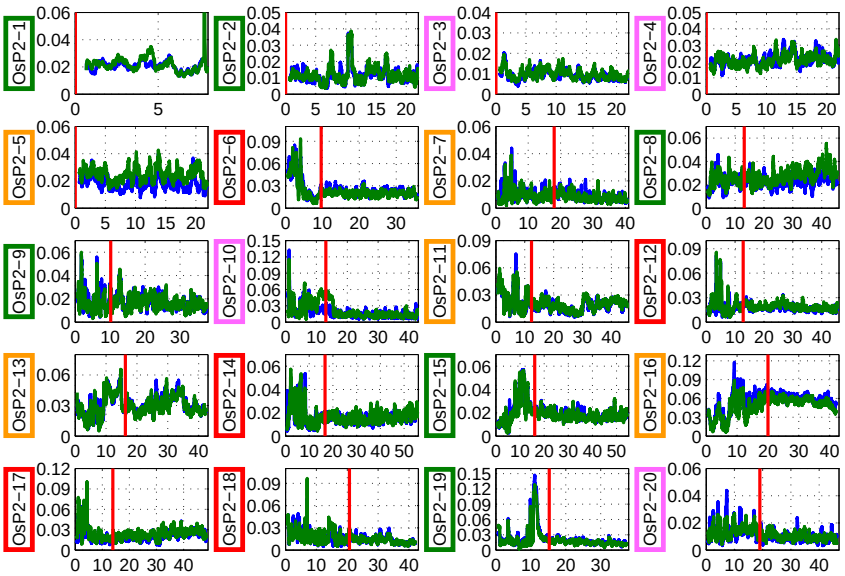

Figure 3.126 – *Synchronization measure $S_{new}(t)$ obtained under anæsthesia by clustering three oscillators (ECG, Respiration and one of EEG1 to EEG4) together on group "Oslo". Horizontal axis is time (min). Blue lines are with EEG1 and green lines are with EEG2. The red lines indicate the beginning of the steady state: The boxes around subject numbers are: (green) Propofol, (orange) Propofol+Curare, (red) Sevoflurane, and (pink) Sevoflurane+Curare.*

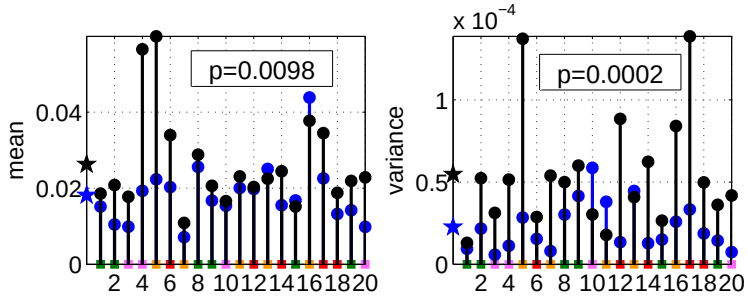

Figure 3.127 – *Mean and variance calculated on $S_{new}(t)$ obtained with the same ED for "p1" and "p2". x axis is the subject number of group "Oslo". p is the result of the Wilcoxon rank sum test: (black round) "p1", (blue round) "p2", (black star) mean of "p1" (blue star) mean of "p2". The colored squares above subject numbers are: (green) Propofol, (orange) Propofol+Curare, (red) Sevoflurane, and (pink) Sevoflurane+Curare.)*

recordings of "Lancaster", we found an increase of the synchronization under anæsthesia on ECG-EEG cluster. However here, even if half of the subjects agree with that, generally, we obtained a decrease of the synchronization under anæsthesia. Accordingly, we should check the fact relevance with more data set. Otherwise, here we found a significant decrease of synchronization on ECG-Resp cluster under anæsthesia, and a decrease of variance under this state "p2" was found on all clusters. These findings were not observed on "Lancaster".

Furthermore, in this data set analyzed with $S_{new}(t)$, we didn't manage to find any difference with respect to the kind of anæsthetic used in the studies. Owing to this, what

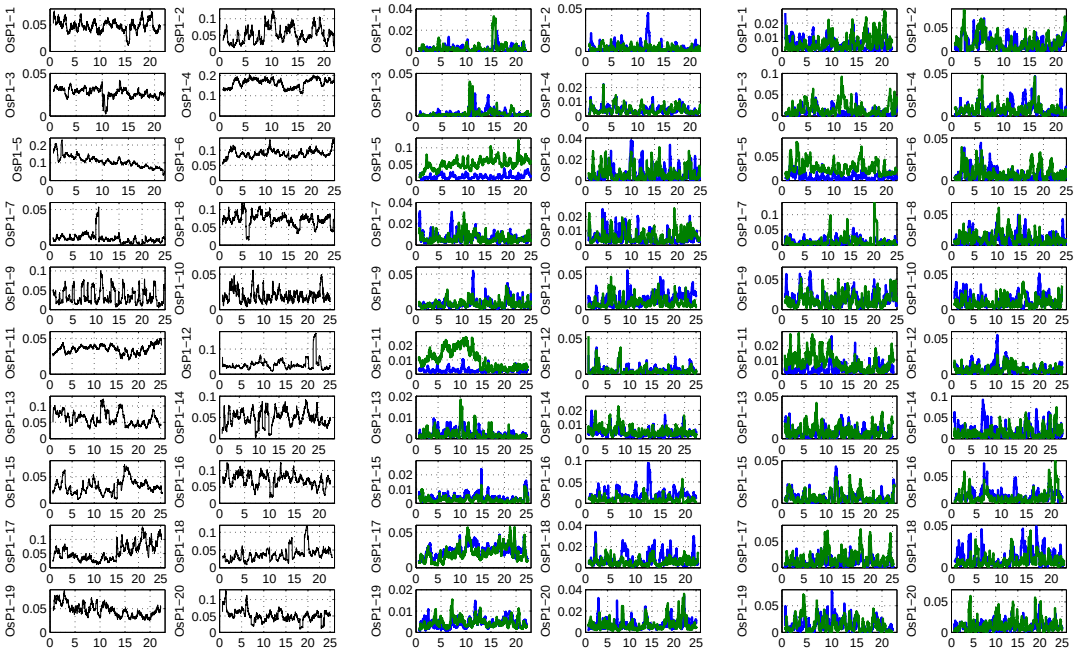

(a) (b) (c)

Figure 3.128 – *$S_{new}(t)$ at resting (awaken) state obtained by clustering two chosen oscillators together on group "Oslo". Horizontal axis is time (min): (a) ECG and Respiration, (b) ECG and EEG, and (c) Respiration and EEG. For (b,c): (blue) EEG1, (green) EEG2, (red) EEG3, and (black) EEG4.*

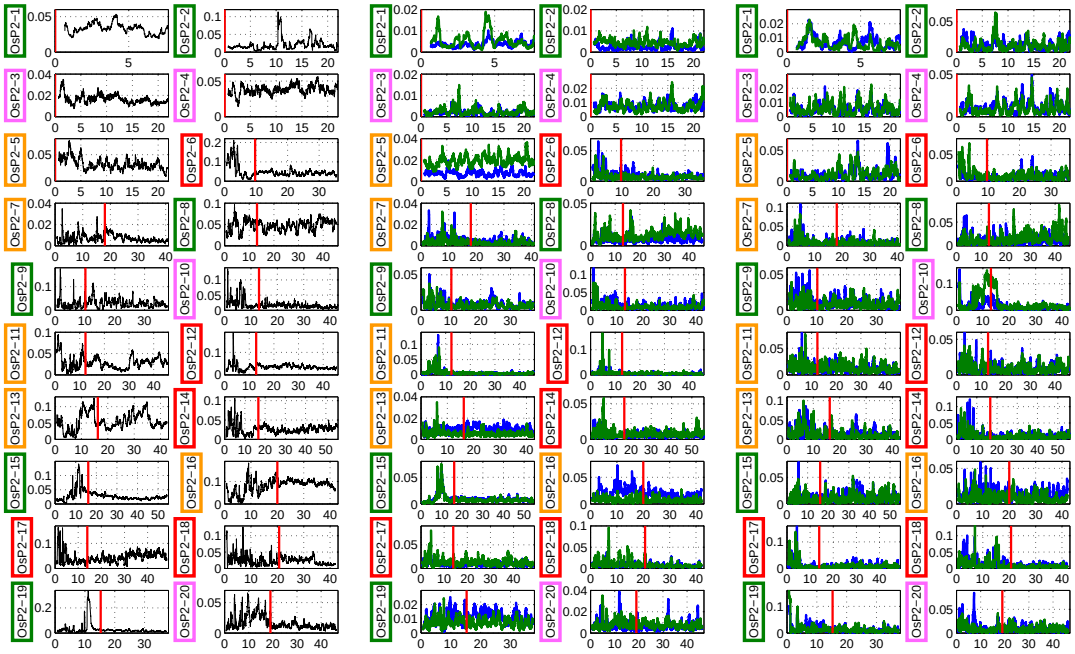

Figure 3.129 – $S_{new}(t)$ *under anæsthesia obtained by clustering two chosen sub-systems on group "Oslo". Horizontal axis is time (min). The same ED was used:(a) ECG and Respiration, (b) ECG and EEG, and (c) Respiration and EEG. For (b,c): (blue) EEG1 and (green) EEG2. Boxes:(green) Propofol, (orange) Propofol+Curare, (red) Sevoflurane, and (pink) Sevoflurane+Curare.*

we commented on the influence of Sevoflurane on EEG signals should be reinvestigated in the future.

Embedding dimension analysis

In Fig. 3.131, we show the obtained results on embedding dimension (ED) for delay embedding. From these figures, we remarked again much more fluctuation on the ED of ECG than the case of rats, except subject no.2, 3 and 5. As the case of subject no.8 in "Lancaster", these obtained ED(t) on these subjects might be a result of some previously dosed drugs. However on the log files, nothing was commented on that such that we don't know the real reason for these stable ED(t). Furthermore, we can see again that nearly half of the ED of ECG signals are equal to 10 at each measurement phase such that, as we mentioned in the studies of "Lancaster", to include higher dimension in the analysis might be necessary. The ED of respiration signal seems to be stable at the resting state as we remarked in the studies of rats and "Lancaster", but more fluctuation can be remarked on the subjects with Propofol with/without Curare under anæsthesia. The ED of EEG signals seem to have similar fluctuation degree as the studies of rats and "Lancaster", and as the case of "Lancaster", the $ED(t)$ obtained form each EEG signals are not exactly the same.

In fig. 3.132 , we show the results of comparison between the state "p1" and "p2" using mean and variance. In "Lancaster", we remarked that the mean values do not change

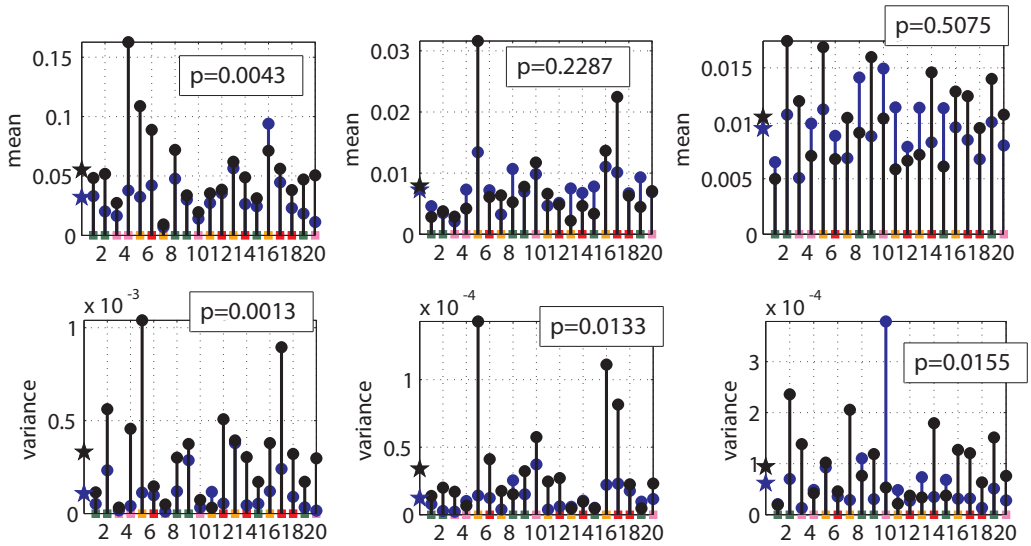

Figure 3.130 – *Mean and variance calculated on $S_{new}(t)$ with clusters of two sub-systems obtained with the same ED for "p1" and "p2". x axis is the subject number of group "Oslo". p is the result of the Wilcoxon rank sum test:(left) ECG-Resp (middle) ECG-EEG (right) Resp-EEG. (black round) "p1", (blue round) "p2", (black star) mean of "p1" (blue star) mean of "p2". The colored squares above subject numbers are: (green) Propofol, (orange) Propofol+Curare, (red) Sevoflurane, and (pink) Sevoflurane+Curare.)*

accoding to the anæsthesia, but here we remarked a significant increase on respiration signal and EEG2 signal. Until now we got the idea that the ED decrease under anæsthesia, such that this decrease was a surprise for us. To understand what going on with the ED according to the anæsthesia needs much more investigation. Apart from this increase in mean, we confirm that the variance of the embedding dimensions of the EEG signals definitively decrease under anæsthesia.

Coupling matrix

Here in "Oslo", the self model for resting state was created taking the first 4 minutes of recordings, but for under anæsthesia, first 4 minutes after the beginning of the steady state was taken. The employed ED and the size of the Toeplitz like matrix K are shown in fig. 3.133. As the ED obtained for delay embedding, the ED of respiration signal for subject no. 11 scores very high for the same reason. Otherwise, we remarked again a decrease in the ED of EEG signals under anæsthesia as the case of delay embedding. However the increase in K of EEG signals under anæsthesia observed in Lancaster cannot be seen here in Oslo, even if the time delay increased under anæsthesia (See fig. 3.119.). Here again, because of the high ED, the creation of the model took very long time. In fig. 3.134, 3.135, 3.136 and 3.137, the obtained results on both phase of measurements are shown. Apart from subject no.11 at resting state and no.3 under anæsthesia, no remarkable difference was found between results with different EEG signals. We remarked that some subjects show huge CM(t) as the case of "Lancaster". We presume that these are also because of the noise. Furthermore, we remarked that the increasing trend under anæsthesia found in the study of "Lancaster" cannot be found, such that this increase is due to the self model

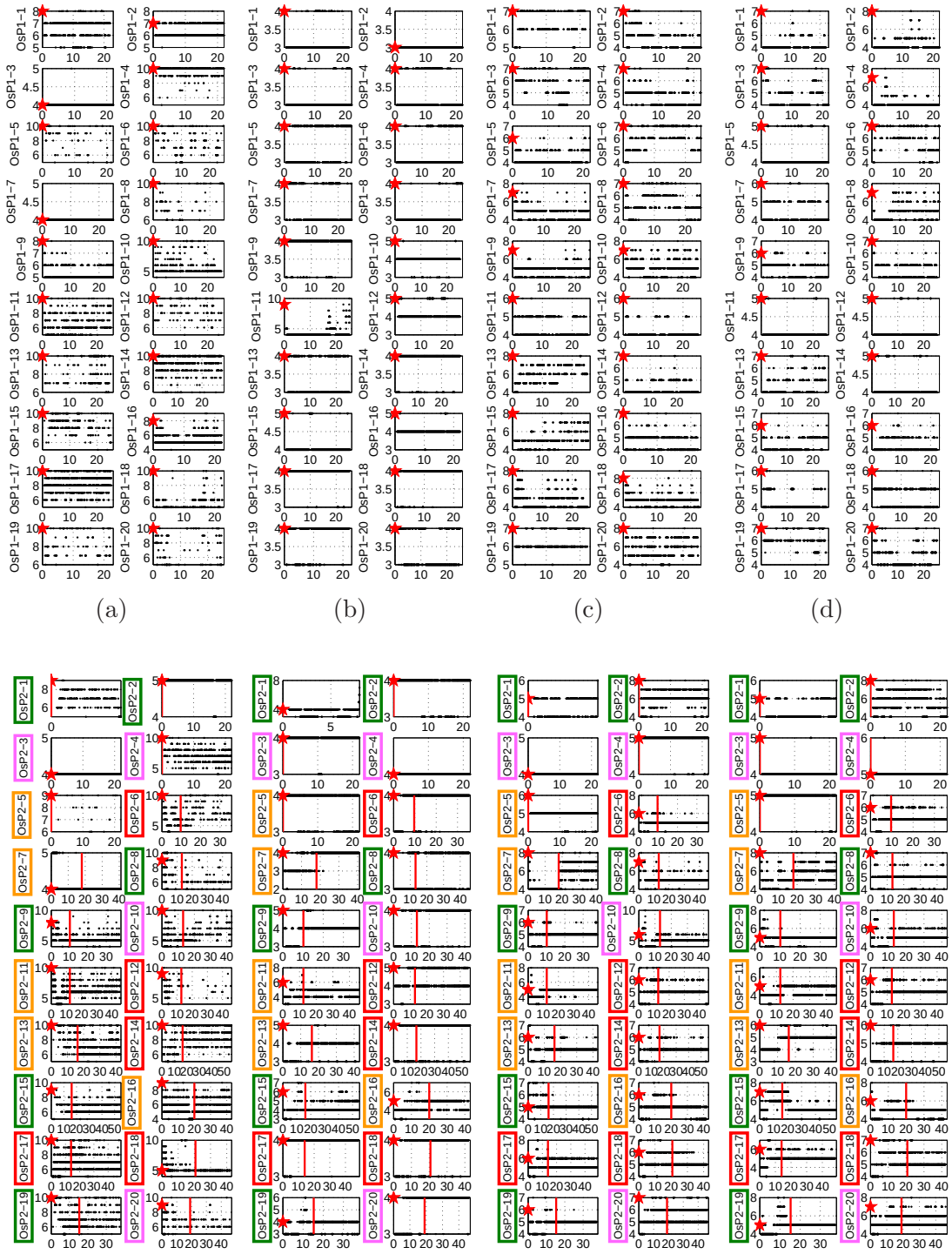

Figure 3.131 – *The study on the embedding dimension (ED) for delay embedding. Horizontal axis is time (min). The red stars indicates the chosen parameters. (upper row) "p1" and (lower row) "p2": (a,e) ECG, (b,f) Respiration , (c,g) EEG1 and (d,h) EEG2. Boxes:(green) Propofol, (orange) Propofol+Curare, (red) Sevoflurane, and (pink) Sevoflurane+Curare.*

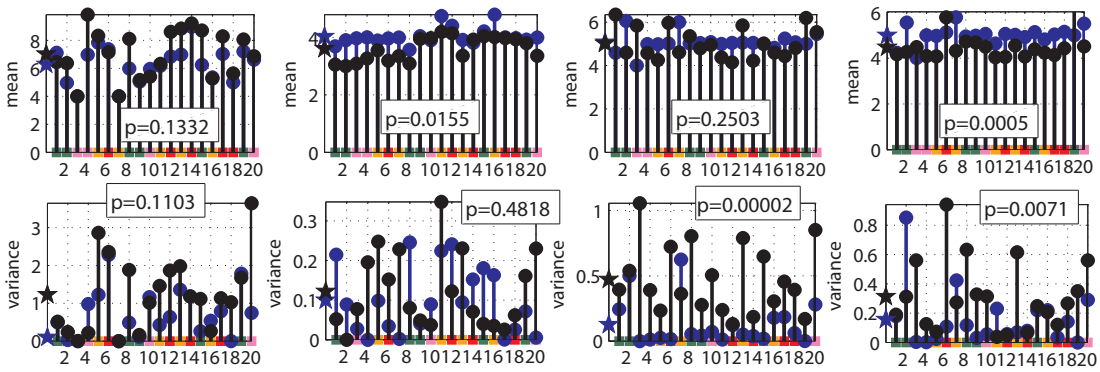

Figure 3.132 – *Mean and variance calculated on Embedding dimension (ED) at each state. Horizontal axis is the subjects number. From the left: ECG, Respiration, EEG1 and EEG2: (black round) "p1", (blue round) "p2", (black star) mean of "p1" (blue star) mean of "p2". The colored squares above subject numbers are: (green) Propofol, (orange) Propofol+Curare, (red) Sevoflurane, and (pink) Sevoflurane+Curare.*

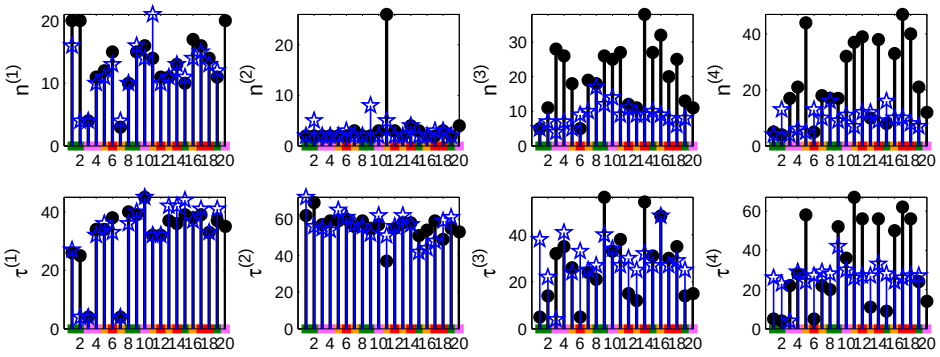

Figure 3.133 – *Embedding dimension (ED) and size of the Toeplitz like matrix (K(samples)) used in the studies. Horizontal axis is the subjects number. Number in (.) means: (1) ECG, (2) Respiration, (3) EEG1 and (4) EEG2. The black rounds are for "p1". The blue stars are for "p2".*

creation with first 4 minutes recordings.

To compare the two phase of measurements, again, we calculated mean and variance. The obtained results are shown in fig. 3.138 and 3.139. From fig. 3.138, except CM:B→H, we remarked significant decrease of the coupling under anæsthesia, which agrees with the case of "Lancaster". And from fig.3.139, we observed a significant decrease in the variance of CM(t) on CM:H→B, CM:B→R, CM:R→B and CM:H→R, and significant increase on CM:R→H under anæsthesia. As the case of "Lancaster", to compare the strength of the coupling, the obtained mean values are summarized in table. 3.31. To remark, in the mean values of this table were recalculated without subjects which shows high means*. From this table, we remarked that all the coupling decrease under anæsthesia. Furthermore, we found the coupling from B to R is the strongest and the coupling from R to H is the smallest at the resting state. Again as "Lancaster", we found strange to have such relationship. But under anæsthesia, we found the coupling from H to R is the strongest and the coupling from B

*More precisely, the removed subject numbers are: [at resting state] (B→H) 3 and 7, (B→R) 7, 8, 12, 14, 17 and 19, (H→R) 12 and 17. [under anæsthesia] (B→H) 2 and 18, (H→B) 3, (R→H) 2 and 18.

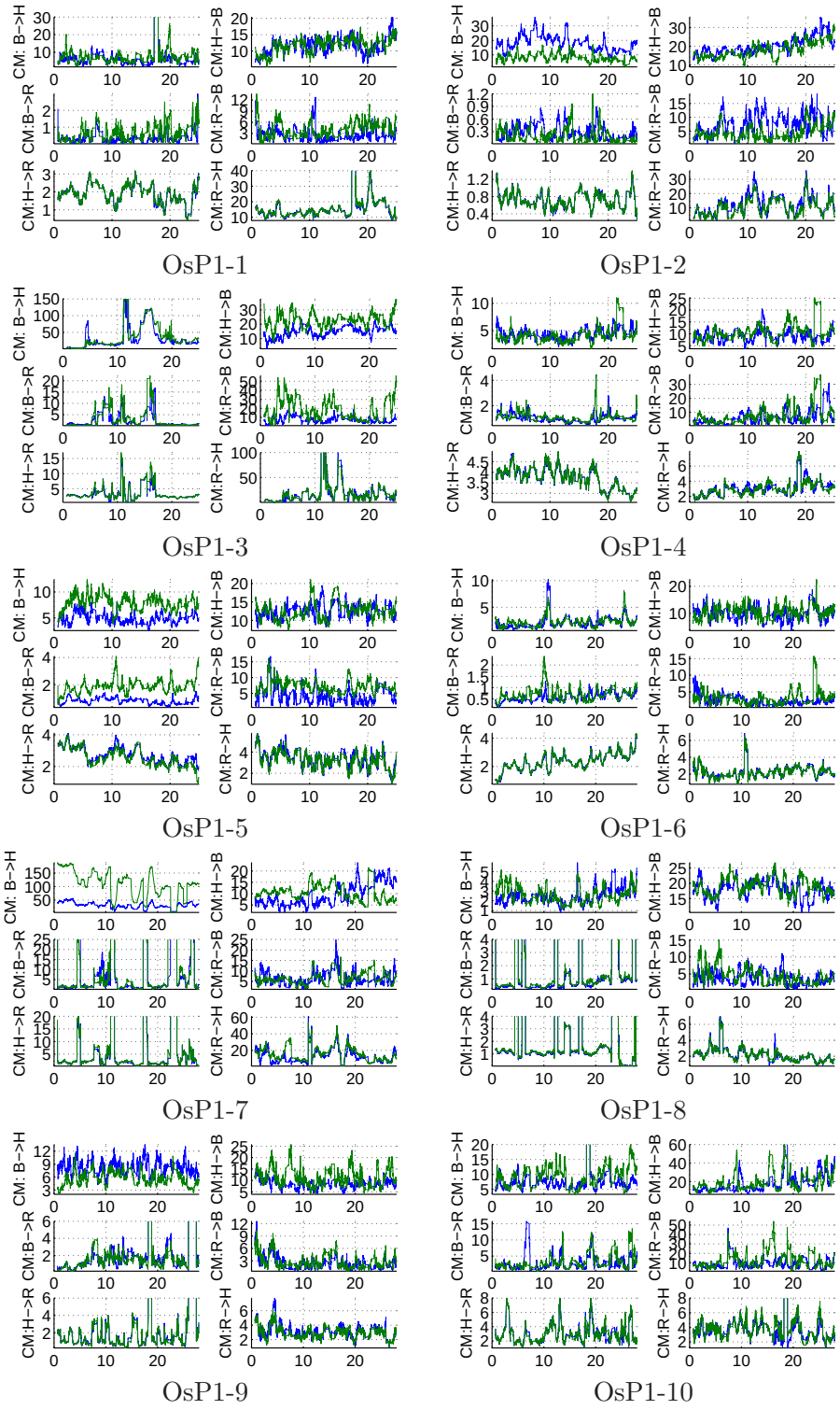

Figure 3.134 – *Coupling matrix $CM(t)$ obtained on "Oslo" at resting (awaken) state PartI. Horizontal axis is time (min): (B) EEG, (H) ECG, and (R) respiration. Note that the results are zoomed to see the major part.*

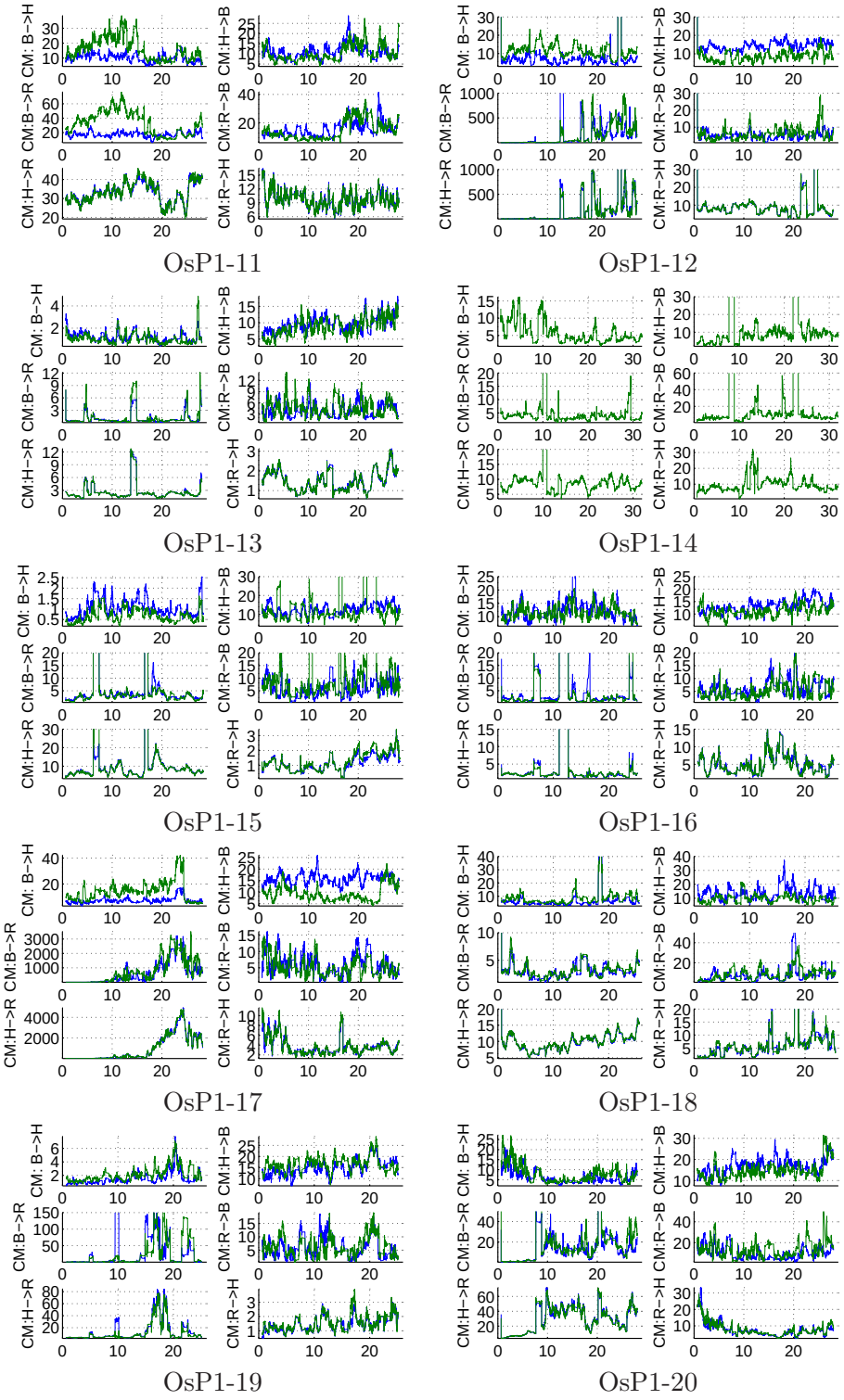

Figure 3.135 – *Coupling matrix $CM(t)$ obtained on "Oslo" at resting (awaken) state PartII. Horizontal axis is time (min). Subject no.14 miss the result with EEG1: (B) EEG, (H) ECG, and (R) respiration. Note that the results are zoomed to see the major part.*

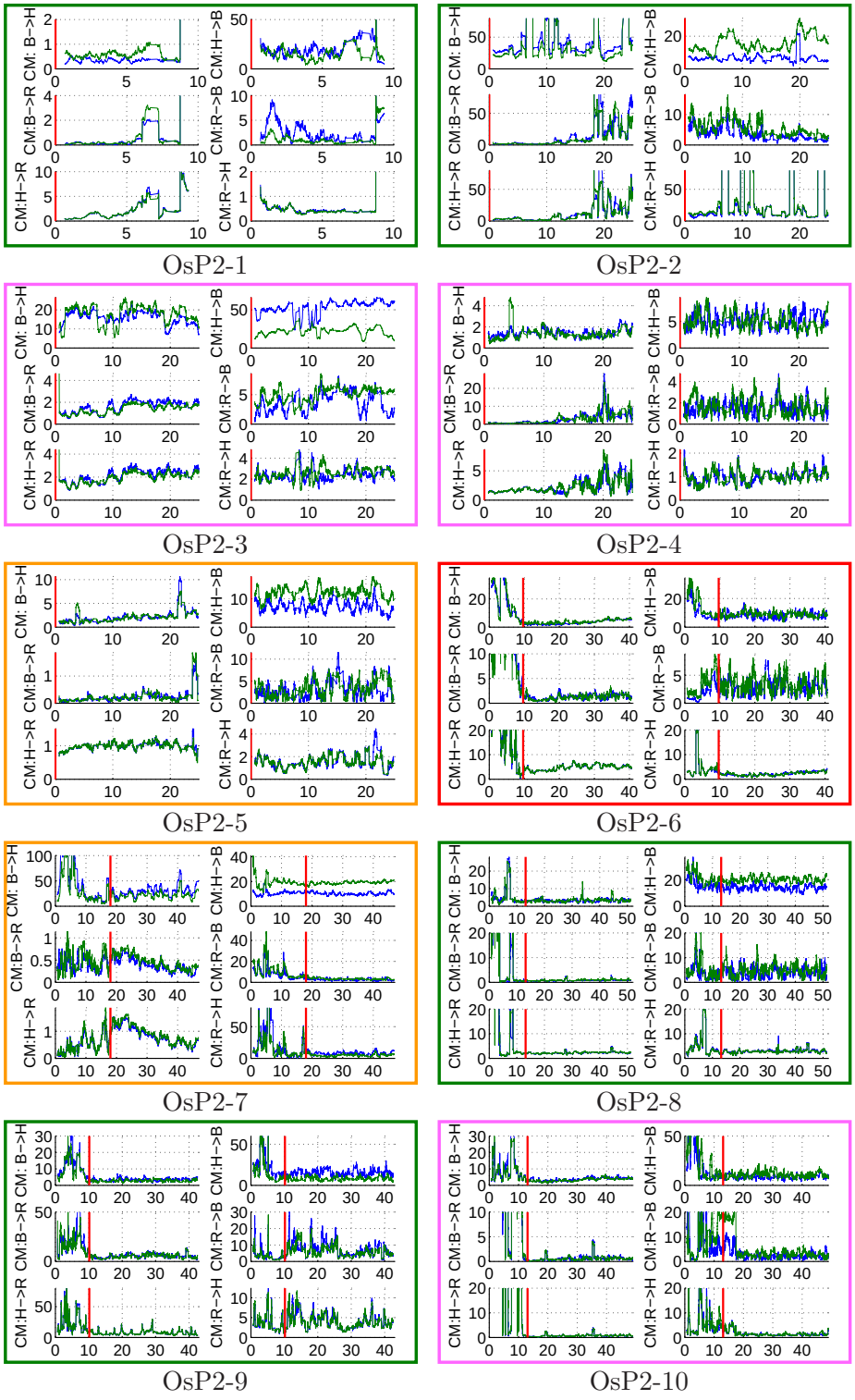

Figure 3.136 – *Coupling matrix $CM(t)$ obtained on "Oslo" under anæsthesia PartI. Horizontal axis is time (min): (B) EEG, (H) ECG, and (R) respiration. Boxes:(green) Propofol, (orange) Propofol+Curare, (red) Sevoflurane, and (pink) Sevoflurane+Curare. Note that the results are zoomed to see the major part.*

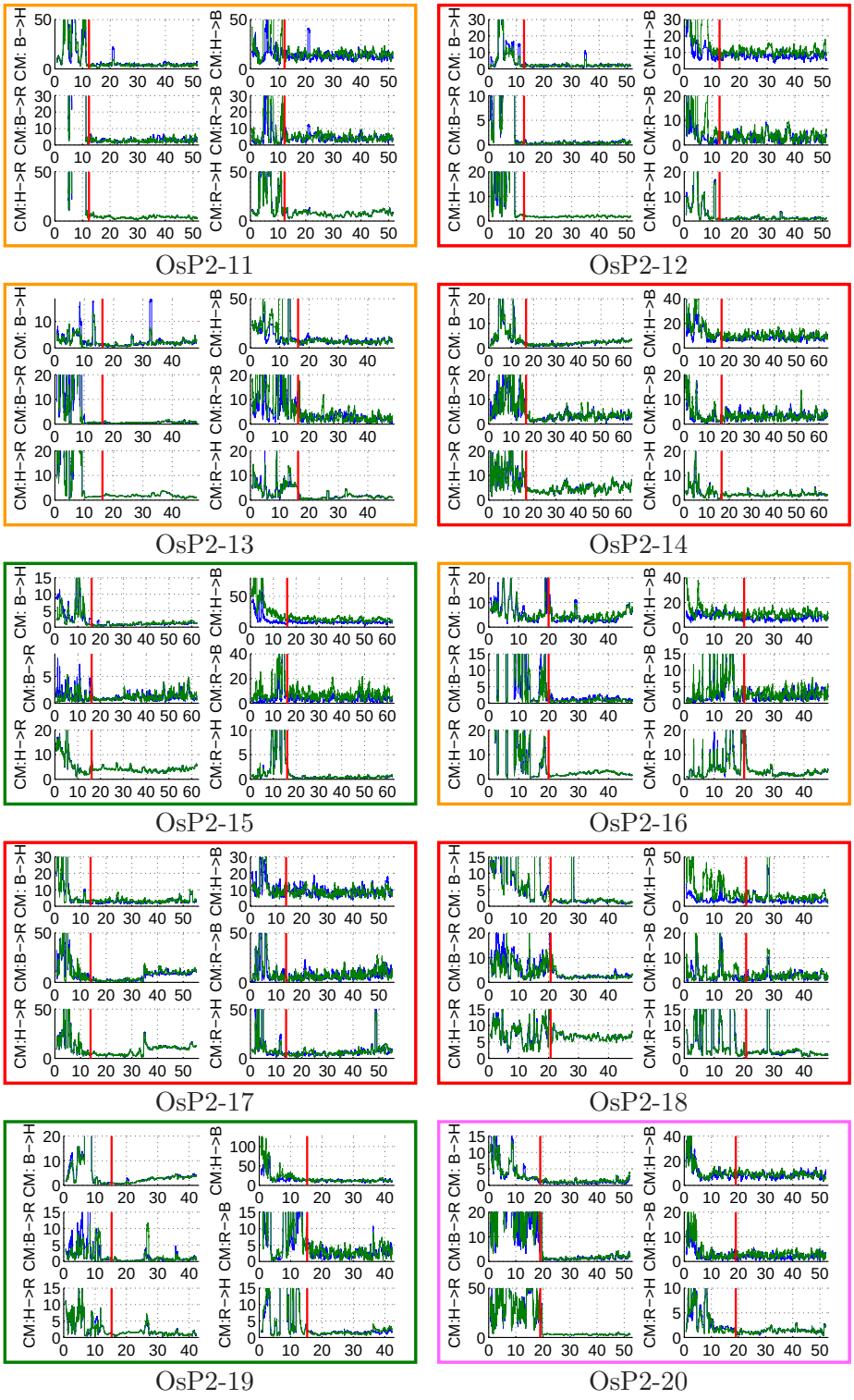

Figure 3.137 – *Coupling matrix $CM(t)$ obtained on "Oslo" under anæsthesia PartII. Horizontal axis is time (min): (B) EEG, (H) ECG, and (R) respiration. Boxes:(green) Propofol, (orange) Propofol+Curare, (red) Sevoflurane, and (pink) Sevoflurane+Curare. Note that the results are zoomed to see the major part.*

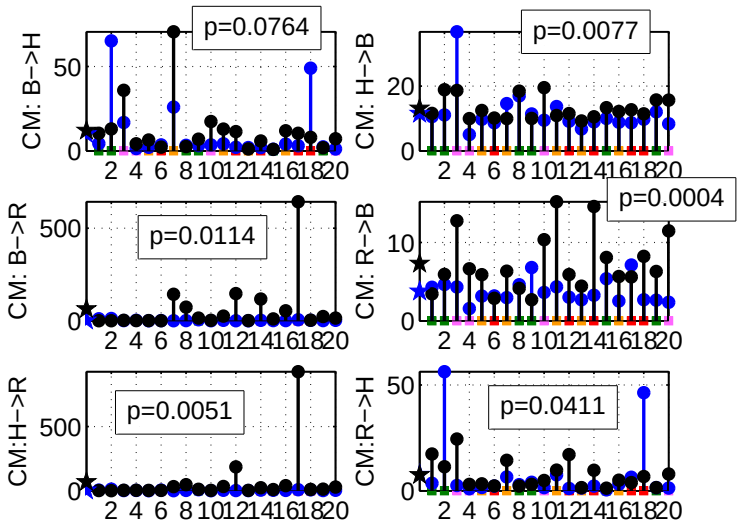

Figure 3.138 – *Mean calculated on CM(t) at each state. Horizontal axis is the subjects number. The black rounds are for "p1". The blue rounds are for "p2". The colored squares above subject numbers are: (green) Propofol, (orange) Propofol+Curare, (red) Sevoflurane, and (pink) Sevoflurane+Curare.*

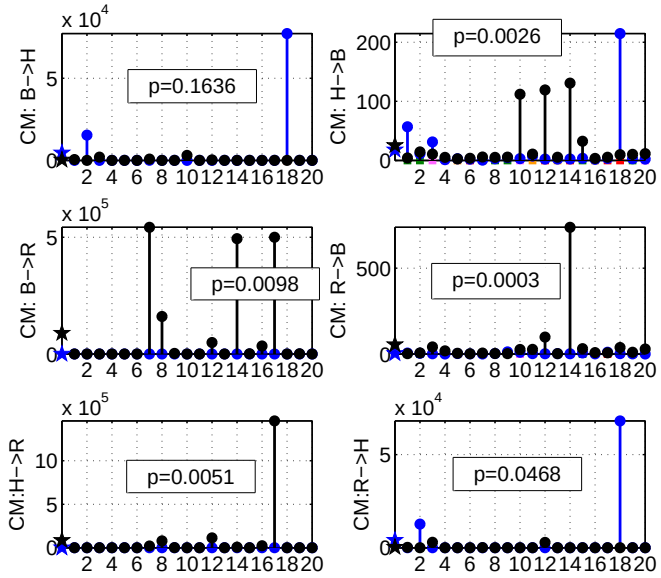

Figure 3.139 – *Variance calculated on CM(t) at each state. Horizontal axis is the subjects number. The black rounds are for "p1". The blue rounds are for "p2". The colored squares above subject numbers are: (green) Propofol, (orange) Propofol+Curare, (red) Sevoflurane, and (pink) Sevoflurane+Curare.*

	CM:B→H	CM:H→B	CM:B→R	CM:R→B	CM:H→R	CM:R→H
resting	7.52	7.48	14.94	10.32	13.15	7.33
anæsthesia	2.81	4.77	3.78	2.85	10.21	3.76

Table 3.31 – *Mean calculated on coupling matrix* $CM(t)$.

to H is the smallest, which seems to be more logical. We think that in case of "Lancaster", still some subjects which include artifact were not excluded from the consideration of this mean values. We think this is also the case for the resting state in "Oslo". So, to confirm, more deeper investigation is necessary in the future.

Now let us check the directionality of the coupling. The obtained results are shown in fig. 3.140, 3.141, 3.142 and 3.143. From these figures, we confirm the case of "Lancaster" that H drives B in both phase since more than half of the subjects indicate this coupling direction. However, the direction from B to R under anæsthesia found in "Lancaster" cannot be seen, and we remarked that B drives R in both phase. For the relationship between H and R, there is no unique trend or it stays around zero such that nothing can be concluded. Looking at the transition to the steady state in fig. 3.142 and 3.143, we remarked that the direction between B and R inverses around the beginning of the steady state. Here, the created self model in unique for each subject such that there is a strong possibilities that B drives R at awaken state and ,in the contrary, R drives under anæsthesia. This is a very interesting result.

Here again we tried to distinguish the results according to the inducted anæsthetics, but no difference was observed in all results with this coupling matrix.

Nonparametric Granger causality

Here, the same window length, shifted time, segment length and segment overlapped length as "Lancaster", i.e. 1min, 30sec, 16sec and 14sec, respectively, are used in this study. In fig. 3.144, 3.145, 3.146 and 3.147, the obtained power spectra are shown. From these figures, as the case of "Lancaster", the spectra of ECG signals show wavy form at the resting state and show straight lines under anæsthesia. Focussing on fig. 3.146, before and after the beginning of the steady state, it seems that the frequency of ECG signals decrease under deep anæsthesia. The spectra of respiration signals are again concentrated at the very low frequency in both phase of measurements such that we analyzed zooming in at the low frequency (See in appendix). From this zoomed in figures, we remarked that, as "Lancaster", the frequency obtained with Sevoflurane without Curare slightly increases under anæsthesia. Furthermore, here we can observe clear effect of mechanical ventilation on the results obtained with Curare from a very straight lines. The reason that this was not observed in "Lancaster" is probably the measuring chest belt which was not tightened enough. For the spectra of EEG signals, again, they are concentrated at the very low frequency in both phase, and under anæsthesia, less fluctuation is observed. To check the presence of α-wave under anæsthesia found in "Lancaster", again we zoomed out the figures to see higher range of frequency (See appendix). From these zoomed out figures, we confirmed that α-waves appear under anæsthesia except subject no.10. On this subject, θ-waves appears instead of α-waves. In "Lancaster", we saw stronger amplitude of α-waves on the results with Sevoflurane with/without Curare, but here, no difference in amplitude

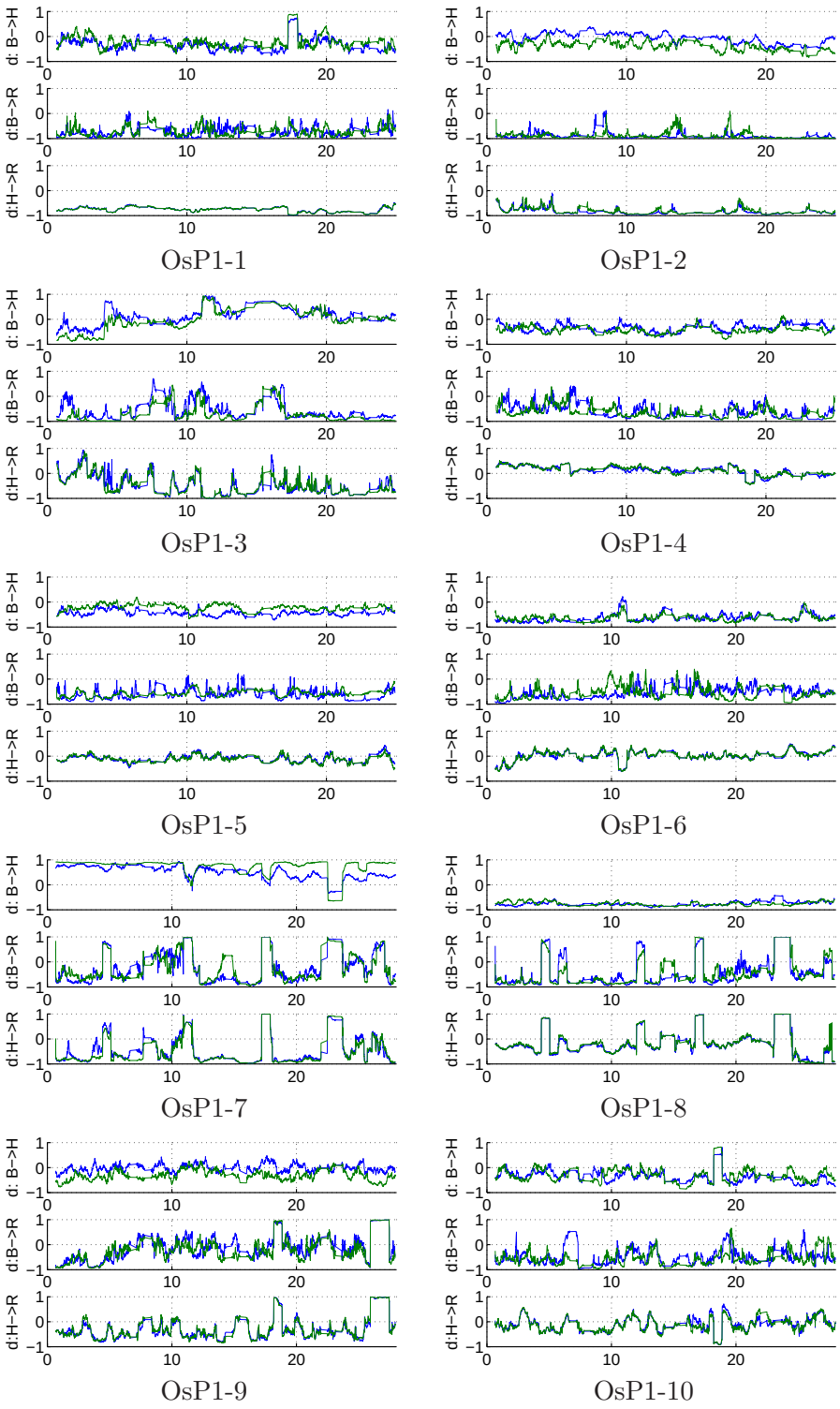

Figure 3.140 – *Direction of the interactions $d(t)$ obtained on "Oslo" at resting (awaken) state PartI. Horizontal axis is time (min): (B) EEG, (H) ECG, and (R) respiration. Note that the results are zoomed to see the major part.*

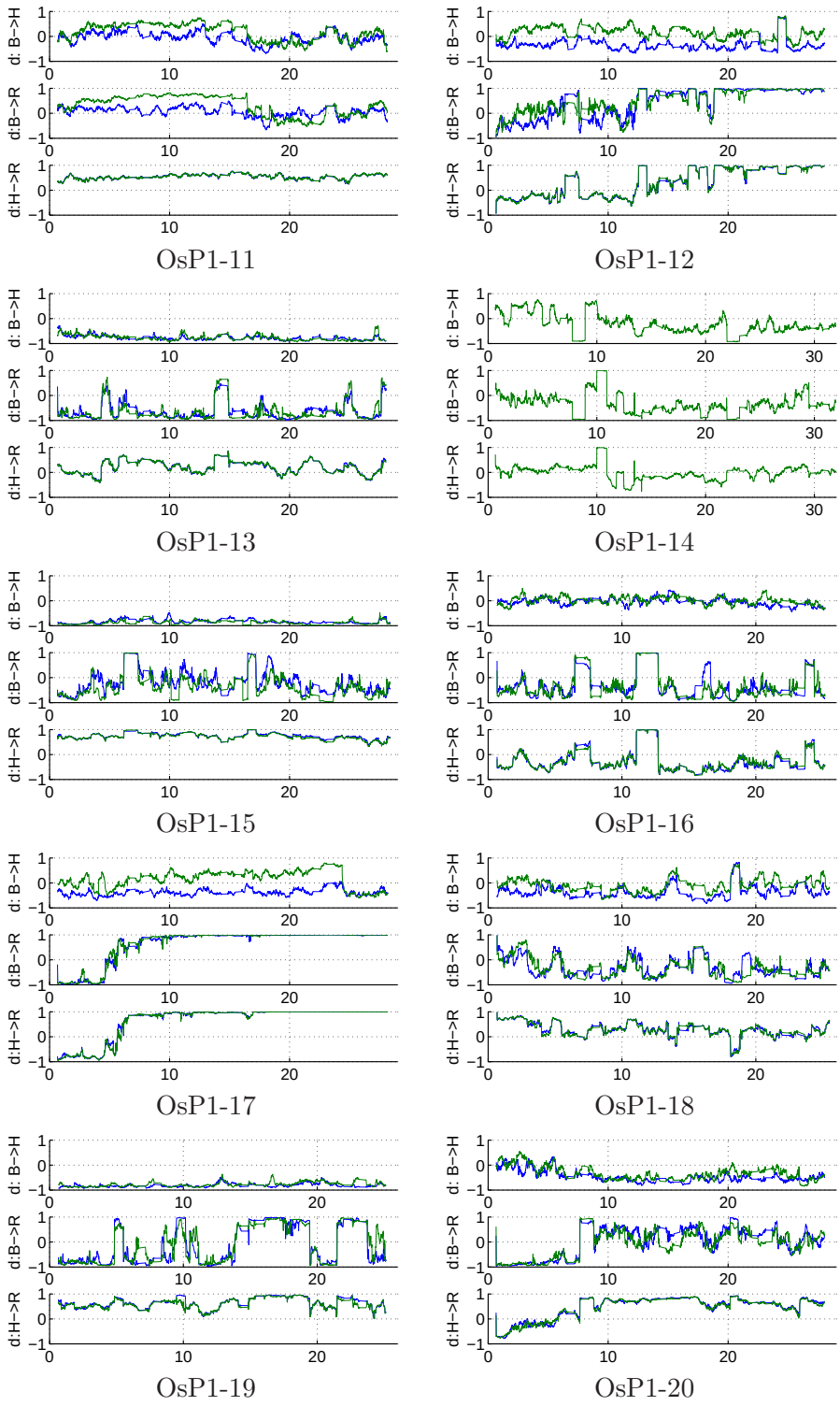

Figure 3.141 – *Direction of the interactions $d(t)$ obtained on "Oslo" at resting (awaken) state PartII. Horizontal axis is time (min): (B) EEG, (H) ECG, and (R) respiration. Note that the results are zoomed to see the major part.*

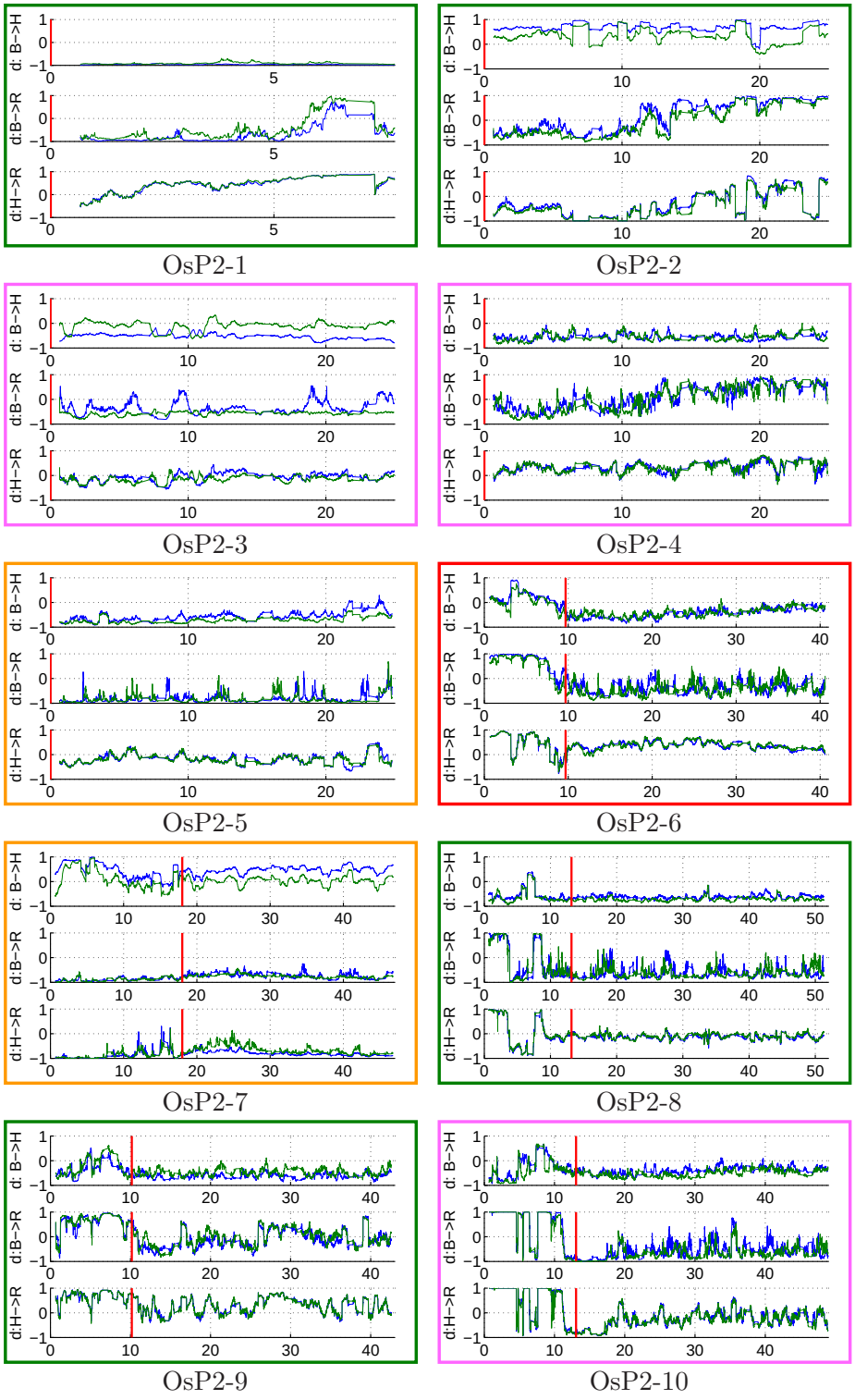

Figure 3.142 – *Direction of the interactions $d(t)$ obtained on "Oslo" under anæsthesia PartI. Horizontal axis is time (min): (B) EEG, (H) ECG, and (R) respiration. Boxes:(green) Propofol, (orange) Propofol+Curare, (red) Sevoflurane, and (pink) Sevoflurane+Curare. Note that the results are zoomed to see the major part.*

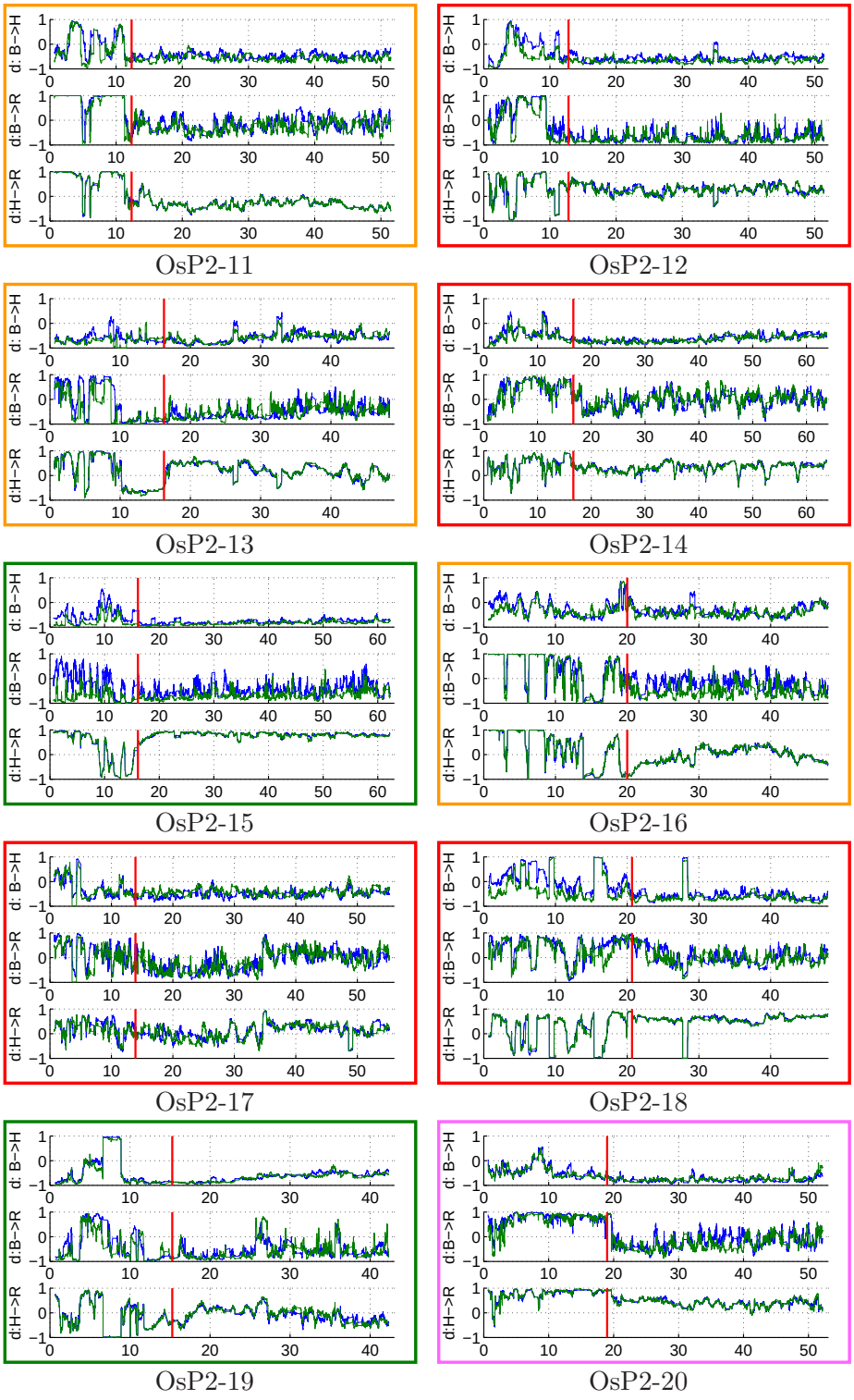

Figure 3.143 – *Direction of the interactions $d(t)$ obtained on "Oslo" under anæsthesia PartII. Horizontal axis is time (min): (B) EEG, (H) ECG, and (R) respiration. Boxes:(green) Propofol, (orange) Propofol+Curare, (red) Sevoflurane, and (pink) Sevoflurane+Curare. Note that the results are zoomed to see the major part.*

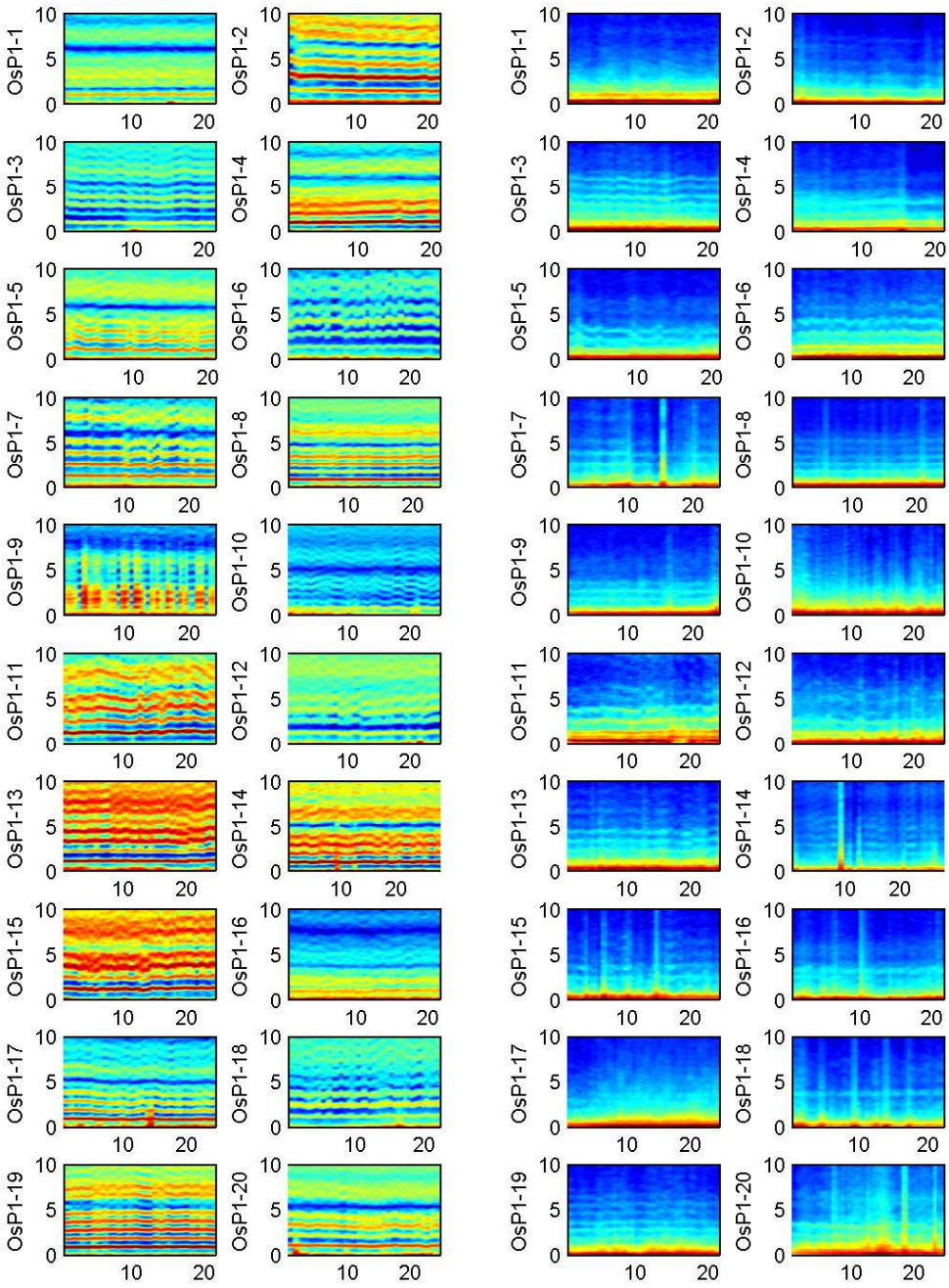

(a) (b)

Figure 3.144 – *Power spectra obtained on "Oslo" at resting (awaken) state PartI. Horizontal axis is time (min). Vertical axis is frequency (Hz). Color axis is omitted: (a) ECG and (b) Respiration.*

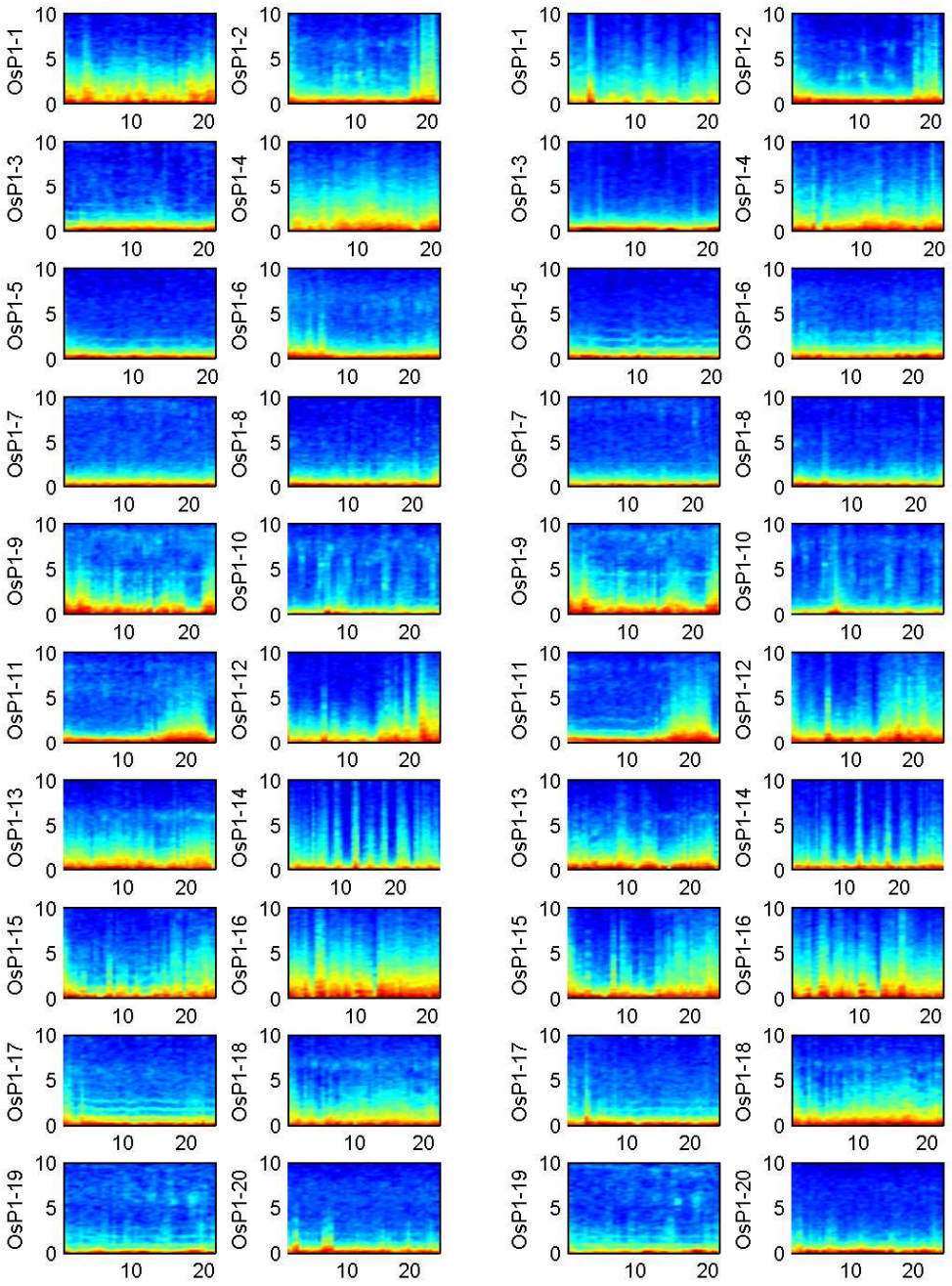

(c) (d)

Figure 3.145 – *Power spectra obtained on "Oslo" at resting (awaken) state PartII. Horizontal axis is time (min). Vertical axis is frequency (Hz). Color axis is omitted: (c) EEG1 and (d) EEG2.*

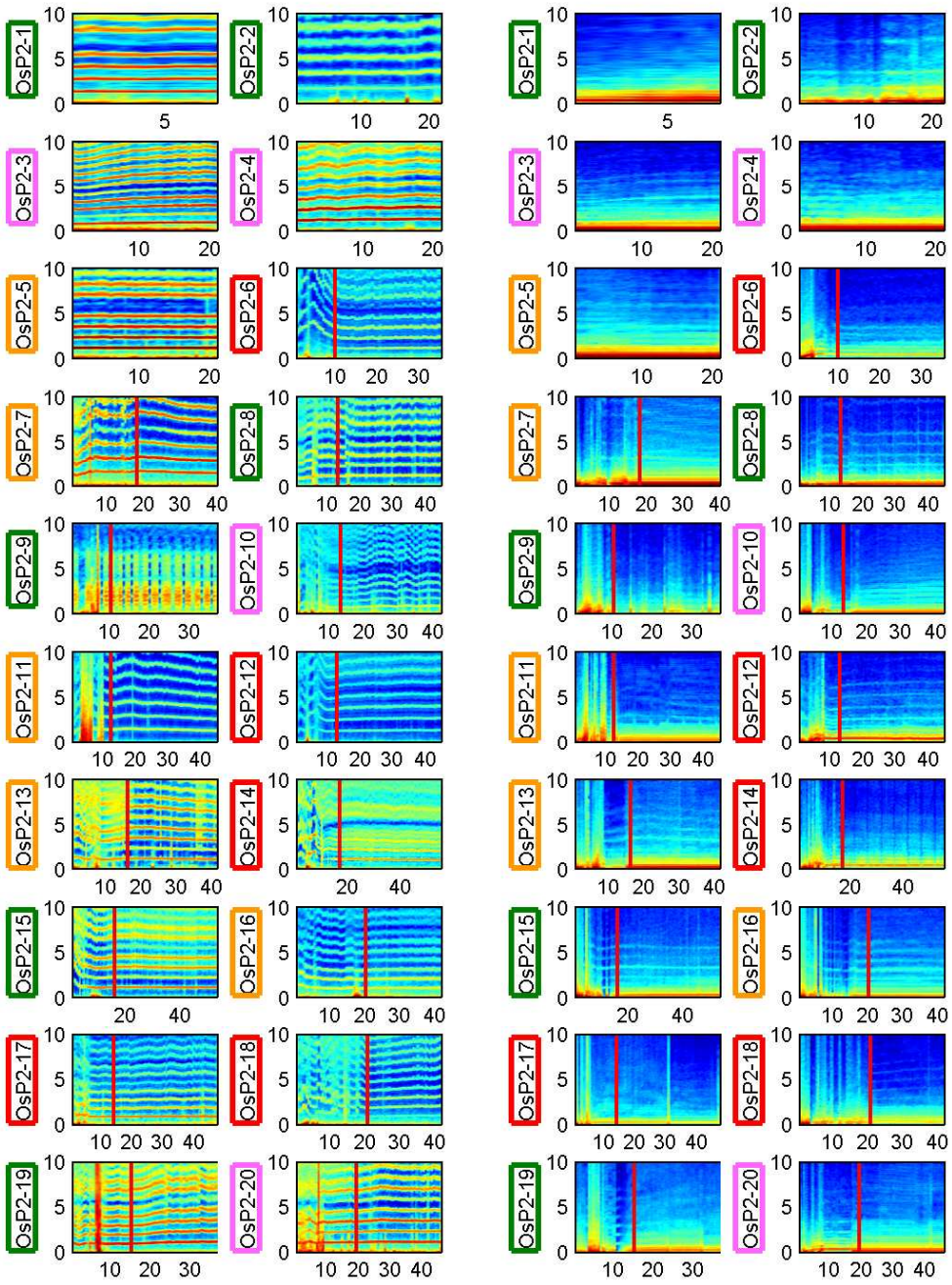

(a) (b)

Figure 3.146 – *Power spectra obtained on "Oslo" under anæsthesia PartI. Horizontal axis is time (min). Vertical axis is frequency (Hz). Color axis is omitted: (a) ECG and (b) Respiration.*

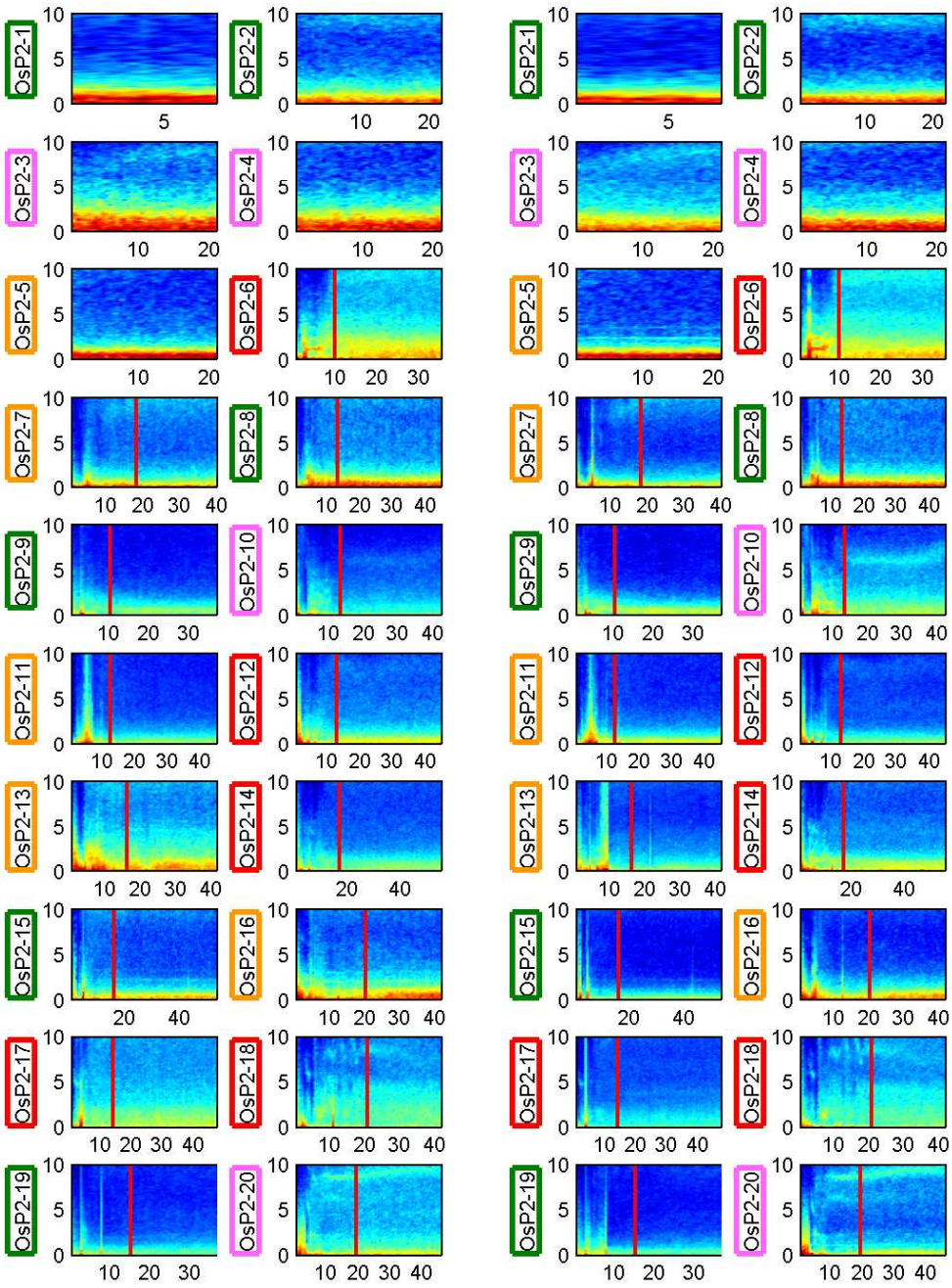

(c) (d)

Figure 3.147 – *Power spectra obtained on "Oslo" under anæsthesia. Horizontal axis is time (min). Vertical axis is frequency (Hz). Color axis is omitted: (c) EEG1 and (d) EEG2.*

according to the induced anæsthetics is observed.

Now let us check the coherence spectra. First, we show the employed thresholds calculated with the permutation test in the table below.

		Coh:H-R	Coh:B-H	Coh:B-R
P1	EEG1	0.19	0.18	0.18
	EEG2	0.19	0.18	0.18
P2	EEG1	0.17	0.18	0.18
	EEG2	0.18	0.17	0.18

Table 3.32 – *Thresholds for coherence spectra defined by the permutation test for "Oslo": (B) EEG, (H) ECG, and (R) respiration. Two cases in each phase are shown according to the chosen EEG signal: (P1) resting (P2) anæsthesia.*

In fig. 3.148 and 3.149, we show the obtained coherence spectra. Again, here the mean result of the results obtained with two different EEG signals is shown. From these figures, as the cases of "Lancaster", high coherence between heart (H) and respiration (R) was observed in both phase of measurements. Also, here again, the strength was not comparable. The coherence between brain (B) and H is also present in both phase, and again it seems weaker under anæsthesia. The coherence between B and R can be seen in some subjects in both phase, but looking carefully, these coherence are in range of heart frequency, such that we presume that these are undirect coherence. Consequently, as nothing appear at the very low frequency, we conclude that there is no direct coherence between B and R.

Now, let us proceed to the final analysis, the nonparametric Granger causality. To begin, the employed thresholds obtained with the permutation test are shown in the table below.

		GC:B→H	GC:H→B	GC:B→R	GC:R→B	GC:H→R	GC:R→H
P1	EEG1	0.13	0.13	0.13	0.13	0.13	0.13
	EEG2	0.23	0.12	0.12	0.13	0.12	0.12
P2	EEG1	0.13	0.15	0.14	0.13	0.16	0.14
	EEG2	0.13	0.12	0.13	0.13	0.12	0.13

Table 3.33 – *Thresholds for nonparametric Granger causality $GC(t)$ defined by the permutation test for "Oslo": (B) EEG, (H) ECG, and (R) respiration. Two cases in each phase are shown according to the chosen EEG signal: (P1) resting (P2) anæsthesia.*

In fig. 3.150, 3.151, 3.152 and 3.153, we show the obtained results. Here again, the mean result of the results obtained with different EEG signals is shown. From these figures, we remarked immediately that there is a causality from H to R in both phase of measurements, except subject no.9 and 10. At this moment, we don't know the reason why these two subjects do not have this causality. In "Lancaster", we mentioned a slightly lower causality under anæsthesia, but here in "Oslo", we have also some subjects which have higher causality, such that to comment on the change of the strength, we need more deeper analysis. The causality from R to H is also observed on some subjects in both phase, and as the case of "Lancaster", it seems to be higher under anæsthesia. Furthermore, the causality from R to B can be observed on some subjects at resting state and on all subjects under anæsthesia. Looking carefully on the frequency range of this causality, we found that the

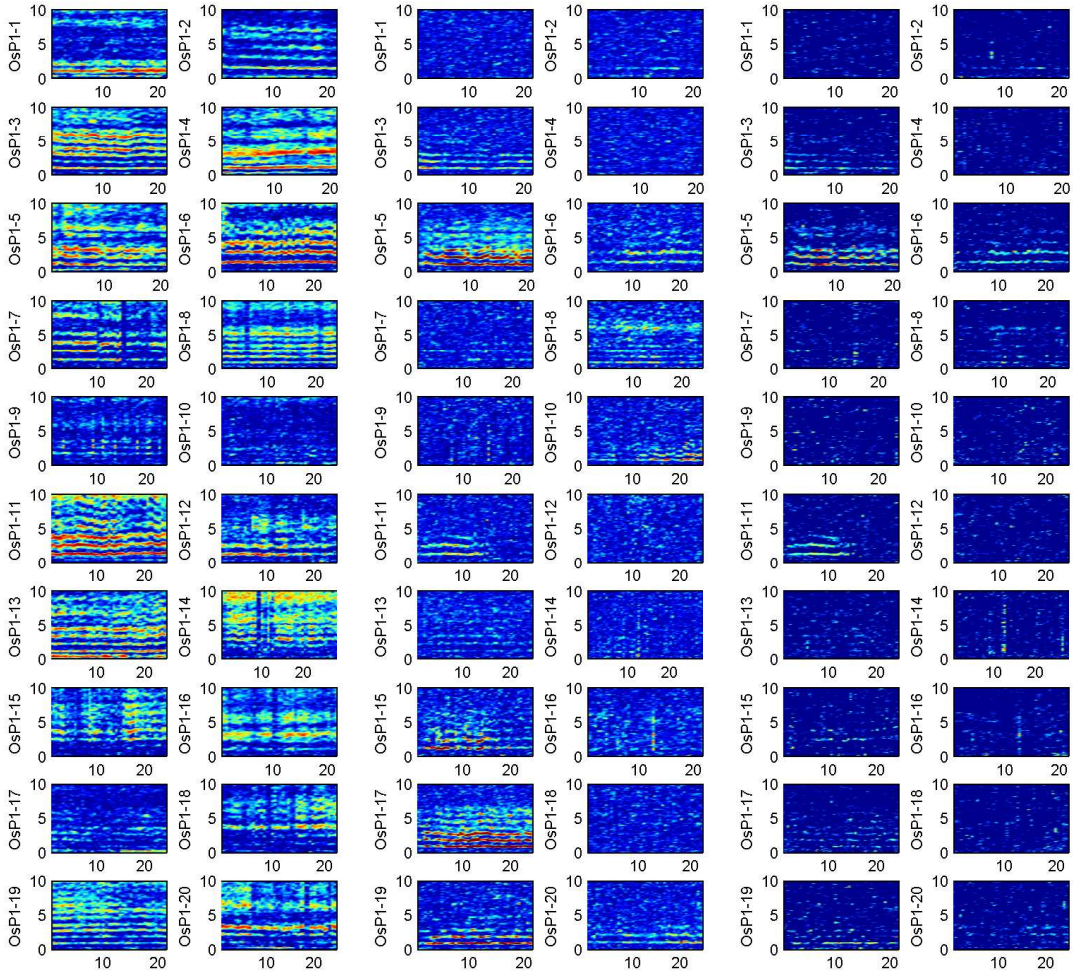

(a) (b) (c)

Figure 3.148 – *Coherence spectra obtained on "Oslo". Horizontal axis is time (min). Vertical axis is frequency (Hz): (a) ECG and respiration; color axis [0 1], (b) EEG and ECG; color axis [0 0.6], and (c) EEG and respiration; color axis [0 0.6].*

causality appears at the frequency of ECG signal. This should mean that there is a indirect causality from H to B through R. We suppose the case of subject no.3 in "Lancaster" is the same. This is a very interesting finding. Additionally, we can say that this indirect causality is stronger under anæsthesia. In the future, it will be very interesting to investigate the partial nonparametric Granger causality which removes the indirect causality.

To end, we tried to find out the difference between the results obtained with different inducted anæsthetics, but we didn't manage to find it.

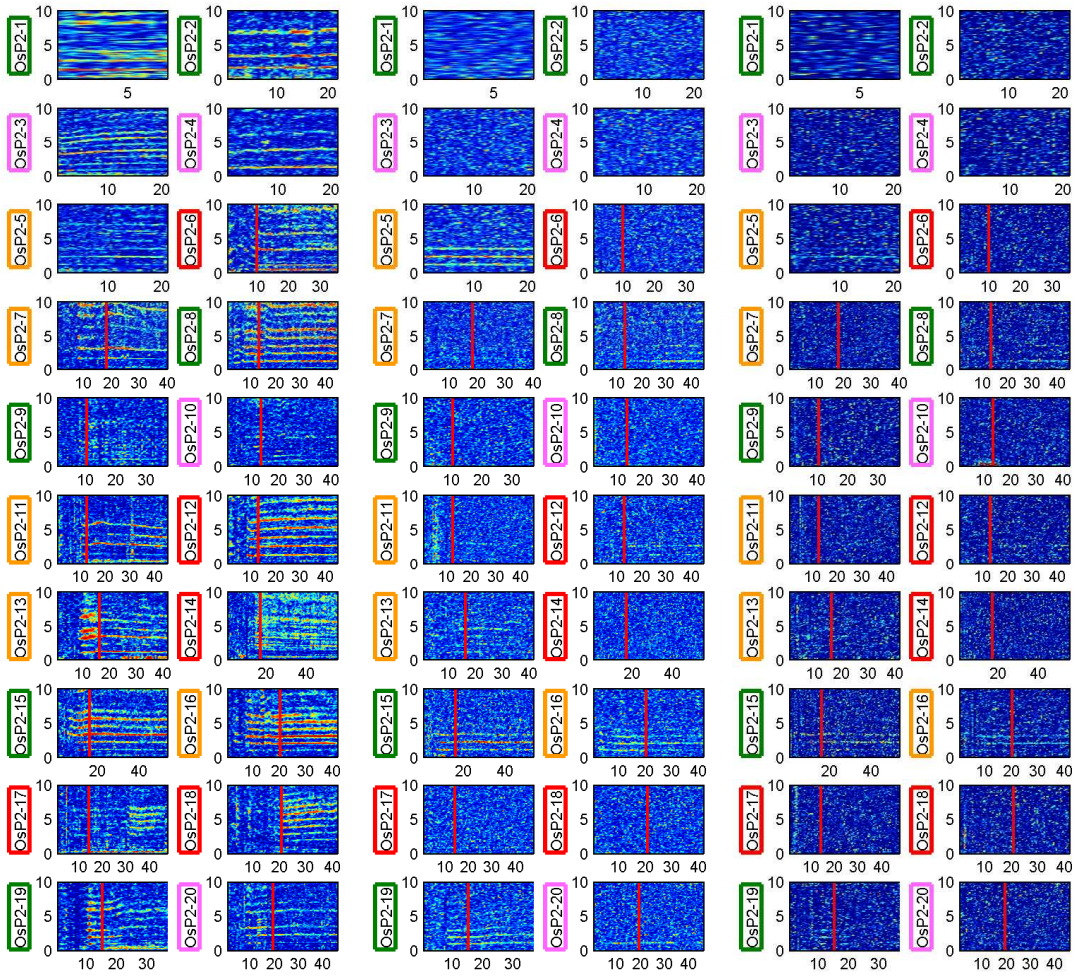

(a) (b) (c)

Figure 3.149 – *Coherence spectra obtained on "Oslo". Horizontal axis is time (min). Vertical axis is frequency (Hz): (a) ECG and respiration; color axis [0 1], (b) EEG and ECG; color axis [0 0.6], and (c) EEG and respiration; color axis [0 0.6]. Boxes: (green) Propofol, (orange) Propofol+Curare, (red) Sevoflurane, and (pink) Sevoflurane+Curare.*

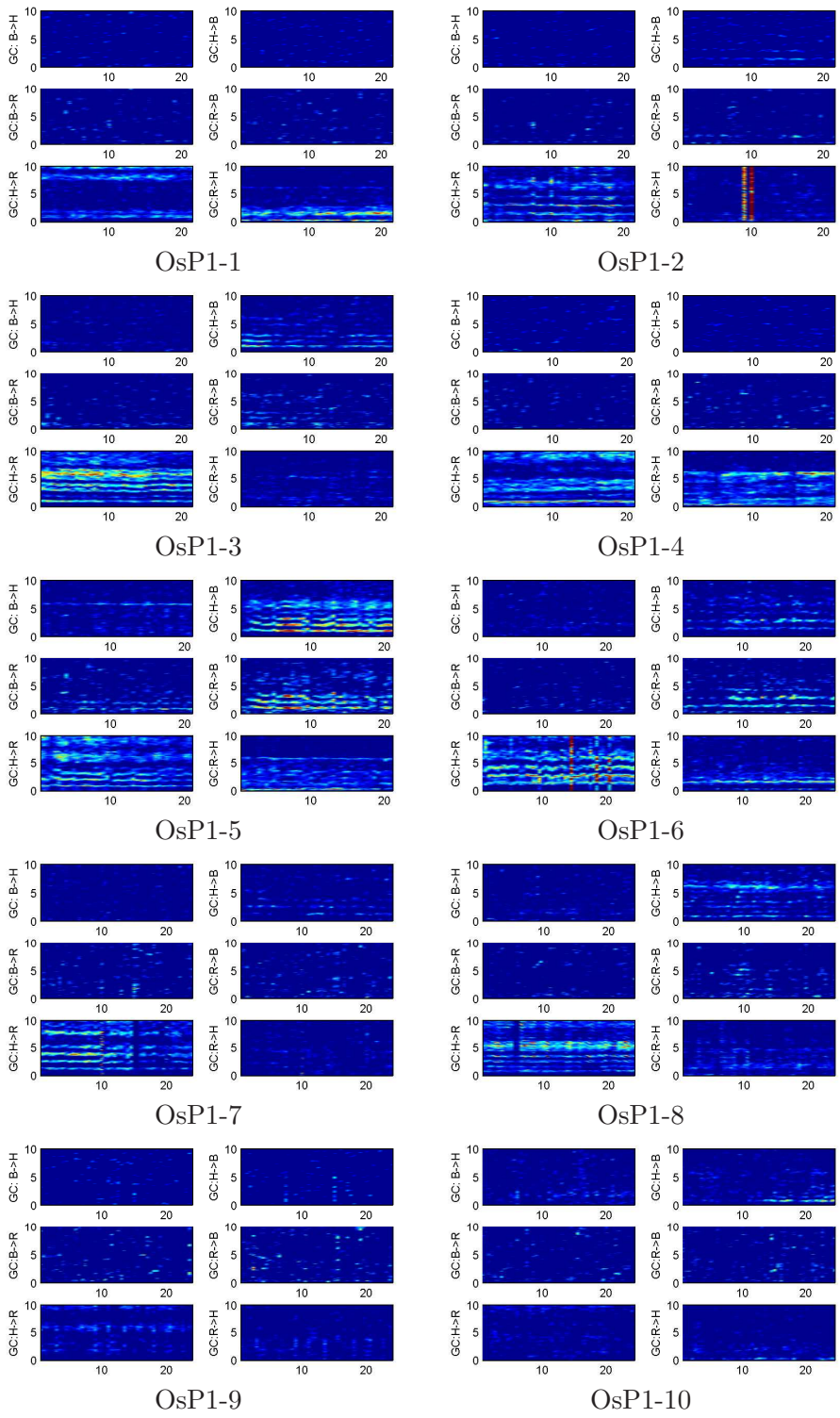

Figure 3.150 – *Nonparametric Granger causality $GC(t, f)$ obtained on "Oslo" at resting (awaken) state PartI. Horizontal axis is time (min): (B) EEG, (H) ECG, and (R) respiration. Color axis: B↔H [0 1], B↔R [0 0.5] and H↔R [0 2].*

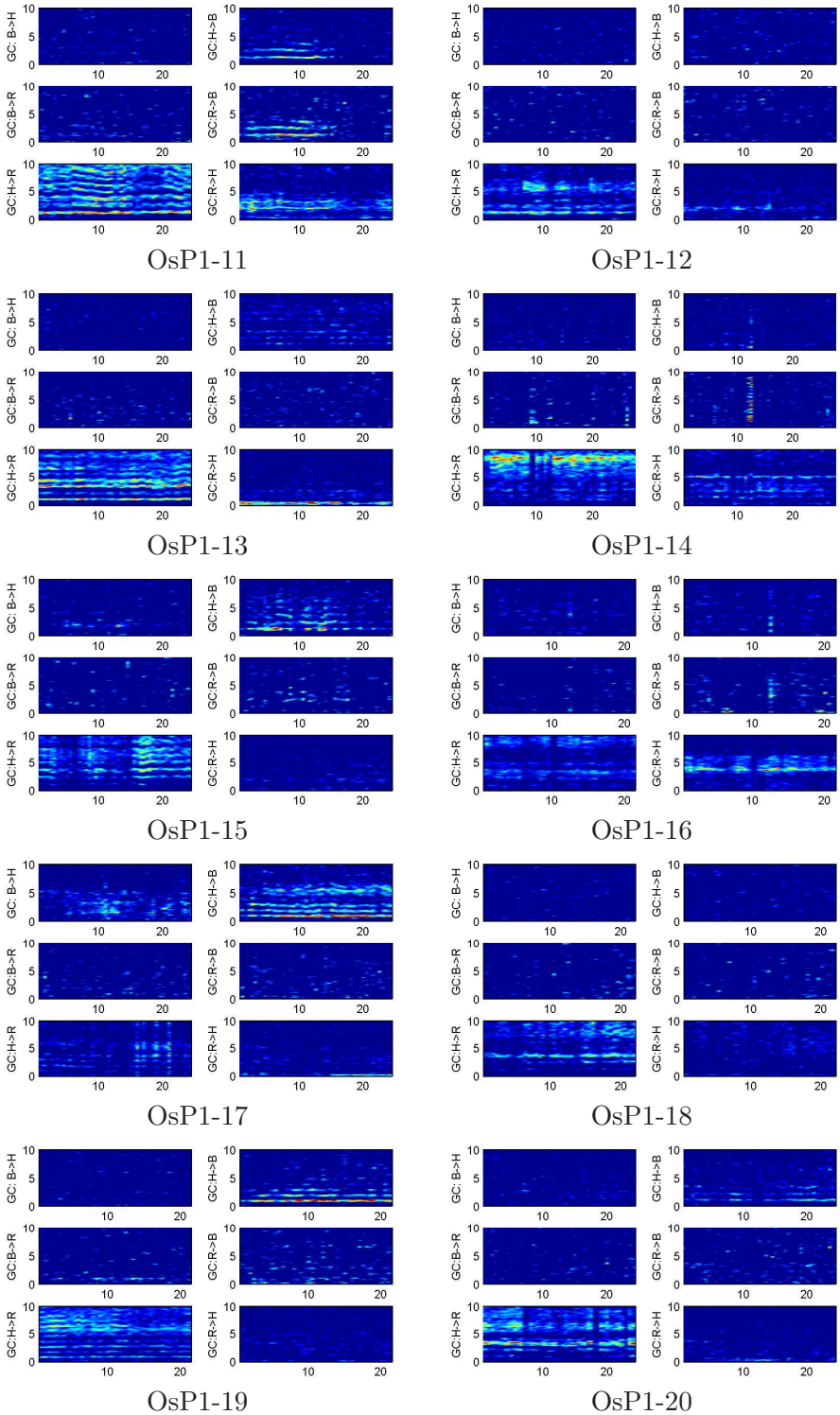

Figure 3.151 – *Nonparametric Granger causality $GC(t, f)$ obtained on "Oslo" at resting (awaken) state PartII. Horizontal axis is time (min): (B) EEG, (H) ECG, and (R) respiration. Color axis: B↔H [0 1], B↔R [0 0.5] and H↔R [0 2].*

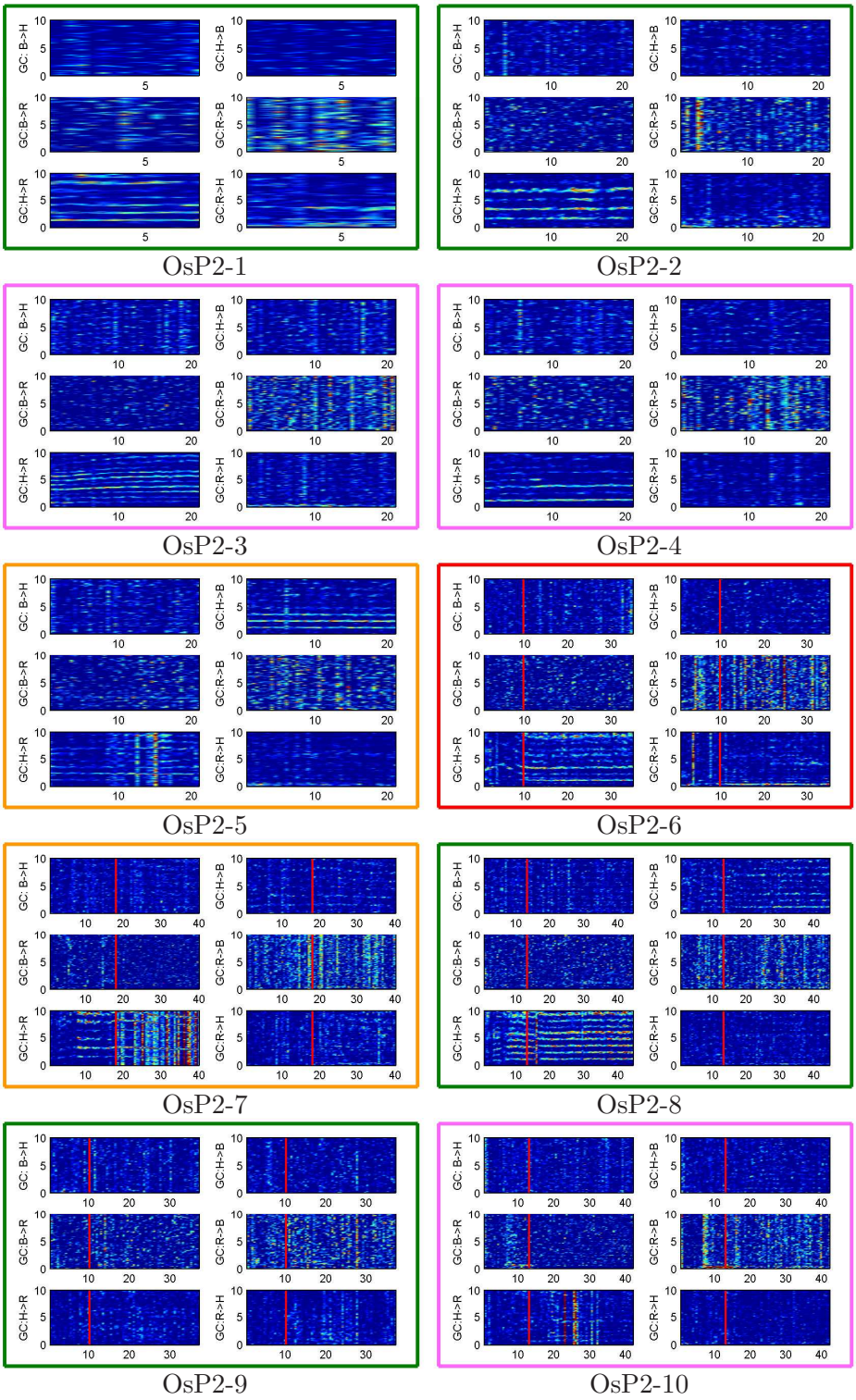

Figure 3.152 – *Nonparametric Granger causality $GC(t, f)$ obtained on "Oslo" under anæsthesia PartI. Horizontal axis is time (min): (B) EEG, (H) ECG, and (R) respiration. Color axis: B↔H [0 1], B↔R [0 0.5] and H↔R [0 2]. Boxes: (green) Propofol, (orange) Propofol+Curare, (red) Sevoflurane, and (pink) Sevoflurane+Curare.*

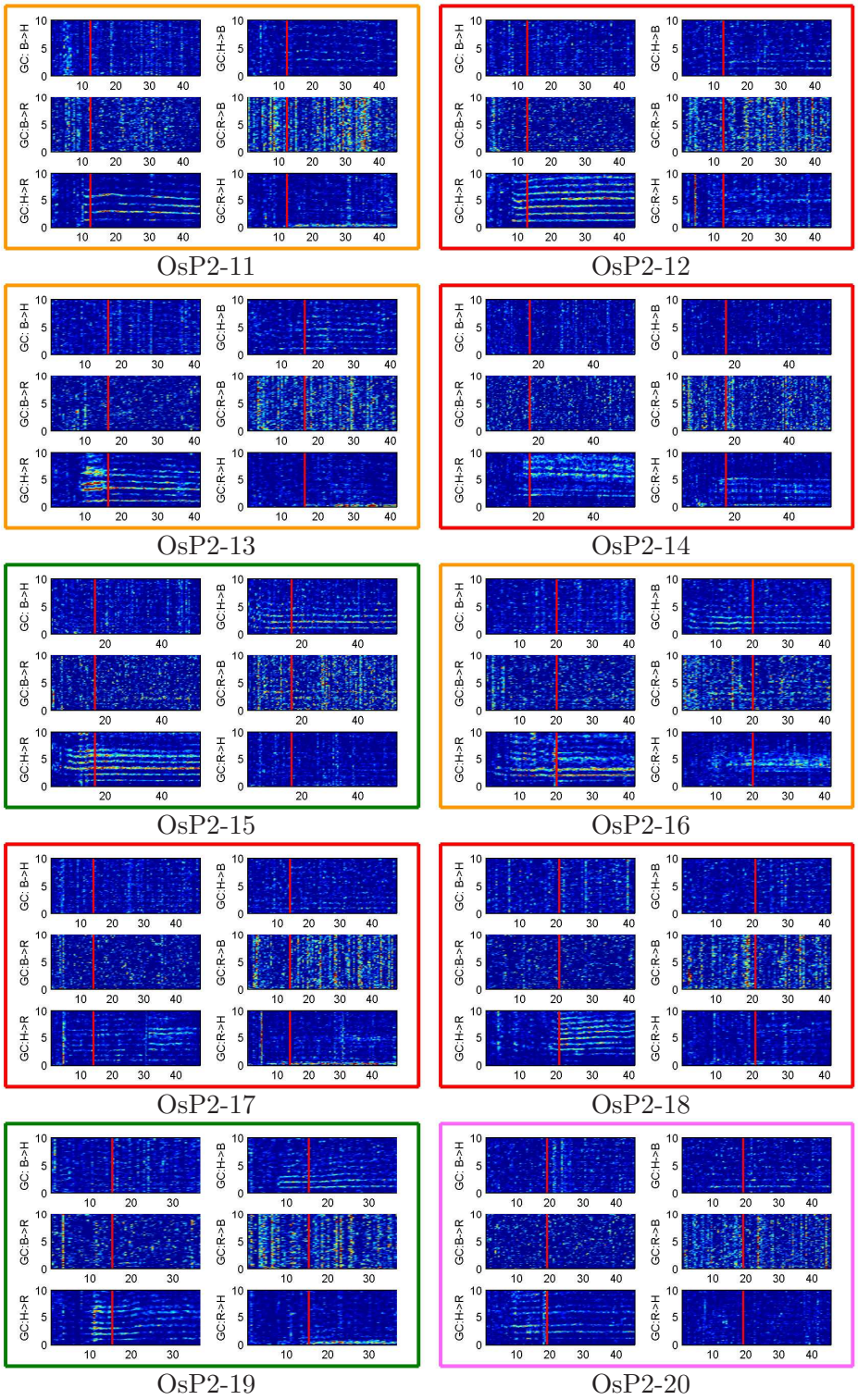

Figure 3.153 – *Nonparametric Granger causality $GC(t, f)$ obtained on "Oslo" under anæsthesia. Color axis: B↔H [0 1], B↔R [0 0.5] and H↔R [0 2]. Boxes: (green) Propofol, (orange) Propofol+Curare, (red) Sevoflurane, and (pink) Sevoflurane+Curare. PartII. Horizontal axis is time (min): (B) EEG, (H) ECG, and (R) respiration.*

3.10.3 Summary of the interdependency for human recordings

In this subsection, again as the case of rats, we summarized the results focussing on the interdependency according to the induced anæsthetics. The analysis results on the embedding dimension are also summarized since these are our brand-new findings. Here, the abbreviation B(brain) for EEG, H(heart) for ECG and R for respiration are used. What we manage to distinguish according to the induced anæsthetics are itemized at the end.

The synchronization inside of whole system is lower under anæsthesia:

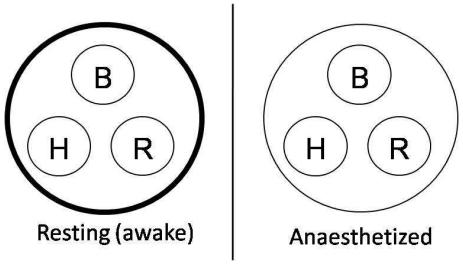

- The variance is also low under anæsthesia.
- This is exactly the inverse case from results of rats.
- The $S(t)$ stays nearly constant at each state such that there is a strong possibility of numerical detection of the change point of the depth of anæsthesia.
- When taking only two sub-sytems into account, we can also see low synchronization under anæsthesia on each system with chosen two sub-systems, but only the decrease on B-R system is significant in both "Lancaster" and "Oslo". In "Oslo", B-H system also shows significant decrease. The variance is also low under anæsthesia but only B-H and B-R system in "Lancaster" show significant decrease.

No change in the synchronization exclusively between sub-systems:

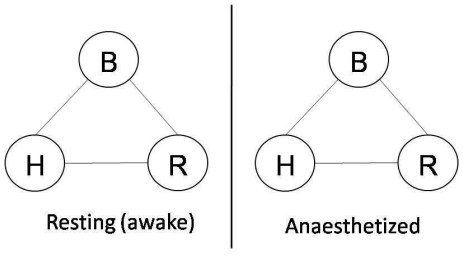

- On "Oslo", we observed a significant decrease in this synchronization, but this is probably because of two patients which score high synchronization at the resting state.
- The level of synchronization is about 10 times smaller than synchronization inside of whole system.

- The variance is low under anæsthesia. In "Oslo" this is significant.
- When taking only two sub-sytems into account, the synchronization between B and R increases significantly in "Lancaster". Half of the subject in "Oslo" agree with this, but taking the mean of the subjects, we observe a decrease instead of increase. Otherwise, synchronization between H and R significantly decrease on "Oslo". Additionally, significant decrease of variance was also observed only on "Oslo".

Estimated embedding dimension is lower under anæsthesia on B and H:

- The decrease on ECG was not observed on all results.
- Even we found the decrease in estimated ED, there is no difference in mean between both phase of measurements in "Lancaster". On "Oslo", we remark even a significant increase on EEG2 ED and Resp ED.
- Definitively the variance of EEG ED decrease under anæsthesia.

Coherence decreases between B and H under anæsthesia:

- High coherence was observed between H and R, but no change can be remarked at the change point of anæsthesia.
- Almost no coherence found between B and R.

The change in coupling strength found with "coupling matrix (CM)":

- All the couplings, except from B to R in "Lancaster", are lower under anæsthesia.
- On "Lancaster", from B to H, from H to B, from R to B and from R to H show significant decrease. On "Oslo", all the couplings show significant decrease except from B to H and from R to H. This coupling from R to H shows significant increase.
- On "Lancaster", from H to B and from R to B show significant decrease in variance under anæsthesia. On "Oslo", all the variance of couplings show significant decrease except from B to H and from R to H. This from R to H, same as coupling, the variance shows significant increase.
- The directionality change in coupling happens like the figure below.
  The change in coupling between B and R is exactly the inverse of the case of rats.

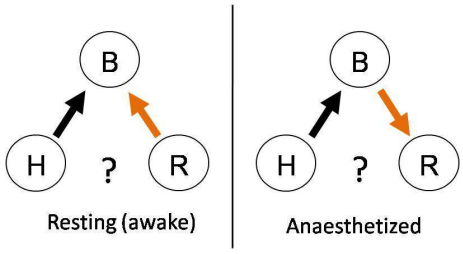

The change in causality strength found with "nonparametric Granger causality (GC)":

- The causality from H to R is present in both state, but no unique change was found.
- The causality from R to H increases under anæsthesia. This agrees the CM.
- The causality from H to B is present on some subjects, but no change can be found between two phase of measurements.
- The causality from R to B found on "Oslo" seems to be the shadow of indirect causaity.

The difference between induced anæsthetics that we managed to find are:

- Propofol with/without Curare show higher $S(t)$ under anæsthesia compared to the others in some subjects.
- The results of $S_{new}(t)$ with different EEG signals obtained on systems with two subsystems with Propofol with/without Curare differ.
- Sevoflurane with/without Curare show lower $S_{new}(t)$ on B-H and B-R system, such that these anæsthetics affect the brain more than Propofol with/without Curare.
- Sevoflurane with/without Curare show stronger α-wave on the obtained power spectrum under anæsthesia in "Lancaster".
- On "Oslo", Propofol with/without Curare have more fluctuation on the ED(t) of respiration under anæsthesia.

Modelling of the brain rhythms

4

Brief - In this study, we will go through three steps. The first step is to investigate the way of modelling brain waves, δ waves in particular, using a large ensemble of locally and/or globally coupled identical and non-identical oscillators. Each neuron will be represented as one oscillator. After establishing the model, the next step is to investigate the effect of anæsthesia changing the related parameters on the model. Here, the collective behavior of the cortical neurons is employed as an observable, since it is said to represent the EEG signal. Finally, the understanding and the analysis of the model is carried out.

Contribution - As I was not specialized on this domain of brain modelling, the model was taken from the literature, but the choice of the model was by myself after a lot of searching information and reading articles and books on the brain modelling. The implementation of the model was carried out collaborating with Borja Ibarz, a PhD student of Universidad Rey Juan Carlos in Spain, who visited our lab for six months during the last half of 2006. The way to include the effect of the anæsthesia was also taken from the literature, but the implementation on our model was my task. All the simulations and the interpretation of the results were my contribution. Furthermore, the understanding and the analysis of the model were also done by myself.

4.1 Motivation

BRAIN science is one of the most attractive research topic of this century and many investigations are in progress to clarify the mechanism of the brain. One example is the "Blue Brain project" here in EPFL. The Blue Brain Project is an attempt to reverse engineer the brain, to explore how it functions and to serve as a tool for neuroscientists and medical researchers using IBM Blue Gene supercomputer. In our project "BRACCIA", even if we don't use this supercomputer, we want also to dive into this challenge.

Modeling the effects of anesthesia upon the brain is a very challenging problem, since even the origin of the electroencephalogram (EEG) oscillations, which are presently used in clinical surgery to estimate the depth of anesthesia, remains a mystery despite more than 100 years of research. So, at the beginning, we had difficulties to set up the research direction. To overcome this, we began to collect the knowledge about the rhythmic activities of the brain and about modelling them from the huge literature. From these readings, we deduce that it is generally accepted in the neuroscience community that the slow rhythms of the EEG are created by the interaction between the cortex and the thalamus[Destexhe and Sejnowski, 2001]. Consequently, the goal of this chapter is to create a model based on this interaction between cortex and the thalamus, and test the effect of the anæsthesia by changing the related model parameters.

4.2 Knowledge acquisition

To get familiar with the field and to accumulate the information about the recent investigations, we refer to the huge literature, but especially to the book of Destexhe and Sejnowski titled "Thalamocortical assemblies" Destexhe and Sejnowski [2001]. Here, we summarize what we learned from these literatures studies.

4.2.1 Neurons

The number of neurons in the brain depends on species. Besides, it is said that the human brain has about 100 billion (10^{11}) neurons and 100 trillion (10^{14}) synapses. The dendrite, is a branching arbor of cellular extensions. Most neurons have several dendrites with profuse dendritic branches. It is traditionally thought to be the main information receiving network

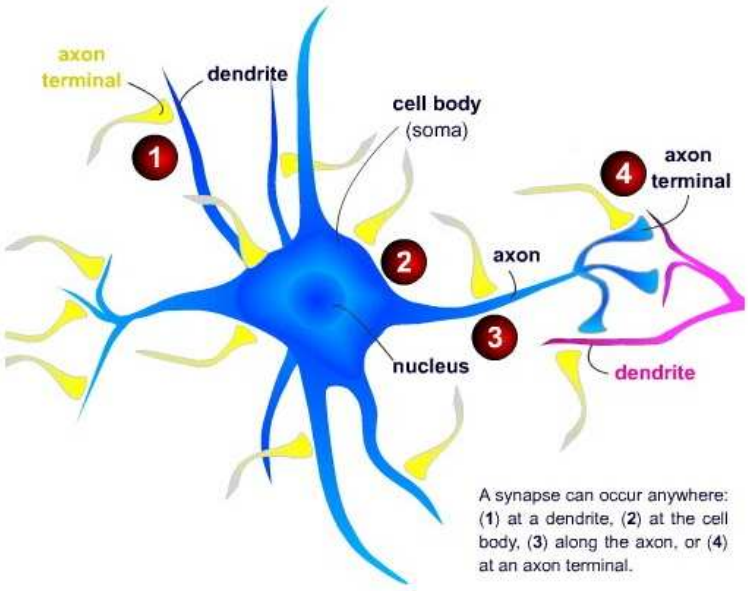

Figure 4.1 – *Neuron-Synapses*

for the neuron. However, information outflow (i.e. from dendrites to other neurons) can also occur. So, in general, when a dendrite is stimulated in a certain way, the neuron to which it is attached suddenly changes its electrical polarity and may fire, sending a signal out along its single axon where it may be picked up by the dendrites of other neurons. (To be precise with the axon, many neurons have only one axon, but this axon may - and usually will - undergo extensive branching, enabling communication with many target cells.) For one neuron to influence another, the two must be connected, and this is accomplished by junctions called synapses. These synaptic junctions usually connect the axon of one neuron with the dendrites of another.

4.2.2 Brain rhythmicities

As mentioned in the motivation, despite more than 100 years of research, the origin of the EEG oscillations remains a mystery. Nevertheless, new techniques are being developed to observe populations of neurons and theories are being developed for how brain may represent information in these populations [Abbott and Sejnowski, 1999].

The earliest theory proposed by Rothberger [Bremer, 1938] explains that EEG rhythmicity are due to action potentials travelling along chains of interconnected neurons. Five years later, Bishop [Bishop, 1936], for the first time, invoked the thalamocortical mechanism and proposed that the rhythmicity is generated by the action potentials travelling back and forth between thalamus and cortex. In 1938, instead of travelling action potentials, Bremer [Bremer, 1938][Bremer, 1949][Bremer, 1958] proposed a new theory that the rhythm is generated by autorhythmic properties of cortical neurons and the EEG results from the synchronized oscillatory activity of large assemblies of oscillating cortical neurons (See fig. 4.2). Following the work of Bremer, Eccles[Eccles, 1951] provided convincing evidence that the EEG reflects summated postsynaptic potentials. Furthermore, to explain the slow time course of EEG waves, he postulated that distal dendritic potentials, and their slow electronic propagation to soma, participate in the genesis of the EEG. Furthermore, Bremer [Bremer, 1949] also proposed that oscillations depend on the 'excitability cycle' of cortical neurons, where the intrinsic properties of cortical neurons were identified as important in generating EEG oscillations for the first time.

4.2.3 Hodgkin-Huxley model

Computational models can make a significant contribution in linking the microscopic properties of ion channels to cellular behavior by simulating their complex interactions.

The model of the sodium current and the potassium current introduced by Hodgkin and Huxley [Hodgkin and Huxley, 1952] was remarkably forward looking. The schematic diagram for Hodgkin-Huxley model is shown in fig. 4.3 [Gerstner and Kistler, 2002]. The semipermeable cell membrane separates the interior of the cell from the extracellular liquid and acts as a capacitor. If an input current I(t) is injected into the cell, it may add further charge on the capacitor, or leak through the channels in the cell membrane. Because of active ion transport through the cell membrane, the ion concentration inside the cell is different from that in the extracellular liquid. The Nernst potential generated by the difference in ion concentration is represented by a battery. When translating this into a

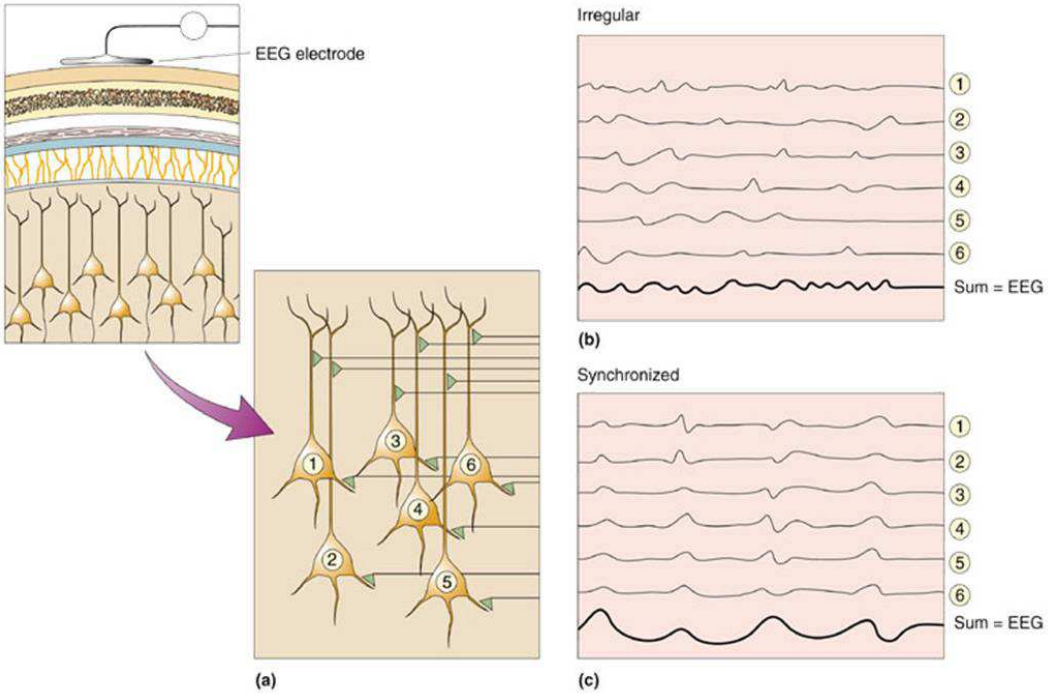

Figure 4.2 – *The mechanism of EEG creation from emsemble of corical neurons [Bear et al., 2002].*

mathematical model, we can represent as:

$$C\frac{dV}{dt} = -\sum_k I_k(t) + I(t), \tag{4.1}$$

where, C is the capacitance of the membrane, V is the voltage across the membrane and $\sum_k I_k$ is the sum of the ionic currents which pass through the cell membrane. In this Hodgkin-Huxley model, there are three types of channels: a sodium channel with index Na, a potassium channel with index K and an unspecific leakage channel with resistance R. All channels may be characterized by their resistance or, equivalently, by their conductance. The leakage channel is described by a voltage-independent conductance $g_L = 1/R$; the conductance of the other ion channels is voltage and time dependent. If all channels are open, they transmit currents with a maximum conductance $\bar{g}_{Na}$ or $\bar{g}_K$, respectively. Nor-

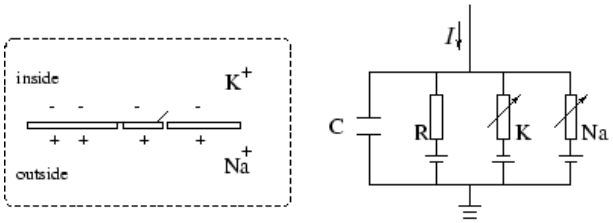

Figure 4.3 – *Schematic diagram for Hodgkin-Huxley model [Gerstner and Kistler, 2002].*

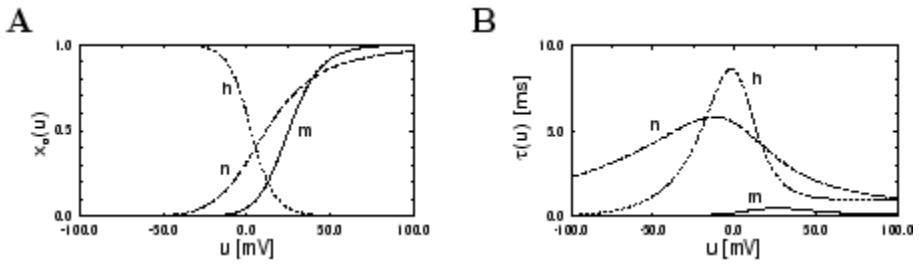

Figure 4.4 – *Kinetics of channel gating: (A) Equilibrium function and (B) time constant. The resting potential is at $V = 0$ [Gerstner and Kistler, 2002].*

mally, however, some of the channels are blocked. The probability that a channel is open is described by additional variables m, n, and h which evolve according to the following differential equations.

$$\frac{dm}{dt} = \alpha_m(V)(1-m) - \beta_m(V)m, \tag{4.2}$$

$$\frac{dn}{dt} = \alpha_n(V)(1-n) - \beta_n(V)n, \tag{4.3}$$

$$\frac{dh}{dt} = \alpha_h(V)(1-h) - \beta_h(V)h, \tag{4.4}$$

where, α is the opening rate and β is the closing rate. Usually this eq.(4.2)-(4.4) are reformalized as follows for better understanding of the kinetics:

$$C\frac{dx}{dt} = -\frac{1}{\tau_x(V)}(x - x_0(V)), \tag{4.5}$$

where, x stands for m, n and h. For fixed voltage V, the variable x approaches the value $x_0(V)$ with a time constant $\tau_x(V)$ (See fig. 4.4). The asymptotic value $x_0(V)$ and the time constant $\tau_x(V)$ are given by the transformation:

$$x_0(V) = \frac{\alpha_x(V)}{\alpha_x(V) + \beta_x(V)}, \tag{4.6}$$

$$\tau_x(V) = \frac{1}{\alpha_x(V) + \beta_x(V)}. \tag{4.7}$$

The combined action of m and h controls the Na channels. The K gates are controlled by n. Now, we can formalized $\sum_k I_k$ with more details on each three channels:

$$\sum_k I_k = \bar{g}_{Na} m^3 h(V - E_{Na}) + \bar{g}_K n^4 (V - E_K) + g_L(V - E_L), \tag{4.8}$$

where, E_{Na}, E_K and E_L are the reversal potentials.

This description of Hodgkin-Huxley not only accounted quite well for the conductances of the squid giant axon, but has been widely applied, with very minor alterations, to describe nearly all of voltage-dependent currents. One of the advantages of this model is that it describes the behavior of ion channels using quantities (activation functions, time constants) that are observable experimentally with relatively simple voltage-clamp protocols. This model is not appropriate for modeling single channels, but it should continue to be the basis for modeling macroscopic currents for many more years.

4.2.4 Rhythmic oscillations in thalamocortical assemblies

The experimental data have demonstrated that corticothalamic feedback may be important in organizing the large-scale synchrony of oscillations [Contreras and Steriade, 1996][Contreras et al., 1997a]. Analysis of multistate field potentials further characterized the remarkable degree of large-scale synchrony of oscillations during natural sleep and how this can be disrupted by cortical depression or by anaesthesia [Contreras et al., 1997b][Destexhe et al., 1999].

During the early stages of sleep or under anesthesia, low frequency oscillations are mostly observed in the EEG. The generation of the slow oscillation is associated with significant hyperpolarization of neocortical neurons. The survival of slow oscillations after extensive thalamic lesions [Steriade et al., 1993] and the absence of slow oscillations in the thalamus of decorticated cat [Timofeev and Steriade, 1996] point to an intracortical origin for this rhythm. Intracellular studies have shown that the hyperpolarizing phase of slow oscillation is associated with disfacilitation, a temporal absence of synaptic activity [Contreras et al., 1996][Timofeev et al., 1996][Timofeev et al., 2001][Steriade et al., 2001].

A computational model of thalamocortical networks was investigated to test possible mechanism for large-scale synchrony [Destexhe et al., 1998]. It also made predictions about the influential role of the cortex in triggering and synchronizing oscillations generated in the thalamus through corticothalamic feedback projections [Destexhe et al., 1999](See fig. 4.5). Intracortical mechanisms may be responsible for synchronizing oscillations over cortical

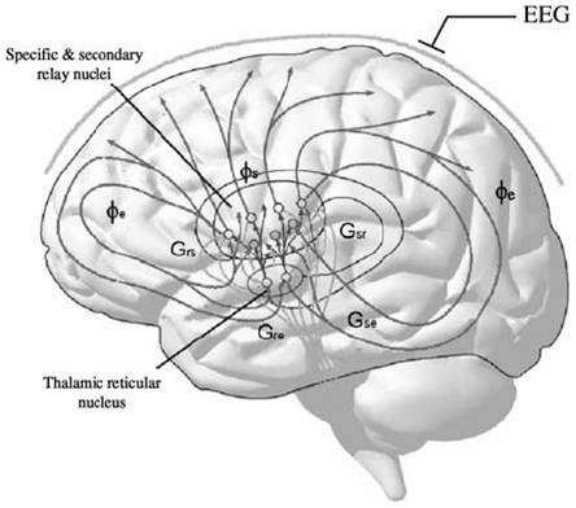

Figure 8 Schematic of interactions between the thalamus and the cortex. The cerebral cortex gives and receives excitatory (red) connections to and from the specific and secondary relay nuclei of the thalamus, and gives connections also to the reticular nucleus of the thalamus. The reticular nucleus gives inhibitory connections to the other thalamic nuclei, and receives inputs from the specific and secondary nuclei. All components are activated by the reticular activating system. Symbols ϕ_{ee}, ϕ_{es}, etc, represent pulse fluxes, and G_{rs}, G_{sr}, etc, synaptic gains, in accord with a related convention to that used in the purely cortical model.

Figure 4.5 – *corticothalamic feedback projections. Figure taken from [Wright et al., 2003].*

distances of several millimeters through cortex-thalamus-cortex loops, even though the generators of the oscillations are in the thalamus. According to this view, the neocortex shapes and controls the spatial pattern of thalamic oscillations.

4.3 The model

4.3.1 Choice of the model

As mentioned before, during deep anaesthesia, EEG is dominated by slow waves, and from literature, the importance of corticothalamic feedback for the slow EEG rhythmicities was pointed out. Accordingly several interesting models were identified [Hill and Tononi, 2005][Rulkov et al., 2004], but one particular thalamocortical model was chosen, since the potential to reflect the effect of anæsthesia was high. This chosen model based on Hodgkin-Huxley kinetics was created by Bazhenov et al.[Bazhenov et al., 2002]. This model includes four layers of neurons, where two of them are for the thalamus (RE: thalamic reticular neurons, TC: thalamic relay neurons) and the other two are for the cortex (PY: pyramical neurons, IN: interneurons). See fig. 4.6 for their connections.

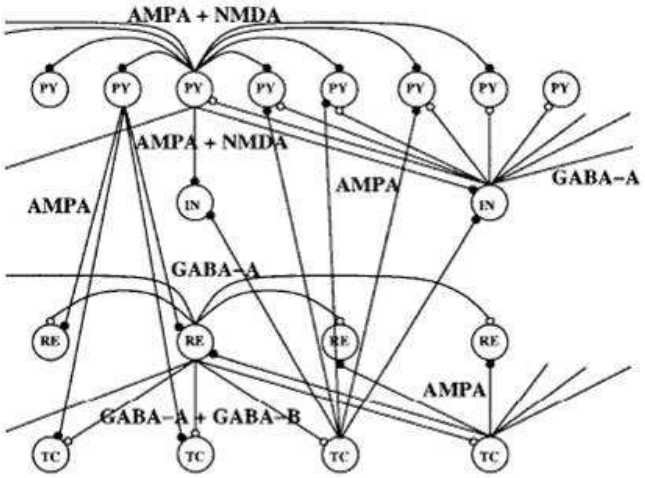

Figure 1. Network geometry. Network model included four layers of neurons with *N PY, M IN, L RE,* and *L TC* cells. In most simulations we used $N = 100$, $M = 25$, and $L = 50$.

Figure 4.6 – *Network geometry taken from [Bazhenov et al., 2002].*

One of the advantages of this network is that each neuron follows the Hodgkin-Huxley formalism[Hodgkin and Huxley, 1952] that describes the behavior of ion channels using quantities as activation functions and time constants such that the implementation of the effect of anæsthesia planned for afterward should be easily possible. Another positive point is the investigation of the transformation from slow waves to higher frequency waves which also takes place in the transition from deep anesthesia to light anesthesia.

In the simulation carried out by the authors, occasional summation of the miniature EPSPs during the hyperpolarized (silent) phase of SWS oscillation activated the persistent

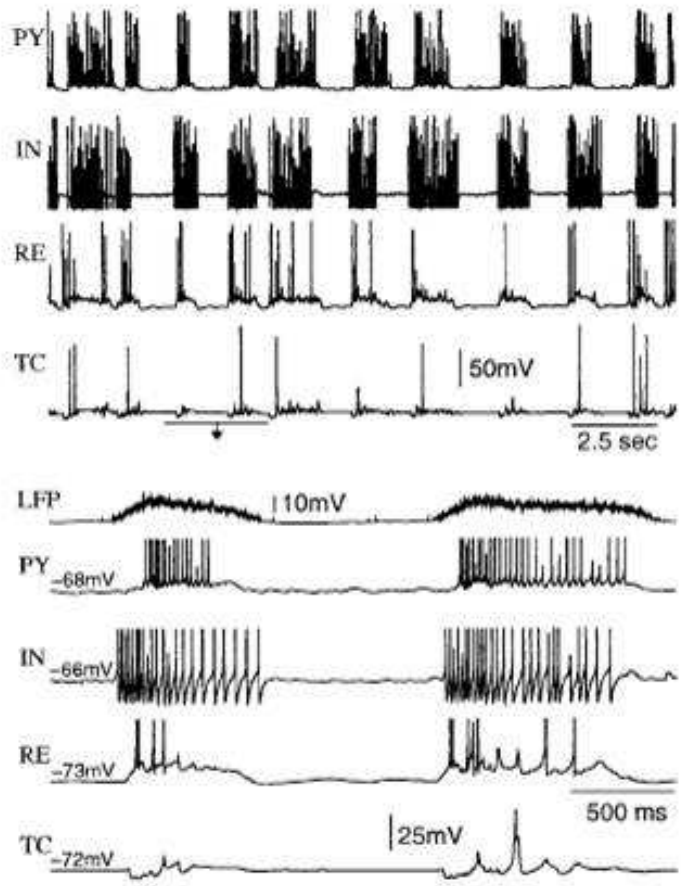

Figure 7. Membrane potential traces of individual *PY, IN, RE,* and *TC* cells from the network in Figure 6. Spontaneous firing in the PY–IN network initiated waning spindles in the RE–TC network. The spindles in TC cells usually started with two to three cycles of subthreshold (no spikes) oscillations mediated by inhibitory input from RE neurons.

Figure 4.7 – *Obtained result by authors [Bazhenov et al., 2002].*

sodium current and depolarized the membrane of cortical pyramidal (PY) cells sufficiently for spike generation. This triggered the active phase, which was maintained by lateral PY-PY excitation and persistent sodium current. Progressive depression of the excitatory interconnections and activation of Ca^{2+}-dependent K^+ current led to termination of the 20-25 Hz activity after 500-1000 msec. Including thalamic relay (TC) and thalamic reticular (RE) neurons in the model increased the duration of the active epochs up to 1-1.5 sec and introduced waning spindle sequences. An increase in acetylcholine activity, which is associated with activated states, was modelled by the reduction in the K^+ leak current in PY and TC cells and by a decrease in intracortical PY-PY synaptic conductances. These changes eliminated the hyperpolarizing phases of network activity and transformed cortical neurons to tonic firing at 15-20 Hz. In fig. 4.7, the obtained result by authors is shown. In this figure, we can remark that the LFP reflects very well the creation of EEG shown in fig. 4.2.

4.3.2 Implementation

As mentioned before, the model consists of four layers of neurons, and the propotion of the number of cells are: N PY, $M = N/4$ IN, $L = N/2$ RE and $L = N/2$ TC cells [Bazhenov et al., 2002]. The synaptic connections between neurons are represented in fig. 4.8, and its adjacency matrix is shown in fig. 4.9.

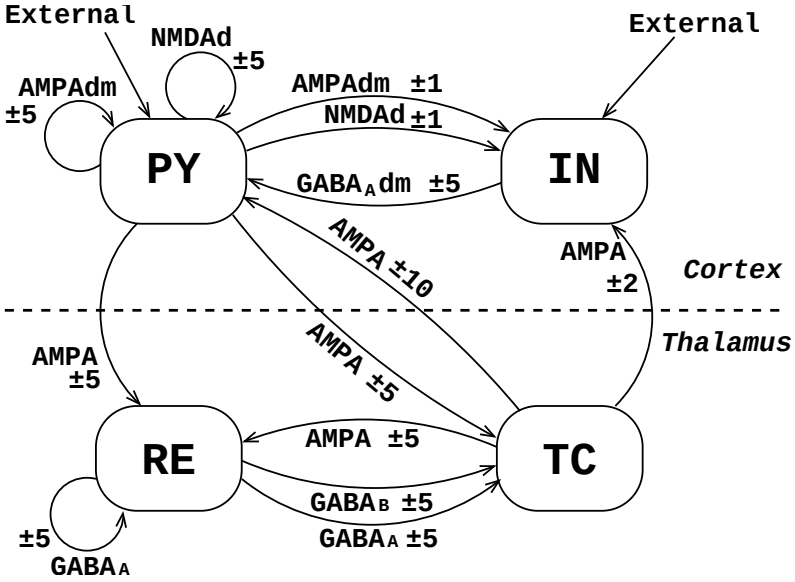

Figure 4.8 – *Synaptic connection between four kinds of neurons. The numbers indicate the outdegree of each neuron for each kind of synapse, while "External" represents a fixed current stimulating the neurons. The lower case d which is next to NMDA connections indicates that short time depression is included in the model. Moreover, the lower case dm next to some AMPA and GABA$_A$ connections means that spontaneous miniature EPSPs or IPSPs are included in addition to the short term depression.*

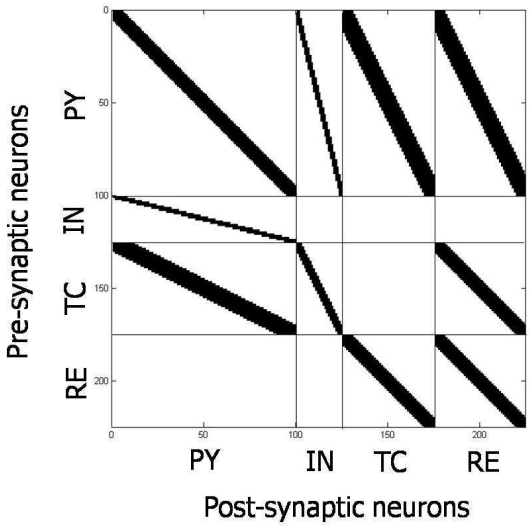

Figure 4.9 – *Adjacency matrix*

The α-amino-3-hydroxy-5-methyl-4-isoxazolepropionic acid (AMPA) and the N-methyl-D-aspartate (NMDA) receptors mediate fast and slow excitatory synaptic interactions respectively, while γ-aminobutyric acid type A ($GABA_A$) and type B ($GABA_B$) receptors mediate fast and slow inhibitory synaptic interactions respectively.

The kinetics of the thalamic neurons, RE and TC cells, are described by a single-compartment model as follows:

$$C_m \frac{dV}{dt} = -I_{leak} - I^{int} - I^{syn}, \tag{4.9}$$

where C_m is the membrane capacitance, V is the membrane potential, $I_{leak}(= g_L(V - E_L))$ is the leakage current, I^{int} is the sum of active intrinsic currents and I^{syn} is the sum of synaptic currents. As intrinsic currents, for both RE and TC cells, a fast sodium (Na^+) current, I_{Na}, a fast potassium (K^+) current, I_K, a low-threshold Ca^{2+} current, I_T, and a potassium leak current are considered. A hyperpolarization-activated cation current, I_h, is also included in TC cells [Bazhenov et al., 1998]. Here below, we show equations describing the intrinsic current of each cell with more details:

$$\begin{aligned} I^{int}_{RE} &= g_{Na}(V - E_{Na}) + g_K(V - E_K) + g_T(V - E_T) + g_{KL}(V - E_{KL}), & (4.10)\\ I^{int}_{TC} &= g_{Na}(V - E_{Na}) + g_K(V - E_K) + g_T(V - E_T) + g_h(V - E_h) \\ &\quad + g_{KL}(V - E_{KL}), & (4.11) \end{aligned}$$

where, g_{Na} ,g_K, g_T and g_h are voltage and time dependent conductance. g_{KL} is voltage-independent. E_* are reversal potentials.

The kinetics of the PY and IN cells are described by a two-compartment model [Mainen and Sejnowski, 1996] as follows:

$$C_m \frac{dV_D}{dt} = -I_{leak} - \frac{g}{S_D}(V_D - V_S) - I^{int}_D - I^{syn},$$

$$\frac{g}{S_S}(V_S - V_D) = -I^{int}_S, \tag{4.12}$$

where C_m and I_{leak} are the membrane capacitance and the leakage current of the dendritic compartment, V_D and V_S are the membrane potentials of dendritic and axosomatic compartments, I^{int}_D and I^{int}_S are the sums of active intrinsic currents in each compartment, S_D and S_S are the areas of each compartment, I^{syn} is the sum of synaptic currents, and g is the conductance between the two compartments. As axosomatic intrinsic currents, for both PY and IN cells, a high density fast Na^+ current (I_{Na}) and fast delayed rectifier K^+ current (I_K) are considered. For dendritic intrinsic currents in both cells, a low density fast Na^+ current, a slow voltage-dependent noninactivating K^+ current (I_{Km}), a slow Ca^{2+}-dependent K^+ current (I_{KCa}), a high-threshold Ca^{2+} current (I_{HVA}), and a K^+ leak current are included. For PY cells, a persistent Na^+ current ($I_{Na(p)}$) is added to both compartments [Timofeev et al., 2000].Here below, we show the equations describing the

intrinsic current of each cell and each compartment with more details:

$$
\begin{aligned}
I_{PY_S}^{int} &= g_{Nas}(V_S - E_{Nas}) + g_K(V_S - E_K) + g_{Naps}(V_S - E_{Naps}), && (4.13)\\
I_{PY_D}^{int} &= g_{Nad}(V_D - E_{Nad}) + g_{HVA}(V_D - E_{HVA}) + g_{KCa}(V_D - E_{KCa}) \\
&\quad + g_{Km}(V_D - E_{Km}) + g_{KL}(V_D - E_{KL}) + g_{Napd}(V_D - E_{Napd}), && (4.14)\\
I_{IN_S}^{int} &= g_{Nas}(V_S - E_{Nas}) + g_K(V_S - E_K)), && (4.15)\\
I_{IN_D}^{int} &= g_{Nad}(V_D - E_{Nad}) + g_{HVA}(V_D - E_{HVA}) + g_{KCa}(V_D - E_{KCa}) \\
&\quad + g_{Km}(V_D - E_{Km}) + g_{KL}(V_D - E_{KL}), && (4.16)
\end{aligned}
$$

where, g_* except g_{KL} are voltage and time dependent conductance. g_{KL} is voltage-independent. E_* are reversal potentials.

Each intrinsic current is modeled as

$$I_i^{int} = \bar{g}_i m_i^{M_i} h_i^{H_i} (V - E_i), \tag{4.17}$$

where $\bar{g}_i$ is the maximal conductance , m_i and h_i represent the fraction of open and non-inactivated gates respectively, M_i and H_i are exponents which indicate the number of gates in each ion channel, and E_i is the reversal potential of the i-th channel.

The synaptic currents through AMPA, NMDA and $GABA_A$ channels are also modeled similarly [Destexhe et al., 1994],

$$I_i^{syn} = \bar{g}_i r_i (V - E_i), \tag{4.18}$$

where $\bar{g}_i$ is the maximal conductance , r_i is the fraction of receptors in the open state, and E_i is the reversal potential of the i-th receptor. The activation parameter r follows the first-order kinetics

$$\frac{dr}{dt} = \alpha[T](1 - r) - \beta r, \tag{4.19}$$

where α and β are voltage-independent forward and backward rate constants, and $[T]$ is the transmitter concentration, represented by a pulse after each presynaptic spike. The $GABA_B$ receptors are modeled by a higher-order reaction scheme that takes into account the activation of K^+ channels by G-proteins. Here below, the synaptic currents of each cell are shown:

$$
\begin{aligned}
I_{RE}^{syn} &= \Big(\bar{g}_{GABAA}^{RE,RE} \cdot r_{GABAA}^{RE,RE} \cdot (V - E_{GABAA}^{RE,RE}) + \bar{g}_{AMPA}^{TC,RE} \cdot r_{AMPA}^{TC,RE} \cdot (V - E_{AMPA}^{TC,RE}) \\
&\quad + \bar{g}_{AMPA}^{PY,RE} \cdot r_{AMPA}^{PY,RE} \cdot (V - E_{AMPA}^{PY,RE})\Big) \cdot \frac{1}{S_{RE}}, && (4.20)\\
I_{TC}^{syn} &= \Big(\bar{g}_{GABAA}^{RE,TC} \cdot r_{GABAA}^{RE,TC} \cdot (V - E_{GABAA}^{RE,TC}) \bar{g}_{GABAB}^{RE,TC} \cdot \frac{(s_{GABAB}^{RE,TC})^n}{(s_{GABAB}^{RE,TC^n})^n + K_d} \cdot (V - E_{GABAB}^{RE,TC}) \\
&\quad + \bar{g}_{AMPA}^{PY,TC} \cdot r_{AMPA}^{PY,TC} \cdot (V - E_{AMPA}^{PY,TC})\Big) \cdot \frac{1}{S_{TC}}, && (4.21)
\end{aligned}
$$

$$
\begin{aligned}
I_{PY}^{syn} &= \Big(\bar{g}_{AMPAd}^{PY,PY} \cdot r_{AMPAd}^{PY,PY} \cdot (1 - D_{AMPAd}^{PY,PY}) \cdot (V - E_{AMPAd}^{PY,PY}) \\
&\quad + \bar{g}_{NMDAd}^{PY,PY} \cdot r_{NMDAd}^{PY,PY} \cdot fn \cdot (1 - D_{NMDAd}^{PY,PY}) \cdot (V - E_{NMDAd}^{PY,PY}) \\
&\quad + \bar{g}_{GABAAd}^{IN,PY} \cdot r_{GABAAd}^{IN,PY} \cdot (1 - D_{GABAAd}^{IN,PY}) \cdot (V - E_{GABAAd}^{IN,PY}) \\
&\quad + \bar{g}_{AMPA}^{TC,PY} \cdot r_{AMPA}^{TC,PY} \cdot (V - E_{AMPA}^{TC,PY})\Big) \cdot \frac{1}{S_{D,PY}}, \qquad (4.22) \\
I_{IN}^{syn} &= \Big(\bar{g}_{AMPAd}^{PY,IN} \cdot r_{AMPAd}^{PY,IN} \cdot (1 - D_{AMPAd}^{PY,IN}) \cdot (V - E_{AMPAd}^{PY,IN}) \\
&\quad + \bar{g}_{NMDAd}^{PY,IN} \cdot r_{NMDAd}^{PY,IN} \cdot fn \cdot (1 - D_{NMDAd}^{PY,IN}) \cdot (V - E_{NMDAd}^{PY,IN}) \\
&\quad + \bar{g}_{AMPA}^{TC,IN} \cdot r_{AMPA}^{TC,IN} \cdot (V - E_{AMPA}^{TC,IN})) \cdot \frac{1}{S_{D,IN}}, \qquad (4.23)
\end{aligned}
$$

where, D is depression parameter, s_{GABAB} is activation parameter which follows higher-order reaction scheme, K_d is dissociation constant of the binding of G on the K^+ channel, and f_n is magnesium block parameter.

A simple phenomenological model was used to describe short time depression of intracortical excitatory connections [Abbott et al., 1997][Tsodyks and Markram, 1997][Galarreta and Hestrin, 1998][Timofeev et al., 2000]. Spontaneous miniature EPSPs and IPSPs followed the same equations as the regular PSPs, and their arrival times were modelled by Poisson processes [Stevens, 1993].

For more detailed description of the model with parameter sets, please refer to the appendix.

4.3.3 Results

Having difficulties to set parameters and equations because of unclear indications of the creator of the model, after several months, collaborating with Borja Ibarz, we reproduced a simulator of this model of Bazhenov [Bazhenov et al., 2002], Hodgkin-Huxley based thalamocortical network model in C language. We used the same number of cells (100 PY, 25 IN, 50 TC, 50 RE) and mostly the same value of parameters (conductances, reversal potentials, etc.) as in [Bazhenov et al., 2002] and performed the simulation for 10 sec length. The integration was performed by the first-order numerical method, "Exponential Euler", with a time step of 0.02 msec. This method is commonly used to simulate models that interact in real time with neurophysiological experiments, and is able to speed up the computation. The program was compiled using a GCC compiler on the PC with Intel(R)Xeon(TM)CPU 2.66GHz 2.66GHz, 200GB RAM. A network of 225 cells took ∼20 min of computation to simulate 10 sec of real time. Our simulator seems to perform better than the original program.

Fig.4.10 shows somatic membrane potentials of PY, IN, TC and RE cells. First indexed neuron is displayed for each kind. As the connection is very complicated, it is impossible to see directly the effect of each synaptic input, but we can remark that the coherence of the period of active state among four neurons are relatively high.

Fig.4.11 shows the spontaneous activity in the PY cells. In this figure, for each neuron, the spikes are marked as a small point. From this, we can observe the propagation of activities among them and form a stripe pattern with respect to time. According to the

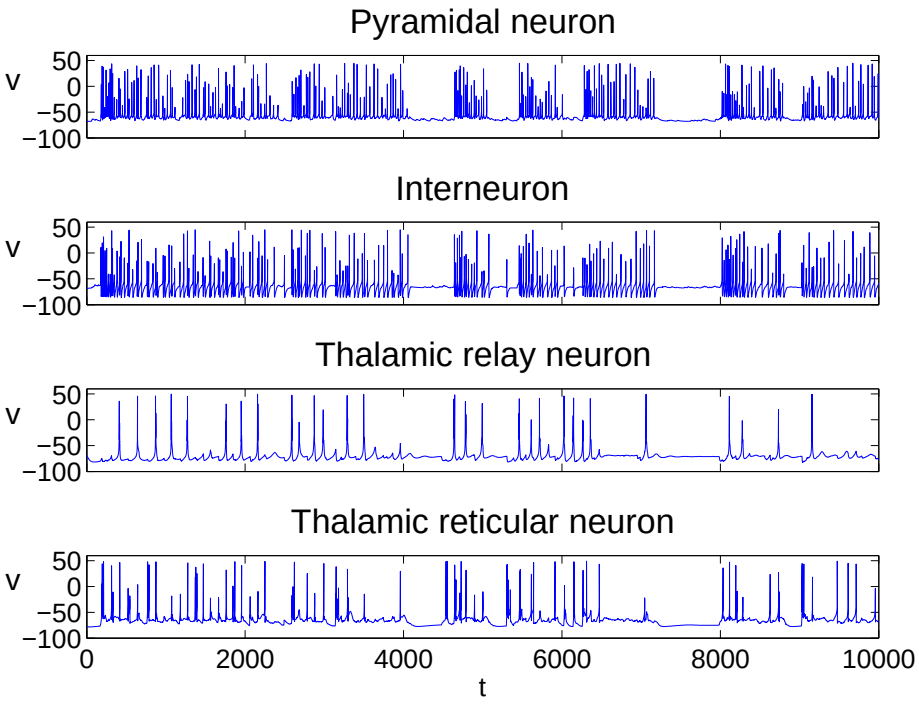

Figure 4.10 – *Membrane potentials (mV) of each individual pyramidal neuron (PY), interneuron (IN), thalamic relay neuron (TC) and thalamic reticular neuron (RE) for 10 sec. Horizontal axis is time (ms).*

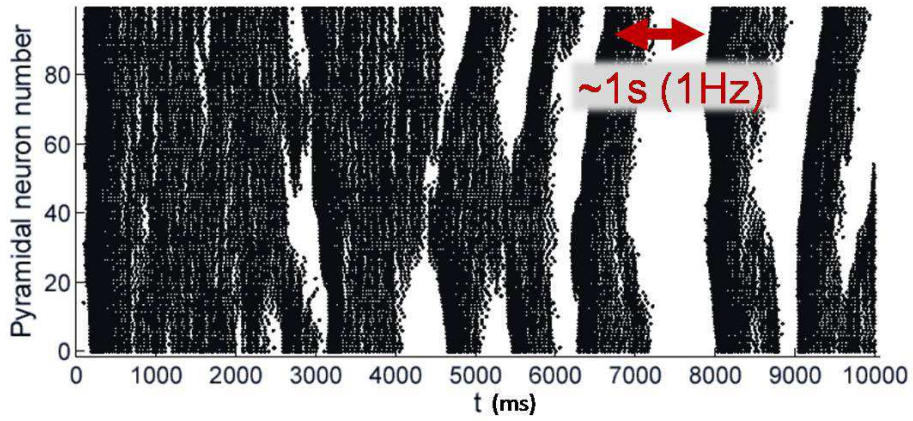

Figure 4.11 – *Spontaneous activity of 100 PY cells for 10 sec. For each neuron, the spikes are marked as a small point.*

parameter setting procedure, it seems that this pattern is induced by the depression of the cortical neurons. But this assumption remains to be verified. As we mentioned in subsec. 4.2.2, EEG reflects the global synchrony of cortical neurons, more precisely, the amplitude of EEG returns a high value when a lot of PY neurons are in spiking activities and, on the contrary, returns a low value during silent activities. From fig. 4.11, we can perceive that the frequency of EEG is about 1 Hz which matches exactly the frequency of δ-waves.

4.4 Effect of anaesthesia on the model

As we succeeded to create a brain simulator from which we can obtain δ-waves, let us move to the next step, the consideration of the effect of anæsthesia on this brain model.

It is known that both volatile and intravenous anesthetics modulate the activity of a variety of ion channels and synaptic receptors of neurons [Yaksh et al., 1998]. However, because of the lack of basic understanding of the workings of general anesthesia at the system level, it is very difficult to determine how microscopic modulation of ion activities can produce general anesthesia. Moreover, the effects of anesthesia differ from one kind of anesthetic to the other. Intravenous anesthetics act on the synaptic receptors, especially on the $GABA_A$ receptors. Volatile anesthetics also seem to act on this $GABA_A$ receptors, but their effect is not completely understood. For instance, concerning our employed anæsthetics on human, we found a paper describing their effect on this $GABA_A$ receptors [Grasshoff and Antkowiak, 2004]. This paper reports that both Propofol and Sevoflurane reduce spontaneous action potential firing of neurons, where the effects of Sevoflurane were mediated predominantly by glycine receptors(45%) and $GABA_A$ receptors (38%), whereas Propofol acted almost exclusively via $GABA_A$ receptors (96%). See fig. 4.12. The modulation of ion channels, among which Ca^{2+} channels are most prominent, is also considered relevant for general anesthesia. However, it is necessary to investigate how the different anesthetic effects are integrated to produce it, but this is a future investigation.

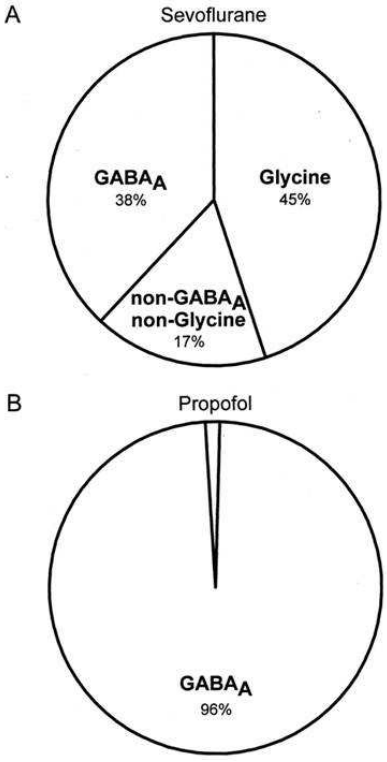

Estimated contributions of molecular targets to the effects of sevoflurane (*A*) and propofol (*B*) on the mean firing rate. Concentrations of 0.5 minimum alveolar concentration sevoflurane (corresponding to 0.175 mm) and 0.5 µm propofol were used because, at these concentrations, both anesthetics depressed spontaneous network activity by approximately 60% and were therefore equieffective. The effects of sevoflurane and propofol on spontaneous action potential firing were measured in the absence or presence of bicuculline (100 µm), strychnine (1 µm), or a combination of both antagonists. Effects of the anesthetics in the absence of bicuculline and strychnine were taken as 100%. Bicuculline decreased sevoflurane-induced depression of ongoing activity by approximately 38%; suppression of action potential firing by propofol was almost completely abolished (γ-aminobutyric acid type A [GABAA]). Strychnine reduced the effects of sevoflurane on the mean firing rate by 45% and did not affect the efficacy of propofol in reducing neuronal activity (glycine).

Figure 4.12 – *Percentage of $GABA_A$ mediation on the effect of Sevofluane and Propofol [Grasshoff and Antkowiak, 2004].*

Neural models are used to link the modulation of ion channel activity due to anesthetics with overall behavior at the system level using computer simulations and analysis of their mathematical structure [Koch and Segev, 1998]. Gottschalk and Haney [Gottschalk and Haney, 2003] examined the response of four simple neural models to the concentration of anesthetics. In each of the models, the inhibitory effects under general anesthesia which decrease the influx of the Ca^{2+} channels are approximated by a decrease in the maximal Ca^{2+} conductance, and an increase of the inhibitory chloride current which evokes the prolongation of the open time of the $GABA_A$ channels by a decrease of the rate of channel closure or an increase of the rate of channel opening in the equations describing $GABA_A$ channel dynamics(eq.4.19). According to the results of [Gottschalk and Haney, 2003], we deduced that we can not attribute the effects of anesthetics to one simple change of parameter. In fact, one single neuron model shows a decrease in the frequency of neuron activity as a function of a decrease in maximum conductance of Ca^{2+} channels, while another model shows an increase in frequency accompanied by a change from a bursting pattern to tonic firing. One network model reflects a decrease of the closing rate of $GABA_A$ channels in the increased amplitude and decreased frequency of the average membrane potential, indicating stronger synchrony of the neurons. Meanwhile, another neural network model doesn't show an increase of synchrony with a decrease of the closing rate but it does show greater degrees of synchronous behavior when the rate of $GABA_A$ channel opening is increased.

Consequently, it is imperative to investigate the reaction of our simulation model to changes of the parameters reflecting the effect of anesthesia.

4.4.1 Effect on Ca^{2+} channel

The inhibitory effect on Ca^{2+} channels, which changes when anesthetic concentration is increased, is frequently modeled with the Hill equation

$$Inhibition = \frac{EC_{50}^n}{[A]^n + EC_{50}^n}, \tag{4.24}$$

where $[A]$ is the anesthetic concentration, n is the Hill coefficient, and EC_{50} is the anesthetic concentration at which channel activity is inhibited by 50%. This leads to the following modulation of maximal conductance which is now effectively modeled as a function of anesthetic concentration:

$$g_i = \bar{g}_i \frac{EC_{50}^n}{[A]^n + EC_{50}^n} m_i^{M_i} h_i^{H_i}, \tag{4.25}$$

4.4.2 $GABA_A$

Unfortunately, the effects on the $GABA_A$ receptors cannot be modeled uniquely like the Ca^{2+} channels as a function of anesthetic concentration because of the complex reaction to the anesthetic quantity which differs from kind to kind. The most pronounced effect, the prolongation of the open time of the $GABA_A$ channels, is modeled by a decrease of β and an increase of α in eq.(4.19) as mentioned before. For some anesthetics, detailed quantitative descriptions of how these parameters vary with anesthetic concentration have been obtained, but still the descriptions for the anesthetics used in our experiments must be defined.

4.4.3 Results

We set the parameters used to reproduce the model of Bazhenov as a default, using the same initial conditions, we perform simulations on the thalamocortical assembly model varying simply the parameter of maximal conductance of Ca^{2+} channels, since we don't have experimental measurements of the concentration of the anesthetics around the neurons, or varying closing/opening rate of $GABA_A$ receptors from one simulation to another (See fig. 4.14 for the exact position of the parameters change in the model), and try to figure out how the collective behavior of PY neurons, which should be interpreted as a field potential analogous to the EEG that is measured from experiments can be modified according to these parameter changes.

In fig. 4.15 we whow the results obtained changing the maximal conductances of Ca^{2+} channels, more precisely, $\bar{g}_T$ in both RE and TC cells and $\bar{g}_{HVA}$ in PY and IN cells are decreased by the same percentage in each simulation. From this figure, we can remark that the number of white stripes increases as the values of $\bar{g}$ decrease, which makes sense because weakening Ca^{2+} currents has an inhibitory effect on neurons. This has as a consequence an increase in global frequency, which is not observed in the experiments. Therefore, further frequency analysis on the mean field of PY neurons is necessary to conclude about that. Moreover, we can also perceive that the synchrony among neurons becomes stronger with the change of this parameter since stripes are more limited by vertical lines when $\bar{g}$ is small.

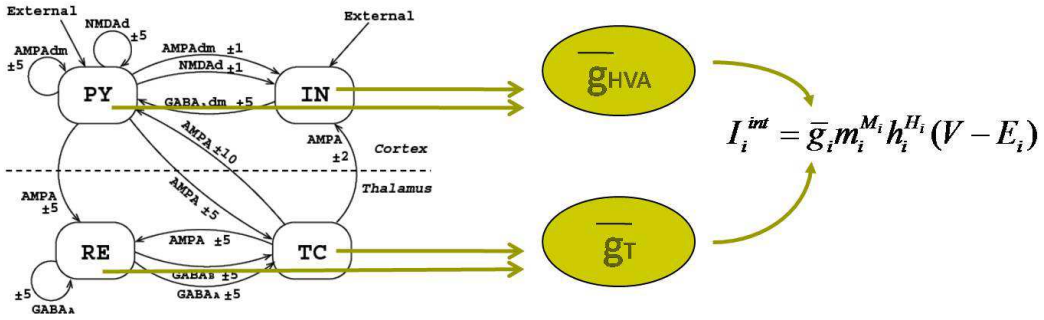

Figure 4.13 – *The implementation of the effect of the anæsthesia on Ca^{2+} channels of the model.*

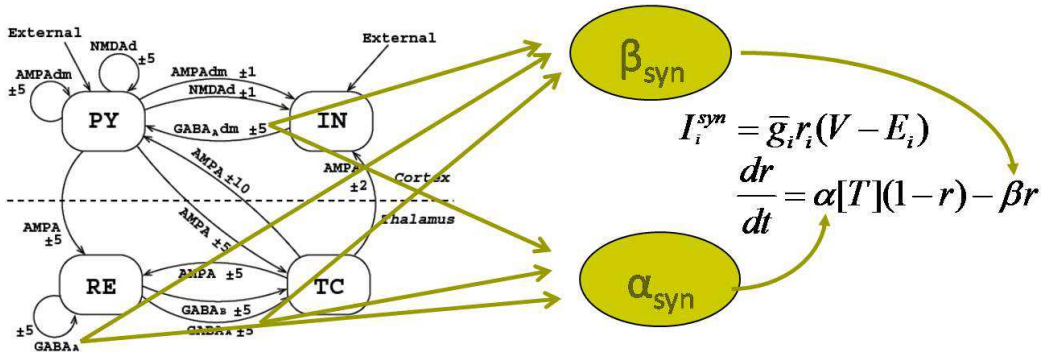

Figure 4.14 – *The implementation of the effect of the anæsthesia on $GABA_A$ synaptic receptors of the model.*

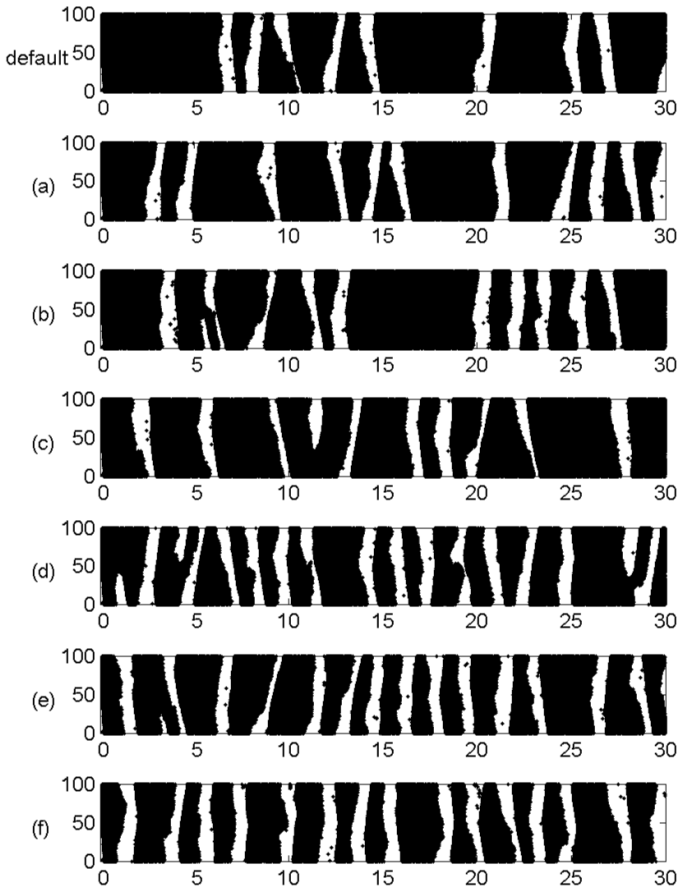

Figure 4.15 – *Spontaneous activity of 100 PY cells depending on maximal conductance $\bar{g}$ of calcium channels ($\bar{g}_{T_{RE}}$, $\bar{g}_{T_{TC}}$, $\bar{g}_{HVA_{PY\&IN}}$). The x axis represents time(s) and the y axis is the PY neuron index. At the top, the default plot is shown for reference: (a)5% less than default $\bar{g}$, (b)10% less, (c)20% less, (d)40% less, (e)60%less, and (f)80% less.*

As a first exploration of the effects on $GABA_A$ channels, we performed simulations decreasing the channel closing rate β in all $GABA_A$ connections by the same ratio, and show the obtained results in fig. 4.16. From this figure, we can see that the effect of inhibition is so powerful that at a certain value of β the coherent spiking activity in the network becomes unsustainable. However, a small decrease of β actually increases the synchrony of neurons.

In fig. 4.17, we show the results obtained in simulations in which we increase the $GABA_A$ channel opening rate α. On this figure, as in the case of β, the network is inhibited by the prolongation of the opening time of the $GABA_A$ channels and duration of silent states which is represented by the white stripes increases. Moreover, we can observe that the neurons are more synchronized due to this increment for the same reason as before. However, the difference among the Fig.4.17(c)(d) and (e) is not large so that the change in the global reaction to the increase of α seems to have some kind of threshold effect.

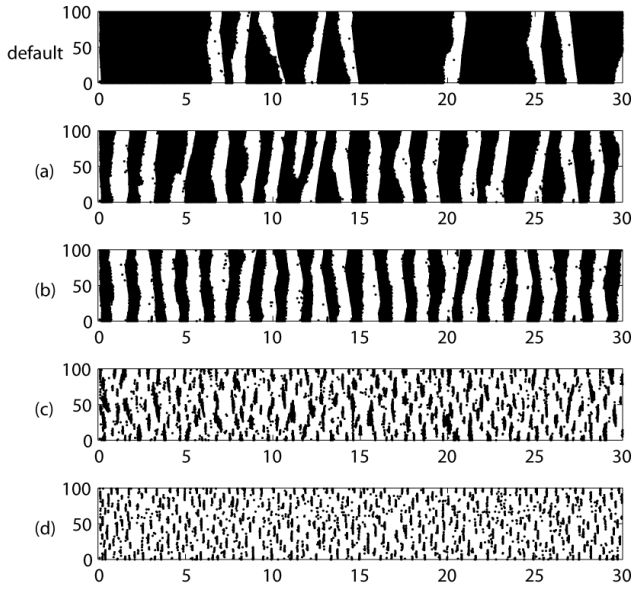

Figure 4.16 – *Spontaneous activity of 100 PY cells depending on $GABA_A$ channel closing rate β. The x axis represents time(s) and the y axis is the PY neuron index. At the top, the default plot is shown for reference: (a)7/8 times default β, (b)3/4 times, (c)1/2 times, and (d)1/4 times.*

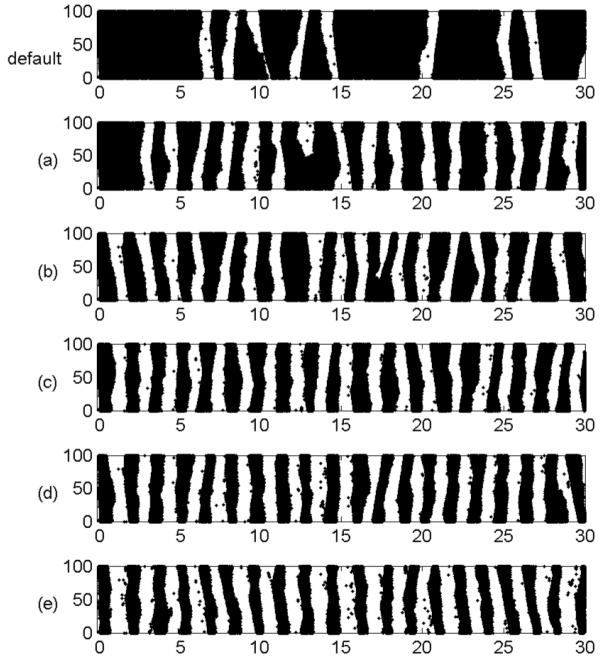

Figure 4.17 – *Spontaneous activity of 100 PY cells depending on $GABA_A$ channel opening rate α. The x axis represents time(s) and the y axis is the PY neuron index. At the top, the default plot is shown for reference: (a)1.25 times default α, (b)1.5 times, (c)1.75 times, (d)2 times, and (e)5 times.*

The conclusion on this study on the effect of anæsthesia is: All the results obtained with different parameter changes have shown effective suppression of the spiking activities by the reinforcement of the inhibition induced by all changes of the parameters, but the degree of the reaction, i.e., the individual/global behavior of the PY neurons is different in each case.

4.5 Understanding and analysis of the model

As the thalamocortical model on which we based for all modelling studies was not created by ourselves, in order to continue with it in the future, we proceeded to the study on the more detailed structure and functioning of the reproduced model described in sec. 4.3. Unfortunately, we saw that the equations describing each of neurons were very complex, and moreover their synaptic connections were also very complex, such that we realized that mathematical analysis, like stability analysis etc., was too difficult to finish, in a short period, before the end of my thesis. Consequently, from the complex network theory point of view, we started with the study on the size of network. And after that, we continued with studying some properties of thalamic neurons and cortical neurons to better understand the basic components of the model.

4.5.1 Size of network

What happens when changing the size of the network? To answer this question, We made simulations of 5min length with different sizes of the network, i.e., $\frac{1}{5}\times, \frac{3}{5}\times, 1\times$(default), $2\times, 4\times, 6\times, 8\times$ and $10\times$ bigger than the size of the original network (100PY, 25IN, 50TC and 50RE)* and investigated the collective behavior of the PY neurons. Here, the degree of local connection was kept unchanged as shown in fig. 4.8. In fig. 4.18, we show the obtained results for 20sec, taken at 160sec from the beginning. From this figure, we can see that the larger the size of the network is, the more the vertical white stripes disappear. This means that global synchrony among PY neurons is not preserved in larger sizes. To check the local synchrony, we plot the same results with the same number of PY neurons in fig. 4.19. From this figure, we can observe that the structure of the collective spiking activities are very similar in all sizes, such that we can confirm that the local synchrony is not influenced by the size of the network.

So, how about the frequency of the mean field? Is the δ-oscillation preserved? To answer these questions, we calculated the mean of the obtained time-series (whole 5min-length) of the membrane potentials of the PY neurons, and calculated the frequency spectrum of them. For this frequency analysis, larger sizes of the network, namely $40\times, 60\times$ and $100\times$(only 2min instead of 5min because of the computation) are added to the study. From the obtained results shown in fig. 4.20, small increase in the main frequency towards 1 Hz can be found between $\frac{1}{5}\times$ and $1\times$, but for larger sizes, the main frequency remains at around 1Hz. As a result, we can conclude that the δ-waves are not influenced either by the size of the network. Just to remark, we can also observe a peak at the very small frequency close to 0Hz in all sizes of the network, but we don't know the reason of this presence.

*Here, when enlarging the network, the proportion of the number of neurons among 4 neurons is kept as $PY : IN : TC : RE = 4 : 1 : 2 : 2$

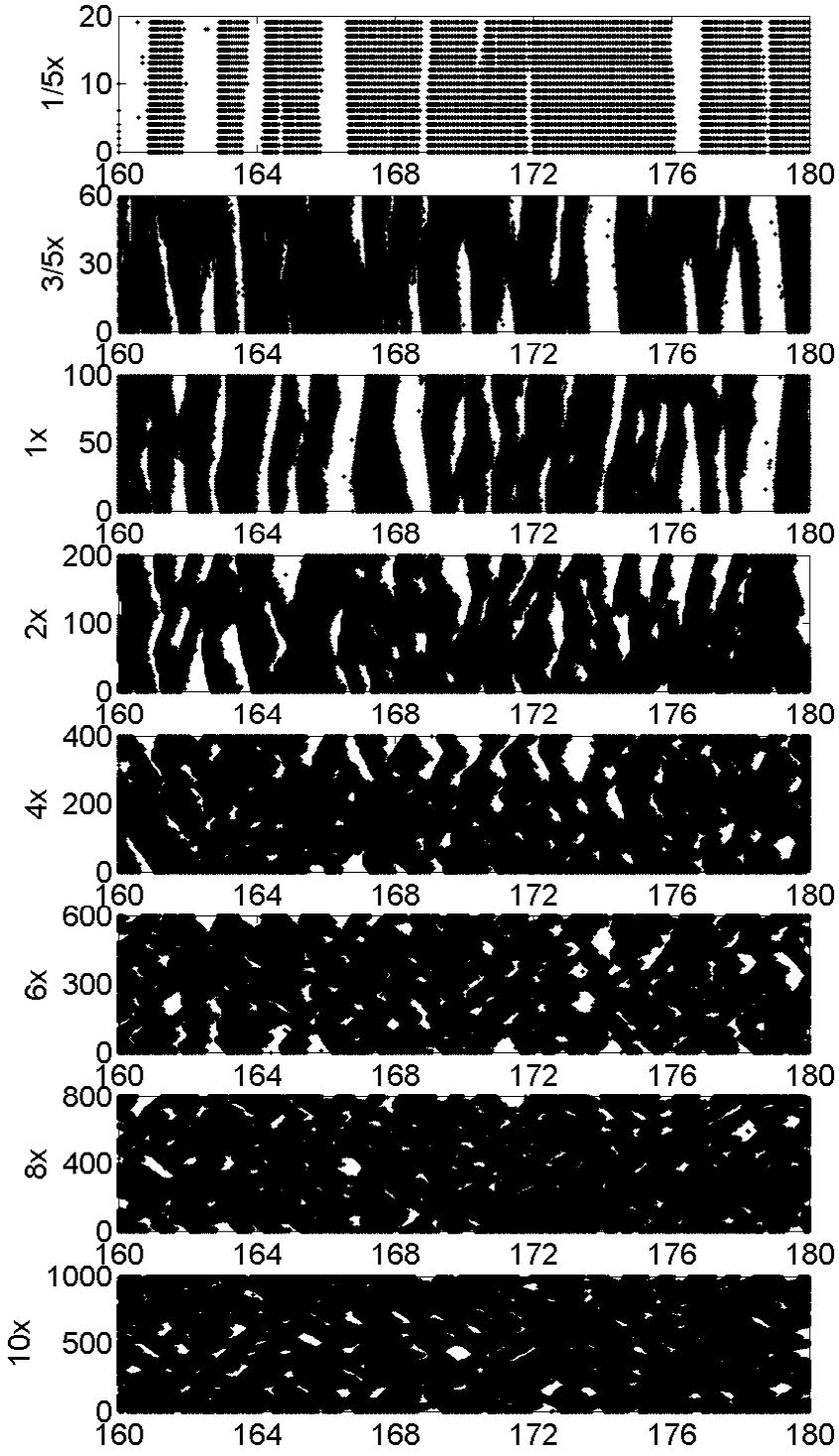

Figure 4.18 – *Spontaneous activity of PY cells with different network size. The x axis represents time(s) and the y axis is the PY neuron index. The default plot (1x) is shown for reference.*

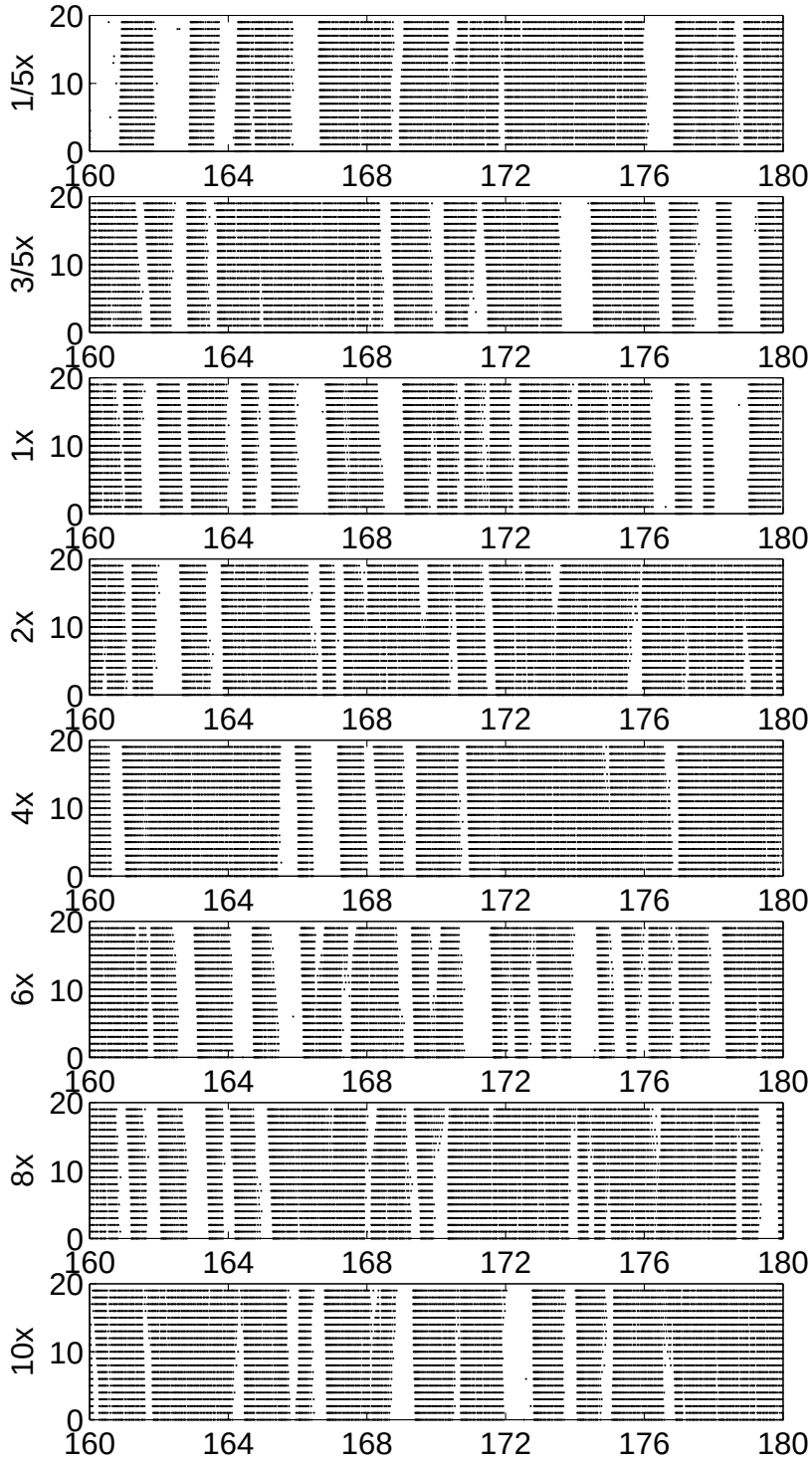

Figure 4.19 – *Spontaneous activity of PY cells with different network size with same number of PY neurons. The x axis represents time(s) and the y axis is the PY neuron index.*

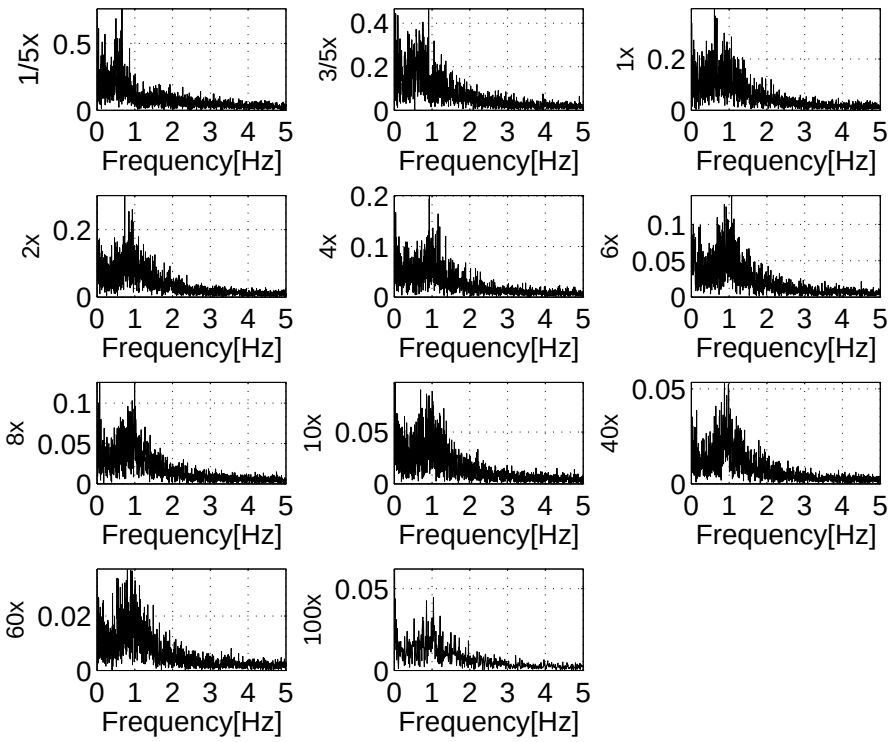

Figure 4.20 – *Power spectrum of the mean field of PY cell membrane potentials with different network size.*

From curiosity and because of lack of time, just to see the reaction of the model to the change of the degree of connections, one simulation with 6× larger size of the network with 6× larger vertex degrees was launched. The obtained result is shown in fig. 4.21. In this figure, the spiking activities of the other neurons, i.e. IN, TC and RE, are also shown in order to see if the periods of the active states in each of four kinds of neurons still coincidence. Comparing fig. 4.21 with fig. 4.22 which is the result of the previously obtained 6 times larger size of network*, we can see the spread of the local synchrony to the global synchrony with larger vertex degrees. However, from their similar spike propagation form, we can confirm that the coincidence of the active period among four kinds of neurons is preserved. Furthermore, from the power spectrum of the mean field, we found not only the main frequency around 1Hz but also another main frequency around 0.5Hz which is still a δ-wave range. Just to remark, here again, a very small frequency component close to 0Hz can be also observed (See fig. 4.23). This analysis of the vertex degrees stands just on one simulation such that further investigation is necessary in the future.

4.6 Studies on the properties of the neurons

To understand the model from the basic components of the model, i.e. neurons, we studied the properties of the neurons from the book of Destexhe [Destexhe and Sejnowski, 2001].

*Just to insist, here, the number of the vertex degrees is unchanged.

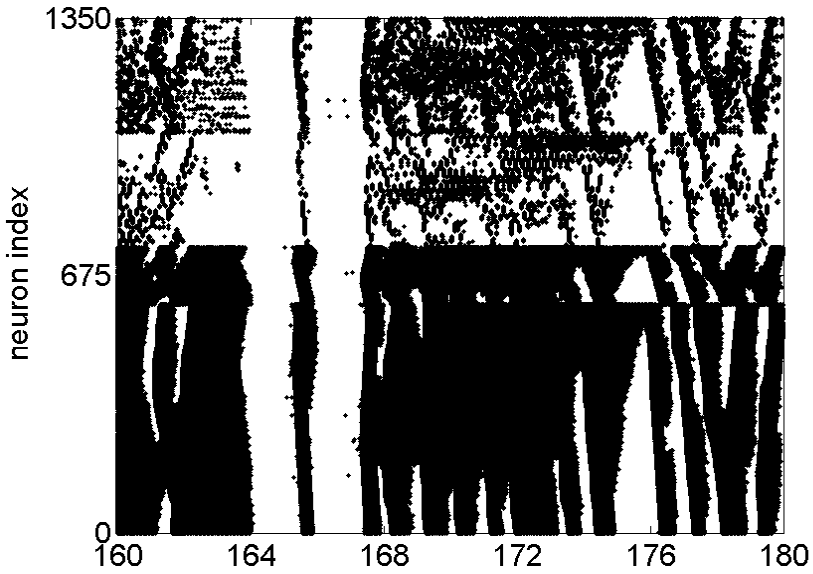

Figure 4.21 – *Spontaneous activity of neurons. The size of the network as well as the vertex degrees are 6 times larger. The x axis represents time(s) and the y axis is the neuron index: PY(0-599), IN(600-749), TC(750-1049) and RE(1050-1349).*

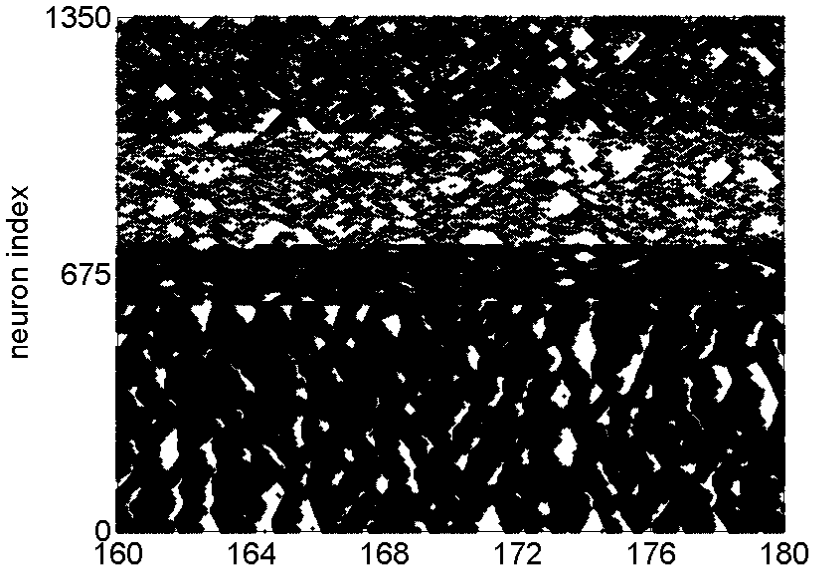

Figure 4.22 – *Spontaneous activity of neurons. The size of the network is 6 times larger. The x axis represents time(s) and the y axis is the neuron index: PY(0-599), IN(600-749), TC(750-1049) and RE(1050-1349).*

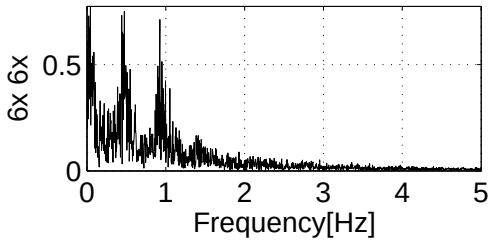

Figure 4.23 – *Power spectrum of the mean field of PY cell membrane potentials for the network with 6 times larger size and connections.*

Thalamic relay neuron (TC)

The Thalamic relay neurons, also called thalamocortical neurons (TC), assume important roles in relaying information in the brain. For instance, sensory inputs (visual, auditory and somatosensory) always first reach these TC neurons, and then these neurons in turn project to the sensory cortex. These TC neurons have properties that allow them to generate activity. There exist two different firing modes, namely "tonic mode" and "burst mode". In "tonic mode", near the resting membrane potential, a TC neuron fires train of action potentials at a frequency proportional to the amplitude of the injected current. This spiking action can be explained by the voltage-dependent Na^+ and K^+ currents (I_{Na} and I_K) that generate action potentials like many other kinds of neurons. In "burst mode", at hyperpolarized membrane potentials, a TC neuron fires high-frequency bursts of action potentials at the end of hyperpolarizing current injection. This rebound responses arise from a low-threshold Ca^{2+} current, called T-current (I_T). In addition to this prominent rebound-burst property, TC neurons can also generate sustained oscillations. This was confirmed from experiments, for instance, performed in cats in vivo with the observation of the clock-like rhythmicities in the δ frequency range (0.5-4Hz). These intrinsic slow oscillations consisted of rebound bursts recurring periodically, and are only possible when TC neuron is maintained at relatively hyperpolarized potentials. It was shown that these oscillations are generated by an interplay between I_T and the hyperpolarization-activated current (I_h) which is a mixed Na^+/K^+ cation current responsible for anomalous rectification in TC neuron. Furthermore, it was concluded that this interaction between I_T and I_h is sufficient to produce also the intrinsic waxing-and-warning oscillations*. In fig. 4.24, we summarized the properties of TC neuron relating with the equation of the TC neuron used in our model.

Thalamic reticular neuron (RE)

The thalamic reticular nucleus (RE) receives input from the cerebral cortex and TC neurons. Most input comes from collaterals of fibers passing through RE. Primary RE efferent fibers project to TC neurons, but never to the cerebral cortex. The precise function of RE neuron is not understood, although it has been suggested that RE neuron receives afferent input from the RE formation and in turn projects to TC neurons, regulating the flow of information through these to the cortex. In common with TC neurons, RE neurons

*Sequence of repeating active periods and silent periods. See fig. 4.24.

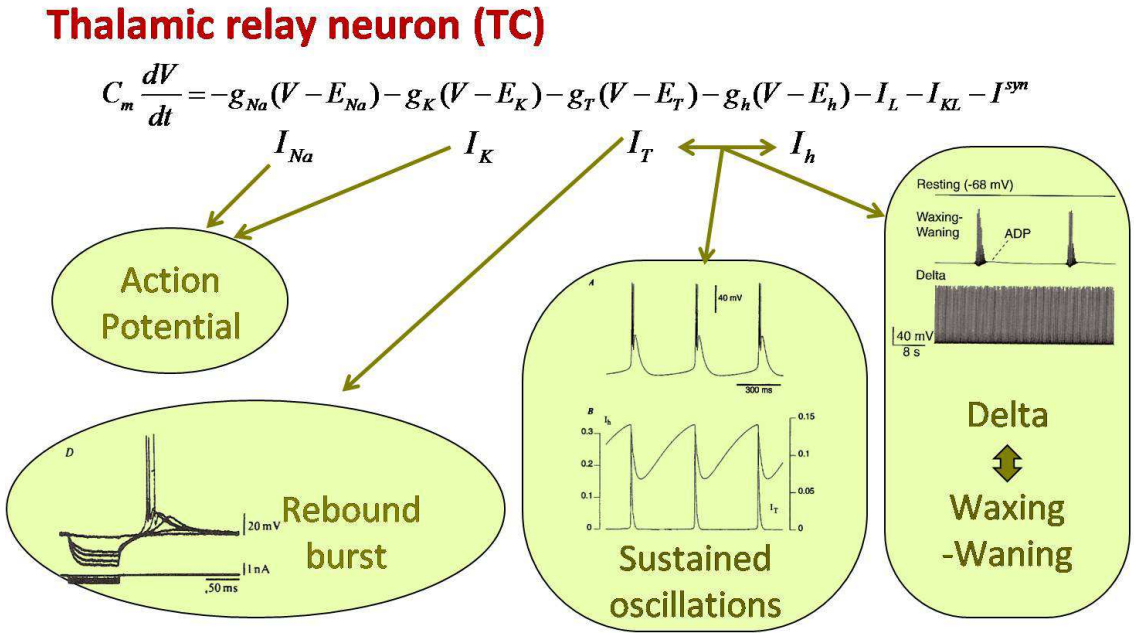

Figure 4.24 – *Properties of the TC neuron related with the equation of the model. All the figures inside of this figure show the experimental/simulation results related to their properties and they were taken from [Destexhe and Sejnowski, 2001]*

have two distinct firing modes, i.e. "tonic mode" and "burst mode". The mediated ionic current for each mode are the same as TC neurons, however the characterization of the I_h in RE is different from TC such that the rebound bursts generated by RE neurons are broader and the amplitude rise is slower than that of TC neurons, and also requires more current to be elicited than TC. This signifies that a RE neuron has slower kinetics and their activation happens over a more depolarized range of membrane potentials. In fig. 4.25, we summarized the properties of RE neurons relating with the equation of the RE neuron used in the model. To add, sustained oscillations is not possible in a single RE neuron, but connecting them with dense proximal $GABA_A$ connections, the oscillations become possible through a sequences of reciprocal inhibitory rebounds.

Cortical neurons

A pyramidal cell (or pyramidal neuron, or projection neuron) is a multipolar neuron located in the hippocampus and cerebral cortex. Pyramidal neurons compose approximately 80% of the neurons of the cortex, and release glutamate as their neurotransmitter, making them the major excitatory component of the cortex. Pyramidal cells are the output neurons of the cerebrum. They transmit signals to other parts of the CNS. Their axons have collaterals that synapse with other neurons in the cortex or in deeper regions of the brain.

The term interneuron is used for small, locally projecting neurons (in contrast to larger projection neurons with long-distance connections). Interneurons are typically inhibitory, and use the neurotransmitter GABA or glycine*.

*Description taken from Wikipedia.

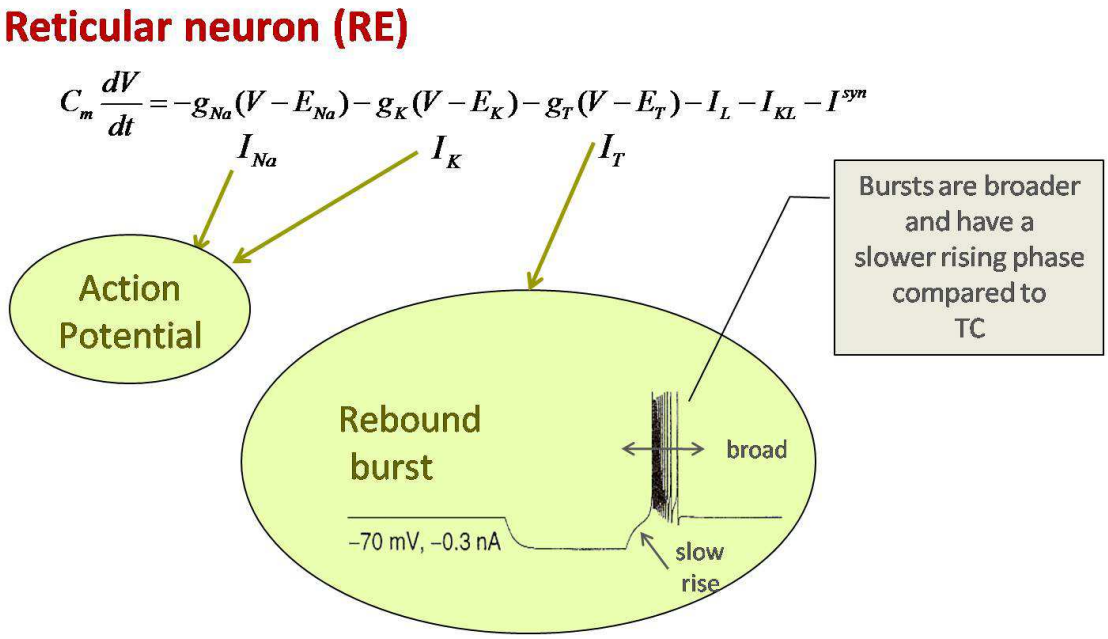

Figure 4.25 – *Properties of the RE neuron related with the equation of the model. The figure inside of this figure show the simulation results related to the rebound burst property and it was taken from [Destexhe and Sejnowski, 2001]*

No clear description of the properties of the cortical neurons was found in the book [Destexhe and Sejnowski, 2001], nor in the paper of our base model [Bazhenov et al., 2002]. However, from one reference paper [Mainen and Sejnowski, 1996], we understood that cortical neurons have several distinct firing patterns, such as spike trains, adaptive spike trains (fast spiking at the beginning and after become slower), spike after-depolarizations (ADPs) and bursting spike trains. The two-compartment model makes it possible to realize such spiking activities normally obtained with several compartments, by adapting just two parameters: the ratio of axo-somatic area to dendritic membrane area ($\rho = S_D/S_S$) and the conductance between the two compartments (g). When $g \to 0$, the two compartments are uncoupled and the firing frequency of each compartment is driven by the ionic current inside of each compartment. The firing frequency of the axo-somatic compartment, which is driven by the fast I_{Na} and I_K is much higher than for the dendritic compartment, which is driven by high-threshold Ca^{2+} current (I_{HVA}), Ca^{2+}-dependent K^+ current (I_{KCa}) and potassium M-current (I_{Km}). When fully coupled ($g \to \infty$) the amount of spike-frequency adaptation varies with ρ, but no bursting nor spike ADPs can be obtained. When partially coupled, changing either ρ or g, all kinds of firing patterns become possible.

To end, we verified that our simulated neurons have these described properties (cf. fig. 4.10). On the results of TC, we can observe tonic spiking at ∼1sec, rebound burst at ∼4.7sec. For RE, we can observe tonic spiking at ∼9.7sec, rebound burst at ∼4.5sec. For cortical neurons, bursting and adaptive spike trains can be observed clearly.

5 Conclusions

5.1 Summary and Discussion

IN this thesis, first we analyzed the experimental recordings on rats and human, namely the heart activity (ECG), the respiration and the cortical activity (EEG), to estimate the depth of anæsthesia and to investigate the interdependency changes depending on the deep-light change of anæsthesia. Furthermore, we investigated a model for the slow brain rhythms, i.e. δ-waves, and the way to include the effect of anæsthesia in this model.

5.1.1 Estimation of the depth of anæsthesia

From the obtained results on Ketamine-Xylazine anæsthetized rats, with the "S-estimator", it was found that the synchronization within the whole system suddenly decreases from the deep-light transition point, and thanks to it, we managed to detect this point precisely in time using a statistical assessment tool. Additionally, even in one of the groups of recordings, namely "Rats1", we pointed out the possibility to detect automatically this deep-light change point in real time with a small delay. On the contrary, no change was found in the synchronization exclusively between the three sub-systems with the "new S-estimator". However, questioning the difference between the original S-estimator and the new S-estimator and analyzing the time evolution of the embedding dimension (ED), which is the basic component of the "S-estimator", interestingly, an increase and a higher variation in the ED were found at the light stage on cortical activities (B) and heart activities (H). Furthermore, with the "coupling matrix" (CM) method, it was found that the coupling between H-Respiration (R) and B-R change and also their directions change at this transition point. On the other hand, only B to R change was confirmed with the "nonparametric Granger causality" (GC).

From the obtained results on Pentobarbital anæsthetized rats, a decrease of the synchronization inside of whole system at the transition point was found in one of the two

groups of recordings, and also a decrease of the synchronization exclusively in-between was found. However, the detection of the transition point was impossible from these decreases. Nothing was concluded for the ED. Furthermore, for the coupling, there was no general agreement among rats, but some changes in H-R, B to H and R to B were found with coupling matrix (CM). Here, only the R to H change was confirmed with nonparametric GC.

From the obtained results on humans, it was found that the synchronization inside of whole system was lower under anæsthesia, which is surprisingly the inverse case of rats. No change was found in the synchronization exclusively between the three sub-systems. However, lower ED and lower variance of ED of B and H were again found under anæsthesia as is the case of rats anæsthetized with KX. Furthermore, it was found that, by taking the mean, the couplings are in general lower under anæsthesia. It was also found that the coupling B to R changes its direction between the two measurement stages. Only an increase of R to H found in group "Oslo" was confirmed with nonparametric GC.

From the studies on rats, we remarked that the synchronization as well as the interdependency among these three physiological systems differed according to the employed anæsthetics. For KX, we can say that our synchronization analysis method, the S-estimator, has a very high application potentiality to the creation of a system which measures the depth of anæsthesia. But for PB, there was no general agreement on the obtained results from all the methods, such that we were not able to confirm the effectiveness of our methods. We saw that the interdependencies identified with the CM and the nonparametric GC disagree in some of the cases. Compared with the results of our project partners, the CM method seems to be correct. Nevertheless, compared with the nonparametric GC, CM uses a parametric approach such that uncertainty in model parameters may play a role. Moreover, GC needs less power of computation which is a big advantage. Consequently, we need to check the reason of this disagreement in order to be able to decide on the causality among these three physiological systems.

From the studies on humans, contrarily to rats, we remarked little difference among Propofol, Sevoflurane and these two anæsthetics with Curare. This may mean that a unique measuring system of the depth of anæsthesia is sufficient for the human patients. And here again, our method, the S-estimator, has a great potentiality to be one of the efficient detection methods of the deep-light anæsthesia, since the obtained results showed two distinct synchronization degrees between the resting state and the anæsthesia state. The interdependencies were identified with both CM and nonparametric GC. But our frequency analysis shows that the main frequency of respiration and brain were very low such that it would be more efficient to consider only these low frequency components, especially for the nonparametric GC.

5.1.2 Modelling of the brain rhythms

From our literature study about the rhythmic activity of the brain, we deduce that it is generally accepted in the neuroscience community that the rhythms of the EEG are created by the interaction between the cortex and the thalamus. Consequently, we chose one of the Hodgkin-Huxley based models which considers the thalamocortical assemblies, the model of Bazhenov et al. [Bazhenov et al., 2002], which includes four layers of neurons where two

of them are for the thalamus (RE: thalamic reticular neuron, TC: thalamic relay neuron) and the other two are for the cortex (PY: pyramidal neuron, IN: interneuron). We had a lot of difficulties to set parameters and equations, since their exact definitions were spread out over several papers, some of them were described twice with different settings and moreover some of them were not described anywhere. But in the end, we succeeded to reproduce this model and simulated it. As a result, from observing the collective spiking activity of the PY cells on this model, we confirmed the presence of slow oscillations, namely the δ-waves.

From the simulations performed on this reproduced model varying the parameter of maximal conductance of Ca^{2+} channels or the closing/opening rate of $GABA_A$ receptors from one simulation to another, it was shown that reinforcement of the inhibition that suppresses the spiking activities was effectively induced by all changes of the parameters. Here, the model show also an increase in global frequency, which is not observed in the experiments. Therefore, further frequency analysis on the mean field of PY neurons is necessary to conclude about the reason of this increase. Furthermore, we perceived that the synchrony among neurons becomes stronger with the change of the parameters. This is especially prominent on the results obtained with an increase in the $GABA_A$ channel opening rate, α. The results obtained with a small decrease in the $GABA_A$ channel closing rate, β, shows also a prominent synchrony, but from a certain value of β, the effect of inhibition becomes so powerful that the coherent spiking activity in the network becomes unsustainable. As a result, we concluded that the degree of the reaction, i.e., the individual/local behavior of the PY neurons differs according to which parameters are changed.

From the studies of the size of the model, we found that the local synchrony and the mean field frequency is not influenced by the size of network, but the global synchrony is not preserved at larger sizes. The fact that the local synchrony is not changed when the size of the network is increased is important, because the simulated networks are much smaller than the biological networks. Thus, we have some confidence, at least within the limits of the considered neuron and network models, that the property of local synchrony remains true at biological network sizes. And from the studies of the properties of the neurons, we confirmed that our simulated model reflects very well the properties of each neuron as reported in the literature.

5.2 Future work

5.2.1 Methodology

As mentioned just before, our method, the "S-estimator" seems very promising. But our method, the "new S-estimator" indicated that there is no synchronization change between heart activity and respiration even though our project partners came to the opposite conclusion. Consequently, it would be interesting to calculate the partialized S-estimator, i.e. calculate the synchronization between two system partializing the third system. This can also be applied to the nonparametric GC.

Furthermore, in this thesis, we found an interesting result in the analysis of the embedding dimension. In this study, we expected to have a well defined ED with respect to time, and not a varying ED. This variation should come from statistical variations when operating the false nearest neighbors method. Consequently, we should test why this happens, simulating with artificial models and mathematically clarify the reason.

Moreover, as we mentioned also just before, there is a disagreement between the CM method and the nonparametric GC. The deep analysis of the CM method is very difficult since we proceeded in several steps, and moreover, for the identification of the nonlinear model, we employed a MATLAB tool box. In consequence, we should proceed to a deep analysis of the nonparametric GC in order to clarify the reason of this disagreement.

5.2.2 Data analysis

In this thesis, we had nine groups of experimental recordings. However, the number of subjects inside of each group was too low in order to reach definite conclusions. Having more data in one kind of group in the future, we can proceed to a statistical analysis. In this case, we are convinced to reach a more concrete results on each of the groups.

Furthermore, we mentioned several times in this thesis some unsolved problems concerning the analysis. These problems should also be treated in the future.

5.2.3 Brain modelling

In this thesis, we just made the first step, and still a lot of problem remain to be solved in order to approach the closing of the gap between the mathematical model and the reality. We think that we should continue with the understanding of the model. Here, we can conceive as a next step, the understanding of the mechanism of the interaction between two identical or non-identical neurons, which could be expanded to analyze a small network and larger networks. A detailed mathematical analysis on a neuron model sounds also promising. As another approach, the transition from Hodkin-Huxley based model to a simplified model could be a good idea. For example, a map based model proposed by Rulkov et al. [Rulkov et al., 2004] seems very promising. However, for this transition, still we should find the way how to include the effect of anæsthesia.

Appendix

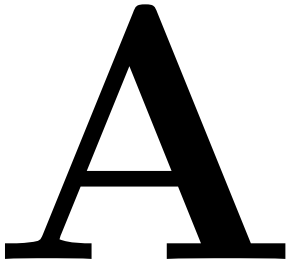

A.1 Figures of analysis results

A.1.1 "Rats1"

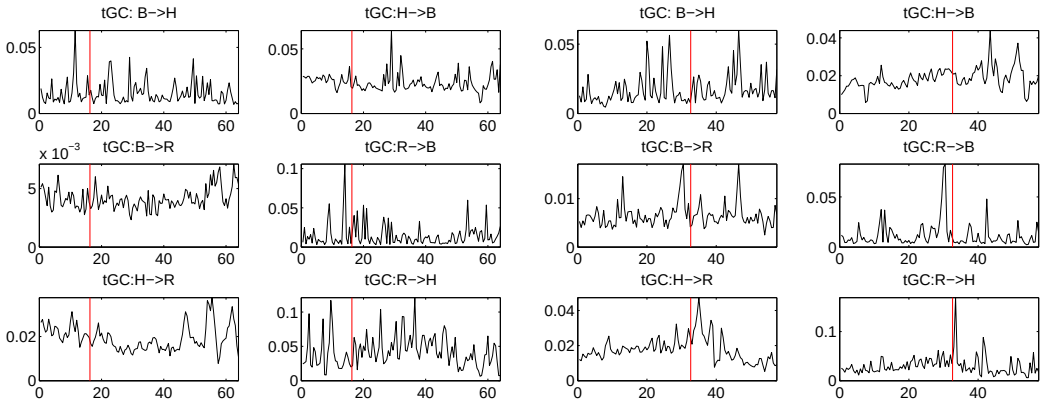

Figure A.1 – *Time domain nonparametric Granger causality $tGC(t)$ obtained on "Rats1" PartI (Rats1-1 to Rats1-2). Horizontal axis is time (min). The red lines indicate the deep-light change of anæsthesia detected by us: (B) EEG, (H) ECG, and (R) respiration.*

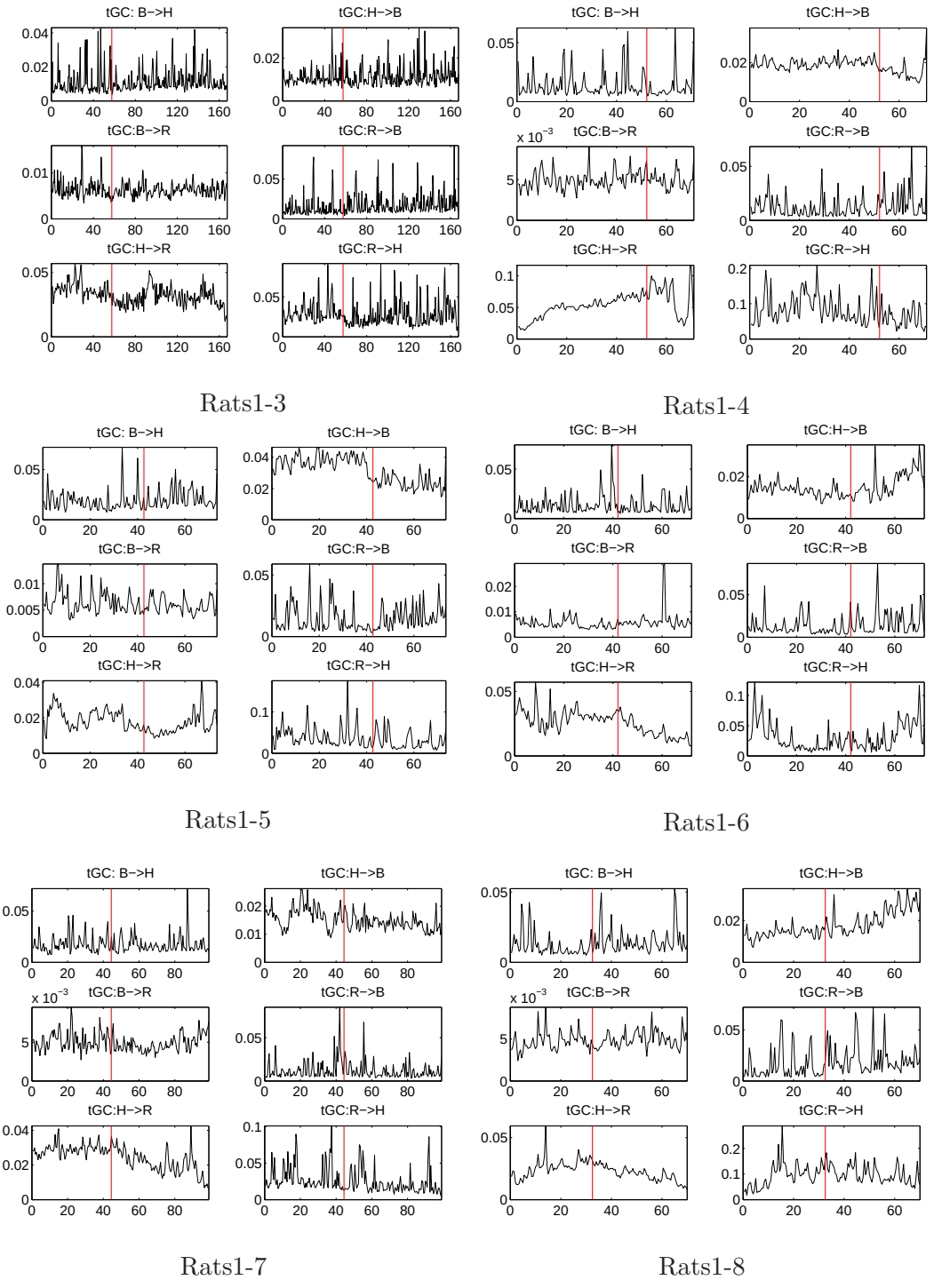

Figure A.2 – *Time domain nonparametric Granger causality $tGC(t)$ obtained on "Rats1" PartII (Rats1-3 to Rats1-8). Horizontal axis is time (min). The red lines indicate the deep-light change of anæsthesia detected by us: (B) EEG, (H) ECG, and (R) respiration.*

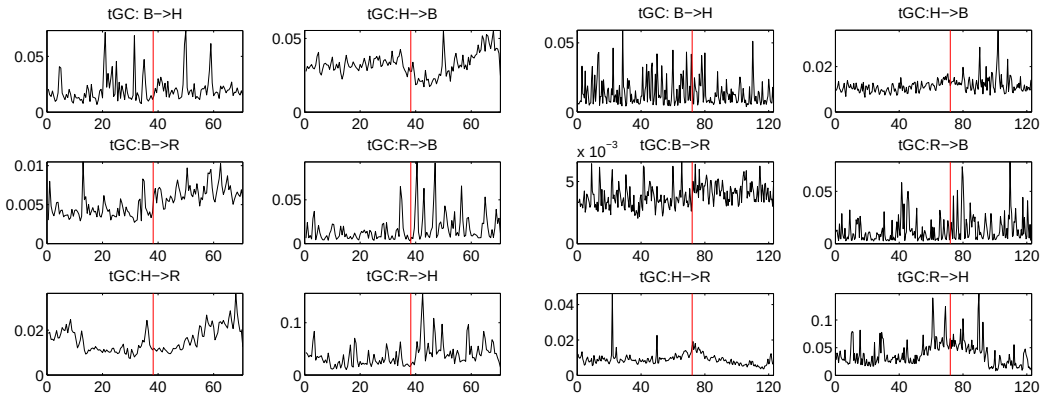

Figure A.3 – *Time domain nonparametric Granger causality $tGC(t)$ obtained on "Rats1" PartIII (Rats1-9 to Rats1-10). Horizontal axis is time (min). The red lines indicate the deep-light change of anæsthesia detected by us: (B) EEG, (H) ECG, and (R) respiration.*

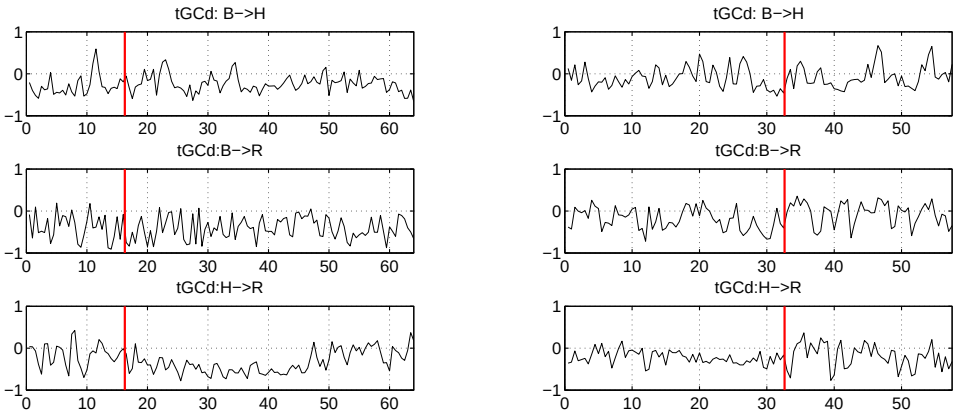

Figure A.4 – *Direction of the interactions $tGCd(t)$ using $tGC(t)$ obtained on "Rats1" PartI (Rats1-1 to Rats1-2). Horizontal axis is time (min). The red lines indicate the deep-light change of anæsthesia detected by us: (B) EEG, (H) ECG, and (R) respiration.*

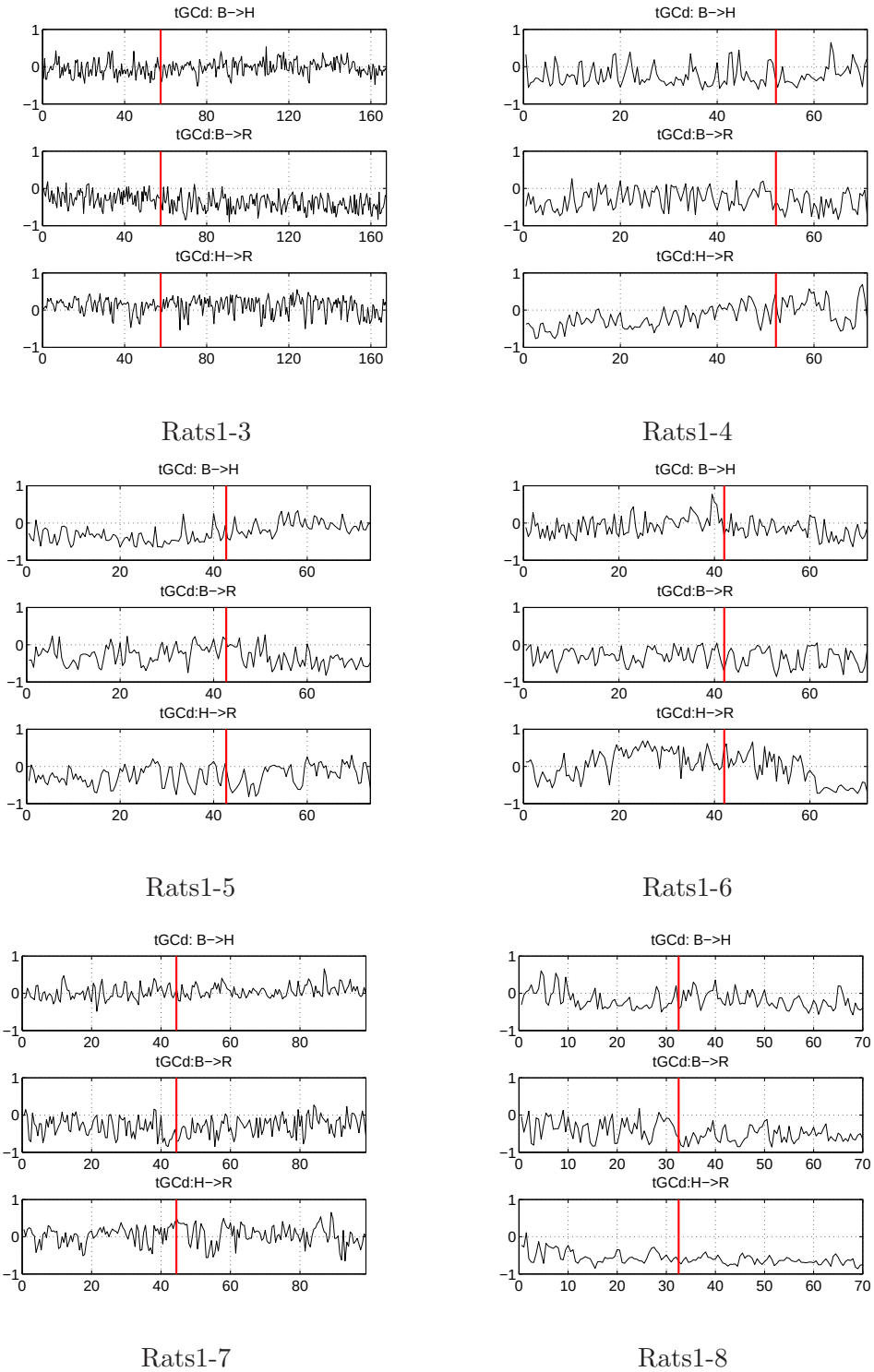

Figure A.5 – *Direction of the interactions $tGCd(t)$ using $tGC(t)$ obtained on "Rats1" PartII (Rats1-3 to Rats1-8). Horizontal axis is time (min). The red lines indicate the deep-light change of anæsthesia detected by us: (B) EEG, (H) ECG, and (R) respiration.*

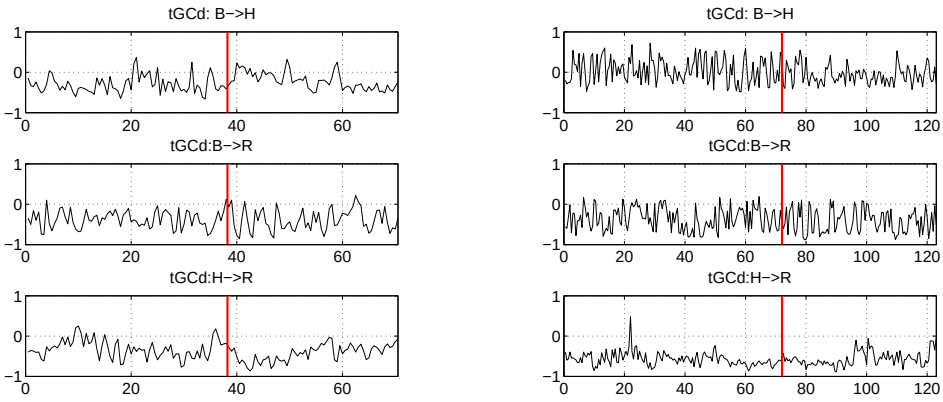

Rats1-9 Rats1-10

Figure A.6 – *Direction of the interactions $tGCd(t)$ using $tGC(t)$ obtained on "Rats1" PartIII (Rats1-9 to Rats1-10). Horizontal axis is time (min). The red lines indicate the deep-light change of anæsthesia detected by us: (B) EEG, (H) ECG, and (R) respiration.*

A.1.2 "Rats2"

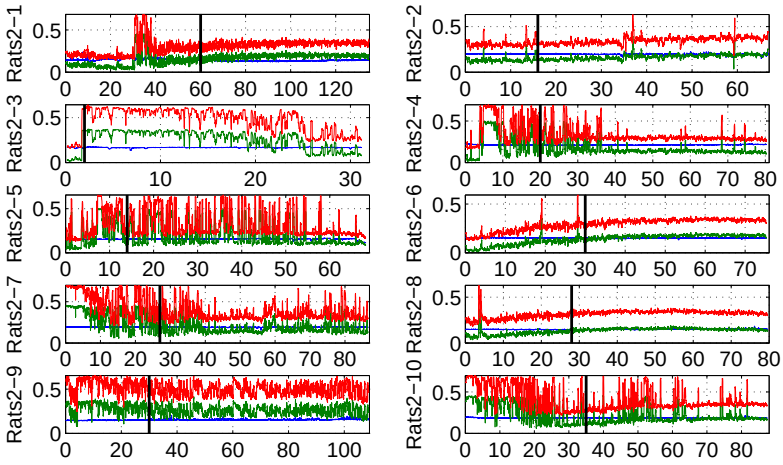

Figure A.7 – *Comparison of the strength of $S(t)$ obtained by clustering two chosen oscillators together on Group "Rats2". Horizontal axis is time (min). The black lines indicate the deep-light change of anæsthesia detected in [Musizza et al., 2007]: (blue) ECG and Respiration, (green) ECG and EEG, and (red) Respiration and EEG.*

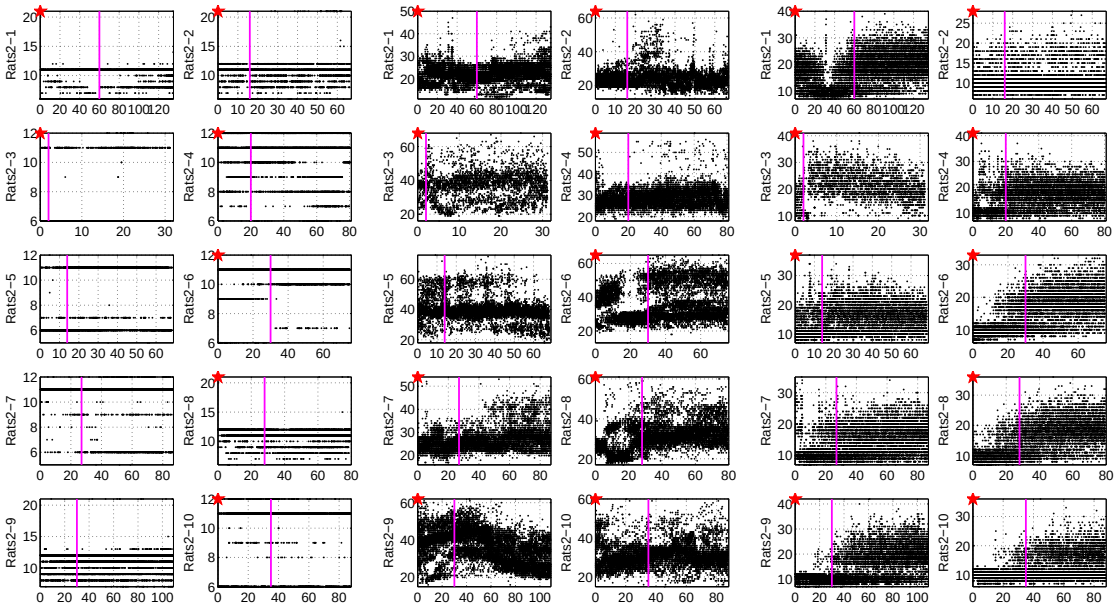

Figure A.8 – *The study on the size of the Toeplitz like matrix (K) (samples) for PCA embedding. Horizontal axis is time (min). The magenta lines indicate the deep-light change of anæsthesia detected in [Musizza et al., 2007]: (a) ECG, (b) Respiration and (c) EEG.*

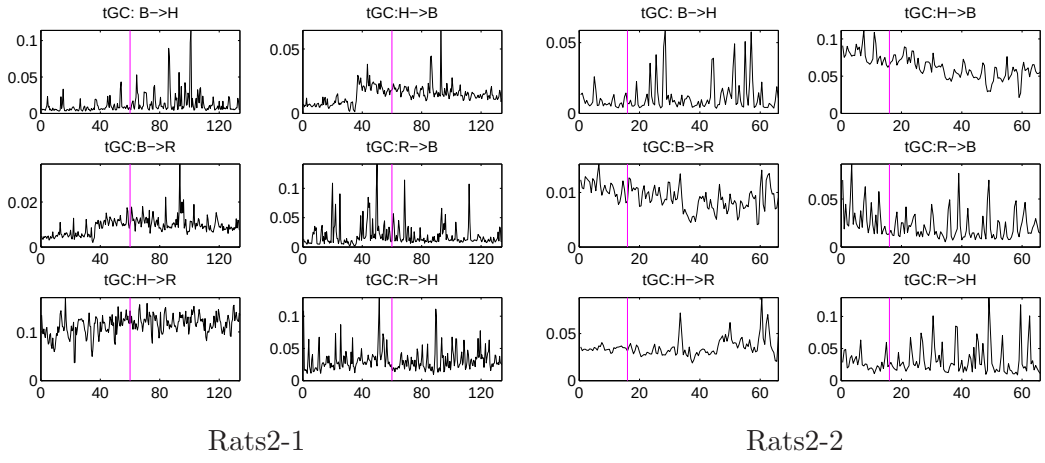

Figure A.9 – *Time domain nonparametric Granger causality $tGC(t)$ obtained on "Rats2" PartI (Rats2-1 to Rats2-2). Horizontal axis is time (min). The magenta lines indicate the deep-light change of anæsthesia detected in [Musizza et al., 2007]: (B) EEG, (H) ECG, and (R) respiration.*

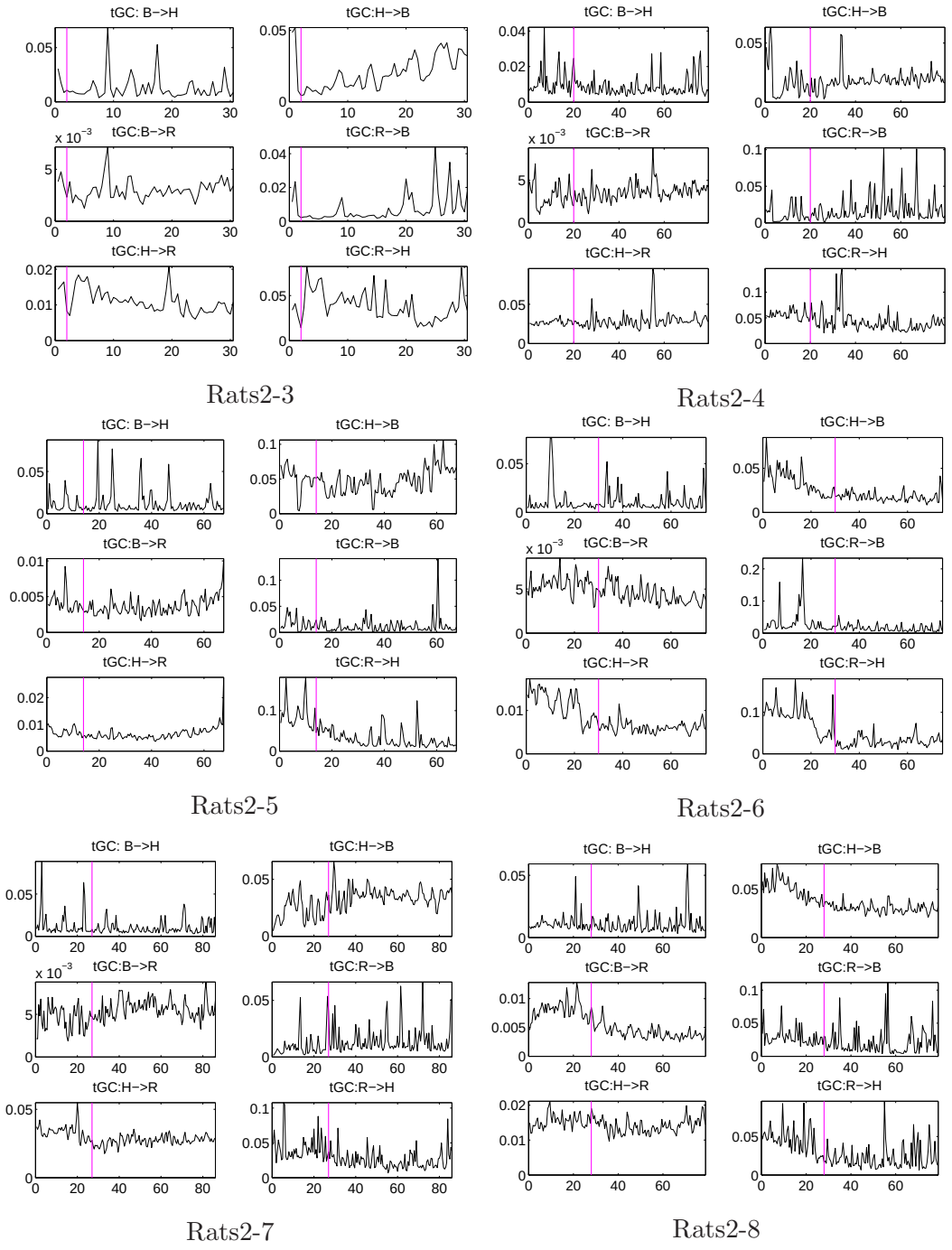

Figure A.10 – *Time domain nonparametric Granger causality $tGC(t)$ obtained on "Rats2" PartII (Rats2-3 to Rats2-8). Horizontal axis is time (min). The magenta lines indicate the deep-light change of anæsthesia detected in [Musizza et al., 2007]: (B) EEG, (H) ECG, and (R) respiration.*

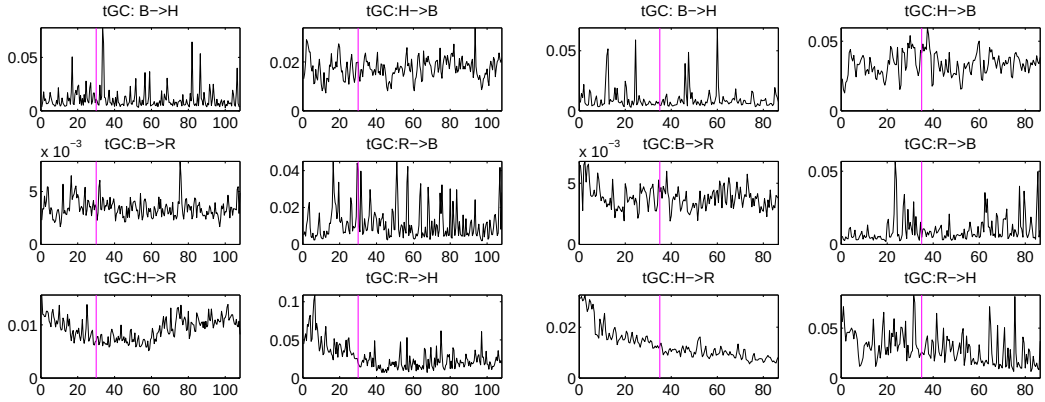

Figure A.11 – *Time domain nonparametric Granger causality $tGC(t)$ obtained on "Rats2" PartIII (Rats2-9 to Rats2-10). Horizontal axis is time (min). The magenta lines indicate the deep-light change of anæsthesia detected in [Musizza et al., 2007]: (B) EEG, (H) ECG, and (R) respiration.*

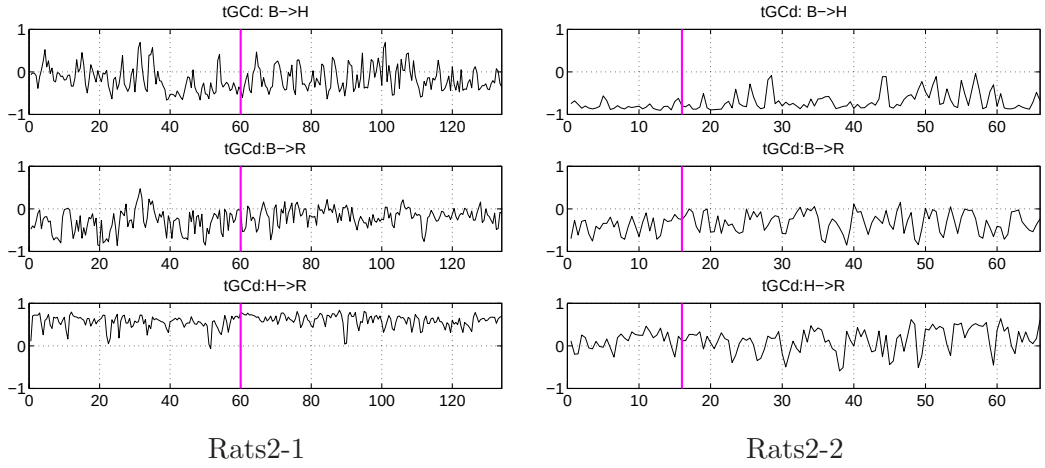

Figure A.12 – *Direction of the interactions $tGCd(t)$ using $tGC(t)$ obtained on "Rats2" PartI (Rats2-1 to Rats2-2). Horizontal axis is time (min). The magenta lines indicate the deep-light change of anæsthesia detected in [Musizza et al., 2007]: (B) EEG, (H) ECG, and (R) respiration.*

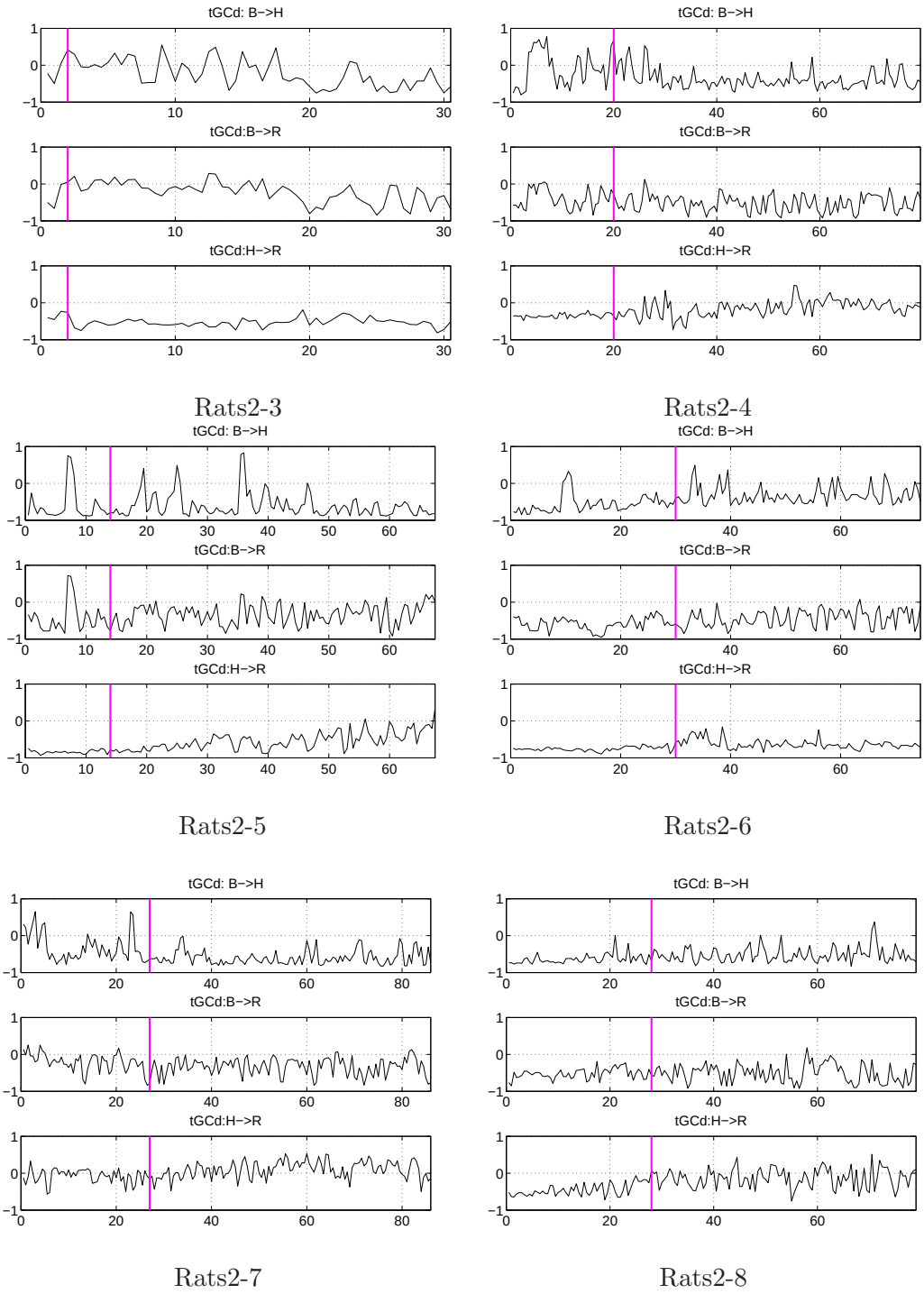

Figure A.13 – *Direction of the interactions $tGCd(t)$ using $tGC(t)$ obtained on "Rats2" PartII (Rats2-3 to Rats2-8). Horizontal axis is time (min). The magenta lines indicate the deep-light change of anæsthesia detected in [Musizza et al., 2007]: (B) EEG, (H) ECG, and (R) respiration.*

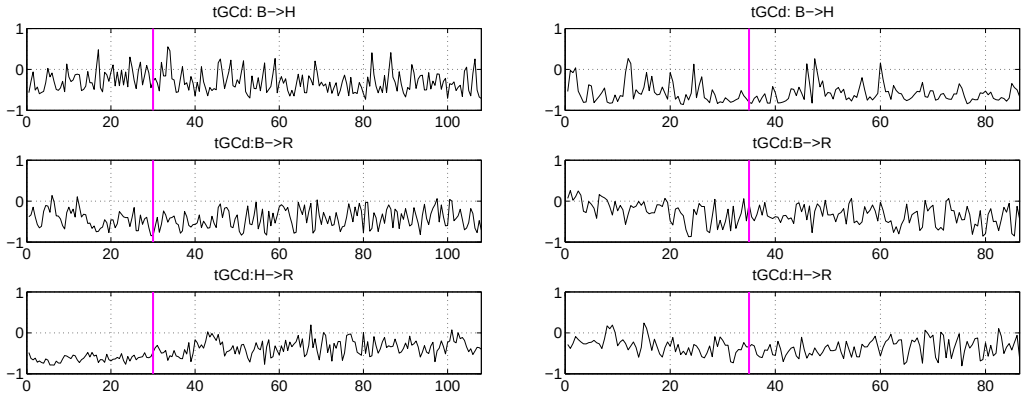

Rats2-9 Rats2-10

Figure A.14 – *Direction of the interactions $tGCd(t)$ using $tGC(t)$ obtained on "Rats2" PartIII (Rats2-9 to Rats2-10). Horizontal axis is time (min). The magenta lines indicate the deep-light change of anæsthesia detected in [Musizza et al., 2007]: (B) EEG, (H) ECG, and (R) respiration.*

A.1.3 "Rats3"

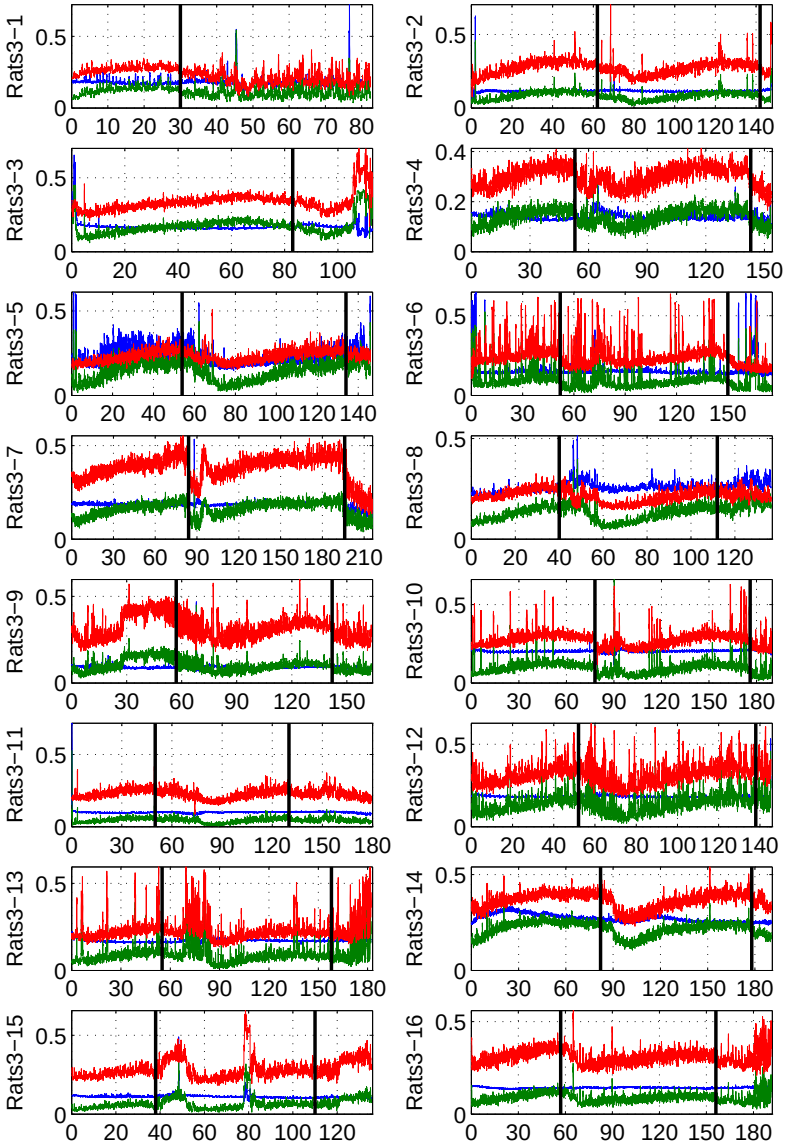

Figure A.15 – *Comparison of the strength of $S(t)$ obtained by clustering two chosen oscillators together on Group "Rats3". Horizontal axis is time (min). The black lines indicate the estimated deep-light change of anæsthesia: (blue) ECG and Respiration, (green) ECG and EEG, and (red) Respiration and EEG.*

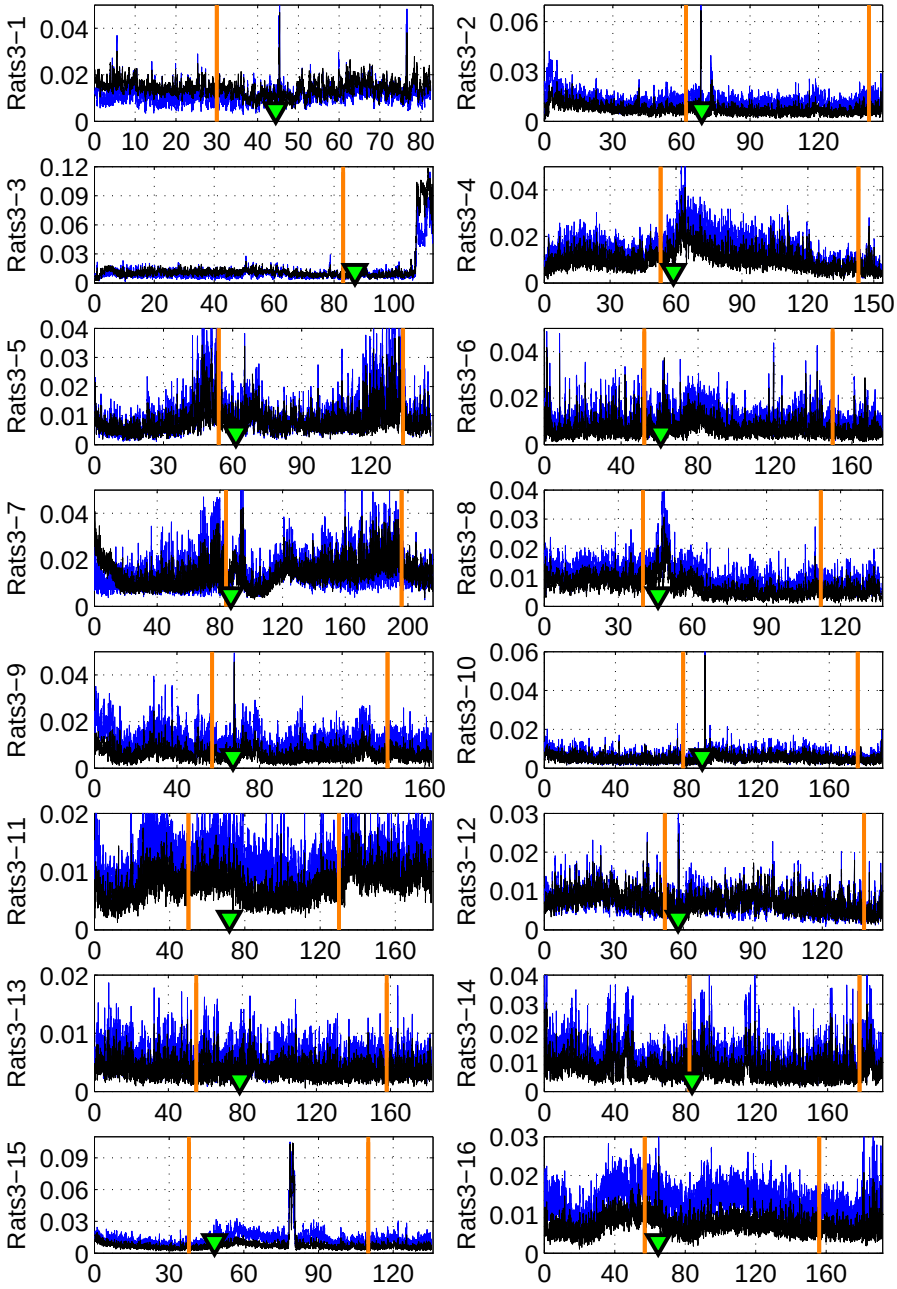

Figure A.16 – *Synchronization measure $S_{new}(t)$ obtained by clustering three oscillators (ECG, Respiration and EEG) together on group "Rats3". Horizontal axis is time (min). Orange lines indicate the estimated deep-light change of anæsthesia. The downward triangles which indicate the reinduction timing are also shown as a reference of strong external stimulation. Sometimes, high value of $S_{new}(t)$ is not plotted since we zoomed in in order to see the variation around the transition point.*

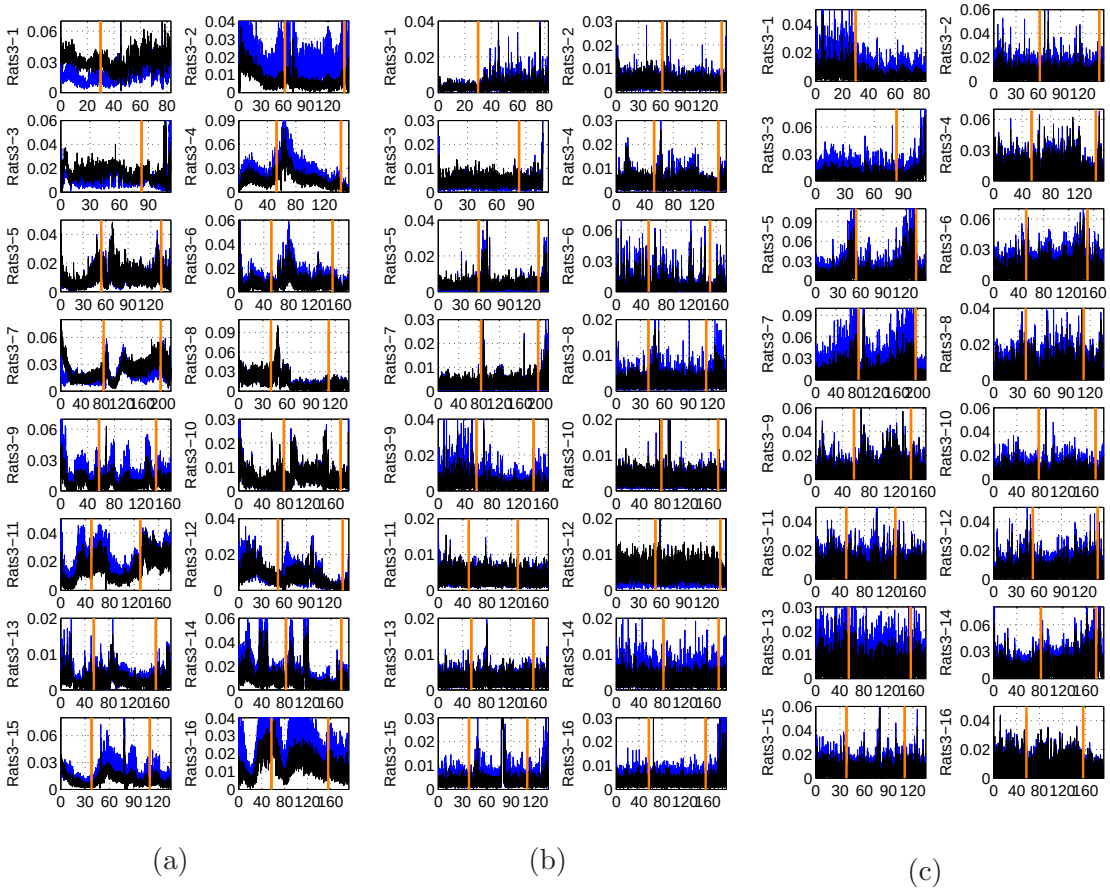

Figure A.17 – *Synchronization measure $S_{new}(t)$ obtained by clustering two chosen oscillators together on group "Rats3". Horizontal axis is time (min). Orange lines indicate the estimated deep-light change of anæsthesia: (a) ECG and Respiration, (b) ECG and EEG, and (c) Respiration and EEG.*

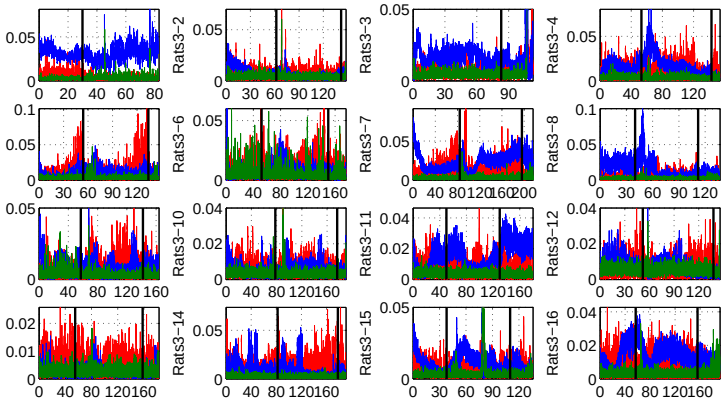

Figure A.18 – *Comparison of the strength of $S_{new}(t)$ obtained by clustering two chosen oscillators together on Group "Rats3". Horizontal axis is time (min). The black lines indicate the estimated deep-light change of anæsthesia: (blue) ECG and Respiration, (green) ECG and EEG, and (red) Respiration and EEG.*

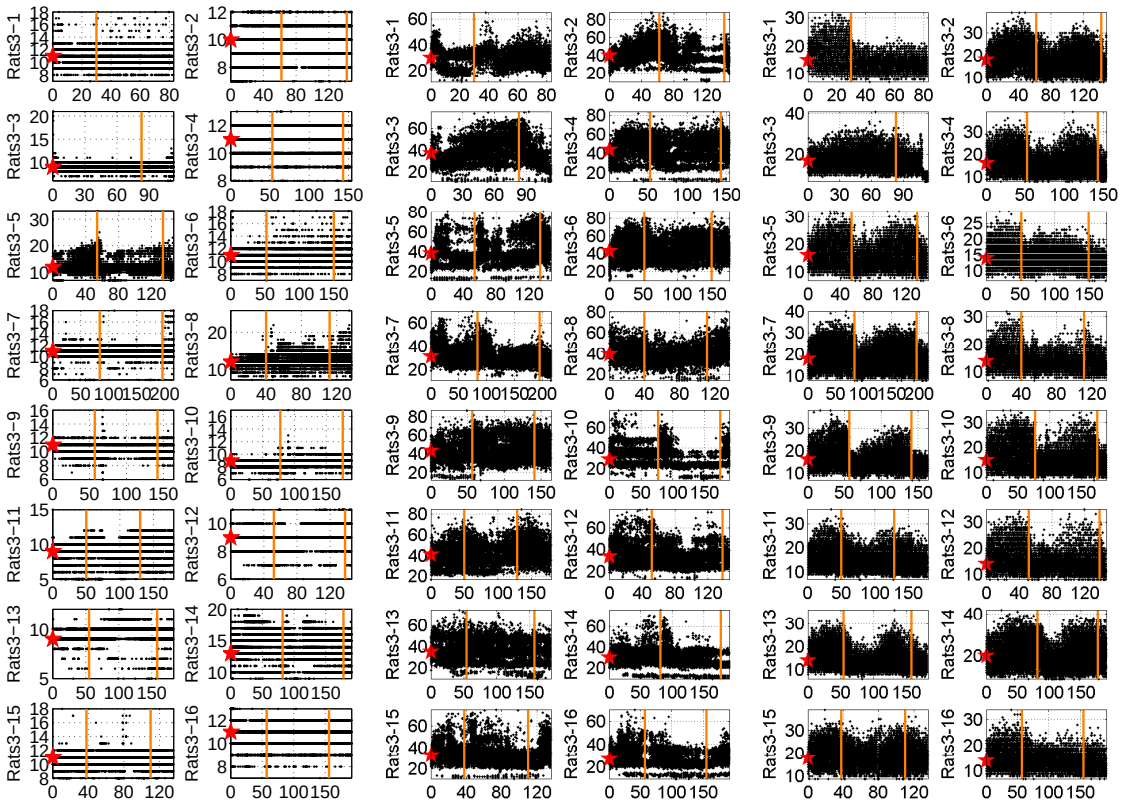

Figure A.19 – *The study on the time delay (τ) (samples) for delay embedding. Horizontal axis is time (min). Orange lines indicate the estimated deep-light change of anæsthesia. The red stars indicates the chosen parameters: (a) ECG, (b) Respiration and (c) EEG.*

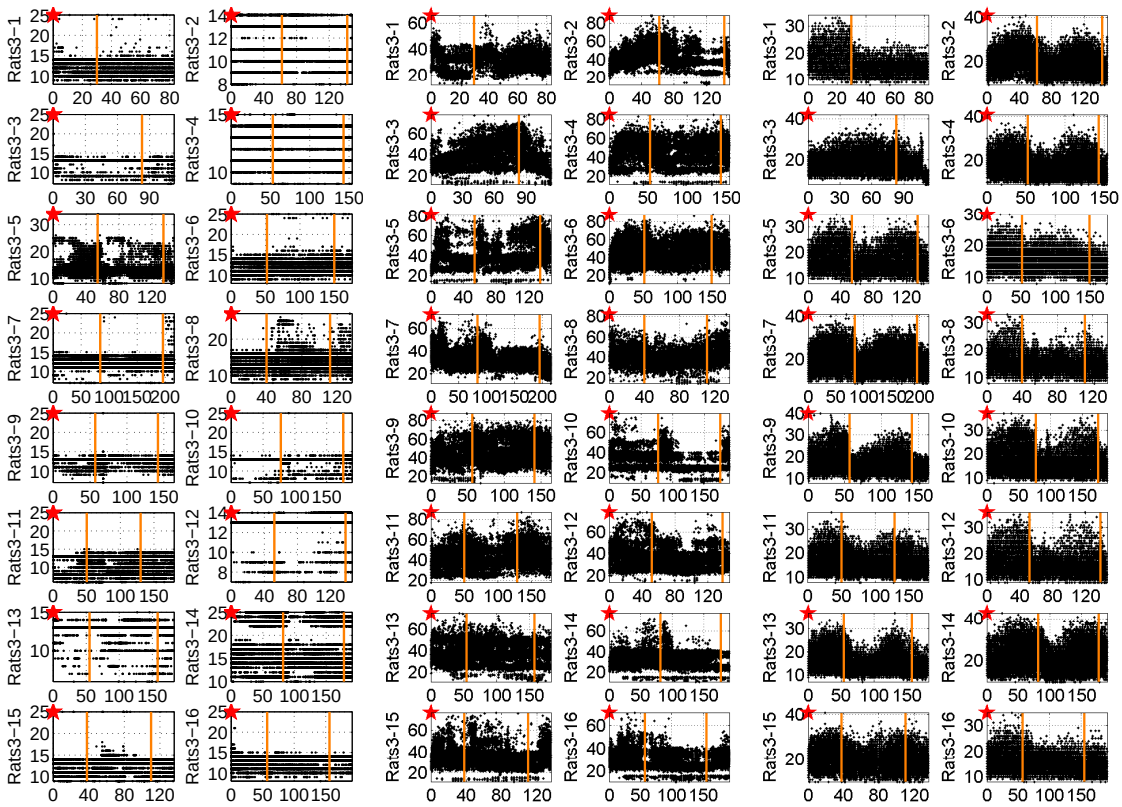

(a) (b) (c)

Figure A.20 – *The study on the size of the Toeplitz like matrix (K) (samples) for PCA embedding. Horizontal axis is time (min). Orange lines indicate the estimated deep-light change of anæsthesia. The red stars indicates the chosen parameters: (a) ECG, (b) Respiration and (c) EEG.*

A.1.4 "Rats4"

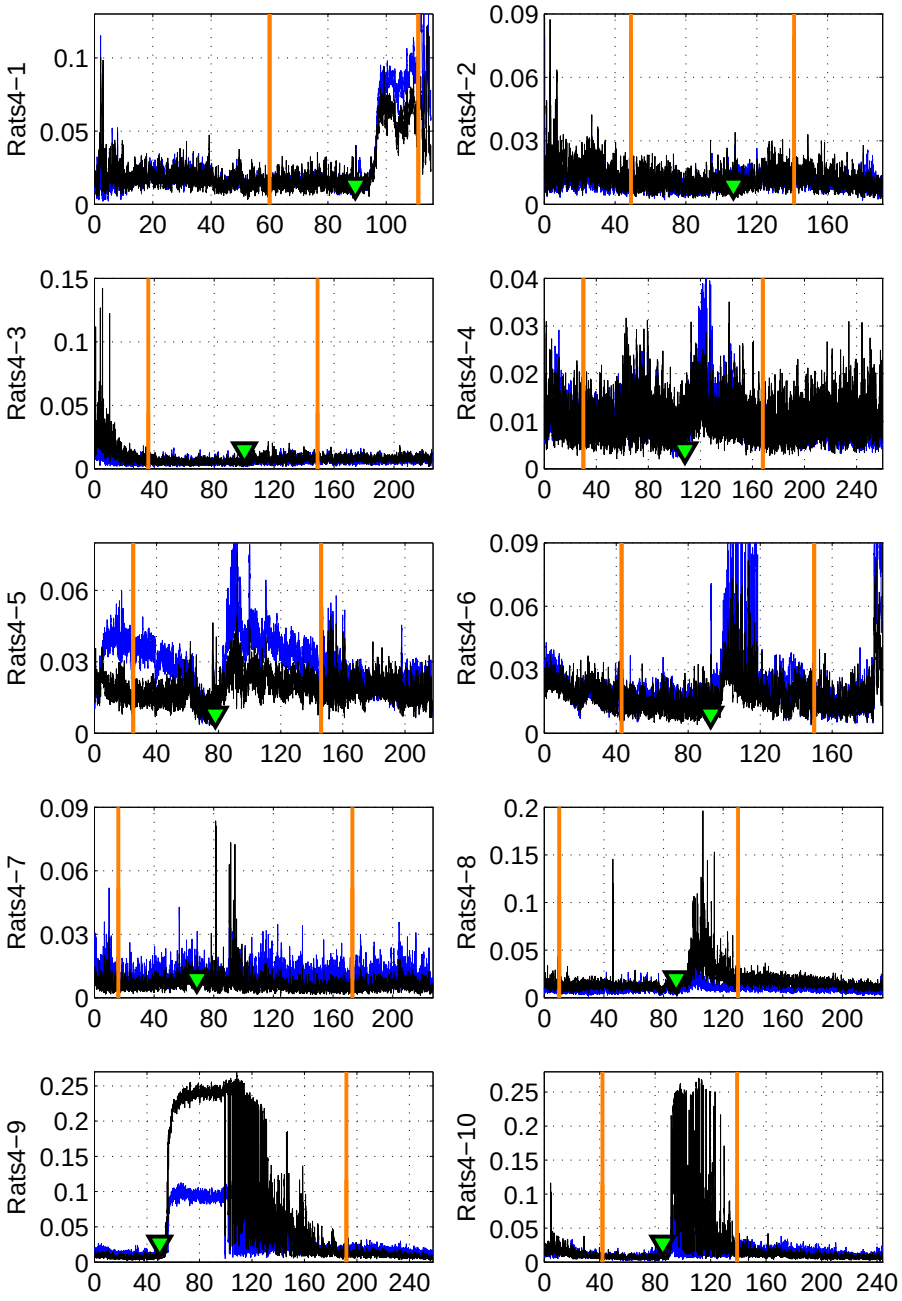

Figure A.21 – *Synchronization measure $S_{new}(t)$ obtained by clustering three oscillators (ECG, Respiration and EEG) together on group "Rats4". Horizontal axis is time (min). Orange lines indicate the estimated deep-light change of anæsthesia.*

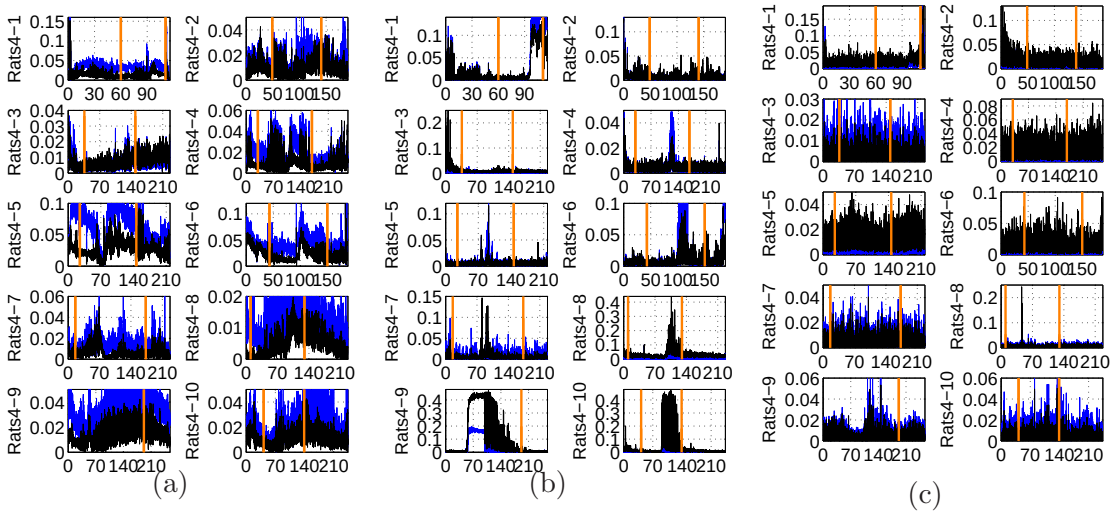

Figure A.22 – *Synchronization measure $S_{new}(t)$ obtained by clustering two chosen oscillators together on group "Rats4". Horizontal axis is time (min). Orange lines indicate the estimated deep-light change of anæsthesia: (a) ECG and Respiration, (b) ECG and EEG, and (c) Respiration and EEG.*

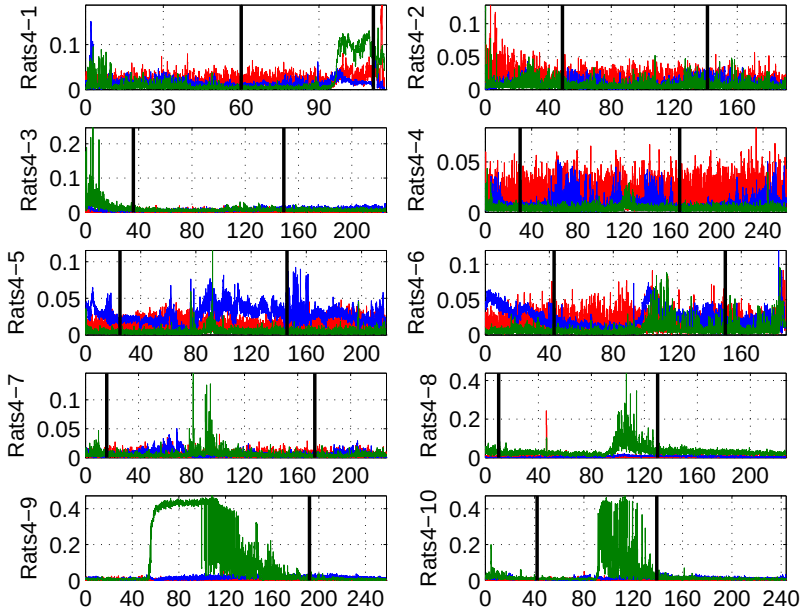

Figure A.23 – *Comparison of the strength of $S_{new}(t)$ obtained by clustering two chosen oscillators together on Group "Rats4". Horizontal axis is time (min). The black lines indicate the estimated deep-light change of anæsthesia: (blue) ECG and Respiration, (green) ECG and EEG, and (red) Respiration and EEG.*

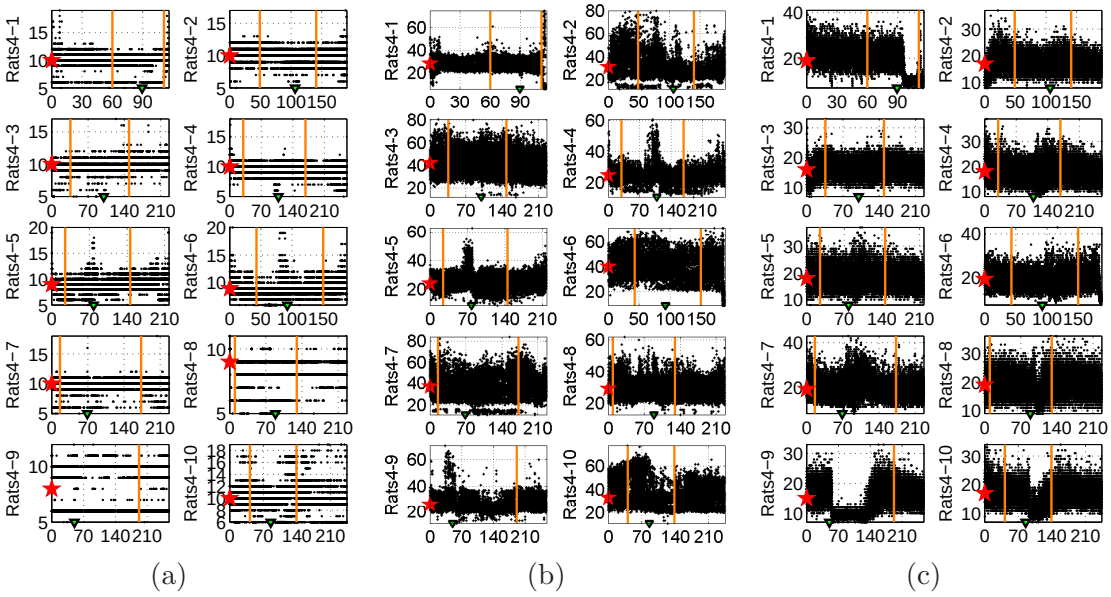

Figure A.24 – *The study on the time delay (τ) (samples) for delay embedding. Horizontal axis is time (min). Orange lines indicate the estimated deep-light change of anæsthesia. The downward triangles show the reinduction timing. The red stars indicates the chosen parameters: (a) ECG, (b) Respiration and (c) EEG.*

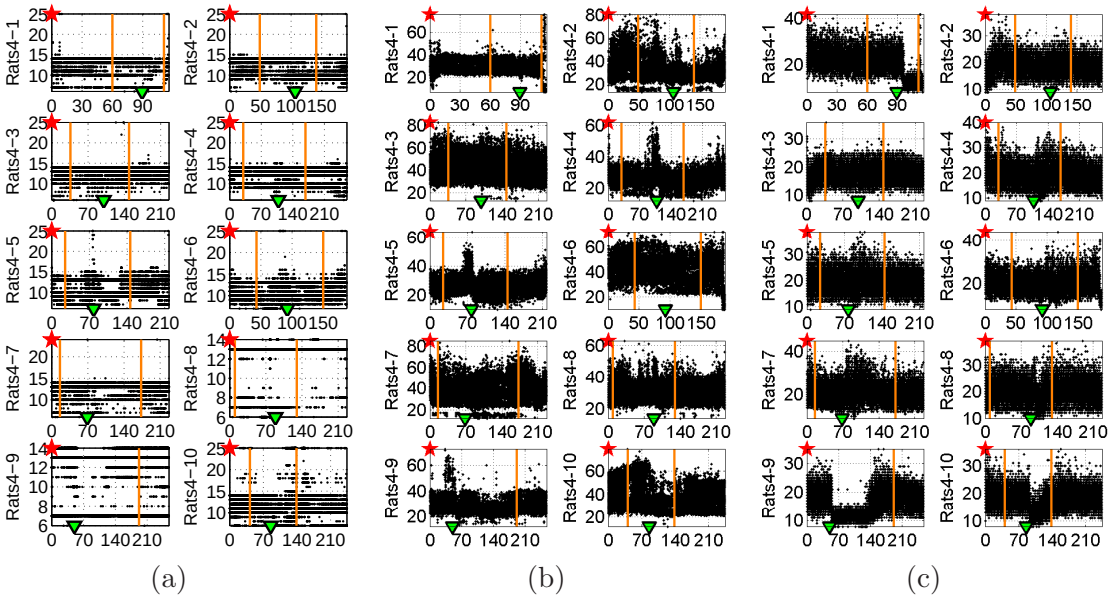

Figure A.25 – *The study on the size of the Toeplitz like matrix (K) (samples) for PCA embedding. Horizontal axis is time (min). Orange lines indicate the estimated deep-light change of anæsthesia. The downward triangles show the reinduction timing. The red stars indicates the chosen parameters: (a) ECG, (b) Respiration and (c) EEG.*

A.1.5 "Rats5"

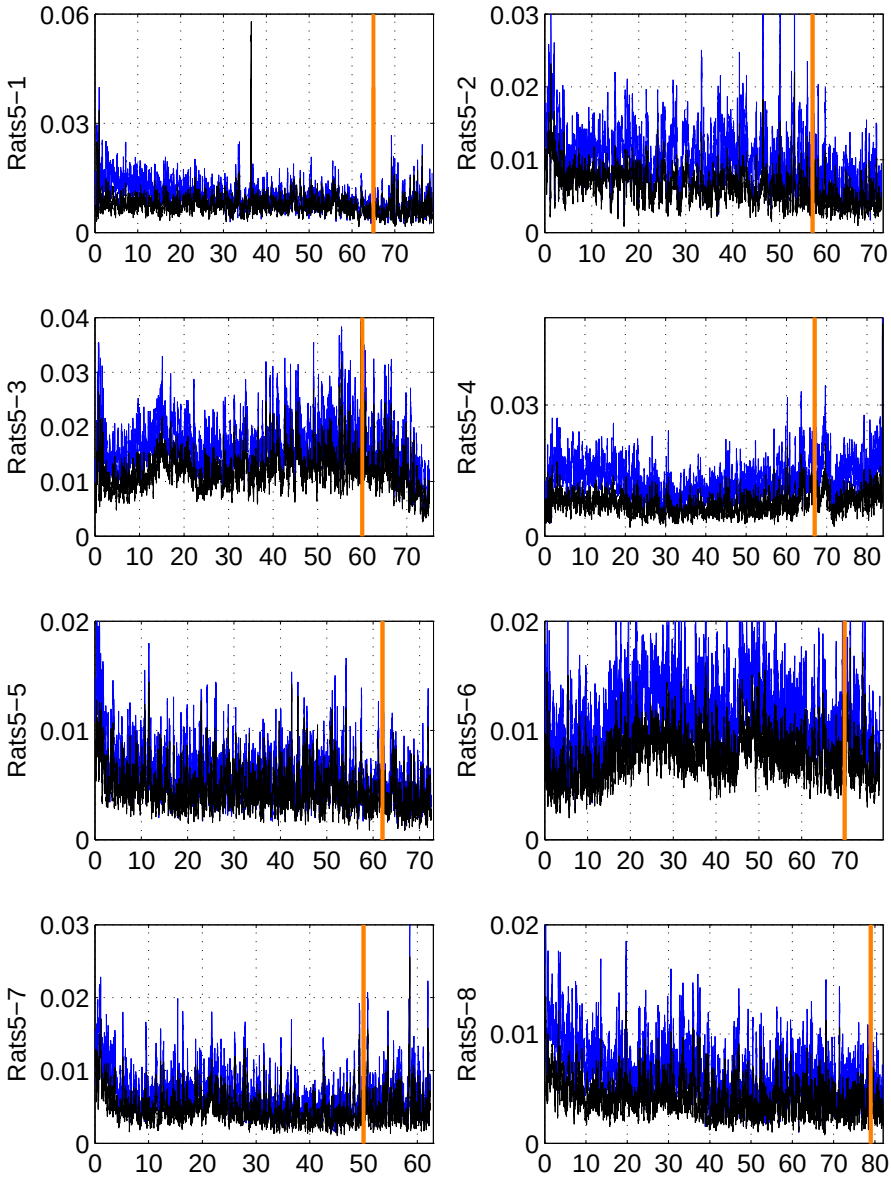

Figure A.26 – *Synchronization measure $S_{new}(t)$ obtained by clustering three oscillators (ECG, Respiration and EEG) together on group "Rats5". Horizontal axis is time (min). Orange lines indicate the estimated deep-light change of anæsthesia.*

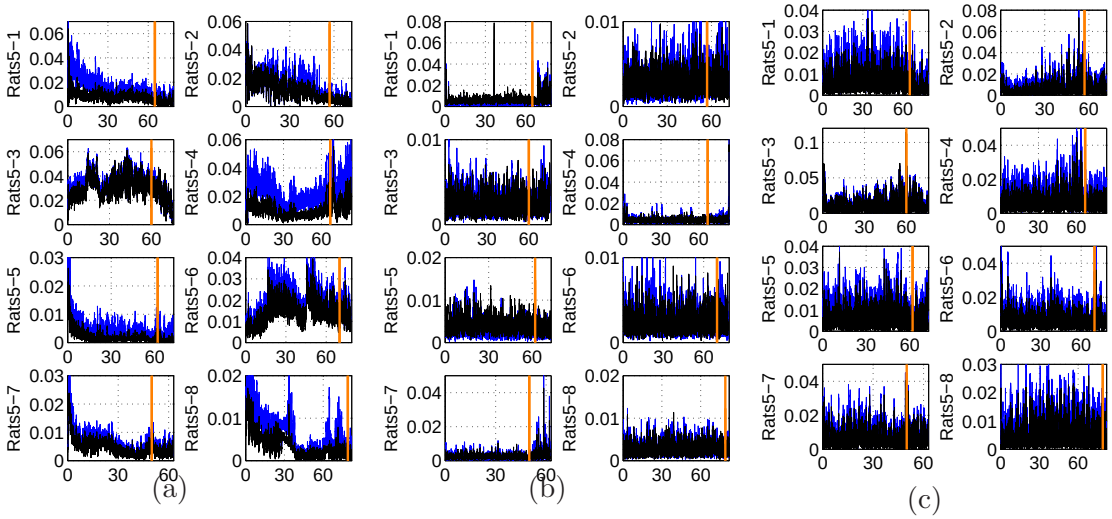

Figure A.27 – *Synchronization measure $S_{new}(t)$ obtained by clustering two chosen oscillators together on group "Rats5". Horizontal axis is time (min). Orange lines indicate the estimated deep-light change of anæsthesia: (a) ECG and Respiration, (b) ECG and EEG, and (c) Respiration and EEG.*

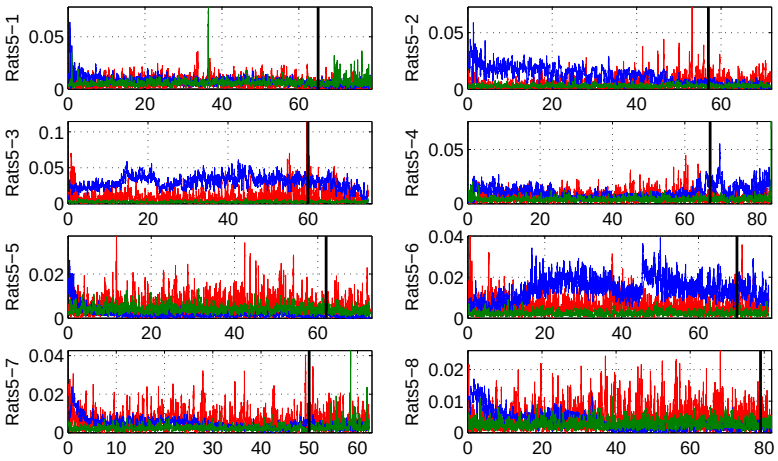

Figure A.28 – *Comparison of the strength of $S_{new}(t)$ obtained by clustering two chosen oscillators together on Group "Rats5". Horizontal axis is time (min). The black lines indicate the estimated deep-light change of anæsthesia: (blue) ECG and Respiration, (green) ECG and EEG, and (red) Respiration and EEG.*

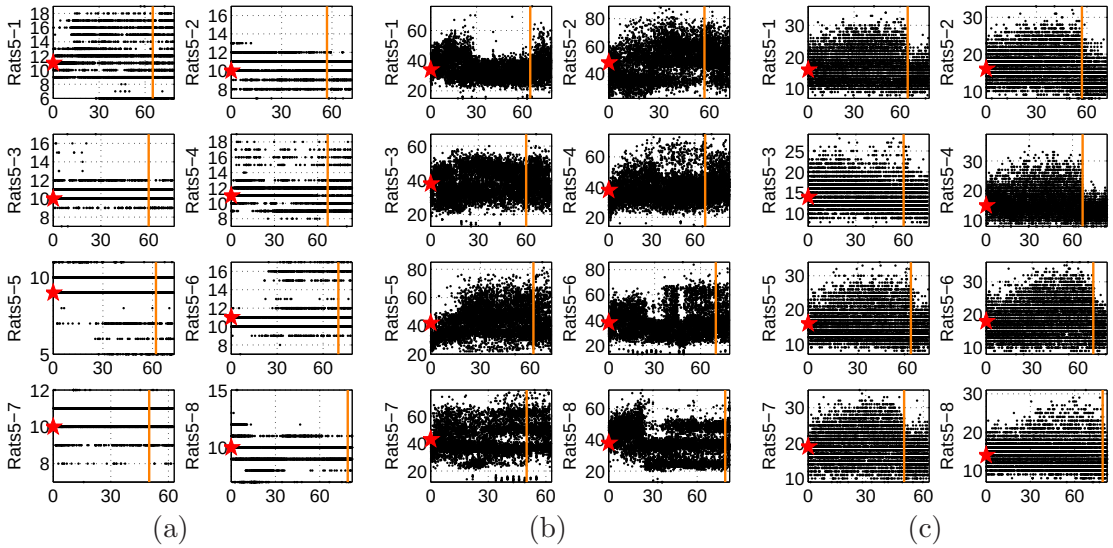

Figure A.29 – *The study on the time delay (τ) (samples) for delay embedding. Horizontal axis is time (min). Orange lines indicate the estimated deep-light change of anæsthesia. The red stars indicates the chosen parameters: (a) ECG, (b) Respiration and (c) EEG.*

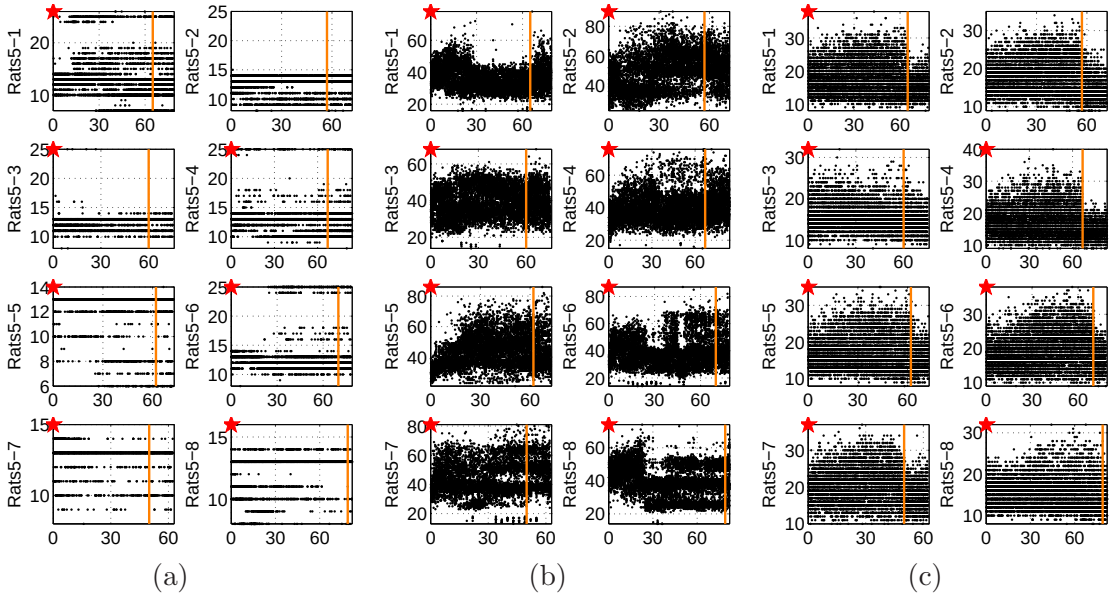

Figure A.30 – *The study on the size of the Toeplitz like matrix (K) (samples) for PCA embedding. Horizontal axis is time (min). Orange lines indicate the estimated deep-light change of anæsthesia. The red stars indicates the chosen parameters: (a) ECG, (b) Respiration and (c) EEG.*

A.1.6 "Lancaster"

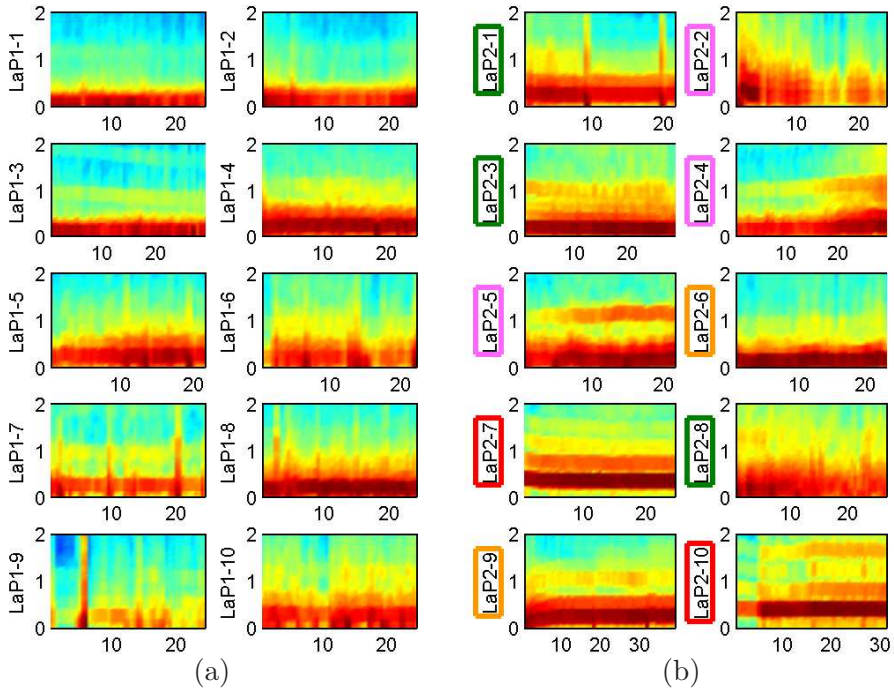

Figure A.31 – *Zoomed in power spectra of respiration signals obtained on "Lancaster". Horizontal axis is time (min). Vertical axis is frequency (Hz). Color axix is omitted: (a) resting (b) anæsthetized.*

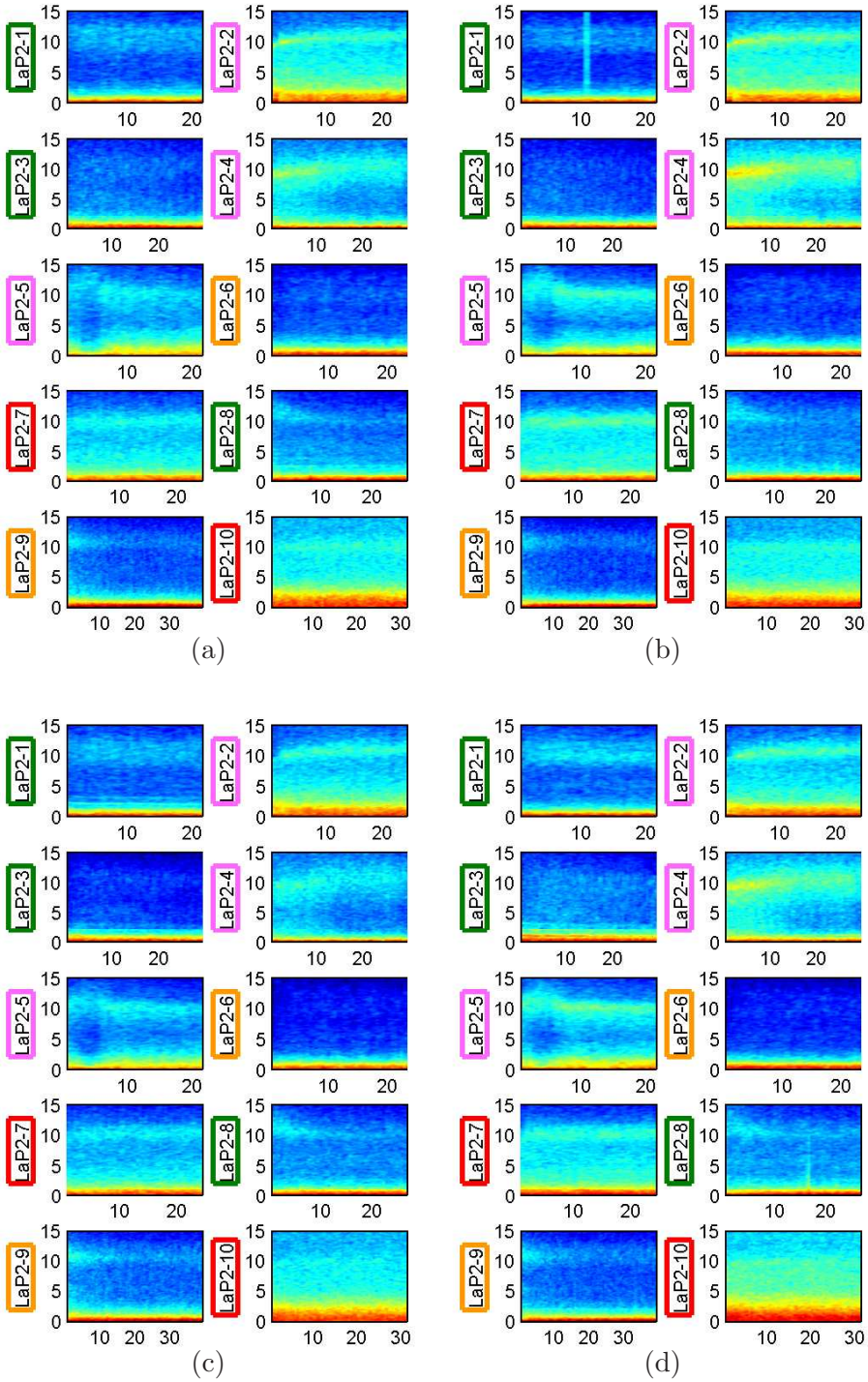

Figure A.32 – *Zoomed out power spectra of EEG signals under anæsthesia obtained on "Lancaster". Horizontal axis is time (min). Vertical axis is frequency (Hz). Color axix is [-3 7]: (a) EEG1, (b) EEG2, (c) EEG3 and (d) EEG4.*

A.1.7 "Oslo"

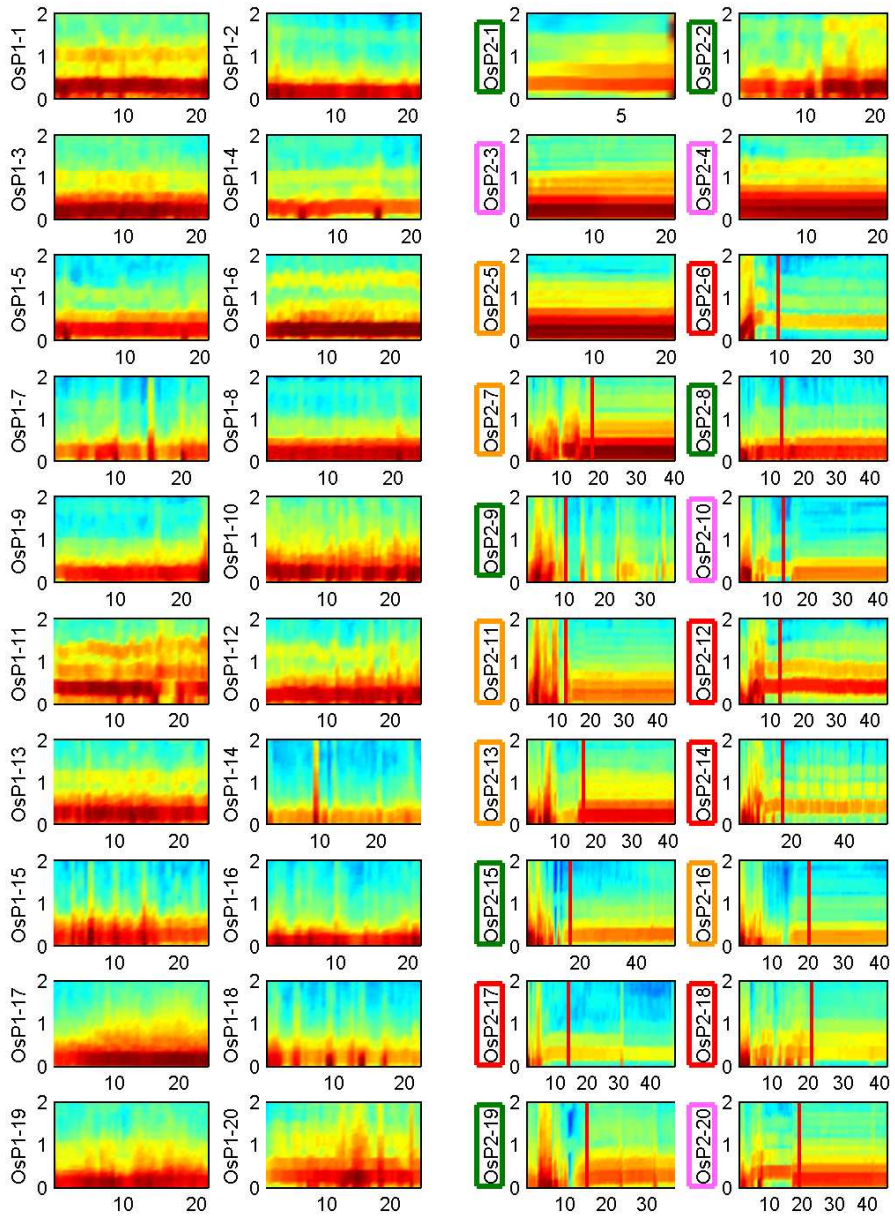

(a) (b)

Figure A.33 – *Zoomed in power spectra of respiration signals obtained on "Oslo". Horizontal axis is time (min). Vertical axis is frequency (Hz). Color axix is omitted: (a) resting (b) anæsthetized.*

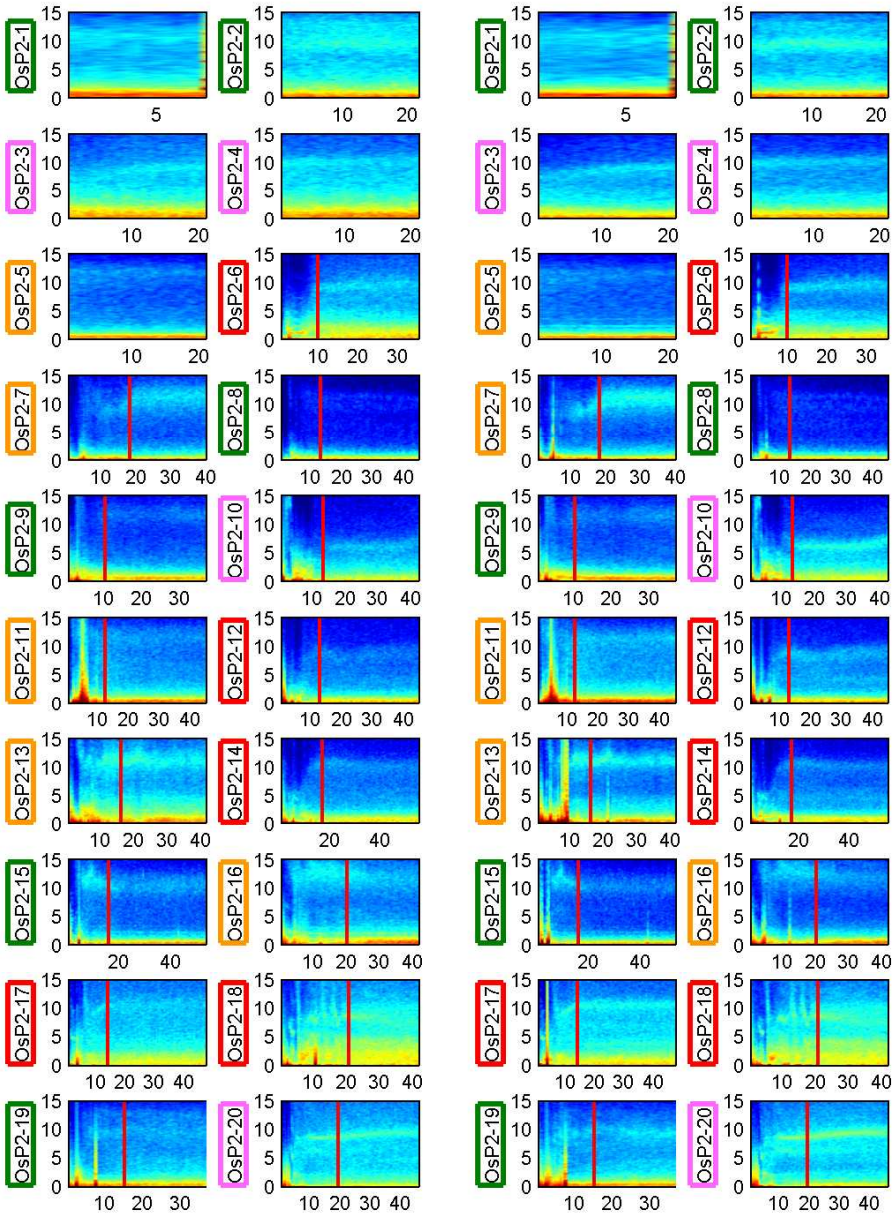

(a) (b)

Figure A.34 – *Zoomed out power spectra of EEG signals under anæsthesia obtained on "Oslo". Horizontal axis is time (min). Vertical axis is frequency (Hz). Color axix is [-3 9]: (a) EEG1 and (b) EEG2.*

Appendix - Model Description

B

B.1 Thalamus

Single-compartment models of TC and RE cells that include voltage- and calcium-dependent currents are described by Hodgkin-Huxley kinetics:

$$C_m \frac{dV}{dt} = -g_L(V - E_L) - I^{int} - I^{syn}, \tag{B.1}$$

membrane capacitance for both RE and TC:

$$C_m = 1(\mu F/cm^2)$$

leakage conductance:

$$g_L^{RE} = 0.05(mS/cm^2), g_L^{TC} = 0.01(mS/cm^2)$$

leakage reversal potential:

$$E_L^{RE} = -77(mV), E_L^{TC} = -70$$

area:

$$S_{RE} = 1.43 \cdot 10^{-4}(cm^2), S_{TC} = 2.9 \cdot 10^{-4}(cm^2)$$

B.1.1 Reticlular neuron (RE)

- **Hodgkin-Huxley kinetics of intrinsic currents of RE:**

$$\begin{aligned} -I_{RE}^{int} &= -g_{Na}(V - E_{Na}) - g_K(V - E_K) - g_T(V - E_T) - g_{KL}(V - E_{KL}) \\ &= -(g_{Na} + g_K + g_T + g_{KL})V + (g_{Na}E_{Na} + g_K E_K + g_T E_T + g_{KL}E_{KL}) \\ &= -g_{intRE}V + I_{leakintRE} \end{aligned} \tag{B.2}$$

- **Fast sodium (Na) channel:**
  Reversal potential:

$$E_{Na} = 50(mV)$$

Conductance:

$$gNa = \bar{g}Na \cdot mNa^3 \cdot hNa$$

Maximum conductance:

$$\bar{g}Na = 100(mS/cm^2)$$

Traub resting potential: $vtraub = -50(mV)$

$$v = V - vtraub$$

Temperature adjustment:

$$tadj = 3^{(\frac{T-36}{10})}$$

Activation parameter mNa:

$$\begin{aligned} \alpha_{mNa} &= \frac{0.32 \cdot (13.001 - v)}{e^{(13.001-v)/4} - 1} \\ \beta_{mNa} &= \frac{0.28 \cdot (v - 40.001)}{e^{(v-40.001)/5} - 1} \end{aligned}$$

$$\begin{aligned} mNa_\infty &= \frac{\alpha_{mNa}}{\alpha_{mNa} + \beta_{mNa}} \\ \tau_{mNa} &= \frac{1}{\alpha_{mNa} + \beta_{mNa}} \cdot \frac{1}{tadj} \end{aligned}$$

Activation dynamics:

$$\begin{aligned} \frac{dmNa}{dt} &= \alpha_{mNa}(1 - mNa) - \beta_{mNa} \cdot mNa \\ &= -\frac{1}{\tau_{mNa}}(mNa - mNa_\infty) \end{aligned} \tag{B.3}$$

Integration of activation parameter mNa:

$$\begin{aligned} factor_{mNa} &= e^{-dt/\tau_{mNa}} \\ constant_{mNa} &= mNa_\infty \cdot (1 - e^{-dt/\tau_{mNa}}) \\ mNa &= factor_{mNa} \cdot mNa_{prev} + constant_{mNa} \end{aligned} \tag{B.4}$$

Inactivation parameter hNa:

$$\begin{aligned} \alpha_{hNa} &= 0.128 \cdot e^{(17-v)/18} \\ \beta_{hNa} &= \frac{4}{1 + e^{(40-v)/5}} \end{aligned}$$

$$\begin{aligned} hNa_\infty &= \frac{\alpha_{hNa}}{\alpha_{hNa} + \beta_{hNa}} \\ \tau_h &= \frac{1}{\alpha_{hNa} + \beta_{hNa}} \cdot \frac{1}{tadj} \end{aligned}$$

Inactivation dynamics:

$$\frac{dhNa}{dt} = -\frac{1}{\tau_{hNa}}(hNa - hNa_{\infty}) \tag{B.5}$$

Integration of inactivation parameter hNa:

$$\begin{aligned} factor_{hNa} &= e^{-dt/\tau_{hNa}} \\ constant_{hNa} &= hNa_{\infty} \cdot (1 - e^{-dt/\tau_{hNa}}) \\ hNa &= factor_{hNa} \cdot hNa_{prev} + constant_{hNa} \end{aligned} \tag{B.6}$$

- **Fast potassium (K) channel:**
  Reversal potential:

$$E_K = -95(mV)$$

  Conductance:

$$gK = \bar{g}K \cdot mK^4$$

  Maximum conductance:

$$\bar{g}K = 10(mS/cm^2)$$

  Traub resting potential: $vtraub = -50(mV)$

$$v = V - vtraub$$

  Temperature adjustment:

$$tadj = 3^{(\frac{T-36}{10})}$$

  Activation parameter mK:

$$\begin{aligned} \alpha_{mK} &= \frac{0.032 \cdot (15.001 - v)}{e^{(15.001-v)/5} - 1} \\ \beta_{mK} &= 0.5 \cdot e^{(10-v)/40} \end{aligned}$$

$$\begin{aligned} mK_{\infty} &= \frac{\alpha_{mK}}{\alpha_{mK} + \beta_{mK}} \\ \tau_{mK} &= \frac{1}{\alpha_{mK} + \beta_{mK}} \cdot \frac{1}{tadj} \end{aligned}$$

  Activation dynamics:

$$\frac{dmK}{dt} = -\frac{1}{\tau_{mK}}(mK - mK_{\infty}) \tag{B.7}$$

  Integration of activation parameter mK:

$$\begin{aligned} factor_{mK} &= e^{-dt/\tau_{mK}} \\ constant_{mK} &= mK_{\infty} \cdot (1 - e^{-dt/\tau_{mK}}) \\ mK &= factor_{mK} \cdot mK_{prev} + constant_{mK} \end{aligned} \tag{B.8}$$

- **Low-threshold Ca^{2+} (T) channel:**
  Temperature adjustment:

$$T_K = T + 273.15(K)$$

Unit conversion constant:

$$k' = 1000$$

Gas constant:

$$R = 8.31441(Jmol^{-1}K^{-1})$$

Extracellular Ca^{2+} concentration:

$$[Ca]_o = 2(mM)$$

Reversal potential:

$$E_T = k' \frac{R \cdot T_K}{2F} log \frac{[Ca]_o}{[Ca]_i}$$

Conductance:

$$gT = \bar{g}T \cdot mT^2 \cdot hT$$

Maximum conductance:

$$\bar{g}T = 2.3(mS/cm^2)$$

Temperature adjustment:

$$phi_m = 5^{\frac{T-24}{10}}$$
$$phi_h = 3^{\frac{T-24}{10}}$$

Shift:

$$shift = 2(mV)$$

Activation parameter mT:

$$\begin{aligned} mT_\infty &= \frac{1}{1 + e^{-(V+shift+50)/7.4}} \\ \tau_{mT} &= (3 + \frac{1}{e^{(V+shift+25)/10} + e^{-(V+shift+100)/15}}) \cdot \frac{1}{phi_m} \end{aligned}$$

Activation dynamics:

$$\frac{dmT}{dt} = -\frac{1}{\tau_{mT}}(mT - mT_\infty) \tag{B.9}$$

Integration of activation parameter mT:

$$\begin{aligned} factor_{mT} &= e^{-dt/\tau_{mT}} \\ constant_{mT} &= mT_\infty \cdot (1 - e^{-dt/\tau_{mT}}) \\ mT &= factor_{mT} \cdot mT_{prev} + constant_{mT} \end{aligned} \tag{B.10}$$

Inactivation parameter hT:

$$\begin{aligned} hT_\infty &= \frac{1}{1 + e^{(V+shift+78)/5}} \\ \tau_{hT} &= (85 + \frac{1}{e^{(V+shift+46)/4} + e^{-(V+shift+405)/50}}) \cdot \frac{1}{phi_h} \end{aligned}$$

Inactivation dynamics:

$$\frac{dhT}{dt} = -\frac{1}{\tau_{hT}}(hT - hT_\infty) \tag{B.11}$$

Integration of inactivation parameter hT:

$$\begin{aligned} factor_{hT} &= e^{-dt/\tau_{hT}} \\ constant_{hT} &= hT_\infty \cdot (1 - e^{-dt/\tau_{hT}}) \\ hT &= factor_{hT} \cdot hT_{prev} + constant_{hT} \end{aligned} \tag{B.12}$$

- **Kinetic of intracellular calcium dynamics ($[Ca]_i$):**
  Faraday constant:
  $$F = 96489(Cmol^{-1})$$
  Depth of the shell beneath the membrane:
  $$d = 1(\mu m)$$
  Unit conversion constant:
  $$k = 10$$
  Influx of Ca^{2+} is governed by:
  $$[\dot{Ca}]_{i,in} = \begin{cases} -\frac{k}{2Fd} I_T & if > 0 \\ 0 & if \leq 0 \end{cases}$$
  Time constant of calcium efflux:
  $$\tau_{Ca} = 5(ms)$$
  Intracellular concentration at rest:
  $$[Ca]_\infty = 2.4 \times 10^{-4}(mM)$$
  Efflux of calcium can be modeled by a first-order decay term:
  $$[\dot{Ca}]_{i,ef} = -\frac{1}{\tau_{Ca}}([Ca]_i - [Ca]_\infty)$$
  Calcium concentration dynamics:
  $$\begin{aligned} \frac{d[Ca]_i}{dt} &= [\dot{Ca}]_{i,in} + [\dot{Ca}]_{i,ef} \\ &= [\dot{Ca}]_{i,in} - \frac{1}{\tau_{Ca}}([Ca]_i - [Ca]_\infty) \\ &= -\frac{1}{\tau_{Ca}}([Ca]_i - ([Ca]_\infty + \tau_{Ca} \cdot [Ca]_{i,in})) \end{aligned} \tag{B.13}$$
  Integration of calcium dynamics $[Ca]_i$:
  $$\begin{aligned} factor_{[Ca]_i} &= e^{-dt/\tau_{Ca}} \\ [Ca]_i &= factor_{[Ca]_i} \cdot [Ca]_{i,prev} + (1 - factor_{[Ca]_i}) \cdot ([Ca]_\infty + \tau_{Ca} \cdot [Ca]_{i,in}) \end{aligned} \tag{B.14}$$
  Minimum of $[Ca]_i$:
  $$minCa = 1e - 6$$
  Update $[Ca]_i$ according to minimum (Avoid negative values):
  $$[Ca]_i = max(minCa, [Ca]_i)$$
- **Potassium leak (Kl) current:**
  Reversal potential:
  $$E_{Kl} = -95(mV)$$
  Conductance:
  $$gKl = 0.005(mS/cm^2)$$

- **Hodgkin-Huxley kinetics of synaptic currents of RE:**

$$\begin{aligned} -I_{RE}^{syn} &= (-\bar{g}_{GABAA}^{RE,RE} \cdot r_{GABAA}^{RE,RE} \cdot (V - E_{GABAA}^{RE,RE}) - \bar{g}_{AMPA}^{TC,RE} \cdot r_{AMPA}^{TC,RE} \cdot (V - E_{AMPA}^{TC,RE}) \\ &\quad -\bar{g}_{AMPA}^{PY,RE} \cdot r_{AMPA}^{PY,RE} \cdot (V - E_{AMPA}^{PY,RE})) \cdot \frac{1}{S_{RE}} \\ &= -\frac{1}{S_{RE}} \cdot (\bar{g}_{GABAA}^{RE,RE} \cdot r_{GABAA}^{RE,RE} \cdot + \bar{g}_{AMPA}^{TC,RE} \cdot r_{AMPA}^{TC,RE} \cdot + \bar{g}_{AMPA}^{PY,RE} \cdot r_{AMPA}^{PY,RE}) V \\ &\quad + \frac{1}{S_{RE}} \cdot (\bar{g}_{GABAA}^{RE,RE} \cdot r_{GABAA}^{RE,RE} \cdot E_{GABAA}^{RE,RE} + \bar{g}_{AMPA}^{TC,RE} \cdot r_{AMPA}^{TC,RE} \cdot E_{AMPA}^{TC,RE} \\ &\quad + \bar{g}_{AMPA}^{PY,RE} \cdot r_{AMPA}^{PY,RE} \cdot E_{AMPA}^{PY,RE}) \\ &= -\frac{1}{S_{RE}} \cdot g_{synRE} V + \frac{1}{S_{RE}} \cdot I_{leaksynRE} \end{aligned} \tag{B.15}$$

- **GABA$_A$ receptors (RE → RE):**
  Maximum conductance and Reversal potential:

$$\bar{g}_{GABAA}^{RE,RE} = 0.0002(mS/cm^2) \ , \ E_{GABAA}^{RE,RE} = -70(mV)$$

  Maximal concentration of the transmitter during the pulse:

$$C_{max} = 0.5(mM)$$

  Release duration:

$$C_{dur} = 0.3(mS)$$

  Voltage-independent forward and backward rate constants:

$$\alpha_{GABAA} = 10.5(/mS \cdot mM)$$
$$\beta_{GABAA} = 0.166(/mS)$$

  Pre-synaptic spike detection thereshold:

$$prethresh = 0(mV)$$

  Deadtime when spike can not occur:

$$deadtime = 1(mS)$$

  Parameters of fraction of receptors in the open state:

$$\begin{aligned} r_{\infty,GABAA} &= \frac{C_{max} \cdot \alpha_{GABAA}}{C_{max} \cdot \alpha_{GABAA} + \beta_{GABAA}} \\ \tau_{r,GABAA} &= \frac{1}{C_{max} \cdot \alpha_{GABAA} + \beta_{GABAA}} \end{aligned}$$

  Conditions and procedures:
  ▷ Release is possible:
  ◇ if ((time)−(lastrelease)−C_{dur} > deadtime)
  ◇ Release occur:
  ◇ if (the presynaptic neuron's voltage > prethresh)
  ◇ → $C = C_{max}$ → lastrelease=time
  ◇ Release doesn't occur: → do nothing
  ▷ Release is not possible:
  ◇ We should close the release
  ◇ if ((time)−(lastrelease)−$C_{dur} \geq 0$) && (C=C_{max})

◇ $\rightarrow C = 0$
◇ Else: $\rightarrow$ do nothing
♣ $C > 0 \rightarrow$ Release is hapenning
♣ $C = 0 \rightarrow$ Release is absent

Dynamics:

$$\begin{aligned}\frac{dr^{RE,RE}_{GABAA}}{dt} &= \alpha \cdot [T] \cdot (1 - r^{RE,RE}_{GABAA}) - \beta \cdot r^{RE,RE}_{GABAA} \\ &= -(C \cdot \alpha_{GABAA} + \beta_{GABAA})(r^{RE,RE}_{GABAA} - \frac{C \cdot \alpha_{GABAA}}{C_{max} \cdot \alpha_{GABAA} + \beta_{GABAA}})\end{aligned} \tag{B.16}$$

Integration of parameter r with respect to release:

$$\begin{aligned}factor_{grow,GABAA} &= e^{-\frac{dt}{\tau_{r,GABAA}}} \\ constant_{grow,GABAA} &= r_{\infty,GABAA} \cdot (1 - e^{-\frac{dt}{\tau_{r,GABAA}}}) \\ factor_{decay,GABAA} &= e^{-\beta_{GABAA} \cdot dt}\end{aligned}$$

$$r^{RE,RE}_{GABAA} = \begin{cases} factor_{grow,GABAA} \cdot r^{RE,RE}_{GABAA,prev} + constant_{grow,GABAA} & C > 0 \\ factor_{decay,GABAA} \cdot r^{RE,RE}_{GABAA,prev} & C \leq 0 \end{cases} \tag{B.17}$$

- **AMPA receptors (TC → RE):**
  Maximum conductance and Reversal potential:

$$\bar{g}^{TC,RE}_{AMPA} = 0.0004(mS/cm^2) \ , \ E^{TC,RE}_{AMPA} = 0(mV)$$

Maximal concentration of the transmitter during the pulse:

$$C_{max} = 0.5(mM)$$

Release duration:

$$C_{dur} = 0.3(mS)$$

Voltage-independent forward and backward rate constants:

$$\begin{aligned}\alpha_{AMPA} &= 0.94(/mS \cdot mM) \\ \beta_{AMPA} &= 0.18(/mS)\end{aligned}$$

Pre-synaptic spike detection threshold:

$$prethresh = 0(mV)$$

Deadtime when spike can not occur:

$$deadtime = 1(mS)$$

Parameters of fraction of receptors in the open state:

$$\begin{aligned}r_{\infty,AMPA} &= \frac{C_{max} \cdot \alpha_{AMPA}}{C_{max} \cdot \alpha_{AMPA} + \beta_{AMPA}} \\ \tau_{r,AMPA} &= \frac{1}{C_{max} \cdot \alpha_{AMPA} + \beta_{AMPA}}\end{aligned}$$

Conditions and procedures:
▷ Release is possible:
◇ if ((time)−(lastrelease)$-C_{dur}$ > deadtime)
◇ Release occur:
◇ if (the presynaptic neuron's voltage > prethresh)
◇ → $C = C_{max}$ → lastrelease=time
◇ Release doesn't occur: → do nothing
▷ Release is not possible:
◇ We should close the release
◇ if ((time)−(lastrelease)$-C_{dur} \geq 0$) && (C=C_{max})
◇ → $C = 0$
◇ Else: → do nothing
♣ $C > 0$ → Release is hapenning
♣ $C = 0$ → Release is absent

Dynamics:

$$\begin{aligned} \frac{dr^{TC,RE}_{AMPA}}{dt} &= \alpha \cdot [T] \cdot (1 - r^{TC,RE}_{AMPA}) - \beta \cdot r^{TC,RE}_{AMPA} \\ &= -(C \cdot \alpha_{AMPA} + \beta_{AMPA})(r^{TC,RE}_{AMPA} - \frac{C \cdot \alpha_{AMPA}}{C_{max} \cdot \alpha_{AMPA} + \beta_{AMPA}}) \end{aligned} \quad \text{(B.18)}$$

Integration of parameter r with respect to release:

$$\begin{aligned} factor_{grow,AMPA} &= e^{-\frac{dt}{\tau_{r,AMPA}}} \\ constant_{grow,AMPA} &= r_{\infty,AMPA} \cdot (1 - e^{-\frac{dt}{\tau_{r,AMPA}}}) \\ factor_{decay,AMPA} &= e^{-\beta_{AMPA} \cdot dt} \end{aligned}$$

$$r^{TC,RE}_{AMPA} = \begin{cases} factor_{grow,AMPA} \cdot r^{TC,RE}_{AMPA,prev} + constant_{grow,AMPA} & C > 0 \\ factor_{decay,AMPA} \cdot r^{TC,RE}_{AMPA,prev} & C \leq 0 \end{cases} \quad \text{(B.19)}$$

- **AMPA receptors (PY → RE):**
Maximum conductance and Reversal potential:

$$\bar{g}^{PY,RE}_{AMPA} = 0.00005(mS/cm^2) \ , \ E^{PY,RE}_{AMPA} = 0(mV)$$

Maximal concentration of the transmitter during the pulse:

$$C_{max} = 0.5(mM)$$

Release duration:

$$C_{dur} = 0.3(mS)$$

Voltage-independent forward and backward rate constants:

$$\alpha_{AMPA} = 0.94(/mS \cdot mM)$$
$$\beta_{AMPA} = 0.18(/mS)$$

Pre-synaptic spike detection thereshold:

$$prethresh = 0(mV)$$

Deadtime when spike can not occur:

$$deadtime = 1(mS)$$

Parameters of fraction of receptors in the open state:

$$\begin{aligned} r_{\infty,AMPA} &= \frac{C_{max} \cdot \alpha_{AMPA}}{C_{max} \cdot \alpha_{AMPA} + \beta_{AMPA}} \\ \tau_{r,AMPA} &= \frac{1}{C_{max} \cdot \alpha_{AMPA} + \beta_{AMPA}} \end{aligned}$$

Conditions and procedures:
▷ Release is possible:
◇ if ((time)−(lastrelease)$-C_{dur}$ > deadtime)
◇ Release occur:
◇ if (the presynaptic neuron's voltage > prethresh)
◇ → $C = C_{max}$ → lastrelease=time
◇ Release doesn't occur: → do nothing
▷ Release is not possible:
◇ We should close the release
◇ if ((time)−(lastrelease)$-C_{dur} \geq 0$) && (C=C_{max})
◇ → $C = 0$
◇ Else: → do nothing
♣ $C > 0$ → Release is hapenning
♣ $C = 0$ → Release is absent

Dynamics:

$$\begin{aligned} \frac{dr^{PY,RE}_{AMPA}}{dt} &= \alpha \cdot [T] \cdot (1 - r^{PY,RE}_{AMPA}) - \beta \cdot r^{PY,RE}_{AMPA} \\ &= -(C \cdot \alpha_{AMPA} + \beta_{AMPA})(r^{PY,RE}_{AMPA} - \frac{C \cdot \alpha_{AMPA}}{C_{max} \cdot \alpha_{AMPA} + \beta_{AMPA}}) \end{aligned} \tag{B.20}$$

Integration of parameter r with respect to release:

$$\begin{aligned} factor_{grow,AMPA} &= e^{-\frac{dt}{\tau_{r,AMPA}}} \\ constant_{grow,AMPA} &= r_{\infty,AMPA} \cdot (1 - e^{-\frac{dt}{\tau_{r,AMPA}}}) \\ factor_{decay,AMPA} &= e^{-\beta_{AMPA} \cdot dt} \end{aligned}$$

$$r^{PY,RE}_{AMPA} = \begin{cases} factor_{grow,AMPA} \cdot r^{PY,RE}_{AMPA,prev} + constant_{grow,AMPA} & C > 0 \\ factor_{decay,AMPA} \cdot r^{PY,RE}_{AMPA,prev} & C \leq 0 \end{cases} \tag{B.21}$$

- **Integration of the membrane voltage of RE:**

$$\begin{aligned} C_m\frac{dV}{dt} &= -g_L(V-E_L) - g_{intRE}V + I_{leakintRE} - \frac{1}{S_{RE}}\cdot g_{synRE}V \\ &\quad + \frac{1}{S_{RE}}\cdot I_{leaksynRE} \\ &= -(g_L + g_{intRE} + \frac{1}{S_{RE}}\cdot g_{synRE})V \\ &\quad + (g_L\cdot E_L + I_{leakintRE} + \frac{1}{S_{RE}}\cdot I_{leaksynRE}) \\ &= -g_{totRE}V + I_{leaktotRE} \\ \frac{dV}{dt} &= -\frac{g_{totRE}}{C_m}(V - \frac{I_{leaktotRE}}{g_{totRE}}) \qquad \text{(B.22)} \\ factor_V &= e^{-\frac{g_{totRE}}{C_m}\cdot dt} \\ constant_V &= \frac{I_{leaktotRE}}{g_{totRE}}\cdot(1 - e^{-\frac{g_{totRE}}{C_m}\cdot dt}) \end{aligned}$$

$$V = factor_V \cdot V_{prev} + constant_V \qquad \text{(B.23)}$$

B.1.2 Thalamocortical neuron (TC)

- **Hodgkin-Huxley kinetics of intrinsic currents of TC:**

$$\begin{aligned} -I_{TC}^{int} &= -g_{Na}(V-E_{Na}) - g_K(V-E_K) - g_T(V-E_T) - g_h(V-E_h) \\ &\quad -g_{KL}(V-E_{KL}) \\ &= -(g_{Na}+g_K+g_T+g_h+g_{KL})V \\ &\quad +(g_{Na}E_{Na}+g_KE_K+g_TE_T+g_hE_h+g_{KL}E_{KL}) \\ &= -g_{intTC}V + I_{leakintTC} \qquad \text{(B.24)} \end{aligned}$$

- **Fast sodium (Na) channel:**
  Reversal potential:

$$E_{Na} = 50(mV)$$

  Conductance:

$$gNa = \bar{g}Na\cdot mNa^3\cdot hNa$$

  Maximum conductance:

$$\bar{g}Na = 90(mS/cm^2)$$

  Traub resting potential: $vtraub = -40(mV)$

$$v = V - vtraub$$

  Temperature adjustment:

$$tadj = 3^{(\frac{T-36}{10})}$$

Activation parameter mNa:

$$\begin{aligned} \alpha_{mNa} &= \frac{0.32 \cdot (13.001 - v)}{e^{(13.001-v)/4} - 1} \\ \beta_{mNa} &= \frac{0.28 \cdot (v - 40.001)}{e^{(v-40.001)/5} - 1} \end{aligned}$$

$$\begin{aligned} mNa_\infty &= \frac{\alpha_{mNa}}{\alpha_{mNa} + \beta_{mNa}} \\ \tau_{mNa} &= \frac{1}{\alpha_{mNa} + \beta_{mNa}} \cdot \frac{1}{tadj} \end{aligned}$$

Activation dynamics:

$$\begin{aligned} \frac{dmNa}{dt} &= \alpha_{mNa}(1 - mNa) - \beta_{mNa} \cdot mNa \\ &= -\frac{1}{\tau_{mNa}}(mNa - mNa_\infty) \end{aligned} \tag{B.25}$$

Integration of activation parameter mNa:

$$\begin{aligned} factor_{mNa} &= e^{-dt/\tau_{mNa}} \\ constant_{mNa} &= mNa_\infty \cdot (1 - e^{-dt/\tau_{mNa}}) \\ mNa &= factor_{mNa} \cdot mNa_{prev} + constant_{mNa} \end{aligned} \tag{B.26}$$

Inactivation parameter hNa:

$$\begin{aligned} \alpha_{hNa} &= 0.128 \cdot e^{(17-v)/18} \\ \beta_{hNa} &= \frac{4}{1 + e^{(40-v)/5}} \end{aligned}$$

$$\begin{aligned} hNa_\infty &= \frac{\alpha_{hNa}}{\alpha_{hNa} + \beta_{hNa}} \\ \tau_h &= \frac{1}{\alpha_{hNa} + \beta_{hNa}} \cdot \frac{1}{tadj} \end{aligned}$$

Inactivation dynamics:

$$\frac{dhNa}{dt} = -\frac{1}{\tau_{hNa}}(hNa - hNa_\infty) \tag{B.27}$$

Integration of inactivation parameter hNa:

$$\begin{aligned} factor_{hNa} &= e^{-dt/\tau_{hNa}} \\ constant_{hNa} &= hNa_\infty \cdot (1 - e^{-dt/\tau_{hNa}}) \\ hNa &= factor_{hNa} \cdot hNa_{prev} + constant_{hNa} \end{aligned} \tag{B.28}$$

- **Fast potassium (K) channel:**
  Reversal potential:

$$E_K = -95(mV)$$

Conductance:

$$gK = \bar{g}K \cdot mK^4$$

Maximum conductance:

$$\bar{g}K = 12(mS/cm^2)$$

Traub resting potential: $vtraub = -25(mV)$

$$v = V - vtraub$$

Temperature adjustment:

$$tadj = 3^{(\frac{T-36}{10})}$$

Activation parameter mK:

$$\begin{aligned} \alpha_{mK} &= \frac{0.032 \cdot (15.001 - v)}{e^{(15.001-v)/5} - 1} \\ \beta_{mK} &= 0.5 \cdot e^{(10-v)/40} \end{aligned}$$

$$\begin{aligned} mK_\infty &= \frac{\alpha_{mK}}{\alpha_{mK} + \beta_{mK}} \\ \tau_{mK} &= \frac{1}{\alpha_{mK} + \beta_{mK}} \cdot \frac{1}{tadj} \end{aligned}$$

Activation dynamics:

$$\frac{dmK}{dt} = -\frac{1}{\tau_{mK}}(mK - mK_\infty) \tag{B.29}$$

Integration of activation parameter mK:

$$\begin{aligned} factor_{mK} &= e^{-dt/\tau_{mK}} \\ constant_{mK} &= mK_\infty \cdot (1 - e^{-dt/\tau_{mK}}) \\ mK &= factor_{mK} \cdot mK_{prev} + constant_{mK} \end{aligned} \tag{B.30}$$

- **Low-threshold Ca^{2+} (T) channel:**
  Temperature adjustment:

$$T_K = T + 273.15(K)$$

Unit conversion constant:

$$k' = 1000$$

Gas constant:

$$R = 8.31441(Jmol^{-1}K^{-1})$$

Extracellular Ca^{2+} concentration:

$$[Ca]_o = 2(mM)$$

Reversal potential:

$$E_T = k' \frac{R \cdot T_K}{2F} log \frac{[Ca]_o}{[Ca]_i}$$

Conductance:

$$gT = \bar{g}T \cdot mT^2 \cdot hT$$

Maximum conductance:

$$\bar{g}T = 2.2(mS/cm^2)$$

Temperature adjustment:

$$phi_m = 3.55^{\frac{T-24}{10}}$$
$$phi_h = 3^{\frac{T-24}{10}}$$

Shift:

$$shift = 2(mV)$$

Activation parameter mT:

$$\begin{aligned} mT_\infty &= \frac{1}{1+e^{-(V+59)/6.2}} \\ \tau_{mT} &= (0.612 + \frac{1}{e^{(V+16.8)/18.2}+e^{-(V+131.6)/16.7}}) \cdot \frac{1}{phi_m} \end{aligned}$$

Activation dynamics:

$$\frac{dmT}{dt} = -\frac{1}{\tau_{mT}}(mT - mT_\infty) \tag{B.31}$$

Integration of activation parameter mT:

$$\begin{aligned} factor_{mT} &= e^{-dt/\tau_{mT}} \\ constant_{mT} &= mT_\infty \cdot (1 - e^{-dt/\tau_{mT}}) \\ mT &= factor_{mT} \cdot mT_{prev} + constant_{mT} \end{aligned} \tag{B.32}$$

Inactivation parameter hT:

$$\begin{aligned} hT_\infty &= \frac{1}{1+e^{(V+83)/4}} \\ \tau_{hT} &= (30.8 + \frac{211.4 + e^{(V+shift+113.2)/5}}{1+e^{(V+shift+84)/3.2}}) \cdot \frac{1}{phi_h} \end{aligned}$$

Inactivation dynamics:

$$\frac{dhT}{dt} = -\frac{1}{\tau_{hT}}(hT - hT_\infty) \tag{B.33}$$

Integration of inactivation parameter hT:

$$\begin{aligned} factor_{hT} &= e^{-dt/\tau_{hT}} \\ constant_{hT} &= hT_\infty \cdot (1 - e^{-dt/\tau_{hT}}) \\ hT &= factor_{hT} \cdot hT_{prev} + constant_{hT} \end{aligned} \tag{B.34}$$

- **Hyperpolarization-activated cation (h) channel:**
  Reversal potential:

$$E_h = -40(mV)$$

Conductance:

$$gh = \bar{g}h \cdot (Oh + g_{inc} \cdot Olh)$$

Maximum conductance:

$$\bar{g}h = 0.017(mS/cm^2)$$

Factor:

$$g_{inc} = 2$$

Temperature adjustment:

$$tadj = 3^{\frac{T-36}{10}}$$

Half-activation of calcium dependence:

$$cac = 0.0015(mM)$$

Half-activation of CB protein dependence:

$$pc = 0.01$$

Inverse of time constant:

$$k2 = 0.0004(ms^{-1})$$

Backward binding on I_h:

$$k4 = 0.001(ms^{-1})$$

Shift:

$$shift = 0(mV)$$

Number of binding sites of Ca^{2+}:

$$nca = 4$$

Number of binding sites on I_h channels:

$$nexp = 1$$

Minimal value of τ_{mh}:

$$taumin = 20(ms)$$

Kinetic scheme:
Normal voltage-dependent opening of I_h channels $-->$

$$C \underset{\beta}{\overset{\alpha}{\rightleftharpoons}} Oh$$

Ca^{2+} binding on CB protein $-->$

$$p0(inactive) + nca \cdot Ca^{2+} \underset{k2}{\overset{k1}{\rightleftharpoons}} ph(active)$$

Binding of active CB protein on the open form $-->$

$$Oh + nexp \cdot ph \underset{k4}{\overset{k3}{\rightleftharpoons}} Olh$$

Activation dynamics:

$$\begin{aligned}
\frac{dOh}{dt} &= \alpha \cdot (1 - Oh - Olh) - \beta \cdot Oh \\
&= -(\alpha + \beta) \cdot Oh + \alpha \cdot (1 - Olh) \\
&= -(\alpha + \beta) \cdot (Oh + \frac{\alpha \cdot (1 - Olh)}{\alpha + \beta}) \\
&= -\frac{1}{\tau_{Oh}} \cdot (Oh - Oh_\infty \cdot (1 - Olh)) \qquad \text{(B.35)} \\
\frac{dPh}{dt} &= k1 \cdot [Ca]_i^{nca} \cdot (1 - Ph) - k2 \cdot Ph \\
&= -(k1 \cdot [Ca]_i^{nca} + k2) \cdot Ph + k1 \cdot [Ca]_i^{nca} \\
&= -(k1 \cdot [Ca]_i^{nca} + k2) \cdot (Ph - \frac{k1 \cdot [Ca]_i^{nca}}{k1 \cdot [Ca]_i^{nca} + k2}) \qquad \text{(B.36)} \\
\frac{dOlh}{dt} &= k3 \cdot Ph \cdot Oh - k4 \cdot Olh \\
&= -k4 \cdot (Olh - \frac{k3}{k4} \cdot Ph \cdot Oh) \qquad \text{(B.37)}
\end{aligned}$$

Activation parameters:

$$\begin{aligned}
Oh_\infty &= \frac{1}{1 + e^{(V - shift + 75)/5.5}} \\
\tau_{Oh} &= (taumin + \frac{1000}{e^{(V - shift + 71.5)/14.2} + e^{-(V - shift + 89)/11.6}}) \cdot \frac{1}{tadj} \\
k1 &= k2 \cdot (\frac{1}{cac})^{nca} \\
k3 &= k4 \cdot (\frac{1}{pc})^{nexp}
\end{aligned}$$

Integration of activation parameters:

$$\begin{aligned}
factor_{Oh} &= e^{-\frac{dt}{\tau_{Oh}}} \\
constant_{Oh} &= Oh_\infty \cdot (1 - e^{-\frac{dt}{\tau_{Oh}}}) \\
Oh &= factor_{Oh} \cdot Oh_{prev} + constant_{Oh} \cdot (1 - Olh_{prev}) \qquad \text{(B.38)} \\
factor_{Ph} &= e^{-(k1 \cdot [Ca]_i^{nca} + k2) \cdot dt} \\
constant_{Ph} &= \frac{k1 \cdot [Ca]_i^{nca}}{k1 \cdot [Ca]_i^{nca} + k2} \cdot (1 - e^{-(k1 \cdot [Ca]_i^{nca} + k2) \cdot dt}) \\
Ph &= factor_{Ph} \cdot Ph_{prev} + constant_{Ph} \qquad \text{(B.39)} \\
factor_{Olh} &= e^{-k4 \cdot dt} \\
constant_{Olh} &= \frac{k3}{k4} \cdot (1 - e^{-k4 \cdot dt}) \\
Olh &= factor_{Olh} \cdot Olh_{prev} + constant_{Olh} \cdot Oh_{prev} \cdot Ph_{prev} \qquad \text{(B.40)}
\end{aligned}$$

- **Kinetic of intracellular calcium dynamics ($[Ca]_i$):**
  Faraday constant:

$$F = 96489(Cmol^{-1})$$

Depth of the shell beneath the membrane:

$$d = 1(\mu m)$$

Unit conversion constant:

$$k = 10$$

Influx of Ca^{2+} is governed by:

$$[\dot{Ca}]_{i,in} = \begin{cases} -\frac{k}{2Fd} I_T & if > 0 \\ 0 & if \leq 0 \end{cases}$$

Time constant of calcium efflux:

$$\tau_{Ca} = 5(ms)$$

Intracellular concentration at rest:

$$[Ca]_\infty = 2.4 \times 10^{-4}(mM)$$

Efflux of calcium can be modeled by a first-order decay term:

$$[\dot{Ca}]_{i,ef} = -\frac{1}{\tau_{Ca}}([Ca]_i - [Ca]_\infty)$$

Calcium concentration dynamics:

$$\begin{aligned} \frac{d[Ca]_i}{dt} &= [\dot{Ca}]_{i,in} + [\dot{Ca}]_{i,ef} \\ &= [\dot{Ca}]_{i,in} - \frac{1}{\tau_{Ca}}([Ca]_i - [Ca]_\infty) \\ &= -\frac{1}{\tau_{Ca}}([Ca]_i - ([Ca]_\infty + \tau_{Ca} \cdot [Ca]_{i,in})) \end{aligned} \tag{B.41}$$

Integration of calcium dynamics $[Ca]_i$:

$$\begin{aligned} factor_{[Ca]_i} &= e^{-dt/\tau_{Ca}} \\ [Ca]_i &= factor_{[Ca]_i} \cdot [Ca]_{i,prev} + (1 - factor_{[Ca]_i}) \cdot ([Ca]_\infty + \tau_{Ca} \cdot [Ca]_{i,in}) \end{aligned} \tag{B.42}$$

Minimum of $[Ca]_i$:

$$minCa = 1e - 6$$

Update $[Ca]_i$ according to minimum (Avoid negative values):

$$[Ca]_i = max(minCa, [Ca]_i)$$

- **Potassium (A) channel:**
  Reversal potential:

$$E_A = -95(mV)$$

Conductance:

$$gA = \bar{g}A \cdot mA^4 \cdot hA$$

Maximum conductance:

$$\bar{g}A = 0(mS/cm^2)$$

Temperature adjustment:

$$tadj = 3^{\frac{T-23.5}{10}}$$

Activation parameter mA:

$$\begin{aligned} mA_\infty &= \frac{1}{1+e^{-(V+60)/8.5}} \\ \tau_{mA} &= (0.37 + \frac{1}{e^{(V+35.82)/19.69}+e^{-(V+79.69)/12.7}}) \cdot \frac{1}{tadj} \end{aligned}$$

Integration of activation parameter mA:

$$\begin{aligned} factor_{mA} &= e^{-dt/\tau_{mA}} \\ constant_{mA} &= mA_\infty \cdot (1 - e^{-dt/\tau_{mA}}) \\ mA &= factor_{mA} \cdot mA_{prev} + constant_{mA} \end{aligned} \tag{B.43}$$

Inactivation parameter hA:

$$\begin{aligned} hA_\infty &= \frac{1}{1+e^{(V+78)/6}} \\ \tau_{hA} &= (\frac{1}{e^{(V+46.05)/5}+e^{-(V+238.4)/37.45}}) \cdot \frac{1}{tadj} && ifV < -63 \\ &= \frac{19}{tadj} && ifV \geq -63 \end{aligned}$$

Integration of inactivation parameter hA:

$$\begin{aligned} factor_{hA} &= e^{-dt/\tau_{hA}} \\ constant_{hA} &= hA_\infty \cdot (1 - e^{-dt/\tau_{hA}}) \\ mh &= factor_{mh} \cdot mh_{prev} + constant_{hA} \end{aligned} \tag{B.44}$$

- **Potassium leak (Kl) current:**
  Reversal potential:

$$E_{Kl} = -95(mV)$$

  Conductance:

$$gKl = 0.03(mS/cm^2)$$

- **Hodgkin-Huxley kinetics of synaptic currents of TC:**

$$\begin{aligned}
-I_{TC}^{syn} &= (-\bar{g}_{GABAA}^{RE,TC} \cdot r_{GABAA}^{RE,TC} \cdot (V - E_{GABAA}^{RE,TC}) \\
&\quad -\bar{g}_{GABAB}^{RE,TC} \cdot \frac{(s_{GABAB}^{RE,TC})^n}{(s_{GABAB}^{RE,TC^n})^n + K_d} \cdot (V - E_{GABAB}^{RE,TC}) \\
&\quad -\bar{g}_{AMPA}^{PY,TC} \cdot r_{AMPA}^{PY,TC} \cdot (V - E_{AMPA}^{PY,TC})) \cdot \frac{1}{S_{TC}} \\
&= -\frac{1}{S_{TC}} \cdot (\bar{g}_{GABAA}^{RE,TC} \cdot r_{GABAA}^{RE,TC} \cdot \\
&\qquad +\bar{g}_{GABAB}^{RE,TC} \cdot \frac{(s_{GABAB}^{RE,TC})^n}{(s_{GABAB}^{RE,TC^n})^n + K_d} \cdot + \bar{g}_{AMPA}^{PY,TC} \cdot r_{AMPA}^{PY,TC}) V \\
&\quad + \frac{1}{S_{TC}} \cdot (\bar{g}_{GABAA}^{RE,TC} \cdot r_{GABAA}^{RE,TC} \cdot E_{GABAA}^{RE,TC} \\
&\qquad +\bar{g}_{GABAB}^{RE,TC} \cdot \frac{(s_{GABAB}^{RE,TC})^n}{(s_{GABAB}^{RE,TC^n})^n + K_d} \cdot E_{GABAB}^{RE,TC} \\
&\qquad +\bar{g}_{AMPA}^{PY,TC} \cdot r_{AMPA}^{PY,TC} \cdot E_{AMPA}^{PY,TC}) \\
&= -\frac{1}{S_{TC}} \cdot g_{synTC} V + \frac{1}{S_{TC}} \cdot I_{leaksynTC} \qquad \text{(B.45)}
\end{aligned}$$

- **GABA$_A$ receptors (RE → TC):**
  Maximum conductance and Reversal potential:

$$\bar{g}_{GABAA}^{RE,TC} = 0.0002(mS/cm^2) \ , \ E_{GABAA}^{RE,TC} = -83(mV)$$

  Maximal concentration of the transmitter during the pulse:

$$C_{max} = 0.5(mM)$$

  Release duration:

$$C_{dur} = 0.3(mS)$$

  Voltage-independent forward and backward rate constants:

$$\alpha_{GABAA} = 10.5(/mS \cdot mM)$$
$$\beta_{GABAA} = 0.166(/mS)$$

  Pre-synaptic spike detection thereshold:

$$prethresh = 0(mV)$$

  Deadtime when spike can not occur:

$$deadtime = 1(mS)$$

  Parameters of fraction of receptors in the open state:

$$\begin{aligned}
r_{\infty,GABAA} &= \frac{C_{max} \cdot \alpha_{GABAA}}{C_{max} \cdot \alpha_{GABAA} + \beta_{GABAA}} \\
\tau_{r,GABAA} &= \frac{1}{C_{max} \cdot \alpha_{GABAA} + \beta_{GABAA}}
\end{aligned}$$

  Conditions and procedures:
  ▷ Release is possible:
  ◇ if ((time)−(lastrelease)$-C_{dur}$ > deadtime)

◇ Release occur:
◇ if (the presynaptic neuron's voltage > prethresh)
◇ $\rightarrow C = C_{max} \rightarrow$ lastrelease=time
◇ Release doesn't occur: $\rightarrow$ do nothing
▷ Release is not possible:
◇ We should close the release
◇ if ((time)−(lastrelease)$-C_{dur} \geq 0$) && (C=C_{max})
◇ $\rightarrow C = 0$
◇ Else: $\rightarrow$ do nothing
♣ $C > 0 \rightarrow$ Release is hapenning
♣ $C = 0 \rightarrow$ Release is absent

Dynamics:

$$\begin{aligned} \frac{dr^{RE,TC}_{GABAA}}{dt} &= \alpha \cdot [T] \cdot (1 - r^{RE,TC}_{GABAA}) - \beta \cdot r^{RE,RTC}_{GABAA} \\ &= -(C \cdot \alpha_{GABAA} + \beta_{GABAA})(r^{RE,TC}_{GABAA} - \frac{C \cdot \alpha_{GABAA}}{C_{max} \cdot \alpha_{GABAA} + \beta_{GABAA}}) \end{aligned} \tag{B.46}$$

Integration of parameter r with respect to release:

$$\begin{aligned} factor_{grow,GABAA} &= e^{-\frac{dt}{\tau_{r,GABAA}}} \\ constant_{grow,GABAA} &= r_{\infty,GABAA} \cdot (1 - e^{-\frac{dt}{\tau_{r,GABAA}}}) \\ factor_{decay,GABAA} &= e^{-\beta_{GABAA} \cdot dt} \end{aligned}$$

$$r^{RE,TC}_{GABAA} = \begin{cases} factor_{grow,GABAA} \cdot r^{RE,TC}_{GABAA,prev} + constant_{grow,GABAA} & C > 0 \\ factor_{decay,GABAA} \cdot r^{RE,TC}_{GABAA,prev} & C \leq 0 \end{cases} \tag{B.47}$$

- **GABA$_B$ receptors (RE → TC):**
  Maximum conductance and Reversal potential:

$$\bar{g}^{RE,TC}_{GABAB} = 0.00004(mS/cm^2) \ , \ E^{RE,TC}_{GABAB} = -95(mV)$$

  Maximal concentration of the transmitter during the pulse:

$$C_{max} = 0.5(mM)$$

  Release duration:

$$C_{dur} = 0.3(mS)$$

  Model parameters:

$$\begin{aligned} k1 &= 0.52(ms^{-1}) \\ k2 &= 0.0013(ms^{-1}) \\ k3 &= 0.098(\mu M \cdot ms^{-1}) \\ k4 &= 0.033(ms^{-1}) \end{aligned}$$

  Pre-synaptic spike detection threshold:

$$prethresh = 0(mV)$$

Deadtime when spike can not occur:

$$deadtime = 1(mS)$$

Dissociation constant of the binding of g on the K^+ channels:

$$K_d = 100(\mu M^4)$$

Binding sites:

$$n = 4$$

Conditions and procedures:
▷ Release is possible:
◇ if ((time)−(lastrelease)−C_{dur} > deadtime)
◇ Release occur:
◇ if (the presynaptic neuron's voltage > prethresh)
◇ → $C = C_{max}$ → lastrelease=time
◇ Release doesn't occur: → do nothing
▷ Release is not possible:
◇ We should close the release
◇ if ((time)−(lastrelease)−$C_{dur} \geq 0$) && (C=C_{max})
◇ → $C = 0$
◇ Else: → do nothing
♣ $C > 0$ → Release is hapenning
♣ $C = 0$ → Release is absent

Dynamics:

$$\begin{aligned} \frac{dr^{RE,TC}_{GABAB}}{dt} &= k1 \cdot C \cdot (1 - r^{RE,TC}_{GABAB}) - k2 \cdot r^{RE,TC}_{GABAB} \\ \frac{ds}{dt} &= k3 \cdot r^{RE,TC}_{GABAB} - k4 \cdot s \end{aligned}$$

Integration of parameters r and s with respect to release:

$$\begin{aligned} factorR_{grow,GABAB} &= e^{-(k1 \cdot C_{max} + k2) \cdot dt} \\ constantR_{grow,GABAB} &= \frac{k1 \cdot C_{max}}{k1 \cdot C_{max} + k2} \cdot (1 - e^{-(k1 \cdot C_{max} + k2) \cdot dt}) \\ factorR_{decay,GABAB} &= e^{-k2 \cdot dt} \\ factorS_{GABAB} &= e^{-k4 \cdot dt} \\ factorRinS_{grow,GABAB} &= \frac{k3}{k1 \cdot C_{max} + k2 - k4} \cdot (e^{-k4 \cdot dt} - e^{-(k1 \cdot C_{max} + k2) \cdot dt}) \\ constantS_{grow,GABAB} &= \frac{k1 \cdot C_{max} \cdot k3}{k1 \cdot C_{max} + k2 - k4} \cdot (\frac{1 - e^{-k4 \cdot dt}}{k4} - \frac{1 - e^{-(k1 \cdot C_{max} + k2) \cdot dt}}{k1 \cdot C_{max} + k2}) \\ factorRinS_{decay,GABAB} &= \frac{k3}{k2 - k4} \cdot (e^{-k4 \cdot dt} - e^{-k2 \cdot dt}) \end{aligned}$$

$$r^{RE,TC}_{GABAB} = \begin{cases} factoR_{grow,GABAB} \cdot r^{RE,TC}_{GABAA,prev} + constantR_{grow,GABAB} & C > 0 \\ factorR_{decay,GABAB} \cdot r^{RE,TC}_{GABAA,prev} & C \leq 0 \end{cases} \quad \text{(B.48)}$$

$$s = \begin{cases} factorS_{GABAB} \cdot s_{prev} + factorRinS_{grow,GABAB} \cdot r^{RE,TC}_{GABAA,prev} \\ \qquad + constantS_{grow,GABAB} & C > 0 \\ factorS_{GABAB} \cdot s_{prev} + factorRinS_{decay,GABAB} \cdot r^{RE,TC}_{GABAA,prev} & C \leq 0 \end{cases} \quad \text{(B.49)}$$

- **AMPA receptors (PY → TC):**
  Maximum conductance and Reversal potential:

$$\bar{g}_{AMPA}^{PY,TC} = 0.000025(mS/cm^2)\ ,\ E_{AMPA}^{PY,TC} = 0(mV)$$

  Maximal concentration of the transmitter during the pulse:

$$C_{max} = 0.5(mM)$$

  Release duration:

$$C_{dur} = 0.3(mS)$$

  Voltage-independent forward and backward rate constants:

$$\alpha_{_{AMPA}} = 0.94(/mS \cdot mM)$$
$$\beta_{_{AMPA}} = 0.18(/mS)$$

  Pre-synaptic spike detection thereshold:

$$prethresh = 0(mV)$$

  Deadtime when spike can not occur:

$$deadtime = 1(mS)$$

  Parameters of fraction of receptors in the open state:

$$\begin{aligned} r_{\infty,AMPA} &= \frac{C_{max} \cdot \alpha_{_{AMPA}}}{C_{max} \cdot \alpha_{_{AMPA}} + \beta_{_{AMPA}}} \\ \tau_{r,AMPA} &= \frac{1}{C_{max} \cdot \alpha_{_{AMPA}} + \beta_{_{AMPA}}} \end{aligned}$$

  Conditions and procedures:
  ▷ Release is possible:
  ◇ if ((time)−(lastrelease)$-C_{dur}$ > deadtime)
  ◇ Release occur:
  ◇ if (the presynaptic neuron's voltage > prethresh)
  ◇ → $C = C_{max}$ → lastrelease=time
  ◇ Release doesn't occur: → do nothing
  ▷ Release is not possible:
  ◇ We should close the release
  ◇ if ((time)−(lastrelease)$-C_{dur} \geq 0$) && (C=C_{max})
  ◇ → $C = 0$
  ◇ Else: → do nothing
  ♣ $C > 0$ → Release is hapenning
  ♣ $C = 0$ → Release is absent

  Dynamics:

$$\begin{aligned} \frac{dr_{AMPA}^{PY,TC}}{dt} &= \alpha \cdot [T] \cdot (1 - r_{AMPA}^{PY,TC}) - \beta \cdot r_{AMPA}^{PY,TC} \\ &= -(C \cdot \alpha_{_{AMPA}} + \beta_{_{AMPA}})(r_{AMPA}^{PY,TC} - \frac{C \cdot \alpha_{_{AMPA}}}{C_{max} \cdot \alpha_{_{AMPA}} + \beta_{_{AMPA}}}) \end{aligned} \tag{B.50}$$

Integration of parameter r with respect to release:

$$\begin{aligned} factor_{grow,AMPA} &= e^{-\frac{dt}{\tau_{r,AMPA}}} \\ constant_{grow,AMPA} &= r_{\infty,AMPA} \cdot (1 - e^{-\frac{dt}{\tau_{r,AMPA}}}) \\ factor_{decay,AMPA} &= e^{-\beta_{AMPA} \cdot dt} \end{aligned}$$

$$r^{PY,TC}_{AMPA} = \begin{cases} factor_{grow,AMPA} \cdot r^{PY,TC}_{AMPA,prev} + constant_{grow,AMPA} & C > 0 \\ factor_{decay,AMPA} \cdot r^{PY,TC}_{AMPA,prev} & C \leq 0 \end{cases} \quad \text{(B.51)}$$

- **Integration of the membrane voltage of TC:**

$$\begin{aligned} C_m \frac{dV}{dt} &= -g_L(V - E_L) - g_{intTC}V + I_{leakintTC} - \frac{1}{S_{TC}} \cdot g_{synTC}V + \frac{1}{S_{TC}} \cdot I_{leaksynTC} \\ &= -(g_L + g_{intTC} + \frac{1}{S_{TC}} \cdot g_{synTC})V + (g_L \cdot E_L + I_{leakintTC} + \frac{1}{S_{TC}} \cdot I_{leaksynTC}) \\ &= -g_{totTC}V + I_{leaktotTC} \\ \frac{dV}{dt} &= -\frac{g_{totTC}}{C_m}(V - \frac{I_{leaktotTC}}{g_{totTC}}) \end{aligned} \quad \text{(B.52)}$$

$$\begin{aligned} factor_V &= e^{-\frac{g_{totTC}}{C_m} \cdot dt} \\ constant_V &= \frac{I_{leaktotTC}}{g_{totTC}} \cdot (1 - e^{-\frac{g_{totTC}}{C_m} \cdot dt}) \end{aligned}$$

$$V = factor_V \cdot V_{prev} + constant_V \quad \text{(B.53)}$$

B.2 Cortex

Two-compartment models of PY and IN cells with channels that are modeled by Hodgkin-Huxley kinetics:

$$C_m \frac{dV_D}{dt} = -g_L(V_D - E_L) - \frac{g}{S_{dend}}(V_D - V_S) - I_D^{int} - I^{syn}, \tag{B.54}$$

$$\frac{g}{S_{soma}}(V_S - V_D) = -I_S^{int}, \tag{B.55}$$

membrane capacitance for both PY and IN:

$$C_m = 0.75(\mu F/cm^2)$$

leakage conductance for both PY and IN:

$$g_L = 0.033(mS/cm^2)$$

leakage reversal potential:

$$E_L^{PY} = -68(mV), E_L^{IN} = -70$$

Conductance between axosomatic and dendritic compartments for both PY and IN:

$$g = 0.0001(mS)$$

area:

$$S_{PYsoma} = 1.0 \cdot 10^{-6}(cm^2), S_{PYdend} = 1.65 \cdot 10^{-4}(cm^2)$$
$$S_{INsoma} = 1.0 \cdot 10^{-6}(cm^2), S_{INdend} = 0.5 \cdot 10^{-4}(cm^2)$$

B.2.1 Pyramidal neuron (PY)

- **Hodgkin-Huxley kinetics of intrinsic currents of PY soma:**

$$\begin{aligned} -I_{PY_S}^{int} &= -g_{Nas}(V_S - E_{Nas}) - g_K(V_S - E_K) - g_{Naps}(V_S - E_{Naps}) \\ &= -(g_{Nas} + g_K + g_{Naps})V_S \\ &\quad +(g_{Nas}E_{Nas} + g_K E_K + g_{Naps}E_{Naps}) \\ &= -g_{intPY_S}V_S + I_{leakintPY_S} \end{aligned} \tag{B.56}$$

- **Fast sodium (Nas) channel:**
  Reversal potential:

$$E_{Nas} = 50(mV)$$

  Conductance:

$$gNas = tadj \cdot \bar{g}Nas \cdot mNas^3 \cdot hNas$$

  Maximum conductance:

$$\bar{g}Nas = 3000(mS/cm^2)$$

  Temperature adjustment:

$$tadj = 2.3^{\frac{T-23}{10}}$$

  Shift:

$$shift = -10(mV)$$

Activation parameters mNas:

$$\begin{aligned} \alpha_{mNas} &= \frac{0.182 \cdot (V + shift + 35.001)}{1 - e^{-(V+shift+35.001)/9}} \\ \beta_{mNas} &= \frac{0.124 \cdot (-(V + shift + 35.001))}{1 - e^{(V+shift+35.001)/9}} \end{aligned}$$

$$\begin{aligned} mNas_{\infty} &= \frac{\alpha_{mNas}}{\alpha_{mNas} + \beta_{mNas}} \\ \tau_{mNas} &= \frac{1}{\alpha_{mNas} + \beta_{mNas}} \cdot \frac{1}{tadj} \end{aligned}$$

Activation dynamics:

$$\frac{dmNas}{dt} = -\frac{1}{\tau_{mNas}}(mNas - mNas_{\infty}) \tag{B.57}$$

Integration of activation parameter mNas:

$$\begin{aligned} factor_{mNas} &= e^{-dt/\tau_{mNas}} \\ constant_{mNas} &= mNas_{\infty} \cdot (1 - e^{-dt/\tau_{mNas}}) \\ mNas &= factor_{mNas} \cdot mNas_{prev} + constant_{mNas} \end{aligned} \tag{B.58}$$

Inactivation parameters hNas:

$$\begin{aligned} \alpha_{hNad} &= \frac{0.024 \cdot (V + shift + 50.001)}{1 - e^{-(V+shift+50.001)/5}} \\ \beta_{hNas} &= \frac{0.0091 \cdot (-(V + shift + 75.001))}{1 - e^{(V+shift+75.001)/5}} \end{aligned}$$

$$\begin{aligned} hNas_{\infty} &= \frac{1}{1 + e^{(V+shift+65)/6.2}} \\ \tau_{hNas} &= \frac{1}{\alpha_{hNas} + \beta_{hNas}} \cdot \frac{1}{tadj} \end{aligned}$$

Inactivation dynamics:

$$\frac{dhNas}{dt} = -\frac{1}{\tau_{hNas}}(hNas - hNas_{\infty}) \tag{B.59}$$

Integration of inactivation parameter hNa:

$$\begin{aligned} factor_{hNas} &= e^{-dt/\tau_{hNas}} \\ constant_{hNas} &= hNas_{\infty} \cdot (1 - e^{-dt/\tau_{hNas}}) \\ hNas &= factor_{hNas} \cdot hNas_{prev} + constant_{hNas} \end{aligned} \tag{B.60}$$

- **Fast potassium (K) channel:**
  Reversal potential:

$$E_K = -90(mV)$$

Conductance:

$$gK = tadj \cdot \bar{g}K \cdot mK$$

Maximum conductance:

$$\bar{g}K = 200(mS/cm^2)$$

Temperature adjustment:

$$tadj = 2.3^{(\frac{T-23}{10})}$$

Activation parameter mK:

$$\begin{aligned} \alpha_{mK} &= \frac{0.02 \cdot (V - 25.001)}{1 - e^{-(V-25.001)/9}} \\ \beta_{mK} &= \frac{-0.002 \cdot (V - 25.001)}{1 - e^{(V-25.001)/9}} \end{aligned}$$

$$\begin{aligned} mK_\infty &= \frac{\alpha_{mK}}{\alpha_{mK} + \beta_{mK}} \\ \tau_{mK} &= \frac{1}{\alpha_{mK} + \beta_{mK}} \cdot \frac{1}{tadj} \end{aligned}$$

Activation dynamics:

$$\frac{dmK}{dt} = -\frac{1}{\tau_{mK}}(mK - mK_\infty) \tag{B.61}$$

Integration of activation parameter mK:

$$\begin{aligned} factor_{mK} &= e^{-dt/\tau_{mK}} \\ constant_{mK} &= mK_\infty \cdot (1 - e^{-dt/\tau_{mK}}) \\ mK &= factor_{mK} \cdot mK_{prev} + constant_{mK} \end{aligned} \tag{B.62}$$

- **Persist sodium (Na(p)) channel:**
  Reversal potential:

$$E_{Naps} = 50(mV)$$

Conductance:

$$gNaps = \bar{g}Naps \cdot mNaps$$

Maximum conductance:

$$\bar{g}Naps = 0.3(mS/cm^2)$$

Temperature adjustment:

$$phi_m = 2.7^{\frac{T-22}{10}}$$

Activation parameter mNaps:

$$\begin{aligned} mNaps_\infty &= \frac{1}{1 + e^{-(V+42)/5}} \\ \tau_{mNaps} &= 0.8 \cdot \frac{1}{phi_m} \end{aligned}$$

Activation dynamics:

$$\frac{dmNaps}{dt} = -\frac{1}{\tau_{mNaps}}(mNaps - mNaps_{\infty}) \tag{B.63}$$

Integration of activation parameter mNaps:

$$\begin{aligned} factor_{mNaps} &= e^{-dt/\tau_{mNaps}} \\ constant_{mNaps} &= mNaps_{\infty} \cdot (1 - e^{-dt/\tau_{mNaps}}) \\ mNaps &= factor_{mNaps} \cdot mNaps_{prev} + constant_{mNaps} \end{aligned} \tag{B.64}$$

- **Hodgkin-Huxley kinetics of intrinsic currents of PY dendrite:**

$$\begin{aligned} -I^{int}_{PY_D} &= -g_{Nad}(V_D - E_{Nad}) - g_{HVA}(V_D - E_{HVA}) - g_{KCa}(V_D - E_{KCa}) \\ &\quad -g_{Km}(V_D - E_{Km}) - g_{KL}(V_D - E_{KL}) - g_{Napd}(V_D - E_{Napd}) \\ &= -(g_{Nad} + g_{HVA} + g_{KCa} + g_{Km} + g_{KL} + g_{Napd})V \\ &\quad +(g_{Nad}E_{Nad} + g_{HVA}E_{HVA} + g_{KCa}E_{KCa} + g_{Km}E_{Km} \\ &\quad\quad +g_{KL}E_{KL} + g_{Napd}E_{Napd}) \\ &= -g_{intPY_D}V + I_{leakintPY_D} \end{aligned} \tag{B.65}$$

- **High-threshold Ca^{2+} (HVA) channel:**
  Reversal potential:

$$E_{HVA} = 140(mV)$$

  Conductance:

$$gHVA = tadj \cdot \bar{g}HVA \cdot mHVA^2 \cdot hHVA$$

  Maximum conductance:

$$\bar{g}HVA = 0.01(mS/cm^2)$$

  Temperature adjustment:

$$tadj = 2.3^{\frac{T-23}{10}}$$

  Shift:

$$shift = 0(mV)$$

  Activation parameters mHVA:

$$\begin{aligned} \alpha_{mHVA} &= \frac{0.055 \cdot (V + shift + 27.001)}{1 - e^{-(V+shift+27.001)/3.8}} \\ \beta_{mHVA} &= 0.94 \cdot e^{-(V+shift+75)/17} \end{aligned}$$

$$\begin{aligned} mHVA_{\infty} &= \frac{\alpha_{mHVA}}{\alpha_{mHVA} + \beta_{mHVA}} \\ \tau_{mHVA} &= \frac{1}{\alpha_{mHVA} + \beta_{mHVA}} \cdot \frac{1}{tadj} \end{aligned}$$

  Activation dynamics:

$$\frac{dmHVA}{dt} = -\frac{1}{\tau_{mHVA}}(mHVA - mHVA_{\infty}) \tag{B.66}$$

Integration of activation parameter mHVA:

$$\begin{aligned} factor_{mHVA} &= e^{-dt/\tau_{mHVA}} \\ constant_{mHVA} &= mHVA_{\infty} \cdot (1 - e^{-dt/\tau_{mHVA}}) \\ mHVA &= factor_{mHVA} \cdot mHVA_{prev} + constant_{mHVA} \end{aligned} \tag{B.67}$$

Inactivation parameters hHVA:

$$\begin{aligned} \alpha_{hHVA} &= 0.000457 \cdot e^{-(V+shift+13)/50} \\ \beta_{hHVA} &= \frac{0.0065}{1 + e^{-(V+shift+15)/28}} \end{aligned}$$

$$\begin{aligned} hHVA_{\infty} &= \frac{\alpha_{hHVA}}{\alpha_{hHVA} + \beta_{hHVA}} \\ \tau_{hHVA} &= \frac{1}{\alpha_{hHVA} + \beta_{hHVA}} \cdot \frac{1}{tadj} \end{aligned}$$

Inactivation dynamics:

$$\frac{dhHVA}{dt} = -\frac{1}{\tau_{hHVA}}(hHVA - hHVA_{\infty}) \tag{B.68}$$

Integration of inactivation parameter hHVA:

$$\begin{aligned} factor_{hHVA} &= e^{-dt/\tau_{hHVA}} \\ constant_{hHVA} &= hHVA_{\infty} \cdot (1 - e^{-dt/\tau_{hHVA}}) \\ hHVA &= factor_{hHVA} \cdot hHVA_{prev} + constant_{hHVA} \end{aligned} \tag{B.69}$$

- **Fast sodium (Nad) channel:**
  Reversal potential:

$$E_{Nad} = 50(mV)$$

  Conductance:

$$gNad = tadj \cdot \bar{g}Nad \cdot mNad^3 \cdot hNad$$

  Maximum conductance:

$$\bar{g}Nad = 0.8(mS/cm^2)$$

  Temperature adjustment:

$$tadj = 2.3^{\frac{T-23}{10}}$$

  Shift:

$$shift = -10(mV)$$

  Activation parameters mNad:

$$\begin{aligned} \alpha_{mNad} &= \frac{0.182 \cdot (V + shift + 35.001)}{1 - e^{-(V+shift+35.001)/9}} \\ \beta_{mNad} &= \frac{0.124 \cdot (-(V + shift + 35.001))}{1 - e^{(V+shift+35.001)/9}} \end{aligned}$$

$$\begin{aligned} mNad_{\infty} &= \frac{\alpha_{mNad}}{\alpha_{mNad}+\beta_{mNad}} \\ \tau_{mNad} &= \frac{1}{\alpha_{mNad}+\beta_{mNad}} \cdot \frac{1}{tadj} \end{aligned}$$

Activation dynamics:

$$\frac{dmNad}{dt} = -\frac{1}{\tau_{mNad}}(mNad - mNad_{\infty}) \tag{B.70}$$

Integration of activation parameter mNad:

$$\begin{aligned} factor_{mNad} &= e^{-dt/\tau_{mNad}} \\ constant_{mNad} &= mNad_{\infty} \cdot (1 - e^{-dt/\tau_{mNad}}) \\ mNad &= factor_{mNad} \cdot mNad_{prev} + constant_{mNad} \end{aligned} \tag{B.71}$$

Inactivation parameters hNad:

$$\begin{aligned} \alpha_{hNad} &= \frac{0.024 \cdot (V + shift + 50.001)}{1 - e^{-(V+shift+50.001)/5}} \\ \beta_{hNad} &= \frac{0.0091 \cdot (-(V + shift + 75.001))}{1 - e^{(V+shift+75.001)/5}} \end{aligned}$$

$$\begin{aligned} hNad_{\infty} &= \frac{1}{1 + e^{(V+shift+65)/6.2}} \\ \tau_{hNad} &= \frac{1}{\alpha_{hNad}+\beta_{hNad}} \cdot \frac{1}{tadj} \end{aligned}$$

Inactivation dynamics:

$$\frac{dhNad}{dt} = -\frac{1}{\tau_{hNad}}(hNad - hNad_{\infty}) \tag{B.72}$$

Integration of inactivation parameter hNa:

$$\begin{aligned} factor_{hNad} &= e^{-dt/\tau_{hNad}} \\ constant_{hNad} &= hNad_{\infty} \cdot (1 - e^{-dt/\tau_{hNad}}) \\ hNad &= factor_{hNad} \cdot hNad_{prev} + constant_{hNad} \end{aligned} \tag{B.73}$$

- **Potassium M-current (Km) channel**
  Reversal potential:

$$E_{Km} = -90(mV)$$

Conductance:

$$gKm = tadj \cdot \bar{g}Km \cdot mKm$$

Maximum conductance:

$$\bar{g}Km = 0.01(mS/cm^2)$$

Temperature adjustment:

$$tadj = 2.3^{\frac{T-23}{10}}$$

Activation parameter mKm:

$$\begin{aligned} \alpha_{mKm} &= \frac{0.001 \cdot (V + 30.001)}{1 - e^{-(V+30.001)/9}} \\ \beta_{mKm} &= \frac{-0.001 \cdot (V + 30.001)}{1 - e^{(V+30.001)/9}} \end{aligned}$$

$$\begin{aligned} mKm_{\infty} &= \frac{\alpha_{mKm}}{\alpha_{mKm} + \beta_{mKm}} \\ \tau_{mKm} &= \frac{1}{\alpha_{mKm} + \beta_{mKm}} \cdot \frac{1}{tadj} \end{aligned}$$

Activation dynamics:

$$\frac{dmKm}{dt} = -\frac{1}{\tau_{mKm}}(mKm - mKm_{\infty}) \tag{B.74}$$

Integration of activation parameter mKm:

$$\begin{aligned} factor_{mKm} &= e^{-dt/\tau_{mKm}} \\ constant_{mKm} &= mKm_{\infty} \cdot (1 - e^{-dt/\tau_{mKm}}) \\ mKm &= factor_{mKm} \cdot mKm_{prev} + constant_{mKm} \end{aligned} \tag{B.75}$$

- **Ca^{2+}-dependent K^+ (K[Ca]) channel:**
  Reversal potential:

$$E_{KCa} = -90(mV)$$

Conductance:

$$gKCa = tadj \cdot \bar{g}KCa \cdot mKCa$$

Maximum conductance:

$$\bar{g}KCa = 0.3(mS/cm^2)$$

Temperature adjustment:

$$tadj = 2.3^{\frac{T-23}{10}}$$

Activation parameter mKCa:

$$\begin{aligned} \alpha_{mKCa} &= 0.01 \cdot [Cai]_i \\ \beta_{mKCa} &= 0.02 \end{aligned}$$

$$\begin{aligned} mKCa_{\infty} &= \frac{\alpha_{mKCa}}{\alpha_{mKCa} + \beta_{mKCa}} \\ \tau_{mKCa} &= \frac{1}{\alpha_{mKCa} + \beta_{mKCa}} \cdot \frac{1}{tadj} \end{aligned}$$

Activation dynamics:

$$\frac{dmKCa}{dt} = -\frac{1}{\tau_{mKCa}}(mKCa - mKCa_{\infty}) \tag{B.76}$$

Integration of activation parameter mKCa:

$$\begin{aligned} factor_{mKCa} &= e^{-dt/\tau_{mKCa}} \\ constant_{mKCa} &= mKCa_{\infty} \cdot (1 - e^{-dt/\tau_{mKCa}}) \\ mKCa &= factor_{mKCa} \cdot mKCa_{prev} + constant_{mKCa} \end{aligned} \tag{B.77}$$

- **Kinetic of intracellular calcium dynamics ($[Ca]_i$):**
  Faraday constant:
  $$F = 96489(Cmol^{-1})$$
  Depth of the shell beneath the membrane:
  $$d = 1(\mu m)$$
  Unit conversion constant:
  $$k = 10$$
  Influx of Ca^{2+} is governed by:
  $$[\dot{Ca}]_{i,in} = \begin{cases} -\frac{k}{2Fd} I_{HVA} & if > 0 \\ 0 & if \leq 0 \end{cases}$$
  Time constant of calcium efflux:
  $$\tau_{Ca} = 165(ms)$$
  Intracellular concentration at rest:
  $$[Ca]_\infty = 2.4 \times 10^{-4}(mM)$$
  Efflux of calcium can be modeled by a first-order decay term:
  $$[\dot{Ca}]_{i,ef} = -\frac{1}{\tau_{Ca}}([Ca]_i - [Ca]_\infty)$$
  Calcium concentration dynamics:
  $$\begin{aligned} \frac{d[Ca]_i}{dt} &= [\dot{Ca}]_{i,in} + [\dot{Ca}]_{i,ef} \\ &= [\dot{Ca}]_{i,in} - \frac{1}{\tau_{Ca}}([Ca]_i - [Ca]_\infty) \\ &= -\frac{1}{\tau_{Ca}}([Ca]_i - ([Ca]_\infty + \tau_{Ca} \cdot [Ca]_{i,in})) \end{aligned} \tag{B.78}$$
  Integration of calcium dynamics $[Ca]_i$:
  $$\begin{aligned} factor_{[Ca]_i} &= e^{-dt/\tau_{Ca}} \\ [Ca]_i &= factor_{[Ca]_i} \cdot [Ca]_{i,prev} + (1 - factor_{[Ca]_i}) \cdot ([Ca]_\infty + \tau_{Ca} \cdot [Ca]_{i,in}) \end{aligned} \tag{B.79}$$
  Minimum of $[Ca]_i$:
  $$minCa = 1e - 6$$
  Update $[Ca]_i$ according to minimum (Avoid negative values):
  $$[Ca]_i = max(minCa, [Ca]_i)$$
- **Potassium leak (Kl) current:**
  Reversal potential:
  $$E_{Kl} = -90(mV)$$
  Conductance:
  $$gKl = 0.0025(mS/cm^2)$$

- **Persist sodium (Na(p)) channel:**
  Reversal potential:

$$E_{Napd} = 50(mV)$$

  Conductance:

$$gNapd = \bar{g}Napd \cdot mNapd$$

  Maximum conductance:

$$\bar{g}Napd = 0.07(mS/cm^2)$$

  Temperature adjustment:

$$phi_m = 2.7^{\frac{T-22}{10}}$$

  Activation parameter mNapd:

$$\begin{aligned} mNapd_\infty &= \frac{1}{1+e^{-(V+42)/5}} \\ \tau_{mNapd} &= 0.8 \cdot \frac{1}{phi_m} \end{aligned}$$

  Activation dynamics:

$$\frac{dmNapd}{dt} = -\frac{1}{\tau_{mNapd}}(mNapd - mNapd_\infty) \tag{B.80}$$

  Integration of activation parameter mNapd:

$$\begin{aligned} factor_{mNapd} &= e^{-dt/\tau_{mNapd}} \\ constant_{mNapd} &= mNapd_\infty \cdot (1 - e^{-dt/\tau_{mNapd}}) \\ mNapd &= factor_{mNapd} \cdot mNapd_{prev} + constant_{mNapd} \end{aligned} \tag{B.81}$$

- **Hodgkin-Huxley kinetics of synaptic currents of PY:**

$$\begin{aligned} -I_{PY}^{syn} &= (-\bar{g}_{AMPAd}^{PY,PY} \cdot r_{AMPAd}^{PY,PY} \cdot (1 - D_{AMPAd}^{PY,PY}) \cdot (V - E_{AMPAd}^{PY,PY}) \\ &\quad -\bar{g}_{NMDAd}^{PY,PY} \cdot r_{NMDAd}^{PY,PY} \cdot fn \cdot (1 - D_{NMDAd}^{PY,PY}) \cdot (V - E_{NMDAd}^{PY,PY}) \\ &\quad -\bar{g}_{GABAAd}^{IN,PY} \cdot r_{GABAAd}^{IN,PY} \cdot (1 - D_{GABAAd}^{IN,PY}) \cdot (V - E_{GABAAd}^{IN,PY}) \\ &\quad -\bar{g}_{AMPA}^{TC,PY} \cdot r_{AMPA}^{TC,PY} \cdot (V - E_{AMPA}^{TC,PY})) \cdot \frac{1}{S_{PYdend}} \\ &= -\frac{1}{S_{PYdend}} \cdot (\bar{g}_{AMPAd}^{PY,PY} \cdot r_{AMPAd}^{PY,PY} \cdot (1 - D_{AMPAd}^{PY,PY}) \\ &\quad +\bar{g}_{NMDAd}^{PY,PY} \cdot r_{NMDAd}^{PY,PY} \cdot fn \cdot (1 - D_{NMDAd}^{PY,PY}) \\ &\quad +\bar{g}_{GABAAd}^{IN,PY} \cdot r_{GABAAd}^{IN,PY} \cdot (1 - D_{GABAAd}^{IN,PY}) + \bar{g}_{AMPA}^{TC,PY} \cdot r_{AMPA}^{TC,PY})V \\ &\quad +\frac{1}{S_{PYdend}} \cdot (\bar{g}_{AMPAd}^{PY,PY} \cdot r_{AMPAd}^{PY,PY} \cdot (1 - D_{AMPAd}^{PY,PY}) \cdot E_{AMPAd}^{PY,PY} \\ &\quad +\bar{g}_{NMDAd}^{PY,PY} \cdot r_{NMDAd}^{PY,PY} \cdot fn \cdot (1 - D_{NMDAd}^{PY,PY}) \cdot E_{NMDAd}^{PY,PY} \\ &\quad +\bar{g}_{GABAAd}^{IN,PY} \cdot r_{GABAAd}^{IN,PY} \cdot (1 - D_{GABAAd}^{IN,PY}) \cdot E_{GABAAd}^{IN,PY} \\ &\quad +\bar{g}_{AMPA}^{TC,PY} \cdot r_{AMPA}^{TC,PY} \cdot E_{AMPA}^{TC,PY}) \\ &= -\frac{1}{S_{PYdend}} \cdot g_{synPY}V + \frac{1}{S_{PYdend}} \cdot I_{leaksynPY} \end{aligned} \tag{B.82}$$

- **AMPA receptors with depression and MINI (PY → PY):**
  Maximum conductance and Reversal potential:

$$\bar{g}^{PY,PY}_{AMPAd} = 0.0001125(mS/cm^2)\ ,\ E^{PY,PY}_{AMPAd} = 0(mV)$$

  Maximal concentration of the transmitter during the pulse:

$$\begin{aligned} C_{max} &= 0.5(mM) \\ C_{max,mini} &= 0.4 \cdot C_{max} = 0.2(mM) \end{aligned}$$

  Release duration:

$$C_{dur} = 0.3(mS)$$

  Voltage-independent forward and backward rate constants:

$$\alpha_{AMPAd} = 0.94(/mS \cdot mM)$$
$$\beta_{AMPAd} = 0.18(/mS)$$

  Pre-synaptic spike detection threshold:

$$prethresh = 0(mV)$$

  Deadtime when spike can not occur:

$$deadtime = 1(mS)$$

  Synaptic depression parameters:

$$U_{AMPAd} = 0.073$$
$$\alpha_D = \tfrac{1}{700}$$

  Parameters of fraction of receptors in the open state:

$$\begin{aligned} r_{\infty,AMPAd} &= \frac{C_{max} \cdot \alpha_{AMPAd}}{C_{max} \cdot \alpha_{AMPAd} + \beta_{AMPAd}} \\ \tau_{r,AMPAd} &= \frac{1}{C_{max} \cdot \alpha_{AMPAd} + \beta_{AMPAd}} \\ r_{\infty,AMPAd,mini} &= \frac{C_{max,mini} \cdot \alpha_{AMPAd}}{C_{max,mini} \cdot \alpha_{AMPAd} + \beta_{AMPAd}} \\ \tau_{r,AMPAd,mini} &= \frac{1}{C_{max,mini} \cdot \alpha_{AMPAd} + \beta_{AMPAd}} \end{aligned}$$

  Conditions and procedures:
  ◇ → $D = D \cdot e^{-\alpha_D \cdot dt}$
  ▷ Release is possible:
  ◇ if ((time)−(lastrelease)−C_{dur} > deadtime)
  ◇ Release occur:
  ◇ if (the presynaptic neuron's voltage > prethresh)
  ◇ → $C = C_{max}$ → lastrelease=time → lastspike=time
  ◇ → $D = D + (1 - D) \cdot U_{AMPAd}$
  ◇ Release doesn't occur but MINI is possible:
  ◇ if ((time)−(lastspike)> 70)
  ◇ → $SS = log(\frac{(time)-(lastspike)+50}{50}) \cdot \frac{1}{400}$ → $S = max(0.000001, rand())$
  ◇ → newrelease = -$\frac{log(S)}{SS}$
  ◇ MINI occur:

◇ if ((time)−(lastrelease) > (newrelease))
◇ → $C = C_{max,mini}$ → lastrelease=time
◇ Neither release nor MINI occur:
◇ → do nothing
▷ Release is not possible:
◇ We should close the release
◇ if ((time)−(lastrelease)−$C_{dur} \geq 0$) && (C>0)
◇ → $C = 0$
◇ Else: → do nothing
♣ $C = C_{max}$ → Release is happening
♣ $C = C_{max,mini}$ → MINI is happening
♣ $C = 0$ → Release and MINI are absent

Dynamics:

$$\begin{aligned} \frac{dr^{PY,PY}_{AMPAd}}{dt} &= \alpha \cdot [T] \cdot (1 - r^{PY,PY}_{AMPAd}) - \beta \cdot r^{PY,PY}_{AMPAd} \\ &= -(C \cdot \alpha_{AMPAd} + \beta_{AMPAd})(r^{PY,PY}_{AMPAd} - \frac{C \cdot \alpha_{AMPAd}}{C_{max} \cdot \alpha_{AMPAd} + \beta_{AMPAd}}) \end{aligned} \tag{B.83}$$

Integration of parameter r with respect to release:

$$\begin{aligned} factor_{grow,AMPAd} &= e^{-\frac{dt}{\tau_{r,AMPAd}}} \\ constant_{grow,AMPAd} &= r_{\infty,AMPAd} \cdot (1 - e^{-\frac{dt}{\tau_{r,AMPAd}}}) \\ factor_{grow,AMPAd,mini} &= e^{-\frac{dt}{\tau_{r,AMPAd,mini}}} \\ constant_{grow,AMPAd,mini} &= r_{\infty,AMPAd,mini} \cdot (1 - e^{-\frac{dt}{\tau_{r,AMPAd,mini}}}) \\ factor_{decay,AMPAd} &= e^{-\beta_{AMPAd} \cdot dt} \end{aligned}$$

$$r^{PY,PY}_{AMPAd} = \begin{cases} factor_{grow,AMPAd} \cdot r^{PY,PY}_{AMPAd,prev} & \\ \quad + constant_{grow,AMPAd} & C = C_{max} \\ factor_{grow,AMPAd,mini} \cdot r^{PY,PY}_{AMPAd,prev} & \\ \quad + constant_{grow,AMPAd,mini} & C = C_{max,mini} \\ factor_{decay,AMPAd} \cdot r^{PY,PY}_{AMPAd,prev} & C \leq 0 \end{cases} \tag{B.84}$$

- **NMDA receptors with depression (PY → PY):**
  Maximum conductance and Reversal potential:

$$\bar{g}^{PY,PY}_{NMDAd} = 0.0000075(mS/cm^2) \ , \ E^{PY,PY}_{NMDAd} = 0(mV)$$

  Magnesium block:

$$fn = \frac{1}{1 + e^{-\frac{V+25}{12.5}}}$$

  Maximal concentration of the transmitter during the pulse:

$$C_{max} = 0.5(mM)$$

Release duration:

$$C_{dur} = 0.3(mS)$$

Voltage-independent forward and backward rate constants:

$$\alpha_{_{NMDAd}} = 1(/mS \cdot mM)$$
$$\beta_{_{NMDAd}} = 0.0067(/mS)$$

Pre-synaptic spike detection threshold:

$$prethresh = 0(mV)$$

Deadtime when spike can not occur:

$$deadtime = 1(mS)$$

Synaptic depression parameters:

$$U_{NMDAd} = 0$$
$$\alpha_D = \tfrac{1}{700}$$

Parameters of fraction of receptors in the open state:

$$r_{\infty,NMDAd} = \frac{C_{max} \cdot \alpha_{_{NMDAd}}}{C_{max} \cdot \alpha_{_{NMDAd}} + \beta_{_{NMDAd}}}$$
$$\tau_{r,NMDAd} = \frac{1}{C_{max} \cdot \alpha_{_{NMDAd}} + \beta_{_{NMDAd}}}$$

Conditions and procedures:
$\diamond \rightarrow D = D \cdot e^{-\alpha_D \cdot dt}$
$\triangleright$ Release is possible:
$\diamond$ if ((time)$-$(lastrelease)$-C_{dur} >$ deadtime)
$\diamond$ Release occur:
$\diamond$ if (the presynaptic neuron's voltage > prethresh)
$\diamond$ $\rightarrow C = C_{max} \rightarrow$ lastrelease=time
$\diamond$ $\rightarrow D = D + (1 - D) \cdot U_{NMDAd}$
$\diamond$ Release doesn't occur:
$\diamond$ $\rightarrow$ do nothing
$\triangleright$ Release is not possible:
$\diamond$ We should close the release
$\diamond$ if ((time)$-$(lastrelease)$-C_{dur} \geq 0$) && (C=C_{max})
$\diamond$ $\rightarrow C = 0$
$\diamond$ Else: $\rightarrow$ do nothing
$\clubsuit$ $C > 0 \rightarrow$ Release is hapenning
$\clubsuit$ $C = 0 \rightarrow$ Release is absent

Dynamics:

$$\begin{aligned} \frac{dr^{PY,PY}_{NMDAd}}{dt} &= \alpha \cdot [T] \cdot (1 - r^{PY,PY}_{NMDAd}) - \beta \cdot r^{PY,PY}_{NMDAd} \\ &= -(C \cdot \alpha_{_{NMDAd}} + \beta_{_{NMDAd}})(r^{PY,PY}_{NMDAd} - \frac{C \cdot \alpha_{_{NMDAd}}}{C_{max} \cdot \alpha_{_{NMDAd}} + \beta_{_{NMDAd}}}) \end{aligned} \tag{B.85}$$

Integration of parameter r with respect to release:

$$\begin{aligned} factor_{grow,NMDAd} &= e^{-\frac{dt}{\tau_{r,NMDAd}}} \\ constant_{grow,NMDAd} &= r_{\infty,NMDAd} \cdot (1 - e^{-\frac{dt}{\tau_{r,NMDAd}}}) \\ factor_{decay,NMDAd} &= e^{-\beta_{NMDAd} \cdot dt} \end{aligned}$$

$$r^{PY,PY}_{NMDAd} = \begin{cases} factor_{grow,NMDAd} \cdot r^{PY,PY}_{NMDAd,prev} & \\ \qquad + constant_{grow,NMDAd} & C > 0 \\ factor_{decay,NMDAd} \cdot r^{PY,PY}_{NMDAd,prev} & C \leq 0 \end{cases} \tag{B.86}$$

- **GABAA receptors with depression and MINI(IN → PY):**
  Maximum conductance and Reversal potential:

$$\bar{g}^{IN,PY}_{GABAAd} = 0.0000375(mS/cm^2)\ ,\ E^{IN,PY}_{GABAAd} = -70(mV)$$

  Maximal concentration of the transmitter during the pulse:

$$\begin{aligned} C_{max} &= 0.5(mM) \\ C_{max,mini} &= 0.1 \cdot C_{max} = 0.05(mM) \end{aligned}$$

  Release duration:

$$C_{dur} = 0.3(mS)$$

  Voltage-independent forward and backward rate constants:

$$\begin{aligned} \alpha_{GABAAd} &= 10(/mS \cdot mM) \\ \beta_{GABAAd} &= 0.25(/mS) \end{aligned}$$

  Pre-synaptic spike detection threshold:

$$prethresh = 0(mV)$$

  Deadtime when spike can not occur:

$$deadtime = 1(mS)$$

  Synaptic depression parameters:

$$\begin{aligned} U_{GABAAd} &= 0.07 \\ \alpha_D &= \tfrac{1}{700} \end{aligned}$$

  Parameters of fraction of receptors in the open state:

$$\begin{aligned} r_{\infty,GABAAd} &= \frac{C_{max} \cdot \alpha_{GABAAd}}{C_{max} \cdot \alpha_{GABAAd} + \beta_{GABAAd}} \\ \tau_{r,GABAAd} &= \frac{1}{C_{max} \cdot \alpha_{GABAAd} + \beta_{GABAAd}} \\ r_{\infty,GABAAd,mini} &= \frac{C_{max,mini} \cdot \alpha_{GABAAd}}{C_{max,mini} \cdot \alpha_{GABAAd} + \beta_{GABAAd}} \\ \tau_{r,GABAAd,mini} &= \frac{1}{C_{max,mini} \cdot \alpha_{GABAAd} + \beta_{GABAAd}} \end{aligned}$$

  Conditions and procedures:
  $\diamond \rightarrow D = D \cdot e^{-\alpha_D \cdot dt}$

▷ Release is possible:
◇ if ((time)−(lastrelease)$-C_{dur}$ > deadtime)
◇ Release occur:
◇ if (the presynaptic neuron's voltage > prethresh)
◇ → $C = C_{max}$ → lastrelease=time → lastspike=time
◇ → $D = D + (1 - D) \cdot U_{GABAAd}$
◇ Release doesn't occur but MINI is possible:
◇ if ((time)−(lastspike)> 70)
◇ → $SS = log(\frac{(time)-(lastspike)+50}{50}) \cdot \frac{1}{400}$ → $S = max(0.000001, rand())$
◇ → newrelease = -$\frac{log(S)}{SS}$
◇ MINI occur:
◇ if ((time)−(lastrelease) > (newrelease))
◇ → $C = C_{max,mini}$ → lastrelease=time
◇ Neither release nor MINI occur:
◇ → do nothing
▷ Release is not possible:
◇ We should close the release
◇ if ((time)−(lastrelease)$-C_{dur} \geq 0$) && (C>0)
◇ → $C = 0$
◇ Else: → do nothing
♣ $C = C_{max}$ → Release is happening
♣ $C = C_{max,mini}$ → MINI is happening
♣ $C = 0$ → Release and MINI are absent

Dynamics:

$$\begin{aligned} \frac{dr^{PY,PY}_{GABAAd}}{dt} &= \alpha \cdot [T] \cdot (1 - r^{PY,PY}_{GABAAd}) - \beta \cdot r^{PY,PY}_{GABAAd} \\ &= -(C \cdot \alpha_{GABAAd} + \beta_{GABAAd})(r^{PY,PY}_{GABAAd} - \frac{C \cdot \alpha_{GABAAd}}{C_{max} \cdot \alpha_{GABAAd} + \beta_{GABAAd}}) \end{aligned} \tag{B.87}$$

Integration of parameter r with respect to release:

$$\begin{aligned} factor_{grow,GABAAd} &= e^{-\frac{dt}{\tau_{r,GABAAd}}} \\ constant_{grow,GABAAd} &= r_{\infty,GABAAd} \cdot (1 - e^{-\frac{dt}{\tau_{r,GABAAd}}}) \\ factor_{grow,GABAAd,mini} &= e^{-\frac{dt}{\tau_{r,GABAAd,mini}}} \\ constant_{grow,GABAAd,mini} &= r_{\infty,GABAAd,mini} \cdot (1 - e^{-\frac{dt}{\tau_{r,GABAAd,mini}}}) \\ factor_{decay,GABAAd} &= e^{-\beta_{GABAAd} \cdot dt} \end{aligned}$$

$$r^{PY,PY}_{GABAAd} = \begin{cases} factor_{grow,GABAAd} \cdot r^{PY,PY}_{GABAAd,prev} \\ \qquad + constant_{grow,GABAAd} & C = C_{max} \\ factor_{grow,GABAAd,mini} \cdot r^{PY,PY}_{GABAAd,prev} \\ \qquad + constant_{grow,GABAAd,mini} & C = C_{max,mini} \\ factor_{decay,GABAAd} \cdot r^{PY,PY}_{GABAAd,prev} & C \leq 0 \end{cases} \tag{B.88}$$

- **AMPA receptors (TC → PY):**
  Maximum conductance and Reversal potential:

$$\bar{g}_{AMPA}^{TC,PY} = 0.000075(mS/cm^2)\ ,\ E_{AMPA}^{TC,PY} = 0(mV)$$

  Maximal concentration of the transmitter during the pulse:

$$C_{max} = 0.5(mM)$$

  Release duration:

$$C_{dur} = 0.3(mS)$$

  Voltage-independent forward and backward rate constants:

$$\alpha_{AMPA} = 0.94(/mS \cdot mM)$$
$$\beta_{AMPA} = 0.18(/mS)$$

  Pre-synaptic spike detection threshold:

$$prethresh = 0(mV)$$

  Deadtime when spike can not occur:

$$deadtime = 1(mS)$$

  Parameters of fraction of receptors in the open state:

$$\begin{aligned} r_{\infty,AMPA} &= \frac{C_{max} \cdot \alpha_{AMPA}}{C_{max} \cdot \alpha_{AMPA} + \beta_{AMPA}} \\ \tau_{r,AMPA} &= \frac{1}{C_{max} \cdot \alpha_{AMPA} + \beta_{AMPA}} \end{aligned}$$

  Conditions and procedures:
  ▷ Release is possible:
  ◇ if ((time)−(lastrelease)$-C_{dur}$ > deadtime)
  ◇ Release occur:
  ◇ if (the presynaptic neuron's voltage > prethresh)
  ◇ → $C = C_{max}$ → lastrelease=time
  ◇ Release doesn't occur: → do nothing
  ▷ Release is not possible:
  ◇ We should close the release
  ◇ if ((time)−(lastrelease)$-C_{dur} \geq 0$) && (C=C_{max})
  ◇ → $C = 0$
  ◇ Else: → do nothing
  ♣ $C > 0$ → Release is hapenning
  ♣ $C = 0$ → Release is absent

  Dynamics:

$$\begin{aligned} \frac{dr_{AMPA}^{TC,PY}}{dt} &= \alpha \cdot [T] \cdot (1 - r_{AMPA}^{TC,PY}) - \beta \cdot r_{AMPA}^{TC,PY} \\ &= -(C \cdot \alpha_{AMPA} + \beta_{AMPA})(r_{AMPA}^{TC,PY} - \frac{C \cdot \alpha_{AMPA}}{C_{max} \cdot \alpha_{AMPA} + \beta_{AMPA}}) \end{aligned} \quad \text{(B.89)}$$

Integration of parameter r with respect to release:

$$\begin{aligned} factor_{grow,AMPA} &= e^{-\frac{dt}{\tau_{r,AMPA}}} \\ constant_{grow,AMPA} &= r_{\infty,AMPA} \cdot (1 - e^{-\frac{dt}{\tau_{r,AMPA}}}) \\ factor_{decay,AMPA} &= e^{-\beta_{AMPA} \cdot dt} \end{aligned}$$

$$r^{TC,PY}_{AMPA} = \begin{cases} factor_{grow,AMPA} \cdot r^{TC,PY}_{AMPA,prev} + constant_{grow,AMPA} & C > 0 \\ factor_{decay,AMPA} \cdot r^{TC,PY}_{AMPA,prev} & C \leq 0 \end{cases} \quad \text{(B.90)}$$

- **Integration of the membrane voltage of PY:**
  First, we calculate the somatic membrane voltage:

$$\begin{aligned} \frac{g}{S_{soma}}(V_S - V_D) &= -I^{int}_S \\ \frac{g}{S_{soma}}(V_S - V_D) &= -g_{intPY_S} V_S + I_{leakintPY_S} \\ (\frac{g}{S_{soma}} + g_{intPY_S}) V_S &= \frac{g}{S_{soma}} V_D + I_{leakintPY_S} \\ V_S &= \frac{\frac{g}{S_{soma}}}{\frac{g}{S_{soma}} + g_{intPY_S}} V_D + \frac{I_{leakintPY_S}}{\frac{g}{S_{soma}} + g_{intPY_S}} \end{aligned}$$

Now we update the dendritic membrane voltage:

$$\begin{aligned} C_m \frac{dV_D}{dt} &= -g_L(V_D - E_L) - \frac{g}{S_{dend}}(V_D - V_S) \\ &\quad -g_{intPY_D} V_D + I_{leakintPY_D} - \frac{1}{S_{PYdend}} \cdot g_{synPY} V_D + \frac{1}{S_{PYdend}} \cdot I_{leaksynPY} \\ &= -g_L(V_D - E_L) - \frac{g}{S_{dend}}(V_D - (\frac{\frac{g}{S_{soma}}}{\frac{g}{S_{soma}} + g_{intPY_S}} V_D + \frac{I_{leakintPY_S}}{\frac{g}{S_{soma}} + g_{intPY_S}})) \\ &\quad -g_{intPY_D} V_D + I_{leakintPY_D} - \frac{1}{S_{PYdend}} \cdot g_{synPY} V_D + \frac{1}{S_{PYdend}} \cdot I_{leaksynPY} \\ &= -g_L(V_D - E_L) - \frac{g}{S_{dend}}((1 - \frac{\frac{g}{S_{soma}}}{\frac{g}{S_{soma}} + g_{intPY_S}}) V_D - \frac{I_{leakintPY_S}}{\frac{g}{S_{soma}} + g_{intPY_S}}) \\ &\quad -g_{intPY_D} V_D + I_{leakintPY_D} - \frac{1}{S_{PYdend}} \cdot g_{synPY} V_D + \frac{1}{S_{PYdend}} \cdot I_{leaksynPY} \\ &= -g_L(V_D - E_L) - \frac{g}{S_{dend}}(\frac{g_{intPY_S}}{\frac{g}{S_{soma}} + g_{intPY_S}} \cdot V_D - \frac{I_{leakintPY_S}}{\frac{g}{S_{soma}} + g_{intPY_S}}) \\ &\quad -g_{intPY_D} V_D + I_{leakintPY_D} - \frac{1}{S_{PYdend}} \cdot g_{synPY} V_D + \frac{1}{S_{PYdend}} \cdot I_{leaksynPY} \\ &= -(g_L + \frac{g}{S_{dend}} \cdot \frac{g_{intPY_S}}{\frac{g}{S_{soma}} + g_{intPY_S}} + g_{intPY_D} + \frac{1}{S_{PYdend}} \cdot g_{synPY}) V_D \\ &\quad +(g_L E_L + \frac{g}{S_{dend}} \cdot \frac{I_{leakintPY_S}}{\frac{g}{S_{soma}} + g_{intPY_S}} + I_{leakintPY_D} + \frac{1}{S_{PYdend}} \cdot I_{leaksynPY}) \\ &= -g_{totPY_D} V_D + I_{leaktotPY_D} \\ \frac{dV}{dt} &= -\frac{g_{totPY_D}}{C_m}(V_D - \frac{I_{leaktotPY_D}}{g_{totPY_D}}) \end{aligned} \quad \text{(B.91)}$$

$$\begin{aligned} factor_V &= e^{-\frac{g_{totPY}}{C_m}\cdot dt} \\ constant_V &= \frac{I_{leaktotPY}}{g_{totPY}} \cdot (1 - e^{-\frac{g_{totPY}}{C_m}\cdot dt}) \end{aligned}$$

$$V_D = factor_V \cdot V_D prev + constant_V \tag{B.92}$$

Finally, we update the somatic membrane potential:

$$V_S = \frac{\frac{g}{S_{soma}}}{\frac{g}{S_{soma}} + g_{intPY_S}} V_D + \frac{I_{leakintPY_S}}{\frac{g}{S_{soma}} + g_{intPY_S}} \tag{B.93}$$

B.2.2 Interneurons (IN)

- **Hodgkin-Huxley kinetics of intrinsic currents of IN soma:**

$$\begin{aligned} -I^{int}_{IN_S} &= -g_{Nas}(V_S - E_{Nas}) - g_K(V_S - E_K)) \\ &= -(g_{Nas} + g_K + g_{Naps})V_S \\ &\quad +(g_{Nas}E_{Nas} + g_K E_K) \\ &= -g_{intIN_S}V + I_{leakintIN_S} \end{aligned} \tag{B.94}$$

- **Fast sodium (Nas) channel:**
  Reversal potential:

$$E_{Nas} = 50(mV)$$

  Conductance:

$$gNas = tadj \cdot \bar{g}Nas \cdot mNas^3 \cdot hNas$$

  Maximum conductance:

$$\bar{g}Nas = 2500(mS/cm^2)$$

  Temperature adjustment:

$$tadj = 2.3^{\frac{T-23}{10}}$$

  Shift:

$$shift = -10(mV)$$

  Activation parameters mNas:

$$\begin{aligned} \alpha_{mNas} &= \frac{0.182 \cdot (V + shift + 35.001)}{1 - e^{-(V+shift+35.001)/9}} \\ \beta_{mNas} &= \frac{0.124 \cdot (-(V + shift + 35.001))}{1 - e^{(V+shift+35.001)/9}} \end{aligned}$$

$$\begin{aligned} mNas_\infty &= \frac{\alpha_{mNas}}{\alpha_{mNas} + \beta_{mNas}} \\ \tau_{mNas} &= \frac{1}{\alpha_{mNas} + \beta_{mNas}} \cdot \frac{1}{tadj} \end{aligned}$$

Activation dynamics:

$$\frac{dmNas}{dt} = -\frac{1}{\tau_{mNas}}(mNas - mNas_{\infty}) \tag{B.95}$$

Integration of activation parameter mNas:

$$\begin{aligned} factor_{mNas} &= e^{-dt/\tau_{mNas}} \\ constant_{mNas} &= mNas_{\infty} \cdot (1 - e^{-dt/\tau_{mNas}}) \\ mNas &= factor_{mNas} \cdot mNas_{prev} + constant_{mNas} \end{aligned} \tag{B.96}$$

Inactivation parameters hNas:

$$\begin{aligned} \alpha_{hNad} &= \frac{0.024 \cdot (V + shift + 50.001)}{1 - e^{-(V+shift+50.001)/5}} \\ \beta_{hNas} &= \frac{0.0091 \cdot (-(V + shift + 75.001))}{1 - e^{(V+shift+75.001)/5}} \end{aligned}$$

$$\begin{aligned} hNas_{\infty} &= \frac{1}{1 + e^{(V+shift+65)/6.2}} \\ \tau_{hNas} &= \frac{1}{\alpha_{hNas} + \beta_{hNas}} \cdot \frac{1}{tadj} \end{aligned}$$

Inactivation dynamics:

$$\frac{dhNas}{dt} = -\frac{1}{\tau_{hNas}}(hNas - hNas_{\infty}) \tag{B.97}$$

Integration of inactivation parameter hNa:

$$\begin{aligned} factor_{hNas} &= e^{-dt/\tau_{hNas}} \\ constant_{hNas} &= hNas_{\infty} \cdot (1 - e^{-dt/\tau_{hNas}}) \\ hNas &= factor_{hNas} \cdot hNas_{prev} + constant_{hNas} \end{aligned} \tag{B.98}$$

- **Fast potassium (K) channel:**
  Reversal potential:

$$E_K = -90(mV)$$

Conductance:

$$gK = tadj \cdot \bar{g}K \cdot mK$$

Maximum conductance:

$$\bar{g}K = 200(mS/cm^2)$$

Temperature adjustment:

$$tadj = 2.3^{(\frac{T-23}{10})}$$

Activation parameter mK:

$$\begin{aligned} \alpha_{mK} &= \frac{0.02 \cdot (V - 25.001)}{1 - e^{-(V-25.001)/9}} \\ \beta_{mK} &= \frac{-0.002 \cdot (V - 25.001)}{1 - e^{(V-25.001)/9}} \end{aligned}$$

$$\begin{aligned} mK_\infty &= \frac{\alpha_{mK}}{\alpha_{mK} + \beta_{mK}} \\ \tau_{mK} &= \frac{1}{\alpha_{mK} + \beta_{mK}} \cdot \frac{1}{tadj} \end{aligned}$$

Activation dynamics:

$$\frac{dmK}{dt} = -\frac{1}{\tau_{mK}}(mK - mK_\infty) \tag{B.99}$$

Integration of activation parameter mK:

$$\begin{aligned} factor_{mK} &= e^{-dt/\tau_{mK}} \\ constant_{mK} &= mK_\infty \cdot (1 - e^{-dt/\tau_{mK}}) \\ mK &= factor_{mK} \cdot mK_{prev} + constant_{mK} \end{aligned} \tag{B.100}$$

- **Hodgkin-Huxley kinetics of intrinsic currents of IN dendrite:**

$$\begin{aligned} -I^{int}_{IN_D} &= -g_{Nad}(V_D - E_{Nad}) - g_{HVA}(V_D - E_{HVA}) - g_{KCa}(V_D - E_{KCa}) \\ &\quad -g_{Km}(V_D - E_{Km}) - g_{KL}(V_D - E_{KL}) \\ &= -(g_{Nad} + g_{HVA} + g_{KCa} + g_{Km} + g_{KL})V \\ &\quad +(g_{Nad}E_{Nad} + g_{HVA}E_{HVA} + g_{KCa}E_{KCa} + g_{Km}E_{Km} + g_{KL}E_{KL}) \\ &= -g_{intIN_D}V + I_{leakintIN_D} \end{aligned} \tag{B.101}$$

- **High-threshold Ca^{2+} (HVA) channel:**
  Reversal potential:

$$E_{HVA} = 140(mV)$$

Conductance:

$$gHVA = tadj \cdot \bar{g}HVA \cdot mHVA^2 \cdot hHVA$$

Maximum conductance:

$$\bar{g}HVA = 0.01(mS/cm^2)$$

Temperature adjustment:

$$tadj = 2.3^{\frac{T-23}{10}}$$

Shift:

$$shift = 0(mV)$$

Activation parameters mHVA:

$$\begin{aligned} \alpha_{mHVA} &= \frac{0.055 \cdot (V + shift + 27.001)}{1 - e^{-(V+shift+27.001)/3.8}} \\ \beta_{mHVA} &= 0.94 \cdot e^{-(V+shift+75)/17} \end{aligned}$$

$$\begin{aligned} mHVA_{\infty} &= \frac{\alpha_{mHVA}}{\alpha_{mHVA} + \beta_{mHVA}} \\ \tau_{mHVA} &= \frac{1}{\alpha_{mHVA} + \beta_{mHVA}} \cdot \frac{1}{tadj} \end{aligned}$$

Activation dynamics:

$$\frac{dmHVA}{dt} = -\frac{1}{\tau_{mHVA}}(mHVA - mHVA_{\infty}) \tag{B.102}$$

Integration of activation parameter mHVA:

$$\begin{aligned} factor_{mHVA} &= e^{-dt/\tau_{mHVA}} \\ constant_{mHVA} &= mHVA_{\infty} \cdot (1 - e^{-dt/\tau_{mHVA}}) \\ mHVA &= factor_{mHVA} \cdot mHVA_{prev} + constant_{mHVA} \end{aligned} \tag{B.103}$$

Inactivation parameters hHVA:

$$\begin{aligned} \alpha_{hHVA} &= 0.000457 \cdot e^{-(V+shift+13)/50} \\ \beta_{hHVA} &= \frac{0.0065}{1 + e^{-(V+shift+15)/28}} \end{aligned}$$

$$\begin{aligned} hHVA_{\infty} &= \frac{\alpha_{hHVA}}{\alpha_{hHVA} + \beta_{hHVA}} \\ \tau_{hHVA} &= \frac{1}{\alpha_{hHVA} + \beta_{hHVA}} \cdot \frac{1}{tadj} \end{aligned}$$

Inactivation dynamics:

$$\frac{dhHVA}{dt} = -\frac{1}{\tau_{hHVA}}(hHVA - hHVA_{\infty}) \tag{B.104}$$

Integration of inactivation parameter hHVA:

$$\begin{aligned} factor_{hHVA} &= e^{-dt/\tau_{hHVA}} \\ constant_{hHVA} &= hHVA_{\infty} \cdot (1 - e^{-dt/\tau_{hHVA}}) \\ hHVA &= factor_{hHVA} \cdot hHVA_{prev} + constant_{hHVA} \end{aligned} \tag{B.105}$$

- **Fast sodium (Nad) channel:**
  Reversal potential:

$$E_{Nad} = 50(mV)$$

  Conductance:

$$gNad = tadj \cdot \bar{g}Nad \cdot mNad^3 \cdot hNad$$

Maximum conductance:

$$\bar{g}Nad = 0.8(mS/cm^2)$$

Temperature adjustment:

$$tadj = 2.3^{\frac{T-23}{10}}$$

Shift:

$$shift = -10(mV)$$

Activation parameters mNad:

$$\begin{aligned} \alpha_{mNad} &= \frac{0.182 \cdot (V + shift + 35.001)}{1 - e^{-(V+shift+35.001)/9}} \\ \beta_{mNad} &= \frac{0.124 \cdot (-(V + shift + 35.001))}{1 - e^{(V+shift+35.001)/9}} \end{aligned}$$

$$\begin{aligned} mNad_\infty &= \frac{\alpha_{mNad}}{\alpha_{mNad} + \beta_{mNad}} \\ \tau_{mNad} &= \frac{1}{\alpha_{mNad} + \beta_{mNad}} \cdot \frac{1}{tadj} \end{aligned}$$

Activation dynamics:

$$\frac{dmNad}{dt} = -\frac{1}{\tau_{mNad}}(mNad - mNad_\infty) \tag{B.106}$$

Integration of activation parameter mNad:

$$\begin{aligned} factor_{mNad} &= e^{-dt/\tau_{mNad}} \\ constant_{mNad} &= mNad_\infty \cdot (1 - e^{-dt/\tau_{mNad}}) \\ mNad &= factor_{mNad} \cdot mNad_{prev} + constant_{mNad} \end{aligned} \tag{B.107}$$

Inactivation parameters hNad:

$$\begin{aligned} \alpha_{hNad} &= \frac{0.024 \cdot (V + shift + 50.001)}{1 - e^{-(V+shift+50.001)/5}} \\ \beta_{hNad} &= \frac{0.0091 \cdot (-(V + shift + 75.001))}{1 - e^{(V+shift+75.001)/5}} \end{aligned}$$

$$\begin{aligned} hNad_\infty &= \frac{1}{1 + e^{(V+shift+65)/6.2}} \\ \tau_{hNad} &= \frac{1}{\alpha_{hNad} + \beta_{hNad}} \cdot \frac{1}{tadj} \end{aligned}$$

Inactivation dynamics:

$$\frac{dhNad}{dt} = -\frac{1}{\tau_{hNad}}(hNad - hNad_\infty) \tag{B.108}$$

Integration of inactivation parameter hNa:

$$\begin{aligned} factor_{hNad} &= e^{-dt/\tau_{hNad}} \\ constant_{hNad} &= hNad_\infty \cdot (1 - e^{-dt/\tau_{hNad}}) \\ hNad &= factor_{hNad} \cdot hNad_{prev} + constant_{hNad} \end{aligned} \tag{B.109}$$

- **Potassium M-current (Km) channel**
  Reversal potential:

$$E_{Km} = -90(mV)$$

  Conductance:

$$gKm = tadj \cdot \bar{g}Km \cdot mKm$$

  Maximum conductance:

$$\bar{g}Km = 0.01(mS/cm^2)$$

  Temperature adjustment:

$$tadj = 2.3^{\frac{T-23}{10}}$$

  Activation parameter mKm:

$$\begin{aligned} \alpha_{mKm} &= \frac{0.001 \cdot (V + 30.001)}{1 - e^{-(V+30.001)/9}} \\ \beta_{mKm} &= \frac{-0.001 \cdot (V + 30.001)}{1 - e^{(V+30.001)/9}} \end{aligned}$$

$$\begin{aligned} mKm_{\infty} &= \frac{\alpha_{mKm}}{\alpha_{mKm} + \beta_{mKm}} \\ \tau_{mKm} &= \frac{1}{\alpha_{mKm} + \beta_{mKm}} \cdot \frac{1}{tadj} \end{aligned}$$

  Activation dynamics:

$$\frac{dmKm}{dt} = -\frac{1}{\tau_{mKm}}(mKm - mKm_{\infty}) \tag{B.110}$$

  Integration of activation parameter mKm:

$$\begin{aligned} factor_{mKm} &= e^{-dt/\tau_{mKm}} \\ constant_{mKm} &= mKm_{\infty} \cdot (1 - e^{-dt/\tau_{mKm}}) \\ mKm &= factor_{mKm} \cdot mKm_{prev} + constant_{mKm} \end{aligned} \tag{B.111}$$

- **Ca^{2+}-dependent K^+ (K[Ca]) channel:**
  Reversal potential:

$$E_{KCa} = -90(mV)$$

  Conductance:

$$gKCa = tadj \cdot \bar{g}KCa \cdot mKCa$$

  Maximum conductance:

$$\bar{g}KCa = 0.3(mS/cm^2)$$

  Temperature adjustment:

$$tadj = 2.3^{\frac{T-23}{10}}$$

Activation parameter mKCa:

$$\begin{aligned} \alpha_{mKCa} &= 0.01 \cdot [Cai]_i \\ \beta_{mKCa} &= 0.02 \end{aligned}$$

$$\begin{aligned} mKCa_\infty &= \frac{\alpha_{mKCa}}{\alpha_{mKCa} + \beta_{mKCa}} \\ \tau_{mKCa} &= \frac{1}{\alpha_{mKCa} + \beta_{mKCa}} \cdot \frac{1}{tadj} \end{aligned}$$

Activation dynamics:

$$\frac{dmKCa}{dt} = -\frac{1}{\tau_{mKCa}}(mKCa - mKCa_\infty) \tag{B.112}$$

Integration of activation parameter mKCa:

$$\begin{aligned} factor_{mKCa} &= e^{-dt/\tau_{mKCa}} \\ constant_{mKCa} &= mKCa_\infty \cdot (1 - e^{-dt/\tau_{mKCa}}) \\ mKCa &= factor_{mKCa} \cdot mKCa_{prev} + constant_{mKCa} \end{aligned} \tag{B.113}$$

- **Kinetic of intracellular calcium dynamics ($[Ca]_i$):**
  Faraday constant:

$$F = 96489(Cmol^{-1})$$

  Depth of the shell beneath the membrane:

$$d = 1(\mu m)$$

  Unit conversion constant:

$$k = 10$$

  Influx of Ca^{2+} is governed by:

$$[\dot{Ca}]_{i,in} = \begin{cases} -\frac{k}{2Fd} I_T & if > 0 \\ 0 & if \leq 0 \end{cases}$$

  Time constant of calcium efflux:

$$\tau_{Ca} = 165(ms)$$

  Intracellular concentration at rest:

$$[Ca]_\infty = 2.4 \times 10^{-4}(mM)$$

  Efflux of calcium can be modeled by a first-order decay term:

$$[\dot{Ca}]_{i,ef} = -\frac{1}{\tau_{Ca}}([Ca]_i - [Ca]_\infty)$$

  Calcium concentration dynamics:

$$\begin{aligned} \frac{d[Ca]_i}{dt} &= [\dot{Ca}]_{i,in} + [\dot{Ca}]_{i,ef} \\ &= [\dot{Ca}]_{i,in} - \frac{1}{\tau_{Ca}}([Ca]_i - [Ca]_\infty) \\ &= -\frac{1}{\tau_{Ca}}([Ca]_i - ([Ca]_\infty + \tau_{Ca} \cdot [Ca]_{i,in})) \end{aligned} \tag{B.114}$$

Integration of calcium dynamics $[\mathrm{Ca}]_i$:

$$\begin{aligned} factor_{[Ca]_i} &= e^{-dt/\tau_{Ca}} \\ [Ca]_i &= factor_{[Ca]_i} \cdot [Ca]_{i,prev} + (1 - factor_{[Ca]_i}) \cdot ([Ca]_\infty + \tau_{Ca} \cdot [Ca]_{i,in}) \end{aligned} \tag{B.115}$$

Minimum of $[\mathrm{Ca}]_i$:

$$minCa = 1e - 6$$

Update $[\mathrm{Ca}]_i$ according to minimum (Avoid negative values):

$$[Ca]_i = max(minCa, [Ca]_i)$$

- **Potassium leak (Kl) current:**
  Reversal potential:

$$E_{Kl} = -90(mV)$$

  Conductance:

$$gKl = 0(mS/cm^2)$$

- **Hodgkin-Huxley kinetics of synaptic currents of IN:**

$$\begin{aligned} -I_{IN}^{syn} &= (-\bar{g}_{AMPAd}^{PY,IN} \cdot r_{AMPAd}^{PY,IN} \cdot (1 - D_{AMPAd}^{PY,IN}) \cdot (V - E_{AMPAd}^{PY,IN}) \\ &\quad -\bar{g}_{NMDAd}^{PY,IN} \cdot r_{NMDAd}^{PY,IN} \cdot fn \cdot (1 - D_{NMDAd}^{PY,IN}) \cdot (V - E_{NMDAd}^{PY,IN}) \\ &\quad -\bar{g}_{AMPA}^{TC,IN} \cdot r_{AMPA}^{TC,IN} \cdot (V - E_{AMPA}^{TC,IN})) \cdot \frac{1}{S_{INdend}} \\ &= -\frac{1}{S_{IN}} \cdot (\bar{g}_{AMPAd}^{PY,IN} \cdot r_{AMPAd}^{PY,IN} \cdot (1 - D_{AMPAd}^{PY,IN}) \\ &\quad +\bar{g}_{NMDAd}^{PY,IN} \cdot r_{NMDAd}^{PY,IN} \cdot fn \cdot (1 - D_{NMDAd}^{PY,IN}) \\ &\quad +\bar{g}_{AMPA}^{TC,IN} \cdot r_{AMPA}^{TC,IN})V \\ &\quad +\frac{1}{S_{IN}} \cdot (\bar{g}_{AMPAd}^{PY,IN} \cdot r_{AMPAd}^{PY,IN} \cdot (1 - D_{AMPAd}^{PY,IN}) \cdot E_{AMPAd}^{PY,IN} \\ &\quad +\bar{g}_{NMDAd}^{PY,IN} \cdot r_{NMDAd}^{PY,IN} \cdot fn \cdot (1 - D_{NMDAd}^{PY,IN}) \cdot E_{NMDAd}^{PY,IN} \\ &\quad +\bar{g}_{AMPA}^{TC,IN} \cdot r_{AMPA}^{TC,IN} \cdot E_{AMPA}^{TC,IN}) \end{aligned} \tag{B.116}$$

$$= -\frac{1}{S_{IN}} \cdot g_{synIN} V + \frac{1}{S_{IN}} \cdot I_{leaksynIN} \tag{B.117}$$

- **AMPA receptors with depression and MINI (PY → IN):**
  Maximum conductance and Reversal potential:

$$\bar{g}_{AMPAd}^{PY,IN} = 0.0000375(mS/cm^2)\ ,\ E_{AMPAd}^{PY,IN} = 0(mV)$$

  Maximal concentration of the transmitter during the pulse:

$$\begin{aligned} C_{max} &= 0.5(mM) \\ C_{max,mini} &= 0.4 \cdot C_{max} = 0.2(mM) \end{aligned}$$

  Release duration:

$$C_{dur} = 0.3(mS)$$

  Voltage-independent forward and backward rate constants:

$$\alpha_{AMPAd} = 0.94(/mS \cdot mM)$$
$$\beta_{AMPAd} = 0.18(/mS)$$

Pre-synaptic spike detection threshold:

$$prethresh = 0(mV)$$

Deadtime when spike can not occur:

$$deadtime = 1(mS)$$

Synaptic depression parameters:

$$U_{AMPAd} = 0.073$$
$$\alpha_D = \frac{1}{700}$$

Parameters of fraction of receptors in the open state:

$$\begin{aligned} r_{\infty,AMPAd} &= \frac{C_{max} \cdot \alpha_{AMPAd}}{C_{max} \cdot \alpha_{AMPAd} + \beta_{AMPAd}} \\ \tau_{r,AMPAd} &= \frac{1}{C_{max} \cdot \alpha_{AMPAd} + \beta_{AMPAd}} \\ r_{\infty,AMPAd,mini} &= \frac{C_{max,mini} \cdot \alpha_{AMPAd}}{C_{max,mini} \cdot \alpha_{AMPAd} + \beta_{AMPAd}} \\ \tau_{r,AMPAd,mini} &= \frac{1}{C_{max,mini} \cdot \alpha_{AMPAd} + \beta_{AMPAd}} \end{aligned}$$

Conditions and procedures:
▷ Release is possible:
◇ if ((time)−(lastrelease)−C_{dur} > deadtime)
◇ Release occur:
◇ if (the presynaptic neuron's voltage > prethresh)
◇ → $C = C_{max}$ → lastrelease=time → lastspike=time
◇ → $D = D \cdot e^{-\alpha_D \cdot dt} + (1 - D \cdot e^{-\alpha_D \cdot dt}) \cdot U_{AMPAd}$
◇ Release doesn't occur but MINI is possible:
◇ if ((time)−(lastspike)> 70)
◇ → $SS = log(\frac{(time)-(lastspike)+50}{50}) \cdot \frac{1}{400}$ → $S = max(0.000001, rand())$
◇ → newrelease = -$\frac{log(S)}{SS}$
◇ MINI occur:
◇ if ((time)−(lastrelease) > (newrelease))
◇ → $C = C_{max,mini}$ → lastrelease=time → $D = D \cdot e^{-\alpha_D \cdot dt}$
◇ Neither release nor MINI occur:
◇ → $D = D \cdot e^{-\alpha_D \cdot dt}$
▷ Release is not possible:
◇ → $D = D \cdot e^{-\alpha_D \cdot dt}$
◇ We should close the release
◇ if ((time)−(lastrelease)−$C_{dur} \geq 0$) && (C=C_{max})
◇ → $C = 0$
◇ Else: → do nothing
♣ $C = C_{max}$ → Release is happening
♣ $C = C_{max,mini}$ → MINI is happening
♣ $C = 0$ → Release and MINI are absent

Dynamics:

$$\begin{aligned}\frac{dr^{PY,IN}_{AMPAd}}{dt} &= \alpha \cdot [T] \cdot (1 - r^{PY,IN}_{AMPAd}) - \beta \cdot r^{PY,IN}_{AMPAd} \\ &= -(C \cdot \alpha_{AMPAd} + \beta_{AMPAd})(r^{PY,IN}_{AMPAd} - \frac{C \cdot \alpha_{AMPAd}}{C_{max} \cdot \alpha_{AMPAd} + \beta_{AMPAd}})\end{aligned} \tag{B.118}$$

Integration of parameter r with respect to release:

$$\begin{aligned} factor_{grow,AMPAd} &= e^{-\frac{dt}{\tau_{r,AMPAd}}} \\ constant_{grow,AMPAd} &= r_{\infty,AMPAd} \cdot (1 - e^{-\frac{dt}{\tau_{r,AMPAd}}}) \\ factor_{grow,AMPAd,mini} &= e^{-\frac{dt}{\tau_{r,AMPAd,mini}}} \\ constant_{grow,AMPAd,mini} &= r_{\infty,AMPAd,mini} \cdot (1 - e^{-\frac{dt}{\tau_{r,AMPAd,mini}}}) \\ factor_{decay,AMPAd} &= e^{-\beta_{AMPAd} \cdot dt} \end{aligned}$$

$$r^{PY,IN}_{AMPAd} = \begin{cases} factor_{grow,AMPAd} \cdot r^{PY,IN}_{AMPAd,prev} & \\ \qquad + constant_{grow,AMPAd} & C = C_{max} \\ factor_{grow,AMPAd,mini} \cdot r^{PY,IN}_{AMPAd,prev} & \\ \qquad + constant_{grow,AMPAd,mini} & C = C_{max,mini} \\ factor_{decay,AMPAd} \cdot r^{PY,IN}_{AMPAd,prev} & C \leq 0 \end{cases} \tag{B.119}$$

- **NMDA receptors with depression (PY → IN):**
  Maximum conductance and Reversal potential:

$$\bar{g}^{PY,IN}_{NMDAd} = 0.000006(mS/cm^2) \ , \ E^{PY,IN}_{NMDAd} = 0(mV)$$

  Magnesium block:

$$fn = \frac{1}{1 + e^{-\frac{V+25}{12.5}}}$$

  Maximal concentration of the transmitter during the pulse:

$$C_{max} = 0.5(mM)$$

  Release duration:

$$C_{dur} = 0.3(mS)$$

  Voltage-independent forward and backward rate constants:

$$\begin{aligned} \alpha_{NMDAd} &= 1(/mS \cdot mM) \\ \beta_{NMDAd} &= 0.0067(/mS) \end{aligned}$$

  Pre-synaptic spike detection threshold:

$$prethresh = 0(mV)$$

  Deadtime when spike can not occur:

$$deadtime = 1(mS)$$

  Synaptic depression parameters:

$$U_{NMDAd} = 0$$
$$\alpha_D = \frac{1}{700}$$

Parameters of fraction of receptors in the open state:

$$\begin{aligned} r_{\infty,NMDAd} &= \frac{C_{max} \cdot \alpha_{NMDAd}}{C_{max} \cdot \alpha_{NMDAd} + \beta_{NMDAd}} \\ \tau_{r,NMDAd} &= \frac{1}{C_{max} \cdot \alpha_{NMDAd} + \beta_{NMDAd}} \end{aligned}$$

Conditions and procedures:
▷ Release is possible:
◇ if ((time)−(lastrelease)−C_{dur} > deadtime)
◇ Release occur:
◇ if (the presynaptic neuron's voltage > prethresh)
◇ → $C = C_{max}$ → lastrelease=time
◇ → $D = D \cdot e^{-\alpha_D \cdot dt} + (1 - D \cdot e^{-\alpha_D \cdot dt}) \cdot U_{NMDAd}$
◇ Release doesn't occur:
◇ → $D = D \cdot e^{-\alpha_D \cdot dt}$
▷ Release is not possible:
◇ → $D = D \cdot e^{-\alpha_D \cdot dt}$
◇ We should close the release
◇ if ((time)−(lastrelease)−$C_{dur} \geq 0$) && (C=C_{max})
◇ → $C = 0$
◇ Else: → do nothing
♣ $C > 0$ → Release is hapenning
♣ $C = 0$ → Release is absent

Dynamics:

$$\begin{aligned} \frac{dr^{PY,IN}_{NMDAd}}{dt} &= \alpha \cdot [T] \cdot (1 - r^{PY,IN}_{NMDAd}) - \beta \cdot r^{PY,IN}_{NMDAd} \\ &= -(C \cdot \alpha_{NMDAd} + \beta_{NMDAd})(r^{PY,IN}_{NMDAd} - \frac{C \cdot \alpha_{NMDAd}}{C_{max} \cdot \alpha_{NMDAd} + \beta_{NMDAd}}) \end{aligned} \tag{B.120}$$

Integration of parameter r with respect to release:

$$\begin{aligned} factor_{grow,NMDAd} &= e^{-\frac{dt}{\tau_{r,NMDAd}}} \\ constant_{grow,NMDAd} &= r_{\infty,NMDAd} \cdot (1 - e^{-\frac{dt}{\tau_{r,NMDAd}}}) \\ factor_{decay,NMDAd} &= e^{-\beta_{NMDAd} \cdot dt} \end{aligned}$$

$$r^{PY,IN}_{NMDAd} = \begin{cases} factor_{grow,NMDAd} \cdot r^{PY,IN}_{NMDAd,prev} & \\ \qquad + constant_{grow,NMDAd} & C > 0 \\ factor_{decay,NMDAd} \cdot r^{PY,IN}_{NMDAd,prev} & C \leq 0 \end{cases} \tag{B.121}$$

- **AMPA receptors (TC → IN):**
Maximum conductance and Reversal potential:

$$\bar{g}^{TC,IN}_{AMPA} = 0.000075(mS/cm^2)\ ,\ E^{TC,PY}_{AMPA} = 0(mV)$$

Maximal concentration of the transmitter during the pulse:

$$C_{max} = 0.5(mM)$$

Release duration:

$$C_{dur} = 0.3(mS)$$

Voltage-independent forward and backward rate constants:

$$\alpha_{AMPA} = 0.94(/mS \cdot mM)$$
$$\beta_{AMPA} = 0.18(/mS)$$

Pre-synaptic spike detection threshold:

$$prethresh = 0(mV)$$

Deadtime when spike can not occur:

$$deadtime = 1(mS)$$

Parameters of fraction of receptors in the open state:

$$\begin{aligned} r_{\infty,AMPA} &= \frac{C_{max} \cdot \alpha_{AMPA}}{C_{max} \cdot \alpha_{AMPA} + \beta_{AMPA}} \\ \tau_{r,AMPA} &= \frac{1}{C_{max} \cdot \alpha_{AMPA} + \beta_{AMPA}} \end{aligned}$$

Conditions and procedures:

▷ Release is possible:
◇ if ((time)−(lastrelease)$-C_{dur}$ > deadtime)
◇ Release occur:
◇ if (the presynaptic neuron's voltage > prethresh)
◇ → $C = C_{max}$ → lastrelease=time
◇ Release doesn't occur: → do nothing
▷ Release is not possible:
◇ We should close the release
◇ if ((time)−(lastrelease)$-C_{dur} \geq 0$) && (C=C_{max})
◇ → $C = 0$
◇ Else: → do nothing
♣ $C > 0$ → Release is hapenning
♣ $C = 0$ → Release is absent

Dynamics:

$$\begin{aligned} \frac{dr^{TC,IN}_{AMPA}}{dt} &= \alpha \cdot [T] \cdot (1 - r^{TC,IN}_{AMPA}) - \beta \cdot r^{TC,IN}_{AMPA} \\ &= -(C \cdot \alpha_{AMPA} + \beta_{AMPA})(r^{TC,IN}_{AMPA} - \frac{C \cdot \alpha_{AMPA}}{C_{max} \cdot \alpha_{AMPA} + \beta_{AMPA}}) \end{aligned} \tag{B.122}$$

Integration of parameter r with respect to release:

$$\begin{aligned} factor_{grow,AMPA} &= e^{-\frac{dt}{\tau_{r,AMPA}}} \\ constant_{grow,AMPA} &= r_{\infty,AMPA} \cdot (1 - e^{-\frac{dt}{\tau_{r,AMPA}}}) \\ factor_{decay,AMPA} &= e^{-\beta_{AMPA} \cdot dt} \end{aligned}$$

$$r^{TC,IN}_{AMPA} = \begin{cases} factor_{grow,AMPA} \cdot r^{TC,IN}_{AMPA,prev} + constant_{grow,AMPA} & C > 0 \\ factor_{decay,AMPA} \cdot r^{TC,IN}_{AMPA,prev} & C \leq 0 \end{cases} \tag{B.123}$$

- **Integration of the membrane voltage of IN:**
  First, we calculate the somatic membrane voltage:

$$\begin{aligned}
\frac{g}{S_{soma}}(V_S - V_D) &= -I_S^{int} \\
\frac{g}{S_{soma}}(V_S - V_D) &= -g_{intIN_S}V_S + I_{leakintIN_S} \\
(\frac{g}{S_{soma}} + g_{intIN_S})V_S &= \frac{g}{S_{soma}}V_D + I_{leakintIN_S} \\
V_S &= \frac{\frac{g}{S_{soma}}}{\frac{g}{S_{soma}} + g_{intIN_S}}V_D + \frac{I_{leakintIN_S}}{\frac{g}{S_{soma}} + g_{intIN_S}}
\end{aligned}$$

  Now we update the dendritic membrane voltage:

$$\begin{aligned}
C_m\frac{dV_D}{dt} &= -g_L(V_D - E_L) - \frac{g}{S_{dend}}(V_D - V_S) \\
&\quad -g_{intIN_D}V_D + I_{leakintIN_D} - \frac{1}{S_{INdend}} \cdot g_{synIN}V_D + \frac{1}{S_{INdend}} \cdot I_{leaksynIN} \\
&= -g_L(V_D - E_L) - \frac{g}{S_{dend}}(V_D - (\frac{\frac{g}{S_{soma}}}{\frac{g}{S_{soma}} + g_{intIN_S}}V_D + \frac{I_{leakintIN_S}}{\frac{g}{S_{soma}} + g_{intIN_S}})) \\
&\quad -g_{intIN_D}V_D + I_{leakintIN_D} - \frac{1}{S_{INdend}} \cdot g_{synIN}V_D + \frac{1}{S_{INdend}} \cdot I_{leaksynIN} \\
&= -g_L(V_D - E_L) - \frac{g}{S_{dend}}((1 - \frac{\frac{g}{S_{soma}}}{\frac{g}{S_{soma}} + g_{intIN_S}})V_D - \frac{I_{leakintIN_S}}{\frac{g}{S_{soma}} + g_{intIN_S}}) \\
&\quad -g_{intIN_D}V_D + I_{leakintIN_D} - \frac{1}{S_{INdend}} \cdot g_{synIN}V_D + \frac{1}{S_{INdend}} \cdot I_{leaksynIN} \\
&= -g_L(V_D - E_L) - \frac{g}{S_{dend}}(\frac{g_{intIN_S}}{\frac{g}{S_{soma}} + g_{intIN_S}} \cdot V_D - \frac{I_{leakintIN_S}}{\frac{g}{S_{soma}} + g_{intIN_S}}) \\
&\quad -g_{intIN_D}V_D + I_{leakintIN_D} - \frac{1}{S_{INdend}} \cdot g_{synIN}V_D + \frac{1}{S_{INdend}} \cdot I_{leaksynIN} \\
&= -(g_L + \frac{g}{S_{dend}} \cdot \frac{g_{intIN_S}}{\frac{g}{S_{soma}} + g_{intIN_S}} + g_{intIN_D} + \frac{1}{S_{INdend}} \cdot g_{synIN})V_D \\
&\quad +(g_L E_L + \frac{g}{S_{dend}} \cdot \frac{I_{leakintIN_S}}{\frac{g}{S_{soma}} + g_{intIN_S}} + I_{leakintIN_D} + \frac{1}{S_{INdend}} \cdot I_{leaksynIN}) \\
&= -g_{totIN_D}V_D + I_{leaktotIN_D} \\
\frac{dV}{dt} &= -\frac{g_{totIN_D}}{C_m}(V_D - \frac{I_{leaktotIN_D}}{g_{totIN_D}}) \qquad \text{(B.124)} \\
factor_V &= e^{-\frac{g_{totIN}}{C_m} \cdot dt} \\
constant_V &= \frac{I_{leaktotIN}}{g_{totIN}} \cdot (1 - e^{-\frac{g_{totIN}}{C_m} \cdot dt})
\end{aligned}$$

$$V_D = factor_V \cdot V_D prev + constant_V \qquad \text{(B.125)}$$

  Finally, we update the somatic membrane potential:

$$V_S = \frac{\frac{g}{S_{soma}}}{\frac{g}{S_{soma}} + g_{intIN_S}}V_D + \frac{I_{leakintIN_S}}{\frac{g}{S_{soma}} + g_{intIN_S}} \qquad \text{(B.126)}$$

B.3 Initial condition

The initial condition of the membrane potentials of all neurons were set to their leakage reversal potentials with $\pm 5(mV)$ of variability. The initial condition of all the other dynamics, namely channel kinetics, were set to the ∞-subindexed values with 10% of variability.

Bibliography

Manual of bis monitor a-2000, 2005.

Nest project proposal no. 517133, June 2005.

L. F. Abbott and T. J. Sejnowski. *Neural Codes and Distributed Representations: Foundations of Neural Computation.* MIT Press, Cambridge, MA, 1999.

L. F. Abbott, J. A. Varela, K. Sen, and S. B. Nelson. Synaptic depression and cortical gain control. *Science*, 275(5297):221–224, 1997.

J. F. Antognini and E. Carstens. *In vivo characterization of clinical anaesthesia and its components.* Br J Anaesth*, 89(1):156–166, 2002.*

M. Bazhenov, I. Timofeev, M. Steriade, and T. J. Sejnowski. Cellular and network models for intrathalamic augmenting responses during 10 hz stimulation. J. Neurophysiol.*, 79: 2730–48, 1998.*

M. Bazhenov, I. Timofeev, M. Steriade, and T. J. Sejnowski. Model of thalamocortical slow-wave sleep oscillations and transitions to activated states. J. Neurosci.*, 22, 2002.*

M. F. Bear, B. W. Connors, and M. A. Paradiso. Neurosciences : A la découverte du cerveau. *Pradel, 2002.*

G. H. Bishop. The interpretation of cortical potentials. Cold Spring Harbor Symp. Qunt. Biol*, 4:305–19, 1936.*

S. Boccaletti, J. Kurths, G. Osipov, D. L. Valladares, and C. S. Zhou. The synchronization of chaotic systems. Phys. Rep.*, 366:1–101, 2002.*

F. Bremer. L'activité électrique de l'écorce cérébrale. Actualités Scientifiques et Industrielles*, 658:3–46, 1938.*

F. Bremer. Considérations sur l'origine et la nature des 'ondes' cérébrales. Electroencephalogr. Clin. Neurophysiol.*, 1:177–93, 1949.*

F. Bremer. Cerebral and cerebellar potentials. Physiol. Reviews*, 38:357–88, 1958.*

R. Brown and L. Kocarev. A unifying definition of synchronization for dynamical systems. Chaos*, 10:344–349, 2000.*

J. Bruhn, P. S. Myles, R. Sneyd, and M. M. R. F. Struys. Depth of anaesthesia monitoring: what's available, what's validated and what's next? BR J Anaesth, *97(1):85–94, 2006.*

C. Carmeli, O. De Feo, and G. M. Innocenti. Macroscopic manifestations of neural connectivity in EEG signals. In International Conference on Nonlinear Theory and its Applications (NOLTA), *number Tu2-A-2, pages 23–26, 2004.*

C. Carmeli, M. G. Knyazeva, G. M. Innocenti, and O. De Feo. Assessment of EEG synchronization based on state-space analysis. Neuroimage, *25(2):339–354, 2005. doi: 10.1016/j.neuroimage.2004.11.049.*

Cristian Carmeli. Assessing cooperative behavior in dynamical networks with applications to brain data. *PhD thesis, Lausanne, 2006. URL* `http://library.epfl.ch/theses/?nr=3651`.

D. Contreras and M. Steriade. Spindle oscillation in cats: The role of corticothalamic feedback in a thalamically-generated rhythm. J. Physiol., *490:159–79, 1996.*

D. Contreras, I. Timofeev, and M. Steriade. Mechanisms of long-lasting hyperpolarizations underlying slow sleep oscillations in cat corticothalamic networks. J. Physiol., *494:251–64, 1996.*

D. Contreras, A. Destexhe, T. J. Sejnowski, and M. Steriade. Spatiotemporal patterns of spindle oscillations in cortex and thalamus. J. Neurosci., *17:1179–96, 1997a.*

D. Contreras, A. Destexhe, and M. Steriade. Spindle oscillations during cortical spreading depression in naturally sleeping cats. Neurosci., *77:933–6, 1997b.*

O. De Feo. Modeling diversity by strange attractors with application to temporal pattern recognition. *PhD thesis, 2001.*

O. De Feo and C. Carmeli. Identifying dependencies among multivariate time series. In International Conference on Nonlinear Theory and its Applications (NOLTA), *number Tu4-A-4, pages 203–206, 2004.*

A. Destexhe and T. J. Sejnowski. Thalamocortical Assemblies: How ion channels, single neurons, and large-scale networks organize sleep oscillations. *Oxford University Press, 2001.*

A. Destexhe, F. Mainen, and T. J. Sejnowski. Synthesis of model for excitable membranes, synaptic transmission and neuromodulation using a common kinetic formalism. J. Comp. Neurosci., *1:195–230, 1994.*

A. Destexhe, D. Contreras, and M. Steriade. Mechanisms underlying the synchronization action of corticothalamic feedback through inhibition of thalamic relay cells. J. Neurophysiol., *79:999–1016, 1998.*

A. Destexhe, D. Contreras, and M. Steriade. Cortically-induced coherence of a thalamic-generated oscillation. Neurosci., *92:427–43, 1999.*

Mukeshwar Dhamala, Govindan Rangarajan, and Mingzhou Ding. Estimating granger causality from fourier and wavelet transforms of time series data. Phys. Rev. Lett., *100(1):018701, 2008.*

J. C. Eccles. Interpretation of action potentials evoked in the cerebral cortex. Electroencephalography and Clinical Neurophysiology*, 3:449–64, 1951.*

Edmond I II Eger. A brief history of the origin of minimum alveolar concentration (mac). Anesthesiology*, 96(1):238–239, 2002.*

M. Galarreta and S. Hestrin. Frequency-dependent synaptic depression and balance of excitation and inhibition in the neocortex. Nat. Neurosci.*, 1:587–594, 1998.*

Wulfram Gerstner and Werner M. Kistler. Spiking Neuron Models. Single Neurons, Populations, Plasticity*. Cambridge University Press, 2002.*

John Geweke. Measurement of linear dependence and feedback between multiple time series. Journal of the American Statistical Association*, 77(378):304–313, June 1982.*

J.D. Gibbons. Nonparametric Statistical Inference*. Marcel Dekker, 2nd edition, 1985.*

A. Gottschalk and P. Haney. Computational aspects of anesthetic action in simple neual models. Anesthesiology*, 98:548–564, 2003.*

C. W. J. Granger. Investigating causal relations by econometric models and cross/spectral methods. Econometrica*, 37(3):424–438, July 1969.*

Christian Grasshoff and Bernd Antkowiak. Propofol and sevoflurane depress spinal neurons in vitro via different molecular targets. Anesthesiology*, 101:1167–76, 2004.*

Sean Hill and Giulio Tononi. Modeling sleep and wakefulness in the thalamocortical system. J Neurophysiol*, 93:1671–1698, 2005.*

A. L. Hodgkin and A. F. Huxley. A quantitative description of membrane current and its application to conduction and excitation in nerve. J. Physiol.*, 117:500–44, 1952.*

I Joliffe. Principal Component Analysis*. Springer-Verlag, 2002.*

Holger Kantz and Thomas Schreiber. Nonlinear Time Series Analysis*. Cambridge Univ. Press, 2004.*

Matthew B. Kennel, Reggie Brown, and Henry D. I. Abarbanel. Determining embedding dimension for phase-space reconstruction using a geometrical construction. Phys. Rev. A*, 45(6):3403–3411, Mar 1992. doi: 10.1103/PhysRevA.45.3403.*

C. Koch and I. Segev. Methods in Neuronal Modeling From Ions to Networks*. Cambridge Univ. Press, 2nd edition, 1998.*

Z. F. Mainen and T. J. Sejnowski. Influence of dendritic structure on firing pattern in model neocortical neurons. Nature*, 382:363–66, 1996.*

Bojan Musizza, Aneta Stefanovska, Peter V. E. McClintock, Milan Paluš, Petrovičič Janko, Samo Ribarič, and Fajko F. Bajrović. Interactions between cardiac, respiratory and eeg-δ oscillations in rats during anaesthesia. J. Physiol.*, 580(1):315–326, 2007.*

M. Orr. Matlab functions for radial basis function networks, 2001. http://www.anc.ed.ac.uk/ mjo/software/rbf2.zip.

Milan Paluš and Aneta Stefanovska. Direction of coupling from phases of interacting oscillators: An information-theoretic approach. Phys. Rev. E*, 67(5):055201, May 2003. doi: 10.1103/PhysRevE.67.055201.*

Milan Paluš, Vladimír Komárek, Zbyn ěk Hrnčíř, and Katalin Štěrbová. Synchronization as adjustment of information rates: Detection from bivariate time series. Phys. Rev. E*, 63(4):046211, Mar 2001. doi: 10.1103/PhysRevE.63.046211.*

C. J. D. Pomfrett. Monitoring depth of anaesthesia. The Royal College of Anaesthetists*, pages 155–157, November 2000.*

Hegger Rainer, Holger Kantz, and Thomas Schreiber. Practical implementation of nonlinear time series methods: The tisean package. Chaos*, 9(2):413–435, 1999.*

Michael G. Rosenblum and Arkady S. Pikovsky. Detecting direction of coupling in interacting oscillators. Phys. Rev. E*, 64(4):045202, Sep 2001. doi: 10.1103/PhysRevE.64.045202.*

Michael G. Rosenblum, Laura Cimponeriu, Anastasios Bezerianos, Andreas Patzak, and Ralf Mrowka. Identification of coupling direction: Application to cardiorespiratory interaction. Phys. Rev. E*, 65(4):041909, Mar 2002. doi: 10.1103/PhysRevE.65.041909.*

N. F. Rulkov, I. Timofeev, and M. Bazhenov. Oscillations in large-scale cortical networks: Map-based model. J. of Comp. Neurosci.*, 17:203–223, 2004.*

J. Schüttler and H. Schwilden. Modern Anesthetics (Handbook of Experimental Pharmacology)*. Springer, 1st edition, 2008.*

D. Scott and M.D. Kelly. Monitoring level of consciousness during anesthesia & sedation*. A Clinician's Guide to the Bispectral Index.*

Aneta Stefanovska and M Bračič. Physics of the human cardiovascular system. Contemporary Physics*, 40(1):31–55, 1999.*

Aneta Stefanovska, H Haken, P. V. E. McClintock, M Hožic, F Majrović, and S Ribarič. Reversible transitions between synchronization states of the cardiorespiratory system. Phys. Rev. Lett.*, 85(22):4831–4834, 2000.*

M. Steriade, A. Nuñez, and F. Amizica. Intracellular analysis of relations between the slow (<1hz) neocortical oscillation and other sleep rhythms of the electroencephalogram. J. Neurosci*, 13:3266–83, 1993.*

M. Steriade, I. Timofeev, and F. Grenier. Natural waking and sleeping states: a view from inside neocortical neurons. J. Neurophysiol.*, 85:1969–85, 2001.*

C. F. Stevens. Quantal release of neurotransmitter and long-term potentiation. Cell*, 72: 55–63, 1993.*

I. Timofeev and M. Steriade. Low-frequency rhythms in the thalamus of intact-cortex and decorticated cats. J. Neurophysiol.*, 76:4152–68, 1996.*

I. Timofeev, D. Contreras, and M. Steriade. Synaptic responsiveness of cortical and thalamic neurones during various phases of slow sleep oscillation in cat. J. Physiol (Lond), *494:265–78, 1996.*

I. Timofeev, F. Grenier, M. Bazhenov, T. J. Sejnowski, and M. Steriade. Origin of slow cortical oscillations in deafferented cortical slabs. Cereb. Cortex, *10:1185–99, 2000.*

I. Timofeev, F. Grenier, and M. Steriade. Disfacilitation and active inhibition in the neocortex during the natural slep-wake cycle: an intracellular study. Proc. Natl. Acad. Sci. USA, *98:1924–29, 2001.*

M. V. Tsodyks and H. Markram. The neural code between neocortical pyramidal neurons depends on neurotransmitter release probability. Proc. Natl. Acad. Sci. USA, *94:719–23, 1997.*

B. W. Urban and M. Bleckwenn. Concepts and correlations relevant to general anaesthesia. Br J Anaesth, *89(1):3–16, 2002.*

Bernd W. Urban, Markus Bleckwenn, and Martin Barann. Interactions of anesthetics with their targets: Non-specific, specific or both? Pharmacology & Therapeutics, *111:729–770, 2006.*

J. J. Wright, C. J. Rennie, G. J. Lees, P. A. Robinson, P. D. Bourke, C. L. Chapman, E. Gordon, and D. L. Rowe. Simulated electrocortical activity at microscopic, mesoscopic, and global scales. Neuropsychopharmacology, *28:S80–S93, 2003.*

T. L. Yaksh, C. Lynch, W. M. Zapol, M. Maze, J. F. Biebuyck, and L. J. Saidman. Anesthesia: Biologic Foundations. *Lippincott Williams & Wilkins, 1998.*

K u m i k o O s h i m a

Av. du Jura 60
1180 Rolle
kumiko.oshima@epfl.ch

November, 11th 1978
Single
Japanese

EDUCATION

Ph. D. thesis mar.2004 – oct. 2008
- Swiss Federal Institute of Technology Lausanne (EPFL),
  Doctoral program in Computer, Communication and
  Information Sciences (EDIC)
  Laboratory of Nonlinear System (LANOS)
  PhD thesis : Estimation of the Depth of Anaesthesia from Interacting
  Physiological Oscillators

Exchange student apr.2002 - mar.2003
- Swiss Federal Institute of Technology Lausanne (EPFL),
  Laboratory of Nonlinear System (LANOS)

Master of Science apr.2001 - mar.2004
- Sophia University, Japan
  Graduate Division of Science and Technology,
  Master's Program in Electrical and Electronic Engineering
  Master thesis : Coded Modulations Using Chaotic Systems Controlled
  by Small Perturbations

Bachelor of Science in Electrical Engineering apr.1997 - mar.2001
- Sophia University, Japan
  Faculty of Science and Technology,
  Department of Electrical and Electronic Engineering
  Diploma work : Adaptive subband image coding using appropriate tree
  rearrangement

EXPERIENCE

Teaching Assistant, EPFL / Lausanne sept.2004 - july.2007
- Teaching assistant for the courses of Circuits and System.
- First assistant for last 2 years.

Semester project supervisor, EPFL / Lausanne mar.2006 - july.2006
- Take care of 2 students in 3rd year of bachelor.

Teaching Assistant, Tokyo Inst. of tech. / Tokyo apr.2003 - mar. 2004
- Teaching assistant for the courses of programming in JAVA and PASCAL language.

Inspector of the cable modem, Xbeam Network/ Tokyo sept.2000 - feb.2002
- Inspection of the cable model with spectrum analyzer.

Teaching Assistant, Sophia Univ. / Tokyo apr.2001 - july.2001
- Teaching assistant for the course "fundament. Computer tech. 1".

Internship, Nikon corp. / Kanagawa aug.1999 - sept.1999
- Programming the software for the digital camera color control system in C language.

LANGUAGE SKILLS

English	Fluent
French	Fluent Speaking, Medium Writing
Japanese	Mother tongue

AWARDS

Outstanding Student Paper Award (March 2006)
- In International Workshop on Nonlinear Circuits and Signal Processing (NCSP), Hawaii, USA

PUBLICATIONS

Journal Papers:

Kumiko Oshima, Tsuyoshi Otake, and Mamoru Tanaka,
Optimal Bandsplitting Considering Spatial Dependency for Adaptive Subband Image Coding
Journal of Signal Processing Vol. 7 No. 2 March 2003.

Kumiko Oshima, Cristian Carmeli and Martin Hasler,
State Change Detection using Multivariate Synchronization Measure from Physiological Signals
Journal of Signal Processing Vol. 10 No. 4 July 2006.

Conference Papers:

Tsuyoshi Otake, Kumiko Oshima and Mamoru Tanaka,
Wavelet Packet Based Image Coding Considering Spatial Dependency with Rearranged Zerotree Algorithm
proceedings of ECCTD2001, Espoo, Finland, August 2001.

Kumiko Oshima, Tsuyoshi Otake, and Mamoru Tanaka,
Wavelet Packet Based Image Coding with Rearrangement Algorithm
proceedings of NOLTA2001, Miyagi, Japan, October 2001.

T. Schimming, K. Oshima, and M. Hasler,
Coded Modulations Using Chaotic Systems Controlled by Small Perturbations
proceedings of NOLTA2002, Xi'an, China, October 2002.

S. Kozic, K. Oshima, and T. Schimming,
Minimum distance properties of coded modulations based on iterated chaotic maps
proceedings of NDES2003, Scuol, Switzerland, May 2003.

S. Kozic, K. Oshima, and T. Schimming,
How to repair CSK using small perturbation control case study and performance analysis
proceedings of ECCTD2003, Cracow, Poland, September 2003.

Kumiko Oshima, Cristian Carmeli and Martin Hasler,
State Change Detection using Multivariate Synchronization Measure from Physiological Signals
Proceedings of NCSP2006, Honolulu, Hawaii, USA, March 2006.

Kumiko Oshima, Borja Ibarz and Martin Hasler,
Consideration of the effect of anesthesia in the thalamocortical assemblies
Proceedings of NDES2007, Tokushima, Japan, July 2007.

Kumiko Oshima, Yuri Shiogai, Mukeshwar Dhamala and Martin Hasler,
Cardio-respiratory-brain interdependency during anaesthesia
Proceedings of NDES2008, Nizhny Novgorod, Russia, July 2008.

With my cordial compliments,

The End